Serpentine Minichannel Liquid-Cooled Heat Sinks for Electronics Cooling Applications

By

Ahmed Fouad Mahmood Al-Neama

Submitted in accordance with the requirements for the degree of
Doctor of Philosophy

The University of Leeds

School of Mechanical Engineering

Institute of ThermoFluids (iTF)

January 2018

The candidate confirms that the work submitted is his own, except where work formed jointly-authored publication has been included. The contribution of the candidate and the other authors to this work has been explicitly indicated overleaf. The candidate confirms that appropriate credit has been given within the thesis where reference has been made to the work of others.

Work Formed from Jointly Authored Publications

The candidate has publications from work contained in this thesis, and these were submitted with the support of supervisors. The contribution of the candidate to these works is explicitly mentioned below.

1- The work in chapters 4, 5 and 6 of the thesis has appeared in publication as follows: Applied Thermal Engineering, 2017, Ahmed F. Al-Neama, Nik Kapur, Jonathan L. Summers, Harvey M. Thompson. The title of the paper is "An experimental and numerical investigation of the use of liquid flow in serpentine microchannels for microelectronics cooling". **116**, pp. 709–723. (***Published online***)

2- The work in part of chapters 4 and 6 and chapter 7 of the thesis has appeared in publication as follows: International Journal of Heat and Mass Transfer, 2018, Ahmed F. Al-Neama, Zinedine Khatir, Nikil Kapur, Jonathan Summers, Harvey M. Thompson. The title of the paper is "An experimental and numerical investigation of chevron fin structures in serpentine minichannel heat sinks". **120**, pp. 1213–1228. (***Published online***)

3- The work in part of chapters 4, 6 and 7 and chapter 8 of the thesis has appeared in publication as follows: Applied Thermal Engineering, 2018, Ahmed F. Al-Neama, Nik Kapur, Jonathan L. Summers, Harvey M. Thompson. The title of the paper is "Thermal management of GaN HEMT devices using serpentine minichannel heat sinks". (***In press***)

The candidate has conducted the majority of the work that appears in the published articles, such as developing the models, collecting the experiment data, optimisation, and presenting and analysing the results. The co-authors as appears in the published papers provided valuable review, contribution and guidance to the candidate.

Acknowledgements

I would like to express my deepest gratitude to my supervisors Prof. Nikil Kapur, Prof. Harvey M. Thompson and Dr. Jonathan L. Summers for their advice, assistance, supportive guidance, and encouragement throughout the entire research.

I would also like to acknowledge the Iraqi Ministry of Higher Education and Scientific Research (MOHE), and Mechanical Engineering Department University of Mosul, Iraq, who offered unlimited help and financial support.

I am most thankful to my mother and father, wife, children, brothers and all my family members for their help, support, encouragement and patience during the years of my study.

Finally, I am grateful to University of Leeds for granting me access to their facilities, such as lab, library and Advanced Research Computing (ARC2).

Above all, I would like to thank the Almighty God for granting me the power and patient to accomplish this work. Without the willing of Allah, nothing is possible.

Abstract

The increasing density of transistors in electronic components is leading to an inexorable rise in the heat dissipation that must be achieved in order to preserve reliability and performance. Hence, improving the thermal management of electronic devices is a crucial goal for future generations of electronic systems. Therefore, a complementary experimental and numerical investigation of single-phase water flow and heat transfer characteristics of the benefits of employing three different configurations of serpentine minichannel heat sink (MCHS) designs has been performed, to assess their suitability for the thermal management of electronic devices. These heat sinks are termed single (SPSMs), double (DPSMs) and triple path serpentine rectangular minichannels (TPSMs), and their performance is compared, both experimentally and numerically, with that of a design based on an array of straight rectangular minichannels (SRMs) in terms of pressure drop (ΔP), average Nusselt number (Nu_{avg}) and total thermal resistance (R_{th}).

The results showed that the serpentine channel bends are very influential in improving heat transfer by preventing both the hydrodynamic and thermal boundary layers from attaining a fully-developed state. The SPSM design provides the most effective heat transfer, followed by the DPSM and TPSM ones, both of which out-performed the SRM heat sink. The SPSM heat sink produced a 35% enhancement in Nu_{avg} and a 19% reduction in R_{th} at a volumetric flow rate (Q_{in}) of 0.5 l/min compared to the conventional SRM heat sink. These improvements in the heat transfer are, however, achieved at the expense of significantly larger ΔP.

It was found that the incorporation of serpentine minichannels into heat sinks will significantly increase the heat-removal ability, but this must be balanced with the pressure drop requirement. Therefore, an experimental and numerical investigation of the benefit of introducing chevron fins has been carried out to examine the potential of decreasing pressure drop along with further thermal enhancement. This novel design is found to significantly reduce both the ΔP across the heat sink and the R_{th} by up to 60% and 10%, respectively, and to enhance the Nu_{avg} by 15%, compared with the SPSM heat sink without chevron fins.

Consequently, the design of the SPSM with and without chevron fins was then optimised in terms of the minichannel width (W_{ch}), number of minichannels (N_{ch}) and chevron oblique angle (θ). The optimisation process uses a 30 (without chevron fins) and 50 (with chevron fins) point Optimal Latin Hypercubes Design of Experiment, generated from a permutation genetic algorithm, and accurate metamodels built using a Moving Least Square (MLS) method. A Pareto front is then constructed to enable the compromises available between designs with a low pressure drop and those with low thermal resistance to be explored and appropriate design parameters to be chosen. These techniques have then been used to explore the feasibility of using serpentine MCHS and heat spreaders to cool GaN HEMTs.

Table of Contents

List of Tables

List of Figures

Nomenclature

A_{base}	Base area of minichannel [m^2]
A_{ch}	Cross-sectional area of minichannel [m^2]
A_{eff}	Effective heat transfer area per minichannel [m^2]
A_{fin}	Surface area of fin [m^2]
A_h	Bottom heated area of the MCHS [m^2]
A_P	Plenum area [m^2]
A_{tube}	Tube area [m^2]
Cp_f	Specific heat of fluid [J/kg.K]
D_{tube}	Tube diameter [m]
D_h	Hydraulic diameter [m]
d_l	Thickness of thermal layer Ethoxy [m]
F	Body force vector per unit volume [N/m^3]
f	Friction factor
f_{ch}	Fanning friction factor in minichannel
f_{app}	Apparent friction factor
g	Gravity vector [m^2/s], $g_x i + g_y j + g_z k$
G	The geometric parameter [$\frac{\propto^2+1}{(\propto+1)^2}$]
H_{ch}	Minichannel height [m]
h	Convective heat transfer coefficient [$W/m^2.K$]
h_x	Local heat transfer coefficient [$W/m^2.K$]
I	Current [A]
I	The unit diagonal matrix
k	Turbulent kinetic energy [m^2/s^2]
k_f	Thermal conductivity of fluid [W/m.K]
k_l	Thermal conductivity of Ethoxy layer [=2.2 W/m.K]
k_s	Thermal conductivity of copper block [W/m.K]
k_T	Turbulent thermal conductivity of fluid [W/m.K]
L	Heat sink Length [m]
L_{ch}	Minichannel length [m]
L_{hy}	Hydrodynamic entry length [m]
L_{th}	Thermal entry length [m]
L_{tube}	Tube length [m]
l_f	Chevron fin length [m]

l_{sc}	Secondary microchannel length [m]
$\dot{m}$	Mass flow rate [kg/s]
n	Number of minichannel
N_{cf}	Number of chevron fin
Nu	Nusselt number
ΔP_{ch}	Minichannel pressure drop [Pa]
ΔP_t	Total pressure drop [Pa]
P_{cf}	Perimeter of chevron fin [m]
p_f	Fin pitch ($= l_f + l_{sc}$) [m]
P_{in}	Inlet pressure [Pa]
P_{out}	Outlet pressure [Pa]
Po	Poiseuille number [$=f \cdot Re$]
Pr	Prandtl number
Pr_T	Turbulent Prandtl number
P_w	The wetted perimeter [m]
Q_{in}	Volumetric flow rate [m^3/sec]
q	Heat transfer rate [W]
q_{in}	Input power to the heater [W]
q_{loss}	Heat loss [W]
Re	Reynolds number
R_{th}	Total thermal resistance [K/W]
$T_{w,tci}$	Minichannel base temperature at thermocouple location [^{o}C]
$T_{f,out}$	Outlet fluid temperature [^{o}C]
$T_{f,in}$	Inlet fluid temperature [^{o}C]
$T_{f,x}$	Local fluid bulk temperature [^{o}C]
$T_{f,avg}$	Average fluid bulk temperature [^{o}C]
$T_{w,avg}$	Average minichannel base temperature [^{o}C]
u	Velocity vector [m/s], $ui + vj + wk$
u, v, w	Velocities in $x-, y-$ and $z-$directions, respectively [m/s]
U_{in}	Inlet water velocity [m/s]
V	Voltage [V]
V_{ch}	Velocity in minichannel [m/s]
V_p	Velocity in plenum [m/s]
V_{tube}	Velocity in tube [m/s]

W	Heat sink width [m]
W_{ch}	Minichannel width [m]
W_{sc}	Secondary microchannel width [m]
W_w	Fin width [m]
x, y, z	Cartesian coordinates
x^+	Dimensionless hydrodynamic axial distance [$x^+ = \frac{x}{Re \cdot D_h}$]
x^*	Dimensionless thermal axial distance [$x^* = \frac{x}{Re \cdot D_h \cdot Pr}$]

Greek symbols

$\propto$	Aspect ratio [$= W_{ch}/H_{ch}$], $W_{ch} < H_{ch}$ $(\propto < 1)$
$\propto^*$	Inverse aspect ratio [$1/\propto = H_{ch}/W_{ch}$], $W_{ch} < H_{ch}$ $(\propto > 1)$
β	Fin spacing ratio [$= W_w/W_{ch}$]
ξ	The excess loss coefficient of bend
η_f	Fin efficiency
ρ_f	Fluid density [kg/m^3]
μ_f	Dynamic viscosity of fluid [kg/m.s]
μ_T	Turbulent viscosity of fluid [kg/m.s]
ν_f	Kinematic viscosity of fluid [m^2/s]
θ	The chevron oblique angle [Degree]
ε	Minichannel surface roughness [μm]
τ_{ij}	Viscous stress tensor [Pa]
∇	Del or Nabla (gradient operator), $\frac{\partial}{\partial x} i + \frac{\partial}{\partial y} j + \frac{\partial}{\partial z} k$
Φ	The viscous dissipation function
Γ	The interface surface between the solid and fluid
δ_u	Hydrodynamic boundary layer thickness [m]
δ_{th}	Thermal boundary layer thickness [m]
ω	Specific dissipation rate [1/sec]
$\kappa(x)$	The Hagenbach factor
κ_c	Contraction loss coefficients
κ_e	Expansion loss coefficients
κ_{90}	The bend loss coefficient, (≈ 1.2)

Abbreviations

AMD	Advanced Micro Devices
CFD	Computational Fluid Dynamics
CPUs	Central Processing Units
DoEs	Design of Experiments
DPSM	Double Path Serpentine Minichannel
FDM	Finite Difference Method
FEM	Finite Element Method
FVM	Finite Volume Method
GaN	Gallium Nitride
HEMTs	High Electron Mobility Transistors
IC	Integrated Circuit
ITRS	The International Technology Roadmap for Semiconductors
MCHS	Minichannel Heat Sink
MLS	Moving Least Squares
MMICs	Monolithic Microwave Integrated Circuits
RF	Radio Frequency
Si	Silicon
SiC	Silicon Carbide
SMCF	Serpentine Minichannel with Chevron Fin
SMPF	Serpentine Minichannel with Plate Fin
SPSM	Single Path Serpentine Minichannel
SRM	Straight Rectangular Minichannel
TPSM	Triple Path Serpentine Minichannel
WBG	Wide Bandgap

Chapter 1: Introduction

1.1 Thermal Management of Microelectronic Devices

The inexorable miniaturisation of electronic components and increase in electronic packaging density (number of transistors per unit area or volume) is leading to a significant rise in the heat dissipation that must be achieved for operation and to preserve component lifespan and reliability. Hence, it becomes necessary to remove high heat flux from highly compact systems such as high-performance computer chips, laser diodes, gallium nitride (GaN) high electron mobility transistors (HEMTs) and nuclear fusion and fission reactors for ensuring their consistent performance with long life.

Since the invention of the integrated circuit (IC) in the late 1960s, the number of transistors on a chip has increased rapidly (ITRS, 2015). In 1965, Intel co-founder Gordon Moore demonstrates in an empirical relation called Moore's law that the density of components that can be integrated onto a microchip doubles roughly every two years (Moore, 1965). This law has held true since the IC's invention even today as shown in Fig. 1.1.

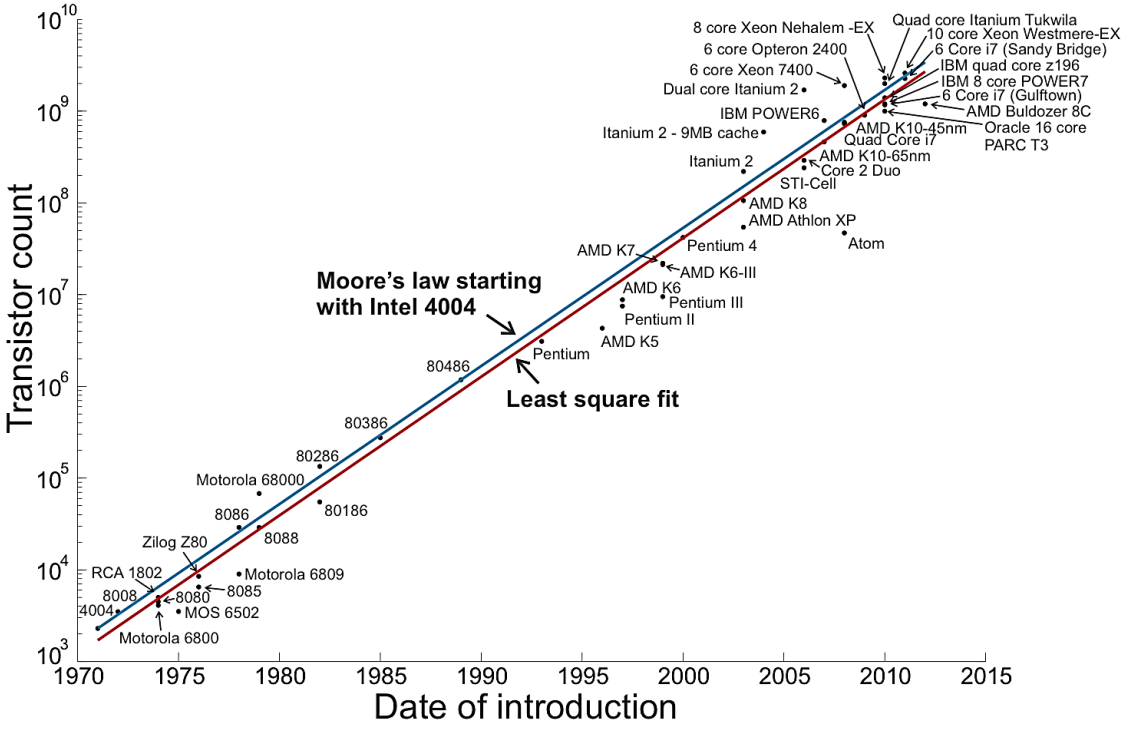

Fig. 1.1: shows the increase in the number of transistors every year. The blue line represents Moore's law applied, starting from the first microprocessor on the graph. The red line denotes the least square fit of the entire set (Saenen, 2013).

With growing use of digital systems, the requirements of data storage have grown exponentially and hence, the size and energy consumption of data centres, that house a large part of the digital infrastructure, has greatly increased (Kant, 2009 and Baliga et al., 2011).

In 2010, cooling of electronics in data centres account for roughly 33% of 1.31% (238 billion kWh annually) of combined worldwide energy consumption, representing a growth of roughly 11% per year over the last decade (Sharma et al., 2015). For example, in that year the United States (U.S.) data centres consumed about 1.8% of total U.S. electricity consumption, which represents about 82 billion kWh at an annual cost of approximately $6.1 billion (Koomey, 2011; EIA, 2011; and Sverdlik, 2016), and this is expected to triple by 2020 (Shehabi et al., 2016). Assuming an annual increase in new energy generation capacity of 1%, data centres could eventually consume all the available electrical energy in the U.S. by 2030 (Utsler, 2010). Therefore, managing power consumption and energy efficiency of data centres has become essential.

The International Technology Roadmap of Semiconductors (ITRS, 2011) predicted that the power dissipation from a microprocessor chip will exceed 270 W by 2015, and it is expected to increase three times (> 800 W) by 2026. Improving the thermal management in electronic devices is one of the major goals in the development of next generation electronic systems such as central processing units (CPUs), Radio Frequency (RF) Power Amplifier, and Satellite and Radar systems.

Conventional macroscopic air-convection fin-array heat sinks are no longer adequate for these levels of heat generation (Tullius et al., 2011), and in order to dissipate higher heat fluxes (>100 W/cm²), a very high air velocity or a significantly larger-dissipation area is need. For example, Khodabandeh and Palm (2002) claimed that if it is necessary to cool a device component contain a large number of transistors, which dissipates at least 90 W/cm² by using air-cooling heat sink type, a heat sink about 2000 times larger than the area of the device itself is required. Conventional two-phase cooling technologies using heat pipes and vapour chambers have been attractive for microprocessor cooling, because they do not need a pump to rotate the working fluid contained within a closed chamber. However, these capillary-driven devices are not well suited for solving the problem of chip powers exceeding a 100 W, due to limitations in the wick thickness and cross-sectional area of the pipe (Jiang et al., 2002). Even with pulsating and loop heat pipes, the maximum achievable heat flux is still modest as stated by Karayiannis and Mahmoud (2017).

Liquid jet impingement cooling technology, on the other hand, has also attracted much attention from researchers due to its ability to dissipate high heat fluxes. For example, Mudawar et al. (2009) reported 150–200 W/cm^2 using a dielectric fluid HFE-7100 and Zhao et al. (2013) reported 674 W/cm^2 using water impingement over a porous structure. However, this technology requires high pumping power and there is a danger of surface erosion, due to

integration of spray cooling into a closed loop system configuration (Silk et al., 2008 and Karayiannis and Mahmoud, 2017).

For high heat fluxes (> 100 W/cm^2), single-phase liquid cooling and flow boiling (two-phase flow) choices in microfluidic systems can provide the required cooling for the microelectronic devices (Kandlikar et al., 2006). The former, first introduced by Tuckerman and Pease in 1981, have emerged as viable cooling devices for high heat flux electronics due to their light weight, ease of implementation, compactness and higher heat transfer surface area to fluid volume ratio (Yadav et al., 2016). Leonard and Phillips (2005) explained that the use of such heat sinks for cooling of chips could produce savings in energy consumption of over 60%. However, high pressure drop and temperature gradients need to be alleviated. The latter have also been widely studied by researchers due to their ability to dissipate high heat fluxes with much lower pumping power than the former (Ghani et al., 2017a), due to their effective utilization of the latent heat of vaporization of the liquid (Karayiannis and Mahmoud, 2017). However, at higher heat fluxes, microchannel flow boiling suffers from pressure fluctuations and flow instabilities, which can lead to serious problems from significant reductions in heat transfer performance due to, for example, liquid dry-out (Kandlikar et al., 2006 and Balasubramanian et al., 2013).

Fig. 1.2 shows the variation of convective thermal resistances, R_{conv} (K/W), with different coolants and heat transfer mechanisms for a typical heat source area of 10 cm^2 and a velocity range of 2–8 m/s. It is shown that when air is used as a coolant the R_{conv} values decreased from 100 K/W to 33 K/W when using natural and forced convection heat transfer mechanisms, respectively, while using fluorocarbon liquids coolant with boiling heat transfer the R_{conv} value decreased significantly to 0.5 K/W.

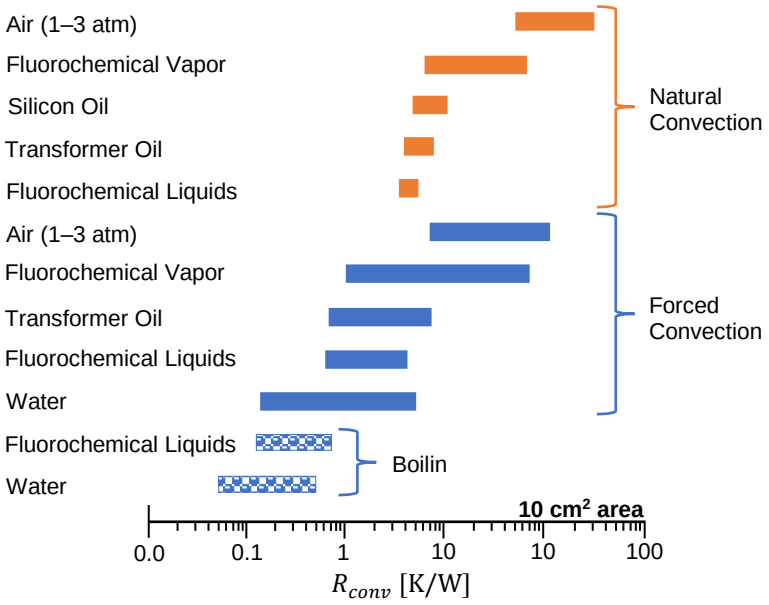

Fig. 1.2: Typical convective thermal resistances for a 10 cm^2 heat source area (Tummala, 2001).

1.2 GaN-Based HEMT Technology

Nowadays, most of traditional integrated circuit technologies and power devices are made of silicon (Si) semiconductors, which are not able to operate at temperatures above 250 °C, especially when high operating temperatures are combined with high-power, high-frequency and high-radiation environments (Seal and Mantooth, 2017). As an alternative, Wide Bandgap (WBG) semiconductors, particularly GaN HEMTs and silicon carbide (SiC), have attracted a lot of attention and are considered to be candidates for the next generation high-power electronics such as radio frequency (RF) power amplifier implementations and logic applications, as compared to silicon (Si) and gallium arsenide (GaAs)-based devices, due to their superior physical properties, such as high breakdown voltage and capability to handle high current and high power densities (Pengelly et al., 2012). However, the very high-power density in the active region of GaN HEMTs leads to significant degradations in performance as the device temperature increases to more than 300 °C. Thus, effective thermal management of GaN-based electronics is a key to enabling the technology to reach its full potential.

Commenting on what was mentioned above, Mishra and Shen (2008) stated that the GaN HEMT technology is becoming the front-runner to be used for power amplifiers, because of its ability to work under robust environments such as higher power levels, high-voltage and high temperatures. Recently, GaN has been used in most power electronic applications, such as: radar and space applications, missiles, satellites, automotive industry, defence and military communications, high frequency Monolithic Microwave Integrated Circuits (MMICs), high power amplifiers for wireless base stations, high voltage electronics for power transmission lines, cell phone infrastructure (base stations), as well as automotive and other general power conversion devices (Flack et al., 2016). This is attributed to a unique combination of GaN material properties, including wide bandgap (3.4 eV), high saturation electron drift velocity (2.5×10^7 cm/s) and large electric breakdown field strengths (~3.3×10^6 V/cm). These properties are explained in Table 1.1 (Kaminski and Hilt, 2014), which compares the benefits of GaN to those of other major and relevant semiconductors.

Table 1.1: Comparison between GaN and other Semiconductor properties (Kaminski and Hilt, 2014).

Property	Si	SiC	GaAs	GaN	Diamond
Bandgap, Eg (eV)	1.12	3.26	1.43	3.39	5.47
Electric Breakdown Field, E_{crit} (MV/cm)	0.23	2.2	0.4	3.3	5.6
Electron Mobility, μ_n (cm^2/V.s)	1400	950	8500	1500	1800
Permittivity, ε_r	11.8	9.7	13.1	9.0	5.7
Saturated Electron Drift Velocity, v_{sat} ($\times10^7$ cm/sec)	1	2	1	2.5	2.7
Thermal Conductivity, k (W/cm.K)	1.5	3.8	0.46	1.3	20

As can be seen, GaN has superior physical properties compared with other semiconductors, especially the conventionally used Si, for power devices operating under high-power, high-temperature and high-frequency conditions. For this reason, GaN HEMTs have proven to be excellent candidate for the radio frequency (RF) power amplifier applications (Nuttinck et al., 2002).

Although GaN has so many advantages that make it a promising technology, significant technological development is still required to improve the reliability and thermal management of devices constructed with this material. Self-heating is one of the critical factors that adversely affect device performance and reliability. Chattopadhyay and Tokekar (2008) claimed that GaN HEMT devices offer high power density, high break-down voltage and therefore generate high chip temperatures that can reach several hundred degrees above ambient base temperature due to self-heating, and their study has demonstrated that increasing the chip temperature not only reduces the performance of the devices but also accelerates their degradation. Severe self-heating effects may damage the gate electrode and can burn metal wires connecting the chip to the package, and hence cause device failures and reliability problems.

To avoid the malfunctions of electronics and to ensure the reliability of the electronic systems, with the rapid increase of heat dissipation from various electronic components such as CPU and graphic card in computers and radio-frequency (RF) power amplifiers, substantial research work has been carried out to explore more effective cooling techniques to keep up with the development pace of new electronic equipment and large electronic systems.

1.3 Liquid Cold Plate Microchannel Heat Sink

Nowadays, the thermal designer faces many challenges to overcome the factors of contracting system size, the requirement to insert more components within a limited space and to reduce the system acoustic noise generated from the heat sinks fans. The thermal solution is required to dissipate the maximum power consumption of the electronic equipment and ensure it remains below its maximum operating temperature (junction temperature). To overcome this dilemma, there are several liquid cooling methods, among these direct and indirect contact liquid cooling techniques. One example of direct contact liquid cooling is that investigated by Almaneea (2014) through immersing servers into dielectric liquid. The indirect contact liquid cooling method, which is the subject of this study, uses a liquid cold plate microchannel heat sink in an open-loop single-phase system, which is a promising solution to thermal challenges (Fan et al., 2014).

Liquid cooling like pure water, dielectric (Hydrofluoroethers, HFE) and nanofluids (nanofluid is a mixture between water and organic material such as Al_2O_3, SiO_2, TiO_2 and CuO) have much higher thermal conductivities and specific heat capacities than air, and thus much higher heat transfer coefficients associated with them. Therefore, by using liquids for cooling of electronic components is more effective than gas or air cooling (Salman et al., 2014).

Microchannel heat sinks can be used as an effective heat dissipation device, which has proven to be a very efficient method to remove high heat loads generated from a chip (Chein and Chuang, 2007). The novel idea of dispelling heat through the use of a silicon based MCHS was first introduced by Tuckerman and Pease in the early 1980s (Tuckerman and Pease, 1981) as shown in Fig. 1.3, which consists of an array of straight rectangular microchannels etched in a 1 cm^2 silicon wafer. They pointed out that decreasing liquid cooling channel dimensions to the micron scale (in the range of 10 μm to 10^3 μm) will lead to an increase in the heat transfer rate. The hydraulic diameter, D_h (m), of the microchannel is inversely proportional to the heat transfer coefficient within a narrowed channel of laminar flow, where the pressure drop is proportional to D_h^{-4} (Bergman et al., 2017). Hence, a higher heat transfer coefficient can be achieved by decreasing the hydraulic diameter of the channels at the expense of increase in pressure drop.

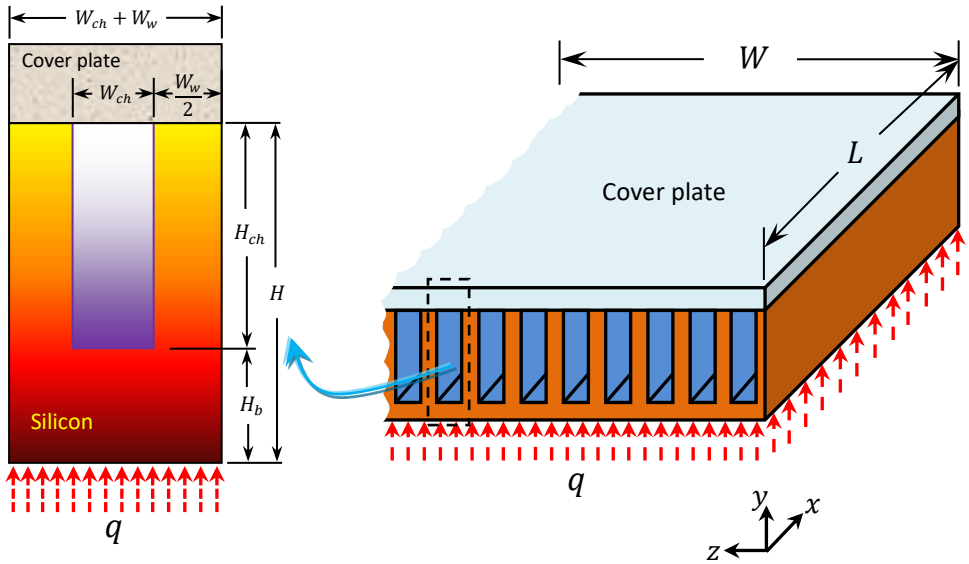

Fig. 1.3: Schematic illustration of a microchannel heat sink with enlarged microchannel.

For channels of rectangular cross-section, the hydraulic diameter (D_h) is defined as:

$$D_h = \frac{4 \cdot A_{ch}}{P_w} = \frac{2(W_{ch} \cdot H_{ch})}{W_{ch} + H_{ch}} \tag{1.1}$$

where A_{ch} is the channel cross sectional area (m^2) and P_w is the channel wetted perimeter (m), while W_{ch} and H_{ch} represent the width and depth of the channel (m), respectively. After this pioneering work, several studies have investigated the fluid flow and heat transfer characteristics of the microchannel heat sink, with a comprehensive review being found in Ghani et al. (2017a).

1.4 Classification of the Microchannels

Classification of the channel size is a controversial issue, and several authors have addressed this problem. Mehendale et al. (2000) had classified the channels according to their dimension, "D_h", being the hydraulic diameter of tube or smallest dimension for other cross-sections. Kandlikar and Grande (2003) had distinguished the channels based on fluid flow which they recommend for both gas and liquid (single-phase flow) as well as two-phase flow applications. The nomenclatures adopted by both these authors are presented in Table 1.2.

Table 1.2: Channel classification by Mehendale et al. (2000) and Kandlikar and Grande (2003).

Mehendale et al. (2000)		Kandlikar and Grande (2003)	
Conventional Channels	$D_h >$ 6 mm	Conventional Channels	$D_h >$ 3 mm
Compact Passages	1 mm $< D_h \leq$ 6 mm	Minichannels	200 μm $< D_h \leq$ 3 mm
Meso-channels	100 μm $< D_h \leq$ 1 mm	Microchannels	10 μm $< D_h \leq$ 200 μm
Micro-channels	1 μm $< D_h \leq$ 100 μm	Transitional Channels	0.1 μm $< D_h \leq$ 10 μm
		Transitional Microchannels	1 μm $< D_h \leq$ 10 μm
		Transitional Nanochannels	0.1 μm $< D_h \leq$ 1 μm
		Molecular Nanochannels	$D_h \leq$ 0.1 μm

Obot (2003) classified channels of hydraulic diameter under 1 mm ($D_h \leq 1$ mm) as microchannels, which was also adopted by many other researchers such as Bahrami et al. (2006) and Bayraktar and Pidugu (2006).

As a consequence, distinguishing between macrochannel and microchannel flows cannot be based on the channel size alone, for this reason Kew and Cornwell (1997) recommend using a confinement number (Co) as a transition criterion between macro and microscale flow boiling (two phase flow) as given by Eq. (1.2):

$$Co = \left(\frac{\sigma}{g(\rho_l - \rho_v) D_h^2} \right)^{\frac{1}{2}} \tag{1.2}$$

where σ represents the surface tension (N/m), while g is the acceleration due to gravity (m/s^2). ρ_l and ρ_v are densities for liquid and vapour case (kg/m^3), respectively. As per their proposed criteria, they observed that the transition happened at Co = 0.5, with Co < 0.5 being macro-scale flow and Co > 0.5 as microchannel flow.

In the present study, the criteria proposed by Kandlikar and Grande (2003) has been adopted here. Since the channel hydraulic diameter of all the heat sinks fabricated were between the 1.334 mm and 2 mm, minichannels are used for the current work.

1.5 Thermal Resistance Network in Heat Sinks

Generally, the heat generated by the chip mounted on the heat sink base is firstly transferred to the microchannels by conduction and then to the coolant by convection (Fan et al., 2014). A convenient way of presenting the cooling capability of a heat sink for electronics cooling is the total thermal resistance, R_{th} (K/W), which is defined as the ratio of the temperature difference across the module from the electronic die to the coolant fluid per watt of energy transferred (Mochizuki et al., 2011), as defined in Eq. (1.3):

$$R_{th} = \frac{T_{max} - T_{f,in}}{q} \tag{1.3}$$

where,

T_{max} = Maximum surface temperature in heat sink [K].

$T_{f,in}$ = Fluid inlet temperature [K].

q = Heat dissipation [W]

A low thermal resistance is desirable in order to minimize the temperature rise of the electronic devices per watt of heat generated. The thermal resistance of the system is the sum of each individual layer's thermal resistance, which depends on the thermal conductivity and thickness of the material. A traditionally used cooling technique with forced water convection through the heat sink is schematically presented in Fig. 1.4. In this figure, a single microchannel with symmetry has been chosen to illustrate the thermal resistance network.

Shao et al. (2009) carried out a study on the MCHS and considered three main thermal resistances given in Fig. 1.4. The conduction thermal resistances of the bottom base and the fin are represented as $R_{cond,base}$ and $R_{cond,fin}$, respectively. While $R_{conv,base}$ and $R_{conv,fin}$ are respectively the thermal resistances due to convection from the heat sink base and the walls (fins) to the fluid. The last thermal resistance is due to bulk temperature rise in the fluid, R_{bulk} (K/W). Hence, the Eq. (1.3) can be modified to written as:

$$R_{th} = \frac{T_{max} - T_{f,in}}{q} = R_{cond} + R_{conv} + R_{bulk} \tag{1.4}$$

where R_{cond} is the equivalent conductive thermal resistances (K/W), and is equal to the network of $(R_{cond,base} + R_{cond,fin})$, while $R_{conv,base} + R_{conv,fin}$ represent the equivalent

convective thermal resistances, R_{conv} (K/W). Each thermal resistance listed here will be explained in detail in the subsection 3.8.3.

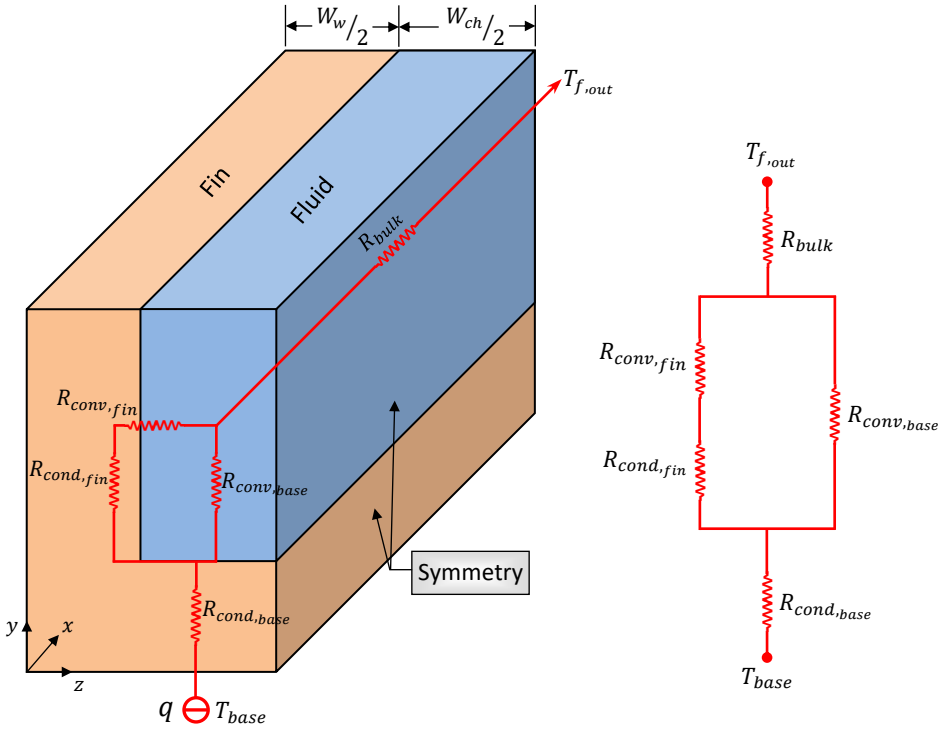

Fig. 1.4: Single microchannel with thermal resistance networks.

1.6 Study Objective and Aims

Thermal management is one of the most critical areas for the electronic product development, and a large proportion of field failures can be attributed to overheating, which in turn is caused by inappropriate thermal design (Sahin et al., 2005). The thermal problem has a significant impact on the cost, overall design, reliability and performance of the next generation of microelectronic devices (ITRS, 2015). The conventional straight rectangular microchannel heat sink has a main problem which is the continuous increase of surface temperature along the flow direction (Li et al., 2004).

Therefore, the main objective of this study is to identify, design, fabricate and test a suitable cooling technique capable to dissipate high heat flux (> 100 W/cm^2) from a chip. There is an urgent need to find an optimal thermal design of a microchannel heat sink cooled by a low flow rate coolant (water). To overcome this limitation, three different configurations of serpentine minichannel heat sink (MCHS) devices have been designed, fabricated and tested as an option to address the problem of thermal management, which they termed single (SPSMs), double (DPSMs) and triple path multi-serpentine rectangular minichannels (TPSMs) as shown in Fig. 1.5. The performance of these types of the minichannel heat sinks have been compared experimentally and numerically with an array of straight rectangular

minichannels (SRMs) in terms of pressure drop (ΔP), average Nusselt number (Nu_{avg}) and total thermal resistance (R_{th}).

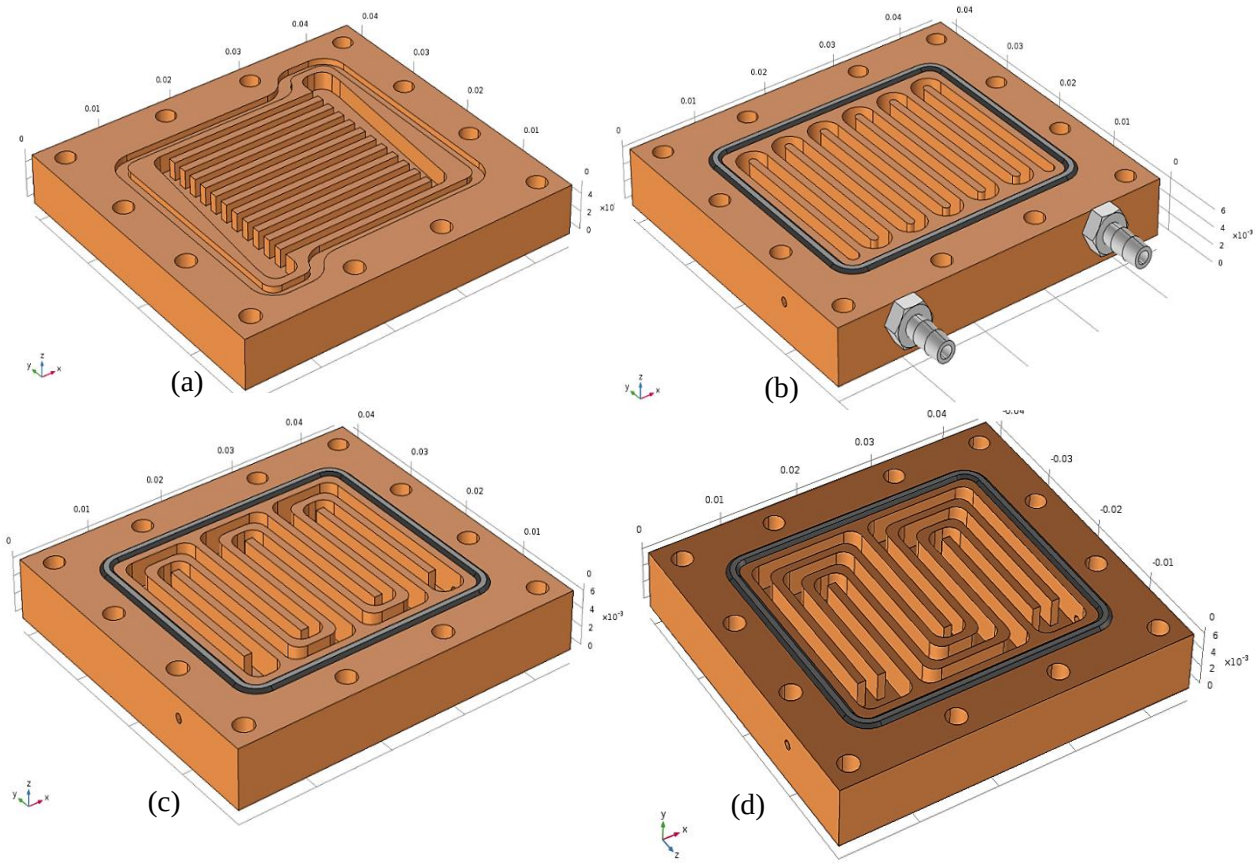

Fig. 1.5: 3-D schematic view of MCHS suggested; a) SRM; b) SPSM; c) DPSM, d) TPSM heat sink.

The key idea behind choosing these types of the MCHSs (Serpentine) in cooling of a chip, that is periodically interrupt hydrodynamic and thermal boundary layers in the corner (bends). In other words, periodic restart in both hydrodynamic and thermal boundary layers hinder the development of the thermal boundary layer on smooth surfaces responsible for limiting the heat transfer rates in MCHS designs. These improvements in heat transfer are, however, achieved at the expense of significantly large increase in ΔP. Additionally, the serpentine MCHS designs have large ratio of heat transfer surface to fluid flow volume compared with the conventional heat sink due to the bends, which leads to absorb as much of a heat from a chip (Lee et al., 2015).

Thermal management in gallium nitride on Silicon carbide (GaN-on-SiC) power amplifier based microelectronic devices is studied numerically. Three-dimensional numerical simulation of the conjugate heat transfer has been carried out within COMSOL Multiphysics. To enhance the hotspot cooling capability of the water-cooled copper SPSM heat sink, four different materials of heat spreader which of Si, SiC, diamond and graphene mounted between the GaN die and the heat sink base are used. The transistor selected for numerical

simulation study was the CREE *CGHV1J070D* GaN HEMT die, as shown in Fig. 1.6, which is attached directly on the heat spreader.

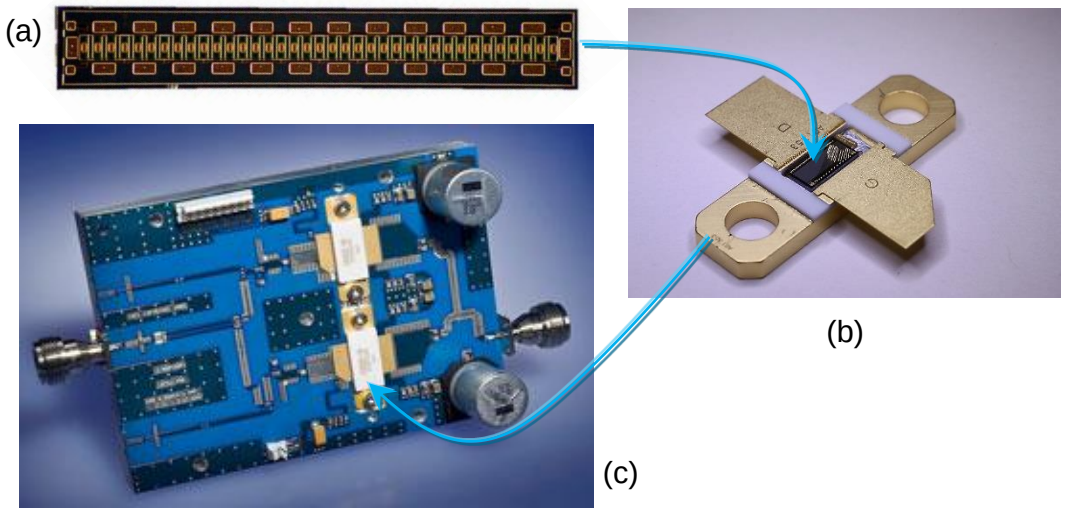

Fig. 1.6: (a) CGHV1J070D GaN-on-SiC HEMT bare die which is inside (b); (b) High voltage GaN HEMT on SiC substrate packaging which is inside (c); (c) Radio Frequency (RF) Power Amplifier (Cree Inc., 2012).

Three small heaters of size 4.8 × 0.8 mm^2 were used to generate a total power of 210 W (power on each GaN is 70 W), resulting in the heat flux on each GaN transistor is 1.823 kW/cm^2. The effect of the heat spreader thickness on the maximum chip temperature also has been investigated.

To enhance the convective heat transfer and achieve a more homogeneous temperature distribution together with reduction in pressure drop penalty, flow obstructions and secondary flows in microchannels can be produced by adding secondary microchannels between the main flow microchannels (Steinke and Kandlikar, 2006a). The present study explores a new design of heat sink where chevrons fins within multiple serpentine minichannels are used to control the hydrodynamic and thermal boundary layers. According to the author's knowledge, no researches have been published on secondary flow using chevron fins with a serpentine MCHS, and this has motivated the present study to develop a SPSM heat sink with chevron fins that could enhance the heat transfer together with significant reduction in pressure drop. Hence, another experimental and numerical work have been carried out to explore the ability of enhancing the heat transfer in SPSM with reduction pressure drop, see Fig. 1.7.

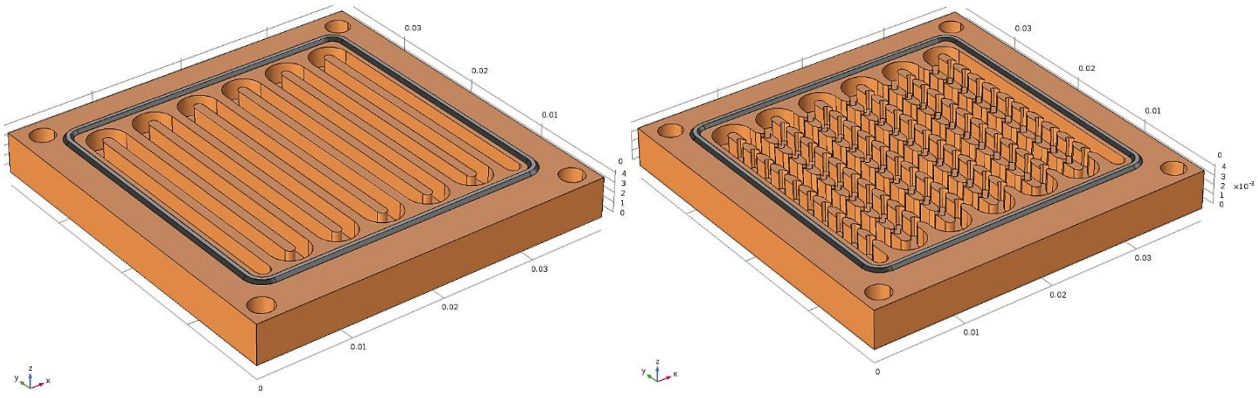

(a) (b)

Fig. 1.7: 3-D schematic view of MCHS suggested; a) single path serpentine MCHS with plate fins; b) single path serpentine MCHS with chevron fins.

In this framework, the specific contributions of this thesis can be summarized as:

1. Develop a suitable design procedure for serpentine minichannel heat sinks.
2. To develop accurate experimental and numerical methods for designing and optimising MCHSs that can remove high heat flux (>100 W/cm^2) from the electronic chip, with maintain maximum chip temperatures in the range of 80-100 ^{o}C for Silicon (Si) chips, and 150-225 ^{o}C for gallium nitride (GaN) high electron mobility transistors (HEMTs).
3. To investigate the fluid flow and forced convective heat transfer characteristic for both a multi-serpentine and multi-straight rectangular minichannel heat sinks.
4. Analyze the effect of different geometry, volumetric flow rate and total power input to the heat sink on the heat transfer coefficient (h), Nu_{avg}, R_{th} and ΔP.
5. Develop optimisation methods for multi-objective optimisation of minichannel heat sinks.

1.7 Scope of the Work

This thesis contains nine chapters in total. The following flow chart is a brief summary of the thesis content:

Chapter 1 introduces the background and motivation of the research. The objectives are also outlined along with scope of the thesis.

↓

Chapter 2 reviews the literature relevant to the present study. These include experimental and numerical studies for both single and two-phase flow heat transport in micro/mini channels heat sinks.

↓

Chapter 3 presents the heat and fluid flow fundamentals such as convective heat transfer, key dimensionless parameters in fluid flow and heat transfer, correlation equations for friction factor and heat transfer, and design optimisation.

↓

Chapter 4 describes the experimental investigation of the SRM, SPSM, DPSM and TPSM heat sinks. Additionally, the experimental set-up, design and fabrication of test sections, minichannel surface roughness measurements, calibrations, procedures of running the test rig, heat loss measurements, experimental data analysis, experimental uncertainty analysis are presented in detail.

↓

Chapter 5 experimental investigation of the four-different configuration of the MCHSs described in Chapter 4. The pressure drop, friction factor, average Nusselt number and total thermal resistance are analysed and discussed.

↓

Chapter 6 develops conjugate heat transfer models for four-different types of the MCHSs listed in Chapter 4, and validates them with the experimental data in terms of total pressure drop, average Nusselt number and total thermal resistance. The Navier-Stokes equations, conjugate heat transfer, finite element method, assumptions, boundary conditions, grid sensitivity, mesh quality and validation with previous study, and design optimisation are explained.

↓

Chapter 7 explores a new design of heat sink where chevrons fins within multiple serpentine minichannels are used. The effect of secondary channel width, chevron fins oblique angle, heat fluxes are examined. Pareto front is generated by using three design variables and metamodels are built using moving least squares approach.

↓

Chapter 8 investigates the thermal management of the GaN-on-SiC HEMTs numerically using the SPSM heat sink. Discussing the effect of changing the volumetric flow rate, heat flux, heat spreader materials and heat spreader thickness on the maximum chip temperature.

↓

Chapter 9 discusses some of points together with the main conclusions and recommendations for future works.

Fig. 1.8: Flow chart to explain the scope of the present thesis work.

Chapter 2: Literature Review

2.1 Introduction

In recent years, various cooling technologies have been applied to microprocessor chips and integrated circuits (ICs), among these impinging jets and heat pipes to achieve effective heat removal, at the device and system levels. The use of microchannel heat sinks is a promising alternative which can dissipate high heat flux and maintain a chip under the critical temperature design (the junction temperature, 85-100 ^{o}C) (ITRS, 2011), to ensure high performance. In this chapter, a brief review of the literature on microchannel and its related cooling devices is described.

The literature review is divided into five broad categories: the single-phase flow in a conventional straight microchannels is reviewed firstly, and the effects of the surface roughness, the geometric parameters and nanofluids on the fluid flow and heat transfer characteristics for the conventional microchannel heat sinks will be described. The effect of a micro-pin fins on the hydrothermal performance of the heat sinks will be discussed. While the second section is a review of the heat transfer augmentation techniques that employed on the single-phase microfluidic cooling devices. The third section is concerned about boiling heat transfer and flow boiling in microchannels, where boiling curve and flow boiling instabilities will be presented. The thermal management of the GaN HEMTs devices will be discussed in fourth section. Summary of this chapter will be drawn in last section of this chapter.

2.2 Single-Phase Flow in Microchannels

Several experimental and numerical studies have been carried out by various researchers to find out an effective way of cooling micro devices. The first idea for the concept of a microchannel heat sink was introduced by Tuckerman and Pease in 1981 (Tuckerman and Pease, 1981) (see Fig. 1.3), at Stanford University, where there seminal paper is considered a valuable reference for most researchers. Microchannel heat sinks with conventional straight rectangular microchannels were first proposed for very large scale integrated (VLSI) electronic components in 1980s. Since then, several other researchers have published theoretical and/or experimental works, generating a significant amount of information in the area of microscale flow and heat transfer processes. The heat transfer between the coolant (water or nano-fluid) and the heat sink contributes a significant fraction of the total thermal resistance in electronic component packages.

2.2.1 Conventional Microchannel Heat Sinks

Tuckerman and Pease (1981 and 1982) fabricated and tested a very compact, water-cooled heat sink for silicon integrated circuit using single phase heat transfer. In this pioneering work, they showed that VLSI circuit can be cooled by means of forced convective flow of water as working fluid through a very small volume of silicon microchannel heat sink. They fabricated heat sinks with an array of straight rectangular microchannels etched in a 1×1 cm^2 silicon wafer, and the channels were 302 μm deep and 50 μm wide and the wall separating the channels was 50 μm thick, which was demonstrated to have thermal resistance as low as 0.09 K/W over 1 cm^2 area for a pumping power 1.84 W. It had a capacity to dissipate 790 W/cm^2 while maintaining a chip temperature below 110 °C and without undergoing any phase change. This heat flux required a mass flow rate of 5700 kg/m^2.s and a high pressure drop of 220 kPa, the temperature of the substrate could rise as high as 71 °C above the temperature of the water inlet (with resulting inlet and outlet fluid temperatures of 23 °C and 94 °C, respectively). This was a milestone in the development of micro-scale heat sinks. Since then, the microchannel heat sink field has grown significantly.

Following the pioneering work of Tuckerman and Pease (1981), another major achievement was conducted by Phillips (1987) when he carried out an experimental study on the straight rectangular microchannel heat sinks under fully developed and developing flow condition for laminar and turbulent flow regimes. He used indium phosphide as a substrate for heat sink and water as the coolant. The channel dimensions used were typically H_{ch} = 0.165 mm, W_{ch} = 0.22 mm and L_{ch} = 9.7 mm. Subsequently, a computer model was developed (MICROHEX) to predict the overall thermal resistance (R_{th}) and fluid flow characteristics of this MCHS. They demonstrated that thermal resistances of the order of 0.072 K/(W/cm^2) can be achieved, albeit with pressure drops in excess of 2.5 bar.

Kawano et al. (1998) conducted an experimental and three-dimensional numerical simulation study of heat transfer and pressure drop in a straight rectangular microchannel heat sink used for cooling electronic components. The experimental setup consisted of an array of 110 microchannels etched in a silicon substrate having surface area 15 × 15 mm^2. The microchannel width was fixed at 57 μm, whilst the height used was either 180 μm or 370 μm. In their experimental study, water was used as the coolant fluid, and a fully developed laminar flow assumption was assumed in the numerical simulations. In the measurement of pressure loss no heat is applied to the chip. For Reynolds numbers ranging from $0 < Re < 200$, the pressure drop results of the experiments and simulations were in good agreement with each other, but in the same range of the Reynolds number, they found that the thermal resistance values at the microchannel heat sink entrance varied by a significant amount. This

discrepancy is due to the heat loss to the ambient surrounding during the experiments by the solid substrate which resulting in a larger measured thermal resistance. Additionally, they indicated these low Reynolds number conditions were unreliable because of large temperature-induced viscosity gradients at the inlet portion. For $Re > 300$, the pressure drop measured was higher than those obtained in the simulations. The change in thermal resistance along the microchannel heat sink (from inlet to outlet) at heat flux of 100 W/cm^2 was about 0.1 K/(W/cm^2).

A numerical study by using a three-dimensional computational model was conducted by Vafai and Zhu (1999) of two-layered microchannel heat sink with counter-current flow arrangement for cooling of electronic equipment. It was found that a counter-flow arrangement reduces the temperature gradient dramatically compared with single-layered microchannel for Re = 143.6. Also, they found that the pressure drop measured with a two-layered microchannel heat sink was also less than that for a single-layer. They observed that the two-layered microchannel heat sink design is a significant improvement over the conventional single-layered microchannel heat sink.

An experimental study was carried out by Xu et al. (2000) on the liquid flow in rectangular microchannels at different Reynolds number ranging from 20 to 4000. Deionized water was used as a coolant fluid in their study with two different heat sink materials. The first six heat sinks were made from aluminium, whereas the second six heat sinks were made from silicon. The microchannel length of the aluminium heat sinks was fixed at 50 mm with hydraulic diameters ranging from 46.8 μm to 344.3 μm, while the microchannel length of the silicon heat sinks were 10 mm and 20 mm with hydraulic diameters varying from 29.6 μm to 79 μm. Their results showed that the transition from laminar to turbulent flow occurred at Re around 1500, which is slightly earlier than the transition observed in the macrosystem, possibly due to dimensional errors in the microchannels rather than the effect of the micro-size dimensions the channels. Furthermore, they observed that as the microchannel size reduces, deviations between the experiment result and the theoretical predictions become more significant. At the same Re, when the hydraulic diameters of the microchannels are smaller than 100 μm, it was shown that the friction coefficient became smaller than that of the prediction.

An experimental study was conducted by Jiang et al. (2001) to investigate the fluid flow and forced convection heat transfer in straight rectangular microchannels filled with porous media. Firstly, numerical studies were carried out on the rectangular microchannel heat sink with different heights without porous media, and the deepest one was chosen for experimental work since this yielded a large heat transfer coefficient. The microchannel heat sink used was fabricated from 0.7 mm thick pure copper plates with base surface area of 21 × 21 mm^2. The

typical width and depth of the microchannels were 0.2 mm and 0.6 mm, respectively; while the fin width and the active length of the microchannels were respectively 0.2 mm and 15 mm to yields 38 channels per sheet. Water was used as a coolant with water flow rate in the microchannel ranging from 0.0093 to 0.34 kg/s.

The measured performance of both microchannels with and without porous media are compared with those of similar microchannel heat sinks tested by other researchers. The experimental values of pressure drop and friction factor for the microchannels without porous media were larger than the values predicted numerically and by theoretical correlations for both laminar and turbulent flow regimes, and this is due to the channels used experimentally having large relative roughness (about 1.9–12.1%) which is non-uniform. Also, they observed that the transition from laminar to turbulent flow in microchannels occurs much earlier (Re = 600) compared to fluid flow in smooth channels (Re = 2300). Compared to the conventional microchannel heat sink, the microchannels with porous media have better heat transfer performance, but this was at the expense of high pressure drop which reached up to 4.6 bar compared with 0.7 bar for a conventional heat sink.

Numerical analysis for heat transfer and fluid flow phenomena were investigated by Toh et al. (2002) inside a three-dimensional heated microchannel. They carried out a detailed numerical analysis on the experimental conditions of Tuckerman and Pease (1981). They solved steady, laminar flow and heat transfer equations using a finite-volume method. They found that at lower Reynolds numbers the temperature of the water increases, leading to a decrease in the viscosity and thus smaller frictional losses (pressure drop).

Qu and Mudawar (2002a) have performed experimental and numerical investigations of pressure drop and heat transfer characteristics of single-phase laminar flow in microchannel heat sinks having 1 cm wide and 4.8 cm long by using twenty-one rectangular microchannels with 231 μm wide and 713 μm deep. Deionized water was employed as the cooling liquid and two heat flux levels, 100 W/cm^2 and 200 W/cm^2. The Reynolds numbers in their study ranged from 139 to 1672 for 100 W/cm^2 and 385 to 1289 for 200 W/cm^2. They also solved the conjugate heat transfer problem analytically by treating both the fluid and solid as a unitary computational domain and they compared the result of the numerical study with experimental data and suggested that the Navier-Stokes and energy equations can successfully predict heat transfer behaviour of the single-phase flow. They found that heat flux and Nusselt number are larger near the inlet and vary around the periphery with Nusselt number approaching zero near the corners.

Fedorov and Viskanta (2000); Qu and Mudawar (2002b); and Li et al. (2004) carried out three-dimensional numerical studies of fluid flow and heat transfer for the $1cm^2$ silicon wafer MCHS with straight rectangular microchannels, used in the experiments of Kawano et al. (1998). Fedorov and Viskanta (2000) demonstrated that the average channel wall temperature along the flow direction was nearly uniform, whereas a very large temperature gradient was observed in the region close to the microchannel inlet. However, Qu and Mudawar (2002b) predicted that the temperature rise in the wall and fluid bulk regions along the flow direction was approximately linear. Li et al. (2004) later explained this discrepancy by noting that Qu and Mudawar (2002b) assumed that the fluid thermophysical properties (i.e. density and viscosity) were temperature-independent, whereas Fedorov and Viskanta (2000) accounted for their temperature-dependence.

Wei and Joshi (2003) numerically investigated the thermal performance of a stacked microchannel heat sink as shown in Fig. 2.1. They conducted an optimization study to determine the minimal thermal resistance by developing a simple thermal resistance network model, under the constraints of fixed pumping power and fixed number of layers. They observed that the overall thermal resistance for a two layered micro-channel stack was 30 % less than for the single layered micro-channel due to doubling of the heat transfer area. Also, they studied the effect of channel length and number of layers on the thermal resistance. Their results showed that the optimal number of layers for a stacked microchannel heat sink under constant pumping power of 0.01 W is 3. The minimal thermal resistance of two-layered microchannel heat sink was found out to be 0.213 K/W, with an optimal channel has a fin width of 41 μm, channel width of 107 μm and inverse aspect ratio ($\propto^* = H_{ch}/W_{ch}$, $H_{ch} > W_{ch}$) of 3.8.

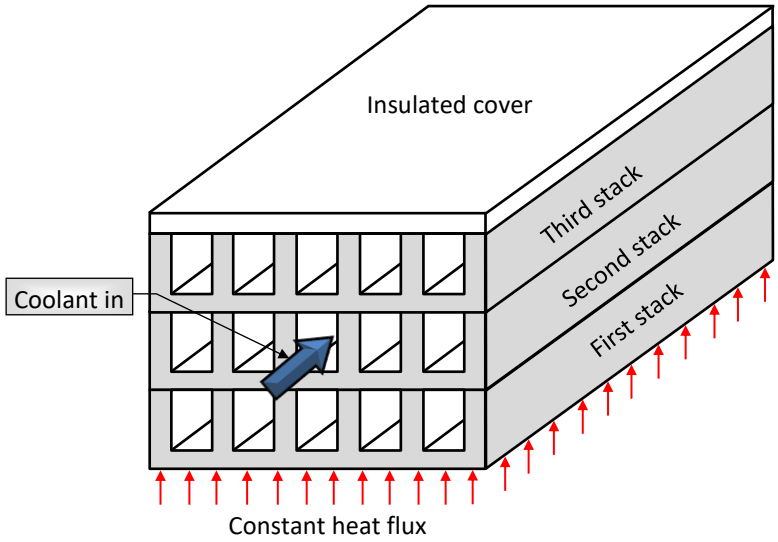

Fig. 2.1: 3-D view of a stacked MCHS design (Wei and Joshi, 2003).

Later, Wei and Joshi (2004) conducted a numerical simulation to study the conjugate heat transfer of a multilayer microchannel heat sink. In their study, the area of a base heat sink was 10 mm by 10 mm, with a height in the range 1.8 mm to 4.5 mm (2–5 layers) was considered. The water flow rate varied from 50 *ml/min* to 400 *ml/min*. The effects of the number of layers in the stack, microchannel aspect ratio, pumping power per unit area of heat sink and channel length on the optimal thermal resistance was investigated by using water as coolant. The overall thermal resistance was calculated and the results of the computational simulations were also compared with that of a single-layered microchannel heat sink.

Pijnenburg et al. (2004) have used conventional silicon processing technology to produce microchannels on the backside of a silicon chip. They used the Bosch process to anisotropically etch silicon microchannels 0.1 mm wide, 0.3 mm deep and 0.1 mm spacing between them and then coated them with a layer of thermal SiO_2. Fluidic connections were created through a Pyrex glass cover, which was glued to the silicon substrate, allowing water to flow into a reservoir, then through parallel channels on the chip. The chip was heated by a copper resistor plated on the opposite side of the silicon. Through Flowtherm Computational Fluid Dynamics (CFD) models and by experimental analysis they found that the thermal resistance of the chip decreases with increasing flow rate and increasing dissipated power. However, the experimental results showed a lower thermal resistance than the Flowtherm model predicted for variable flow rates. They demonstrated cooling densities of 370 W/cm^2 with a maximum junction temperature of 120 °C, 0.1 l/min flow rate, and 15 kPa pressure drop.

Steinke and Kandlikar (2006b) conducted an experimental study on the straight rectangular microchannel with a width of 200 µm, a depth of 250 µm, and a length of 10 mm to get 26 parallel channels connected to a common header. The data presented is for water with single-phase laminar flow and covers the range of Reynolds numbers from 14 to 789. The temperature and pressure are measured in the plenums. From the measured total pressure drop, the apparent friction factor (f_{app}) is calculated and then plotted versus Re after they calculated the experimental uncertainty. The expanded uncertainty expression for $f \cdot Re$, based upon measured variables such as channel width (W_{ch}), channel height (H_{ch}), channel length (L_{ch}), total pressure drop (ΔP_t) and water flow rate (Q_{in}) is given by Eq. (2.1).

$$\frac{U_{f\cdot Re}}{f\cdot Re}=\left(\begin{array}{c} 2\left(\frac{U_\rho}{\rho}\right)^2+\left(\frac{U_\mu}{\mu}\right)^2+\left(\frac{U_{\Delta P_t}}{\Delta P_t}\right)^2+\left(\frac{U_{L_{ch}}}{L_{ch}}\right)^2+3\left(\frac{U_{Q_{in}}}{Q_{in}}\right)^2+ \\ 5\left(\frac{U_{W_{ch}}}{W_{ch}}\right)^2+5\left(\frac{U_{H_{ch}}}{H_{ch}}\right)^2+2\left(\frac{U_{W_{ch}}}{H_{ch}+W_{ch}}\right)^2+2\left(\frac{U_{H_{ch}}}{H_{ch}+W_{ch}}\right)^2 \end{array}\right)^{1/2} \tag{2.1}$$

From the Eq. (2.1), it can be seen that the most dominant terms in the $f \cdot Re$ uncertainty are the measurements of microchannel width and height, and the flow rate. It can be concluded that due to the measurement errors of the microchannel dimensions and the flow rate there is still going to be a large uncertainty, even with the most careful pressure drop measurements. To calculate the total pressure drop in the microchannels, four components were included which are the inlet and outlet losses, the fully developed flow losses, and the developing flow losses as shown in Eq. (2.2):

$$\Delta P_t = \frac{\rho_f \kappa_c \bar{V}_{ch}^2}{2} + \frac{\rho_f \kappa_e \bar{V}_{ch}^2}{2} + \frac{2\mu_f (f \cdot Re) \bar{V}_{ch} L_{ch}}{D_h^2} + \frac{\kappa(x) \rho_f \bar{V}_{ch}^2}{2} \tag{2.2}$$

where ρ_f and μ_f represent the density (kg/m^3) and viscosity (kg/m.s) of the fluid and $\bar{V}_{ch}$ is the average velocity inside the microchannel (m/s). κ_c and κ_e are, respectively, the inlet and outlet loss coefficients due to sudden contraction and expansion between the microchannel and the plenum. The difference between the apparent friction factor (f_{app}) over a length x and fully developed friction factor (f_{FD}) is expressed in terms of an incremental pressure defect, $\kappa(x)$, as given by:

$$\kappa(x) = \left(f_{app} - f_{FD}\right) \frac{4x}{D_h} \tag{2.3}$$

The incremental pressure defect (also known as Hagenbach factor) will begin at a value of zero and increase to some fully developed constant value $\kappa(\infty)$. For a rectangular channel, the fully developed Hagenbach factor can be calculated by (Steinke and Kandlikar, 2006b):

$$\kappa(\infty) = 0.6796 + 1.2197 \propto +3.3089 \propto^2 - 9.5921 \propto^3 + 8.9089 \propto^4 - 2.9959 \propto^5 \tag{2.4}$$

From the Eq. (2.4), it is shown that the Hagenbach factor has a dependence upon channel aspect ratio ($\propto = \frac{W_{ch}}{H_{ch}}$), where $W_{ch} < H_{ch}$.

Jiang et al. (2008) studied experimentally the fluid flow and heat transfer characteristics of deionized water flowing in parallel rectangular microchannels. The test section was made from oxygen-free copper; it was 3 mm thick, 20 mm wide and 80 mm long. The height and width of the rectangular microchannels were 350 μm and 900 μm respectively. They measured the flow rate, the pressures and temperatures of water at the inlet and outlet of the microchannel. Their experimental friction factors in the microchannel were only 20% to 30% lower than the conventional theory. The transitional Reynolds number found was 1100 which was also lower than conventional theory. At low flow rate, the Nusselt number for the microchannel is found to be lower than the conventional theory, while at high flow rate, the Nu significantly increased and exceeds the value of Nu for conventional theory. They also stated that the Nu almost remained constant when the flow rate was small, however, as the

flow rate was increased, significant increase of the Nu occurred. Furthermore, the Nu was affected by the heat flux when the mass flow rate was large.

Koşar (2010) used COMSOL Multiphysics to conduct a numerical investigation to study the effects of microchannel material and substrate thickness on the heat transfer and fluid flow. The microchannel had size (200 μm wide × 200 μm deep × 5 cm long) with different base thicknesses ranging from 100 μm to 1000 μm and different materials such as Polyimide, Silica Glass, Quartz, Steel, Silicon and Copper. He discussed the trends of local and average Nusselt numbers in the microchannels. He presented a general Nusselt number correlation for fully developed laminar flow as a function of two dimensionless parameters, namely Biot number (Bi) and relative conductivity, $k^* = k_{Solid}/k_{Copper}$, to take the conduction effects of the solid substrate on heat transfer into account.

2.2.2 Surface Roughness Effects

The effect of surface roughness on single-phase liquid flow in microchannels has been investigated in the literature both numerically and experimentally. As the channel size becomes smaller and smaller, the roughness effects need to be considered especially in the laminar flow regime. The surface roughness plays a more important role in predicting the flow in the channels, and it has significant effect on the transition from laminar-to-turbulent flow.

Wu and Little (1983) conducted experiments to measure the friction factor for nitrogen (N_2), hydrogen (H_2) and argon (Ar) gases flow in fine microchannels used for micro–miniature Joule–Thomson refrigerators, of trapezoidal and rectangular cross-section, for both laminar and turbulent flow regimes. The test microchannels were etched in glass and silicon with hydraulic diameter ranging from 45.5 μm to 83.1 μm and sealed with Pyrex by using anodic bonding. A unique aspect of the microchannels is that the heat transfer surfaces were relatively rough. For glass microchannels, they found that the flow transition from laminar to turbulent flow occurred at Reynolds number (Re) of 350 without heat treatment and 900 with heat treatment, which is much earlier than the traditional transitional Re = 2300 (Yang et al., 2005). They attributed these deviations to the relatively high surface roughness effects caused by the fabrication technique and uncertainty in the determination of the channel dimensions. Furthermore, the results indicated that the friction factors for both flow regimes in these channels were larger than predictions from the established correlations for macroscale pipes. However, the trend obtained from Choi et al. (1991) was inconsistent with that obtained by Wu and Little (1983), who used nitrogen gas as a working fluid flow through micro-tubes in both the laminar and turbulent flow regimes, and the measured friction factors for both flow

regimes were found to be lower than those predicted by conventional correlations shown in Eqs (2.5-2.8):

For fully developed laminar flow regime, Darcy friction factor (f_D) for round tube is depends only on Re as given (Shah and London, 1978):

$$f_D = \frac{64}{Re} \qquad (Re \leq 2300) \tag{2.5}$$

Colebrook (1939) conducted experiments of turbulent flow using rough and smooth pipes which led to the most famous equation for f_D shown as follows:

$$\frac{1}{\sqrt{f_D}} = -2\log_{10}\left(\frac{\varepsilon/D_h}{3.7} + \frac{2.51}{Re\sqrt{f_D}}\right) \qquad (3000 \leq Re \leq 10^5) \tag{2.6}$$

As shown from Eq. (2.6), f_D depends on both Re and the relative roughness (ε/D_h), where ε is the surface roughness (m). For hydraulically smooth pipes, $\varepsilon/D_h = 0$, and Eq. (2.6) can be rewritten to be:

$$\frac{1}{\sqrt{f_D}} = 2\log_{10} Re\sqrt{f_D} - 0.8 \tag{2.7}$$

Eq. (2.7) is called Prandtl equation. The friction factor in rough pipes can be calculated from von Karman's expression:

$$\frac{1}{\sqrt{f_D}} = 2\log_{10}\left(\frac{3.7}{\varepsilon/D_h}\right) \tag{2.8}$$

Later, Wu and Little (1984) considered heat transfer characteristics of nitrogen gas flow in micro heat exchangers for both laminar and turbulent flow regimes. Microchannels in the counterflow heat exchangers were fabricated using the same photolithography technique as in their former work, with hydraulic diameters between 134 μm and 164 μm. The unique features of such channels are their asymmetric roughness (part of the channel walls are smooth and part are very rough compared to those of most conventional heat exchangers), their large relative roughness and a large variation of the heat flux and temperature over the walls of the channels. For the channels heated on one side, the results indicated that the position of the heat source does appear to have some effect in determining the heat transfer in the laminar zone, while for the turbulent flow it did not appear to be a significant factor. The transition zone occurred between Re = 1000 and 3000. The average Nusselt number was larger for the two-side heated channel than for one-side heated channel. The roughened channels have an improved heat transfer coefficient but have an increased friction factor also. For both flow regimes, the measured heat transfer coefficient was found to be higher than those predicted by correlations shown in Eqs. (2.9-2.11) (Kraus, 2013), and this is attributed

to the rougher surfaces of the channels. Important correlations include Sieder-Tate's correlation for simultaneously developing laminar flow:

$$Nu = 1.86\left(Re\,Pr\frac{D_h}{L}\right)^{1/3}\left(\frac{\mu_f}{\mu_w}\right)^{0.14} \qquad (Re \le 2300) \qquad (2.9)$$

Hausen's correlation for transitional regime:

$$Nu = 0.116\left(Re^{2/3} - 125\right)Pr^{1/3}\left(\frac{\mu_f}{\mu_w}\right)^{0.14}\left[1 + \left(\frac{D_h}{L}\right)^{2/3}\right] \qquad (2300 \le Re \le 10000) \qquad (2.10)$$

Dittus – Boelter's correlation for turbulent fully developed flow:

$$Nu = 0.023\,Re^{0.8}\,Pr^{1/3} \qquad (Re \ge 10000) \qquad (2.11)$$

where $\frac{\mu_f}{\mu_w}$ is the viscosity correction, while μ_f and μ_w are the dynamic viscosity of the fluid (kg/m.s) calculated at the bulk fluid and wall temperature, respectively.

Wu and Cheng (2003) performed experimental investigations of the laminar convective heat transfer and friction factor of deionised water flow in a silicon microchannel with 13 different surface conditions (trapezoidal and triangular microchannels). It is found that the values of the Nusselt number (Nu) and apparent friction coefficient ($C = f_{app} \cdot Re$, where f_{app} is apparent friction factor) depend greatly on different geometric parameters. In addition, these two values were found to increase with the increase of surface roughness and surface hydrophilicity (to increase the surface hydrophilic capability of the silicon microchannels, some of them were deposited by a thermal oxide layer), and these increases become more obvious at larger Reynolds numbers. The experimental results showed that the Nu increases almost linearly with very low Reynolds number flow ($10 < Re < 100$), while if the $Re > 100$ ($100 < Re < 1500$) the rate of increase of Nu with Re gradually decreases. Based on the experiments, dimensionless correlations for the Nu and the apparent friction constant are obtained as shown:

For $10 < Re < 100$

$$Nu = C_1 Re^{0.946} Pr^{0.488}\left(1 - \frac{W_b}{W_t}\right)^{3.547}\left(\frac{W_t}{H_{ch}}\right)^{3.577} \times \left(\frac{\varepsilon}{D_h}\right)^{0.041}\left(\frac{D_h}{L}\right)^{1.369} \qquad (2.12)$$

For $100 < Re < 1500$

$$Nu = C_2 Re^{0.148} Pr^{0.163}\left(1 - \frac{W_b}{W_t}\right)^{0.908}\left(\frac{W_t}{H_{ch}}\right)^{1.001} \times \left(\frac{\varepsilon}{D_h}\right)^{0.033}\left(\frac{D_h}{L}\right)^{0.798} \qquad (2.13)$$

For $10 < Re < 1500$

$$f_{app} \cdot Re = C_3 Re^{0.089} Pr^{0.163}\left(1 - \frac{W_b}{W_t}\right)^{4.359}\left(\frac{W_t}{H_{ch}}\right)^{4.444} \times \left(\frac{\varepsilon}{D_h}\right)^{0.028}\left(\frac{D_h}{L}\right)^{1.023} \qquad (2.14)$$

For silicon surfaces, the factors C_1, C_2 and C_3 are respectively equal to 6.7, 47.8 and 508.7, while for thermal oxide surfaces equal to 6.6, 54.4 and 540.5. The symbols W_t, W_b and H_{ch} are respectively top width, bottom width and depth of the trapezoidal microchannel.

Kandlikar et al. (2003) experimentally investigated the effect of surface roughness on the pressure drop and heat transfer characteristics in circular stainless steel tubes having inner diameters of 1.067 mm and 0.62 mm. In their experiments, distilled water as the working fluid was used. The roughness of the tubes was varied by etching them with an acid solutions to get three different roughness values for each tube. Thus, they obtained relative roughness values of 0.00161 to 0.00355 for the tube with inner diameter of 0.62 mm, and 0.00178 to 0.00281 for the tube of 1.067 mm diameter. For the 0.62 mm diameter tube, the experiments were conducted at a Reynolds number ranging from 900 to 3000, and from 500 to 2600 for 1.067 mm tube. Their results revealed that the effect of surface roughness on pressure drop and heat transfer for the larger tube were negligible, however, these became more dependence on the surface roughness with the smaller one, namely highest heat transfer and pressure drop occurred in the tube with highest relative roughness value of 0.00355.

As a result of the literature presented above, the structured roughness elements on channel walls resulted in heat transfer enhancements as compared to smooth channels due to the combined effects of area increase and flow modification. However, this heat transfer enhancement will be at the expense of higher pressure drop.

2.2.3 Geometric Parameters Effects

There have been several attempts to study the effects of the geometric parameters on the thermal performance of the microchannel heat sink. Among these parameters, different channel shapes, parallel channels with different aspect ratios and different inlet/outlet arrangements, as will be described below.

2.2.3.1 Channel Shapes Effects

The size and shape of the microchannels may have remarkable influence on the thermal and hydrodynamic performance of microfluidic cooling devices. In this subsection, the experimental and numerical studies that performed on the microchannel heat sinks with different types of channel shapes such as rectangular, trapezoidal, triangular and circular will be presented.

Jiang et al. (1995) experimentally investigated the microfluid flow behaviour through different cross-section shapes, namely, rectangular, trapezoidal, triangular and circular microchannels. The microchannels used in their study were etched in a silicon substrate and then sealed by bonding it with a glass wafer. The dimensions of the rectangular, trapezoidal

and triangular microchannel heat sinks ranged with height varying from 13.4 μm to 46 μm and width ranging from 25 μm to 100 μm, whereas the lengths varied from 2.5 mm to 10 mm, while the diameter of the circular microchannel ranged from 0.008 mm to 0.042 mm and the length from 1 cm to 10 cm. The experiments showed good agreement with the theoretical equation for the friction factor.

Another experimental study was conducted by Jiang et al. (1997) on a silicon microchannel heat sink with circular and trapezoidal cross-sections on the laminar flow of liquid (water) with a hydraulic diameter ranging from 35 μm to 120 μm and Reynolds numbers varying from 1 to 30. The measurements of the circular microtubes agreed well with the theoretical prediction for conventional ducts in terms of friction coefficient. For trapezoidal microchannel, it is noticed that the Poiseuille number ($Po = f.Re$) depended not only on the shape and the cross-section sizes but also on the microchannel length. Their measurements revealed that the friction factors were lower than that of the conventional theory and this is due to the surface roughness of the microchannel.

Experiments were conducted by Qu et al. (2000a) to investigate fluid flow characteristics of water flowing through three heated walls of trapezoidal silicon microchannels with a hydraulic diameter ranging from 51 μm to 169 μm and a 54.7^o sidewall angle. The friction factor and pressure drop measured across the microchannels at steady states were compared with the predictions from the conventional laminar flow theory. Experimental results indicate that pressure gradient and flow friction in microchannels are higher than those given by the theory, and this was probably due to the effect of the microchannel surface roughness. Later, experiments were carried out by Qu et al. (2000b) for the same test sections above to study heat transfer characteristics of water flow in trapezoidal microchannels. The experimental data obtained were compared with the results predicted by the numerical calculation solved by a conjugate heat transfer analysis. The comparison results indicated that the experimentally determined Nusselt number is much lower than that given by the numerical analysis, and this may be due to the effects of surface roughness of the microchannel walls. For both studies, a roughness-viscosity model was proposed to interpret the experimental data, and good agreement between the experimental data and the predictions was found for both friction factor and Nusselt number, when an adjusted coolant viscosity was included to account for surface roughness of the microchannels.

The laminar fluid flow and heat transfer characteristics of water in three-dimensional symmetric silicon microchannels with trapezoidal and triangular cross-sections were studied by Zhuo et al. (2006) using the finite volume method. The numerical results of their study were compared with the experimental data available of Wu and Cheng (2003), and a good

agreement between the two was achieved. The thermal properties of solid and water are assumed to be constant except the water viscosity, which varied with the temperature. From the numerical results, it was found that the intensity of heat transfer between the solid and the fluid is highest at the microchannel inlet for both trapezoidal and triangular microchannels and decreases along the flow direction. For the two microchannels simulated the heat transfer coefficient of the fully developed region of the trapezoidal microchannel was much better than that of the triangular microchannel, indicating the significant effect of the cross section geometric on the microchannel system.

An optimisation study of a trapezoidal microchannel heat sink was carried out by Yang and Liao (2014) using the response surface methodology and the genetic algorithm approach to find out the optimal geometries. Three design variables from the geometric parameters are selected namely, the ratio of the upper width of the microchannel to the whole width, the depth of the microchannel to the whole depth, and the ratio of upper width and lower width of the microchannel. In their optimisation, water was used as the cooling fluid in a silicon substrate with Reynolds number ranging between 50 to 600 while heat flux varied between 20 to 40 W/cm^2. In their study, they showed that the average Nusselt number increases with an increase in the Reynolds number or pumping power, while thermal resistance was reduced.

2.2.3.2 Aspect Ratios Effects

In this subsection, the experimental and numerical studies that carried out to investigate the heat transfer enhancement and fluid flow characteristics for microchannels with various aspect ratios will be discussed.

Wang and Peng (1994) studied experimentally the single-phase forced convective heat transfer characteristics by using six microchannel heat sinks made of stainless steel plate, 18 mm wide and 125 mm long, each microchannel cross-section was rectangular with different widths and identical channel height of 0.7 mm. The tested length of the microchannel was 45 mm with a thickness of 2 mm, with microchannels characteristics of (Width (mm), height (mm) and number of channels) (0.8, 0.7, 4), (0.6, 0.7, 4), (0.4, 0.7, 4), (0.4, 0.7, 6), (0.2, 0.7, 4) and (0.2, 0.7, 6). There were 4 or 6 microchannels with identical geometries evenly distributed on each test plate. Methanol and deionized water were employed as the working fluids in their experiments, and the liquid velocities evaluated varied from 0.2 to 2.1 m/s for water and 0.2 to 1.5 m/s for methanol. The working liquid temperature varied from 10 to 35 °C for deionized water and 14 to 19 °C for methanol.

The results provide significant data and considerable insight into the behaviour of the forced-flow convection in microchannels. They observed three different trends for the variation of

single phase heat transfer coefficient in the above microchannels. In first the trend on (0.8, 0.7, 4) heat sink, heat transfer coefficient smoothly increased with wall temperature. In the second trend on (0.6, 0.7, 4), (0.4, 0.7, 4) and (0.4, 0.7, 6) heat sink, a steep increase in heat transfer coefficient at low wall temperature was observed. This was followed by moderate increase in heat transfer coefficient at high wall temperature. In third trend on (0.2, 0.7, 4) and (0.2, 0.7, 6) heat sink, the heat transfer coefficient decreased first and then moderately increased as the wall temperature was increased. They further concluded that heat transfer characteristics in laminar and transition region of microchannels are highly complicated when compared to a conventional channel. This was attributed to the considerable change in thermo-physical properties of the flowing fluid because of large variation in liquid temperature along the length of microchannel. Compared with conventional theory, they found that fully turbulent flow is induced much earlier with Re of about 1000-1500 for liquid flow in microchannels.

Peng et al. (1994a and 1994b) experimentally studied friction flow and heat transfer characteristics of water flowing through rectangular stainless steel microchannels with hydraulic diameters (D_h) varying from 0.133 mm to 0.367 mm and with aspect ratios ($\propto$) ranging from 0.33 to 1.0. Under steady-state and fully developed flow conditions they conducted measurements for the liquid temperatures, the liquid flow rates, inlet and outlet pressures, wall surface temperatures and heat input to the substrate. To calculate the heat transfer coefficient (h) at the downstream end of the microchannel, two thermocouples were used for recording of the fluid temperature at the inlet of the microchannel ($T_{f,in}$), and three thermocouples were used for measuring the local wall temperature (T_w) at the downstream end. In their experimental studies, they showed that their results of both flow friction and heat transfer in microchannels deviated from the value predicted by the classical correlations (see Eqs. (2.5-2.11)), and also they observed that the laminar heat transfer occurred at a Re of 200 to 700, and that the fully turbulent convective heat transfer was achieved at a value of Re ranging from 400 to 1500. Their data analysis revealed that the flow was found to be most strongly affected by the D_h and $\propto$. For the laminar heat transfer regime, experimental Nusselt number (Nu) values were smaller than the predicted ones and they were dependent on the Reynolds number, Nu is being to $Re^{0.62}$. For the turbulent flow, the experimental Nusselt number were higher than those predicted although trend correctly captured by correlation. The heat transfer coefficient values for both laminar and turbulent flow regimes were changed significantly for different values of D_h and $\propto$. They reported an optimum value of $\propto$ as 0.75 for laminar and 0.5–0.75 for turbulent flows. The friction factor was found to be proportional to $Re^{-1.98}$ under laminar conditions and $Re^{-1.72}$ for turbulent flow.

Peng and Peterson (1996) also investigated experimentally the heat transfer coefficient (h) and Nusselt numbers (Nu) for single-phase forced convective heat transfer microchannel structures with small rectangular straight channels having hydraulic diameters between 0.133 mm and 0.367 mm. Water was employed as a working fluid with a relatively high velocity, ranging from 0.2 to 12 m/s, the Reynolds number spanned a range of pure laminar to highly turbulent cases, 50–4000. They created empirical heat transfer correlations for both the laminar and turbulent flow regimes which indicated that the geometric configuration of the microchannel heat sink (specifically the $\propto$, D_h, and the ratio of hydraulic diameter and microchannel centre to centre distance (D_h/W_c)) were very influential.

Poh and Ng (1998) carried out a numerical analysis of fluid flow and thermal resistance with a uniform wall heat flux and uniform inlet velocity in manifold microchannels. They used a commercial CFD package, ANSYS, to simulate the manifold microchannels of sixteen cases with different geometric parameters of the heat sink. Fluorocarbon liquid FX-3250 was used as the coolant and the flow was laminar. In their study the effects of channel geometries (width, height and length), wall heat flux and inlet velocity of the coolant were investigated and compared to an analytical model. The numerical results showed a very strong relationship between thermal resistance and inlet velocity. It was found that the thermal resistance of the heat sink decreased with increasing inlet velocity and channel depth. The numerical results were compared with available analytical results and found to be in good agreement.

A three-dimensional numerical study was conducted by Zhang et al. (2008) on the microchannel heat sink cooler. The commercial Fluent package was used to simulate the temperature distribution in MCHS under uniform and non-uniform heating source. In their study, water was chosen as the coolant with velocity varying from 0.01 m/s to 10 m/s. A comparison between two heating conditions was carried out, and the results showed that the heat sink has better heat dissipation character under uniform heating conditions. A new type of micro channel heat sink with various ranges in channel width was adopted to enhance the heat transfer under non-uniform heating conditions. They observed that the heat dissipation rate increased by about 10% with the narrower width channel at the same inlet velocity.

2.2.3.3 Inlet/Outlet Arrangements Effects

Flow maldistribution caused by improper channels and headers design can significantly effect on the thermal and hydraulic performance of the microchannel heat sinks. The fluid flow may enter and exit in different directions according to the inlet and outlet port locations. For example, it can enter in vertical direction and exits out to vertical or lateral direction or vice

versa. In this subsection, various types of flow arrangements in the heat sinks will be presented.

Five inlet flow configurations (namely I-, Z-,]-, L-, and Γ-arrangement) are investigated numerically by Lu and Wang (2006) to explore the influence of inlet locations on the hydrothermal performance of the multichannel cold-plates (see Fig. 2.2). The size of the cold-plate is fixed for all models with width, length and depth of 60 mm, 64 mm, and 7.8 mm, respectively. The corresponding inlet and outlet port diameter is 5.8 mm. They observed that]-flow arrangement displayed uniform flow distribution and lowest pressure drop with moderate heat transfer performance. In contrast, I- and Γ-flow configurations revealed the highest pressure drop and excellent heat transfer performance due to their impingement configurations. The Z- and L-flow arrangements showed deteriorate in heat transfer performance due to the flow maldistribution. These observations can be attributed to the flow-recirculation that eventually leads to a significant temperature difference along the surface of the cold-plate as well as flow maldistribution. These findings provoked the researchers to examine the effects of flow maldistribution on the microchannel heat sink performance.

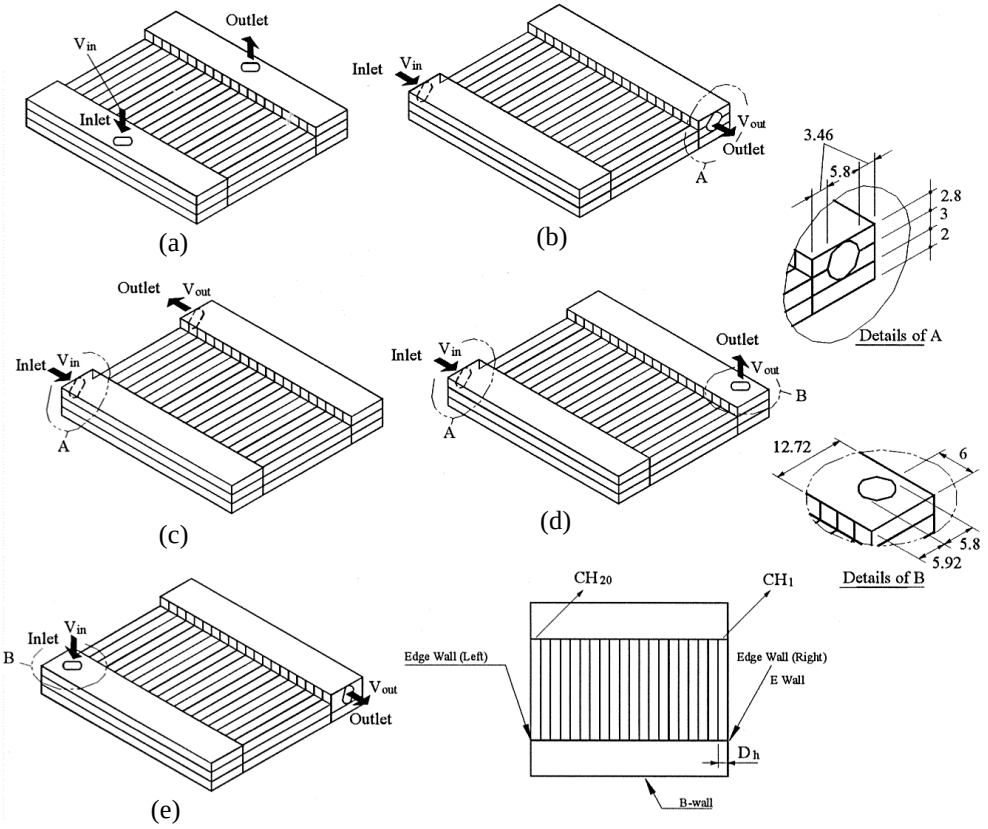

Fig. 2.2: Various inlet/outlet flow arrangements for: (a) I-type; (b) Z-type; (c)]-type; (d) L-type; and (e) Γ-type (Lu and Wang, 2006).

Chein and Chen (2009) carried out three-dimensional numerical study on the microchannel heat sinks with various inlet/outlet arrangements. They considered six inlet/outlet flow arrangements to inspect the fluid flow and heat transfer in microchannel heat sink including D, I, N, S, U and V-types as shown in Fig. 2.3. The size of microchannel heat sink is fixed with width, length and depth of 6.2 mm, 18 mm, and 0.5 mm, respectively, with microchannels dimensions of W_{ch} = 200 μm, H_{ch} = 400 μm, and L_{ch} = 10 mm. For horizontal inlet/outlet flow arrangements (D, I, N and S-type), their results revealed that the flow maldistribution is more pronounced in the microchannel heat sink which leads to temperature non-uniformity. This finding is ascribed to the manifestation of recirculation at the corners of dividing and combining manifolds. In contrast, the vertical flow inlet (V-type and U-type) arrangement revealed lower flow maldistribution, and this due to the effect of jet impingement at the manifold surface that suppressed the appearance of flow recirculation. Overall, it is found that the V-type heat sink has the best hydrothermal performance among the heat sinks studied. For all of the heat sinks studied (U-, V-, I-, N-, D-, and S-types), the highest heat sink temperature took place at the edge of the heat sink since there is no heat dissipation by fluid convection.

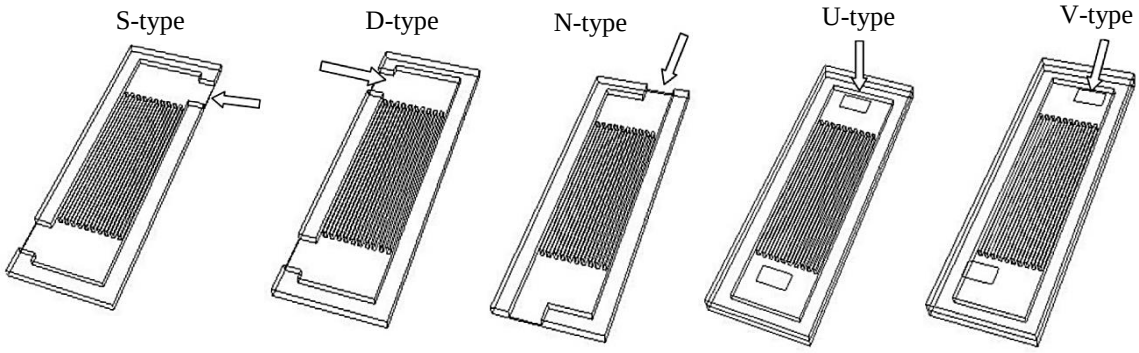

Fig. 2.3: Typical inlet/outlet configurations for S, D, N, U and V-arrangement of a straight rectangular microchannel heat sink (Chein and Chen, 2009).

Sehgal et al. (2011) experimentally explored the effect of different flow arrangements on the hydro-thermal performance of straight rectangular microchannel heat sink. Three different flow arrangements were considered (S-type, U-type, and P-type) as shown in Fig. 2.4. Three different heat fluxes of 125 W, 225 W, and 375 W are supplied at the bottom of the heat sink with Reynolds number ranging from 224 to 1121. The results indicated that the U-type flow arrangement demonstrated the maximum heat transfer followed by P-type and S-type. This is due to the fact that the U-type arrangement ensured the longest flow path and contributed to maximum heat absorption by the fluid. The S-type, on the other hand, is exposed to change in its direction in two bends which maximized the pressure drop more than other types. It is shown that the P-type flow arrangement is preferred in terms of having lowest pressure drop

with acceptable heat transfer performance, indeed it is the optimum one for practical applications.

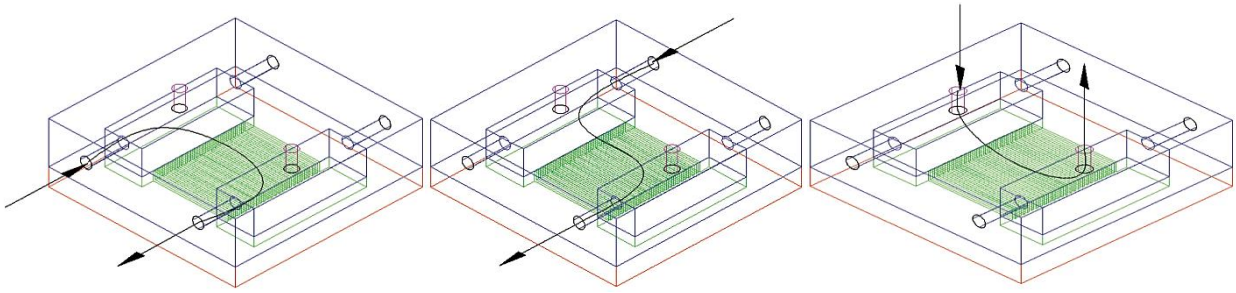

(a) (b) (c)

Fig. 2.4: Different flow arrangements in a straight rectangular microchannel heat sink: (a) U-type; (b) S-type; and (c) P-type (Sehgal et al., 2011).

Numerical studies were carried out by Vinodhan and Rajan (2014) on fluid flow and heat transfer characteristics in four new microchannel heat sink configurations consisting of four compartments with separate coolant inlet and outlet plenums for each compartment as shown in Fig. 2.5, to compare their performance with the conventional microchannel heat sink. At the same pumping power for a heat flux of 100 W/cm^2, it is found that the thermal resistances and temperature gradient of the substrate in the four new designs are lower than the thermal resistances in conventional heat sink.

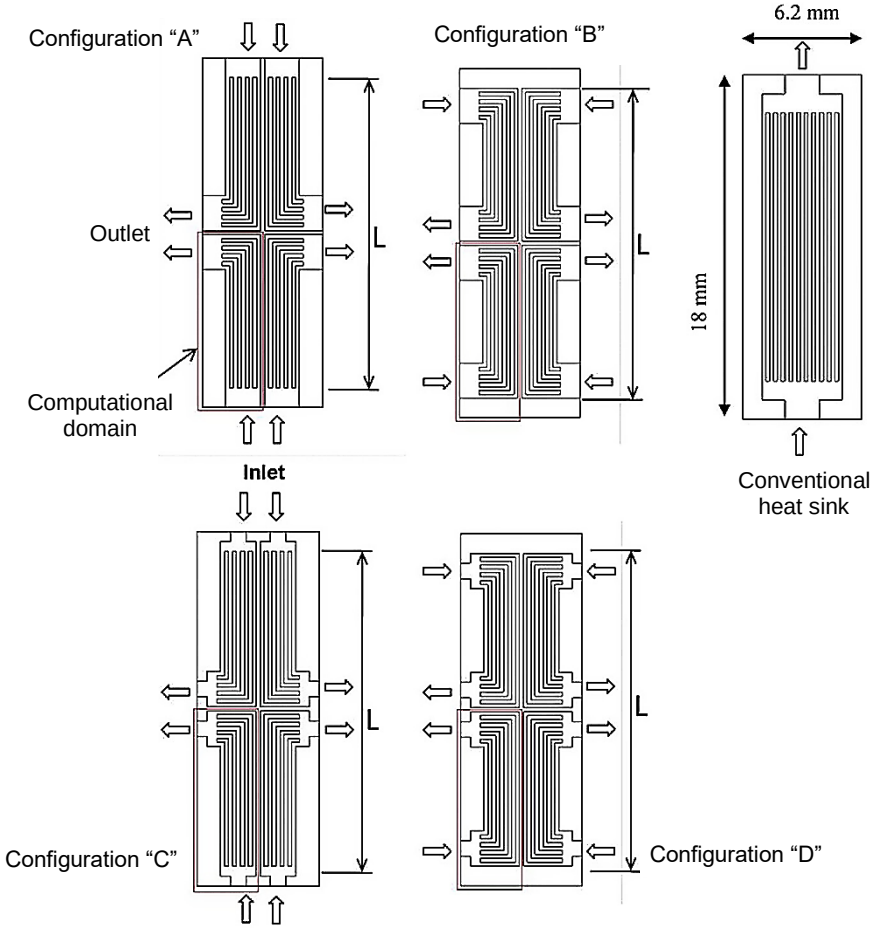

Fig. 2.5: Schematic diagram of heat sink configurations (Vinodhan and Rajan, 2014).

Anbumeenakshi et al. (2014) experimentally examined the flow distribution over a multiple microchannel with two different types of header geometries namely rectangular and trapezoidal with inlet flow arrangement at three different flow rates. Their experimental investigation was carried out with a micro channel setup having 25 numbers of rectangular channels of 0.42 mm width, 4.2 mm depth and 100 mm length. In their study, the computational fluid dynamics (CFD) simulation is done for inline flow by using the CFD software Fluent 6.3.26. The results were compared with experiments and found to be in good agreement. From the experimental results, it was found that micro channel with trapezoidal header gives less flow maldistribution when compared to rectangular header.

It can be concluded from the above studies that the performance of the microchannel heat sinks can be severely deteriorated by the flow maldistribution caused by inappropriate manifold design.

2.2.4 Nanofluid Flow in Microchannel Heat Sinks

One of the methods for enhancing heat transfer in the microfluidic cooling devices is the application of additives to the working fluid. Therefore, one possible route is increase the thermal conductivity of the working fluids. Nanofluids, i.e., dilute suspensions of nanoparticles in liquids (water, ethylene glycol, and oil), have been found to possess enhanced thermophysical properties, and it can enhance the convective heat transfer coefficient since has higher thermal conductivities and viscosities than the base fluids. Nanofluid consists of a base fluid such as water and nano scale metallic or non-metallic particles. The commonly used nanoparticles are metals – e.g., Cu, Au, Ag, Fe, Al, and Zn; metal oxides – e.g., Al_2O_3, CuO, Fe_2O_3, Fe_3O_4, SiO_2, TiO_2, and ZrO_2; carbide ceramics (SiC and TiC), nitride ceramics (AlN and SiN); carbon materials – e.g., carbon nanotubes, graphite, and diamond (Tullius et al., 2011 and Sundara et al., 2017). Nanoparticle suspensions in liquids have received great attention in recent years because the nanofluids having unprecedented stability of suspended nanoparticles were proven to be having anomalous thermal conductivity even with small volume fraction of the nanoparticles (Jung et al., 2009).

Lee and Mudawar (2007) experimentally investigated the heat transfer coefficient in the straight rectangular microchannels heat sink by using a nanofluid as the cooling fluid containing small solid particles of Aluminium oxide (Al_2O_3) mixed with water, where two volumetric concentrations of Al_2O_3 particles, 1% and 2%, were tested in their study. Twenty-one parallel rectangular microchannels were etched on the copper plate with width and length of 1 cm and 4.48 cm, respectively, while the cross-section area of the microchannel was 215

μm wide by 821 μm deep. Operating conditions for their study were as follows: Re = 140–941, total power = 100–300 W, water inlet temperature = 30 ^{o}C, inlet pressure = 1.17–1.36 bar, and outlet pressure = 1.12 bar. Both single- and two-phase convective heat transfer results were obtained.

Their measurements showed that the high thermal conductivity of nanoparticles significantly enhanced the heat transfer coefficient especially in the microchannel entrance region; while in the downstream fully developed region the enhancement was weaker, proving that nanoparticles have an appreciable effect on thermal boundary layer development. They found that there are 13% increase in heat transfer coefficient for 2% Al_2O_3 in water. Also, they concluded that increasing nanoparticle concentration increases single-phase pressure drop compared to that of water alone as the coolant at the same Reynolds number. However, increasing nanoparticle concentration does not have a clear influence on the friction factor. They noticed that increasing the heat flux has a very weak effect on the heat transfer coefficient for pure water, but an appreciable effect for the nanofluid and this effect was increased as the volumetric concentrations of Al_2O_3 within the nanofluid was increased. For single-phase turbulent flow regime, the heat transfer enhancement by using nanofluids becomes weak compared with that of single-phase laminar flow regime, because the heat transfer coefficient has a weak thermal conductivity dependence at high flow rate as well as decreased specific heat.

In the case of two-phase flow cooling, they proposed not to use nanoparticles in the microchannel heat sinks. Despite of small size of these particles, it is caused catastrophic failure for cooling system once boiling commenced by depositing into relatively large clusters near the channel exit due to localized evaporation. They filled the entire microchannels and prevented coolant from entering the heat sink.

Jung et al. (2009) measured the friction factor and convective heat transfer coefficient of Al_2O_3–water nanofluids with diameter of 170 nm in straight rectangular microchannels. Various particle volume fractions of nanofluids were examined in the experiments to investigate the effect of the volume fraction of nanoparticles (φ) on the fluid flow and convective heat transfer in microchannels. With a 1.8% volume fraction of Al_2O_3 in water, in the laminar flow regime, they found that the measured convective heat transfer coefficient increased up to 32% over that of the distilled water, with an acceptable increase for friction loss. With considering the volume fraction of nanoparticles, the measured data of the Nusselt number (Nu) for the various nanofluids of laminar flow regime in microchannels was correlated by the following equation:

$$Nu = 0.014\,\varphi^{0.095}\,Re^{0.4}\,Pr^{0.6} \quad (2.15)$$

Experiments were performed by Ho et al. (2010) to investigate the influence of using Al_2O_3–water nanofluid of 1 and 2 vol.% as the coolant on the forced convective cooling performance of a copper microchannel heat sink. The heat sink fabricated consisted of 25 parallel rectangular microchannels, and each microchannel had a length of 50 mm and a cross-sectional area of 283 μm in width by 800 μm in height. With the Reynolds number ranging from 226 to 1676, the hydrothermal performance of the nanofluid-cooled microchannel heat sink has been investigated in terms of the friction factor, the average heat transfer coefficient, the thermal resistance, and the maximum wall temperature. For the largest flow rate tested for the nanofluid of 1 vol.%, the measured data showed that the nanofluid cooled microchannel outperformed the water cooled microchannel, having significantly higher heat transfer rates (the average heat transfer coefficient increases by about 70%) and thereby marked reductions in the thermal resistance (reduced by about 25%) as well as in the maximum wall temperature were found. Despite the nanofluid-cooled heat sink markedly enhancing heat transfer rate due to the presence of the nanoparticles in water, the nanofluid of 1 or 2 vol.% Al_2O_3 flowing through the heat sink appeared to give only slightly increase in the friction factor.

Mohammed et al. (2011a) carried out numerical simulations on laminar nanofluids flow and heat transfer characteristics in triangular shaped microchannel heat sink made from aluminum. The performance of microchannel heat sink was examined by using water as a base fluid with different types of nanofluids such as Al_2O_3, Ag, CuO, diamond, SiO_2, and TiO_2 as the coolants with nanoparticle volume fraction of 2%. Based on their results, they found that diamond nanoparticles dispersed in water is preferable to attain overall heat transfer enhancement. In the other hand, Ag nanoparticles dispersed in water is recommended to achieve low pressure drop and low wall shear stress, compared with pure water.

Naphon and Nakharintrthe (2013) investigated experimentally the pressure drop and heat transfer characteristics of nanofluids cooling (Titanium Dioxide (TiO_2) particles with deionized water) in a mini-rectangular fin heat sink. The aluminium heat sinks with three different channel heights of 1, 1.5 and 2 mm were fabricated and the effects of the nanofluids inlet temperature, coolant Reynolds number and heat flux on the pressure drop and heat transfer characteristics of mini-rectangular fin heat sink were examined. It was found that average heat transfer rates obtained from nanofluids as coolant are higher than those for the deionized water as a coolant at the same operating conditions. Also, they showed that the heat flux has an insignificant effect on the pressure drop of the nanofluids, where pressure drop decreased slightly as heat flux increases and this due to nanofluids viscosity.

Although adding nanoparticles to a base fluid can influence the cooling process positively, there are still challenges. Overall, these fluids leave sedimentation of particles, fouling, erosion, high pressure drop, and may even clog the channel over time.

2.2.5 Micro Pin–Fins and Offset-Strip Fins

Micro-scale pin–fins with different shapes such as circles, squares, rhombus, elliptical, eye-shaped, and sine-shaped cross sections that protrude out of the surface have shown significant improvements in removing heat. These usually made from materials have high thermal conductivity such as silicon, aluminium and copper. Using this type of pin-fins can increase the wall surface area, and interrupt the steady flow of the fluid allows better flow mixing and as a result, enhanced heat transfer. To improve the thermal heat transfer performance, micro pin-fins can take different shapes and sizes and be placed in different patterns (aligned and staggered).

Peles et al. (2005) investigated experimentally the convective heat transfer and pressure drop across a pin-fin micro heat sink by comparing its thermal resistance with that of a microchannel heat sink (see Fig. 2.6). They discovered that the thermo-hydraulic performance of a cylindrical micro-pin-fin heat sink is superior to that of a microchannel heat sink as very high heat fluxes can be dissipated with low wall temperature rises across the heat sink. Their results showed that for fin diameters larger than 50 μm, the thermal resistance is less sensitive to changes in the fin diameter and for increased efficiency short pins should be used.

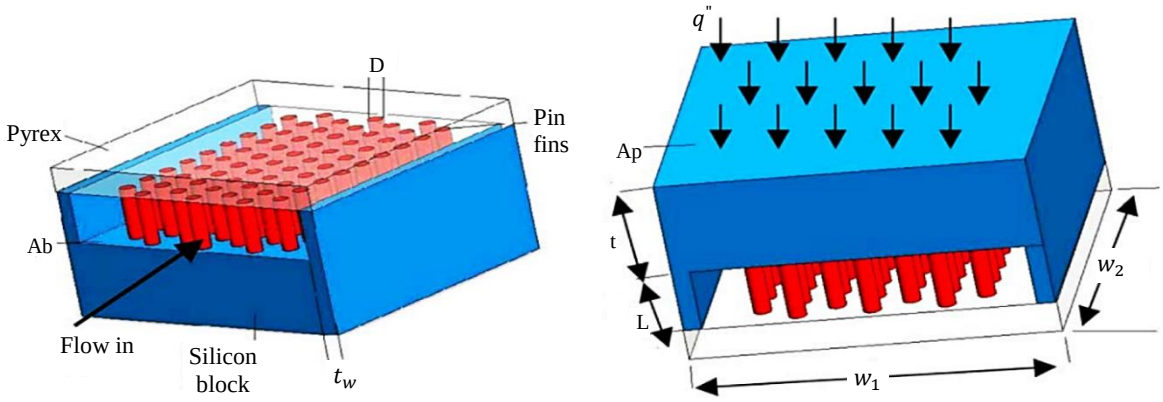

Fig. 2.6: 3-D schematic view of micro pin fin heat sink suggested by Peles et al. (2005).

Colgan et al. (2007) tested an offset strip fin silicon microchannel cooler for a single phase flow bonded to a high power chip with power density of 300 W/cm^2 (see Fig. 2.7). In their study, the offset strip fin microchannels offer enhancements in heat transfer several times higher than a plain microchannel, depending on the fin length, but this was at the expense of increased pressure drop. To keep the pressure drop reasonable, shorter flow lengths were used by using multiple entry and exit ports.

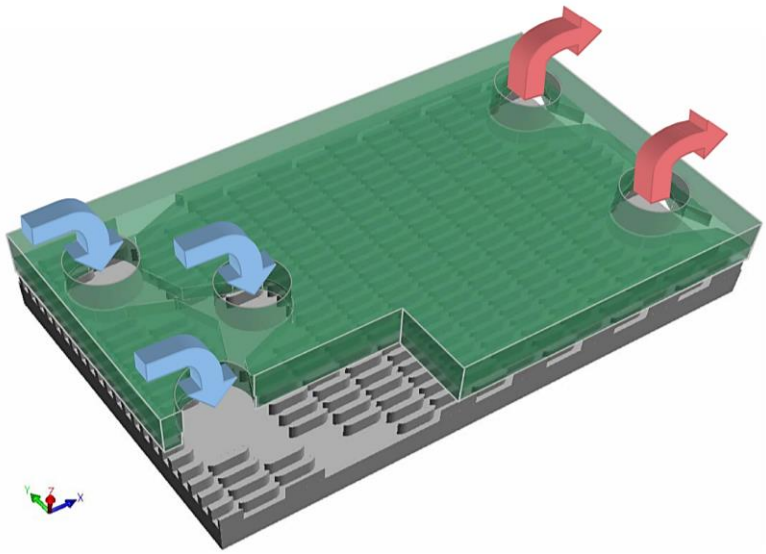

Fig. 2.7: 3-D rendering of assembled microchannel cooler (Colgan et al., 2007).

Experimental studies of single phase flow through micro pin-fin heat sinks have been conducted by Siu-Ho et al. (2007) and Qu and Siu-Ho (2008a and 2008b) to study the heat transfer and pressure drop characteristics. The heat sink model that they used in their work was composed of an array of 1950 staggered square micro-pin-fins with a cross section area of 0.2 × 0.2 mm^2 and a height of 0.67 mm. They tested the model at various inlet water flow velocities with Reynolds number varying from 93 to 634 (Siu-Ho et al., 2007) and 46 to 180 (Qu and Siu-Ho, 2008a and 2008b) with two different temperature of 30 ºC and 60 ºC. According to their experimental results, Qu and Siu-Ho (2008a and 2008b) proposed two new heat transfer correlations for the low Re range ($Re < 1000$) which showed much better accuracy as shown:

$$Nu_{avg} = 0.0285\, Re_{avg}^{0.932} Pr_{f,avg}^{1/3} \tag{2.16}$$

$$Nu_{avg} = 0.0241\, Re_{avg}^{0.953} Pr_{f,avg}^{0.36} \left(\frac{Pr_{f,avg}}{Pr_{w,avg}}\right)^{0.25} \tag{2.17}$$

where Re_{avg} is the average Reynolds number, while $Pr_{f,avg}$ and $Pr_{w,avg}$ are respectively the water Prandtl numbers at average water bulk temperature and at average micro-pin-fin base temperature. The term $\frac{Pr_{f,avg}}{Pr_{w,avg}}$ in Eq. (2.17) represents a property correction factor to account for the effect of fluid property variation on heat transfer. Local Nusselt numbers were predicted with a mean absolute error (MAE) of 13.7% and 13.0% respectively for the two new correlations. A new correlation was proposed for the friction factor in the micro-pin-fin array (f_{fin}), and good agreement is achieved with MAE of 6.9% as:

$$f_{fin} = 20.09\, Re^{-0.547} \tag{2.18}$$

An experimental study was carried out by Nguyen et al. (2007) on the copper pin fin heat sink to investigate the behaviour and heat transfer enhancement of a nanofluid (namely, Al_2O_3 nanoparticle – distilled water mixture). The experiments were conducted within the single phase turbulent flow regime with two different particle average diameters and various volume concentrations. From the experimental data obtained, they observed that the heated block average temperature has considerably decreased with an increase of particle volume concentration. For example, at a given mass flow rate of 0.06 kg/s, the heated block average temperature has as approximate values, 40.9 ^oC, 39.3 ^oC, 38.7 ^oC and 37.3 ^oC, respectively for water and nanofluids with 1%, 3.1% and 6.8% particle concentration. Additionally, for a particle volume concentration of 6.8%, the heat transfer coefficient increased around 40% compared to that of the distilled water. The influence of particle size on nanofluid heat transfer behaviour was also studied, and the comparison was performed only for the particular particle volume concentration of 6.8%. The experimental results showed that a nanofluid with smaller particle size does provide a better heat transfer. For two different particle average diameters, a nanofluid with 36 nm particle size provides higher convective heat transfer coefficients than the ones given by nanofluid with 47 nm particles.

The efficacy of nanofluids containing copper oxide (CuO) nanoparticles in water as coolants has been investigated experimentally and numerically by Pantzali et al. (2009) in a similar miniature plate heat exchanger to that used experimentally by Nguyen et al. (2007). First, the thermophysical properties (i.e., thermal conductivity, heat capacity, viscosity, density and surface tension) of a typical nanofluid (CuO in water, 4% Particle volume fraction) were measured. The thermo-hydraulic behaviour of the miniature plate heat exchanger was also simulated using a CFD code and then compared with that of the flat plate (without pin fins), and the prediction results were in very good agreement with the experimental measurements. The results predicted showed that the presence of the nanoparticles greatly affects the properties of the base fluid (i.e., water). The measurements revealed that the increase in the thermal conductivity was accompanied by a significant decrease in specific heat capacity and an increase in viscosity. For example, with respect to the water at a temperature of 25 ^oC, the thermal conductivity of a nanofluid increases by about 10%, the specific heat capacity decreases by 20% and the viscosity is significantly higher (almost 100%). They found that at a given heat load, the nanofluid volumetric flow rate required for a given load is lower than that of water causing lower pressure drop. For example, at the specific heat load of 90 W, the water and nanofluid volumetric flow rates required were 11 and 3 *ml/s*, respectively, while the pressure drop produced was 240 Pa and 45 Pa, respectively. For all cases studied, it was observed that the nanofluid flow rate required is up to 4 times lower (compared to water)

while the respective pressure drop is up to 6 times lower, and thus less pumping power required.

A numerical study was performed by Seyf and Feizbakhshi (2012) on single-phase heat transfer and pressure drop of two types of nanofluids (Al_2O_3–water and CuO–water) in a circular micro-pin-fin heat sink. The effects of Reynolds number, volume fraction, type and size of nanoparticles on thermal and hydrodynamic behaviour of system have been studied. The results showed that the transition from laminar to turbulent flow occurs very early ($Re \sim 100$) compared with the flow in ordinary pin-fins arrays. For both types of nanofluids, it is found that the Nusselt number increases with increasing volume fraction, because the heat transfer coefficient is proportional to the thermal conductivity of coolant, which is increasing with volume fraction of the nanoparticles. At Reynolds number ranging from 25 to 75, it demonstrates that adding low volume fraction of nanoparticle (0.01-0.04) to the base fluid (deionized water) leads to significant increase in Nusselt number between 1.62%–4.5% and 8.37%–11.44% for Al_2O_3 with particle diameter of 47 nm and CuO with particle diameter of 29 nm nanoparticles, respectively, as shown in Fig. 2.8. However, with increasing particle volume fraction the nanofluid viscosity increases, thus thicker boundary layer thicknesses on pin fins will be formed with a corresponding reduction in convection. With decreasing particle diameters the Nusselt number increases for Al_2O_3–water nanofluid while the trend is reverse for CuO–water nanofluid. This is due to the fact that for CuO nanoparticles decreasing the diameter of nanoparticles leads to decreasing thermal conductivity of nanofluids.

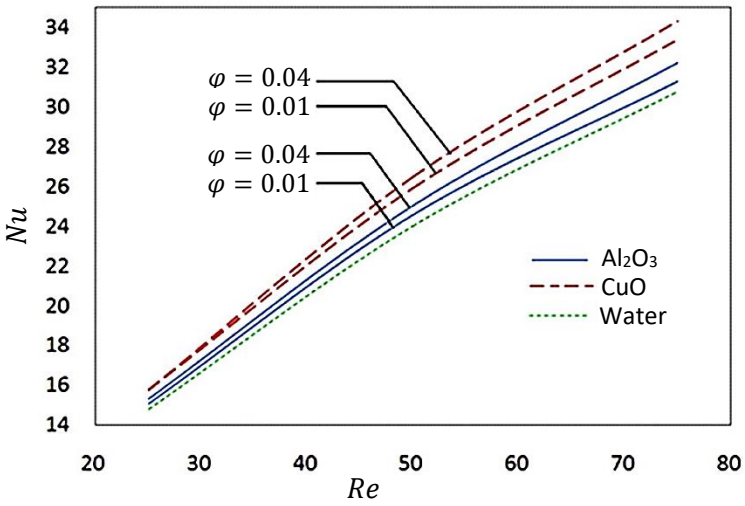

Fig. 2.8: Effect of nanofluid volume fraction on Nusselt number at different Reynolds number (Seyf and Feizbakhshi, 2012).

Online and offset micro pin-fin heat sinks arranged in variable fin density configurations were studied numerically by Rubio-Jimenez et al. (2013) to cool 10 × 10 mm^2 integrated chip (IC).

Each configuration consists of three zones (SI, SII, and SIII) with different fin densities as shown in Fig. 2.9. Water was used as the coolant in the single phase and laminar flow regime under nondeveloped flow conditions. The cooling system is formed by 4748 flat fins with rounded sides having a radius of 25 μm placed on a 200 μm thick silicon substrate, which are distributed in three different sections along the flow length. The fin width, length, and height are 50, 100, and 200 μm, respectively. These fins are formed on a microchannel heat sink has 33 rectangular channels with aspect ratio of 1.0 and space between channels 100 μm.

The results revealed that the cooling system using the offset micro pin-fin configuration can achieve a thermal resistance as low as 0.1 K/W with a pumping power requirement of 0.45 W. Furthermore, it is observed that the offset fin configuration produces a more uniform substrate temperature profile compared with online fin configuration, and this belongs to that a large part of fluid in the online fin configurations passing through the straight gaps between the fins. Thus, the interaction between the coolant and the walls of the fins is significantly reduced, affecting the heat diffusion. From the results obtained, it is shown that the offset micro pin-fin configuration is not recommended for cooling systems that required thermal resistance < 0.1 K/W because of their large increase of the pressure drop.

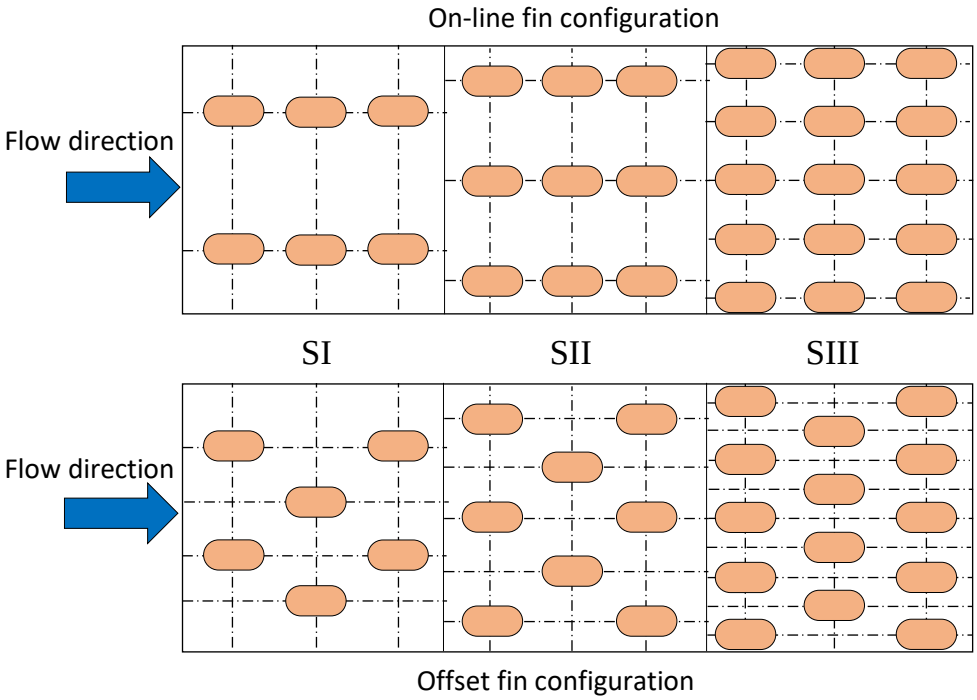

Fig. 2.9: Online and offset micro pin-fin heat sinks (Rubio-Jimenez et al., 2013).

An experimental and numerical investigation was conducted by Yu et al. (2016a) for single-phase fluid flow and heat transfer in a microchannel with Piranha Pin Fins (PPFs) as shown in Fig. 2.10. In their study, and depending on the channel hydraulic diameter, the Re varied from 508 to 2114. Numerically, a conjugate convection/conduction heat transfer model was

developed within COMSOL Multiphysics, which the pressure drop and Nu predictions showed good agreement with experiments. Friction factor and Nusselt number obtained from the PPF heat sinks were compared with available correlations for conventional straight and pin fin channels.

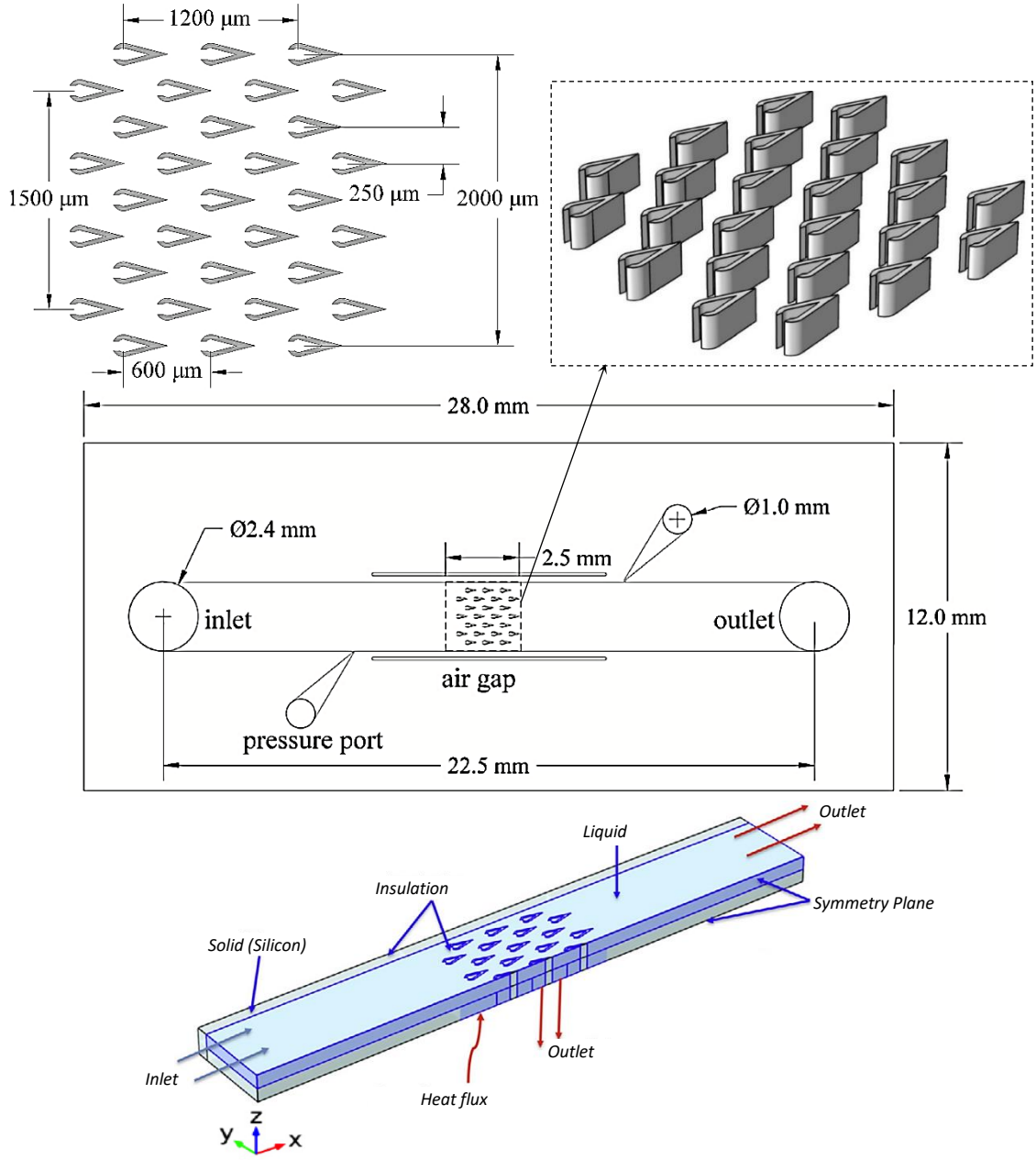

Fig. 2.10: Dimensions of the test device with enlarge for the PPF arrays and silicon-based microchannel with PPFs (half of the channel) (Yu et al., 2016a).

From the results obtained, it is found that the friction factor for the PPFs heat sink is larger than for a plain channel. However, it is still much smaller than the friction factor predicted from most correlations developed for channels with pin fins (Kosar et al., 2005) and previous existing studies such as Chilton and Generaux (1933); Jacob (1938); and Metzger et al. (1982). Also, it is shown that the microchannel with PPFs enhances heat transfer due to the

larger area for heat spreading and interfacing with a cold fluid. Additionally, the extruded PPFs disturbed the velocity field, and the subsequent separation and mixing further enhances heat transfer.

An experimental and numerical study was carried out by Yang et al. (2017) for an array of microchannel heat sinks with five different staggered pin-fin configurations, namely triangle, square, pentagon, hexagon and circle geometries. A uniform heat flux was applied at the top surface of the microchannel heat sink, and deionized water was used as the coolant. The results showed that the lowest thermal resistance and uniformity of the chip's top surface was found with a staggered hexagonal cross section pin fins and the lowest pressure drop with the staggered circular cross section pin fins because of the channels distribution that provides continuous and stable flow. For pin fins with staggered triangular cross section, it is found there are maximum blocking effects for the coolant flowing happened because of the narrowest channel between the adjacent triangle pin fins and the biggest back side area, which leads to an increase in the pressure drop.

2.3 Heat Transfer Augmentation Techniques

From the literature described above, it is found that the conventional straight rectangular microchannel heat sinks suffering from an increase in surface temperature along the flow direction, and this rise in surface temperature limits the efficiency of this type of the microchannel heat sinks; and to enhance the convective heat transfer and achieve a more homogeneous temperature distribution methods for disrupting the flow are needed to reinitialise both the hydrodynamic and thermal boundary layers.

One may consider the use of augmentation techniques to satisfy any of the following thermal-hydraulic objectives: (1) to reduce prime surface area, (2) to reduce the approach temperature difference for the process streams, (3) to reduce pumping power consumption, or (4) to increase heat transfer capacity. Generally, heat transfer augmentation mechanisms can be classified into three broad categories: (i) active method, (ii) passive method, and (iii) compound (hybrid) method (Bergles, 2001).

Those which require external power input to maintain the heat transfer enhancement mechanism are named active methods. On the other hand, the passive enhancement methods are those which do not require external power to sustain the enhancements' characteristics, those method are mostly consist of increasing the transfer surface area. Compound method is a combination of above two methods. Since the external power is not easy to provide in several applications, active method has not shown much potential owing to complexity in design. Some examples of active methods are well stirring the fluid or vibrating the surface

(Nesis et al., 1994), using a magnetic field to disturb the seeded light particles in a flowing stream, electrostatic fields, jet impingement, and induced pulsation by cams and reciprocating plungers, etc. Examples of passive enhancing methods are smooth surfaces, rough surfaces, extended surfaces, displaced enhancement devices, additives for fluids, coiled tubes, and many others (Siddique, 2010). The compound method involves complex design and hence has limited applications.

Passive techniques, where inserts are used in the flow passage to augment the heat transfer rate, are advantageous and more attractive compared with active techniques, because no power is required to facilitate the enhancement and the insert manufacturing process is simple (Rainieri et al., 2014), and these techniques can be easily employed in an existing microchannel heat sinks. Therefore, in this section, a review on progress with the passive augmentation techniques that employed on the microchannel heat sinks will be presented.

2.3.1 Corrugated Channels

Corrugated channels such as wavy, zig-zag, serpentine and convergent-divergent, are one of the important applications in the field of passive heat transfer augmentation methods. Using this technique a significant enhancement in the flow mixing between hotter fluid layers near channel wall and cooler fluid layers in core region is demonstrated (Ghani et al., 2017a). The following sub-sections briefly explain their operational principles.

Tsuzuki et al. (2007) used CFD to optimize the geometry of wavy, zigzag and S-shaped fins. In their study, the parametric dependence of fin angle, guiding wing, thickness, length, and roundness were studied. They evaluated the thermal and hydraulic performance by calculating the heat transfer and pressure drop, and showed that the fin angle was the most influential parameter on the performance of the microchannel heat exchanger.

A numerical study has conducted by Sui et al. (2010) on the laminar water flow and heat transfer in three-dimensional wavy microchannels with rectangular cross sections under constant wall heat flux, constant wall temperature and conjugate conditions (see Fig. 2.11). In their study, the Navier-Stokes equations have been solved using the general-purpose finite-volume based CFD. To analyze the fluid mixing, the dynamical system technique (Poincaré section) is employed. The simulation results stated that the secondary flow (Dean vortices patterns) may change considerably along the flow channel direction when liquid coolant flows through the wavy microchannels, leading to chaotic advection as suggested by Poincaré sections, which can greatly enhance the convective fluid mixing, and thus the heat transfer performance with a much smaller pressure drop penalty, as compared to straight baseline microchannels.

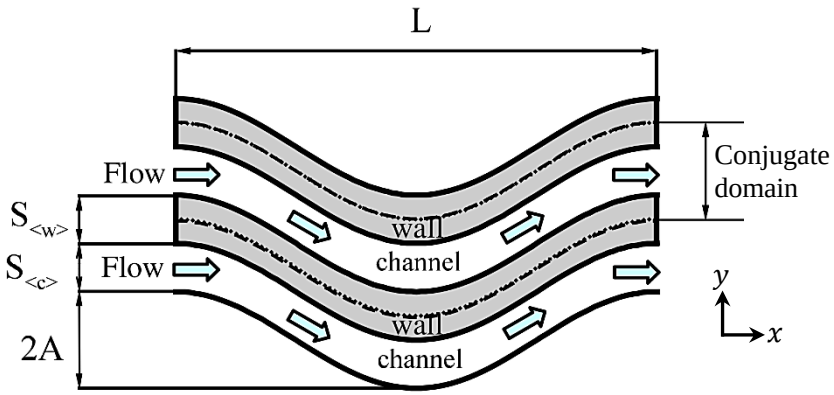

Fig. 2.11: Cross section view of wavy MCHS (Sui et al., 2010).

Extending this study, Sui et al. (2011) carried out experiments on the heat transfer and flow friction using deionized water as the working fluid on three wavy microchannels with rectangular cross sections. The width and depth of test pieces were 205 μm and 404 μm respectively with different wavelengths (magnitude 0, 138 and 259 μm). Each test piece is made of copper and contains 60 – 62 wavy (Sinusoidal) microchannels in parallel. The Reynolds numbers ranged from approximately 300 to 800. They compared the heat transfer performance of the wavy microchannels with straight microchannels and concluded that wavy microchannels had superior heat transfer performance than straight microchannels. Three-dimensional conjugate simulations for similar experimental conditions are also carried out, and the simulation results are compared with experimental data, the numerical results agree reasonably well with experimental data.

Numerical investigation of laminar forced convective heat transfer was performed in two types of a 3D wavy microchannel heat sinks by Gong et al. (2011), including serpentine wavy microchannels and raccoon wavy microchannels with rectangular cross-section having hydraulic diameter of 500 μm. They studied the effect of wave amplitude, wavelength, and inverse aspect ratio ($\propto^* = H_{ch}/W_{ch}, H_{ch} > W_{ch}$) for three different Reynolds numbers (50, 100 and 150) on the heat transfer performance. In both wavy microchannels, it shown that the performance factor improved by increasing Reynolds number and wave amplitude and decrease in wavelength.

For serpentine wavy microchannel heat sinks, the maximum velocity got shifted from the centreline towards the trough and crest regions, which caused a reduction of thermal boundary layer thickness and enhanced the heat transfer as shown in Fig. 2.12. Additionally, it is observed that the boundary layers thickness was reduced at increasing the $\propto^*$. For raccoon wavy microchannel heat sink, vortices and secondary flow at the furrows were formed which in turn enhanced the heat transfer as illustrated in Fig. 2.13. In general, it was observed that the performance factor of serpentine wavy configuration is discerned to be superior over the

raccoon wavy configuration due to a lower rise in the pressure drop in the former case compared to the heat transfer improvement.

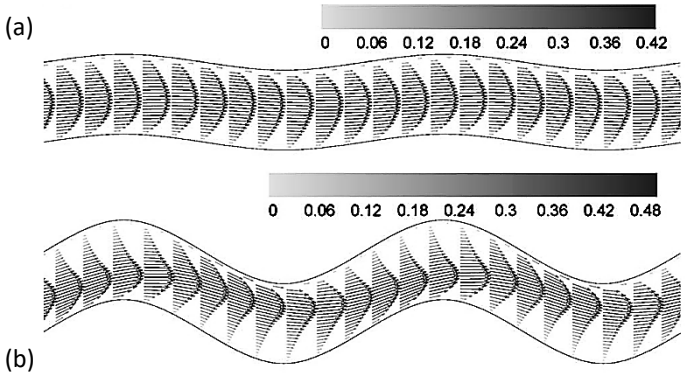

Fig. 2.12: Velocity vectors for serpentine wavy microchannel; a) A=50 µm; and b) A=200 µm (Gong et al., 2011).

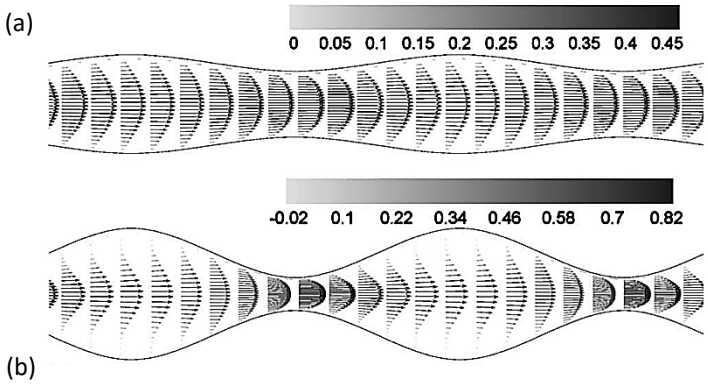

Fig. 2.13: Velocity vectors for raccoon wavy microchannel; a) A=50 µm; and b) A=150 µm (Gong et al., 2011).

Mohammed et al. (2011b) investigated numerically the water flow characteristics and heat transfer in wavy microchannel heat sink with various wavy amplitudes from 125 to 500 µm. This study considered Reynolds numbers ranging from 100 to 1000. The results show that the wavy microchannel has better heat transfer performance than the straight microchannels. It was also found that as the wavy amplitude decreases, the temperature of the microchannel heat sink increases and it is lower than the straight micro channel heat sink.

Another numerical analysis using finite volume method (FVM) for water flow based microchannel heat sink to solve the three-dimensional steady and conjugate heat transfer governing equations has been carried out by Mohammed et al. (2011c). The performance of microchannel heat sink for different channel shapes such as zigzag, curvy, and step microchannels was compared with straight and wavy channels (see Fig. 2.14). Temperature profile, heat transfer coefficient, pressure drop, friction factor, and wall shear stress were used as parameters for analyzing the performance of microchannel heat sink. As expected the

pressure drop penalty for all the studied channel shapes was higher than the conventional straight micro channel heat sink.

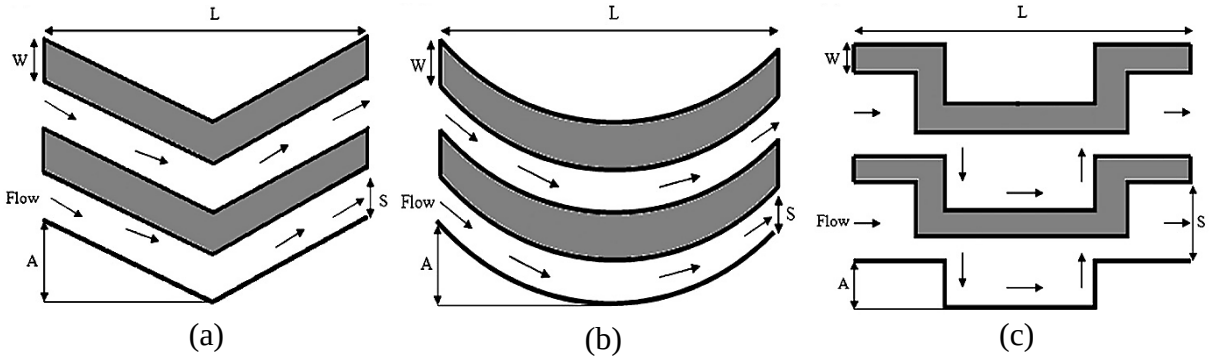

Fig. 2.14: A schematic view of a heat sink unite with (a) zigzag channels; (b) curvy channels; and (c) step channels (Mohammed et al., 2011c).

A numerical simulation was carried out by Fan and Hassan (2011) to investigate the cooling performance of a swirl microchannel heat sink (see Fig. 2.15). Copper was used for this novel module that which enhanced the cooling of uniform heat flux through multiple swirl microchannels positioned on a circular flat plate. The channel depth and width are fixed as 0.5 mm and 0.4 mm, respectively. The heat flux was supplied from the bottom of a swirl microchannel heat sink which varied from 10 W/cm^2 to 60 W/cm^2 with inlet velocities of 0.5 m/s and 1 m/s. The effects of channel curvature and channel number were studied and compared with a straight channel. It was observed that increase in curvature and channel number improved the cooling performance of the heat sink by enhancing temperature uniformity. Pressure drop decreased at higher channel number because of the reduction in velocity in the channel.

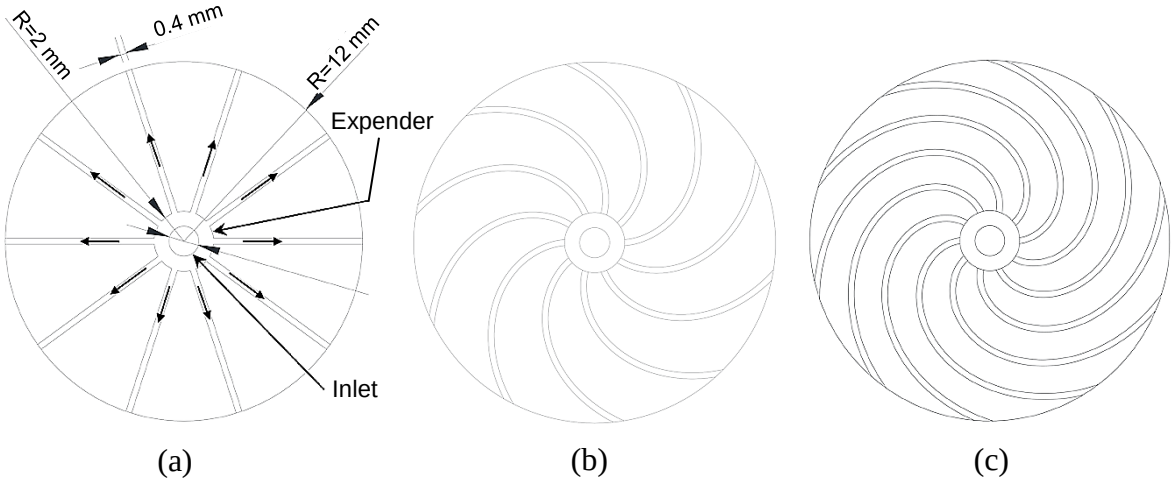

Fig. 2.15: A schematic view of a swirl MCHS with (a) straight channels; (b) Cω3; and (c) Cω5 (Fan and Hassan, 2011).

Chu et al. (2012) experimentally and numerically investigated the behaviour of deionised water through curved rectangular microchannels for Reynolds numbers ranging from 10 to 600 with different aspect ratios ($\propto$) and curvature ratios (D_h/R_c), where R_c is the curvature radius. Six different curved rectangular microchannel chips with different geometric parameters were designed and fabricated on the silicon substrate. The experimental data were compared with the numerical predictions and the available empirical correlation from previous studies of curved and straight microchannels. Over a range of channel sizes and flow rates the average discrepancy between the experimental data and numerical predictions was 8%, and this due to the uncertainties in mass flow rate and configuration. At the same inlet flow rate, it is observed that increasing the channel curvature radius (R_c) while keeping the same $\propto$ leads to a larger increase in the pressure drop. Within $\propto$ ranging from 0.5 to 1 and $100 < Re < 600$, the predicted values from the empirical correlation proposed by Hua and Yang (1985) for friction factor in curved channels that shown in Eq. (2.19) were in good agreement with those obtained from the experimental data. However, more deviation was observed with microchannels for $\propto$ in the range of 0.1–0.2, since Eq. (2.19) was based on data obtained for a square channel. Also, it was observed that the main flow velocity of the inner part of the curved microchannel with $\propto$ varying from 0.5 to 1 was lower compared with that of the outer part, and this attributed to the centrifugal forces produced by the channel curvature pushing the water flow from the centre of the microchannel to the outside of it.

$$f = \frac{5}{Re^{0.65}}\left(\frac{W_{ch}}{2R_c}\right)^{0.175} \tag{2.19}$$

Li et al. (2013) conducted a numerical study to optimize a serpentine microchannel heat sink. A CFD package was used for simulations using water as the coolant. In their study, they developed a simple thermal resistance network model to investigate the total thermal performance of the serpentine microchannel heat sink. A correlation of pressure loss coefficient for 180 degree sharp bend was obtained which was function of the inverse aspect ratio, $\propto^*$, (ratio of channel height to channel width) which ranging of ($1 < \propto^* < 6$) and ratio of fin width to channel width, β, ($0.25 < \beta < 2$) at different Reynolds number ranging at ($1000 < Re < 2200$). Next, a multi-objective genetic algorithm was carried out to minimize the total thermal resistance and pressure drop of the serpentine MCHS with fixed length, the width and base substrate of microchannel heat sink, and they obtained good agreement with the results of numerical calculation.

Yong and Teo (2014) carried out an experimental and theoretical study and used CFD simulations to investigate the fully-developed flow and heat transfer in periodic converging-diverging channels with rectangular cross sections. The heat sink in their study consisted of

15–20 of such converging-diverging passages, with each passage also containing 15–20 converging-diverging repeating units, and the wavelength has been kept constant at 1.5 mm (see Fig. 2.16). Heat transfer simulations have been conducted under constant wall temperature conditions using liquid water as the working fluid. They investigated the effects of channel aspect ratio on the respective flow behaviour and transformation of the recirculating vortices, and their results showed that the optimal channel aspect ratio ranges from 0.5 to 1.0.

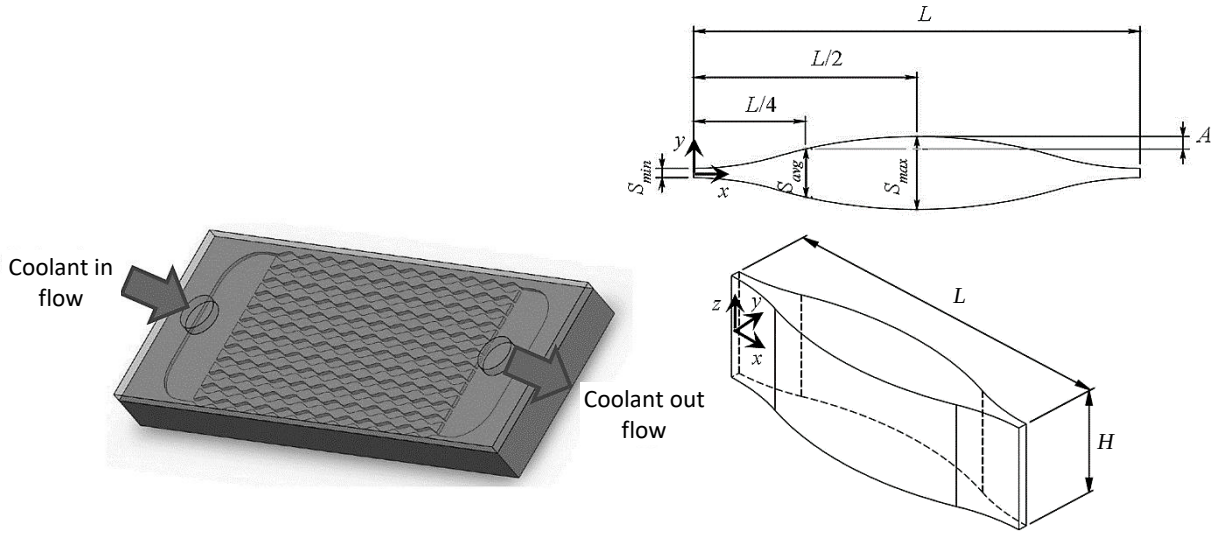

Fig. 2.16: 3-D and cross section view for MCHS design containing converging-diverging flow passages (Yong and Teo, 2014).

Also, they studied the heat transfer enhancement and pressure drop penalty for converging-diverging channels of various amplitude ratios with constant curvature and sinusoidal profiles. They claimed a 60% improvement in the overall thermal-hydraulic performance compared to the straight microchannels. It was observed a pair of symmetrical recirculating vortices formed in both the upper and lower furrows of the channel as shown in Fig. 2.17, and these recirculating vortices lead to enhance the fluid mixing, and thus convective heat transfer rates.

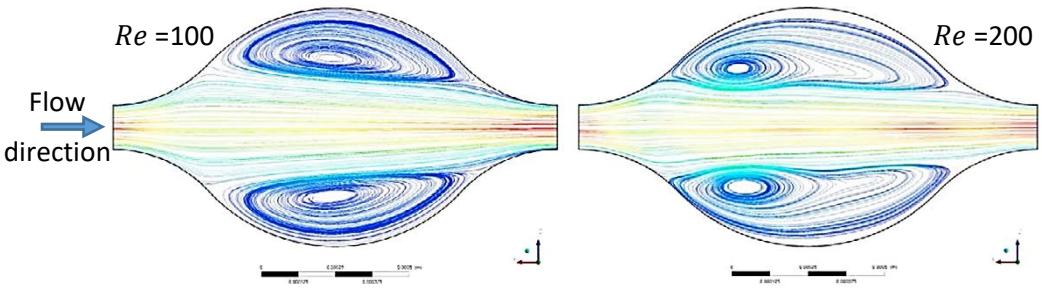

Fig. 2.17: Numerical results for streamline plots at Re =100 and Re =200 (Yong and Teo, 2014).

Recently, Gong et al. (2016) studied numerically the characteristic of fluid flow and heat transfer of the three wavy microchannels with dimples placed in the microchannel base. The three different configurations of wavy microchannels proposed were compared with the wavy microchannel without dimples and with straight microchannel. The prediction results showed that the local Nusselt number in the wavy microchannels is increased especially in the throat regions, which causes an increase in the speed of the fluid and creates a high velocity gradient near the wall as illustrated in Fig. 2.18. Overall, Channel I provides the best thermal performance, which shows that using a dimpled structure in the throat of a channel is useful for enhancing heat transfer in wavy mirochannel heat sinks.

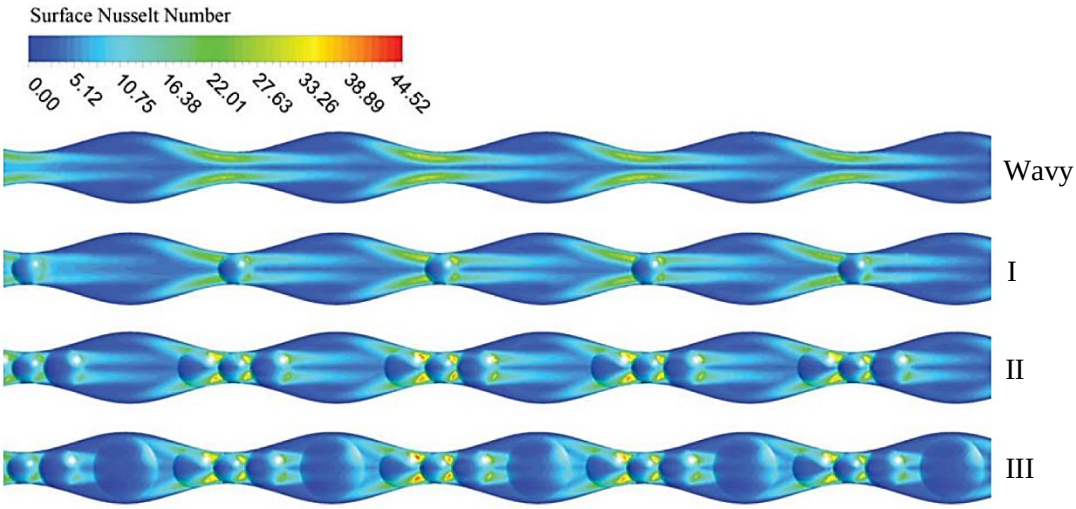

Fig. 2.18: Local Nusselt numbers of a wavy and a wavy microchannel with dimples (Gong et al., 2016).

2.3.2 Flow Disruption

By introducing flow disruption techniques, the hydrodynamic and thermal boundary layers development in microchannel heat sink can be disrupted. Flow disruption can trigger flow instabilities which are responsible for increased flow mixing and enhancement of heat transfer. Recently, dedicated efforts are made to utilise the appropriate geometrical modifications to the side walls of the conventional microchannels for promoting the flow instabilities and improved mixing. Periodic disturbance promoters such as offset strip fins, interrupted-wall channel, reentrant cavities, grooves, ribs and combinations between ribs and grooves simultaneously along the flow direction are shown to be effective flow disrupters. These techniques can create a secondary flow and disrupt the growth of the boundary layer, enhanced mixing of flow at the leading edge resulting in an increased heat transfer.

Greiner et al. (1991) and Wirtz et al. (1999) examined the influence of V-grooved microchannels on both heat transfer and pressure drop. From their studies, they found that

both Nusselt number and pressure drop are larger than for flat channels. Kandlikar and Grande (2004); Steinke and Kandlikar (2004); and Steinke and Kandlikar (2006a) suggested several techniques to promote heat transfer in microchannel heat sinks including increasing the surface area of heat transfer and improve mixing flow using interrupted and staggered strip-fin designs. Among these, two techniques have been proposed by Steinke and Kandlikar (2004) to generate secondary flow in a microchannel heat sink. Fig. 2.19(a) shows one of their proposed designs with cross mixing of adjacent liquid streams. They suggested to add smaller secondary channels which induce flow between the main channels, this technique can be applied by various kinds of fins and plates arrangement. While the second makes use of the Venturi effect as shown in Fig. 2.19(b). Both methods enhance the convective heat transfer by increasing fluid mixing without inducing significantly larger pressure losses.

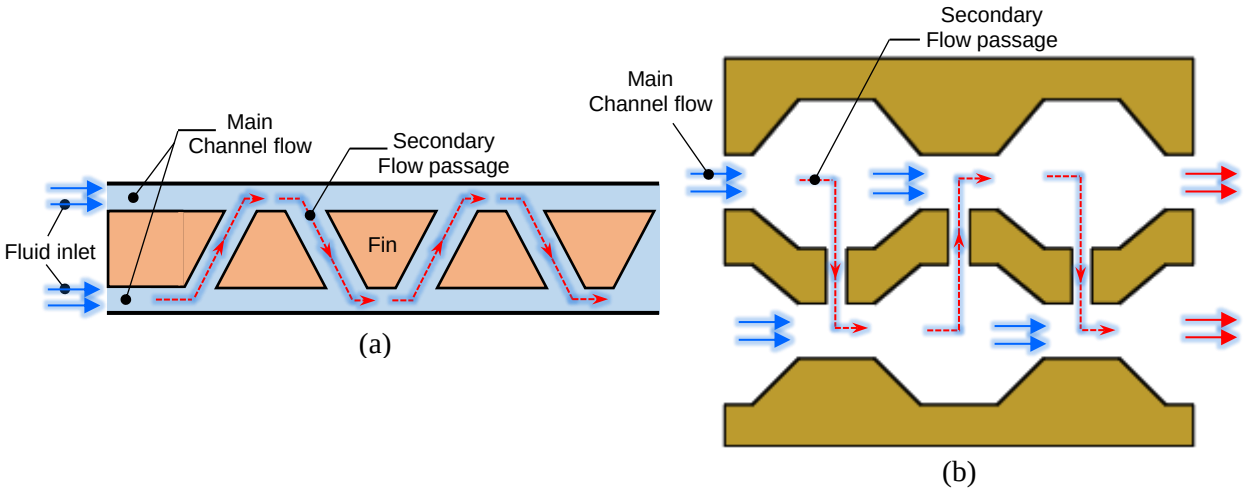

Fig. 2.19: Schematic view for MCHS proposed by Steinke and Kandlikar (2004) for: (a) Secondary flow channels; and (b) Venturi based secondary flow.

Advanced microchannel structures, such as stacked microchannels (Joshi and Wei, 2005), double-layered microchannels (Leng et al., 2015), tree-shaped microchannel networks (Hong et al., 2007 and Luo and Mao, 2012), microchannel with Y-shaped bifurcation plate (Li et al., 2014), offset strip-fin microchannels (Hong and Cheng, 2009) and micro-pin fins (Peles et al., 2005; Koşar et al., 2005; Koşar and Peles, 2006; and Siu-Ho et al., 2007), have also been proposed to enhance temperature uniformity and reduce the pressure drop.

2.3.2.1 Interrupted-Wall Channel

Xu et al. (2005) proposed experimentally a new silicon microchannel heat sink and compared it with a conventional heat sink in terms of the temperature distribution and heat transfer characteristics. The novel straight microchannel heat sink that was used in their work composed of ten triangular microchannels along the flow direction with five transverse trapezoid microchambers placed to separate the whole straight microchannels into six

independent zones (see Fig. 2.20). The purpose of using the transverse microchannel is to interrupt the thermal boundary layer which leads to an enhancement of the heat transfer coefficient. Also, they observed that the pressure drop characteristics were reduced for the interrupted microchannel design compared to the conventional microchannel heat sink design, which demonstrated that pressure drop decreased by 27% in the new design. The main reasons behind the reduction of pressure drop in this design was due to the very low water mass flow rate and shortened flow length. The experiments were tested under different ranges of conditions for inlet pressure, inlet temperature, mass flow rate, pressure drop, and heat flux are respectively 1–2 bar, 30–70 ºC, 534.8–4132.85 kg/m^2.s, 10–100 kPa, and 10–100 W/cm^2.

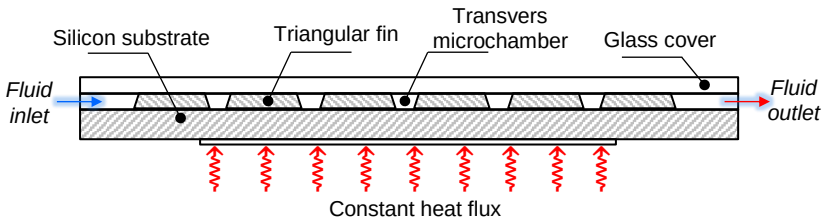

Fig. 2.20: Cross section view for a MCHS used by Xu et al. (2005).

Xu et al. (2008) conducted three-dimensional numerical simulations of conjugate heat transfer in conventional and interrupted microchannel heat sink following their earlier experimental work (Xu et al., 2005). Their numerical results predicted that the mass flux and received heat were larger in the central channels than the edge channels by 0.2% and 2% respectively. The hydraulic and thermal boundary layers were redeveloping at the entrance of each separated zone and this mechanism enhanced the heat transfer in the microchannel heat sink. Also, they observed that the pressure drop in an interrupted microchannel heat sink was smaller compared with a conventional heat sink. The numerical results showed good agreement with the experimental data.

Lee et al. (2012 and 2013) used the technique proposed by Steinke and Kandlikar (2004), where the conventional straight fin microchannels are modified by breaking the continuous fins into oblique sections as illustrated in Fig. 2.21, except the secondary flow is induced in only one direction. Their experimental study compared this new arrangement with a corresponding straight conventional microchannel and showed that the heat transfer enhancement factor (the average Nusselt number of the MCHS with oblique fins divided by the Nusselt number of conventional straight channels) was increased by a factor of 1.6 at $Re \sim 300$ with a negligible pressure drop penalty.

The results showed that the oblique sections reduce the thickness of the boundary layer in the main channels, by causing both the hydrodynamic and thermal boundary layers to re-develop

at the leading edge of each oblique fin. The oblique channels divert a small fraction of flow into the adjacent main channels, causing further improvements in heat transfer due to improved mixing.

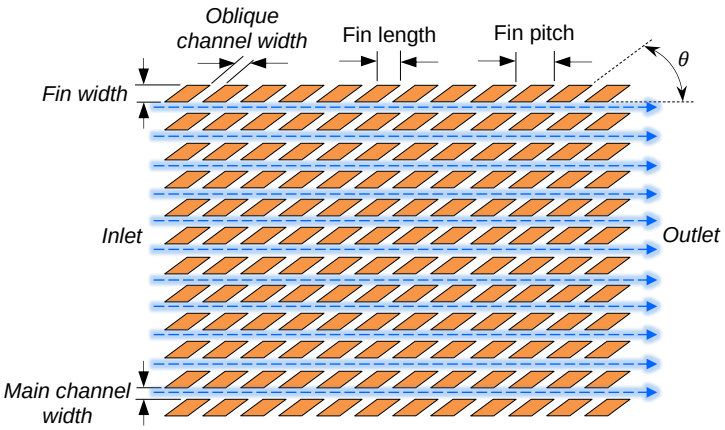

Fig. 2.21: Cross section view of oblique fins suggested by Lee et al. (2012 and 2013).

Recently, an experimental and numerical study by Lee et al. (2015) proposed a microchannel heat sink with sectional oblique fins inside the flow channels to enhance heat transfer. The numerical design optimisation was carried out using two variables: the oblique angle and fin pitch. The results indicated that a smaller oblique angle and smaller fin pitch both lead to improved heat transfer.

Khan et al. (2010 and 2017) carried out an experimental investigation into single-phase heat transfer in commercial plate heat exchangers for symmetric and non-symmetric (mixed) chevron angle plates for Re ranging from 500 to 2500. Their experimental results demonstrated the significant effects of both chevron angle and Re on the heat transfer coefficient and friction factor and they used their results to propose a correlation to estimate Nusselt number and friction factor.

2.3.2.2 Cavities in Microchannel Heat Sinks

Chai et al. (2013a) experimentally and numerically investigated the pressure drop and heat transfer characteristics of two microchannel heat sinks, fan-shaped and triangular reentrant cavities, with periodic expansion-constriction cross-sections, see Fig. 2.22. In their study, the microchannel heat sink consisted of ten parallel microchannels and each one has depth and width of 0.2 mm and 0.1 mm, respectively. The averaged Nusselt number for the proposed heat sinks with periodic expansion-constriction cross-sections was observed to increase by about 1.8 times with an acceptable pressure drop compared with the straight rectangular microchannel, and this was attributed to the interruption of boundary layer formation and provision of more surface area.

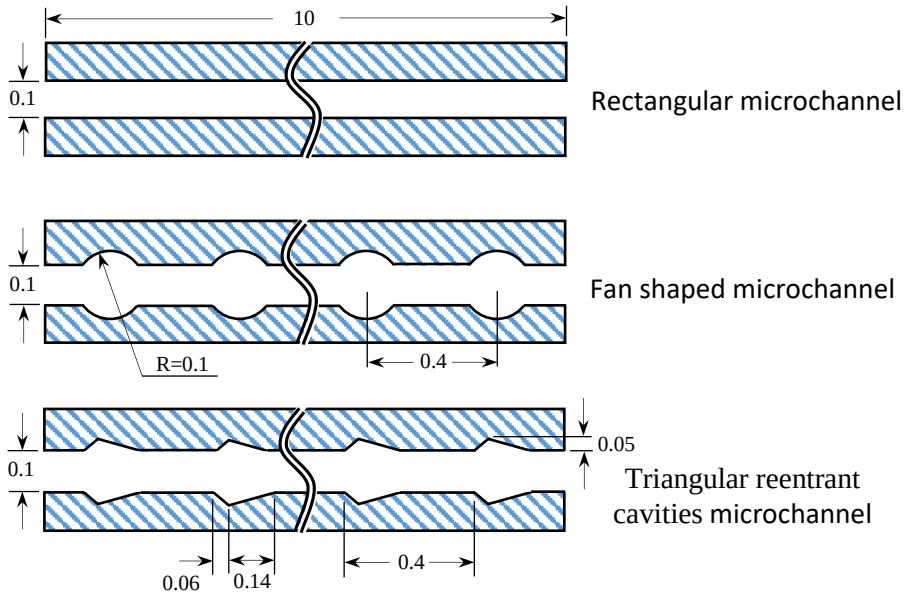

Fig. 2.22: Straight rectangular, fan-shaped and triangular reentrant cavities microchannels (Chai et al., 2013a), all dimensions in mm.

It is interesting to note that the pressure drop in periodic expansion construction is lower for Re < 300, but it increased rapidly for Reynolds number in the range of 300–750. For thermal resistance components, the capacitive and convective thermal resistances show a significant downward trend with an increase of volumetric flow rate (Q_{in}) for all heat sinks, while the conductive term thermal resistance remains fixed, see Fig. 2.23. In addition, it can be seen that the newly proposed heat sinks have lower convective thermal resistance compared with conventional one, and this due to significant enhancement of heat transfer coefficient with an increase of the Q_{in}.

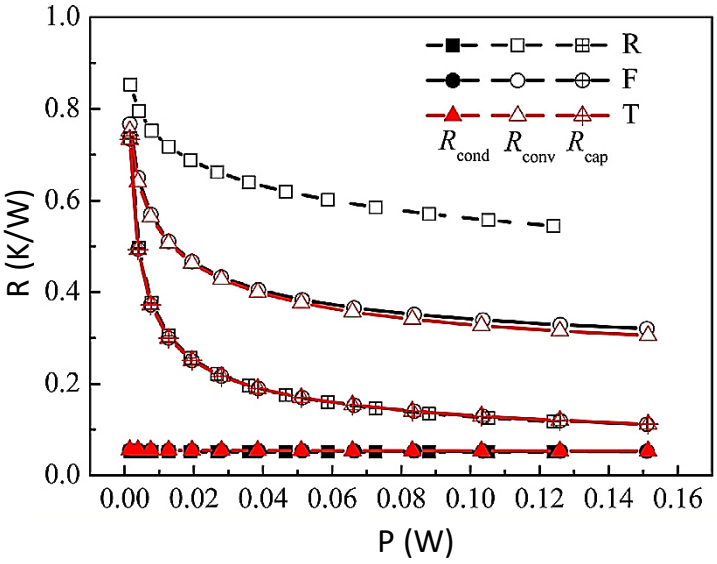

Fig. 2.23: Thermal resistance versus pumping power (Chai et al., 2013a).

Deng et al. (2015a) carried out experimental and numerical studies to investigate single-phase convective flow and heat transfer performance of a unique Ω–shaped reentrant copper

microchannel heat sink, see Fig. 2.24. The width, length and thickness of the heat sink used were 20 mm, 45 mm and 2 mm, respectively, and consisted of 14 parallel Ω–shaped reentrant microchannels with a hydraulic diameter of 781 μm. In their study, deionized water as the coolant was used with two inlet temperatures of 33 and 60 °C, and the tests were conducted at Reynolds number of 150–1100 at three different heat fluxes of 133, 200 and 267 kW/m^2 supplied underneath the heat sink base. Compared to the straight rectangular microchannel, the new proposed microchannel provided a 10–30% heat transfer enhancement and 22% reduction of total thermal resistance with overall 10% increase of the frictional factor ratios. This heat transfer enhancement is associated with the fluid mixing and the flow separation caused by the throttling effects (the narrow slot played a restriction role on the fluid flow, while the abrupt protrusion between the bottom circular cavity and upper vertical narrow slot interrupted the hydrodynamic and thermal boundary layers). Additionally, for both microchannels, the pressure drop was found to decrease with increasing heat flux, with the higher inlet temperature cases showing a smaller thermal resistance.

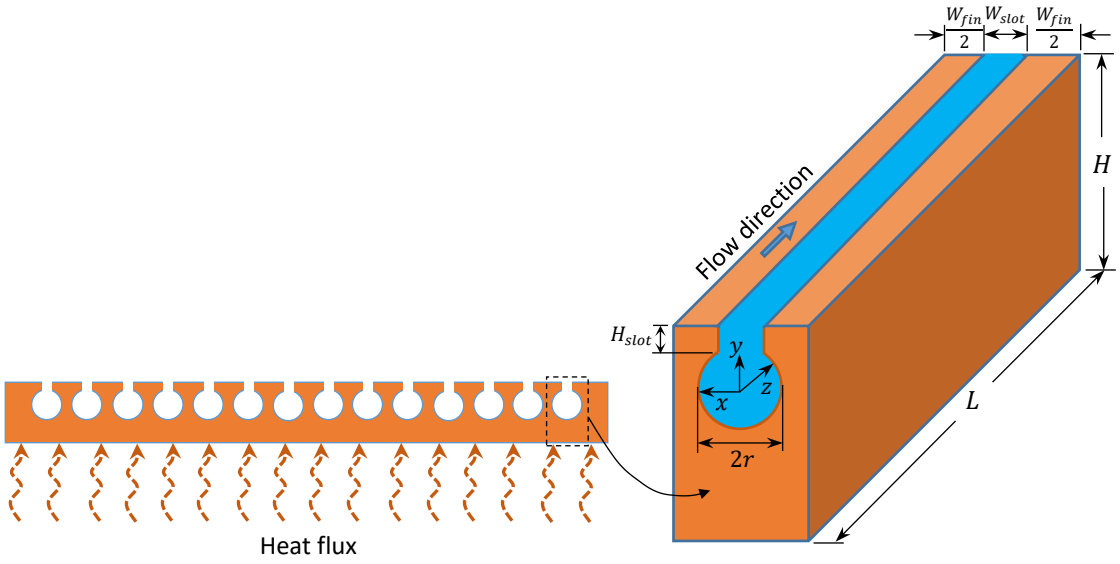

Fig. 2.24: Schematic diagram of computational domain for reentrant microchannels (Deng et al., 2015a).

Xia et al. (2015) numerically investigated the fluid flow and heat transfer in microchannel heat sinks with different inlet/outlet locations (I, C and Z-type), header shapes (triangular, trapezoidal and rectangular) and microchannel cross-section shapes (the conventional rectangular microchannel, the microchannel with offset fan-shaped reentrant cavities and the microchannel with triangular reentrant cavities) with a computational domain including the entire microchannel heat sink. The simulation results revealed that the I-type inlet-outlet flow arrangement produced the best flow distribution compared to the other configurations. Likewise, the rectangular header shape generated better flow uniformity than other shapes. The overall evaluation for microchannel heat sink performance showed that microchannel

with cavities is thermally more efficient than simple microchannel with superiority of triangular cavities over fan-shaped cavities. This enhancement in heat transfer is attributed to the throttling and jetting effects associated with increased pressure drops.

2.3.2.3 Ribs and Grooves in Microchannel Heat Sinks

An experimental investigation was conducted by Liu et al. (2011) for fluid flow and heat transfer in rectangular micochannels with longitudinal vortex generators (LVGs) for the Reynolds numbers ranging from 170 to 1200. Five rectangular microchannel test chips of the same dimension with LVGs were designed for the experiment, while the sixth test chip is with a smooth rectangular microchannel. All microchannels were etched on a silicon wafer with a 4 inch (101.6 mm) diameter and a 0.55 mm thickness, whereas the height, width and length of rectangular microchannels used were 0.1 mm, 1.5 mm and 20 mm, respectively, resulting in a hydraulic diameter 0.1875 mm. The length and width of LVGs was fixed at 0.4 mm and 0.05 mm, respectively. The effect of the attack angle and the number of LVG pairs was also investigated.

Compared with the smooth microchannel, the laminar-to-turbulent transition in microchannel with LVGs occurs at Reynolds numbers of 600–720 instead of 2300. Furthermore, it is found that changing the direction of attack angle of one pair of LVGs in the stream-wise direction can to some extent delay the occurrence of laminar-to-turbulent transition. The experiments indicated that the rectangular microchannel with LVGs can enhance heat transfer, compared with the smooth rectangular microchannel, but this was at the expense of a large pressure drop. From laminar to turbulent flow, the heat transfer performance was improved by 9–90%, while encountering larger pressure drops by 34–169%.

Chai et al. (2013b) introduced staggered rectangular ribs into the transverse microchambers of the interrupted microchannels, and studied the heat transfer characteristics in such heat sinks. For optimum thermal design, the geometry parameters (e.g. the length and width of rib) and the effect of the position parameters (e.g. the distance from the parallel microchannels to the rib row and the space between two adjoining transverse microchambers) were investigated. Their results showed that considering the staggered rectangular ribs could further improve the heat transfer largely due to better flow separation and mixing of hot and cold liquids.

Five different microchannel heat sink configurations with multiple length bifurcation plates and various arrangements were investigated numerically by Xie et al. (2014). The local pressure drop, flow structures, temperature distributions and average heat transfer coefficients are presented at different Reynolds number ranging from 220 to 520 to evaluate the cooling

performance of the bifurcating microchannel heat sinks. The numerical results obtained showed that the thermal performance of the bifurcated microchannel heat sink is better than that of the corresponding straight microchannel heat sink with an enhancement factor of up to 2. Additionally, it is found that the bifurcated microchannel with a longer bifurcation plate might be better for heat dissipation but this was at the expense of a higher pressure drop.

The thermal and fluid flow characteristics of silicon straight rectangular microchannel heat sinks integrated with the internal vertical Y-shaped bifurcation plates in laminar liquid flow were analysed numerically by Xie et al. (2015). The Y-shaped bifurcation fin structure is not in contact with the internal microchannel walls (see Fig. 2.25), which increases fluid mixing. Optimization of the Y-shaped plate lengths (10, 15 and 25 mm) and the angles (60^o, 90^o, 120^o, 150^o and 180^o) between the two arms of the Y-shaped bifurcation was carried out. The silicon heat sink used consist of 100 microchannels with surface area of 35 × 35 mm^2 and length of 35 mm to dissipate a total power of 300 W (24.49 W/cm^2) using water as the coolant. The channel width, channel height and fin width are respectively 0.315 mm, 0.4 mm and 0.035 mm, while the thickness of the heat sink substrate and cover plate are both 0.05 mm, and the length of the bifurcation arm is set as a fixed value at 0.15 mm.

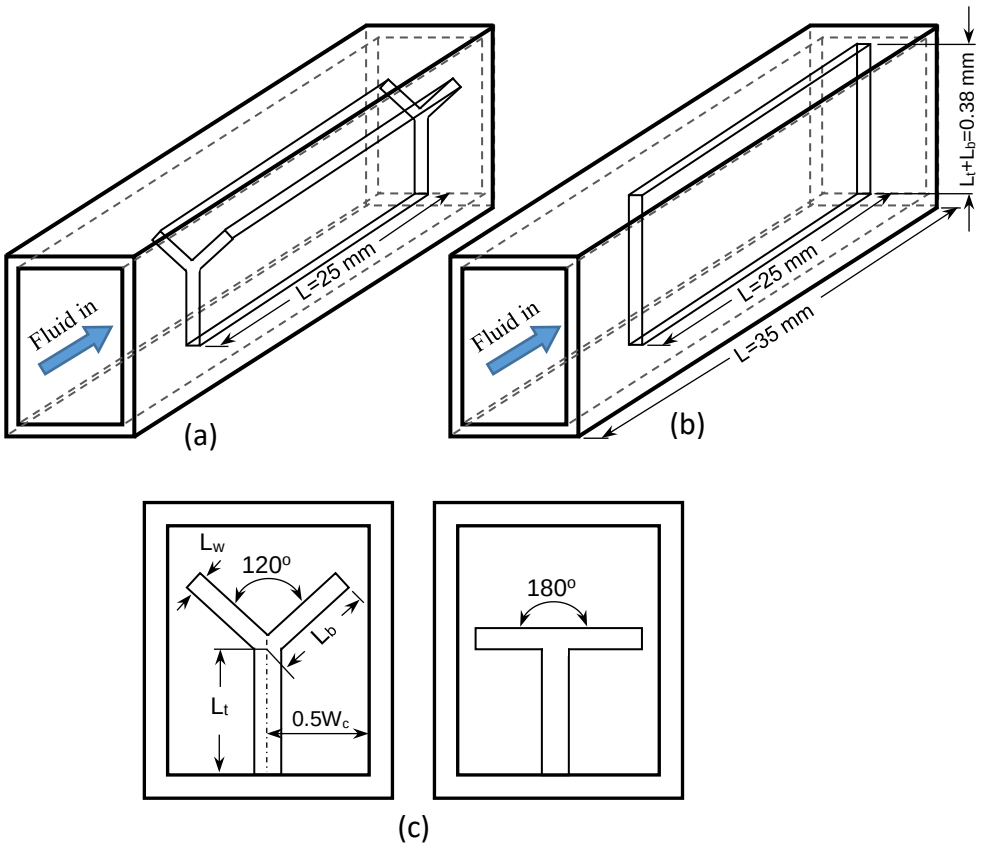

Fig. 2.25: Schematic diagrams of (a) internal Y-shaped bifurcation microchannel; (b) vertical fin without Y-shaped bifurcation microchannel; (c) The cross profiles of microchannel heat sinks with Y-shaped bifurcation at angle of 120^o and 180^o (Xie et al., 2015).

The numerical predictions indicate that the thermal performance of the 25 mm internal Y-shaped bifurcation microchannel is much better than that of the traditional rectangular microchannel and the other two microchannels with internal Y-shaped bifurcations. At an inlet velocity of 1.0 m/s, it is found that using the Y-shaped bifurcation, the thermal resistance decreased by 41% when compared to the straight rectangular microchannel. The results show that the microchannel with internal Y-shaped bifurcations with an angle of 180^{o} gives the best thermal performance, but this was at the expense of high pressure drop.

An experimental investigation was carried out by Ferhati et al. (2015) to evaluate the hydro-thermal characteristics for single-phase laminar regime of deionized water flowing through three electron beam surface enhancement technology. Three test samples with different surface protrusion patterns were produced for testing, namely S1, S2 and S3. The test sample S1 consist of four-bladed groups arranged on a repeating square pattern, while test samples S2 and S3 both feature pyramidal-like protrusions arranged in staggered rows, and each one has different protrusion spacing and protrusion sizes. The mass flow rates of coolant and the input power were respectively varied from 0.005 kg/s to 0.045 kg/s and from 100 W to 600 W. These three test samples are compared to those for a smooth surface tested in terms of friction factor and Nusselt number operating under the same conditions. The width, length and thickness of the test samples are respectively 35, 55 and 6.5 mm, each one was mounted on the heater block made from copper with cross-section area of 28 mm × 32 mm matching the heat transfer surface base area in the test sample.

The average protrusion densities for the three samples S1, S2, and S3 were 13, 11, and 25 per cm^2 with hydraulic diameters of 3, 2.8 and 1.59 mm and protrusion heights of 2.5, 2.8, and 1.6 mm, respectively. The experiments showed that the three test samples have significantly higher Nusselt numbers compared to the smooth test section due to an increase in the heat transfer area, improve mixing and disturb both the hydrodynamic and thermal boundary layers. The test sample S1 gave the highest Nusselt number followed by samples S3 and S2, but this enhancement is accompanied by an increase in pressure drop. They observed that with increase of the protrusion density the friction factor increased also and the sample S3 gave the highest pressure drop since it has the highest protrusion density. To trade-off between the heat transfer and pressure drop optimization of these structures was suggested, and the protrusion geometry and density can be considered.

Numerical simulations were carried out by Chai et al. (2016a) for laminar flow and heat transfer in microchannel heat sinks with offset ribs on the sidewalls. In their study, five different shapes of offset ribs are designed, including rectangular, backward triangular, isosceles triangular, forward triangular and semicircular, see Fig. 2.26. The results showed

that the microchannel heat sink with forward triangular offset ribs performed the highest performance evaluation criteria as $Re < 350$, while for $Re > 400$ the one with semicircular offset ribs yielded the best performance evaluation criteria.

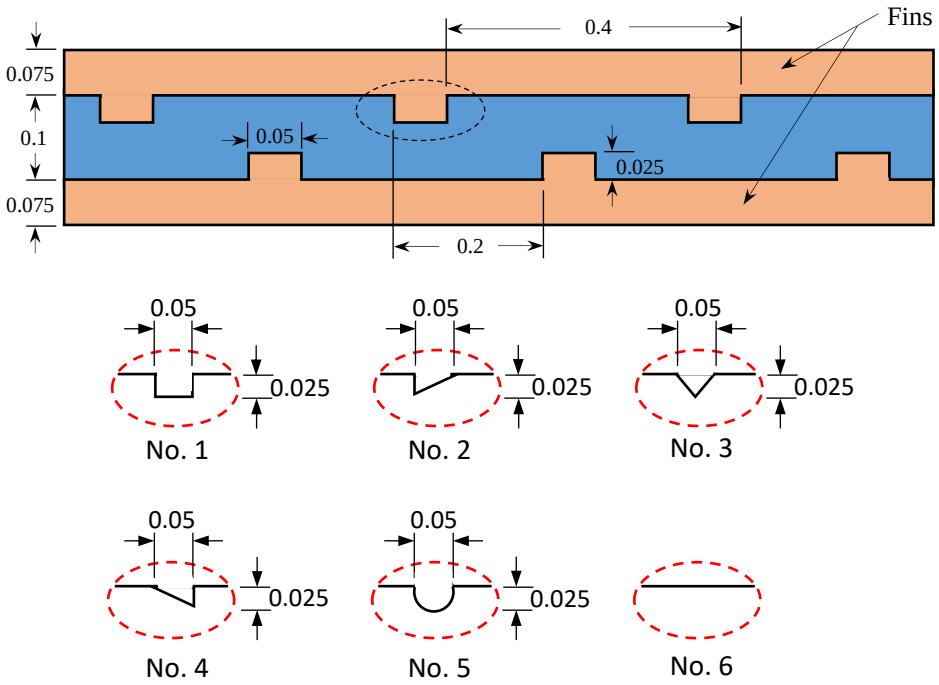

Fig. 2.26: Structure and dimensions of offset ribs suggested by Chai et al. (2016a) (all dimensions in mm).

Three-dimensional numerical simulations have been conducted by Chai et al. (2016b) to investigate laminar flow and heat transfer characteristics in the interrupted microchannel heat sink with ribs in the transverse microchambers. In their study five different rib configurations are considered as shown in Fig. 2.27, including rectangular, backward triangular, forward triangular, diamond and ellipsoidal. Their findings indicated that the new interrupted microchannel with ellipsoidal ribs can effectively enhance the heat transfer coefficient along the flow direction compared with the other ribs and the conventional microchannel heat sink, due to redevelopment of the thermal boundary layer. The rectangular and backward triangular ribs in the transverse microchambers show the largest pressure drop compared with the other three configurations.

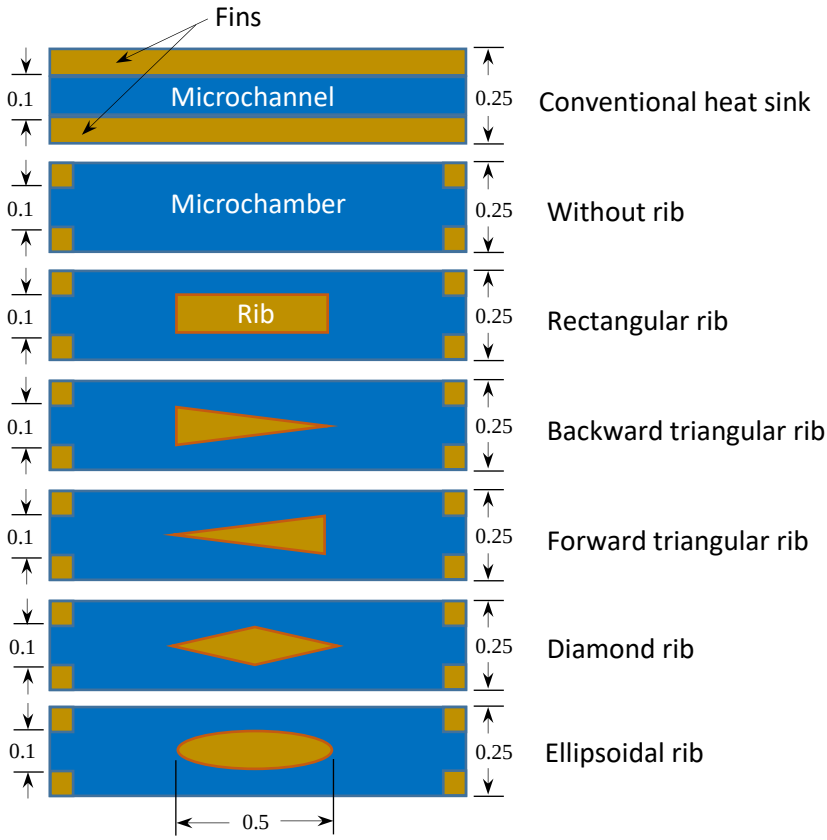

Fig. 2.27: Structure and dimensions of offset ribs proposed by Chai et al. (2016b) (all dimensions in mm).

A three-dimensional numerical simulation was conducted by Ghani et al. (2017b) to study the fluid flow and heat transfer characteristics for single phase laminar flow in new microchannel heat sinks with sinusoidal cavities and rectangular ribs (MC-SCRR) in the central portion of channel (see Fig. 2.28). The performance factor of the proposed new design was compared with a microchannel with rectangular ribs, microchannel with sinusoidal cavities and a conventional rectangular channel. The new design promotes flow mixing and provided larger heat transfer and flow area compared with other three microchannel geometries, which significantly enhances the heat transfer and reduces the pressure drop.

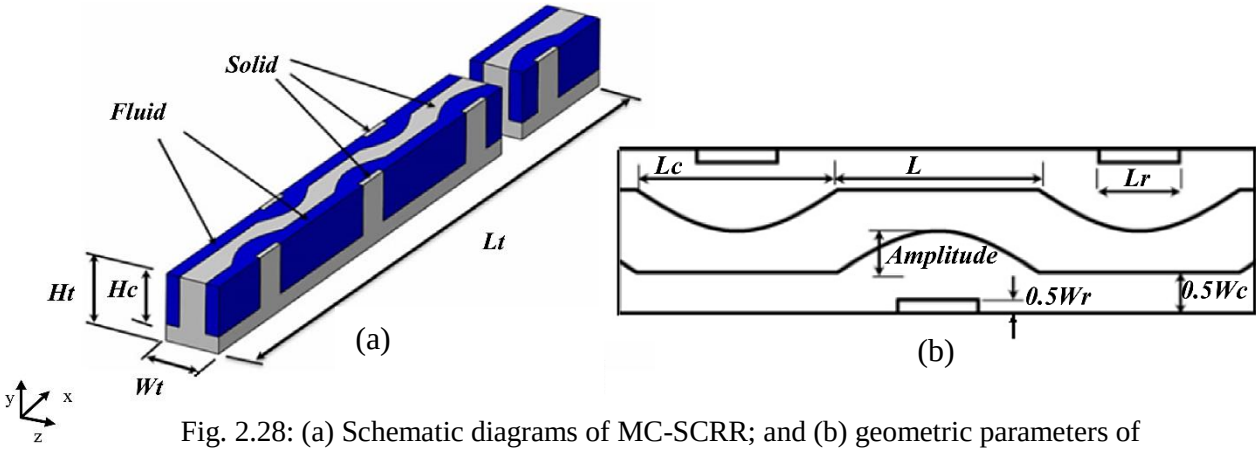

Fig. 2.28: (a) Schematic diagrams of MC-SCRR; and (b) geometric parameters of MC-SCRR (Ghani et al., 2017b).

The effect of three geometrical parameters; relative cavity amplitude, relative rib width and relative rib length on the convective heat transfer and pressure drop have been investigated. The optimisation results revealed that as the relative cavity increases, the Nusselt number increases while the friction factor decreases. Furthermore, it is found that as the relative rib width and relative rib length increases, the Nusselt number and friction factor increase also.

Recently, Ghani et al. (2017c) studied numerically the fluid flow and heat transfer characteristics of microchannel heat sinks with rectangular ribs and secondary oblique channels in alternating directions (MC-SOCRR) at different Reynolds number (Re) ranging from 100 to 500 (see Fig. 2.29). This type of heat sink has been compared with microchannels with secondary oblique channels, microchannels with rectangular ribs and straight rectangular microchannels.

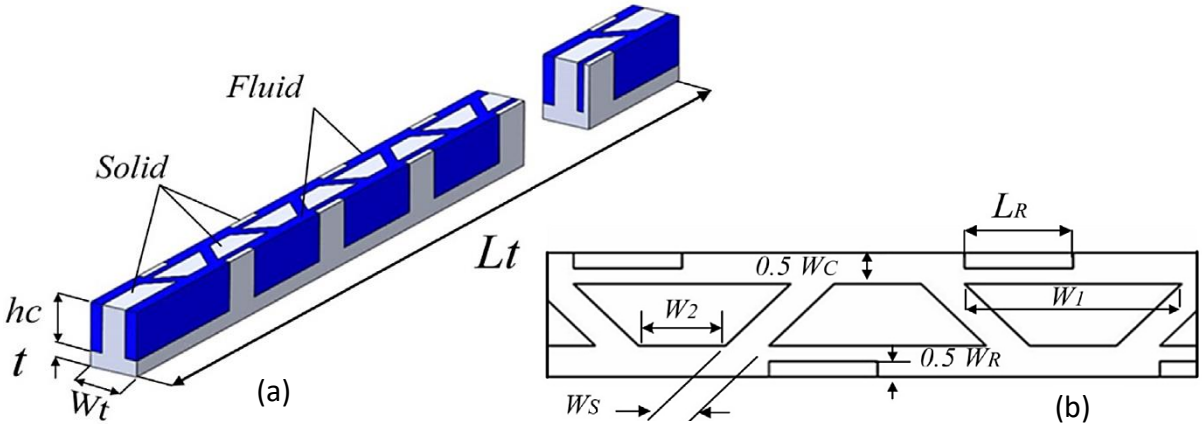

Fig. 2.29: (a) Schematic diagrams of MC-SOCRR; and (b) geometric parameters of MC-SOCRR (Ghani et al., 2017c).

The proposed design provides a larger heat transfer area in comparison with the other three microchannel geometries whilst also reducing the pressure drop caused by ribs by around 50%. Three parameters were selected to explore the effects of geometrical parameters on the hydrothermal performance of the heat sink: (i) the relative secondary channel width, (ii) the relative rib width, (iii) the angle of the secondary channel. The results revealed that the average Nusselt number and friction factor increase as the angle of secondary channel decreases and decrease as the relative secondary channel width increases, while the friction factor increases as the relative rib width increases.

Recently, an experimental study of single-phase water flow inside a commercial gasket plate heat exchanger with chevron angles (θ) of 30° and 60° was carried out by Nilpueng et al. (2018). The heat transfer coefficient, pressure drop, and thermal performance factor, TPF, which is defined as the ratio of the Nusselt number and friction factor between the rough surface and smooth surface, under different chevron angles, surface roughness (0.95 μm <

$\varepsilon < 2.75$ μm), and working conditions are investigated. The experiments are performed at cold and hot water temperatures of 25 °C and 40 °C, respectively, with Reynolds numbers ranging from 1200 to 3500 (3-10 *l/min*). Their results demonstrate that the chevron angle and surface roughness have a significant effect on the TPF, and the heat transfer coefficient and pressure drop of the 30° chevron angle are higher than those of the 60° chevron angle by about 2.51 times and 1.87 times, respectively. Additionally, a correlations of the Nusselt number and friction factor at the different chevron angles and surface roughness are proposed as a function of the Reynolds number, Prandtl number, relative roughness (ε/D_h), and chevron angle as follows:

$$Nu = 0.343Re^{0.604}Pr^{0.33}(\varepsilon/D_h)^{0.133}(\theta/30)^{-1.327} \quad (2.20)$$

$$f = 1.98Re^{-0.237}(\varepsilon/D_h)^{0.168}(\theta/30)^{-0.903} \quad (2.21)$$

2.4 Flow Boiling in Microchannels

When a liquid is brought into contact with a heated surface maintained at a temperature sufficiently above the saturation temperature of the liquid, boiling will eventually take place at that liquid–solid interface. Based on the relative bulk motion of the body of a liquid to the heating surface, the boiling is divided into two categories: pool and flow boiling (Johnson, 2016). Boiling is called pool boiling in the absence of bulk fluid flow (boiling under natural convection conditions and the motion of the bubbles is due to buoyancy effect) while flow boiling in the presence of it (boiling under forced convection conditions and the motion of the fluid and bubbles is due to external means such as a pump) (Çengel, 2002).

Depending on the bulk liquid temperature, pool and flow boiling are further classified as subcooled or saturated boiling. Subcooled boiling occurs if the bulk liquid temperature is below the saturation temperature at corresponding pressure, and in this case the bubbles formed on the heated surface may collapse in the liquid due to the subcooled fluid. While saturated boiling takes place if the bulk liquid temperature is maintained at saturation temperature and the bubble formed can depart the heated surface (Çengel, 2002).

2.4.1 Boiling Curve

There are four different boiling regimes has been observed by experiments of Nukiyama (1934) who used electrically heated nichrome and platinum wires submerged in liquids. These regimes are natural convection boiling, nucleate boiling, transition boiling, and film boiling as indicated in Fig. 2.30. This figure for water and is called boiling curve which is a plot of boiling heat flux versus the excess temperature ($\Delta T_e = T_s - T_{sat}$, where T_s and T_{sat} are respectively the surface and saturation temperatures) (Bergman et al., 2017), and each boiling regime will be described briefly as shown in Table 2.1.

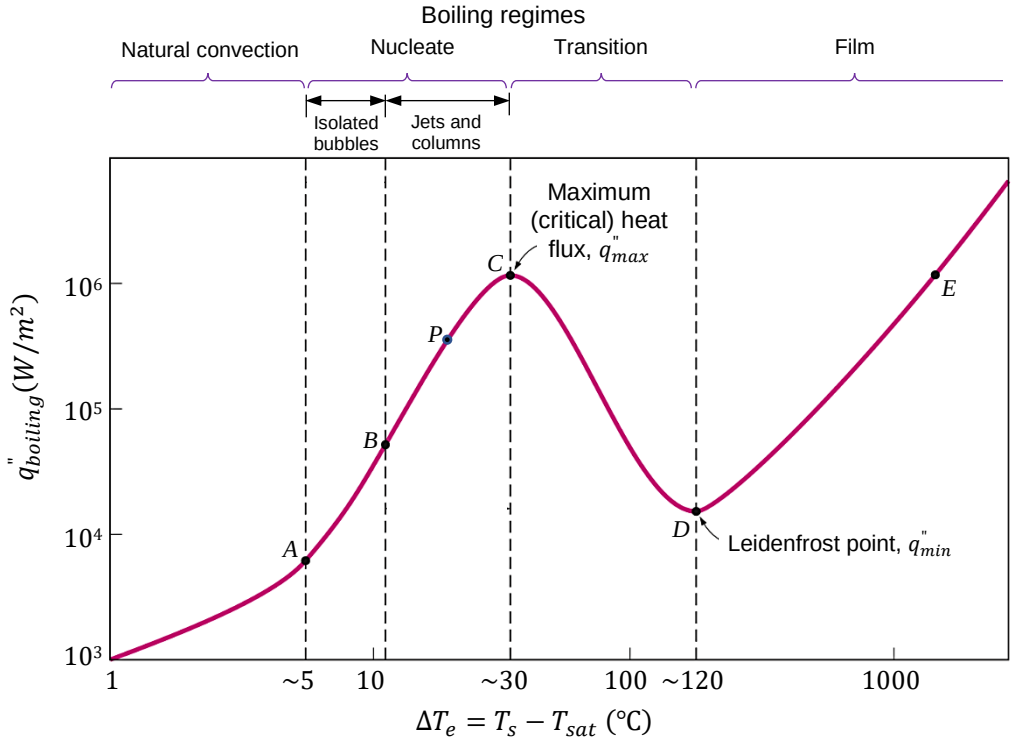

Fig. 2.30: Typical features of a boiling curve for water at 1 atmospheric pressure (Bergman et al., 2017).

Table 2.1: Boiling regimes.

Boiling regimes	Remarks
Natural convection boiling	• Bubbles don't form on the heating surface until the liquid is heated a few degrees above the saturation temperature (about 2 to 6 °C). • The liquid in this regime is slightly superheated, and the process ends at an excess temperature of about 5 °C. • The heat transfer from the heating surface to the fluids and the fluid motion is governed by natural convection currents.
Nucleate boiling	• This regime exists in the range 5 °C ≤ ΔT_e ≤ 30 °C (see Fig 2.30), and in this range two different flow regimes may be distinguished as: i) In the region A–B, isolated bubbles form at nucleation sites and separate from the surface. These bubbles may be dissipated in the liquid after breaking away from the surface. ii) In the region B–C, the vapour escapes as jets or columns. After point P, the heat flux increases more slowly as ΔT_e is increased. • The heat flux at the point C is called the critical heat flux (CHF), and is of prime engineering importance.
Transition boiling	• This regime exists in the range 30 °C ≤ ΔT_e ≤ 120 °C (see Fig 2.30), and also called the unstable film. • In this process the heat flux is beginning decrease monotonically, and this is because the fraction of the heater surface is covered by vapour film, which acts as an insulation. • In this regime, both nucleate and film boiling occur partially. • Operation under this regime is avoided in practice.
Film boiling	• Beyond point D in Fig 2.30, the heater surface is completely covered by continuous stable vapour film. • Point D, where the heat flux reaches a minimum is called Leidenfrost point. • The presence of a vapour film between the heater surface and the liquid is responsible for the low heat transfer rates in the film boiling region. • The heat transfer rate increases with increasing excess temperature due to radiation to the liquid.

The performance of two phase cooling solutions is limited by the critical heat flux (CHF) (point C in Fig 2.30), which is also called a boiling crisis, burnout, and departure

from nucleate boiling (DNB). It is defined as the maximum heat flux that can be transferred without encountering a reduction in heat transfer efficiency, and if the heat flux exceeds the CHF the transition from nucleate boiling to film boiling occurs as shown in the typical boiling curve of Fig. 2.30. In film boiling, the formation of a vapour film covers the heating surface completely and separating the surface from the liquid leads to a significant rise in thermal resistance and, as a result, reduction in heat transfer efficiency.

2.4.2 Flow Boiling Instability

During the last three decades, various technologies, such as pin fins, changing surface roughness, modifying the continuous fins through cutting it into different small shapes such as oblique or rhombus fins to generate secondary flow and adding nanoparticles to the working fluid have been dedicated within single-phase liquid-cooled microchannel heat sink to enhance cooling (Steinke and Kandlikar, 2004 and Morini, 2004). These methods were also investigated with flow boiling as it leverages the latent heat of evaporation and promotes extensive mixing (Kandlikar, 2002; Koşar and Peles, 2007; and Reeser et al., 2014). Moriyama et al. (1992) experimentally demonstrated that the two-phase heat transfer coefficient was up to 3–20 times larger than the corresponding single-phase coefficient. As a result of the enhanced thermal performance compared to other processes, fairly uniform stream-wise temperatures distributions that eliminates the possibility of hot-spot formation on the substrate of electronic devices, reduced coolant flow rates, and thus smaller pumping powers are obtained in microchannel heat sinks incorporating two-phase flow boiling cooling technology (Karayiannis et al., 2010; Karayiannis and Mahmoud, 2017; and Cheng and Xia, 2017). However, the main disadvantage of such technology at high heat flux dissipation is generating massive amount of vapour in the smooth/straight microchannels, which causes the extremely rapid bubble growth in both upstream and downstream directions and vapour bubble clogging leading to flow instabilities and backflow (Prajapati et al., 2015 and Prajapati and Bhandari, 2017).

The effect of flow instabilities on flow boiling heat transfer in microchannels can be further characterised by vigorous pressure and temperature fluctuations, maldistribution of coolant between microchannels, and intermittent flow reversal leading to local dry-out (Prajapati and Bhandari, 2017). Furthermore, instabilities are undesirable, as they can lead to modify the hydrodynamics inside the microchannels that create mechanical vibrations which in turn lead to damage of the device and also may cause premature critical heat flux (CHF) (Bogojevica et al., 2009).

To address such problems, researchers in both heat transfer and microelectronic communities have attempted to develop more advanced microchannels. Among the reported enhancement methods, one way is to modify the flow passages. Flow instabilities can be mitigated by using one of these methods such as tapered microchannels (Kandlikar et al., 2013), diverging microchannels (Lee and Pan, 2008; Lu and Pan, 2008; Lu and Pan, 2011; and Prajapati et al., 2015), expanding microchannels (Balasubramanian et al., 2011), cross-linked microchannels (Xu et al., 2006 and Megahed, 2011), Ω–shaped reentrant microchannels (Deng et al., 2015b), installing inlet restrictors or orifices in the upstream of heat sink (Koşar et al., 2006) and fabrication of artificial reentrant microcavities on the bottom (Kandlikar et al., 2006) or sidewall (Kuo and Peles, 2007 and Kuo and Peles, 2009) surface of rectangular microchannels.

2.4.2.1 Influence of Inlet/Outlet Configurations

To suppress flow instability, to reduce the severe reduction in the critical heat flux, and to enhance heat transfer during two phase flow boiling, Kandlikar et al. (2006) experimentally introduced two modifications in a set of six 1054 μm wide, 197 μm high and 63.5 mm long parallel rectangular microchannels. They fabricated inlet area restriction (pressure drop elements) and artificial nucleation sites (cavities), these are studied alone and in conjunction with each other. The microchannel heat sinks used were made from copper, and water was employed as coolant. Artificial cavities of diameters 5–30 μm are drilled on the bottom surface of the microchannel using a laser beam, these are spaced at a regular interval of 762 μm. Two different areas of restrictive inlet header are machined on the Lexan cover, the first and second sets consisting of circular holes with a cross sectional area 4% and 51% of a single microchannel flow area, and both sets of restrictors had a length of 1.6 mm. These pressure restrictors are expected to eradicate the backflow by forcing an expanding vapor bubble in the downstream direction and not allowing the liquid-vapor mixture to enter the inlet manifold.

In their work five cases have studied and flow stability is determined through high-speed digital video camera and measurement of pressure drop fluctuations across the microchannels. These are carried out under the same mass flow and heat flux conditions. They observed that introducing the 51% area pressure drop elements (restrictors) in the inlet manifold alone seem to reduce the severity of backflow partially with lower pressure drop fluctuations, while using the artificial cavities alone actually increased the instabilities. The presence of both the 51% area pressure drop elements and the artificial cavities partially reduced the vapour backflow and significantly reduced the pressure drop fluctuations. However, introduction of artificial cavities in conjunction with the 4% area pressure drop

elements completely eliminated the instabilities, but this was at the expense of high pressure drop.

Koşar et al. (2006) investigated experimentally the effects of introducing inlet restrictors (orifices) on the suppression of boiling flow instabilities in parallel microchannels. They used a microchannel device consisting of five 1 cm long, 200 μm wide, and 264 μm high, parallel microchannels, spaced 200 μm apart. Five 20 μm wide orifices with different lengths varying from 50 μm to 400 μm were installed at the entrance of each microchannel, see Fig. 2.31. To get homogeneous distribution of flow in the inlet, flow distributive pillars have been introduced, these are arranged in 2 columns of 12 circular pillars having a diameter of 100 μm. Once boiling occurs, they observed severe flow oscillations in the device without the restrictors. However, with increasing restrictor length, they found a decrease in the instabilities and larger heat fluxes could be obtained before reaching critical heat flux.

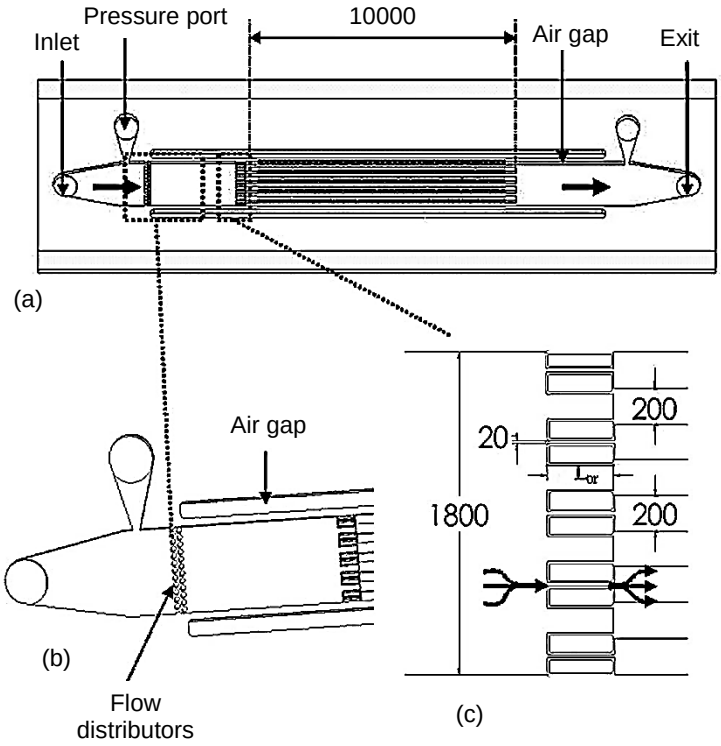

Fig. 2.31: (a) Schematic illustration of the heat sink device used by Koşar et al. (2006); (b) flow distributive pillars; (c) geometry of the inlet orifices (dimensions in μm).

Experimental study has been carried out by Wang et al. (2008) to investigate effects of inlet/outlet configurations on the flow boiling instabilities in eight parallel trapezoidal microchannels etched in a silicon substrate, having the same length of 30 mm and a hydraulic diameter of 186 μm. In their study, water is employed as coolant in three types of inlet/outlet connections, these are classified as Type-A, Type-B and Type-C connections, see Fig. 2.32. In the Type-A connection, the water flow in both inlet and outlet plenums were restricted by the conduits that being perpendicular to the parallel microchannels. In the Type-B connection,

the fluid flow could enter to and exit from the microchannels without any restriction. In the Type-C connection, the entrance of each microchannel was restricted whereas fluid flow could freely discharge from the outlet, this type of connection was used previously by both Kandlikar et al. (2006) and Koşar et al. (2006) in their experiments on flow boiling in microchannels. In their study, they found that the Type-B connection had the largest oscillations followed by the Type-A connection and finally the Type-C connection had nearly complete steady flow boiling.

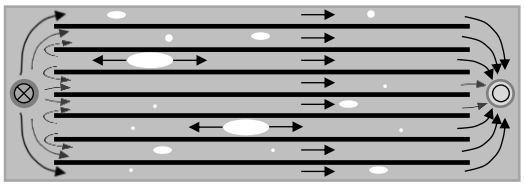

(a) Type–A connection: flow entering and exiting from parallel microchannels with restrictions because inlet/outlet conduits perpendicular to microchannels.

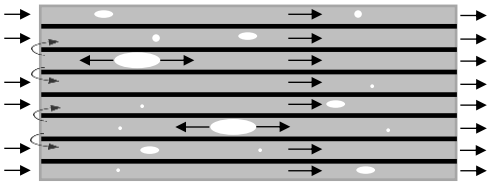

(b) Type–B connection: flow entering to and exiting from microchannels freely without restriction.

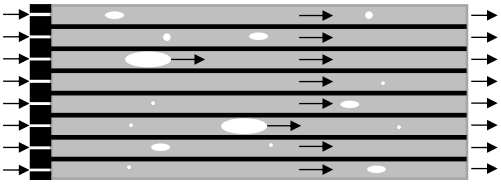

(i) Arrangement of parallel microchannels with restrictive inlet.

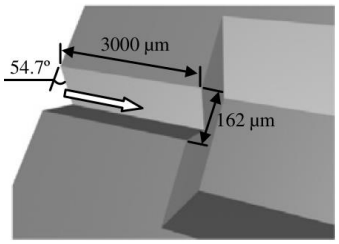

(ii) Sketch of the microchannel with a restrictive inlet.

(c) Type–C connection: flow entering with restriction and exiting without restriction in microchannels.

Fig. 2.32: Different inlet/outlet configurations investigated by Wang et al. (2008).

Further experiment study was carried out by Harirchian and Garimella (2008) to investigate the effect of four mass fluxes of a perfluorinated dielectric fluid (Fluorinert FC-77) ranging from 250 to 1600 kg/m^2.s and microchannel size on the local flow boiling heat transfer and pressure drops. Seven silicon microchannel heat sink test sections with cross-sectional area of 12.7 mm × 12.7 mm and thickness of 0.65 mm are fabricated for experiments, and each one was mounted on a printed circuit board. These heat sinks consisting of parallel rectangular microchannels having a constant depth of 400 µm and variable widths ranging from 100 to 5850 µm, with the channel length held constant at 12.7 mm. The heat transfer coefficients obtained are compared to values predicted using a number of existing correlations for pool boiling and saturated flow boiling in different channel size. For a fixed wall heat flux, their experiments revealed that the microchannel width has a modest effect on both of the heat transfer coefficient and boiling curves, whilst the opposite was shown when a base heat flux is fixed, where the heat transfer coefficient and wall temperature were increased as

the microchannels width increases. In the nucleate boiling region, the heat transfer coefficient and boiling curves are found to be independent of mass flux when channel size is fixed. However, when convective boiling dominates, the boiling curves diverge and more heat is dissipated as the mass flux increases. Also, a strong dependence of pressure drop on both channel size and mass flux was observed at a fixed wall heat flux.

Harirchian and Garimella (2009) then extended their work to include a study of the effect of changing channel depth as well. Their experiments are performed with five additional microchannel test sections with channel depths of 100 and 250 μm and widths ranging from 100 to 1000 μm. They presented the variation in heat transfer coefficient graphically as a function of channel cross-sectional area at different heat fluxes. They observed that the heat transfer coefficient remained constant without any noticeable change with microchannels with a cross-sectional area of 0.089 mm^2 and larger, due to vapour confinement as they affect the heat transfer mechanisms in flow boiling.

2.4.2.2 Influence of Microchannel Shape

Law and Lee (2015) conducted a comparative study on the flow boiling performance of copper oblique-finned microchannels and straight parallel microchannels. Both heat sink geometries consist of 40 parallel microchannels, and FC-72 dielectric fluid was used as coolant at inlet temperature of 29.5 ^oC. The periodic breaking and redevelopment of the thin liquid-film in the convective boiling regime led to the thinner boundary layer. Hence, significant reduction in the wall temperature gradients and pressure fluctuations have been obtained for the oblique-finned microchannels, which in turn led to enhancement in the flow boiling stability. As a result, significant augmentation in heat transfer and delay in the critical heat flux (CHF) have been observed. Unfortunately, it was accompanied by a higher pressure drop penalty due to the sudden change in the flow direction through secondary channels, and this drawback can be alleviated by modification the oblique-finned geometry.

An experimental study of flow boiling performance in unique Ω–shaped reentrant copper microchannel was carried out by Deng et al. (2015b) that had previously been studied experimentally and numerically by Deng et al. (2015a) to investigate the single-phase flow performance, see Fig. 2.24. In their study, deionized water and ethanol were used as coolants at inlet subcooling of 10 and 40 ^oC, and mass fluxes of 200–300 $kg/m^2.s$. Such microchannels with reentrant shape were compared with the straight rectangular microchannels and both microchannel heat sinks have the same dimensions. For both coolants tests, they observed significant heat transfer enhancement, reduction of pressure drop and alleviation of severe

two-phase flow instabilities in the reentrant microchannels compared with the rectangular one, due to the uniform liquid film distribution in the circular cavities.

Yu et al. (2016b) examined a new configuration of microchannel named as piranha pin fins (PPFs) that had previously been studied experimentally by Yu et al. (2016a) to investigate the single-phase flow performance, see Fig. 2.10. Two silicon microchannel devices at a deep of 200 μm embedded with different PPF configurations were investigated at different flow conditions. The first device is consisted of microchannel having PPFs with a narrow mouth opening (70 μm), while the second device having PPFs with a wide mouth opening (90 μm). In their study, heat transfer enhancement, critical heat flux (CHF) behaviour and pressure drop have been studied experimentally, and HFE7000 as the working fluid was used. They showed that a microchannel with PPFs is capable of dissipating high heat flux with reasonable pressure drop. Under a given mass flux, they observed that the device contains PPFs with a narrow mouth opening can achieve a higher CHF compared to those with a wide mouth opening, but this was at the expense of high pressure drop.

Li et al. (2017) proposed a microchannel configuration with triangular cavities at channel sidewall to enhance heat transfer and suppress instabilities as shown in Fig. 2.33. The flow pattern, pressure drop, heat transfer and wall temperature performances of the proposed design are analyzed and compared with that of the conventional rectangular microchannel.

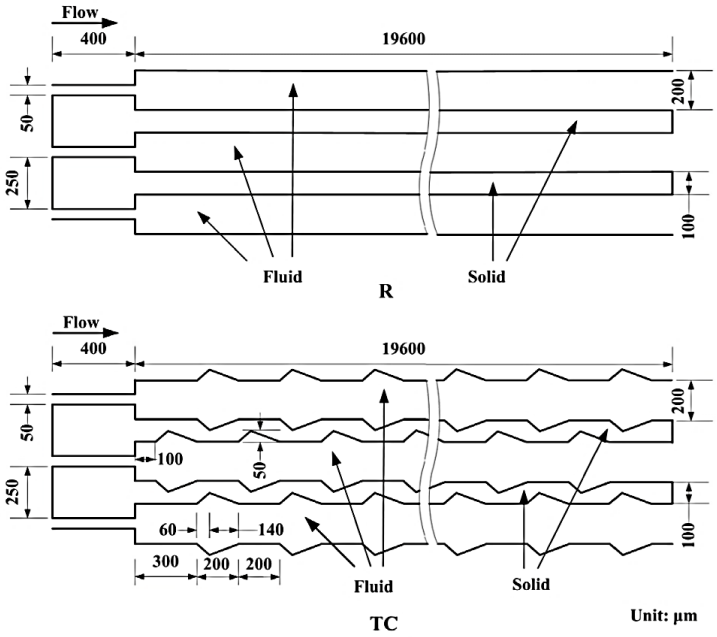

Fig. 2.33: Schematic illustration for different microchannel configurations proposed by Li et al. (2017); (a) conventional microchannel (R); and (b) microchannel with triangular cavities (TC).

Acetone as working fluid with inlet temperature of 29 ^{o}C and mass flux ranging from 83 to 442 kg/m^2.s was used in the experiments. They have obtained significant enhancement of heat transfer, uniform wall temperature, obvious reduction of pressure drop and more stable

flow boiling with flow reversal mitigation in triangular cavities type microchannels compared to conventional rectangular channels.

2.5 Gallium Nitride (GaN) High Electron Mobility Transistor (HEMT) Devices

Over the last decade, gallium nitride (GaN) high-electron-mobility transistors (HEMTs) have become increasingly popular for radio-frequency (RF) and microwave applications due to their robustness, wide band-gap and high thermal conductivities and saturated electron velocities that enable them to function in harsh environments (Millan et al., 2014 and Tsou et al., 2015), see Table 1.1. However, GaN HEMTs dissipate large heat fluxes which create hotspots that can cause significant degradation in performance (Agarwal et al., 2017) when maximum operating temperatures of ~250 ^{o}C are exceeded. To alleviate the problem of hot spots, Silicon carbide (SiC) heat spreaders have been used due to their high thermal conductivity of 370 W/m.K at 20 ^{o}C (Lee et al., 2016). However, since the thermal conductivity of SiC decreases significantly as temperature increases (Dowling et al., 2015), the use of SiC alone is not practical for hot spot mitigation. For high heat fluxes (>100 W/cm^2) single-phase liquid-cooled micro-/minichannel heat sinks can provide the required cooling, due to their effective ability to cool microelectronic devices (Wang et al., 2015).

A number of investigations into the thermal management of GaN HEMTs have appeared in the literature. For example, Calame et al. (2007) used experiments and numerical simulations to study the dissipation of 4 kW/cm^2 over a 1.2 × 5 mm^2 active area of a GaN-on-SiC semiconductor using water-cooled microchannel coolers, while the experimental study of Lee et al. (2012) investigated how to dissipate a heat flux of 11.9 kW/cm^2 over eight heat sources of size 350 × 150 μm^2 on a 7 × 7 mm^2 silicon (Si) die with a maximum hotspot temperature of 175°C. Recently, Lee et al. (2015) and Lee et al. (2016) used three-dimensional numerical simulations to analyse the thermal conditions when a total power of 92.4 W is applied to 40 multiple gates (a heat flux of 330 kW/cm^2 is applied to each gate) located on GaN HEMTs on a SiC-based microchannel heat sink using water and methanol as a coolants in single and two phase flow conditions.

Other relevant studies have focused on the effect of using very high thermal conductivity substrates to enhance heat spreading for GaN HEMT and a number of these have analysed diamond heat spreaders (Felbinger et al., 2007; Babić et al., 2013; and Chu et al., 2015) since diamond's thermal conductivity is 2200 W/m.K – 5.5 times greater than copper (Wort and Balmer, 2008). Han et al. (2014) used experiments and numerical simulations to investigate the effect of 300 μm thick diamond heat spreaders on copper-based microchannel heat sinks containing twenty-one parallel straight rectangular microchannels with a water flow rate of

$0.4\ l/min$ to dissipate 11.9 kW/cm^2 from a GaN-on-Si device. They found that the use of the diamond heat spreader within the liquid-cooled microchannel heat sink enabled, the maximum gate finger temperature to be reduced from 237 ^{o}C to 193 ^{o}C compared with a heat sink without a heat spreader.

Graphene, on the other hand, may be a viable alternative to diamond not only because it is less expensive, but also because of its extremely high thermal conductivity which ranges from 3080–5300 W/m·K at room temperature (Balandin et al., 2008 and Ghosh et al., 2008). In addition, its low density and strength (50-times stronger than steel (Allen et al., 2010)) has created excitement within research teams worldwide. The effect of graphene heat spreaders on operating temperatures have been investigated numerically by Subrina et al. (2009); Barua et al. (2012); and Bae et al. (2014), while Reddy and Dulikravich (2017) used a three-dimensional conjugate heat transfer model to investigate the effect of the thickness of thin film graphene heat spreaders applied to the top wall of micro pin-fin heat sinks on the maximum electronic chip temperature. The latter's results showed that the use of thin graphene heat spreaders can lead to significant reductions in the maximum chip temperature.

However, research has shown that heat spreaders by themselves are insufficient for high heat flux applications and that nanocrystalline diamond (NCD) around the gates can be extremely beneficial under these condition. In recent years, NCD thin-films have advanced significantly (Williams, 2011) due to their unique properties, notably high thermal conductivity (up to 1300 W/m.K for $t_{NCD} > 3$ µm) (Meyer et al., 2014). To mitigate the self-heating effect, NCD has been demonstrated as a top-side coating for improved heat spreading in AlGaN/GaN HEMT devices by Anderson et al. (2017). As a result, HEMTs with NCD heat spreading layers exhibit a 20% decrease in peak channel temperature compared to HEMTs without NCD film. Tadjer et al. (2012) and Tadjer et al. (2016) also used Nanocrystalline diamond heat-spreading film with thickness of 0.5 µm mounted on the top surface of the AlGaN/GaN HEMT device in order to reduce self-heating. Their results showed significant reduction in temperature near the GaN/Si substrate interface, from 340 ^{o}C to 120 ^{o}C after NCD capping.

2.6 Summary

The literature review has shown that the single and two-phase microchannel heat sinks in conjunction with electronics cooling have been investigated quite extensively during the last three decades. Experimental, numerical and analytical studies have been used for a range of different geometries, substrate materials and working fluids in order to investigate the heat transfer and the fluid flow behaviours in different types of mini/micro-scale heat sink.

The experiments and numerical predictions have revealed several advantages of single-phase liquid forced convection in microchannel heat sinks making them more efficient at dissipating heat compared to their conventional counterparts (such as air cooled heat sinks and heat pipes), namely, high surface area-to-volume ratio, very compact and lightweight. However, large heat transfer coefficients cannot be achieved with microchannels having large hydraulic diameter (the heat transfer coefficient is inversely proportional to hydraulic diameter), namely higher heat transfer coefficients, results in high pressure drops. Another drawback can be seen that since the single-phase microfluidic devices rely on sensible heat rise to achieve the cooling, a large temperature gradient will occur in the direction of fluid flow.

Two-phase (flow boiling) microchannel heat sinks offer several distinct benefits over their single-phase counterparts, due to their utilisation of the latent heat of vaporization of a liquid for dissipating high heat fluxes, thus, less coolant flow rates are needed, which consequently results to lower pumping powers. Furthermore, better temperature uniformity can be obtained for fluid and solid. Despite these benefits, several disadvantages can be found in the two-phase microchannel cooling, among these pressure fluctuations and flow instabilities, which lead to flow reversal and this may degrade the heat transfer performance in the microchannel heat sink devices, and also may cause premature critical heat flux (CHF), that CHF is a working limit that needs to be avoided at all times.

Overall, single-phase flow systems are very popular and it is the focus in the current work. It has been shown here there is a broad body of work examining the heat transfer and fluid flow behaviour in conventional microchannel heat sinks including straight rectangular, triangular and trapezoidal microchannels and micro-pin fin heat sinks or other channel shape such as wavy, zigzag and curved microchannels. However, studies of heat transfer and fluid flow of a multi-serpentine rectangular microchannel heat sink with a 180-degree sharp bend or round turned channel are very rare and the implementation of this type of microchannel heat sink is still in its infancy. It can be thought that the main obstacle behind the limited study of this type of heat sinks is due to the lack of substantial understanding in the behaviour of

microchannel system in terms of heat transfer, fluid flow and pressure drop. Therefore, the current study mainly focuses on investigate a multi-serpentine rectangular minichannel heat sink experimentally and numerically using three-dimensional computational simulations of heat transfer for single phase laminar and turbulent liquid flow characteristics. These results will be compared to those obtained with a multi-straight rectangular minichannel heat sink in terms of thermal resistance, pressure drop and Nusselt number. So, the present work is presented to generate understanding in this area.

The review highlights that earlier studies (from 1981 to 1999) were largely conducted using experimental or analytical approaches, whereas the studies after this date (from 2000 to the end of 2017) showed that there is a large dependence on numerical simulations and evolutionary algorithms.

The above studies have demonstrated that flow obstructions and secondary flows in microchannels can enhance the thermal performance without significantly increasing pressure drop. The present study explores a new design of heat exchanger where chevrons fins within multiple serpentine minichannels are used to control the hydrodynamic and thermal boundary layers.

Chapter 3: Heat and Fluid Flow Fundamentals

3.1 Introduction

The basic concepts of fluid flow and heat transfer characteristics in internal flow such as circular pipes and rectangular channels are described in this chapter. Firstly, the types of heat transfer and the non-dimensional parameters that are utilized in this work will be presented. Secondly, the types of flow in channels, hydrodynamic and thermal entrance length, and the types of thermal boundary conditions will be explained. Thirdly, the correlation equations proposed by other researches for friction factor and heat transfer will be discussed. Finally, the optimisation design will be presented.

3.2 Convective Heat Transfer

There are three types of heat transfer which are conduction, convection and radiation. The heat transfered between the microchannel heat sink wall and fluid is by conduction through the heat sink and convection to the liquid. The convective heat transfer can be subdivided into three types as shown in Fig. 3.1. In this chapter, we will focus and deal with the theory and correlation equations proposed for internal forced convection heat transfer.

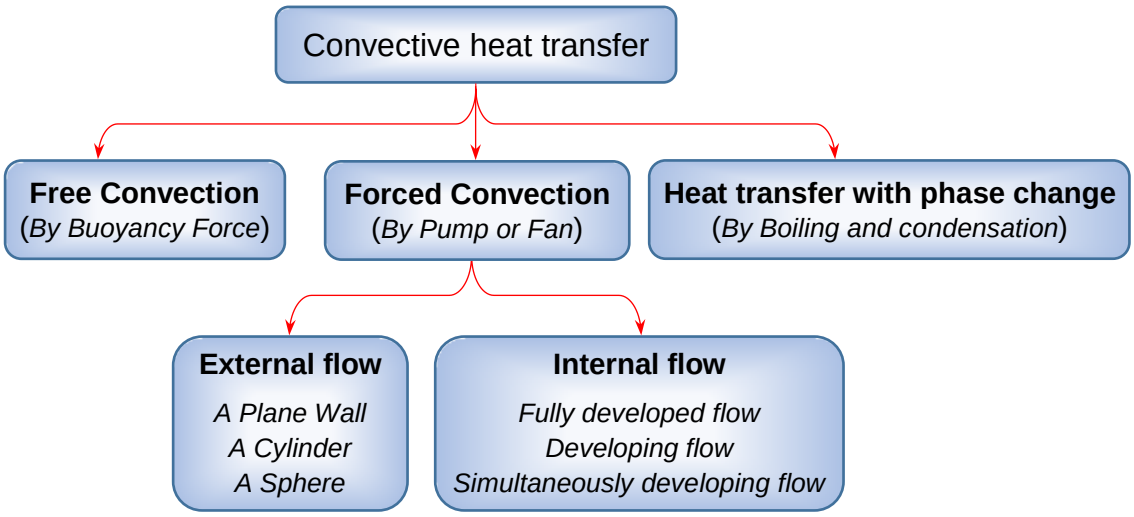

Fig. 3.1: Simple flowchart for types of convective heat transfer.

3.3 Dimensionless Parameters in Fluid Flow and Heat Transfer

3.3.1 Reynolds Number (Re)

The Reynolds number (Re) is used to describe the nature and regime of the flow, and it is defined as the ratio of the inertial force to the viscous force within the flowing fluid as:

$$Re = \frac{\rho_f \cdot V_{ch} \cdot D_h}{\mu_f} = \frac{V_{ch} \cdot D_h}{\nu_f} \tag{3.1}$$

where μ_f, ν_f and ρ_f are respectively the dynamic viscosity (kg/m.s), kinematic viscosity (m^2/s) and fluid density (kg/m^3), while D_h denotes the characteristic length or hydraulic diameter (m) and traditionally defined by $D_h = \frac{4A_{ch}}{P_w}$, for both circular and non-circular cross sections, see Eq. (1.1). For non-circular cross sections, for example consider a rectangular duct having width (W_{ch}) and depth (H_{ch}) the D_h become:

$$D_h = \frac{2\,(W_{ch} \cdot H_{ch})}{W_{ch} + H_{ch}} = \frac{2H_{ch}^2\left(\frac{W_{ch}}{H_{ch}}\right)}{H_{ch}\left(1 + \frac{W_{ch}}{H_{ch}}\right)} = H_{ch}\left(\frac{2 \propto}{1 + \propto}\right) \tag{3.2}$$

where $\propto$ is the channel aspect ratio and it is defined as the short side of the channel (channel width, W_{ch}) divided by the long side of the channel (channel height, H_{ch}) as:

$$\propto = \frac{W_{ch}}{H_{ch}}, \quad W_{ch} < H_{ch} \quad , \quad 0.1 \leq \propto \leq 1.0 \tag{3.3}$$

3.3.2 Prandtl Number (Pr)

The Prandtl number (Pr) is an important dimensionless parameter in convection heat transfer, because of it is provides a measure of the relative ability of a fluid to transport momentum and energy (Nellis and Klein, 2009). The Pr is defined as the ratio of the momentum diffusivity to the thermal diffusivity as:

$$Pr = \frac{\text{Momentum diffusivity}}{\text{Thermal diffusivity}} = \frac{\nu}{\alpha} = \frac{\mu_f/\rho_f}{k_f/\rho_f . C_{p_f}} = \frac{\mu_f . C_{p_f}}{k_f} \tag{3.4}$$

where C_{p_f} and k_f respectively denotes the specific heat capacity (J/kg.K) and the thermal conductivity (W/m.K) of the fluid. The relative thickness of the velocity (δ_u) and the thermal (δ_{th}) boundary layers can be described by the Prandtl number as:

$$Pr = \left(\frac{\delta_u}{\delta_{th}}\right)^{\frac{1}{n}} \tag{3.5}$$

where n is a positive exponent ($n > 0$). Fig. 3.2 shows the Pr as a function of temperature for a variety of fluids at atmospheric pressure. For fluids with laminar flow and low Prandtl number ($Pr << 1$) (e.g., liquid metals such as Mercury), the thermal boundary layer is thicker than the velocity boundary layer; the fluid is low viscosity but very conductive (the fluid will transport thermal energy very well but not momentum). While in the case of $Pr >> 1$, such as engine oils, the thermal boundary layer is fully contained within the velocity boundary layer, as shown in Fig. 3.3, and the fluid in this case is viscous and non-conductive (the fluid will transport momentum very well but not thermal energy).

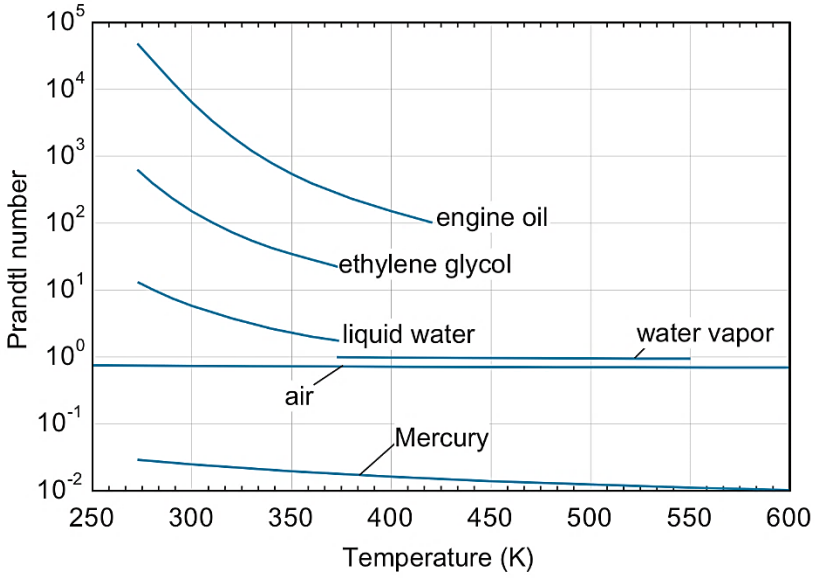

Fig. 3.2: Prandtl number versus temperature for various fluids (Nellis and Klein, 2009).

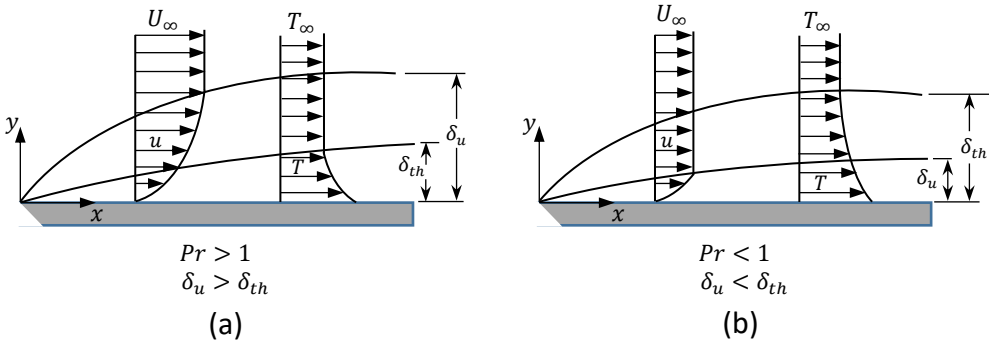

Fig. 3.3: The hydrodynamic and thermal boundary layer thicknesses for (a) $Pr > 1$; and (b) $Pr < 1$.

For turbulent flow regime, the boundary layer development is influenced strongly by the random fluctuations in the fluid and not by the molecular diffusion and both thicknesses are similar ($\delta_u = \delta_{th}$), (Bejan, 2013).

3.3.3 Nusselt Number (Nu)

The non-dimensional heat transfer coefficient in forced convection heat transfer is usually expressed by the Nusselt number (Nu), it is defined as the ratio of the convective to the conductive heat transfer rates across the boundary as represented:

$$Nu = \frac{\text{Convective heat transfer}}{\text{Conductive heat transfer}} = \frac{h \cdot A \cdot \Delta T}{k_f \cdot A \cdot \frac{\Delta T}{\Delta x}} = \frac{h \cdot L}{k_f} \tag{3.6}$$

where L and k_f are respectively the characteristic length of the channel (m) and the fluid thermal conductivity (W/m.K). The Nu value can be easily determined if the convective heat

transfer coefficient (h) is known. The Nu depends on the Reynolds number (Re), the Prandtl number (Pr) and fluid properties. Therefore, the heat transfer experimental data for internal flow can be generalized in the following functional relationships:

$$Nu = yRe^{m}Pr^{n}\left(\frac{\mu_b}{\mu_w}\right)^{p} \tag{3.7}$$

where y is the coefficient and the terms m, n, and p are the exponents determined by experimental analyses and curve fitting. The symbols μ_b and μ_w are respectively the viscosity of the fluid (kg/m.s) calculated at the bulk fluid temperature and the wall temperature.

3.4 Hydrodynamic and Thermal Entrance Region

To calculate the pressure drop (ΔP) and heat transfer coefficient (h) inside the straight rectangular mini/microchannel, it is important to know whether the flow is a hydrodynamically fully developed and/or thermally developing flow, or a simultaneously developing flow (hydrodynamically and thermally developing flow). In this case, the hydrodynamic entry length (L_{hy}) must be firstly calculated to establish the type of the flow, which is defined as the distance from the channel entrance to the point at which the hydrodynamic boundary layer merges at the centreline, as shown in Fig. 3.4.

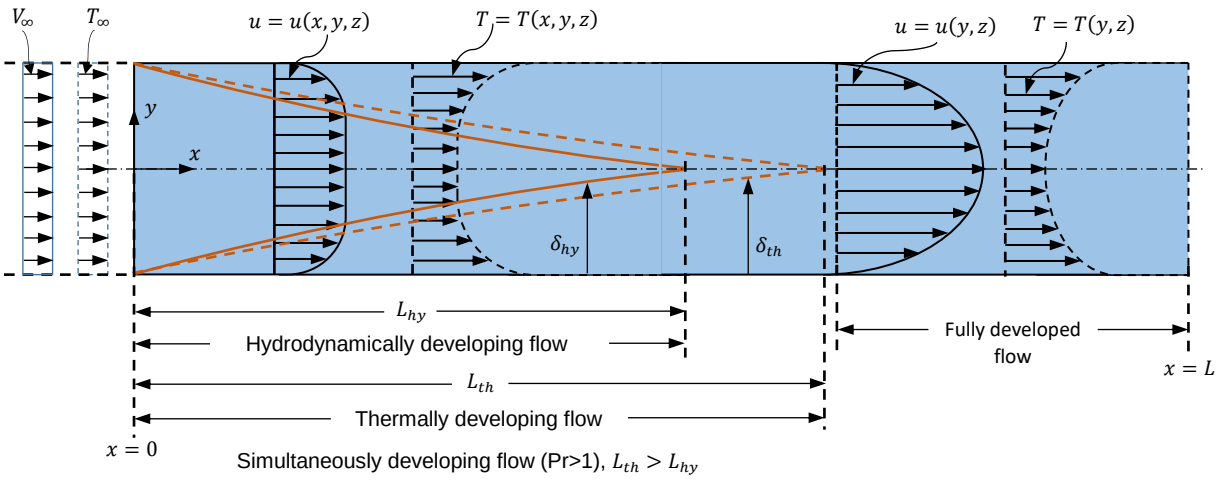

Fig. 3.4: Developing flow (hydrodynamically and thermally developing flow), followed by fully developed (hydrodynamically and thermally fully developed flow) in channel under constant wall temperature boundary condition (Shah and Bhatti, 1987).

The velocity profile develops in the entrance region and the flow in this region is called hydrodynamically developing flow. After the hydrodynamic entrance region the shape of velocity profile is parabolic and remains unchanged and the flow become hydrodynamically fully developed. In laminar flow regime, the L_{hy} can be calculated based on the well accepted equation proposed by Shah and London (1978):

$$L_{hy} = L_{hy}^{+} \cdot Re \cdot D_h \quad (3.8)$$

where L_{hy}^{+} represents the dimensionless hydrodynamic entry length which depends on the aspect ratio ($\propto$) of the channel geometry, and in the present study was taken to be 0.05 to reach a fully developed conditions (Kandlikar, 2014). For single-phase laminar flow in a rectangular channel, the length of the hydrodynamic developing (entrance) region (L_{hy}) can be estimated by the following equation given by Shah and London (1978):

$$L_{hy} = (0.06 + 0.07 \propto -0.04 \propto^2)\, Re \cdot D_h \quad (3.9)$$

Another entry length should be determined which is thermal entry length (L_{th}). It is defined as the distance from the channel entrance to the point at which the thermal boundary layer merges at the centreline, see Fig. 3.4. The temperature profile in the entrance region is developed and the flow is called thermally developing flow. Beyond the thermal entrance region the thermal profile remains unchanged and the flow become thermally fully developed. For laminar flow regime, the L_{th} can be estimated using equation proposed by Shah and London (1978) as given by:

$$L_{th} = L_{th}^{*} \cdot Re \cdot D_h \cdot Pr \quad (3.10)$$

where L_{th}^{*} denotes the dimensionless thermal entry length, and following Lee et al. (2005) was taken to be 0.05 in this study for fully developed conditions.

In fully developed region in which the flow is both hydrodynamically and thermally developed, the friction factor (f) and heat transfer coefficient (h) are lowest and remained constant along the length of the channel (Çengel and Cimbala, 2013). Simultaneously developing flow is flow in which both the velocity and the temperature profiles are developing, as shown in Fig. 3.4. In simultaneously developing flow both of the f and h vary in the flow direction. Table 3.1 demonstrates the relationships between the types of flow, boundary layers, velocity and temperature distributions, the friction factor, and the Nusselt number (Nu) (Rohsenow et al., 1998).

Table 3.1: Flow types.

Flow type	Hydrodynamic boundary layer	Velocity distribution in the flow direction	Friction factor	Thermal boundary layer	Dimensionless temperature distribution in the flow	Nusselt number
Fully developed flow	Developed	Invariant	Constant	Developed	Invariant	Constant
Hydrodynamically developing flow	Developing	Variant	Variant	----	----	----
Thermally developing flow	Developed	Invariant	Constant	Developing	Variant	Variant
Simultaneously developing flow	Developing	Variant	Variant	Developing	Variant	Variant

3.5 Effect of Transition on Local Heat Transfer Coefficient

Fig. 3.5 illustrates the velocity boundary layer (δ_u) development of fluid flowing over a flat plate surface. The fluid velocity at the entrance (x=0) is uniform and become zero at the plate surface due to the no-slip condition. The fluid velocity reaches the free-stream velocity (u_∞) at a certain distance from the plate surface. This distance is known as the δ_u and is defined as the distance at which $u = 0.99u_\infty$. In the turbulent boundary layer, three different regions may be delineated as a function of distance from the surface. The first region is a very thin layer formed above the flat plate surface called viscous sublayer (laminar sublayer) in which transport is dominated by diffusion and the velocity profile is nearly linear. Buffer layer is a second region generated above the viscous layer directly in which diffusion and turbulent mixing are comparable, while the third region is the turbulent layer in which transport is dominated by turbulent mixing.

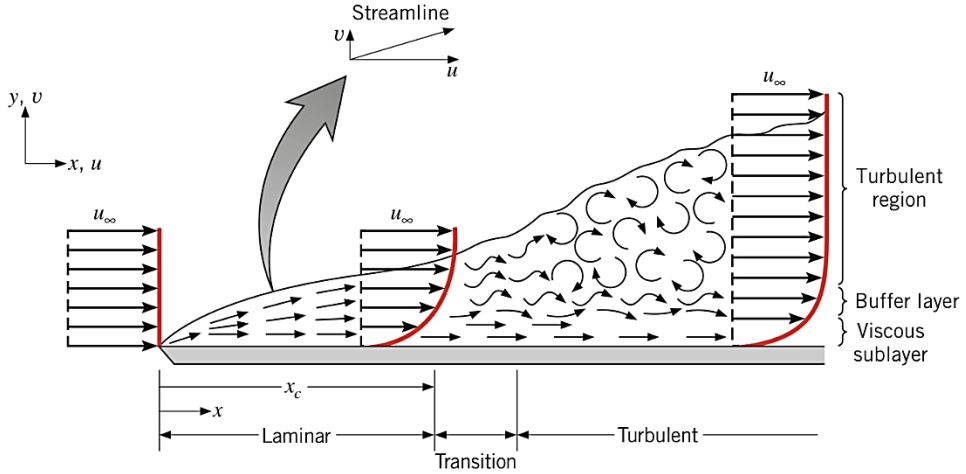

Fig. 3.5: Velocity boundary layer development on a flat plate (Bergman et al., 2017).

Fig. 3.6 shows the variation of the velocity boundary layer thickness (δ_u) and the local heat transfer coefficient (h) for flow over an isothermal flat plate. Boundary layers are essentially an insulation layer, so that when they are thin the flow of heat is greatest, as the temperature gradient will decrease as the boundary layer thickens. In the laminar flow regime, the heat transfer coefficient is very high at the entrance region and this belong to the boundary layer thickness which is zero, and as the δ_u increase the heat transfer coefficient decrease. When the boundary becomes turbulent there is a mixing of warm and colder fluid, which increases the heat transfer coefficient, and then the local heat transfer coefficient return to decrease again as δ_u increase. In the transition region, a significant increase in the local heat transfer coefficient can be found despite the increase in the boundary layer thickness. This behaviour can be explained that in the transitional region mixing turbulent mixing starts and since the boundary layer is thinner the impact of the first stages of mixing are greatest and then the

boundary layer continues to thicken by mixing still takes place however its impact on heat transfer gradually reduces.

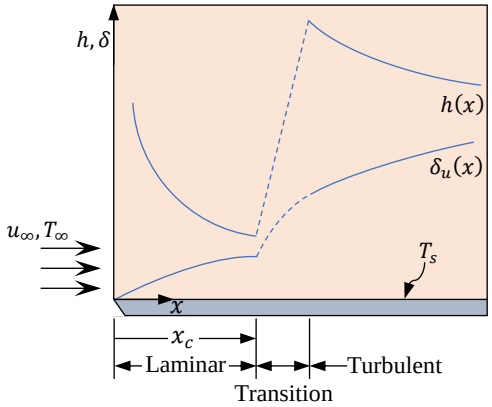

Fig. 3.6: Variation of velocity boundary layer thickness and the local heat transfer coefficient for flow over an isothermal flat plate (Bergman et al., 2017).

3.6 Surface Thermal Conditions for Convection Heat Transfer

The thermal conditions at the surface can usually be approximated either constant heat flux boundary condition or constant wall temperature boundary condition as explained below. The corresponding temperature variations with tube length for these two conditions are shown in Fig. 3.7. If there is fluid flow inside the tube having length L and diameter D and heat is convected through the tube wall by applying the steady-flow energy balance to a control volume (C.V) in a tube as shown in Fig. 3.7, gives (Bergman et al., 2017):

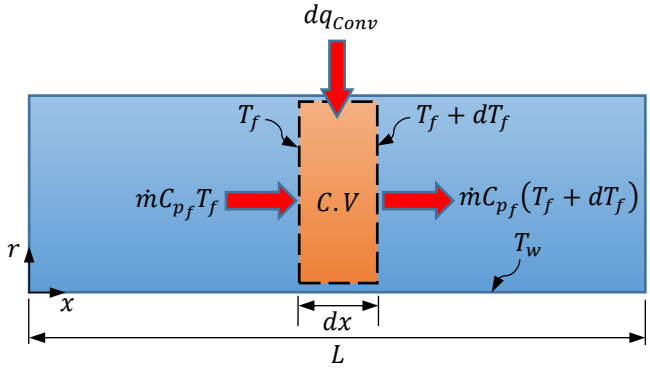

Fig. 3.7: Control volume of fluid flowing in a tube.

Rate of heat flow through wall + Rate of energy inflow = Rate of energy outflow

$$dq_{Conv} + \dot{m} \cdot C_{p_f} \cdot T_f = \dot{m} \cdot C_{p_f}\left(T_f + dT_f\right) \tag{3.11}$$

The heat applied (dq_{Conv}) to the control volume throughout convection can be expressed as:

$$dq_{Conv} = q_s^{"} \cdot dA \tag{3.12}$$

where $dA = Pdx$ and P is the perimeter of the tube (m). By using the Newton's law of cooling, the convective heat transfers from the tube wall to the fluid stream can be determined as:

$$q_s^{"} = h(T_w - T_f) \tag{3.13}$$

By substituting Eq. (3.12) and Eq. (3.13) in Eq. (3.11) gives:

$$\frac{dT_f}{dx} = \frac{P}{\dot{m} \cdot C_{p_f}} h(T_w - T_f) \tag{3.14}$$

3.6.1 Constant Wall Heat Flux Boundary Condition (CWHF)

In the fully developed region, the wall temperature (T_w) will increase linearly in the flow direction as the same mean fluid temperature ($T_{f,x}$), and the difference temperature between the wall and the mean fluid remains constant, as shown in Fig. 3.8(a). In the developing region, the wall temperature will vary non-linearly in this region.

In the case of fully developed region under the constant wall heat flux (CWHF) boundary condition, the local (h_x) and average heat transfer coefficient (h_{avg}) is constant, since the fluid properties remain constant during flow, and the differentiation of Eq. (3.13) with respect to x gives:

$$\frac{dT_f}{dx} = \frac{dT_w}{dx} \tag{3.15}$$

From Eq. (3.15) the temperature gradient ($T_w - T_f$) remains constant and the temperature profile shape does not change along the tube.

3.6.2 Constant Wall Temperature Boundary Condition (CWT)

As shown in Figs. 3.8 (a and b), the constant wall temperature (CWT) boundary condition shows a very different behaviour than the constant wall heat flux (CWHF) boundary condition.

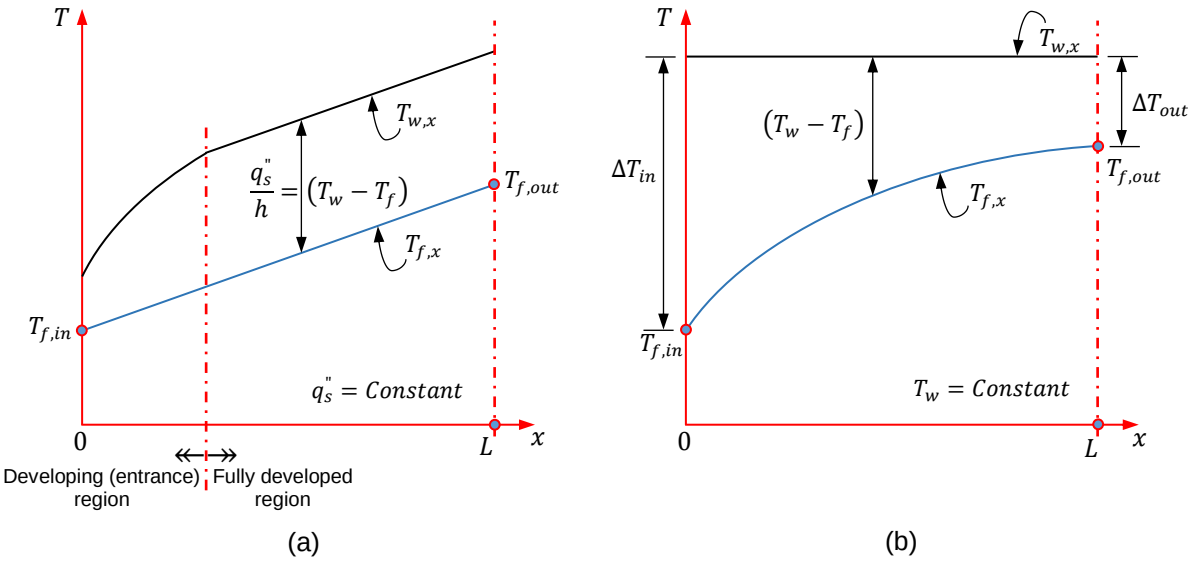

Fig. 3.8: Axial temperature variation for heat transfer in a channel; (a) Constant surface heat flux; and (b) Constant surface temperature.

By integrating Eq. (3.14) from $x = 0$ ($T_f = T_{f,in}$) to $x = L$ ($T_f = T_{f,out}$):

$$\int_{T_{f,in}}^{T_{f,out}} \frac{d(T_w - T_f)}{(T_w - T_f)} = -\frac{h.P}{\dot{m} \cdot C_{p_f}} \int_0^L dx \tag{3.16}$$

$$ln\left(\frac{T_w - T_{f,out}}{T_w - T_{f,in}}\right) = -\frac{h.A}{\dot{m} \cdot C_{p_f}} \tag{3.17}$$

The rate of heat transfer can also be determined as:

$$q = h \cdot A(T_w - T_f) = \dot{m} \cdot C_{p_f}(T_{f,out} - T_{f,in}) \tag{3.18}$$

Rearrangement Eq. (3.17) for $\dot{m} \cdot C_{p_f}$ and then substituting it into Eq. (3.18), it can be obtained:

$$q = h \cdot A \cdot \Delta T_{ln} \tag{3.19}$$

where ΔT_{ln} is the logarithmic mean temperature difference, and equal to:

$$\Delta T_{ln} = \frac{T_{f,in} - T_{f,out}}{ln\left(\frac{T_w - T_{f,out}}{T_w - T_{f,in}}\right)} = \frac{\Delta T_{out} - \Delta T_{in}}{ln\left(\frac{\Delta T_{out}}{\Delta T_{in}}\right)} \tag{3.20}$$

where $\Delta T_{in} = T_w - T_{f,in}$ and $\Delta T_{out} = T_w - T_{f,out}$

3.7 Types of Thermal Boundary Conditions

There are three main types of thermal boundary conditions are the most commonly used in the case of microchannel heat sink. The first one is uniform (Constant) wall temperature boundary condition, T, (uniform wall temperature, axially, and circumferentially). The other two are constant heat flux boundary conditions. The first one is the constant wall heat flux boundary condition, H1, (axially constant wall heat flux and circumferentially constant wall temperature). While the second one is the constant wall heat flux boundary condition, H2, (circumferentially and axially uniform heat flux). The Nusselt number (Nu) for T, H1, and H2 boundary conditions for fully developed laminar flow with four side heating in rectangular channel are respectively (Shah and London, 1978):

$$Nu_T = 7.541\,(1 - 2.61 \propto + 4.97 \propto^2 - 5.119 \propto^3 + 2.702 \propto^4 - 0.548 \propto^5) \tag{3.21}$$

$$Nu_{H1} = 8.235\,(1 - 2.0421 \propto + 3.0853 \propto^2 - 2.4765 \propto^3 + 1.0578 \propto^4 - 0.1861 \propto^5) \tag{3.22}$$

$$Nu_{H2} = 8.235\,(1 - 10.6044 \propto + 61.1755 \propto^2 - 155.1803 \propto^3 + 176.9203 \propto^4 - 72.923 \propto^5) \tag{3.23}$$

3.8 Friction Factor, Heat Transfer and Thermal Resistance Correlations

3.8.1 Friction Factor

The Fanning friction factor for fully developed laminar flow ($f_{fd,lam}$) in a rectangular microchannel can be obtained using the following correlation equation given by Shah and London (1978):

$$f_{fd,lam} = \frac{24}{Re}(1 - 1.3553 \propto +1.9467 \propto^2 - 1.7012 \propto^3 + 0.9564 \propto^4 - 0.2537 \propto^5) \quad (3.24)$$

The Reynolds number (Re) can be calculated using Eq. (3.1). In the present work, the water properties were determined using the equations proposed by Popiel and Wojtkowiak (1998) at the bulk-fluid temperature. More detail of this can be found in Appendix B. The experimental Poiseuille number (Po) can be determined by multiplying the friction factor obtained from Eq. (3.24) by Reynolds number:

$$Po = f_{fd,lam} \cdot Re \quad (3.25)$$

Another correlation equation can be used to determine the Fanning friction factor for fully developed laminar flow in a rectangular mini/microchannel as introduced by Knight et al. (1991):

$$f_{fd,lam} = \frac{4.7 + 19.64\, G}{Re} \quad (3.26)$$

where G is the geometric parameter and defined as:

$$G = \frac{\left(\frac{W_{ch}}{H_{ch}}\right)^2 + 1}{\left(\frac{W_{ch}}{H_{ch}} + 1\right)^2} = \frac{\propto^2 + 1}{(\propto +1)^2} \quad (3.27)$$

The vast majority of studies and research for fluid flow and heat transfer characteristic in microchannels have been conducted under fully developed flow condition by neglecting the entrance region in microchannel, whilst the effects of the entrance region are entirely clear on the results obtained in terms of friction factor (f) and heat transfer coefficient (h) for both flow laminar and turbulent regimes. Therefore, to get accurate results the effect of the entrance region must be considered by calculating the friction factor and heat transfer coefficient in both the developing and fully developed flow regions.

By taking into account the entrance region, the apparent Fanning friction factor for hydrodynamically developing laminar flow ($f_{app,lam}$) can be determined according to an empirical formula of Churchill and Usagi (1972) type obtained by Copeland (1995) using data obtained from Shah and London (1978):

$$f_{app,lam} = \frac{\sqrt{\left(\frac{3.2}{(x^+)^{0.57}}\right)^2 + \left(f_{fd,lam} \cdot Re\right)^2}}{Re} \quad , \quad x^+ < 0.05 \tag{3.28}$$

$$x^+ = \frac{x}{Re \cdot D_h} \tag{3.29}$$

where x^+ is the dimensionless hydrodynamic axial distance at the axial distance downstream from the channel entrance, x. For hydrodynamic developing laminar flow, Shah (1978) proposed the following correlation equation for estimating apparent friction factor in the hydrodynamic entry region for circular and non-circular channels (ducts).

$$f_{app,lam} = \frac{3.44}{Re\sqrt{x^+}} + \frac{\left(f_{fd,lam} \cdot Re\right) + \frac{\kappa(\infty)}{4x^+} - \frac{3.44}{\sqrt{x^+}}}{Re\left(1 + \frac{C}{x^{+2}}\right)} \tag{3.30}$$

where C is a constant dependent on the channel geometry which is in the range of 29×10^{-6} – 29×10^{-5} and can be interpolated from Table 3.2 that suggested by Shah (1978) for rectangular channel at different aspect ratio. $\kappa(\infty)$ is the incremental pressure drop number which depends on the channel aspect ratio ($\propto$) for rectangular microchannels which is presented in graphical form by Shah and London (1978). Qu et al. (2006) and Lee and Qu (2007) obtained the curve-fit equation for the incremental pressure drop number and constant C in terms of aspect ratio, and can be expressed as the following equation:

$$\kappa(\infty) = 0.674 + 1.2501 \propto + 0.3417 \propto^2 - 0.8358 \propto^3 \tag{3.31}$$

$$C = (0.1811 + 4.3488 \propto + 1.6027 \propto^2) \times 10^{-4} \tag{3.32}$$

Table 3.2: Values of Incrementał pressure drop, Poiseuille number and constant C for rectangular channel at different aspect ratio (Shah, 1978).

Aspect ratio, $\propto$	$\kappa(\infty)$	$f_{fd,lam} \cdot Re$	C	% Error
0.0	0.674	24.000	0.000029	± 2.4
0.2	0.931	19.071	0.000076	± 1.7
0.5	1.280	15.548	0.00021	± 1.9
1.0	1.430	14.227	0.00029	± 2.3

Phillips (1987) and Kandlikar (2014) used the data collected from the work of Curr et al. (1972) and Shah and London (1978) and plotted $f_{app} \cdot Re$ versus x^+ at different inverse aspect ratio **($\propto^*$)** as shown in Fig. 3.9.

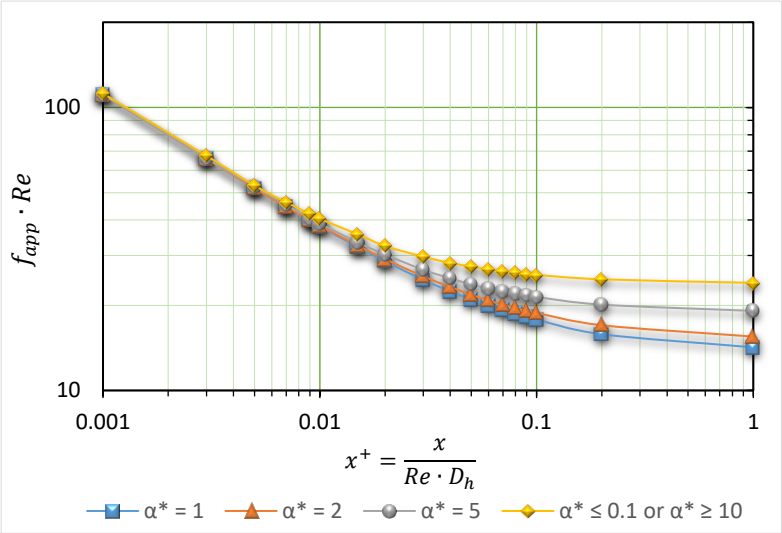

Fig. 3.9: Developing laminar flow apparent friction factor in rectangular channel employed in computer simulation of Phillips (1987).

The friction factor in laminar flow regime depends only on the Reynolds number ($Re < 2300$), while in turbulent flow regime it depends only on the relative roughness ($\frac{\varepsilon}{D_h}$), where ε is the surface roughness parameter. In the transition zone, the friction factor depends on both Re and $\frac{\varepsilon}{D_h}$ (Wu and Little, 1983). For fully developed turbulent flow in smooth pipes, in a range of $3000 < Re < 10^5$. The following equation proposed by Blasius has shown that the Fanning friction factor can be approximated by (Hager, 2003):

$$f_{Blasius,turb} = \frac{0.079}{(Re)^{1/4}} \tag{3.33}$$

The Blasius' equation is valid when the relative roughness ($\frac{\varepsilon}{D_h}$) is $\leq 10^{-6}$ (smooth surface). In order to take into account the effect of the surface roughness on the friction factor, Haaland (1983) modified the Colebrook (1939) equation to calculate the Darcy friction factor in tube under fully developed turbulent flow condition as:

$$f_{Haaland} = \left(-1.8 . \log_{10} \left(\frac{6.9}{Re} + \left(\frac{\frac{\varepsilon}{D_h}}{3.7} \right)^{1.11} \right) \right)^{-2} \tag{3.34}$$

In the case of developing turbulent flow, Phillips (1988 and 1990) offered a correlation equation to evaluate the apparent friction factor of a rectangular microchannel:

$$f_{Phillips,turb} = A\left(Re_{eq}\right)^B \tag{3.35}$$

$$A = 0.0929 + \frac{1.01612}{\left(\frac{L_t}{D_h}\right)} \tag{3.36}$$

$$B = -0.268 - \frac{0.3193}{\left(\frac{L_t}{D_h}\right)} \tag{3.37}$$

L_t is the total length (m) of the mini/microchannel, whereas Re_{eq} and $D_{h_{eq}}$ represent the equivalent Reynolds number and the equivalent hydraulic diameter (m), respectively, which proposed by Jones (1976) for rectangular channels as:

$$Re_{eq} = \frac{\rho_f \cdot V_{ch} \cdot D_{h_{eq}}}{\mu_f} \tag{3.38}$$

$$D_{h_{eq}} = \left(\frac{2}{3} + \frac{11}{24} \cdot \propto (2 - \propto)\right) D_h \tag{3.39}$$

3.8.2 Heat Transfer

The average Nusselt number of the fluid (Nu_{avg}) which represents a *dimensionless* heat transfer coefficient, can be determined as follows:

$$Nu_{avg} = \frac{h_{avg} \cdot D_h}{k_f} \tag{3.40}$$

where h_{avg} represents the average heat transfer coefficient (W/m^2.K). With water as the working fluid and for a fully developed laminar flow in a four-sided heated channel, the Nusselt number can be calculated as proposed by Shah and London (1978):

$$Nu_{fd\_4,lam} = 8.235\,(1 - 2.0421 \propto + 3.0853 \propto^2 - 2.4765 \propto^3 + 1.0578 \propto^4 - 0.1861 \propto^5) \tag{3.41}$$

Eq. (3.41) presents the fully developed Nusselt numbers for commonly used geometries under H1 boundary conditions (Constant circumferential wall temperature, uniform wall heat flux axially) with four-sided heating (Kandlikar, 2014). This boundary condition is found if the wall is highly conductive. The Nusselt number under H1 boundary conditions for laminar thermally fully developed flow in a heated channel (three sides heated and top side is insulated) is:

$$Nu_{fd\_3,lam} = 8.235\,(1 - 1.883 \propto + 3.767 \propto^2 - 5.814 \propto^3 + 5.361 \propto^4 - 2 \propto^5) \tag{3.42}$$

To simulate the real case, in which three walls are heated, Phillips (1988 and 1990) suggests that the Nusselt number for thermally developing flow can be calculated using:

$$Nu_{x,3}(x^*, \propto) \approx Nu_{x,4}(x^*, \propto) \cdot \frac{Nu_{fd\_3,lam}(\propto)}{Nu_{fd\_4,lam}(\propto)} \tag{3.43}$$

where $Nu_{fd\_4,lam}$ and $Nu_{fd\_3,lam}$ denotes the Nusselt numbers in the fully-developed region in the microchannel for the four-sided and three-sided heating cases respectively as defined

above in Eqs. (3.41) and (3.42). These values can be determined either from Eqs. (3.41) and (3.42) or using Table 3.3 proposed by Phillips (1987) at different channel aspect ratio ($0.1 \leq \propto \leq 10$).

Table 3.3: Fully developed laminar flow Nusselt number in rectangular channel for the H1 boundary condition with three and four walls transferring heat, and with uniform axial heat flux (Phillips, 1987).

$\propto = \frac{W_{ch}}{H_{ch}}$	$Nu_{fd\_4,lam}$	$Nu_{fd\_3,lam}$	$\propto = \frac{W_{ch}}{H_{ch}}$	$Nu_{fd\_4,lam}$	$Nu_{fd\_3,lam}$
0	8.235	8.235	0.9	3.620	—
0.1	6.785	6.939	1	3.608	3.556
0.2	5.738	6.072	1.43	3.750	3.195
0.3	4.990	5.393	2	4.123	3.146
0.4	4.472	4.885	2.5	4.472	3.169
0.5	4.123	4.505	3.33	4.990	3.306
0.6	3.895	—	5	5.738	3.636
0.7	3.750	3.991	10	6.785	4.252
0.8	3.664	—	∞	8.235	5.385

Unheated wall (Adiabatic)

The $Nu_{x,4}$ represents the Nusselt number for thermally developing region for the four-sided heating case at a distance x. The value of $Nu_{x,4}$ can be obtained using the data tabulated in Table 3.4 suggested by Phillips (1987 and 1990) at different inverse aspect ratio ($\propto^*$) and dimensionless thermal axial distance (x^*).

Table 3.4: Developing laminar flow Nusselt number in rectangular channel for the H1 boundary condition used in the computer simulation of Phillips (1987 & 1990).

$x^* = \frac{x}{Re \, . D_h \, . Pr}$	$Nu_{x,4}$					
	$\propto^* \leq 0.1$	$\propto^* = 1$	$\propto^* = 2$	$\propto^* = 3$	$\propto^* = 4$	$\propto^* \geq 10$
0.0001	31.6	25.2	23.7	27	26.7	31.4
0.0025	11.2	8.9	9.2	9.9	10.4	11.9
0.005	9	7.1	7.46	8.02	8.44	10
0.00556	8.8	6.86	7.23	7.76	8.18	9.8
0.00625	8.5	6.6	6.96	7.5	7.92	9.5
0.00714	8.2	6.32	6.68	7.22	7.63	9.3
0.00833	7.9	6.02	6.37	6.92	7.32	9.1
0.01	7.49	5.69	6.05	6.57	7	8.8
0.0125	7.2	5.33	5.7	6.21	6.63	8.6
0.0167	6.7	4.91	5.28	5.82	6.26	8.5
0.025	6.2	4.45	4.84	5.39	5.87	8.4
0.033	5.9	4.18	4.61	5.17	5.77	8.3
0.05	5.55	3.91	4.38	5	5.62	8.25
0.1	5.4	3.71	4.22	4.85	5.45	8.24
≥ 1	5.38	3.6	4.11	4.77	5.35	8.23

By taking into account the thermal entrance effect in a microchannel, the average Nusselt number for developing laminar flow in a rectangular microchannel can be calculated by the following correlation:

$$Nu_{avg} = \sqrt[3]{\left(\frac{2.22}{(x^*)^{1/3}}\right)^3 + \left(Nu_{fd,lam}\right)^3} \tag{3.44}$$

Eq. (3.44) was proposed by Copeland (2000) who took the data from Shah and London (1978) and fitted these data to an equation of the same form as that of Eq. (3.28) for the apparent friction factor. The dimensionless thermal axial distance (x^*) can be expressed as:

$$x^* = \frac{x}{Re \cdot Pr \cdot D_h} \tag{3.45}$$

The Nusselt number for fully developed laminar flow in a rectangular mini/microchannel can be approximated by the following equation (Copeland, 2000):

$$Nu_{fd,lam} = 8.31 \times G - 0.02 \tag{3.46}$$

Hwu and Qu (2010) obtained a new correlation equation for rectangular microchannels with a three-sided wall and four-sided wall heating under H1 boundary conditions, which are capable of predicting heat transfer in the thermally developing region for single phase laminar flow. From their numerical results, a correlation equation for the local average Nusselt number for the thermally developing region for both three sided and four-sided heating wall were determined as a function of x^* and $\propto^*$ as given below:

$$Nu_{x,4} = Nu_{fd\_4,lam} + 8.68(x^* \times 10^3)^{-0.506} \cdot e^{(-8.779\propto^* - \mathbf{23.157})x^*} \tag{3.47}$$

$$Nu_{x,3} = Nu_{fd\_3,lam} + 8.68(x^* \times 10^3)^{-0.506} \cdot e^{(-9.427\propto^* - \mathbf{23.472})x^*} \tag{3.48}$$

The correlation equations proposed above by Hwu and Qu (2010) have been compared with two correlation equations. The first comparison was with a correlation equation proposed by Phillips (1987 and 1990) for three-sided heating and a good agreement was achieved by submitting Eq. (3.47) in the equation proposed by Phillips. Whilst, the other comparison was conducted against the Lee and Garimella (2006) correlation equation who utilized a CFD package, FLUENT, to solve numerically heat transfer in rectangular microchannel for laminar single flow. The numerical study of Lee and Garimella (2006) was used to calculate the local average Nusselt number in the thermally developing region for the four-sided heating case under the H1 boundary condition and for $\propto^*$ ranging from 1 to 10. The local average Nusselt number in the thermally developing region can be calculated when the dimensionless thermal axial distance (x^*) is less than the dimensionless thermal entrance length (x^*_{th}) as given by:

$$Nu_{x,4} = \frac{1}{C_1(x^*)^{C_2} + C_3} + C_4 \quad \text{for} \quad 1 \leq \propto^* \leq 10 \quad \text{and} \quad x^* < x^*_{th} \tag{3.49}$$

where x^*_{th}, C_1, C_2, C_3 and C_4 can be determined as follows:

$$x_{th}^{*} = \frac{-1.275\times10^{-6}}{\propto^{6}} + \frac{4.709\times10^{-5}}{\propto^{5}} - \frac{6.902\times10^{-4}}{\propto^{4}} + \frac{5.014\times10^{-3}}{\propto^{3}} - \frac{1.769\times10^{-2}}{\propto^{2}} + \frac{1.845\times10^{-2}}{\propto} + 0.05691 \quad (3.50)$$

$$C_1 = \frac{-2.757\times10^{-3}}{\propto^{3}} + \frac{3.274\times10^{-2}}{\propto^{2}} - \frac{7.464\times10^{-5}}{\propto} + 4.476 \quad (3.51a)$$

$$C_2 = 0.6391 \quad (3.51b)$$

$$C_3 = \frac{1.604\times10^{-4}}{\propto^{2}} - \frac{2.622\times10^{-3}}{\propto} + 2.568\times10^{-2} \quad (3.51c)$$

$$C_4 = 7.301 - \frac{13.11}{\propto} + \frac{15.19}{\propto^{2}} - \frac{6.094}{\propto^{3}} \quad (3.51d)$$

By substituting $Nu_{x,4}$ in Eq. (3.43) proposed by Phillips (1987 and 1990), the Nusselt number for three-sided heating wall can be obtained. When x^{*} is larger than x_{th}^{*}, the flow can be assumed to be fully developed and Eq. (3.42) can be employed to calculate the local average Nusselt number for three-sided heating wall microchannels.

The Nusselt number for fully developed turbulent flow regime in rectangular microchannel can be estimated by using the empirical correlation equation that was proposed by Dittus and Boelter (1930) for a smooth circular tube. This equation is known as the Dittus-Boelter equation as given:

$$Nu_{D-B\_tfd} = 0.023 \cdot Re^{0.8} \cdot Pr^{n} \quad (3.52)$$

where $n = 0.4$ if the wall is heating the fluid and $n = 0.3$ if the fluid is cooled by the wall.

Another correlation equation for Nusselt number is utilized in this study to compare it with the present experimental work; this equation is proposed by Petukhov (1970). The Petukhov's correlation equation for thermally fully developed turbulent flow in smooth circular tube is given by:

$$Nu_{P\_tfd} = \frac{\left(\frac{f_D}{8}\right) Re \cdot Pr}{C + 12.7\sqrt{\frac{f_D}{8}}\left(Pr^{\frac{2}{3}} - 1\right)} \quad (3.53)$$

The parameter C is determined by:

$$C = 1.07 + \frac{900}{Re} - \frac{0.63}{1 + 10Pr} \quad (3.54)$$

f_D in Eq. (3.53) denotes the Darcy friction factor and can be obtained using the Petukhov friction factor correlation used for smooth tube as follows:

$$f_D = (0.79\, ln(Re) - 1.64)^{-2} \qquad \text{for} \quad 3000 < Re < 5\times10^{6} \quad (3.55)$$

In order to take into account the thermal entrance region effects in a microchannel, a correlation equation by Al-Arabi (1982) was used for circular tube with constant wall temperature and constant heat flux conditions as presented by Rohsenow et al. (1998):

$$Nu_{P\_tdf} = Nu_{P\_tfd}\left(1 + \frac{B}{\frac{L_{ch}}{D_h}}\right) \tag{3.56}$$

Nu_{P_tdf} represents the Nusselt number in the thermally developing turbulent flow region and the parameter B can be determined by:

$$B = \frac{\left(\frac{L_{ch}}{D_h}\right)^{0.1}\left(0.68 + \frac{3000}{Re}\right)}{Pr^{\frac{1}{6}}} \tag{3.57}$$

Then, the final form for the Petukhov's correlation for the thermally developing turbulent flow can be written as:

$$Nu_{P\_tdf} = \left(\frac{\left(\frac{f_D}{8}\right)Re \cdot Pr}{\left(1.07 + \frac{900}{Re} - \frac{0.63}{1+10Pr}\right) + 12.7\sqrt{\frac{f_D}{8}}\left(Pr^{\frac{2}{3}} - 1\right)}\right)\left(1 + \frac{\left(\frac{L_{ch}}{D_h}\right)^{0.1}\left(0.68 + \frac{3000}{Re}\right)}{Pr^{\frac{1}{6}}\left(\frac{L_{ch}}{D_h}\right)}\right) \tag{3.58}$$

To take into account the effect of the surface roughness on the Nusselt number, Haaland's equation for friction factor must be used in Eq. (3.58) instead of Petukhov's friction factor correlation, see Eq. (3.34).

In addition, the Dittus-Boelter equation can also be adjusted by using a correlation equation of Al-Arabi to include the effects of thermally developing flow. Since the Dittus-Boelter equation is used for smooth surface, it can be corrected to take the influence of the surface roughness by using the correlation equation suggested by Norris (1971) as expressed:

$$\frac{Nu_{Rough}}{Nu_{Smooth}} = \left(\frac{f_{Rough}}{f_{Smooth}}\right)^n \tag{3.59}$$

where $n = 0.68Pr^{0.215}$. Norris found that the Nusselt number no longer increases with increasing roughness if the ratio $\left(\frac{f_{Rough}}{f_{Smooth}}\right)$ is greater than 4. This ratio can be calculated by using the Haaland's equation for both smooth walls ($\varepsilon = 0$) and for walls with the roughness of the microchannels ($\varepsilon > 0$). So, the final form for the Dittus-Boelter correlation for the thermally developing turbulent flow and surface roughness can be written as:

$$Nu_{D-B\_tdf} = (0.023Re^{0.8} \cdot Pr^{0.4})\left(\frac{f_{Rough}}{f_{Smooth}}\right)^{0.68Pr^{0.215}}\left(1 + \frac{\left(\frac{L_{ch}}{D_h}\right)^{0.1}\left(0.68 + \frac{3000}{Re}\right)}{Pr^{\frac{1}{6}}\left(\frac{L_{ch}}{D_h}\right)}\right) \tag{3.60}$$

Another widely accepted empirical correlation equation for the thermally fully developed turbulent flow regime in a circular smooth tube was proposed by Gnielinski (1976), in his study the correlation equation of Petukhov (Eq. (3.53)) was used as the basis for the development of his Nusselt number correlation:

$$Nu_{Gn\_tfd} = \frac{\frac{f_F}{2}(Re - 10^3)Pr}{1 + 12.7\sqrt{\frac{f_F}{2}}\left(Pr^{\frac{2}{3}} - 1\right)} \tag{3.61}$$

Eq. (3.61) is valid under $3 \times 10^3 \leq Re \leq 5 \times 10^6$ and $0.5 \leq \mathrm{Pr} \leq 2000$. The Fanning friction factor (f_F) for smooth circular tubes in fully developed turbulent flow can be computed using the method employed by Filonenko (1954):

$$f_F = (1.58\ln(Re) - 3.28)^{-2} \quad \text{for} \quad 4000 \leq Re \leq 5 \times 10^6 \quad \text{and} \quad 0.5 \leq Pr \leq 10^6 \tag{3.62}$$

To take into account the effect of the thermal entry region, Gnielinski (1976) modified correlation Eq. (3.61) to become as given (Kakaç et al., 1987):

$$Nu_{Gn\_tdf} = \frac{\frac{f_F}{2}(Re - 10^3)Pr}{1 + 12.7\sqrt{\frac{f_F}{2}}\left(Pr^{2/3} - 1\right)} \cdot \left(1 + \left(\frac{D_h}{L_{ch}}\right)^{2/3}\right) \tag{3.63}$$

Phillips (1987) used the correlation equation provided by Gnielinski (1976) to predict the Nusselt number in a circular duct in the turbulent developing region. This equation is simplified form of Eq. (3.63) and can be expressed as:

$$Nu = 0.012\left(1 + \left(\frac{D_h}{L_{ch}}\right)^{\frac{2}{3}}\right) \cdot (Re^{0.87} - 280)Pr^{0.4} \tag{3.64}$$

3.8.3 Thermal Resistance Analysis

The total thermal resistance, R_{th} (K/W), is used to evaluate the thermal performance of the liquid-cooled MCHS. R_{th} measures the resistance of the MCHS to dissipating the input power (Steinke and Kandlikar, 2006a), and is a commonly used parameter within the field of electronic cooling. It is defined by the ratio of the temperature difference of the substrate and the inlet fluid of the minichannel to the heating power received by water in the minichannel region, see Eq. (3.65). The R_{th} of the MCHS for single-phase fully developed flow and constant heat flux is composed of six main components as given by Phillips (1987, 1988 and 1990):

$$R_{th} = \frac{T_{surf,max} - T_{f,in}}{q} = R_{cond} + R_{conv} + R_{bulk} + R_{const} + R_{inter} + R_{spread} \tag{3.65}$$

where $T_{surf,max}$ and $T_{f,in}$ are the maximum measured MCHS base temperature at the exit and inlet water temperature, respectively. Fig. 3.10 illustrates the components of the thermal resistances, and a brief description of each term in Eq. (3.65) is given in the following section:

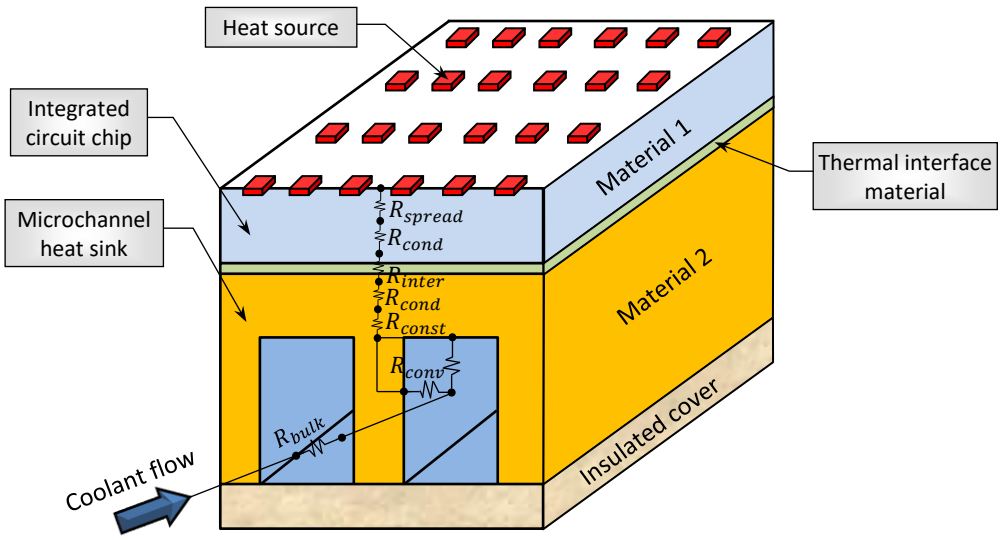

Fig. 3.10: Schematic diagram showing the thermal resistance components (Phillips, 1990).

The first term is the conduction thermal resistance (R_{cond}), which can be obtained simply by dividing the thickness of the minichannel substrate, H_b (m), on the thermal conductivity of the MCHS, k_S (W/m.K), multiplied by the area of heat sink, A_h (m^2) as:

$$R_{cond} = \frac{T_{surf,max} - T_{w,out}}{q_{cond}} = \frac{H_b}{k_S \cdot A_h} \tag{3.66}$$

$T_{w,out}$ (^{o}C) represents the base fin temperature at the outlet of the minichannel. The second term is the convective thermal resistance, R_{conv}, which depends on the convective heat transfer coefficient, h (W/m^2.K), and the effective heat transfer area, A_{eff} (m^2).

$$R_{conv} = \frac{T_{w,out} - T_{f,out}}{q_{conv}} = \frac{1}{h \cdot A_{eff}} \tag{3.67}$$

The heat transfer coefficient (h) can be determined using Eq. (3.6), and Nu in that equation can be calculated using the correlation equations proposed by Phillips (1990) and Lee and Garimella (2006), see Eqs. (3.43) and (3.49). The effective heat transfer area (A_{eff}) of the multiple straight rectangular minichannel (SRM) heat sink can be calculated as:

$$A_{eff\_straight} = A_{base} + \eta_f \cdot A_{fin} = n \cdot L_{ch}\left(W_{ch} + 2H_{ch} \cdot \eta_f\right) \tag{3.68}$$

where n represents the number of the total minichannels in the heat sink, and in the present work is equal to 12, while the term η_f is defined as the fin efficiency assuming an adiabatic tip condition which is correlated by:

$$\eta_f = \frac{tanh(m \cdot H_{ch})}{m \cdot H_{ch}} \tag{3.69}$$

where the fin parameter (m), given by:

$$m = \sqrt{\frac{2h}{W_w \cdot k_S}} \tag{3.70}$$

A_{eff} and h can be written in terms of $\propto$ to be:

$$A_{eff} = n \cdot L_{ch} \cdot H_{ch}(\propto + 2\eta_f) \tag{3.71}$$

$$h = \frac{Nu \cdot k_f}{H_{ch}\left(\frac{2\propto}{1+\propto}\right)} \tag{3.72}$$

Then, the convective thermal resistance will be:

$$R_{conv} = \frac{1}{N_u \cdot k_f} \cdot \frac{1}{n \cdot L_{ch}(\propto + 2\eta_f)} \cdot \frac{2 \propto}{1+\propto} \tag{3.73}$$

The third component is the bulk temperature-rise thermal resistance (R_{bulk}) or sometimes called caloric thermal resistance. The R_{bulk} is caused by the heating of the liquid as it flows through the minichannels and absorbs heat and can be determined as:

$$R_{bulk} = \frac{T_{f,out} - T_{f,in}}{q_{bulk}} = \frac{1}{\rho_f \cdot C_{p_f} \cdot Q_{in}} = \frac{1}{C_{p_f} \cdot \mu_f \cdot Re \cdot n \cdot W_{ch}} \cdot \frac{2 \propto}{1+ \propto} \tag{3.74}$$

The fourth term is the constriction thermal resistance (R_{const}) which is caused by the area change between base and the fin (Wei and Joshi, 2003), and can be calculated as:

$$R_{const} = \frac{W_w + W_{ch}}{\pi k_S \cdot A_h} \ln\left(\frac{1}{\sin\left(\frac{\pi W_w}{2\,(W_w + W_{ch})}\right)}\right) = \frac{1+\beta}{\pi k_S \cdot A_h} \ln\left(\frac{1}{\sin\left(\frac{\pi \beta}{2\,(1+\beta)}\right)}\right) W_{ch} \tag{3.75}$$

where β is the ratio of the fin width (W_w) to the channel width (W_{ch}) as ($\beta = \frac{W_w}{W_{ch}}$). The fifth term is the interface thermal resistance (R_{inter}), which is due to the thermal interface material (e.g., solder, epoxy, thermal grease, etc) mounted between the chip and the minichannel heat sink.

The last term is the spreading thermal resistance (R_{spread}), which is caused due to thermal spreading from each discrete heat source (e.g., integrated circuit, IC) on the chip surface

(Phillips, 1988). The R_{spread} is a function of shape and size of the heat source, and for a square chip the following equation can be used:

$$R_{spread} = \frac{1}{4k_s \cdot D_h} \tag{3.76}$$

This thermal resistance can be ignored when the thermal conductivity of the heat sink is high (Thermal conductivity of copper (Cu) = 385 W/m.K at 20 ^{o}C), and also when the D_h of the chip is large. Thus, the total thermal resistance for the straight rectangular mini/microchannel heat sinks can be calculated as:

$$R_{th} = \frac{H_b}{k_S \cdot A_h} + \frac{1}{N_u \cdot k_f} \cdot \frac{1}{n \cdot L_{ch}(\propto +2\eta_f)} \cdot \frac{2 \propto}{1+ \propto} + \frac{1}{n \cdot C_{p_f} \cdot \mu_f \cdot R_e \cdot W_{ch}} \cdot \frac{2 \propto}{1+ \propto} + \frac{W_{ch}(1+\beta)}{\pi k_S \cdot A_h} \ln\left(\frac{1}{\sin\left(\frac{\pi\beta}{2\,(1+\beta)}\right)}\right) \tag{3.77}$$

3.9 Temperature Dependent Properties

The fluid bulk temperature which is also referred to as the mean fluid temperature, T_m (^{o}C), can be calculated by using the equation proposed by Qu and Mudawar (2002a) as:

$$T_m = \frac{\int_{A_c} \rho . u . T . dA_c}{\int_{A_c} \rho . u . dA_c} \approx \frac{T_{f,in} + T_{f,out}}{2} \tag{3.78}$$

where u represents the velocity component (m/s) in x-direction and T is the temperature (^{o}C). Eq. (3.78) was used to calculate the fluid bulk temperature at any axial location along the middle channel. The numerator of Eq. (3.78) represents the total energy carried by the liquid while the denominator calculates the total mass flow rate through a cross-sectional area along the axial distance of the channels. The fluid bulk temperature can be used to determine the properties of fluid such as density (ρ_f), thermal conductivity (k_f), specific heat (C_{p_f}), kinematic viscosity (μ_f) and Prandtl number (Pr).

3.10 Design Optimisation

Optimisation aims to achieve the best possible solution to a specific problem while satisfying certain restrictions (Myers et al., 2016). The aim is to find the design variables x that minimise an objective function $f(x)$. A general optimisation problem can be formulated as follows:

Objective function	$min\,(f(x))$
Constraints	$g\,(x) \leq 0$
Design space	$x^{lower} \leq x \leq x^{upper}$

where $g(x)$ denotes the inequality constraints that should be fulfilled, while x^{lower} and x^{upper} respectively represent the lower and the upper limit for the design variables. This section is concerned with optimising heat sinks using CFD-based shape optimisation methods, and explains the process of optimisation from the stage of selection of design variables to the stage of obtaining the optimum design.

3.10.1 Design of Experiments (DoEs)

Design of Experiments (DoEs) is used for building the response surface (Metamodel) over the range of the input variables. Several methods can be used to create the DoE points, among those Random, Full Factorial, Latin Hypercube (LHC) and Optimal Latin Hypercube (OLHC) which is used in this study (Cavazzuti, 2013). The reason behind our choice for the OLHC sampling method that it is effective at providing uniform sampling throughout the design space with the fewest number of design points. It is very important to fill the entire design space to get an accurate response surface over the range of the input variables, and also to reduce the expense of performing each experiment (Keane and Nair, 2005). In addition an insufficient number of DoE points will lead to a poor representation of the response and an inaccurate metamodel. In order to create a DoE, it is necessary to select appropriate design parameters that used for building the response surface.

To generate DoE points using OLHC, the Audze-Eglais objective function (AE) was used, which is based on a potential energy (E^{AE}) among the design points (see Audze and Eglais, 1977 and Bates et al., 2004). These points will reach equilibrium when the potential energy of the repulsive forces between the masses is at a minimum. The points are distributed as uniformly as possible when the potential energy of repulsive forces inversely proportional to the squared distance between the points is minimised (Narayanan et al., 2007):

$$min\ E^{AE} = min \sum_{i=1}^{N} \sum_{j=i+1}^{N} \frac{1}{L_{i,j}^2} \tag{3.79}$$

where $L_{i,j}$ is the Euclidean distance between the points i and j ($i \neq j$) and N is the number of the sampling points.

3.10.2 Response Surface Modelling (RSM)

Response surface modelling (RSM) is a collection of mathematical and statistical techniques for empirical model building (Altenbach and Becker, 2003), which is strongly dependent on design of experiment (DoE) points (Box and Draper, 2007). The objective of the RSM is to approximate a response variable with respect to the corresponding design variables over the

entire design space. The approximation is called a response surface or meta-model and can be built for any output parameter (Cavazzuti, 2013).

The concept of RSM was first introduced by Box and Wilson (1951) who suggested using a first-degree polynomial model for approximating response variables. First and second order polynomials can be used to approximate the response surface. The general form of the first-order polynomial model is (Myers et al., 2016):

$$f_i = \beta_0 + \sum_{j=1}^{k} \beta_j x_{ij} \quad , \quad i = 1, 2, 3, \dots, N \tag{3.80}$$

where f_i is the response which is a function of the design variable x_{ij}, β is the polynomial or regression coefficient, k is the number of parameters, and N the number of DoE points.

The second order (Quadratic) polynomial includes all the terms in the first-order model, plus all quadratic terms as (Montgomery, 2013):

$$f_i = \beta_0 + \sum_{j=1}^{k} \beta_j x_j + \sum_{j=1}^{k} \beta_{jj} x_j^2 + \sum_{i=1}^{k-1} \sum_{j=i+1}^{k} \beta_{ij} x_i x_j \tag{3.81}$$

The second-order polynomial model is widely used in RSM because it can represent curvature in the response surface. There are several different methods that can be used to evaluate these two polynomial approximations, for example are named Kriging, Radial Basis Functions, Least Squares (LS) method and Moving Least Squares (MLS) method, and the latter will be used in this study.

3.10.2.1 Least Squares (LS) Method

To plot line, summarise the relationship between two variables x_1 and x_2, the least squares (LS) method can be used as a mathematical method for data fitting. For example, a linear regression fit for two design variables can be expressed as shown in Eq. (3.80), and if there are N points giving a response f as a function of number of design variables x_1 and x_2, the purpose is to look for polynomial fit of the data. Eq. (3.80) can be rewritten to be:

$$f_i = \beta_0 + \beta_1 x_{i1} + \beta_2 x_{i2} + \cdots + \beta_k x_{ik} \tag{3.82}$$

The main goal is then to find the three regression coefficients β_0, β_1 and β_2. The least squares method solves for the best fit of the data set by minimising the sum of squares of the differences (Square Errors, SE) between the data points and the fitted curve as follows (Cavazzuti, 2013):

$$SE = \sum_{i=1}^{N} \left(f_i - \beta_0 - \sum_{j=1}^{k} \beta_j x_{ij} \right)^2 \tag{3.83}$$

In order to obtain the regression coefficients β_0 and β_j, it is necessary to minimise the Square Errors (SE). So, Eq. (3.83) is differentiated with respect to each of its components and set equal to zero yielding Eqs. (3.84a) and (3.84b).

$$\frac{\partial SE}{\partial \beta_0} = -2 \sum_{i=1}^{N} \left(f_i - \beta_0 - \sum_{j=1}^{k} \beta_j x_{ij} \right) = 0 \tag{3.84a}$$

$$\frac{\partial SE}{\partial \beta_j} = -2 \sum_{i=1}^{N} \left(f_i - \beta_0 - \sum_{j=1}^{k} \beta_j x_{ij} \right) x_{ij} = 0 \tag{3.84b}$$

In general, the model in terms of the response variables (observations), Eq. (3.80), can be written in matrix notation as (Myers et al., 2016):

$$\boldsymbol{f} = \boldsymbol{X}\boldsymbol{\beta} \tag{3.85}$$

where $\boldsymbol{f}$ is the vector of the observations, $\boldsymbol{X}$ is the model matrix of DoE points and $\boldsymbol{\beta}$ is the vector of the regression coefficients. Eqs. (3.84a) and (3.84b) can be rewritten as follows:

$$\frac{\partial SE}{\partial \boldsymbol{\beta}} = -2\boldsymbol{X}^T\boldsymbol{f} + 2\boldsymbol{X}^T\boldsymbol{X}\boldsymbol{\beta} = 0 \tag{3.86}$$

where $\boldsymbol{X}^T$ is the transpose of $\boldsymbol{X}$. The least squares estimator of $\boldsymbol{\beta}$ is:

$$\boldsymbol{\beta} = (\boldsymbol{X}^T\boldsymbol{X})^{-1}\boldsymbol{X}^T\boldsymbol{f} \tag{3.87}$$

The least squares fit with the regression coefficients for the vector of response surface approximations $\hat{\boldsymbol{f}}$ at the interpolation locations $\widehat{\boldsymbol{X}}$ can be read as:

$$\hat{\boldsymbol{f}} = \widehat{\boldsymbol{X}}\boldsymbol{\beta} \tag{3.88}$$

3.10.2.2 Moving Least Squares (MLS) Method

To build the Response Surface (Metamodel), the Moving Least Squares (MLS) method has been used, which has been proposed for design optimisation applications (Gilkeson et al. 2014; Khatir et al., 2015; and de Boer et al., 2016). MLS method is a generalisation of a traditional weighted least squares method where the weights do not remain constant but are functions of the position in the design space (Loweth et al., 2011).

The first step of the MLS method is to define an estimate $\hat{y}$ at an arbitrary design point $\{x\} = \{x_1, x_2, x_3, \dots, x_{ndv}\}$ in the design space based on the values at a series of responses $\{f_i\} =$

$\{f_1, f_2, f_3, \dots, f_n\}$ at a series of design points $\{x_{1,i}, x_{2,i}, x_{3,i}, \dots, x_{ndv,i}\}$ in order to estimate the following:

$$\hat{y}(x) = \sum_{i=1}^{N} w_i \ (L_i) \ f_i \tag{3.89}$$

where the weights, w_i, are functions of the Euclidian norm $L_i = |x - x_i|$ between the sample points x_i and the assessment point x. The metamodel tuning can also be controlled by varying the type of decay function used to create the weighting. The weighting of points in the regression coefficients calculation is determined using a Gaussian weight decay function:

$$w_i = \ e^{-\theta \, . \, L_i^2} \tag{3.90}$$

The value of the closeness of fit parameter (θ) can vary between zero which is equivalent to traditional least squares regression and any value until a very close fitting is obtained, which can be used to account for numerical noise in the response. The optimal value of θ parameter can be achieved by calibrating the MLSM metamodels using Cross Validation (CV) techniques for instance Leave-One-Out Cross-Validation (LOOCV) and k-fold CV (de Boer et al., 2014). The LOOCV method is based on an iterative approach which removes one point from a data set, while the remaining points are used to build the MLS metamodel and calculates the error between the approximated and actual response at the removed point. The k-fold CV method is similar to the LOOCV method, but a random subset of k points is used for validation whilst the remaining points are used to build the MLS metamodel (Loweth et al., 2011). In these two methods a sample is taken from the DoE and the error is diagnosed and assessed when the metamodel is evaluated without those points.

In this study the Root Mean Squared Error (RMSE) is adopted to evaluate the accuracy of the metamodel prediction in Eq. (3.91). As the values of RMSE decrease, the accuracy of the metamodel improves (Choi et al., 2001).

$$RMSE = \sqrt{\frac{1}{N}\sum_{i=1}^{N}\left(\hat{f}_i - f_i\right)^2} \tag{3.91}$$

where N is the number of DoE points, while $\hat{f}_i$ and f_i are respictively the predicted and the actual response values as shown in Fig. 3.11.

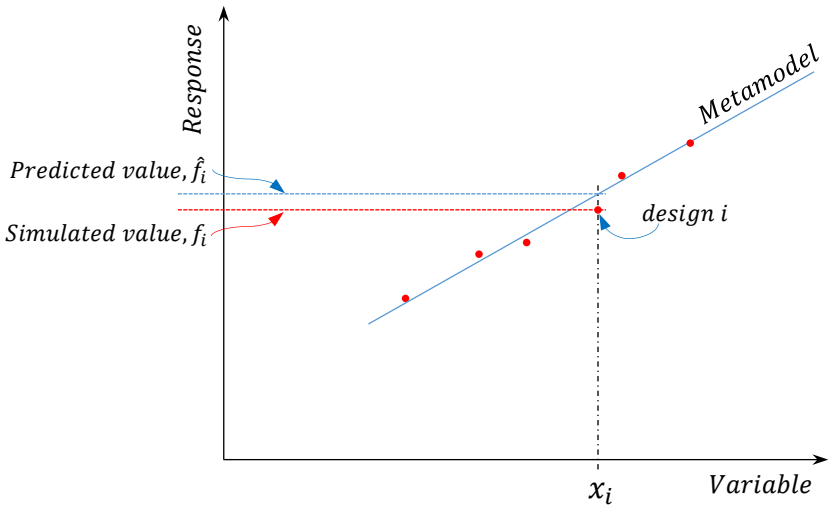

Fig. 3.11: Description of definition used for calculating error measures.

For the second order (Quadratic) regression fit, MLS method can be used to estimate the response (f) by using Eq. (3.81), and the sum of squared errors (SE) leads to Eq. (3.92) which is include the weights associated with each sample location.

$$SE = \sum_{i=1}^{N} w_{ij} \left(f_i - \beta_0 - \sum_{j=1}^{k} \beta_j x_j - \sum_{j=1}^{k} \beta_{jj} x_j^2 - \sum_{i=1}^{k-1} \sum_{j=i+1}^{k} \beta_{ij} x_i x_j \right)^2 \tag{3.92}$$

where w_{ij} is the weight decay function between output point j and sample point i. By differentiating Eq. (3.92) with respect to each of the design variables and setting equal to zero solves for the minimum SE between the approximation and sample values, this yields Eqs. (3.93a – d).

$$\frac{\partial SE}{\partial \beta_0} = -2 \sum_{i=1}^{N} w_{ij} \left(f_i - \beta_0 - \sum_{j=1}^{k} \beta_j x_j - \sum_{j=1}^{k} \beta_{jj} x_j^2 - \sum_{i=1}^{k-1} \sum_{j=i+1}^{k} \beta_{ij} x_i x_j \right) = 0 \tag{3.93a}$$

$$\frac{\partial SE}{\partial \beta_j} = -2 \sum_{i=1}^{N} w_{ij} \left(f_i - \beta_0 - \sum_{j=1}^{k} \beta_j x_j - \sum_{j=1}^{k} \beta_{jj} x_j^2 - \sum_{i=1}^{k-1} \sum_{j=i+1}^{k} \beta_{ij} x_i x_j \right) x_j = 0 \tag{3.93b}$$

$$\frac{\partial SE}{\partial \beta_{jj}} = -2 \sum_{i=1}^{N} w_{ij} \left(f_i - \beta_0 - \sum_{j=1}^{k} \beta_j x_j - \sum_{j=1}^{k} \beta_{jj} x_j^2 - \sum_{i=1}^{k-1} \sum_{j=i+1}^{k} \beta_{ij} x_i x_j \right) x_j^2 = 0 \tag{3.93c}$$

$$\frac{\partial SE}{\partial \beta_{ij}} = -2 \sum_{i=1}^{N} w_{ij} \left(f_i - \beta_0 - \sum_{j=1}^{k} \beta_j x_j - \sum_{j=1}^{k} \beta_{jj} x_j^2 - \sum_{i=1}^{k-1} \sum_{j=i+1}^{k} \beta_{ij} x_i x_j \right) x_i x_j = 0 \tag{3.93d}$$

After Eqs. 3.93(a – d) are solved to find the regression coefficients β_0, β_j, β_{jj} and β_{ij} the MLS method approximation of f is obtained.

Chapter 4: Experimental Methods

4.1 Introduction

In order to examine the minichannel heat sink (MCHS) experimentally in terms of the friction factor (f), heat transfer coefficient (h) and thermal resistance (R_{th}), four different configurations of MCHS were designed, fabricated and tested with the main study being the effect of flow arrangements on heat transfer and pressure drop. In this chapter, the main parts of the experimental set-up, the minichannel heat sink test sections, procedure of running the test rig, calibration, data analysis for f, h and R_{th} are described in detail.

4.2 The Experimental Set-up

Conventional heat sinks that use air as a working fluid are common devices used to prevent overheating in the integrated circuits such as central processing unit (CPU) of a computer. However, dissipating very high amount of heat using this type of heat sink is difficult because of the poor thermal conductivity of air (0.0252 W/(m.K) at 20 ^{o}C), and it can no longer meet the need to reduce the chip junction temperature because of limited heat transfer rate (Gunnasegaran et al., 2010). As a result of these deficiencies, micro-/minichannel heat sinks with liquid coolants such as water have become commonly used in cooling of electronic devices because of its ability to provide very high convective heat transfer rates with small surface area, which have been shown to be a very effective way to remove a high heat load. In addition, water has a higher thermal conductivity, density and specific heat compared to the air properties. The water that used in the MCHS device as a coolant can absorb heat in terms of the temperature rise across the working fluid stream is approximately 3500 times that of air (Chu et al., 2004).

The main components of the test rig used in this experimental investigation consisted of a minichannel heat sink (MCHS) test section machined from copper, a DC-power supply device, power film resistors (heat source), a mini water pump, a reservoir or a tank in order to provide water for a MCHS test section, a clear plastic cover to allow a view of the fluid flow inside the minichannels, a flow meter (Rotameter) to measure the water flow rate, plastic tubes, valves, digital thermometer with thermocouples to measure the temperature of the water inlet and outlet and also surface temperature of MCHS and digital pressure gauge to measure the water difference pressure in the MCHS test section. A schematic diagram of the main components of the experimental test rig used in the present study is depicted in Fig. 4.1, and a photograph of the test facility is shown in Fig. 4.2.

In the experiments, a set of measurements are needed to determine the pressure drop, heat transfer coefficient and thermal resistance. These measurements are as follows: the junction

temperature of the resistor (heater), temperature distribution along the heat sink surface, inlet and outlet water temperature, pressure drop of water between inlet and outlet of heat sinks, mass flowrate of water and power supplied to the power film resistors.

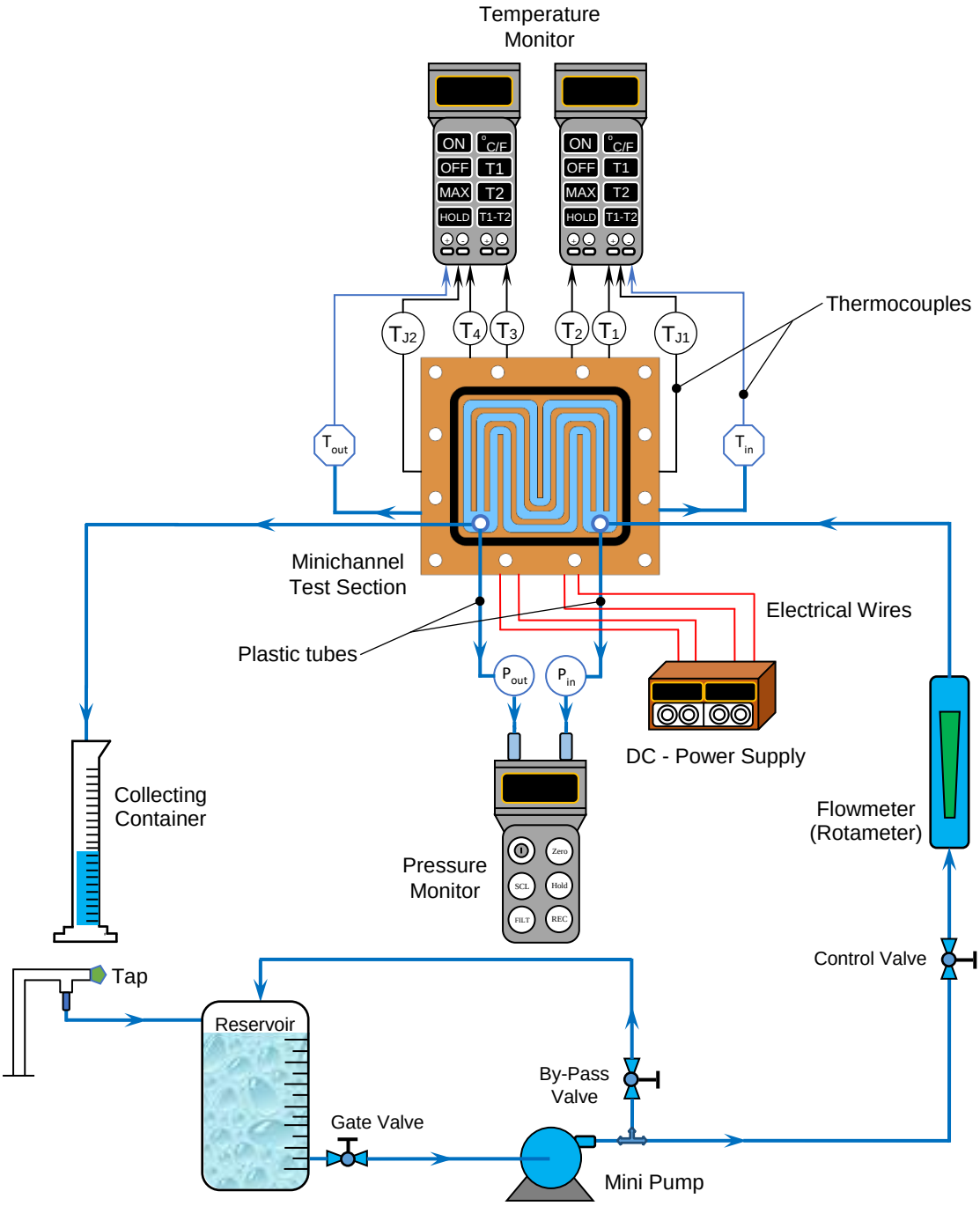

Fig. 4.1: Schematic diagram of the experiment setup.

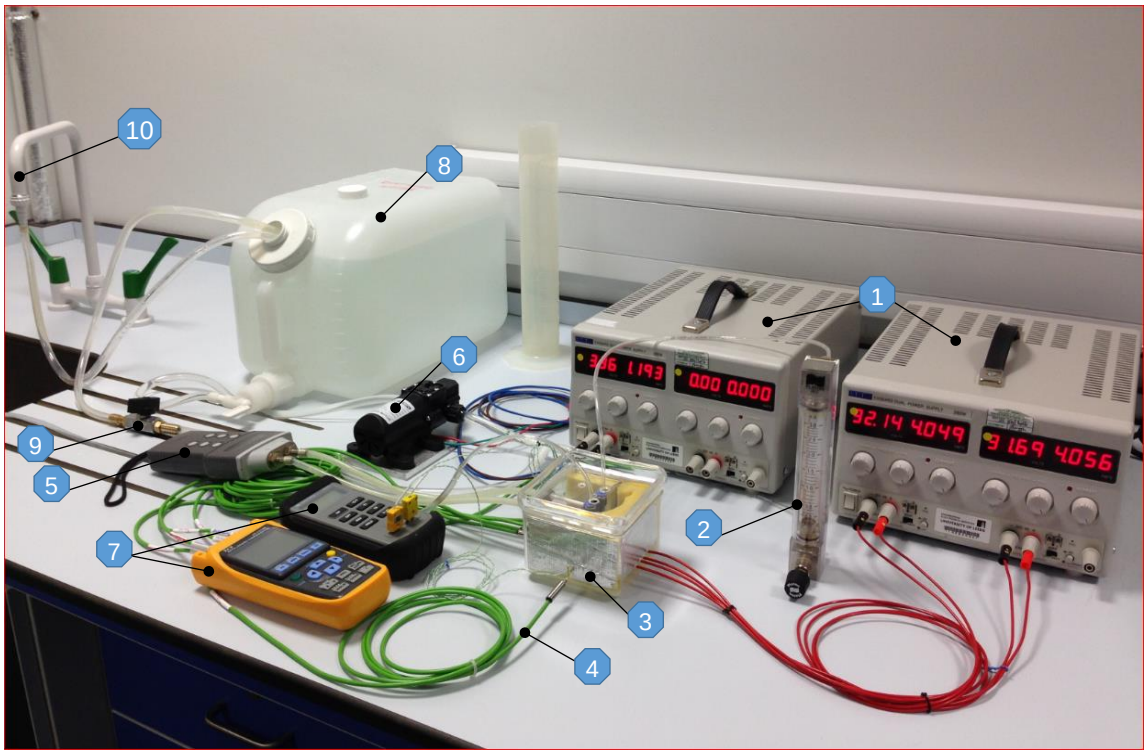

1. DC – Power supply	2. Flow meter (Rotameter)	3. MCHS test section	4. Thermocouple	5. Pressure gauge
6. Mini-water pump	7. Monitor digital thermometer	8. Reservoir	9. Valve	10. Tap

Fig. 4.2: Photograph of the experimental facility.

4.2.1 Design and Fabrication of Test Sections

The minichannel heat sink (MCHS) test section is the most important component of the flow loop on which the experiments were performed. Four different types of minichannel heat sinks were firstly designed by using the SolidWorks software (Shih and Schilling, 2015), then they were manufactured and tested to investigate the effect of heat fluxes and velocity of fluid flow on the heat transfer characteristics and pressure drop. The MCHS specimens were fabricated using a high-accuracy Computer Numerical Control (CNC) milling machine (FANUC ROBODRIL). Copper is used as a material for the MCHS because of its high thermal conductivity, i.e. 388 $\frac{W}{m \cdot K}$ at 20 °C. The entire thickness (H_s) of the straight and serpentine MCHS models was 5.5 mm and 6.5 mm, respectively, while all the MCHS designs had the same surface area of 45 mm × 41 mm (length, L_s × width, W_s), the same base plate thickness (H_b) of 3.5 mm and twelve parallel rectangular minichannels with a 1 mm wall thickness (W_w) between each minichannel.

The first one of these MCHS test sections had a multi-straight rectangular cross section with lengths (L_{ch}) of 21 mm. The depth (H_{ch}) and width (W_{ch}) of the rectangular minichannels are respectively 2 mm and 1 mm, thus giving a hydraulic diameter (D_h) of 1.334 mm. The inlet and outlet manifolds of this type of MCHS model are designed and fabricated to have a trapezoidal shape with tapered longitudinal section for distributing the fluid flowing into and

collecting fluid flowing out of the minichannels, as shown in Fig. 4.3. This type of the manifold was chosen to ensure that each minichannel had approximately the same mass flow rate of water. A manifold with a tapered longitudinal section having inlet width of 4 mm ($W_{m,in}$) and end width of 2 mm ($W_{m,out}$) with the depth (H_m) being the same as that of the minichannel.

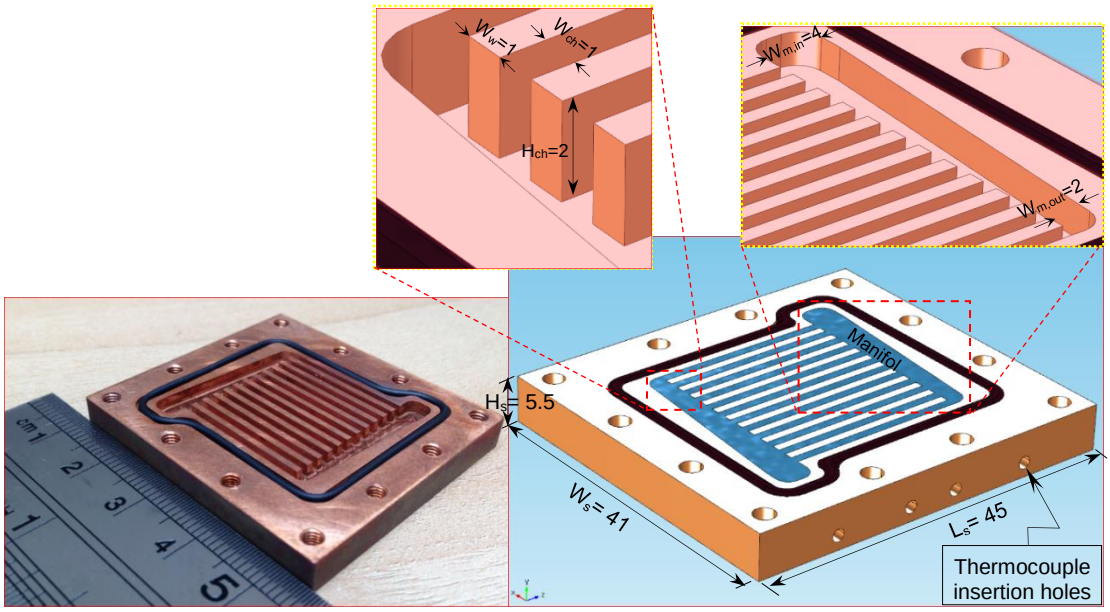

Fig. 4.3: Model and actual pictures of the straight rectangular MCHS test section, all dimensions in mm.

Fig. 4.4 shows both the model and the actual pictures of the other three categories of the MCHS models that have a multi-serpentine rectangular cross section, referred to as the single path serpentine minichannel (SPSM), a double path multi-serpentine minichannel (DPSM), and a triple path multi-serpentine minichannel (TPSM) heat sink. The cross-sectional area of the serpentine rectangular passage is 1.5 mm × 3 mm (width, W_{ch} × depth, H_{ch}) for all three models used to give hydraulic diameters (D_h) of 2 mm. The details of the all MCHS test sections used experimentally are described in Table 4.1.

Table 4.1: Specification of parameters of four MCHSs.

MCHS Sample	Material	Sample dimension, $W \times L \times H\ (mm)$	Channel dimension, $H_{ch} \times W_{ch}(mm)$	Hydraulic diameter, $D_h(mm)$	Wall thickness, $W_W(mm)$	Number of channels, n	Effective area, A_{eff} (mm^2)
SRM	Pure copper	41 × 45 × 5.5	2 × 1.0	1.334	1	12	1260.00
SPSM	Pure copper	41 × 45 × 6.5	3 × 1.5	2.0	1	12	2142.93
DPSM	Pure copper	41 × 45 × 6.5	3 × 1.5	2.0	1	12	2123.73
TPSM	Pure copper	41 × 45 × 6.5	3 × 1.5	2.0	1	12	2064.16

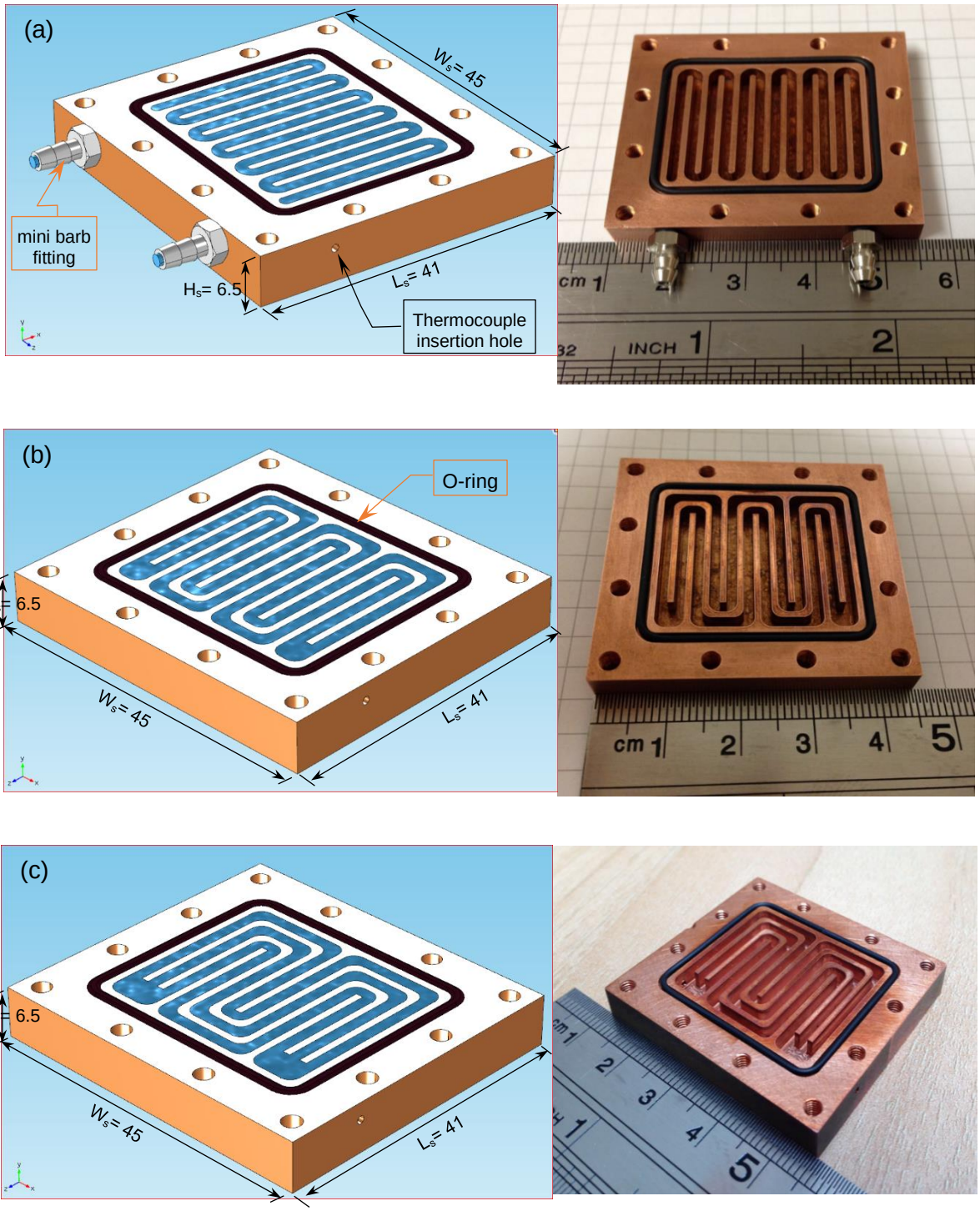

Fig. 4.4: Model and actual pictures of the (a) single, (b) double and (c) triple path multi-serpentine rectangular MCHS test section respectively from top to bottom, all dimensions in mm.

On top of the copper block a clear Acrylic Perspex plastic sheet is placed to serve as a transparent cover through which the flow can be observed. The Acrylic Perspex plastic cover is held onto the copper block by twelve mounting screws (M3×0.5) and sealed with an O-ring and a force provided by the mounting screws was sufficient to seal the minichannels from the ambient environment and prevent water leakage to the outside of the MCHS models. Around each minichannel top there is a groove made for an O-ring seal with a depth of 0.7 mm and a

width of 1.5 mm to prevent water leakage. This seal also provided an easy way to assemble the test section with the cover. For water inlet and exit, two holes were made on the side view of a single path serpentine MCHS test section with diameter of 3 mm to fix a mini barb fitting (M3×0.5); this means that the inlet and outlet adapters are positioned in the axial direction of the minichannels, as shown in Fig. 4.5. For the other MCHS test sections, two 5 mm circular through holes were drilled on the top side surfaces of the plastic covers and a male run tee union adapters are fixed on these threaded holes to create inlet and outlet water passage and also to measure the inlet and outlet pressure, as shown in Fig. 4.6.

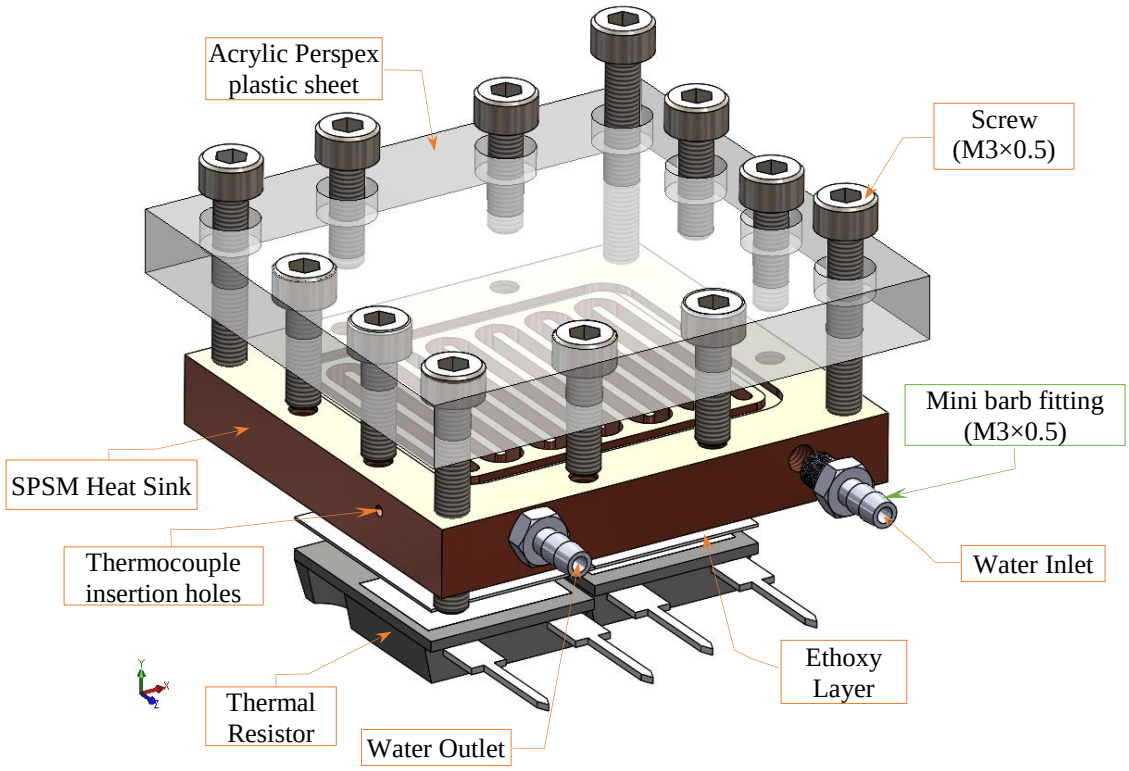

(a)

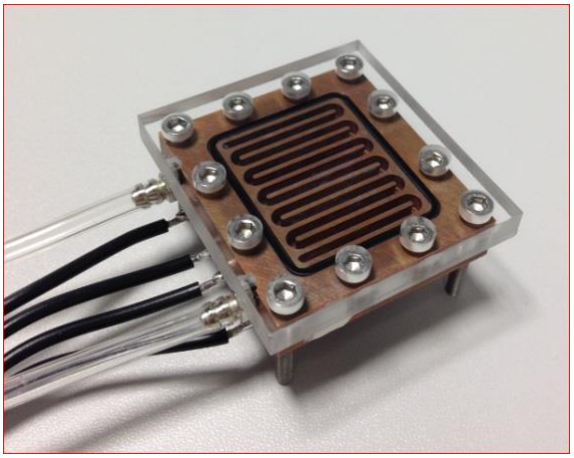

(b)

Fig. 4.5: (a) SolidWorks model; and (b) actual picture for the single path serpentine rectangular MCHS assembly.

[103]

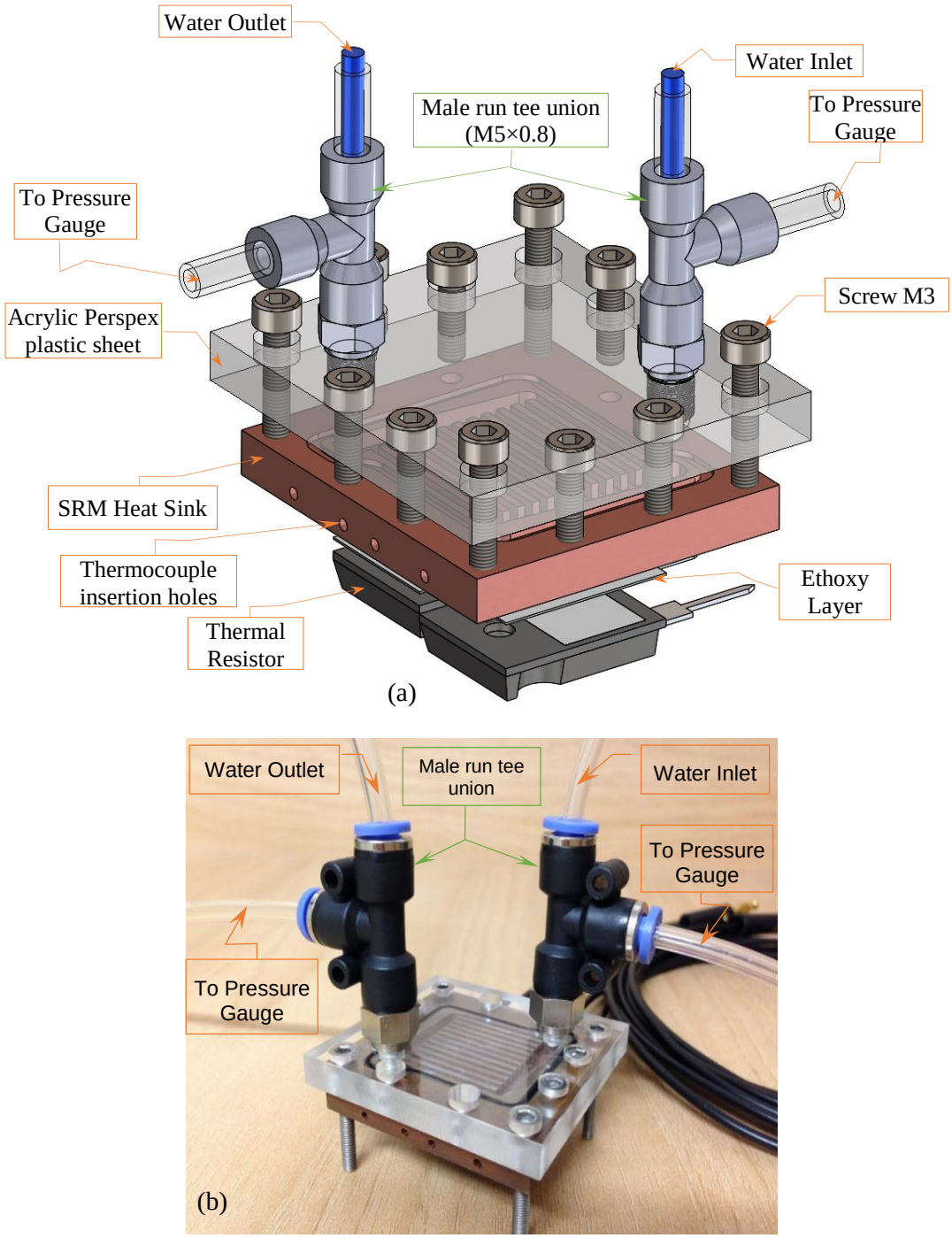

Fig. 4.6: (a) SolidWorks model; and (b) actual picture for the multi-straight rectangular MCHS assembly.

In order to measure the wall temperature distribution along the MCHS, four holes were drilled in the side of each copper test section into which thermocouples were inserted. The diameter of the thermocouple holes was 1.5 mm and located 1.75 mm below the minichannel base. The locations of the thermocouple holes, as measured from the inlet of the MCHS and along its length are 10 mm, 19.5 mm, 25.5 mm and 35 mm as shown in Fig. 4.7. K-type thermocouples have been chosen to be used for the wall temperature measurements, which were inserted into the copper block until it reaches half the width of the MCHS. A thermal paste has been put

inside the holes that were made for the thermocouples to fill the existing gaps in the wall thermocouple holes and to ensure that there is no contact between air and thermocouple for the sake of reducing the error in temperature measuring. Another two thermocouples were installed one in the entrance and the other in the exit of the MCHS to measure the inlet and outlet water temperature.

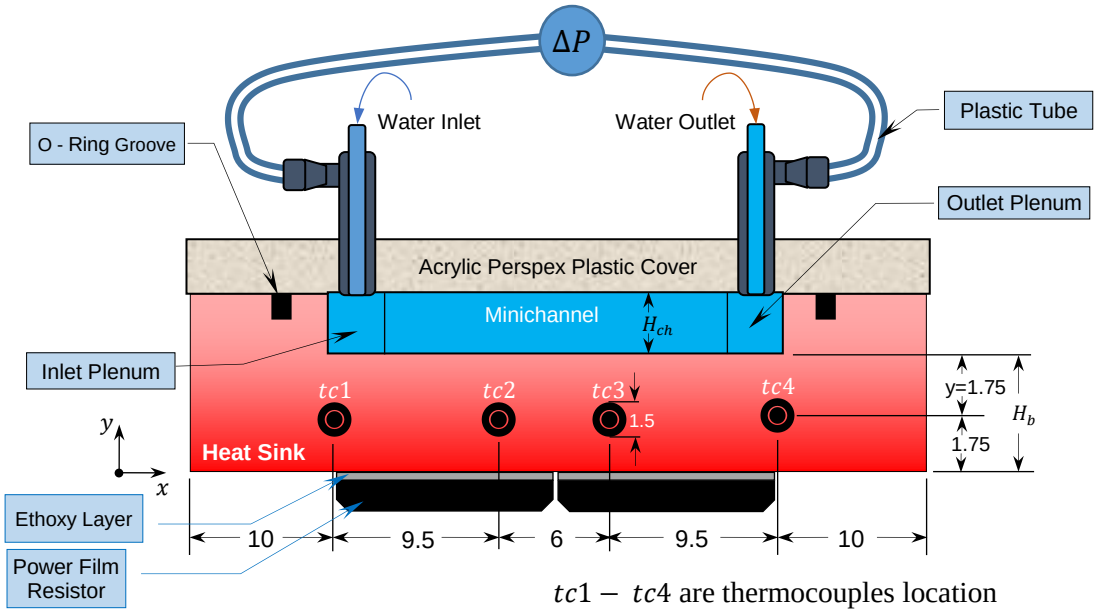

Fig. 4.7: Cross-sectional view of the SRM design to explain the thermocouples location. All dimensions in mm.

To minimise heat loss to the surrounding environment, the MCHS copper block was packed with an insulating fibres glass, and then placed inside a clear, covered Acrylic Perspex plastic box having dimensions (10×10×10) cm^3.

4.2.2 Power Film Resistor

In the present experimental work, two power film resistors as a heat source are placed on the bottom side of each MCHS test section, and the heat flux from the resistor can be controlled by adjusting the electric current supplied to the power film resistors from a DC-power supply, an Aim-TTi EX354RD model from RS, as shown in Fig. 4.2. The power supply has two outputs and each one has an upper limit of 35 V and 4 A. In order to supply variable power to the resistors a variac was used to vary the power supply within the range of 0 to 140 W.

In this study, MP9100 (TO-247) model was used as a heat source with a maximum power supply reaching 100 W and 20 Ω resistance (Caddock). The width and length of the encapsulate resistor are 15.5 mm × 20 mm respectively whereas the effective heating area is 11.5 mm length and 14 mm width as shown in Fig. 4.8. From deconstruction of the resistor it

was found that the heat source is a very thin rectangular layer of Nickel-Chromium sitting on top of a 1 mm slab of alumina ceramic of equal rectangular dimensions.

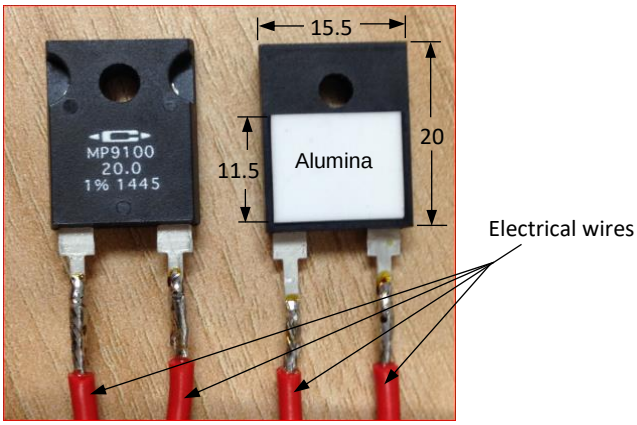

Fig. 4.8: Photograph of the power film resistor, all dimensions in millimeter.

To record the maximum junction temperature of the resistor as accurately as possible, a small hole of diameter of 1 mm was bored from one side of the resistor until it reached half the width of the resistor. In order to reduce the likelihood of defects to the thermal resistor and to bring a thermocouple as close to the junction temperature as possible, a gap of 0.25 mm is left from the Nickel-Chromium (Ni-Cr) layer. Following this, a multi-meter was used to check that resistance had not changed, with any defects being rejected. Then, a K-type thermocouple is embedded inside the bored hole in the heater surface until it reached the middle of the resistor, and the void filled with thermal Ethoxy material to prevent thermocouple movement and to fill the air-gap that existed between the hole and the thermocouple as shown in Fig. 4.9.

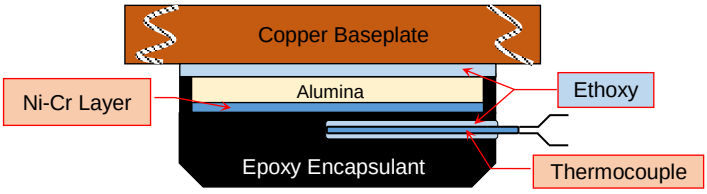

Fig. 4.9: Schematic diagram to describe the junction temperature measurement technique.

Before putting the resistors on the MCHS base, the bottom surface of the copper block needs to be cleaned and care was taken to ensure a clean and smooth contact surface by wiping with fine wire wool. The cleaning process was repeated several times until no debris or dirt is captured on the wipe.

After cleaning, two power film resistors were then permanently adhered on the bottom side of each MCHS test section using a thin consistent layer of thermal Ethoxy (Electrolube, TCER) with thermal conductivity of 2.2 $\frac{W}{m \cdot K}$. Thermal Ethoxy provided a uniform contact

and eliminated the air-gaps between the resistors and specimen surfaces. The thickness of the thermal Ethoxy layer is measured manually using a "Digital Vernier Caliper" and was found to be 200 ± 6 µm. In order to spread the thermal paste (Ethoxy) on the bottom surface of the MCHS test section a small knife edge was used for this purpose. The knife edge was used several times until the surface of interest is covered uniformly. Fig. 4.10(a) shows how it should look like after the thermal paste is applied properly on the bottom of the copper block. Can now be positioned the power film resistors on the thermal Ethoxy layer, and the loading resistor alumina junction was positioned centrally as shown in Fig. 4.10(b). A small G style clamp was used to hold the power film resistors with MCHS together and apply a pressure to the test device. A torque wrench can be used to apply different pressures to the test device, but at the same time great care must be taken in order not to destroy the power film resistors by the force. The clamp was placed on the resistors slowly at the centre, and if shift or movement is found, the resistors position is manually adjusted to the original location.

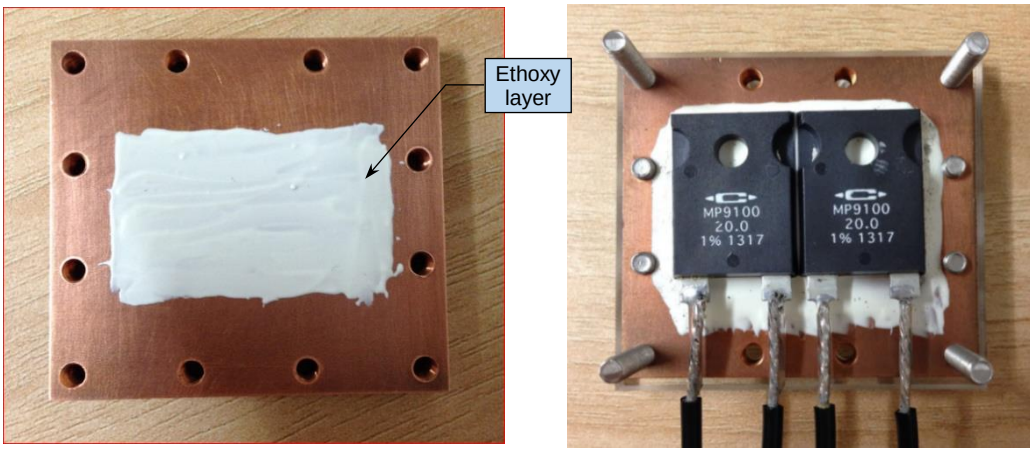

Fig. 4.10: Photograph of (a) applying thermal Ethoxy adhesive to the loading area of the device; and (b) After applied resistors on the Ethoxy adhesive.

4.2.3 Water Pump

A miniature diaphragm-water pump drives water as a cooling fluid from the reservoir through the flow meter to the test module, as shown in Fig. 4.2. In order to regulate the water flow rate in the minichannel heat sink a bypass loop is used to adjust the system flow rate and pressure, and two control valves were used to adjust the flow rate to the flow meter. The allowable working temperature range is 5 to 50 °C, but in this work the liquid inlet temperature was kept below 25 °C to keep the mini-pump safety as recommended by the manufacturer. It is capable of delivering from 1 to 6000 *ml/min* at a maximum differential pressure of 0.9 MPa. The reservoir used in this study was a tank with a capacity of five gallons

(22.7 litres), it was used to supply the miniature pump by water in order to give a constant flow rate without significant fluctuations.

4.3 Minichannel Surface Roughness (ε) Measurements

The surface roughness (ε) of the minichannel walls was be measured, since it can has an effect on the friction factor and heat transfer coefficient. ***Sa*** and ***Sq*** which are respectively the Average Roughness and Root Mean Square Roughness are measured for four MCHS models using the BRUKER-NPFLEX-LA 3D Surface Metrology System. Fig. 4.11 shows the surface roughness measurements that were made on the channel base surface at mid-length minichannel for each heat sink model.

To determine the average surface roughness value, three different axial locations were chosen to measure the local surface roughness which are near the inlet, middle and near outlet of the channel base surface as shown in Table 4.2. From the table, it is observed that the relative surface roughness (ε/D_h) values of the straight rectangular MCHS is higher than those having serpentine passages, because of the smaller hydraulic diameter (D_h).

Table 4.2: Surface roughnesses of four MCHSs.

MCHS Sample	$\varepsilon\ (\mu m)$ $At\ 1\ mm\ after\ channel\ inlet$	$\varepsilon\ (\mu m)$ $Channel\ middle$	$\varepsilon\ (\mu m)$ $At\ 1\ mm\ before\ channel\ outlet$	$Average\ of\ \varepsilon\ (\mu m)$	Hydraulic diameter $D_h(mm)$	ε/D_h
SRM	1.13	1.21	1.16	1.17	1.334	0.875×10^{-3}
SPSM	1.09	1.28	1.07	1.14	2.0	0.573×10^{-3}
DPSM	1.07	1.18	1.13	1.13	2.0	0.563×10^{-3}
TPSM	1.15	1.23	1.17	1.18	2.0	0.591×10^{-3}

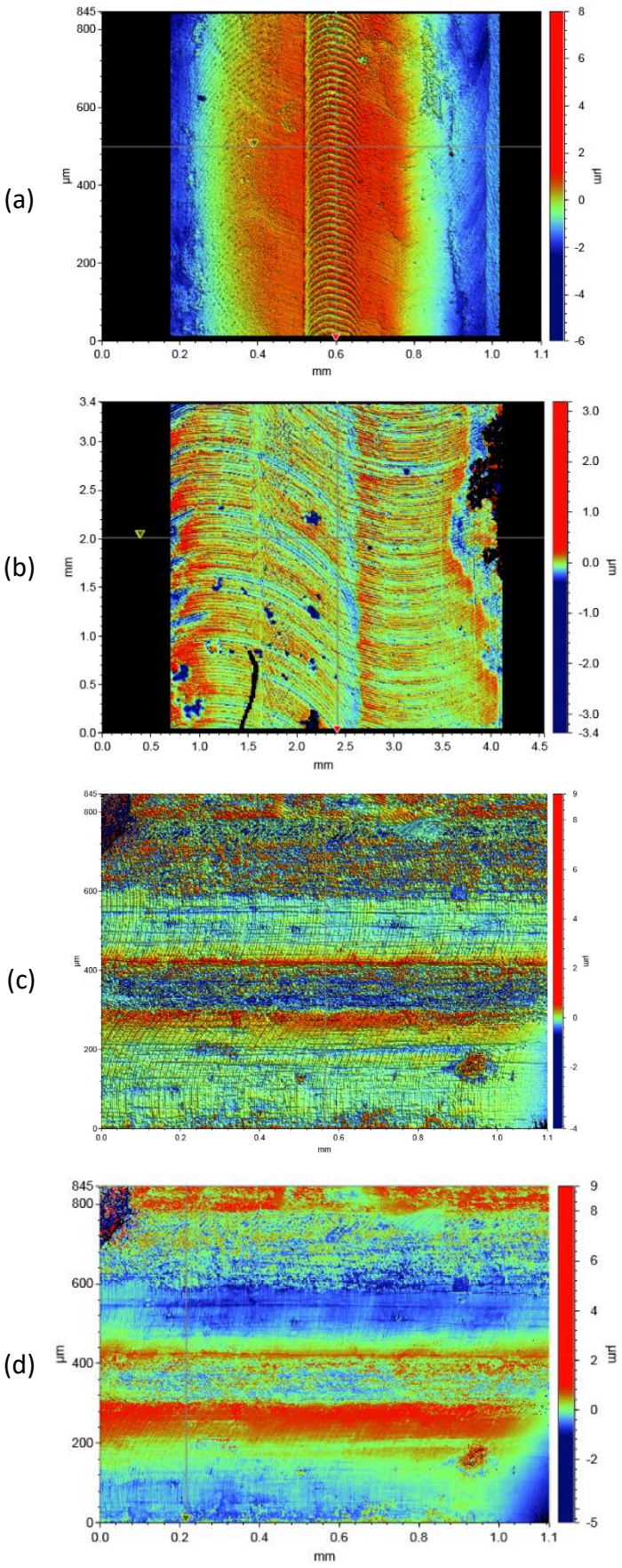

Fig. 4.11: Photographs of surface roughness measurements for (a) SRM; (b) SPSM; (c) DPSM; and (d) TPSM heat sinks.

4.4 Experimental Calibration Procedures

Calibration is a comparison between a known measurement (the standard) and the measurement using your instrument. To ensure that the experimental measurements obtained are accurate the experimental equipment must be calibrated. In the present work, calibration of the thermocouples, flow meter and pressure gauge has been achieved as described below.

4.4.1 Thermocouples Calibration

In order to measure the water temperature at the minichannel inlet and outlet and the axial wall temperature distribution along the flow channel at four different locations, mineral insulated, stainless steel sheathed, type K thermocouple probes are used. The length and diameter of all the thermocouple probes were 40 mm and 0.5 mm respectively, whereas the extension cable length is 2 m as shown in Fig. 4.12(a). The thermocouples are commercially available from Thermosense, model (TPMA-K-310-0.5-I-40-2000 mm CP10KX-RSPK). These thermocouples have a wide temperature range from as low as -100 °C and up to +1300 °C. In order to get the temperature reading, a sub-miniature plastic connector was attached to the thermocouple for easy connection to the digital temperature monitor. From the information given by the manufacturer, the specified tolerance (Class 1) for Type K thermocouples over the temperature range -40 °C to 375 °C is ±1.5 °C. A second type of K-type thermocouple (RS) was used in the present work to measure a junction temperature with length and diameter of 1m and 0.5 mm respectively as shown in Fig. 4.12(b). The range of this type of thermocouple is from -50 °C to 1100 °C.

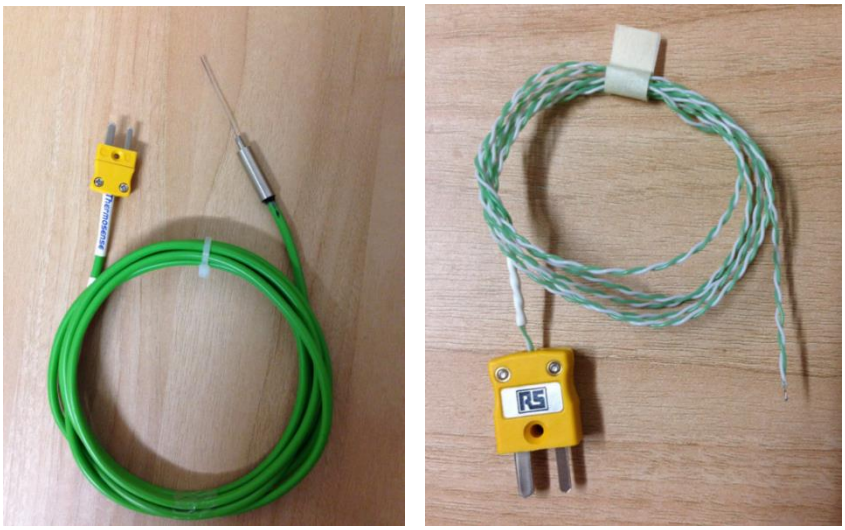

(a) (b)

Fig. 4.12: Photographs of type-K thermocouples.

In order to measure the temperature of the water inlet and outlet in the MCHS test section, two procedures were used. In the multi-straight rectangular MCHS specimen, a type-K thermocouple similar to the picture in Fig. 4.12(a) was used, where one thermocouple was

inserted into the 4 mm tubing and filled with Acetoxy curing silicon at the tee-end. Thermocouple tips extended from the tubing end to ensure that they sat directly within the centre-stream during flow to obtain an approximate mean temperature as shown in Fig. 4.13. While the inlet and outlet water temperature in the other three MCHS test sections were obtained by inserting the probe of thermocouple directly inside the MCHS plenum.

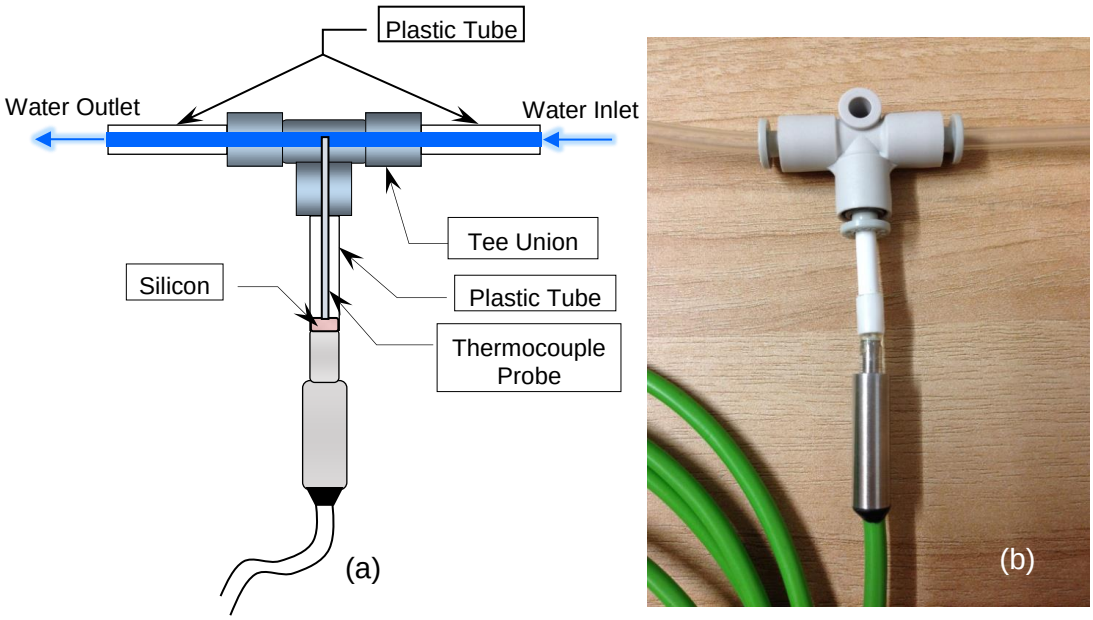

Fig. 4.13: (a) Schematic showing the placement of inlet thermocouple; and (b) Picture of the connection.

For measurement of temperatures, two types of digital thermometer have been used. The first one from RS, Model "Kane-May KM340" has a twin input differential thermometer that can be used for many applications, such as heating and ventilation and other industrial processes. Three display modes can be selected in this type to show values from either input, or the difference between them, in °C or F scales. The measurement temperature ranges of -50 °C to +1300 °C with an accuracy of ±0.2% of reading +1 °C for the temperature range of 0 °C to +1100 °C as mentioned by manufacturer, and this model only has the ability to read K-type thermocouples. The other type of digital thermometer is a multi-channel thermocouple data logger from Thermosense, Model "YC-747UD" which has four Thermocouple input channels (T1-T4) equipped with LCD display and is backlit. It can measure, record and display up to 4 temperature channels using thermocouple or RTD probes and also it can accept J, K, R, S, T thermocouple. This type of thermometer has a temperature range of -100 °C to +1300 °C with an accuracy of ±0.1% as given by the manufacturer. Since calibration of these two digital thermometers are challenging, they have not been calibrated.

Each thermocouple was calibrated against a Mercury thermometer by using an ice bath. The specified accuracy of this thermometer was ±0.05 °C according to the manufacturer over the

range from 0 °C to 100 °C. In our calibration the mercury-in-glass thermometer and thermocouples were immersed in the ice flask (bath) and given a reference temperature of 0 °C. The temperatures measured using the thermocouples and mercury thermometer were recorded simultaneously. Nineteen readings were chosen for calibration of thermocouples over a temperature range of 0 °C to 90 °C. After that, a linear curve fit is plotted for the collected points to determine the equation for the thermocouple. Fig. 4.14 shows the calibration curve for a thermocouple at different temperatures with the calibration equation and with an excellent correlation coefficient (R^2) of 0.99. Each thermocouple is calibrated in the same way with an accuracy of ± 0.3 °C.

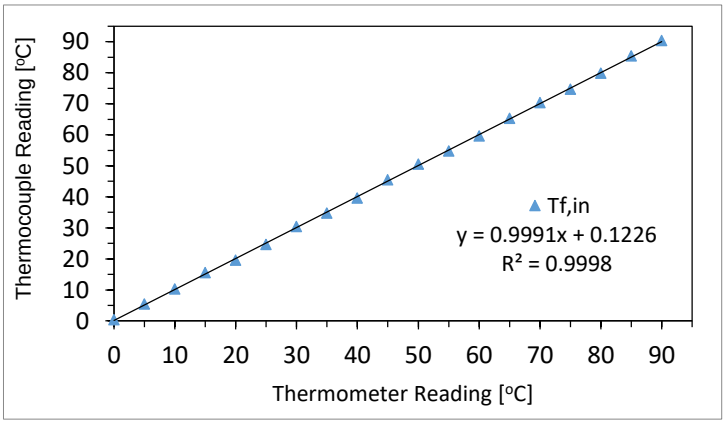

Fig. 4.14: A typical thermocouple calibration curve.

4.4.2 Flow Meter Calibration

A PLATON NG glass model flow meter (Rotameter) was used to measure the water flow rates with a range of 0.2 *l/min* to 3.0 *l/min*, as shown in Fig. 4.2. The rotameter has a direct reading scale, and it has a throttle control valve to provide fine adjustment and isolation of the flow entering the flow meter. The rotameter is provided by a valve to adjust the water flow rate, which is located at the bottom of the rotameter. In the back side of the rotameter there are two stainless steel female fittings of 1/4" FNPT which is fit to a 4 mm male stud pneumatic push-in fitting for water house tube.

In order to calibrate the rotameter, a mini diaphragm water pump is set for a specific flow rate and a volumetric beaker was used to collect the water that drained from the MCHS test section over a measured period of time. After calibration, the flow rate of the water can be determined to calculate the average velocity and Reynolds number in the minichannel.

The volumetric beaker has a scale of 0 to 1000 *ml* with resolution of 2.5 *ml*. A RS digital electronic stop watch was used for timing the water collections during calibration of the flow meter. The stopwatch used has a resolution of 0.01 sec. A linear curve fit is determined to get the calibration equation for the flow meter as shown in Fig. 4.15.

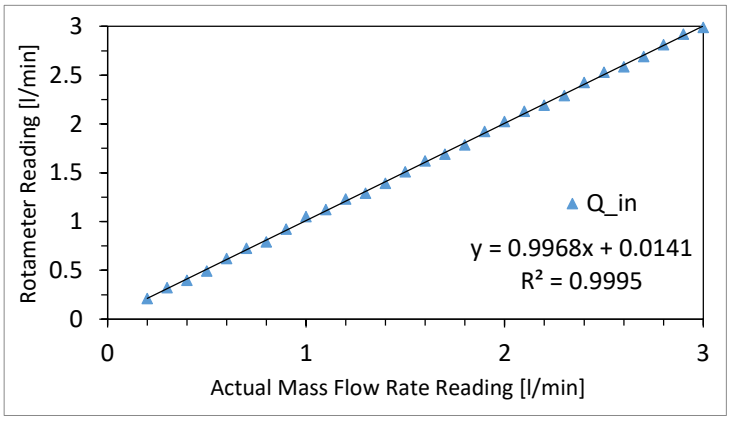

Fig. 4.15: Rotameter calibration curve for the inlet water to the MCHS.

4.4.3 Pressure Gauge Calibration

To measure the total pressure drop between the inlet and outlet of the minichannel heat sink, a Comark C9555 digital pressure meter was used. The digital pressure meter is portable, hand-held and easy to use, it can read up to seven common English and metric pressure units (psi, in. H_2O, in. Hg, mm Hg, kPa, bar or mbar). In order to display the readings of the water differential pressure, LCD screen was provided and the power needed to operate this device was provided by 9 V DC alkaline battery. This device has a range of 0 to 2.1 bar with an accuracy of ±0.5% of its full scale as given by the manufacturer. It also has a memory function that allows up to 40 readings for later recall and a backlight for providing auxiliary lighting at hard-to-see locations. The digital pressure meter was provided by 1/8" FNPT fittings stainless steel, which was constructed to fit to the tubing coming from the pressure taps on the minichannel heat sink.

The inclined manometer was used to calibrate the pressure gauge that measures the differential pressure drop in the inlet and outlet of the minichannel heat sink test section. A linear curve fit was obtained to get the calibration equation for the water differential pressure as shown in Fig. 4.16.

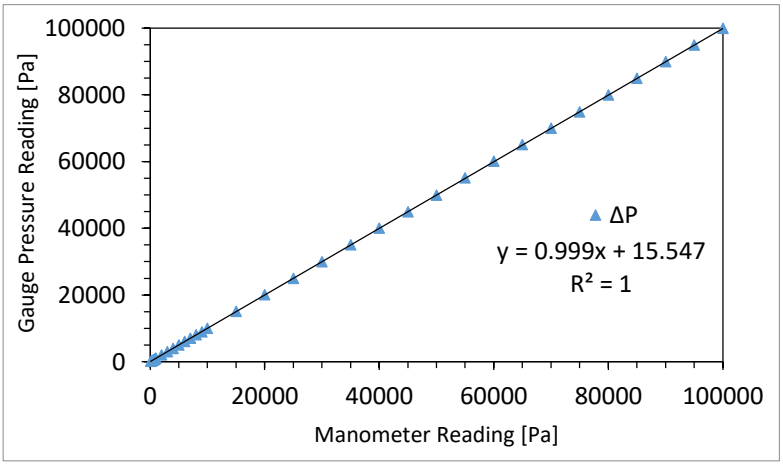

Fig. 4.16: Pressure gauge calibration curve results.

4.5 Procedures of Running the Test Rig

The procedure involved in running the test rig is now described.

1. First, fill the reservoir (tank) with water from the tap.
2. Open the valve and then run the pump to circulate the water through the flow loop.
3. Leave the water circulating inside the test rig until the air escapes fully from connecting tube and minichannel heat sink.
4. Adjust the pump speed to give the required mass flow rate by regulating the voltage and current on the DC power supply device.
5. Switch on the power supply unit to provide DC electrical power to the thermal resistors heater and use the Variac to adjust the power to the required value, for instance 25, 37.5 and 50 W for each resistor in the present work. In order to avoid water boiling inside the test section, the power setting chosen should not cause boiling to occur inside the test section, at the minimum mass flow rate selected which ranges between 0.1 and 3.0 *l/min*.
6. Adjust the mass flow rate by using a bypass valve, e.g. 0.5 *l/min*, and wait until conditions become steady. The measured values are considered to be at steady state if the values do not fluctuate more than the uncertainty in the measurements and also when there are no changes in conditions with time in the mass flow rate, pressure and temperature readings. In the present work, the steady condition is achieved after approximately 35 minutes.
7. After adjusting the water flow rate entering the test section, set the voltage and current applied to the resistors. After steady state is reached, record all data for every mass flow rate used. The data collection includes recording each of the total water differential pressure, water inlet and outlet temperature, wall temperature distribution along the channel flow, water flow rate and power of the water pump and the resistors by measuring the voltage and the current of the power supply.
8. Repeat procedures 6 and 7 for different mass flow rates with a fixed heat flux.
9. After finishing the experiment, firstly, switch off the resistors power supply device, secondly, decrease the mass flow rate and turn off the pump, finally, shut off the valves connecting the main reservoir and the flow loop.

Fig. 4.17 shows the experimental measurement of temperature values measured at total input power of 100 W and volumetric flow rate of 0.10 *l/min* (Re = 92.5) for a straight rectangular minichannel (SRM) heat sink. Since the fluid inlet temperature was fixed at 20 ^{o}C for all time, there is no need to sketch it. In this figure the fluid outlet temperature ($T_{f,out}$) and the temperature close to the minichannel base wall ($T_{y,tci}$) at a distance y = 1.75 mm were

measured experimentally using a thermocouple, see Fig. 4.7. The subscript *i* denotes the location of thermocouple used to measure minichannel base temperature (*i* = 1, 2, 3 and 4). As it can be appreciated in the curves, once the power is switched on the temperature increases until reach steady state after approximately half hour. The maximum values measured for $T_{f,out}$ is 34.85 °C while the maximum temperature of the thermocouples that located underneath the minichannel base from the water inlet side to the outlet side were 26, 46.6, 53.4 and 61.2 °C, respectively.

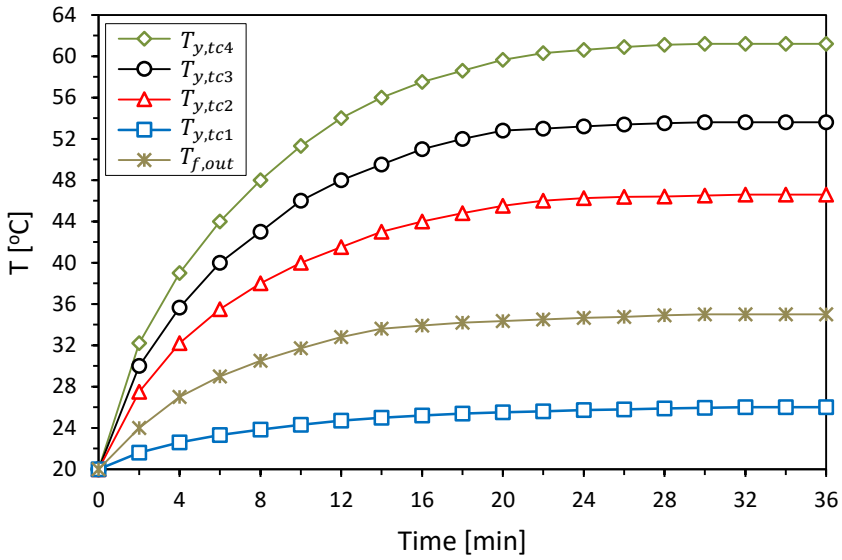

Fig. 4.17: The time history of experimental temperature measured at each thermocouple for the SRM heat sink at total input power of 100 W and volumetric flow rate of 0.10 *l/min*.

4.6 Heat Loss Measurements

Before conducting an experiment, the rate of heat loss dissipated from the MCHS specimen to the surrounding via natural convection, radiation and conduction was estimated. The heat lost due to the conduction occurred through the wires that came out of the MCHS test sections to connect the thermal resistances (Heater) to the power. The other possible source of heat loss was through twelve stainless steel screws mounted on the top of the clear cover, which were used to prevent the water from leaking to the outside of the MCHS test. To calculate the rate of heat losses from the MCHS models, the heat transferred to the working fluid must be calculated and then compared with the heat supplied by the thermal resistances.

The steady-state sensible heat gain by the working fluid can be obtained from an energy balance:

$$q = \rho_f \cdot Q_{in} \cdot Cp_f\left(T_{f,out} - T_{f,in}\right) \tag{4.1}$$

where $T_{f,in}$ and $T_{f,out}$ are respectively the inlet and outlet water temperatures (°C), which were obtained experimentally using the two thermocouples mounted upstream and downstream of the minichannels. The ρ_f and Cp_f are the density (kg/m^3) and specific heat capacity (J/kg.K) of the water, respectively, which are determined based on the average of the fluid inlet and outlet temperatures. The term Q_{in} (m^3/sec) represents the volumetric flow rate of water which is measured with a flowmeter (Rotameter) calibrated using a volumetric beaker and stopwatch and can be expressed as:

$$Q_{in} = n \cdot V_{ch} \cdot A_{ch} \tag{4.2}$$

where n and V_{ch} are respectively the number of channels and water velocity in minichannel, while A_{ch} represents the cross-sectional area of the minichannel as shown:

$$A_{ch} = H_{ch} \cdot W_{ch} \tag{4.3}$$

The power supplied to the heaters (q_{in}) can be calculated by:

$$q_{in} = V \cdot I \tag{4.4}$$

where V and I respectively represent the voltage (V) and current (A) supplied to the resistors by a DC-power supply device. So, the rate of heat losses (q_{loss}) can be written in the final form as:

$$q_{loss} = q_{in} - \rho_f \cdot Q_{in} \cdot Cp_f\left(T_{f,out} - T_{f,in}\right) \tag{4.5}$$

Eq. (4.5) also used in the work of Liu and Garimella (2007) to estimate the heat loss from the test section. The procedure that was used in the present study to calculate the heat losses can be briefly described as follows. Firstly, a constant water flowrate is provided to the MCHS model(s). Secondly, a constant power is applied to the test section heaters using a DC-power supply, which causes the temperature of the MCHS test section to increase. Finally, when conditions become steady (no change in the temperatures of the water inlet and outlet and also in the body of the MCHS model) the inlet and outlet water temperatures from the test section are recorded by the two thermocouples inserted at the inlet and exit of the MCHS test section. This procedure is repeated for several levels of water flow rate and three input power of 50, 75 and 100 W.

In the present work, the maximum average heat loss was estimated to be approximately 8% of the input power from each model. This value was obtained from energy balance tests, where the enthalpy rise of the water flowing inside the MCHS test sections is compared with the electrical input power supplied to the heater. Therefore, the rate of heat removal by the fluid for all MCHS models can be estimated as given:

$$q = V \cdot I - q_{loss} = 0.92(V \cdot I) \tag{4.6}$$

4.7 Experimental Data Analysis

This section will present the equations used to determine pressure drop, friction factor, Poiseuille number, heat transfer coefficient and Nusselt number in the single-phase flow experiments.

4.7.1 Pressure Drop (ΔP) and Friction Factor (f) Measurements in MCHS

4.7.1.1 Pressure Drop

The measurement of the differential pressure drop inside each minichannel heat sink (MCHS) is not a trivial task; it is complicated by the small size of the minichannels. The most common method used in the literature to measure the differential pressure drop involves making pressure measurements inside the inlet and outlet plenums or manifolds such as experimental work conducted by Qu and Mudawar (2002a) and Steinke and Kandlikar (2006b). In the present work, a digital pressure gauge was used to measure the total differential pressure drop (ΔP_t) directly by using two plastic tubes connected to the inlet and outlet MCHS plenum. The overall measured differential pressure drop between the inlet and outlet MCHS is calculated using Eq. (4.7).

$$\Delta P_t = P_{in} - P_{out} \tag{4.7}$$

In order to calculate the total pressure drop across the MCHS, there is a need to calculate the major pressure drop in the minichannel, which represents the developing and fully developed flow regions, and also the minor pressure losses that occur in the inlet and outlet of the minichannels and plenums due to the change in the cross sectional area. Therefore, the overall differential pressure drop for the straight rectangular minichannel (SRM) heat sink can be obtained by summing the major and minor pressure losses as:

$$\Delta P_t = \Delta P_{ch} + \Delta P_{minor\ losses} \tag{4.8}$$

The minor losses have eight components as depicted in Fig. 4.18. The first two components are due to flow of water inside the inlet and outlet tube of the male run tee union positioned on the top of the MCHS cover, while the third and fourth components are due to the bend (90 degree turn), κ_{90}, that forms between the outlet of the tube and the inlet plenum (header) from the inlet side of the MCHS and the bend that forms between the outlet plenum and the tube inlet from the outlet side of the MCHS. The fifth and sixth pressure losses occur respectively due to the sudden expansion between the outlet tube and inlet plenum ($\kappa_{e_{inlet}}$) and the sudden expansion between the minichannel exit and the outlet plenum (κ_e). Similar flow feature pressure losses occur due to sudden contractions to give the last two pressure loss components, the first one was at the inlet plenum and minichannel inlet ($\kappa_{c_{outlet}}$) and the

second at the outlet plenum and the inlet tube (κ_c). Thus, the minor pressure losses in the straight rectangular minichannel (SRM) heat sink can be expressed by Eq. (4.9).

$$\Delta P_{minor\ losses} = 2\left(\frac{1}{2}\cdot \rho_f \cdot V_{tube}^2\left(4f_{tube}\cdot\frac{L_{tube}}{D_{tube}}\right)\right) + \frac{\rho_f \cdot V_{tube}^2}{2}\left(\frac{A_{tube}}{A_P}\right)^2\left(\kappa_{e_{inlet}} + \kappa_{c_{outlet}}\right) + \frac{\rho_f \cdot V_{ch}^2}{2}\left((2\kappa_{90})\cdot\left(\frac{A_{ch}}{A_p}\right)^2 + \kappa_c + \kappa_e\right) \quad (4.9)$$

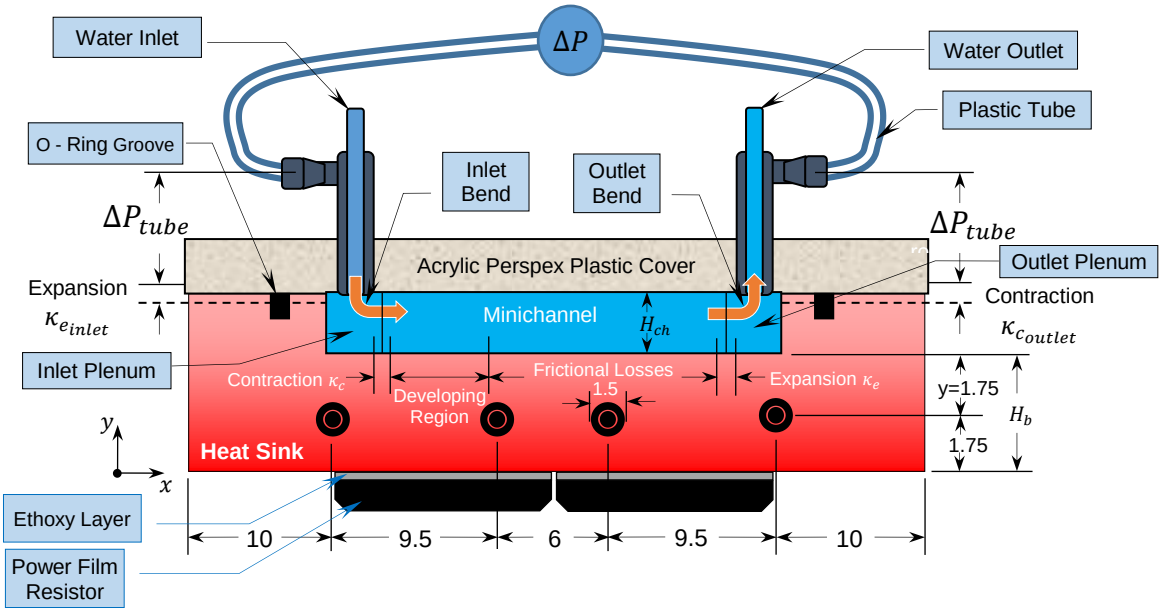

Fig. 4.18: Schematic representation for SRM design showing the thermocouple locations and pressure drop components. All dimensions in mm.

In the present experimental work, the plenum area of the SRM heat sink model is 79.64 mm^2, while the length and diameter of the inlet and outlet tube of the male run tee union are 25 mm and 2.5 mm, respectively. The sudden expansion loss ($\kappa_{e_{inlet}}$) and the sudden contraction loss ($\kappa_{c_{outlet}}$) can be predicted using the simple relationships found in the handbook source of Blevins (1984) and Idelchik (1986):

$$\kappa_{e_{inlet}} = \left(1 - \frac{A_{tube}}{A_P}\right)^2 \quad (4.10)$$

$$\kappa_{c_{outlet}} = 0.42\left(1 - \frac{A_{tube}}{A_P}\right) \quad (4.11)$$

The area and velocity of the male run tee union tube can be calculated by:

$$A_{tube} = \frac{\pi}{4}\cdot D_{tube}^2 \quad (4.12)$$

$$V_{tube} = \frac{Q_{in}}{A_{tube}} \tag{4.13}$$

The κ_{90} denotes the bend loss coefficient associated with each of the 90° turns at the channel inlet and outlet and Phillips (1987) recommended κ_{90} to be approximately 1.2. Whereas κ_c and κ_e respectively represent the contraction and expansion loss coefficients due to area changes which are based on the ratio of the channel area to the plenum flow area ($\sigma = \frac{A_{ch}}{A_P}$) and the flow regime (laminar or turbulent), their values can be estimated from the graphical information given by Kays and London (1984), as shown in Fig. 4.19.

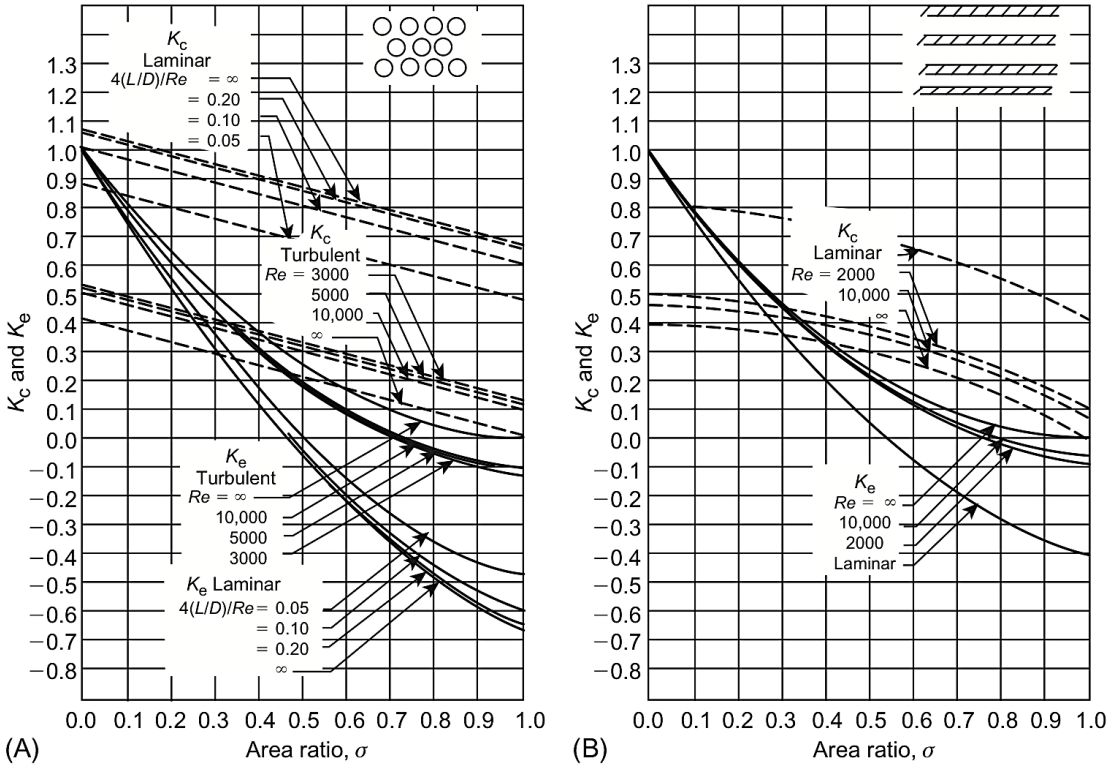

Fig. 4.19: Contraction and expansion loss coefficients for flow between inlet and outlet manifolds and the microchannels: (A) $\propto < 0.1$; and (B) $0.1 \leq \propto \leq 1.0$ (Kays and London, 1984).

Since the flow inside the tubes was found to be in the turbulent regime for most of the water flow rates used, the following correlation equation offered by Phillips (1988 and 1990) can be used to estimate the friction factor:

$$f_{tube} = \left(0.0929 + \frac{1.01612}{\frac{L_{tube}}{D_{tube}}}\right) Re_{tube}^{-\left(0.268 + \frac{0.3193}{\frac{L_{tube}}{D_{tube}}}\right)} \tag{4.14}$$

The Reynolds number in the tube is given by:

$$Re_{tube} = \frac{\rho_f \cdot V_{tube} \cdot D_{tube}}{\mu_f} \tag{4.15}$$

The major component of the pressure drop occurs in the core of the minichannels and can be obtained by summing two components, the first component is due to the frictional factor in the developing region which occurs in the entrance region of the minichannel, while the second component is obtained in the fully developed region in the remaining length of the channel, as shown in Fig. 4.18. The components of the major pressure drop can be seen in Eq. (4.16).

$$\Delta P_{major} = \Delta P_{ch} = \frac{1}{2} \cdot \rho_f \cdot V_{ch}^2 \left(4 f_{app.} \cdot \frac{L_{ch}}{D_h} \right) \tag{4.16}$$

For the straight rectangular minichannel (SRM) heat sink, the total differential pressure drop ($\Delta P_{t,SRM}$) between the inlet and outlet MCHS can be expressed as:

$$\Delta P_{t,SRM} = \frac{\rho_f \cdot V_{ch}^2}{2} \left((2\kappa_{90}) \cdot \left(\frac{A_{ch}}{A_p} \right)^2 + \kappa_c + \kappa_e + 4 f_{app.} \cdot \frac{L_{ch}}{D_h} \right) + \left(\rho_f \cdot V_{tube}^2 \left(4 f_{tube} \cdot \frac{L_{tube}}{D_{tube}} \right) \right) + \frac{\rho_f \cdot V_{tube}^2}{2} \left(\frac{A_{tube}}{A_P} \right)^2 \left(\kappa_{e_{inlet}} + \kappa_{c_{outlet}} \right) \tag{4.17}$$

In order to obtain the pressure drop along the microchannel (ΔP_{ch}) due to the friction and the developing flow, it is necessary to subtract the minor pressure losses from the total measured pressure drop.

With regard to the single path serpentine rectangular minichannel (SPSM) heat sink with n minichannels and a total $n-1$ fins (U-bends), see Fig. 4.4(a), the total pressure drop is caused by two components, namely pressure drop due to straight minichannel friction and U-bends. Thus, the total pressure drop for the serpentine MCHS can be written in general form as follows (Maharudrayya et al., 2004):

$$\Delta P_t = \frac{1}{2} \cdot \rho_f \cdot V_{ch}^2 \left(4 \, f_{app} \cdot \frac{L_t}{D_h} + \sum_{i=1}^{n-1} \xi_i \right) \tag{4.18}$$

where the symbol ξ_i represents the excess loss coefficient of bend i in the MCHS, while f_{app} and L_t respectively represent the apparent friction factor and the total length including the length in the bends and/is the friction factor given. In order to calculate the value of the excess bend loss coefficient (ξ), Maharudrayya et al., (2004) carried out a CFD simulation of laminar single-phase flow through 180^o bends and serpentine rectangular channels. In their study, a three-regime correlation were proposed to determine the ξ as a function of the Reynolds number (Re), inverse aspect ratio ($\propto^*$), curvature ratio (C) and fin width as follows:

For $Re < 100$:

$$\xi = 0 \tag{4.19a}$$

For $100 < Re < 1000$:

$$\xi = 0.46(Re)^{\frac{1}{3}}(1 - 0.18C + 0.016C^2) \times \left(1 - 0.2 \propto^* + 0.0022 \propto^{*^2}\right) \times \left(1 + 0.26\left(\frac{W_w}{D_h}\right)^{\frac{2}{3}} - 0.0018\left(\frac{W_w}{D_h}\right)^2\right) \quad (4.19b)$$

For $1000 < Re < 2200$:

$$\xi = 3.8(1 - 0.22C + 0.022C^2) \times \left(1 - 0.1 \propto^* + 0.0063 \propto^{*^2}\right) \times \left(1 + 0.12\left(\frac{W_w}{D_h}\right)^{\frac{2}{3}} - 0.0003\left(\frac{W_w}{D_h}\right)^2\right) \quad (4.19c)$$

The hydraulic diameter (D_h) of the rectangular channel can be calculated from Eq. (1.1). The curvature ratio (C) is defined as the ratio of the mean bend radius (R_c) to the hydraulic diameter. The inverse aspect ratio ($\propto^*$) in their study was taken to be the long side of the channel divided by the short side of the channel.

The three correlations above (Eqs. 4.19(a-c)) are valid under the laminar regime $\left(0 < Re = \frac{\rho_f \cdot V_{ch} \cdot D_h}{\mu_f} < 2200\right)$ and the following parameters range:

$$1 < \propto^* = \frac{H_{ch}}{W_{ch}} < 6$$

$$0 < C = \frac{R_c}{D_h} < 6$$

$$1 < \frac{W_w}{D_h} < 30$$

In the present study, the total pressure drop for the single path serpentine rectangular minichannel (SPSM) heat sink can be simplified to be:

$$\Delta P_{t,SPSM} = \frac{1}{2} \cdot \rho_f \cdot V_{ch}^2 \left(4 f_{app} \cdot \frac{L_t}{D_h} + \sum_{i=1}^{n-1} \xi_i + \kappa_c + \kappa_e\right) \quad (4.20)$$

The pressure distribution in every straight minichannel in SPSM heat sink is represented by the maximum and minimum pressure, which are given by (Hao et al., 2013):

$$P_{min,i} = \Delta P_{t,SPSM} - (i-1)\frac{1}{2} . \ \rho_f . V_{ch}^2 \left(4 f_{app} \cdot \frac{L_{ch}}{D_h} + \xi\right) \quad (4.21a)$$

$$P_{max,i} = \Delta P_{t,SPSM} - \frac{1}{2} . \ \rho_f . V_{ch}^2 \left(4i f_{app} \cdot \frac{L_{ch}}{D_h} + (i-1)\xi\right) \quad (4.21b)$$

For double path multi-serpentine rectangular minichannel (DPSM) heat sink, the total pressure drop can be written as:

$$\Delta P_{t,DPSM} = \frac{\rho_f \cdot V_{ch}^2}{2}\left(4f_{app} \cdot \frac{L_t}{D_h} + \sum_{i=1}^{n-2} \xi_i + \kappa_c + \kappa_e + 2\kappa_{90}\left(\frac{A_{ch}}{A_p}\right)^2\right) + \rho_f \cdot V_{tube}^2\left(4f_{tube} \cdot \frac{L_{tube}}{D_{tube}}\right) + \frac{\rho_f \cdot V_{tube}^2}{2}\left(\frac{A_{tube}}{A_P}\right)^2\left(\kappa_{e_{inlet}} + \kappa_{c_{outlet}}\right) \quad (4.22)$$

While the total pressure drops for a triple path multi-serpentine rectangular minichannel (TPSM) heat sink can be expressed by:

$$\Delta P_{t,TPSM} = \frac{\rho_f \cdot V_{ch}^2}{2}\left(4f_{app} \cdot \frac{L_t}{D_h} + \sum_{i=1}^{n-3} \xi_i + \kappa_c + \kappa_e + 2\kappa_{90}\left(\frac{A_{ch}}{A_p}\right)^2\right) + \rho_f \cdot V_{tube}^2\left(4f_{tube} \cdot \frac{L_{tube}}{D_{tube}}\right) + \frac{\rho_f \cdot V_{tube}^2}{2}\left(\frac{A_{tube}}{A_P}\right)^2\left(\kappa_{e_{inlet}} + \kappa_{c_{outlet}}\right) \quad (4.23)$$

4.7.1.2 Friction Factor

Due to the short length and small size of the minichannel, the local pressure drop cannot be easily measured directly within the channel. Alternatively, the total pressure drop was measured in the upstream and downstream of the MCHS test section. In this case, the measurement of the differential pressure drop was affected by the inlet and outlet losses. In order to measure the minichannel pressure drop, the pressure losses were calculated individually at different water flow rates (Re) and subtracted from the total pressure drop. The experimental pressure drops over the minichannel were measured and arranged in non-dimensional form by using the friction factor (f). In the present work, the Fanning friction factor (f_F) will be utilized which also called friction coefficient (C_f), it is defined as the ratio of wall friction forces to the inertia forces and can be expressed as presented by Bergman et al. (2017):

$$f_F = \frac{\text{Wall friction force}}{\text{Inertia force}} = \frac{2\tau_w}{\rho \cdot V^2} = \frac{f_D}{4} \quad (4.24)$$

where τ_w is wall shear stress (Pa) and f_D is the Darcy-Weisbach friction factor. The Fanning friction factor is widely used to express the fluid flow behaviour. The Fanning friction factor inside the straight rectangular minichannel can be also rewritten in another form using the following equation:

$$f_{ch} = \frac{\Delta P_{ch} \cdot D_h}{2\rho_f \cdot L_{ch} \cdot V_{ch}^2} = \frac{\Delta P_{ch} \cdot D_h \cdot A_{ch}^2}{2\rho_f \cdot L_{ch} \cdot Q_{in}^2} = \frac{W_{ch}^3 \cdot H_{ch}^3 \cdot \Delta P_{ch}}{\rho_f \cdot L_{ch} \cdot Q_{in}^2 (W_{ch} + H_{ch})} \quad (4.25)$$

The Fanning friction factor occurring inside the curved minichannel is given by:

$$f_{curve} = \frac{\Delta P_{ch} \cdot D_h}{2\rho_f \cdot L_{curve} \cdot V_{ch}^2} = \frac{180}{\pi \cdot R_c \cdot \theta} \times \frac{W_{ch}^3 \cdot H_{ch}^3 \cdot \Delta P_{ch}}{\rho_f \cdot Q_{in}^2 \, (W_{ch} + H_{ch})} \quad (4.26)$$

where θ and R_c are the angle of the channel (in degrees) and curvature radius (m) respectively as shown in Fig. 4.20, while L_{curve} is represents the length of the curved channel (m) which equal to be:

$$L_{curve} = \frac{\pi \cdot R_c \cdot \theta}{180} \tag{4.27}$$

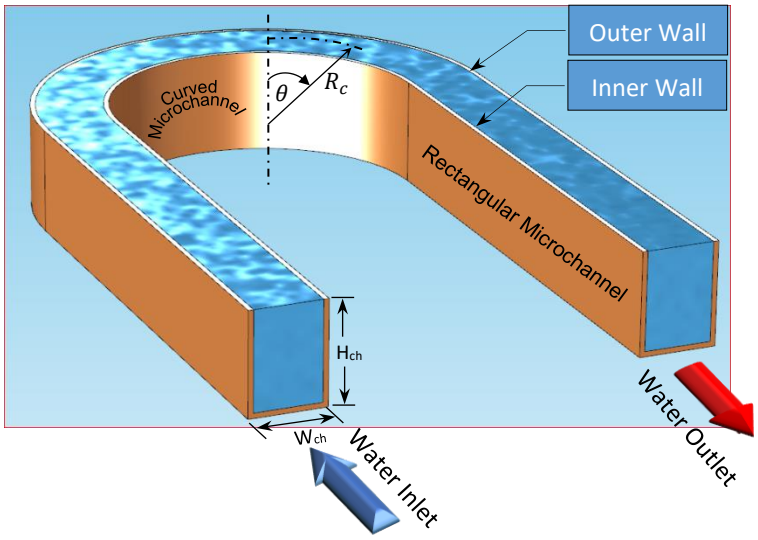

Fig. 4.20: Schematic representation of the geometry for the curved rectangular minichannel.

4.7.2 Heat Transfer Coefficient and Nusselt Number Measurements in MCHS

For a single-phase flow, the heat convected from the inner surface of the minichannels to the working fluid stream can be equated to the steady-state sensible heat carried away by the coolant given by an energy balance, see Eq. (4.1). The convective heat transfer from the walls of the channels to the fluid stream is calculated using Newton's law of cooling as follows:

$$q = n \cdot h \cdot A_{eff} \cdot (T_w - T_f) \tag{4.28}$$

where h is the convective heat transfer coefficient ($\frac{W}{m^2 \cdot K}$), T_w and T_f are the channel base wall temperature and the fluid bulk temperature (^oC), respectively. A_{eff} denotes the effective surface area available for convective heat transfer per minichannel (m^2) and in the present experimental work the heat is transferred to the fluid through three channel walls only and the fourth wall is assumed to be adiabatic as the top cover used was made from an Acrylic Perspex plastic, so the effective heat transfer area of the multiple straight rectangular minichannel can be calculated by using Eq. (3.68).

The effective heat transfers area of the single path serpentine rectangular minichannel (SPSM) heat sink can be obtained by:

$$A_{base} = nW_{ch} \cdot L_{ch} + (n-1)\frac{\pi}{2}(r_1^2 - r_2^2) + 2W_{ch}(W_s + r_1) \quad (4.29)$$

$$A_{fin} = 2n \cdot H_{ch} \cdot L_{ch} + (n-1)\,\pi H_{ch}(r_1 + r_2) + 4H_{ch}(W_s + r_1) \quad (4.30)$$

where L_{ch} represents the minichannel length (m) given by:

$$L_{ch} = L - 2W_s - 2r_1 \quad (4.31)$$

The symbols r_1 and r_2 denotes the outer and inner radius of the curved minichannel (m) respectively, while W_s represents the outlet wall thickness (m) as shown in Fig. 4.21.

$$A_{eff,SPSM} = \left(nW_{ch} \cdot L_{ch} + \frac{\pi}{2}(n-1)(r_1^2 - r_2^2) + 2W_{ch}(W_s + r_1)\right) + \eta_f\left(2n \cdot H_{ch} \cdot L_{ch} + \pi H_{ch}(n-1)(r_1 + r_2) + 4H_{ch}(W_s + r_1)\right) \quad (4.32)$$

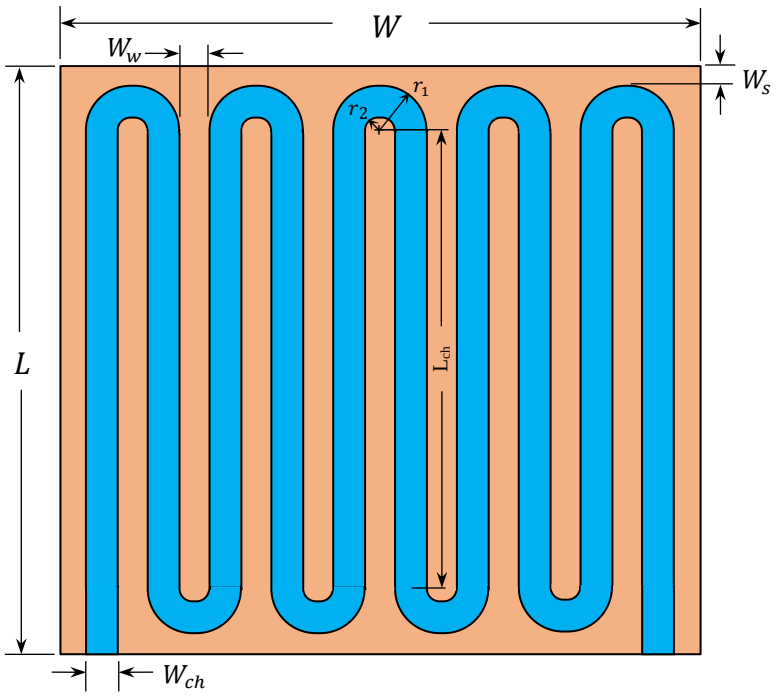

Fig. 4.21: Schematic representation of the geometry for the serpentine rectangular minichannel.

The average minichannel base temperature ($T_{w,avg}$) can be obtained by:

$$T_{w,avg} = \frac{T_{w,tc1} + T_{w,tc2} + T_{w,tc3} + T_{w,tc4}}{4} = \frac{\sum_{i=1}^{4} T_{w,tci}}{4} \quad (4.33)$$

Since direct measurement of the minichannel base temperatures is challenging, it is determined by assuming one-dimensional steady state heat conduction between the thermocouple location (tci) and the minichannel base in the $y-$direction as shown in Fig. 4.22.

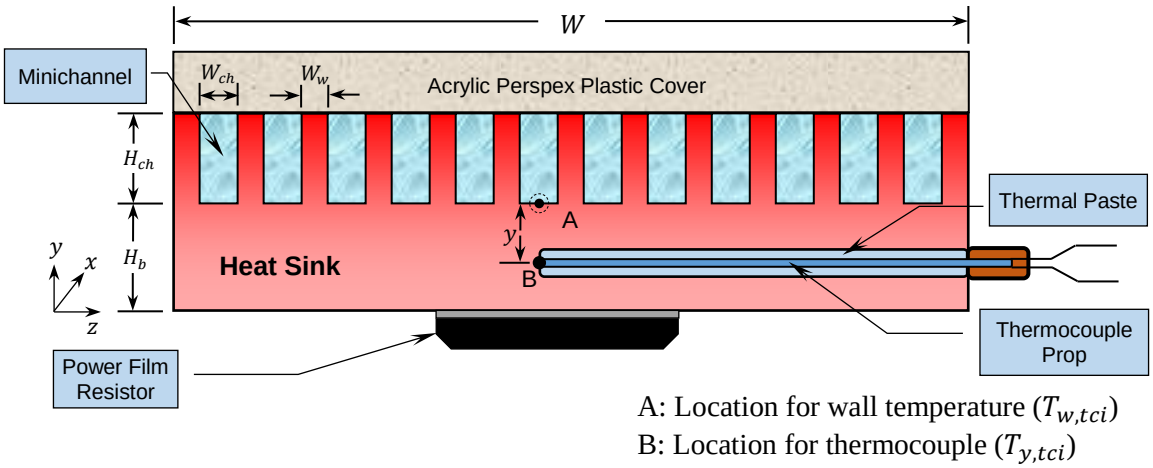

Fig. 4.22: Cross-section view of the test section to explain the arrangement of the wall temperature measurement.

The local minichannel base temperature ($T_{w,tci}$) can be evaluated by:

$$q = k_s \cdot A_h \frac{(T_{y,tci} - T_{w,tci})}{y} \tag{4.34}$$

To get the minichannel base temperature ($T_{w,tci}$) at different location in the minichannel, Eq. (4.34) can be rearrangement as follows (Lee et al., 2012):

$$T_{w,tci} = T_{y,tci} - \frac{y \cdot q''_{eff}}{k_s} \tag{4.35}$$

where A_h is the bottom heated area of the minichannel heat sink (m^2) over which heating is provided by the resistors, while k_s is the thermal conductivity of the heat sink material, and y is the distance between the bottom wall of the minichannel and the thermocouple that is embedded to measure $T_{y.tci}$ as shown in Fig. 4.22. The q''_{eff} denotes the effective average heat flux based on the bottom heated area (A_h) of the MCHS test section as given by:

$$q''_{eff} = \frac{q}{A_h} = \frac{\rho_f \cdot Q_{in} \cdot Cp_f (T_{f,out} - T_{f,in})}{A_h} \tag{4.36}$$

The inlet and outlet water temperatures can be measured directly by thermocouples that are located at the entrance and exit of the MCHS or by using an overall system energy balance as given by Eq. (4.1), while the fluid bulk temperature along the axial location of the minichannel can be calculated by using Eq. (4.37).

$$T_{f,x} = T_{f,in} + \frac{x}{L_{ch}} (T_{f,out} - T_{f,in}) \tag{4.37}$$

By substituting Eq. (4.1) into Eq. (4.37) we obtain Eq. (4.38) as follows:

$$T_{f,x} = T_{f,in} + \left(\frac{q}{\rho_f \cdot Q_{in} \cdot c_{p_f}} \cdot \frac{x}{L_{ch}} \right) \tag{4.38}$$

After determining T_w and T_f, the convective heat transfer coefficient can be calculated from Eq. (4.28).

4.8 Experimental Uncertainty Analysis

In any experimental work, a set of measurements and data is obtained, and these measurements have errors and uncertainties associated with them which must be estimated. Moffat (1988) defines the uncertainty of a measurement to be the difference between the true value and the measured value of the parameter. Several researchers have given guidelines for planning and conducting experiments by taking into account the experimental errors and uncertainties, for instance, Kline and McClintock (1953); Moffat (1985 and 1988); Coleman and Steel (1995 and 2009); and Holman (2012).

The total uncertainty in experiment data is normally composed of two parts; namely, bias error (fixed or systematic error) and precision error (random error) that occurs when making repeated measurements. Therefore, when estimating the overall uncertainty in measured and calculated quantities, both bias and precision errors need to be combined and the preferred method for doing this is the root-sum-square (RSS) technique, as given by Eq. (4.39):

$$U_x = \pm \sqrt{P_x^2 + B_x^2} \tag{4.39}$$

where U_x is represents the absolute overall uncertainty in the measured quantity x. The estimation of bias errors (B) is based on the accuracy of the instruments, while the estimation of precision errors (P) is based on statistical analysis of the data. The detailed uncertainty analyses procedure and a sample calculation for selected key parameters are presented in Appendix A, and a summary of the uncertainties for the experimental data in this work is shown in Table 4.3.

Table 4.3: Measurement uncertainty summary.

Variable	Symbol	Value or Range	Total Relative Uncertainty, %
Channel width	W_{ch} [mm]	1, 1.5	±0.6%, ±0.4%
Channel depth	H_{ch} [mm]	2, 3	±0.3%, ±0.2%
Channel length	L_{ch} [mm]	21, 300	±0.03%, ±0.002%
Fin width	W_w [mm]	1	±0.6%
Hydraulic diameter	D_h [mm]	1.334, 2	±0.412%, ±0.275%
Volumetric flow rate	Q_{in} [L/min]	0.1 – 3.0	±2.5% – ±0.083%
Pressure drop	ΔP [Pa]	250 – 140000	±2.55% – ±18.15%
Friction factor	f [–]	0.02 – 0.185	±3.35% – ±19.3%
Thermal resistance	R_{th} [K/W]	0.1 – 0.5	±2.86% – ±7.3%
Nusselt number	Nu [–]	7 – 34	±3.65% – ±14%

Chapter 5: Experimental Results

5.1 Introduction

In this chapter, the experimental data for four categories of minichannel heat sinks (MCHSs) will be presented in terms of the pressure drop (ΔP), Fanning friction factor (f), Poiseuille number ($Po = f.Re$), heat transfer coefficient (h), Nusselt number (Nu) and total thermal resistance (R_{th}). The details of the four test sections that are used in the experimental study have been described thoroughly in chapter 4. All results presented in this chapter were obtained from experiments at a water inlet temperature of 20 °C and atmospheric pressure.

Comparisons were made between the experiments, empirical correlation equations and conventional theory for both fully developed and developing flow regions in terms of f, Nu and R_{th} at different Reynolds number (Re).

5.2 Flow and Pressure Drop Characteristics of MCHS

Fig. 5.1 depicts the effect of water flow rate ($0.1 \leq Q_{in} \leq 2.0\ l/min$) on the experimental measurements of the total pressure drops (ΔP_t) for the straight rectangular minichannel (SRM) heat sink model with input heating powers of 50, 75 and 100 W. With the inlet tube diameter of 2.5 mm, the flow is considered turbulent when $Q_{in} \geq 0.15\ l/min$. As expected, ΔP_t increases rapidly with Q_{in} and as the input power increases the ΔP_t decreases monotonically. For example, at $Q_{in} = 1.0\ l/min$ the ΔP_t decreased by 18%, fall down from 12.2 kPa at 50 W to 10 kPa at 100 W.

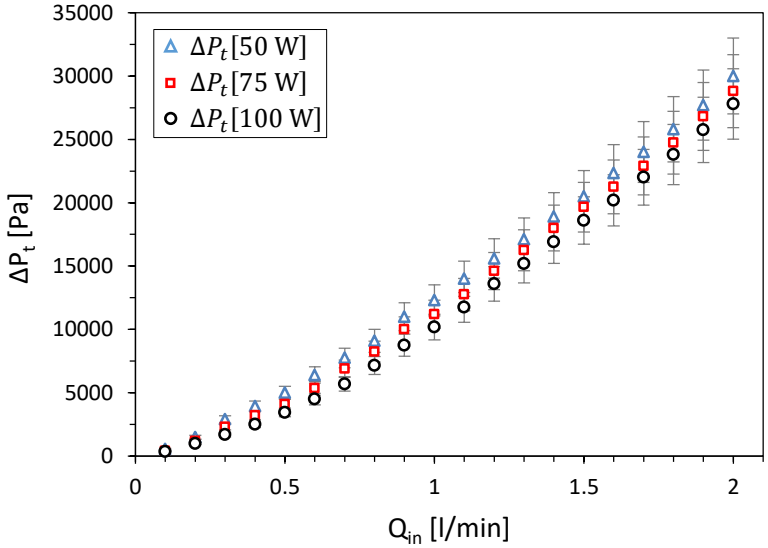

Fig. 5.1: The total pressure drop in a straight rectangular MCHS model versus Q_{in} at three different input powers of 50, 75 and 100 W.

For a given Q_{in}, the pressure drop for flow at an input power of 50 W is higher than those at 75 W and 100 W, and this behaviour is due to the change in the fluid density and viscosity with temperature. As expected, when these properties decrease the pressure drop decreases

also, and this behaviour in unaffected by whether the water flow is in the laminar or turbulent flow regime. Fig. 5.2 shows that as the temperature increases, the density (ρ_f) and kinematic viscosity (μ_f) of the fluid (water) decreases. The density and viscosity of water were obtained using equations proposed by Popiel and Wojtkowiak (1998) as described in Appendix B, which were solved by using MATLAB software version-14.

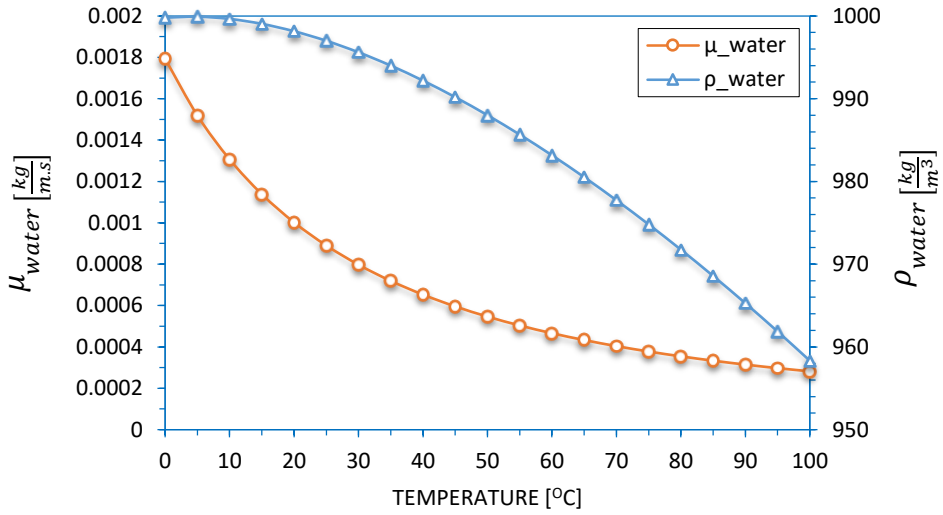

Fig. 5.2: Density and kinematic viscosity of water at different temperature.

Fig. 5.3 shows the data of the total pressure drop (ΔP_t) obtained experimentally for the heating power of 100 W for a SRM heat sink test section, together with those obtained from the equation derived in the present study as a function of volumetric flow rate ($0.1 \leq Q_{in} \leq 1.0\ l/min$), see Eq. (4.17). Using mean absolute error (MAE) as defined by Eq. (5.1), Eq. (4.17) can predict the experimental total pressure drop data in both laminar and turbulent flow regimes with a MAE of 14.3%.

$$MAE = \frac{1}{N}\sum \frac{|predict - experiment|}{experiment} \times 100\% \tag{5.1}$$

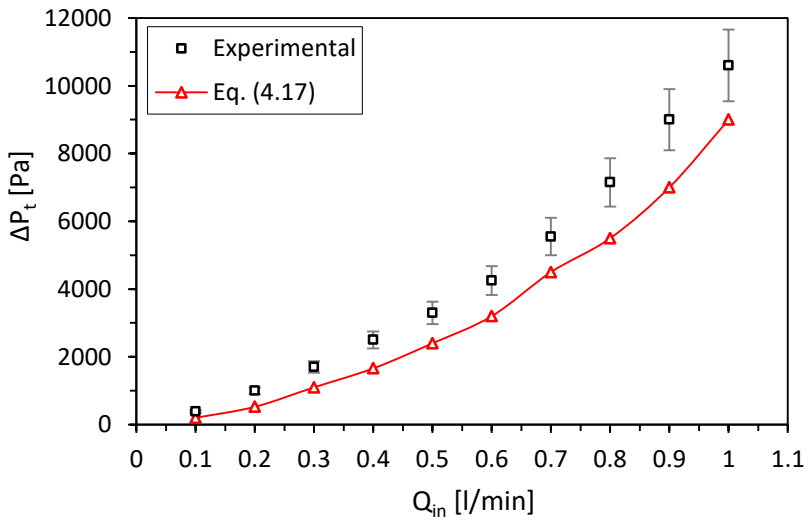

Fig. 5.3: Comparison of the total experimental pressure drop with Eq. (4.17) for SRM heat sink model at different Q_{in} for input power of 100 W.

The minichannel pressure drops (ΔP_{ch}) for the SRM heat sink test section are plotted in graphical form, excluding the minor pressure losses (contraction, expansion and bend pressure losses) to allow a fair comparison with correlations for straight channels. To obtain channel pressure drops, the minor pressure losses are subtracted from the total measured pressure drops, see Eqs. (4.8 and 4.9).

Fig. 5.4 shows the minichannel pressure drop (ΔP_{ch}) measured in the SRM heat sink versus different Reynolds number (Re) for three input powers of 50, 75 and 100 W supplied to the MCHS test section. The range of the volumetric flow rate (Q_{in}) was varied from 0.1 to 3.0 l/min to get both laminar and turbulent flow regimes inside the minichannels. It is apparent from the figure given that Q_{in} has a significant effect on the pressure drop, and as can be seen the pressure drop increases proportionally with volumetric flow rate. For example, at $Re = 1400$ the value of ΔP_{ch} decreased by half from 2000 Pa at 50 W to 1000 Pa at 100 W.

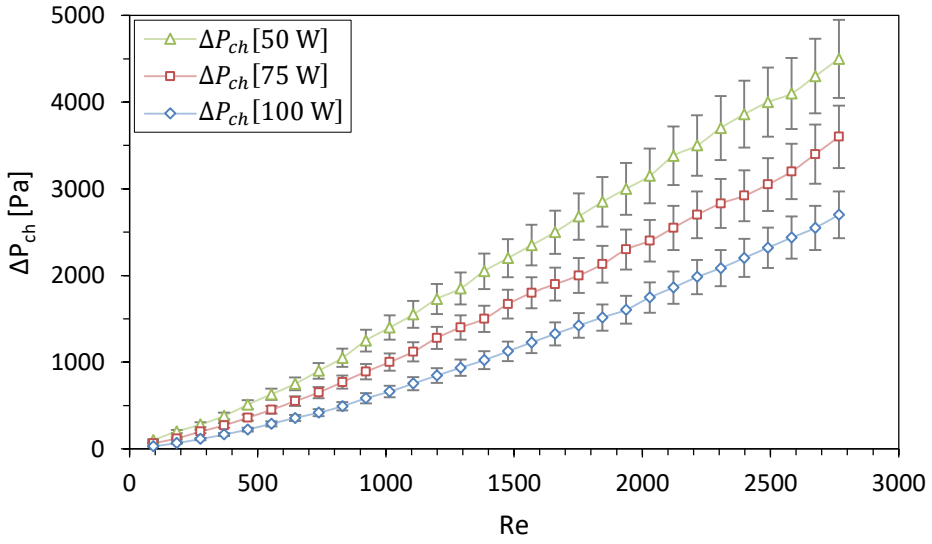

Fig. 5.4: The experimental minichannel pressure drop versus Re at three different input powers of 50 W, 75 W and 100 W.

Fig. 5.5 demonstrates the experimental friction factor (f) in the SRM heat sink versus different Reynolds number (Re) for input power of 100 W. To get laminar and turbulent flow regime inside the minichannel, the volumetric flow rate of water was varied in the range ($0.1 \leq Q_{in} \leq 4.0\ l/min$). The values of f are calculated from the minichannel pressure drop (ΔP_{ch}) obtained experimentally using Eq. (4.25). It can clearly be seen from the figure that when the water flow rate increases the friction factor decreases monotonically.

Comparisons for experimental friction factor have been conducted with available empirical correlation equations for both developing and fully developed regions in laminar and turbulent flow regimes. Shah and London (1978) and Shah (1978) suggested correlation equations for friction factor under single-phase laminar flow condition, while Phillips (1987

and 1990); Haaland (1983); and Blasius (Hager, 2003) proposed correlation equations for friction factor under single-phase turbulent flow regime (Kandlikar, 2014).

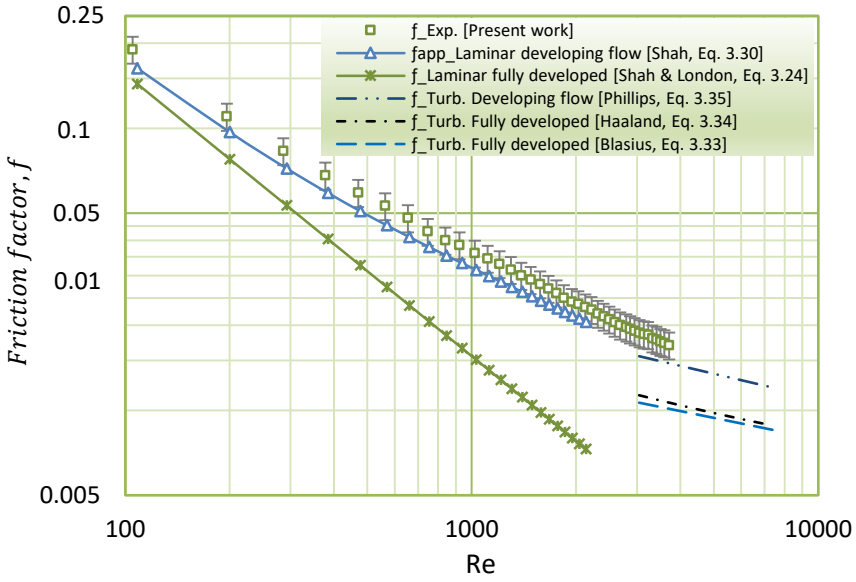

Fig. 5.5: The minichannel friction factor versus Re at input power of 100 W.

In the laminar flow regime, the results of the f_{ch} obtained experimentally exhibit good agreement with the empirical correlation equation proposed by Shah (1978) for developing flow, see Eq. (3.30), with a MAE of 7.8%. The agreement with the correlation proposed by Shah and London (1978) for fully developed flow was not as good, see Eq. (3.24).

For the turbulent flow regime, comparisons have been conducted between the friction factor obtained experimentally and those obtained using correlation equations proposed by Blasius (Hager, 2003) for fully developed and Phillips (1990) for developing flow, see Eqs. (3.33) and (3.35). The maximum Reynolds number in the present study was 3712 due to the limited range of the Rotameter used experimentally. As shown in Fig. 5.5, an acceptable match has been achieved between the experimental friction factor and correlation equation suggested by Phillips (1990) with a MAE of 10%, while 25% MAE was found with equation proposed by Blasius. In conclusion, it could be argued that the conventional correlation equations proposed by Shah (1978) for developing laminar flow and Phillips (1990) for developing turbulent flow regime are still applicable to some extent with regard to straight rectangular minichannel for single phase flow condition.

In order to take into account the effect of the surface roughness on the friction factor, a correlation equation proposed by Haaland (1983) was used in this study for comparison. Haaland's equation is used to calculate the Darcy friction factor in tube under fully developed turbulent flow regime, see Eq. (3.34). As can be seen, 24.7% MAE has been found between the present experimental work and Haaland's equation; though the developing flow region of the experimental work is not accounted for in Haaland's equation.

In the experiments, the relative surface roughness, ε/D_h, where ε and D_h are respectively the surface roughness and hydraulic diameter of the minichannel, for four MCHS test sections studied is therefore 0.875×10^{-3} for the SRM heat sink and between 0.563×10^{-3} and 0.591×10^{-3} for the other three serpentine MCHS designs. These are less than the relative surface roughness of stainless steel micro-tubes (1.76×10^{-3} to 2.80×10^{-3}) in the study of Kandlikar et al. (2003) who showed this ε/D_h had negligible effect on pressure drop and heat transfer characteristics; consequently the effect of the surface roughness (ε) on the pressure drop and heat transfer coefficient is neglected in the present study.

The hydrodynamic entry length (L_{hy}) can be calculated from the equation proposed by Shah and London (1978), see Eq. (3.8). For instance, at low Reynolds number of 92.3, the entrance length was found to be 6.15 mm (29.3% of minichannel length), while, at Reynolds number of 315, the entrance length was 21 mm which is equal to the minichannel length, this means that the flow never become fully developed until it reached the minichannel exit, so the most of flow can be considered in the developing flow regime for this study.

Fig. 5.6 shows the experimental Poiseuille number (Po) for the SRM heat sink design against dimensionless length (x^+) at input power of 100 W. As can be seen from the figure, the values of the experimental Po are in reasonable agreement with the correlation equation proposed by Shah (1978) for developing laminar flow with MAE of 8%. Whereas in a turbulent flow regime, the values of the experimental Po are higher than those obtained by the Blasius's correlation for fully developed conditions. In contrast, an acceptable agreement was achieved particularly with the correlation equation proposed by Phillips (1987) for developing turbulent flow with a MAE of just 10%.

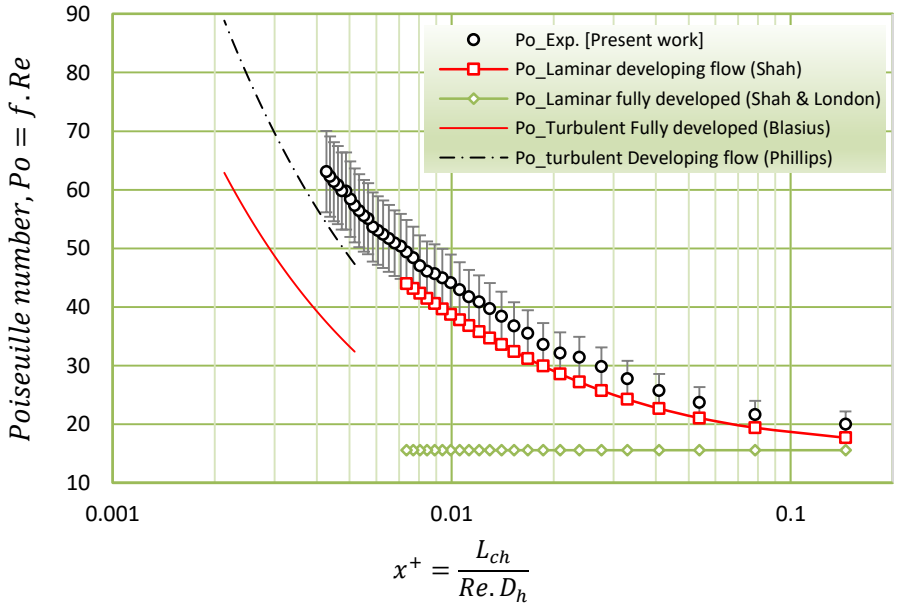

Fig. 5.6: The experimental Poiseuille number against dimensionless length for rectangular MCHS test section at input power of 100 W.

Figs 5.7(a and b) show the experimental measurements of the total pressure drops (ΔP_t) versus volumetric flow rate ($0.1 \leq Q_{in} \leq 1.0\ l/min$) for the three other MCHS models used, namely single (SPSM), double (DPSM) and triple path multi-serpentine rectangular minichannel (TPSM) heat sinks, with an input power of 100 W. The inlet tube diameter for the SPSM was 1.5 mm, and 2.5 mm for both the DPSM and TPSM heat sinks. In all cases, it can be clearly seen that as Q_{in} is increased, the total pressure drop increases rapidly due to both the larger friction forces generated inside the straight and curved minichannels and increases to the minor pressure losses. It is clear from the Fig. 5.7(a) that the SPSM has a higher pressure drop compared with the other MCHS models, while the second and third highest pressure drop were seen in the DPSM and TPSM, respectively. The reason behind this decrease in ΔP_t for the TPSM design belong to that the water flow rate enters to the MCHS manifold is distributed into three minichannels compared to one minichannel in SPSM and two minichannels in DPSM, which leads to reduction in water velocity and friction force.

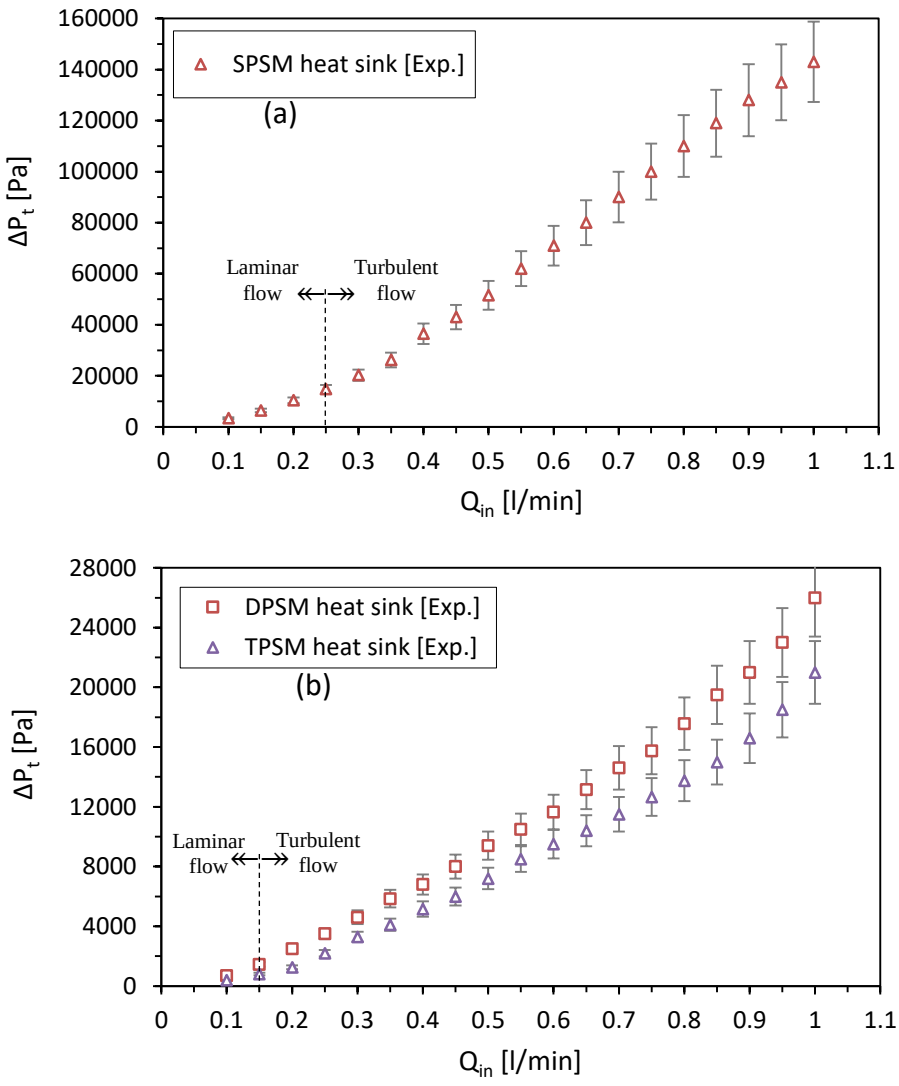

Fig. 5.7: The total experimental pressure drop for: a) SPSM heat sink; b) DPSM & TPSM heat sinks at different Q_{in} and input power of 100 W.

5.3 Heat Transfer Characteristics of MCHS

In this subsection, the local heat transfer coefficient (h_x), the average heat transfer coefficient (h_{avg}), and the Nusselt number (Nu) data obtained from the experimental work for the straight rectangular MCHS test section will be presented in graphical form for different Reynolds numbers (Re). After that, the Nusselt number data obtained experimentally are compared with existing correlation equations for both flow regimes (laminar and turbulent). Among these conventional correlation equations are: Shah and London (1978) for fully developed flow and Lee and Garimella (2006) for laminar single-phase developing flow for the straight rectangular minichannel. For turbulent single-phase flow in a circular cross-section conduit, Dittus-Boelter (1930) for fully developed and Petukhov (1970) and Gnielinski (1976) for both fully developed and developing flow.

5.3.1 Wall and Fluid Bulk Temperature Distribution in the MCHS

To obtain the heat transfer coefficient (h) and Nusselt number (Nu), the minichannel base and the fluid bulk temperature in the MCHS test section must first be determined. The local minichannel base temperature ($T_{w,tci}$) along the axial location of the minichannel can be calculated using Eq. (4.35); whereas the local fluid bulk temperature ($T_{f,x}$) can be determined using Eq. (4.37) in subsection (4.7.2).

Fig. 5.8 compares the measured water temperature rise between the channel inlet and outlet in the SRM heat sink test section versus different inlet Reynolds number (Re_{in}), and theoretical values predicted from the simple energy balance for the two input power of 50 W and 100 W, respectively, see Eq. (4.1). These Reynolds number correspond to water flow rates from 0.1 to 2.0 l/min.

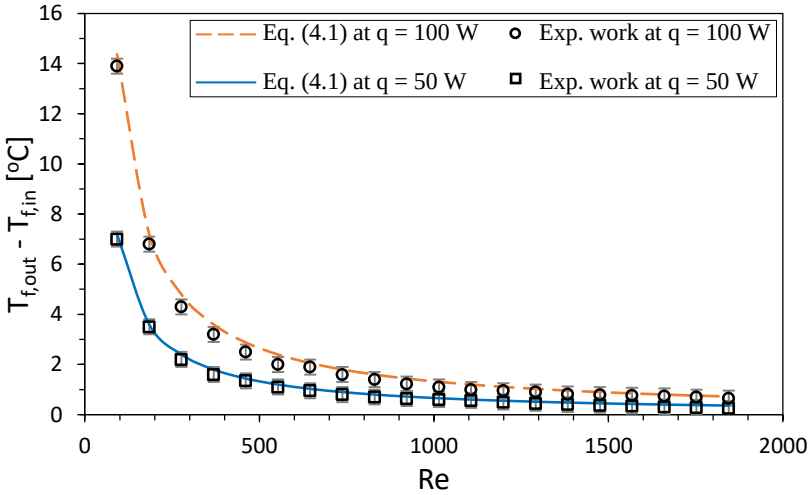

Fig. 5.8: Comparison of experimental data and energy balance predictions for water temperature rise from MCHS inlet to outlet at two input power of 50 and 100 W.

From the figure, it can be seen a good agreement has been achieved between experimental data obtained and the results determined from using the energy balance equation with MAE of 3.35%. From the results obtained, it is evident that when the water flow rate increases the water different temperature decreases.

Figs. 5.9(a and b) show the variation of the microchannel base temperature ($T_{w,tci}$) measured at four locations along the minichannel flow direction for SRM heat sink test section. The experimental temperature data are obtained using thermocouples inserted inside the MCHS model as shown in Fig. 4.7 and Fig. 4.22 with different Reynolds number for two input power of 50 W and 100 W.

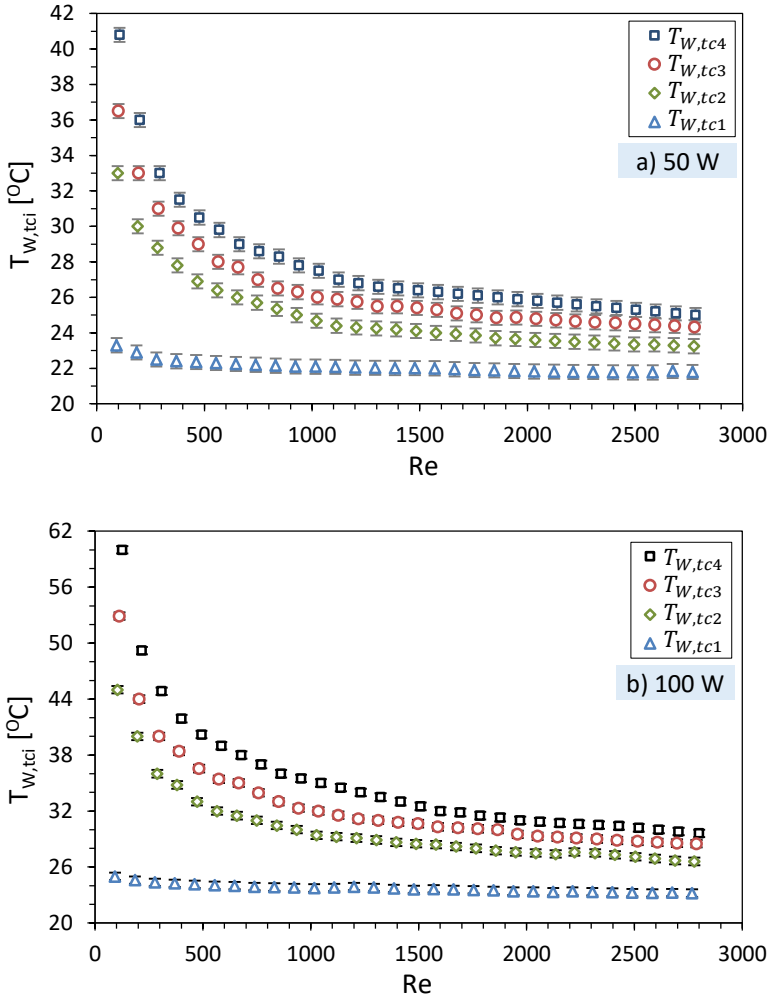

Fig. 5.9: Thermocouple temperature readings at different locations inside MCHS versus Reynolds number for input power of a) 50 W and b) 100 W.

It can clearly be seen from the two figures that as the Reynolds number increase the $T_{w,tci}$ decreases. Additionally, it can be also shown that at the same Reynolds number, $T_{w,tci}$ increases along the minichannel flow direction. This finding is similar to that of Qu and Mudawar (2002a), whose wall temperature gradient at a low Reynolds number was larger

than at a high Reynolds number. Also, it can be seen from the figures that for the same Reynolds number the $T_{w,tci}$ is higher for 100 W than 50 W.

5.3.2 Heat Transfer Coefficient (h) and the Nusselt Number (Nu)

The average heat transfer coefficient (h_{avg}) can be determined experimentally using Newton's law of cooling, see Eq. (4.28). The T_f in Eq. (4.28) represents the mean bulk temperature of the water, it was determined by taking the average of the inlet and outlet bulk temperature of the water. Whereas the T_w in Eq. (4.28) denotes the minichannel base temperature, which is an average of the minichannel base temperatures ($T_{w,tci}$, see Eq. (4.35)) measured experimentally by inserting thermocouple inside the MCHS wall that located at a distance y = 1.75 mm under the minichannel base. T_w can be calculated by using Eq. (4.33).

Fig. 5.10 illustrates the experimental local heat transfer coefficient (h_{tci}) and the experimental average heat transfer coefficient (h_{avg}) as a function of Reynolds number in the SRM heat sink test section. The local heat transfer coefficients are calculated at each measured temperature using thermocouple inserted inside the heat sink model for input power of 100 W, for both laminar and turbulent flow regimes. Each value of h_{tci} has been calculated at the local Reynolds number (Re_{tci}) that is evaluated based on the local fluid bulk temperature ($T_{f,x}$), see Eq. (4.37). The values of h_{avg} are determined at average Reynolds number that is calculated at the average of the water inlet and outlet temperature.

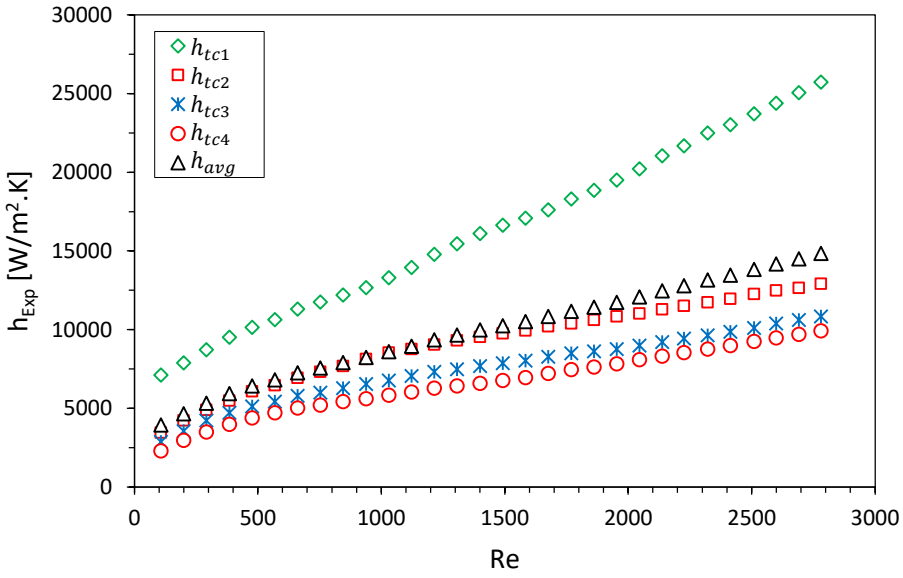

Fig. 5.10: The experimental local and average heat transfer coefficient at different locations versus Reynolds number for input power of 100 W.

For the laminar flow regime, it is noticeable from Fig. 5.10 that the experimental heat transfer coefficient increases monotonically with increasing Reynolds number at each thermocouple streamwise location. In addition, it can be noted that the higher value of the heat transfer

coefficient was found to be in the minichannel entrance region which is calculated at $T_{w,tc1}$, and this is attributed to the effects of entrance developing flow and also due to the very thin thermal boundary layers thickness in the developing region especially at high Reynolds numbers. Additionally, from the experimental results obtained, it was seen that the locations of the first and second thermocouples ($T_{w,tc1}$ and $T_{w,tc2}$) at in the entrance region of the minichannel have smaller temperature differences between the minichannel base and the fluid; accordingly, higher heat transfer coefficients can be obtained.

For the turbulent flow regime, it is evident from Fig. 5.10 that the experimental heat transfer coefficients are generally higher in turbulent region than those obtained in laminar region. This is due to small temperature difference between the fluid and minichannel base.

The length of the thermally developing entrance region was estimated using the equation proposed by Shah and London (1978), and can be calculated by using Eq. (3.10). Table 5.1 demonstrates the values of the thermal entrance length at different range of Reynolds number for the SRM heat sink test section at an input power of 100 W. From the data given in Table 5.1, it is noticeable that the thermally developing entrance length (L_{th}) exceeds the total minichannel length at every Reynolds number chosen, which indicates that the entire flow inside the minichannel is thermally developing.

Table 5.1: Calculated thermal entrance length for the straight rectangular MCHS test section at different Reynolds number and input power of 100 W.

q = 100 W							
Q_{in} [l/min]	Re	Pr	L_{th} [mm]	Q_{in} [l/min]	Re	Pr	L_{th} [mm]
0.1	108.4642	5.8008	41.9	1.1	1031.2	6.833	469.8
0.2	200.5414	6.3367	84.7	1.2	1123.3	6.8442	512.5
0.3	292.7522	6.5328	127.5	1.3	1215.8	6.8513	555.3
0.4	385.02	6.6339	170.3	1.4	1308.1	6.8584	598.1
0.5	477.29	6.696	213.1	1.5	1400.2	6.8656	640.9
0.6	569.6	6.7375	255.8	1.6	1492.859	6.8692	683.6
0.7	661.9365	6.7671	298.6	1.7	1585.174	6.8740	726.4
0.8	754.2297	6.7899	341.4	1.8	1677.393	6.8787	769.2
0.9	846.5251	6.8077	384.2	1.9	1769.840	6.8820	812.0
1.0	938.84	6.8218	427	2.0	1862.148	6.8854	854.7

Fig. 5.11 shows the measured averaged heat transfer coefficient versus the non-dimensional thermal length (x^*) at input power of 100 W for the SRM heat sink test section. As can be seen from Fig. 5.11, the convective heat transfer coefficient is not constant but decreases with increasing x^*, this issue is probably belonging to that the fluid flow is completely within the thermally developing region for most channel length.

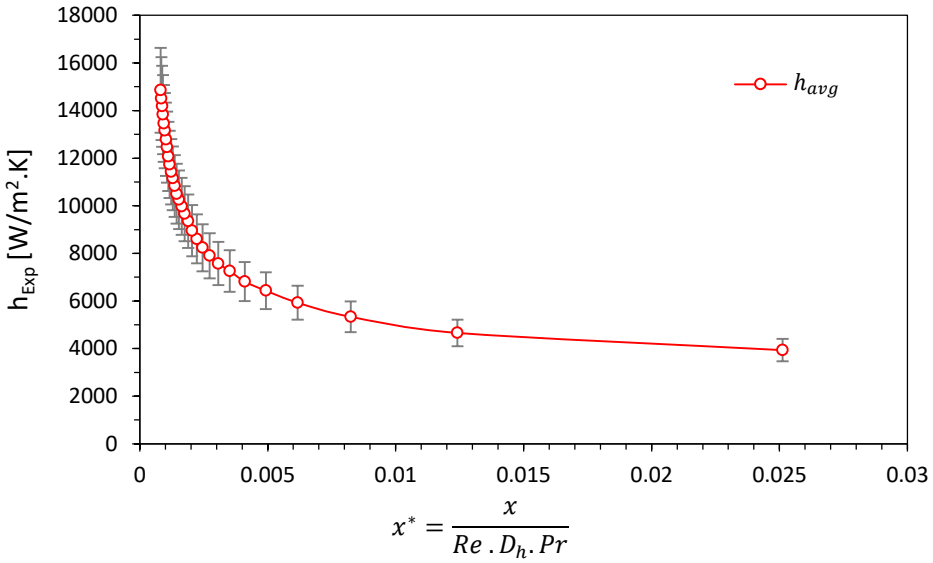

Fig. 5.11: The local average heat transfer coefficient versus the non-dimensional thermal length for input power of 100 W.

After obtaining the average heat transfer coefficient (h_{avg}), the corresponding average Nusselt number (Nu_{avg}) can be calculated using Eq. (3.40), where the experimental values of h_{avg} are determined at $T_{f,avg}$ and $T_{w,avg}$ over a wide range of Q_{in} from 0.1 to 3.0 l/min. In this study, the experimental average Nusselt number data obtained from the SRM heat sink test section was compared with a number of conventional correlation equations for both laminar and turbulent flow regimes as shown in Fig. 5.12.

The experimental Nu_{avg} data in the simultaneously developing laminar flow region (Hydrodynamically and thermally developing flow) are compared with correlation equations proposed by Shah and London (1978) for fully developed flow and Lee and Garimella (2006) for thermally developing flow; the two available correlation equations are used for the straight rectangular cross-section channels, and they are applicable to cases of uniform heat flux with circumferentially constant temperature and axially constant heat flux on the walls (Kandlikar et al., 2014), see Eqs (3.42) and (3.49). The correlation equation of Lee and Garimella (2006) is used with aspect ratios ranging between 1 and 10, and is valid when the dimensionless axial distance (x^*) is less than the length of the dimensionless thermally developing region (x^*_{th}), see Eq. (3.50). Otherwise the flow is considered to be fully developed and Eq. (3.42) from Shah and London (1978) will be used instead. The theoretical correlation used from Lee and Garimella (2006) is used to calculate the local Nu_{avg} for four-sided heating wall minichannels, by using the correction factor proposed by Phillips (1988 and 1990) the local Nu_{avg} for three-sided heating can be estimated, see Eq. (3.43).

The values of the experimental Nu_{avg} for SRM heat sink test section are plotted against the Reynolds number for input power of 100 W as shown in Fig. 5.12. From this, it can clearly be seen that experimental Nu_{avg} values obtained significantly increased with increase of Re and this is because the thermal boundary layer thickness decreases with increased fluid velocity (Fan et al., 2013). Another reason contributing to the increase in the values of Nu_{avg} is that the flow inside the minichannel is thermally developing for most volumetric flow rate, see Table 5.1.

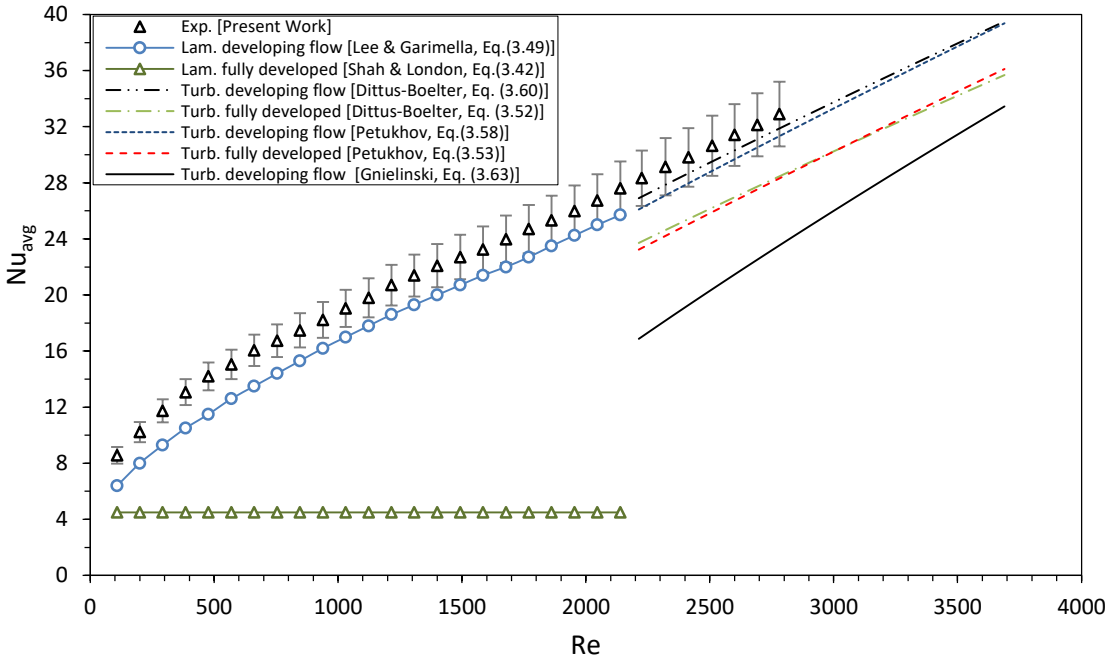

Fig. 5.12: The average Nusselt number versus Re for input power of 100 W.

It is clear from the Fig. 5.12 that there is good agreement between the experimental Nu_{avg} data obtained and the equation of Lee and Garimella (2006) in the laminar flow regime for three-sided wall heating, with MAE of 6.8%. These small differences in the Nu_{avg} values may be due to the fact that the flows in the present study feature both hydrodynamically- and thermally-developing flow, whereas Lee and Garimella's equation is for flow which is hydrodynamically fully developed but thermally developing.

For the turbulent flow regime, the experimental Nu_{avg} values for the SRM heat sink were compared with the experimental correlations proposed by Dittus-Boelter (1930); Petukhov (1970); and Gnielinski (1976) that used for fully developed and thermally developing region in circular cross-section conduits; see Eqs. (3.52), (3.53), (3.58), (3.60) and (3.63). The range of the Reynolds number was 108.5 – 2781, due to the limited range of the Rotameter used experimentally.

It is clear from Fig. 5.12 that the experimental Nu_{avg} results obtained are generally higher than predictions from correlation equations of Dittus-Boelter (1930) and Petukhov (1970), with MAE of 15% for both correlations. This mismatched trend possibly because of both correlation equations are proposed for the case of fully developed turbulent flow and smooth surface (The roughness parameter (ε) = 0), while results obtained in the present experimental study were for developing flow. However, even the Gnielinski (1978) correlation equation proposed for developing turbulent flow, see Eq. (3.63), does not provide satisfactory prediction with experimental data obtained, and this may be due to the inlet condition which is assumed as hydrodynamically fully developed but thermally developing and smooth surface.

A correlation equation proposed by Al-Arab (1982) was applied in this study on the Petukhov and Dittus–Boelter correlation equations to include the effects of the thermal entrance region. Furthermore, an empirical equation suggested by Norris (1971) was used on the Dittus–Boelter correlation equation to take into account the influence of the surface roughness, see Eqs. (3.58) and (3.60). As can be seen from the Fig. 5.12 that corrected Dittus–Boelter and Petukhov correlation equations gave good agreement with the measured Nu_{avg} data much better than their uncorrected counterparts, with MAE of 5.2%.

Fig. 5.13 compares the values of Nu_{avg} obtained experimentally versus different volumetric flow rate ($0.1 \leq Q_{in} \leq 1.0\ l/min$), for the four MCHS test sections with an input heating power of 100 W. As can be seen from the figure, the values of Nu_{avg} determined for all MCHS models increase monotonically with Q_{in}.

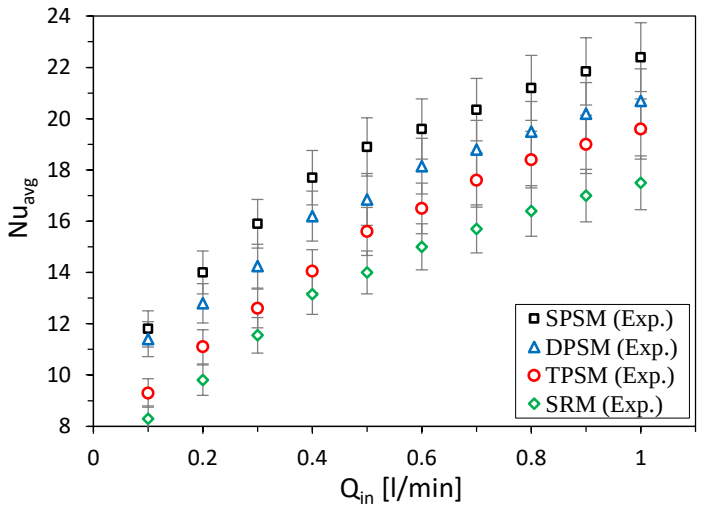

Fig. 5.13: The average Nusselt number versus Q_{in} for four MCHS models at input power of 100 W.

Although all the serpentine MCHS specimens have approximately the same effective heat transfer area (A_{eff}), which are respectively 2142.93 mm^2, 2123.73 mm^2 and 2064.16 mm^2

for SPSM, DPSM and TPSM designs, it is noted that the Nu_{avg} values for SPSM heat sink, for the same Q_{in}, are the largest, followed by those for the DPSM and TPSM heat sinks with those from the SRM the lowest. For example, at a volumetric flow rate is 0.5 l/min, Nu_{avg} for the SPSM is 18.9, which is 35.0%, 21.2% and 12.2% higher than the values for the SRM, TPSM and DPSM respectively. One possible reason for this is that the SPSM and DPSM designs experiences a greater number of bends which disrupt the thermal boundary layer more effectively, reducing the wall temperature and leading to higher heat transfer. Note that, as seen above, the improved heat transfer for the SPSM and DPSM designs comes at the price of a significantly larger pressure drop compared to the other MCHS designs.

5.4 Thermal Resistance

Total thermal resistance (R_{th}) is used to evaluate the performance of MCHS. Where the maximum surface temperature (T_{max}) was measured by using four thermocouples inserted in the copper block (see Fig. 4.7) and the highest temperature reading from those thermocouples was taken, while the inlet water temperature ($T_{f,in}$) was measured by inserting thermocouple into inlet manifold. Fig. 5.14 shows experimental measurements of R_{th} for the four different MCHS designs as a function of volumetric flow rate ($0.1 \leq Q_{in} \leq 1.0\ l/min$) for an input heating power of 100 W and an inlet water temperature of 20 °C.

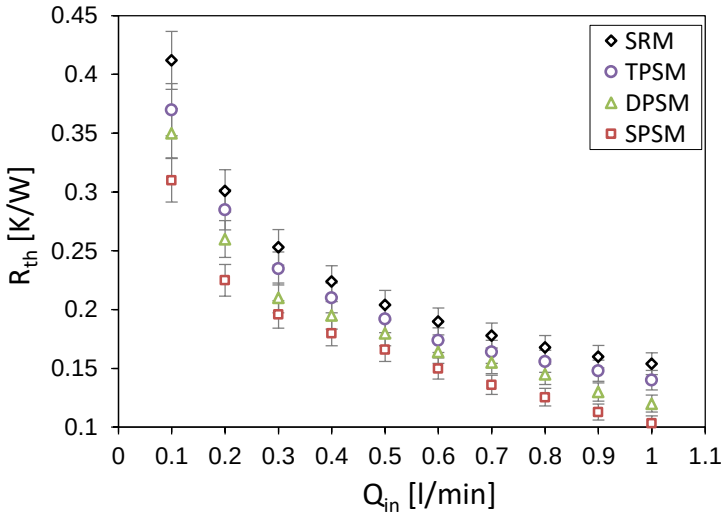

Fig. 5.14: Thermal resistance versus volumetric flow rate at 100 W input power.

The figure shows that the R_{th}values decrease for higher flow rates and those for the SPSM design are the smallest followed by the DPSM, TPSM and the conventional SRM. For example, at a $Q_{in} = 1.0\ l/min$, R_{th} for the SPSM is 0.1 K/W, which is 32.8%, 26.2% and 13.7% lower than the values for the SRM, TPSM and DPSM respectively.

5.5 Performance Evaluation Analysis

As indicated by the above experimental results for fluid flow and heat transfer, the SPSM heat sink designs can enhance heat transfer at the expense of a higher pressure drop. Thus, the benefits and disadvantages of the new serpentine MCHSs are assessed using a performance evaluation criterion (PEC) index based on the same pumping power consumption, as defined in (Rosaguti et al., 2006 and Manca et al., 2012):

$$PEC = \frac{E_{Nu_{avg}}}{\left(E_f\right)^{1/3}} = \frac{\frac{Nu_{avg}}{Nu_{avg,SRM}}}{\left(\frac{f}{f_{,SRM}}\right)^{1/3}} \tag{5.2}$$

where $E_{Nu_{avg}}$ and E_f are respectively the heat transfer enhancement and friction factor parameters, which are defined as the average Nusselt number (Nu_{avg}) and friction factor (f) of the present enhanced MCHSs (SPSM, DPSM and TPSM) divided by those of SRM heat sinks, respectively. To calculate the f values for the three different serpentine MCHS configurations, Eqs. (4.20, 4.22 and 4.23) were used to determine the apparent friction factor (f_{app}) since the total pressure drop and the minor pressure losses are known, while Eq. (4.17) was used to estimate the f_{app} for the SRM heat sink. The PEC values of all the MCHS designs are plotted as functions of volumetric water flow rate (Q_{in}) as shown in Fig. 5.15. It is observed that the PEC of the SPSM heat sink is the smallest. This implies that the SPSM requires higher pumping power to achieve a higher heat transfer coefficient, while the PEC of the TPSM heat sink is the highest which implies that the higher thermal performance is achievable with less pumping power.

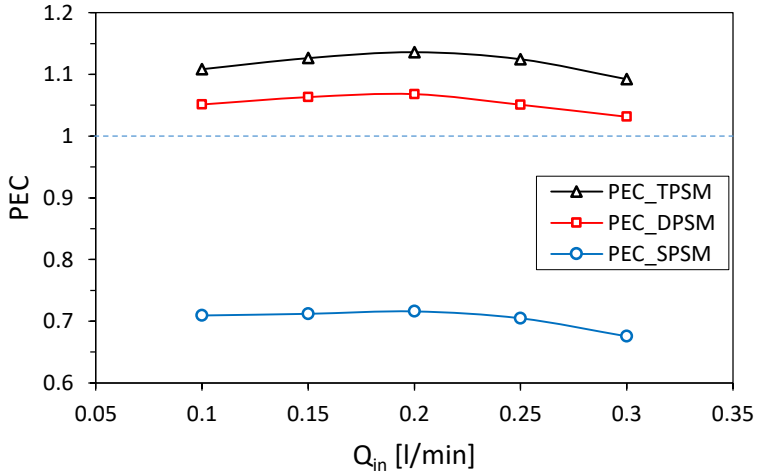

Fig. 5.15: Performance evaluation criterion obtained from experiments for three serpentine MCHS designs versus Q_{in} at input power of 100 W.

In addition, it can be seen that the values of PEC decreased when $Q_{in} > 0.2\ l/min$ for all MCHS test sections, and this due to the high pressure drop penalty which outweighs the heat

transfer enhancement ($E_{Nu_{avg}}$) especially in the SPSM heat sink. It should be noted that the PEC values for both DPSM and TPSM designs are larger than 1 compared with the SPSM which is around 0.71, and this belong to the high pressure drop penalty for the SPSM design although the increase in the $E_{Nu_{avg}}$.

5.6 Repeatability of Measurements

Repeatability is the variation in measurements taken by an instrument on the same device under the same conditions over a short period of time. Repeatability is important because it directly affects the agreement between methods. It has been well-known that the surfaces of channels made of copper material easily suffer fouling or deformation due to the thermal stress, which in turn maybe effects on the fluid flow and the heat transfer characteristics.

In the present study, the experiments were repeated after two months from the first experiments. Fig. 5.16 presents the repeatability measurements of total pressure drop (ΔP_t) and average Nusselt number (Nu_{avg}) of a SPSM heat sink design versus different volumetric flow rate ($0.1 \leq Q_{in} \leq 1.0\ l/min$) at input heating power of 100 W. It is worth mentioning that the repeatability of the experimental results is reasonably good since the deviations are less than 5% for the average Nusselt number and 8.5% for the total pressure drop.

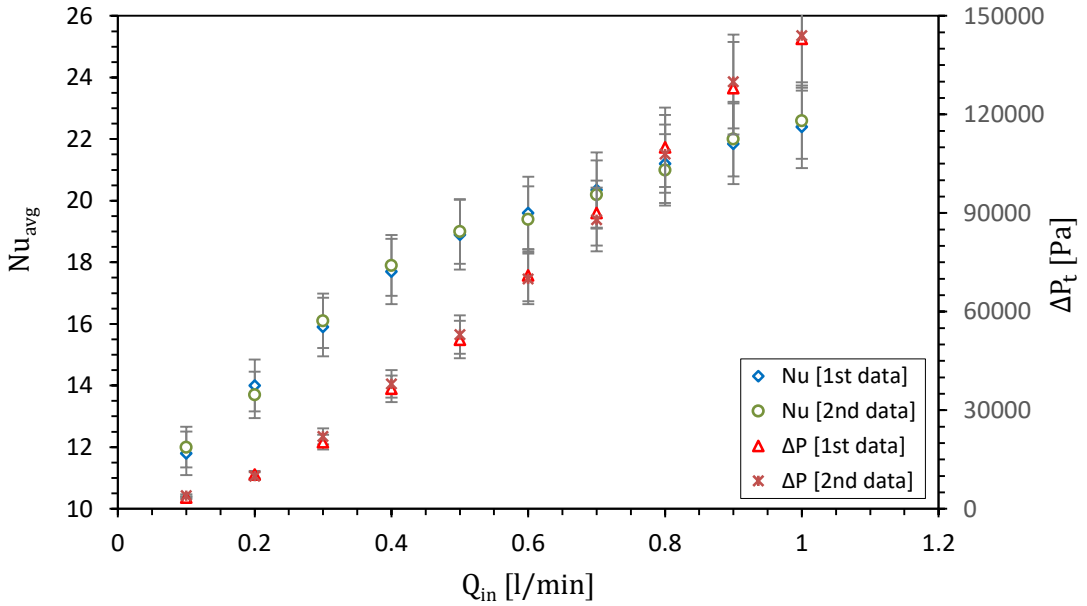

Fig. 5.16: Repeatability of Nu_{avg} and ΔP_t measurements at different volumetric flow rate and total input power of 100 W.

5.7 Summary

In the present study, four categories of minichannel heat sink (MCHS) test sections have been designed and fabricated using copper material as a heat sink, each one of these MCHS specimens have the same surface area of 45 × 41 mm^2 and the same base plate thickness of 3.5 mm. Furthermore, it also has the same minichannel number which is 12 parallel rectangular minichannels. Experiments for pressure drop and heat transfer characteristics have been conducted for the single-phase laminar and turbulent flow of water as a coolant through small hydraulic diameters, over a wide range of Reynolds numbers. The experimental results obtained are evaluated in terms of pressure drop, friction factor, Nusselt number and thermal resistance. One of these minichannel heat sinks is a multi-straight rectangular minichannel (SRM) heat sink and others are a multi-serpentine rectangular MCHS. Three different categories of a serpentine minichannel heat sinks are suggested as an option to address the problem of thermal management, which are single (SPSM), double (DPSM) and triple path multi-serpentine rectangular minichannel (TPSM) heat sink.

Three input power of 50 W, 75 W and 100 W were used in the experimental work as a heat supply to the MCHS models to dissipate it. It is found that the effect of the input power variation is significant on the water pressure drop as shown in Fig. 5.1 for SRM test section. Good agreement was found between the experimental friction factors data and correlation equation proposed by Shah (1978) for developing laminar flow, with MAE of less than 7.5%. For turbulent flow, an acceptable agreement was achieved with correlation suggested by Phillips (1987) for developing flow with MAE of 10%. From the experimental data obtained, it is noticeable that the SPSM test section has a much larger pressure drop penalty compared with other MCHS models.

The results obtained experimentally have shown that the Nu_{avg} for all MCHS models increase with Reynolds number because the thermal boundary layer thickness decreases with increased fluid velocity. Comparisons with existing correlations for Nu_{avg} for SRM heat sink show that the present experimental results agree well with the correlation of Lee and Garimella (2006) in the laminar flow regime, with MAE of 7%, and with that of Dittus-Boelter (1939) and Petukhov (1970) corrected in the turbulent flow regime, with MAE of around 5.2%. In the present experimental work, it is found that the whole rectangular minichannel was simultaneously developing, that means that fully developed flow will not occur at any distance in the minichannel. As a result of this, it is observed that the experimental Nu_{avg} decreases along the minichannel due to formation and developed of thermal boundary layer, and it is extremely high in the entrance region because the thermal boundary layer is very thin.

The experimental total thermal resistances (R_{th}) data are decreased with higher flow rates, and it is found that the SPSM design are the smallest followed by the DPSM, TPSM and the SRM heat sink.

Chapter 6: Numerical Methods

6.1 Introduction

This chapter provides a description of the numerical simulation method adopted for the four minichannel heat sink (MCHS) models used experimentally and is divided into four main sections. In sections 6.2 and 6.3, the finite element method and grid generation are described. In sections 6.4, 6.5 and 6.6, the governing equations, assumptions and boundary conditions, grid independence study, discretisation schemes and validation with previous studies are explained. In sections 6.7 and 6.8, numerical predictions of the pressure drop, Nusselt number, maximum surface temperature of the MCHSs, and thermal resistance are discussed and compared with experimental data. In section 6.9, the optimisation strategy of the SPSM design will be presented. The chapter is summarised in section 6.10.

6.2 Computational Fluid Dynamics (CFD) Methodology

CFD is an increasingly popular method employed for analysing complex systems involving fluid flow, heat transfer and mass transport problems by means of computer-based simulation. For example, in the electronics industry CFD is utilised to optimize energy systems and heat transfer for the cooling of electronic devices. CFD creates discretised forms of partial differential equations (PDEs) for fluid flow and heat transfer to find approximate solutions of the governing equations at a predetermined number of points that are specified by a grid of elements formed within a geometric boundary (Versteeg and Malalasekera, 2007; and Nithiarasu et al., 2016).

Depending on the discretisation method chosen, the governing equations are expressed in either integral or differential form (Oh, 2012). The three main discretisation methods are the finite-difference method (FDM), the finite-volume method (FVM) and the finite-element method (FEM). In all three methods, the continuous problem that is represented by PDEs is converted into a discrete algebraic problem, allowing the governing equations to be solved numerically (Nithiarasu et al., 2016). The FVM and FEM are integral schemes, while the FDM is a differential scheme, based on a Taylor series expansion. The FDM is the oldest technique used among the three methods and may bring in some approximation error (Patankar, 1980) particularly in complex geometries.

The present problem is solved by using a CFD model based on the finite-element method, using the COMSOL Multiphysics software package v.5.2 which is well-suited to multiphysics problems. COMSOL uses the Galerkin method to convert PDEs into FEM integral scheme (COMSOL, 2015). The FEM is a numerical technique, which uses an integral form of the governing equations as its starting point (Minkowycz et al., 2006). In the FEM

algebraic forms of the governing equations are discretized over the entire domain. The smallest sub-geometry is called the element which consists of a number of nodes (see Fig. 6.1). Through this element, various properties continuously change by interaction between any two adjacent elements (Zienkiewicz et al., 2013).

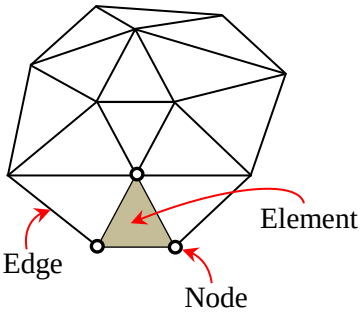

Fig. 6.1: Typical finite element mesh.

The CFD codes used in carrying out numerical modelling of fluid flow and heat transfer problems consist of three stages (Versteeg and Malalasekera, 2007). The process is described below and also shown schematically in Fig. 6.2.

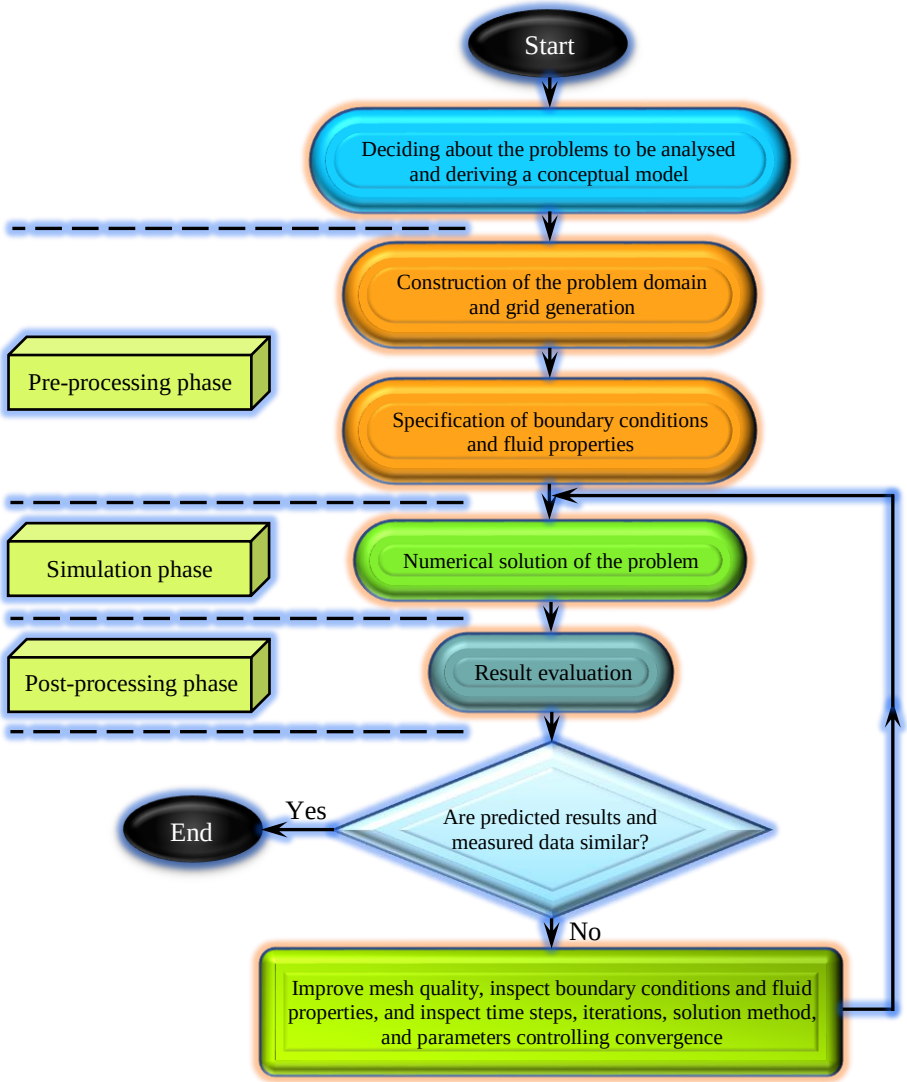

Fig. 6.2: Main stages in a CFD simulation.

1. Pre-processing: This step involves defining the geometry, that is, the computational domain, the subdivision of this domain into sub-domains, which is called the grid generation, the selection of the physical and chemical phenomena that need to be modelled, the defining of all fluid properties and specifications of boundary conditions.
2. Solver execution (Processing): The solution of all the equations that govern the flow and heat transfer over the computational domain is carried out during this next stage.
3. Post-processing: Results obtained from numerical simulations are analysed here. This includes presenting the results, graphics, animations, plots, analyses and full reports that are created.

6.3 Pre – processing (Grid generation)

The finite element method (FEM) within COMSOL Multiphysics v.5.2 was used to solve the governing PDE equations for both laminar and turbulent flow regimes. To generate mesh for the computational domain, there are two different 2D element types, namely triangular and quadrilateral elements. For 3D models, there are four different element types available, namely tetrahedral (tets), triangular prisms (prisms), hexahedral (bricks), and pyramids. These four types of elements can be used, in various combinations, to mesh any 3D model. Each mesh element comprises of different boundaries shown in Fig. 6.3.

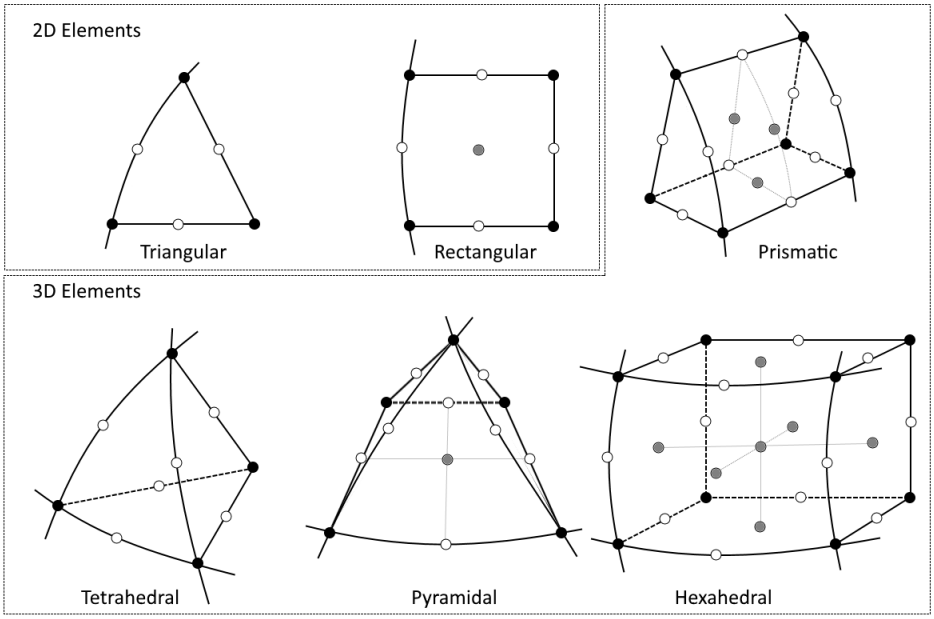

Fig. 6.3: Types of elements. The source (https://www.comsol.fr/multiphysics/finite-element-method)

The pyramids are only used when creating a transition in the mesh between tetrahedral and hexahedral. In a complex geometry it can be more difficult to create a conforming hex mesh leading to worse mesh quality and difficulties to converge the pressure solver. In the present

simulation work the default free tetrahedral mesh feature is applied to the entire model, where the tetrahedral element is chosen for irregular geometry such as curved surfaces or the existence of small objects. To get accurate results, second order (quadratic) tetrahedral mesh was used, which represent the best compromise between growth in memory requirements and accuracy. COMSOL usually uses a second-order Lagrangian element to discretize the geometry and the solution.

6.3.1 Structured and Unstructured Grids

In general, computational mesh generation could be either structured or unstructured or hybrid (combination of structured and unstructured), depending on the geometry shape. A structured mesh is used for generating simple geometries, such as straight rectangular channels or straight pipes, and usually consists of quadrilateral and hexahedral elements. In contrast with unstructured meshes, a triangular and tetrahedral meshes are widely used for computational simulations because of their flexibility for complex geometries (Ito et al., 2008). Structured mesh is less susceptible to numerical diffusion and usually preferred due to the simplicity of computation and doesn't require large computational memory. Unstructured mesh generation, on the other hand, has two important advantages: it can deal with complex geometry and don't require domain decomposition. Fig. 6.4 shows a difference between the structured and unstructured mesh of simple 2D computational domain (curved channel).

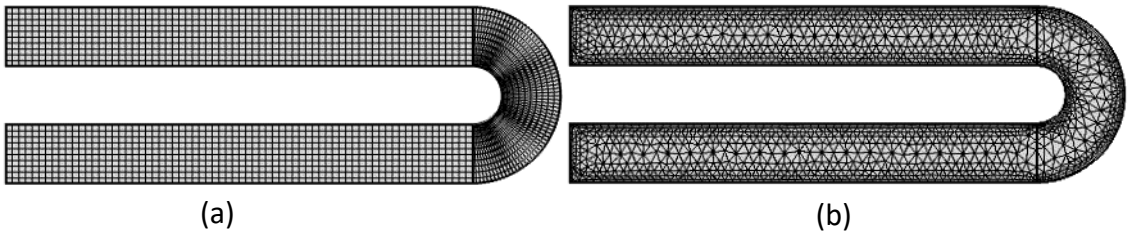

Fig. 6.4: Difference between the 2D (a) structured; and (b) unstructured mesh (Own Figure).

6.3.2 Mesh Quality

The accuracy of the solution is affected by the mesh quality (Q_{mesh}), and COMSOL could be checked the mesh element quality automatically for both laminar and turbulent flow regimes. Due to the complex geometry for all MCHS designs used in the present study, free meshing was used with tetrahedral elements. The curved and small geometry were meshed with extra grid refinement.

For the laminar flow regime, COMSOL calculates Q_{mesh} for the tetrahedral element by:

$$Q_{mesh} = \frac{72\sqrt{3}\,V}{(h_1^2 + h_2^2 + h_3^2 + h_4^2 + h_5^2 + h_6^2)^{1.5}} \tag{6.1}$$

where V represents the volume, while h_1, h_2, h_3, h_4, h_5, and h_6 are the edge lengths of the element (COMSOL, 2015). To avoid the effect of low quality on the solution, mesh quality (Q_{mesh}) should be larger than 0.1.

For the turbulent flow regime, the value of the wall lift-off in viscous units (δ_w^+ or y^+) must be checked, and can be calculated using (Kuzmin et al., 2007):

$$\delta_w^+ = y^+ = \frac{\delta_w \cdot u_\tau}{\nu} \tag{6.2}$$

The wall lift-off (δ_w) is the distance at which the computational domain is located if wall functions are applied, as shown in Fig. 6.5. The symbol ν represents the fluid kinematic viscosity ($= \frac{\mu}{\rho}$), and u_τ is the friction velocity and it can be defined as:

$$u_\tau = C_\mu^{\frac{1}{4}} \cdot \sqrt{k} \tag{6.3}$$

where k denotes the Von Karman constant and it is equal to 0.418 for wall lift-off, while C_μ is an empirical constant which is equal to 0.09 (Kuzmin et al., 2007).

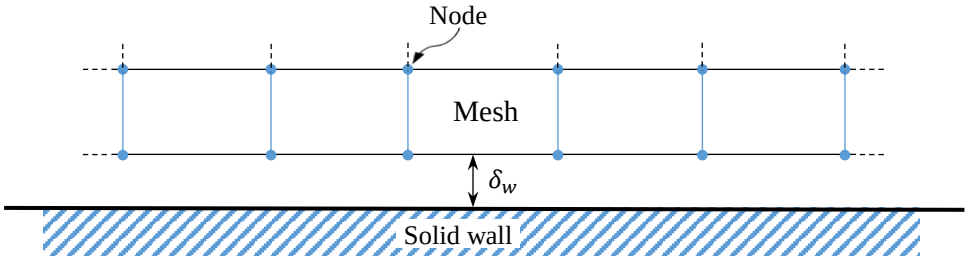

Fig. 6.5: Distance δ_w from wall to computational domain.

The value of δ_w^+ has significant effect on the accuracy of the solution, and COMSOL computes it automatically. For the greatest accuracy, the value of δ_w^+ should be equal to 11.06 (Kuzmin et al., 2007), this is the value used in grids 3 and 4 in the present work. Figs. 6.6 and 6.7 demonstrates the mesh quality for the TPSM and SRM heat sink designs for both laminar and turbulent flow regimes, and as can be seen the δ_w^+ values in two MCHS cases for turbulent flow are within the recommended range ($11.06 \leq \delta_w^+ \leq 300$).

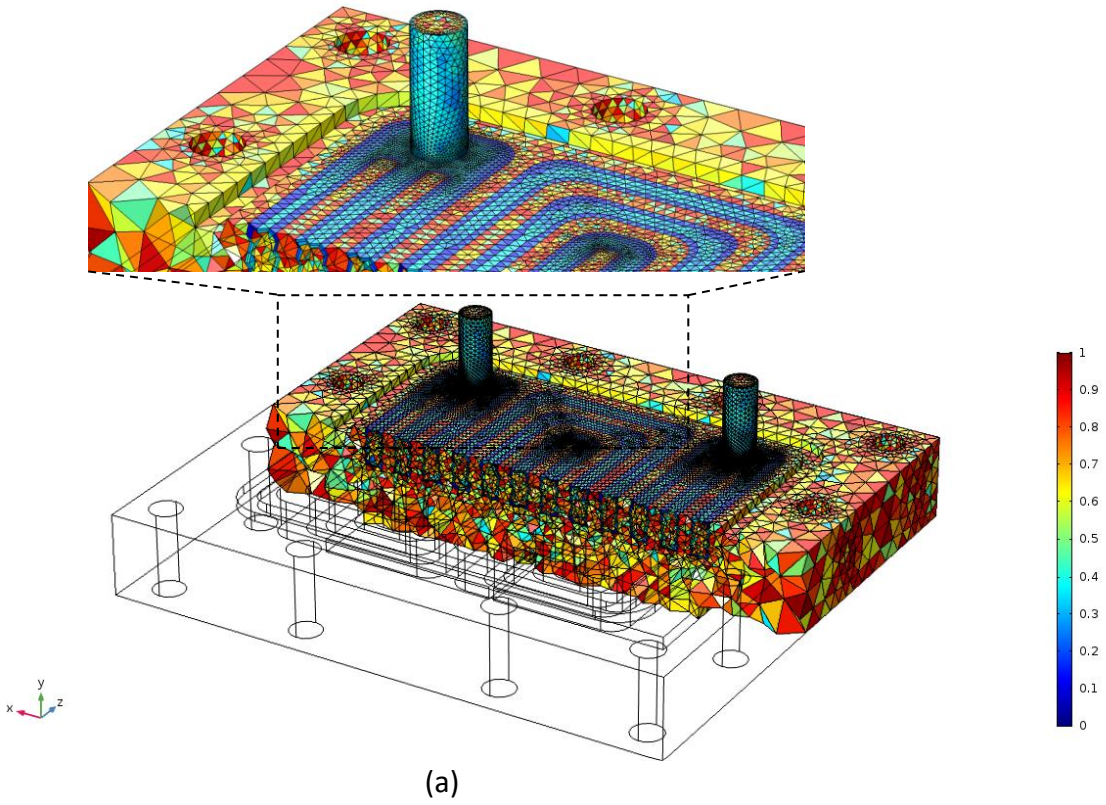

(a)

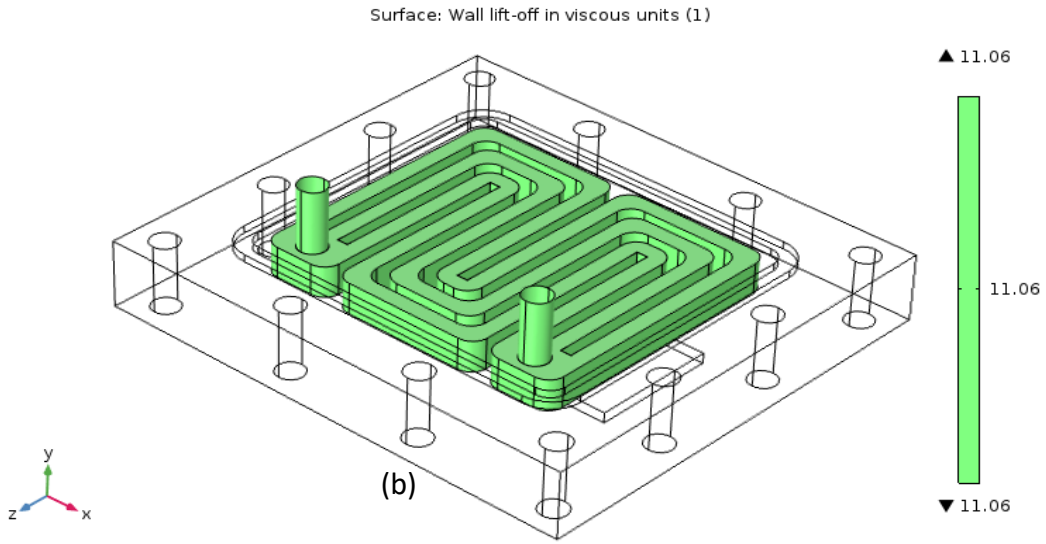

(b)

Fig. 6.6: Mesh quality for the TPSM heat sink: a) Laminar flow; b) Turbulent flow.

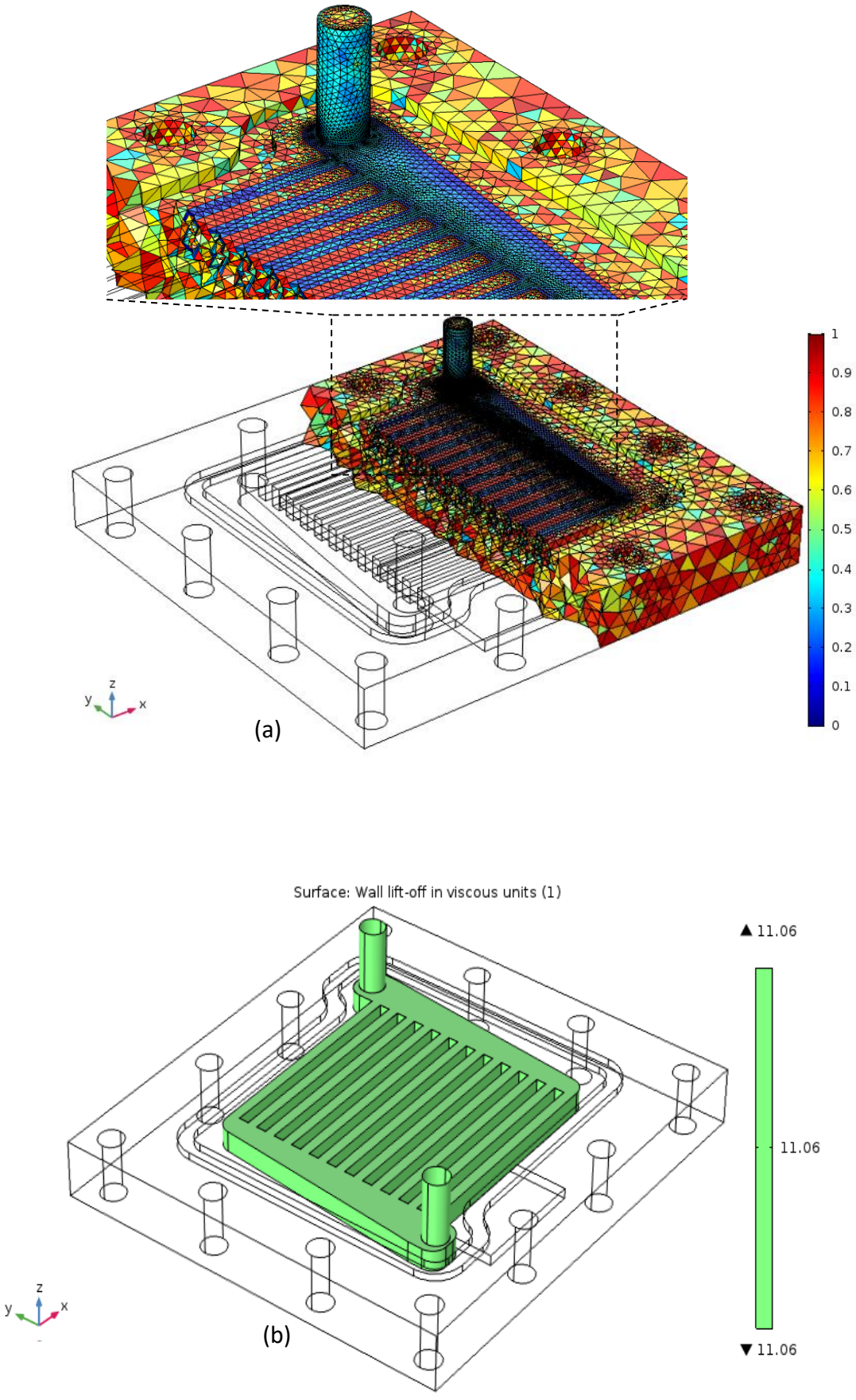

Fig. 6.7: Mesh quality for the SRM heat sink: a) Laminar flow; b) Turbulent flow.

6.4 Processing (Computational Model)

A numerical model of the three-dimensional flow and heat transfer in the minichannel heat sink (MCHS) was developed under assumptions that will be explained in section 6.5. Flow is modelled using the following continuity and Navier-Stokes momentum equations for both laminar and turbulent flow regimes:

6.4.1 Navier – Stokes Equations

The flow and heat transfer in MCHS are governed by the Navier-Stokes equations for the conservation of mass (continuity), momentum and energy for liquid and solid media, as explained below.

6.4.1.1 The Continuity Equation

In a three-dimensional flow, the continuity equation is given by:

$$\frac{\partial \rho}{\partial t} + \frac{\partial}{\partial x}(\rho u) + \frac{\partial}{\partial y}(\rho v) + \frac{\partial}{\partial z}(\rho w) = 0 \tag{6.4}$$

This may be written more compactly in the vector form:

$$\frac{\partial \rho}{\partial t} + \nabla \cdot (\rho \mathbf{u}) = 0 \tag{6.5}$$

where ρ is the fluid density (kg/m^3), del (or nabla), ∇, denotes the vector gradient operator and $\mathbf{u}$ is the fluid velocity vector, and is defined as follows:

$$\nabla = \frac{\partial}{\partial x} i + \frac{\partial}{\partial y} j + \frac{\partial}{\partial z} k \qquad , \qquad \mathbf{u} = ui + vj + wk$$

where u, v and w are respectively the velocity components of flow in the x-, y- and z-directions. The continuity equation above applies to the general case of unsteady, compressible and three-dimensional flow. When the fluid flow is incompressible, ρ = constant, then $\frac{\partial \rho}{\partial t} \approx 0$ regardless of whether the flow is steady or unsteady state condition (White, 2011), Eq. (6.5) can then be reduced to express in a vector form as:

$$\nabla \cdot \mathbf{u} = 0 \tag{6.6}$$

6.4.1.2 The Momentum Equation

The momentum equation for single-phase laminar flow can be written in general form as:

$$\frac{\partial (\rho \mathbf{u})}{\partial t} + \nabla \cdot (\rho \mathbf{u}\mathbf{u}) = -\nabla p + \nabla \cdot \tau_{ij} + \mathbf{F_b} \tag{6.7}$$

The term $\mathbf{F_b}$ is the body force vector per unit volume (N/m^3) due to gravitational forces, while p is the fluid pressure (Pa). The symbol τ_{ij} denotes the viscous stress tensor (Pa) and can be written as a matrix:

$$\tau_{ij} = \begin{bmatrix} \tau_{xx} & \tau_{xy} & \tau_{xz} \\ \tau_{yx} & \tau_{yy} & \tau_{yz} \\ \tau_{zx} & \tau_{zy} & \tau_{zz} \end{bmatrix} \tag{6.8}$$

For a compressible Newtonian fluid, Eq. (6.7) can be written in another form as:

$$\rho\frac{\partial \mathbf{u}}{\partial t} + \rho\mathbf{u}\cdot\nabla\mathbf{u} = -\nabla p + \nabla\cdot\underbrace{\left[\mu(\nabla\mathbf{u} + (\nabla\mathbf{u})^T) - \frac{2}{3}\mu(\nabla\cdot\mathbf{u})\mathbf{I}\right]}_{\tau} + \rho\mathbf{g} \tag{6.9}$$

where μ is the molecular viscosity coefficient, and $\mathbf{I}$ denotes the unit diagonal matrix (unit tensor). $\mathbf{g}$ is the gravity vector (m^2/s) $\left(\mathbf{g} = g_x i + g_y j + g_z k\right)$. The strain-rate tensor, $\dot{\gamma}$, can be defined as:

$$\dot{\gamma} = \nabla\mathbf{u} + (\nabla\mathbf{u})^T \tag{6.10}$$

Multiplying $\dot{\gamma}$ by μ, yields the viscous stress tensor, $\tau = \mu\left(\dot{\gamma} - \frac{2}{3}(\nabla\cdot\mathbf{u})\mathbf{I}\right)$. For incompressible flows, the divergence of the velocity vector is zero, i.e., $\nabla\cdot\mathbf{u} = 0$, and Eq. (6.9) reduces to:

$$\rho\frac{\partial \mathbf{u}}{\partial t} + \rho\mathbf{u}\cdot\nabla\mathbf{u} = -\nabla p + \nabla\cdot[\mu(\nabla\mathbf{u} + (\nabla\mathbf{u})^T)] + \rho\mathbf{g} \tag{6.11}$$

When viscosity is constant ($\mu = \text{constant}$), Eq. (6.11) can be further simplified and can be expressed in component form as:

<u>x- direction:</u>

$$\rho\frac{\partial u}{\partial t} + \rho\left(u\frac{\partial u}{\partial x} + v\frac{\partial u}{\partial y} + w\frac{\partial u}{\partial z}\right) = -\frac{\partial p}{\partial x} + \mu\left(\frac{\partial^2 u}{\partial x^2} + \frac{\partial^2 u}{\partial y^2} + \frac{\partial^2 u}{\partial z^2}\right) + \rho g_x \tag{6.12a}$$

<u>y- direction:</u>

$$\rho\frac{\partial v}{\partial t} + \rho\left(u\frac{\partial v}{\partial x} + v\frac{\partial v}{\partial y} + w\frac{\partial v}{\partial z}\right) = -\frac{\partial p}{\partial y} + \mu\left(\frac{\partial^2 v}{\partial x^2} + \frac{\partial^2 v}{\partial y^2} + \frac{\partial^2 v}{\partial z^2}\right) + \rho g_y \tag{6.12b}$$

<u>z- direction:</u>

$$\rho\frac{\partial w}{\partial t} + \rho\left(u\frac{\partial w}{\partial x} + v\frac{\partial w}{\partial y} + w\frac{\partial w}{\partial z}\right) = -\frac{\partial p}{\partial z} + \mu\left(\frac{\partial^2 w}{\partial x^2} + \frac{\partial^2 w}{\partial y^2} + \frac{\partial^2 w}{\partial z^2}\right) + \rho g_z \tag{6.12c}$$

Equations (6.12a-c) are the momentum equations for an unsteady, incompressible flow and in a three-dimensional Cartesian coordinate. These can be expressed in vector form as:

$$\rho\frac{\partial \mathbf{u}}{\partial t} + \rho(\mathbf{u}\cdot\nabla)\mathbf{u} = -\nabla P + \mu(\nabla^2\mathbf{u}) + \rho\mathbf{g} \tag{6.13}$$

When the fluid flow is steady, $\frac{\partial \mathbf{u}}{\partial t} = 0$.

For single-phase turbulent flow, the standard k-ω turbulence model has been used to solve the governing equations, as this model has captured the physics well for other similar heat transfer studies (Dhinsa et al., 2005 and Sharma et al., 2013). For a compressible Newtonian fluid, the momentum equation for turbulent flow is:

$$\rho\frac{\partial \mathbf{u}}{\partial t} + \rho(\mathbf{u}\cdot\nabla)\mathbf{u} = \nabla\cdot\left[-p\mathbf{I} + (\mu+\mu_T)(\nabla\mathbf{u} + (\nabla\mathbf{u})^T) - \frac{2}{3}(\mu+\mu_T)(\nabla\cdot\mathbf{u})\mathbf{I} - \frac{2}{3}\rho k\mathbf{I}\right] + \mathbf{F_b} \tag{6.14}$$

Eq. (6.14) is applicable for unsteady and compressible flow. The k-ω turbulence model introduces two additional variables: the turbulent kinetic energy, k (m^2/s^2), and specific dissipation rate, ω $(1/s)$. The transport equations for k and ω are based on those given by Wilcox (2006) as given respectively by:

$$\rho\frac{\partial k}{\partial t} + \rho(\mathbf{u}\cdot\nabla)k = P_k - \beta^*\rho\omega k + \nabla\cdot[(\mu+\mu_T\sigma_k^*)\nabla k] \tag{6.15}$$

$$\rho\frac{\partial w}{\partial t} + \rho(\mathbf{u}\cdot\nabla)\omega = \alpha\frac{\omega}{k}P_k - \rho\beta\omega^2 + \nabla\cdot[(\mu+\mu_T\sigma_\omega)\nabla\omega] \tag{6.16}$$

The production term and the turbulent (eddy) viscosity can be defined by:

$$P_k = \mu_T\left[\nabla\mathbf{u}\colon(\nabla\mathbf{u} + (\nabla\mathbf{u})^T) - \frac{2}{3}(\nabla\cdot\mathbf{u})^2\right] - \frac{2}{3}\rho k\nabla\cdot\mathbf{u} \tag{6.17}$$

$$\mu_T = \rho\frac{k}{\omega} \tag{6.18}$$

The empirical turbulent model constants parameters are (COMSOL, 2015):

$$\alpha = \frac{13}{25},\quad \sigma_\omega = \frac{1}{2},\quad \sigma_k^* = \frac{1}{2},\quad \beta = \frac{9}{125},\quad \beta^* = \frac{9}{100}$$

6.4.1.3 The Energy Equation

The conservation of energy equation for single-phase laminar flow can be written in Cartesian coordinates as follows:

$$\rho C_p\left(\frac{\partial T}{\partial t} + u\frac{\partial T}{\partial x} + v\frac{\partial T}{\partial y} + w\frac{\partial T}{\partial z}\right) = k_f\left(\frac{\partial^2 T}{\partial x^2} + \frac{\partial^2 T}{\partial y^2} + \frac{\partial^2 T}{\partial z^2}\right) + \mu\Phi \tag{6.19}$$

where C_p , k_f and T are respectively the specific heat $[\frac{J}{kg\cdot K}]$, the thermal conductivity $[\frac{W}{m\cdot K}]$ and the absolute temperature $[K]$ of the fluid, whereas Φ is the viscous dissipation function:

$$\Phi = 2\left[\left(\frac{\partial u}{\partial x}\right)^2 + \left(\frac{\partial v}{\partial y}\right)^2 + \left(\frac{\partial w}{\partial z}\right)^2\right] + \left[\left(\frac{\partial u}{\partial y} + \frac{\partial v}{\partial x}\right)^2 + \left(\frac{\partial v}{\partial z} + \frac{\partial w}{\partial y}\right)^2 + \left(\frac{\partial w}{\partial x} + \frac{\partial u}{\partial z}\right)^2\right] - \frac{2}{3}\left(\frac{\partial u}{\partial x} + \frac{\partial v}{\partial y} + \frac{\partial w}{\partial z}\right)^2 = \tau : \nabla \mathbf{u} \quad (6.20)$$

Eq. (6.19) can be written in a vector form as:

$$\rho C_p\left(\frac{\partial T}{\partial t} + \mathbf{u} \cdot \nabla T\right) = \nabla \cdot (k \nabla T) + \mu(\tau : \nabla \mathbf{u}) \quad (6.21)$$

In the solid, heat transfer is by conduction only and satisfies:

$$\frac{\partial}{\partial x}\left(k_s \frac{\partial T}{\partial x}\right) + \frac{\partial}{\partial y}\left(k_s \frac{\partial T}{\partial y}\right) + \frac{\partial}{\partial z}\left(k_s \frac{\partial T}{\partial z}\right) = 0 \quad (6.22)$$

or

$$\nabla \cdot (k_s \nabla T) = 0 \quad (6.23)$$

The energy equation for the liquid can be expressed as:

$$\rho C_p\left(\frac{\partial T}{\partial t} + \mathbf{u} \cdot \nabla T\right) = \nabla \cdot \left((k_f + k_T)\nabla T\right) \quad (6.24)$$

where the symbols k_f and k_s represent the thermal conductivity of the fluid and the thermal conductivity of the solid (heat sink), respectively. k_T is the turbulent thermal conductivity $\left(k_T = \frac{\mu_T \cdot C_{p_f}}{Pr_T}\right)$, and Pr_T is the turbulent Prandtl number (following Kays - Crawford, 1994) (Kays, 1994). Eq. (6.24) is the energy equation for the liquid in three-dimensional and turbulent flow, with $\mu_T = 0$ for laminar flow.

6.4.2 Conjugate Heat Transfer

The heat conduction in the solid and convective heat transfer to the fluid are coupled by the continuities of heat flux and temperature at the interface between the fluid and the solid walls. The variations of temperature within solids and fluids in the MCHS models, due to thermal interaction between the solids and fluids can be expressed in a conjugate heat transfer model. Fig. 6.8 demonstrates the conjugate heat flow between solid and fluid, and in the interface wall the temperature of the solid and fluid have the same value ($T_{s,\Gamma} = T_{f,\Gamma}$). The heat flux in the interface wall can be described by Fourier's law as:

$$-k_s \left.\frac{\partial T_s}{\partial n}\right|_\Gamma = -k_f \left.\frac{\partial T_f}{\partial n}\right|_\Gamma \quad , \quad u = v = w = 0 \quad (6.25)$$

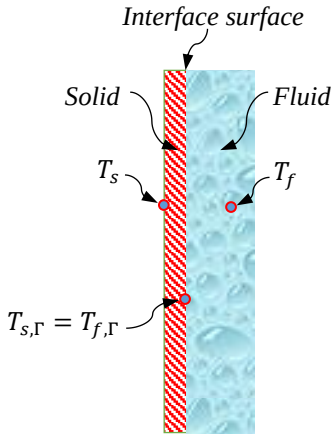

Fig. 6.8: Schematic diagram for conjugate heat transfer between solid and fluid domains.

6.5 Assumptions and Boundary Conditions

6.5.1 Assumptions

To solve the governing equations and simplify the numerical solution, some simplifications have to be made as employed by other studies such as Fedorove and Viskanta (2000); Qu and Mudawar (2002a and 2002b); Xie et al. (2009); Kuppusamy et al. (2014); and Lee et al. (2015) and others. Here the following assumptions are used:

(1) Both fluid flow and heat transfer are three-dimensional and steady;

(2) Fluid is single-phase and heat transfer in the MCHSs is modelled by assuming the flow is incompressible;

(3) All the surfaces of MCHS exposed to the surroundings are assumed to be insulated except the bottom surface of MCHS where a heat flux is applied;

(4) The effect of radiation and natural convection heat transfer are negligible;

(5) Negligible viscous dissipation;

(6) Smooth surface of the channel;

(7) It is well known that the Navier-Stokes equations are dependent dramatically on the continuum hypothesis, which is applicable when the characteristic dimension of the channel, D_h, is much larger than the mean free path of the fluid molecules, λ, and the ratio of λ to D_h, is defined as the Knudsen number, $Kn = \frac{\lambda}{D_h}$. If the $Kn < 10^{-3}$, continuum theory can be applied to treatment of micro/minichannel flows (Federov and Viskanta, 2000; and Kandlikar, 2003). In the present experimental work, the Kn is small enough so that, the fluid is a continuous medium and "No-Slip" velocity boundary conditions $\mathbf{u_s} = 0$ are used at solid wall temperature are defined by $T_s = T_{f\ at\ wall}$.

6.5.2 Boundary Conditions

To simulate the four configurations of the MCHS test sections based on the above assumptions, a whole heat sink has been used as a computational domain and the boundary conditions (BCs) used are:

(1) The boundary condition of inlet flow is volumetric flow rate in (m^3/sec) which is applied at the MCHS entrance and the water inlet temperature (T_o) was fixed at 20 °C (293.15 K). For turbulent flow regime, the standard k-ω turbulence model was used. Therefore, the turbulent length scale (L_T) and turbulent intensity (I_T) at the inlet boundary condition must be specified. For all heat sink models, the I_T and L_T are set to be 5% and $0.07D_h$ (m), respectively (COMSOL, 2015), where D_h is the hydraulic diameter of the inlet tube.

(2) The boundary conditions of outlet flow are:

$$P = P_o = 0$$

(3) Since the whole heat sink test section was insulated in the experimental work, except at the MCHS bottom wall that exposed to the heat, all the outer surface boundaries (The top surface of minichannel and fluid, four side walls and also the bottom wall that was not exposed to the heat (the wall around the two heaters, see Fig. 6.9)) are considered to be adiabatic:

$$-\boldsymbol{n} \cdot (-k\nabla T) = 0$$

where $\boldsymbol{n}$ denotes the outward normal vector on the boundary of the domain.

(4) Heating power was supplied at the bottom surface of the MCHS using two resistance heaters via:

$$-\boldsymbol{n} \cdot (-k\nabla T) = q$$

(5) A thin layer of Ethoxy (heat transfer paste), with thickness (d_l) of $200\ \mu m$ and thermal conductivity (k_l) of 2.2 W/(m.K), was mounted between the heater and the base of the heat sink, which represented by "Thin Layer" boundary condition as:

$$-\boldsymbol{n} \cdot (-k_d\nabla T_d) = -\frac{k_l}{d_l}(T_u - T_d)$$

$$-\boldsymbol{n} \cdot (-k_u\nabla T_u) = -\frac{k_l}{d_l}(T_d - T_u)$$

where k_d and k_u are the thermal conductivities of the contacted surfaces, while T_u and T_d denote the contact surface temperatures. The boundary conditions used are summarised in Table 6.1, while Fig. 6.9 (a and b) shows a three-dimensional schematic view of the boundary

conditions used in the numerical simulation of both the SRM heat sink and SPSM heat sink test sections.

Table 6.1: The boundary conditions of the conjugate heat transfer model.

Locations	Fluid conditions	Thermal conditions
Inlet	Q_{in} = 0.1 – 3.0 *l/min* (1.667×10^{-6} –5×10^{-5} m^3/s)	$T_o = T_{f,in} = 20$ ℃
Outlet	$P = P_o = 0$	The temperature gradient in the normal direction is zero.
Interface surface	No – slip $\boldsymbol{u} = 0$	$-k_s \frac{\partial T_s}{\partial n}\Big\|_\Gamma = -k_f \frac{\partial T_f}{\partial n}\Big\|_\Gamma$ $T_{s,\Gamma} = T_{f,\Gamma}$
Top wall and outer side walls	Thermal insulation (adiabatic) $\boldsymbol{u} = 0$	$-\boldsymbol{n}.(-k\nabla T) = \boldsymbol{q} = 0$
Bottom wall of the heat sink	$\boldsymbol{u} = 0$	$Q = \frac{q}{V}$ (W/m^3) Q is the heat source. $\boldsymbol{q} = 25, 37.5$ and $50\ W$ (total power dissipated per heater). V is the total volume of the selected domains (heaters).
Thin layer	$\boldsymbol{u} = 0$	$-\boldsymbol{n}\cdot(-k_d\nabla T_d) = -\frac{k_l}{d_l}(T_u - T_d)$ $-\boldsymbol{n}\cdot(-k_u\nabla T_u) = -\frac{k_l}{d_l}(T_d - T_u)$

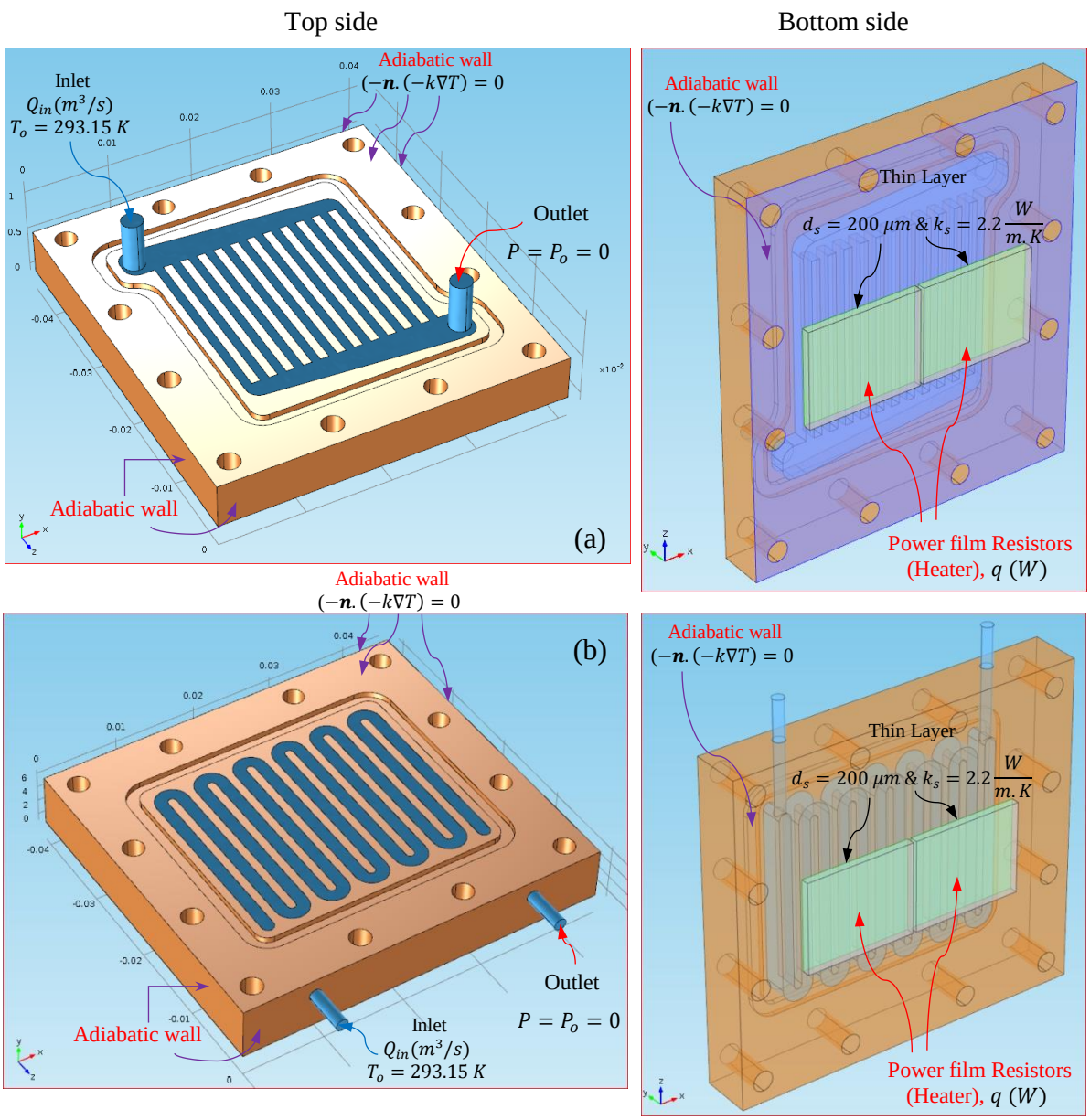

Fig. 6.9: 3D geometry with boundary conditions of (a) the straight rectangular MCHS; (b) single path serpentine MCHS.

6.6 Discretisation Schemes

COMSOL use a segregated and fully coupled solver approaches to solve the governing equations. The segregated solver requires iterations for nonlinear problems. It is also can use direct or iterative linear solvers. The segregated solver splits the Jacobian matrix into smaller sub-problems, usually by degree of freedom (DoF) type. The degrees of freedom are the number of variables that must be assigned to solve the (non)linear algebraic system describing the operational unit. The memory (and time) needed to compute a solution depends strongly upon the number of degrees of freedom solved for, as well as the average connectivity of the nodes, and other factors. The segregated solver solves the governing equations sequentially

(i.e., segregated from one another), while the coupled solver solves them simultaneously (i.e., coupled together). In the present study, segregated solver was used for the best compromise between growth in memory requirements and accuracy.

In COMSOL v.5.2, there are three types of discretisation elements which are P1 + P1 (the default), P2 + P1, and P3 +P2, and each one refers to as follows:

P1+P1 is first-order elements for velocity and pressure fields.

P2+P1 is second-order elements for velocity field and first-order elements for pressure field.

P3+P2 is third-order elements for velocity field and second-order elements for pressure field.

The second order discretisation will be suitable just for creeping flows. In the present study numerical simulations, first-order discretisation type (P1+P1) was used with quadratic elements for temperature field. In many numerical studies, relative error tolerance is generally set to a value between 10^{-3} and 10^{-6}. In a conventional sense, as the relative tolerance reduces, accuracy of the results increases, but this at the expense of the computation time which also increases to reach the desired tolerance level. Therefore, in the current simulations, the relative tolerance is set to 10^{-6}. A numerical method is said to be convergent if the numerical solution of the discrete problem approaches the exact solution of the differential equation as the mesh size and time step go to zero. For all the heat sink models simulated, the numerical solution is converged between 10^{-4} – 10^{-5} with a relaxation factor about 0.5.

6.7 Post – processing

After the governing equations are solved depending on the assumptions and boundary conditions applied to the domain, the results can be analysed. However, it is important to determine whether the numerical results obtained are reliable, mesh verification and other validation with the previous literature must be carried out. Therefore, grid independence tests comparisons with the previous validation studies of straight rectangular MCHS are carried out.

6.7.1 Grid Sensitivity

The effects of grid density on the numerical solutions for all MCHS models were tested using four different mesh sizes, as indicated in Table 6.2, where grid 1 is the coarsest and grid 4 the finest for each particular MCHS model. The predicted values of the temperature between the heater and the heat sink bottom ($T_{junction}$) and average Nusselt number (Nu_{avg}) for all MCHS models for a water flow rate of $0.15\ l/min$, water inlet temperature set at 20 °C and input power of 100 W (power on each heater is 50 W to generate heat flux of 31 W/cm^2) are given in Table 6.2. The deviation percentages, *E*, are calculated with respect to the solutions on grid

4 in each case; these are small (~2%) and thus grid 3 is employed for all MCHS computations reported below as a suitable compromise between efficiency and accuracy. Fig. 6.10 shows grid 3 in the TPSM heat sink design, which shows that resolution was increased near the bends.

Table 6.2: Grid dependency test.

Heat sink model	Grid No.	Number of elements×10^6	$T_{junction}$ (°C)	E%	Nu_{avg}	E%
SRM	1	0.979	57.4	5.7	9.7	9.0
	2	1.897	56.0	3.1	9.3	4.5
	3	2.637	55.0	1.3	9.1	2.2
	4	3.356	54.3	—	8.9	—
SPSM	1	0.937	47.4	7.5	14.3	8.3
	2	1.992	46.0	4.3	13.8	4.6
	3	2.788	44.9	1.8	13.5	2.3
	4	4.834	44.1	—	13.2	—
DPSM	1	0.852	51.3	6.2	12.8	7.5
	2	1.836	49.4	2.3	12.4	4.2
	3	2.526	48.9	1.2	12.1	1.7
	4	3.703	48.3	—	11.9	—
TPSM	1	0.844	54.0	8.0	11.4	8.6
	2	1.776	52.6	5.2	11.0	4.8
	3	2.486	51.0	2.0	10.7	1.9
	4	3.649	50.0	—	10.5	—

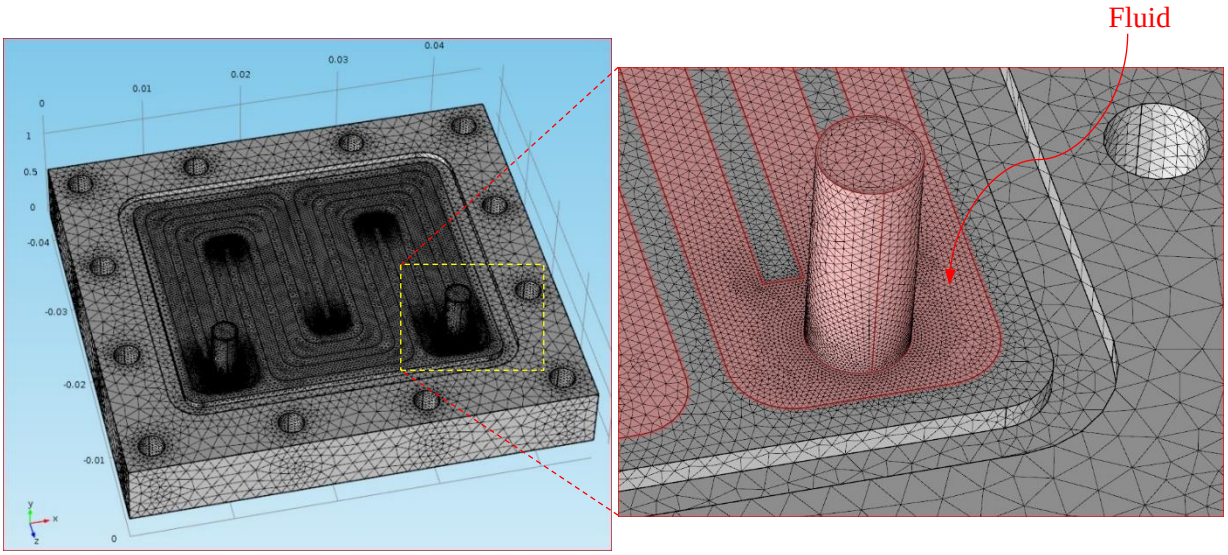

Fig. 6.10: Numerical mesh using grid 3 for a TPSM design.

6.7.2 Impact of Grid and Cell Types

In this subsection, the impact of grid type and cell type on the CFD solutions will be examined using structured and unstructured elements. In this comparison, a single straight rectangular microchannel will be considered, and the dimensions and boundary conditions adopted are described in Fig. 6.11. To reduce the computational effort a symmetry plane was employed, and No-slip boundary conditions were used on all solid walls. Constant heat flux of 100 W/cm^2 was applied at the bottom of the microchannel. The turbulent flow regime was considered in this comparison, and the standard $k-\omega$ turbulence model was used for

numerical simulation since this model provides more accurate solutions in the near wall boundary regions, and is preferred to work with internal flow with a low Reynolds number. The steady state, incompressible, three-dimensional turbulent flow, and heat transfer in the rectangular microchannel are considered. At the inlet boundary condition, the turbulent intensity, I_T, and the turbulent characteristic length, L_T, are set to be 5% and $0.07D_h$ (m), respectively, where D_h is the hydraulic diameter of the inlet microchannel.

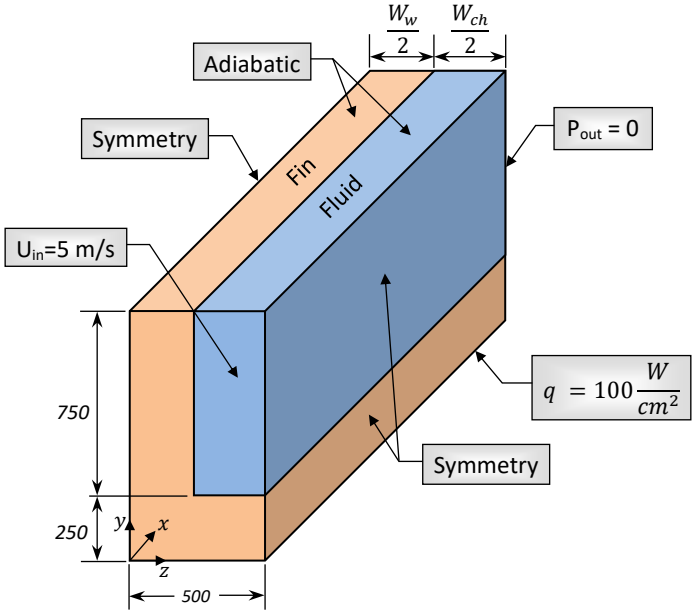

Fig. 6.11: Schematic diagram of the straight rectangular microchannel with symmetry planes and boundary conditions. (all dimensions in μm)

In the present simulations, the segregated solver approach was used to solve the governing equations. To deal with the problem of velocity and pressure coupling, first-order discretisation type P1+P1 (first-order elements for velocity and pressure fields) was used with quadratic elements for temperature field. In the current simulations, the relative tolerance is set to 10^{-5}. In the present exploration two grid densities are considered for each of the following cell types: (i) hexahedral and (ii) tetrahedral. Fig. 6.12 shows the local grid structure for the normal hexahedral and tetrahedral grids respectively, which they generated with COMSOL Multiphysics v.5.2. For mesh independence, three meshes of single straight rectangular microchannel geometry were used for each cell types, namely coarse, normal and fine. All meshes were generated using same topology, and Table 6.3 summarises each grid together with their results. The computed maximum temperature (T_{max}) generally reduce as the grid density increases regardless of the turbulence model, while the opposite was occurred with ΔP.

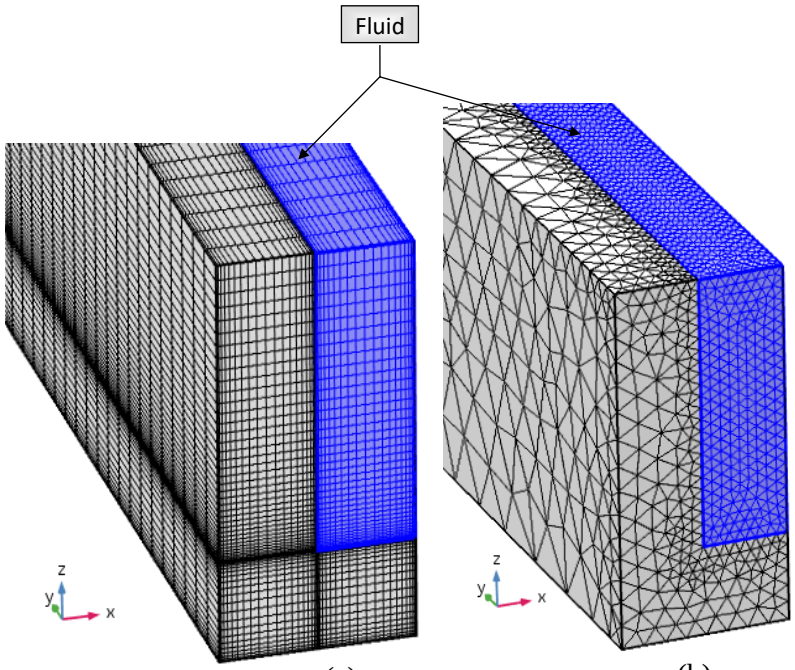

Fig. 6.12: Local grid structure on the straight rectangular microchannel for: (a) hexahedral (structured); and (b) tetrahedral (unstructured) meshes.

Table 6.3: Summary of mesh properties and calculated values used in mesh independence tests.

Grid type	*Global cell count*		*Hexahedral*				*Tetrahedral*			
	Hexahedral	*Tetrahedral*	*T (°C)*	*E%*	*ΔP (Pa)*	*E%*	*T (°C)*	*E%*	*ΔP (Pa)*	*E%*
Coarse	240168	251780	39.13	2.65	19677	2.03	39.58	2.51	19144	2.86
Normal	535224	647553	38.48	0.94	19865	1.09	39.02	1.06	19419	1.47
Fine	940343	1067976	38.12	—	20084	—	38.61	—	19708	—

The deviation percentage, E, of T_{max} and ΔP are calculated with respect to the solutions on fine grid in each case; these are small (~1.5%), thus normal grid can be used to simulate the straight rectangular microchannel heat sinks. Figs. 6.13 and 6.14 show respectively the predicted velocity vectors and temperature contours for the straight rectangular microchannel heat sink for hexahedral and tetrahedral cell types. Both sketches are taken at the mid-depth plane of the microchannel ($H_{ch}/2$) at inlet velocity of 5 m/s and constant heat flux of 100 W/cm^2 for normal grid.

From Table 6.3 it can be observed that the MAE between the hexahedral and tetrahedral cell types for normal grid is 1.38% for T_{max} and 2.24% for ΔP. Therefore, tetrahedral cell type can be employed for complex geometric as a suitable compromise between efficiency and accuracy, also to reduce the effort and the time required to generate meshes.

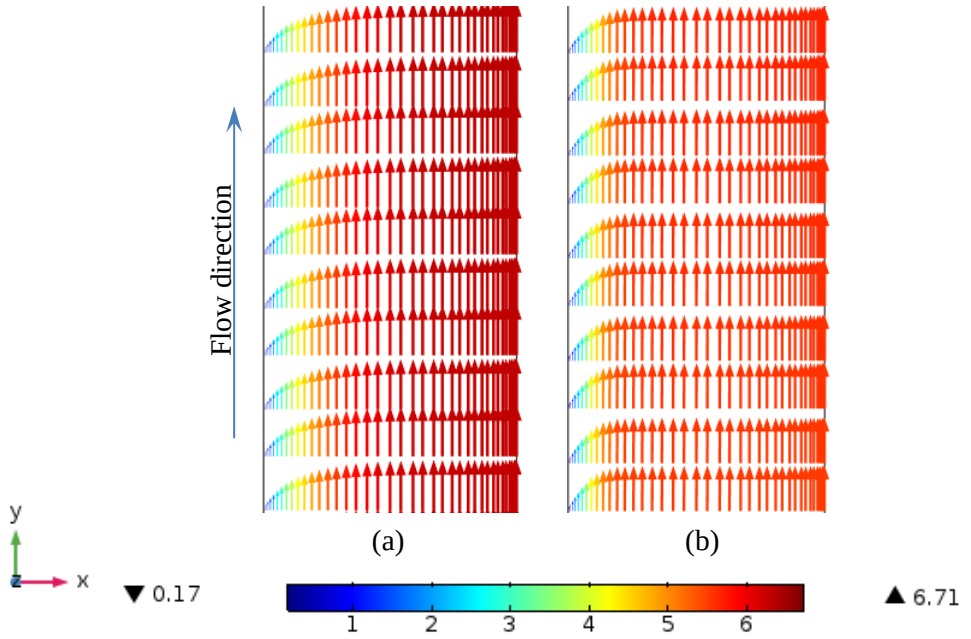

Fig. 6.13: Velocity vector (m/s) distribution along the streamwise on the $x-y$ section at $H_{ch}/2$ in the middle of the microchannel with inlet velocity of 5 m/s and heat flux of 100 W/cm^2 for: (a) hexahedral; and (b) tetrahedral meshes.

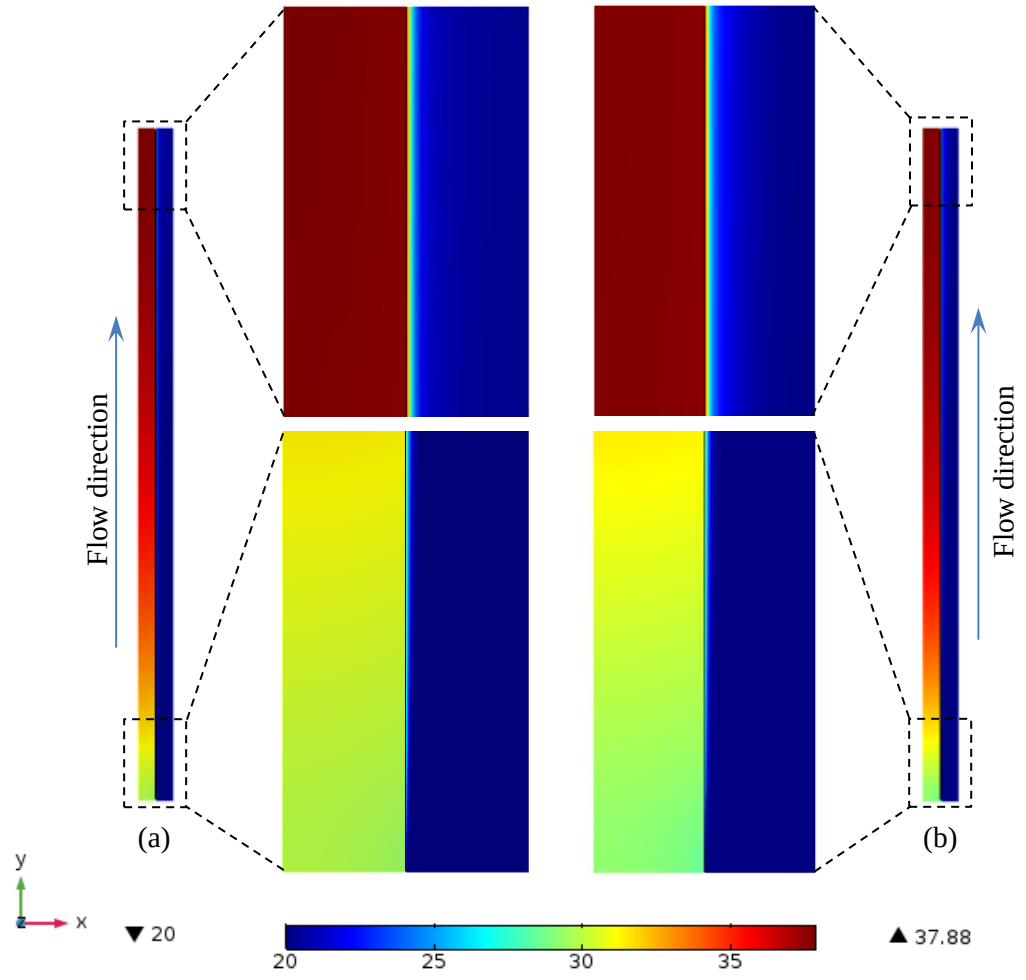

Fig. 6.14: Temperature contours (°C) on the $x-y$ section at $H_{ch}/2$ at velocity inlet of 5 m/s and heat flux of 100 W/cm^2 for: (a) hexhedral; and (b) tetrahedral meshes.

6.7.3 Validation with Previous Studies

The computational model was validated with numerical and experimental results obtained by Qu and Mudawar (2002b) and Kawano et al. (1998) respectively, who considered laminar water flow in a single rectangular microchannel cooling a chip. The water inlet temperature is set at 20 °C and a constant heat flux of 90 W/cm^2 is supplied at the upper boundary. The silicon microchannels have a width and depth of 57 µm and 180 µm, respectively, with a separating wall of 43 µm (see Fig. 6.15).

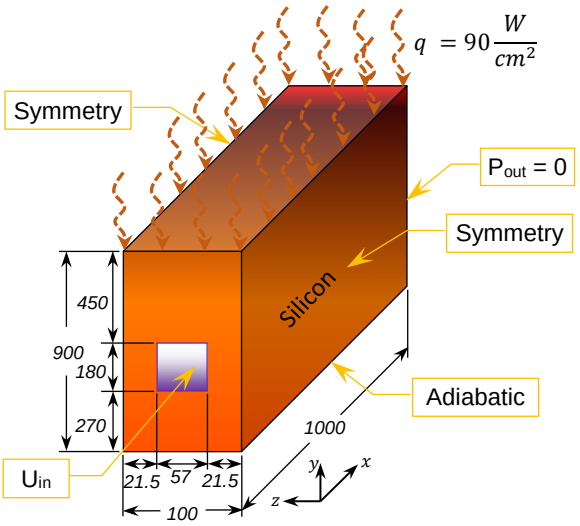

Fig. 6.15: Schematic of unit cell of rectangular microchannel with boundary condition adopted from the work of Qu & Mudawar (2002b).

A free-tetrahedral mesh was used to simulate the single microchannel with 200180 elements. The results obtained were evaluated in terms of the outlet thermal resistance ($R_{th,out} = (T_{surf,max} - T_{f,in})/q$) over a range of Reynolds number of 80 ≤ Re ≤ 400. It is clear from Fig. 6.16 that the predictions of $R_{th,out}$ agree well with the previous studies: a MAE of 3.5% with Qu and Mudawar's (2002b) numerical predictions and a MAE of 6.5% with the experimental study of Kawano et al. (1998). These provide confidence in the accuracy of the numerical approach used here.

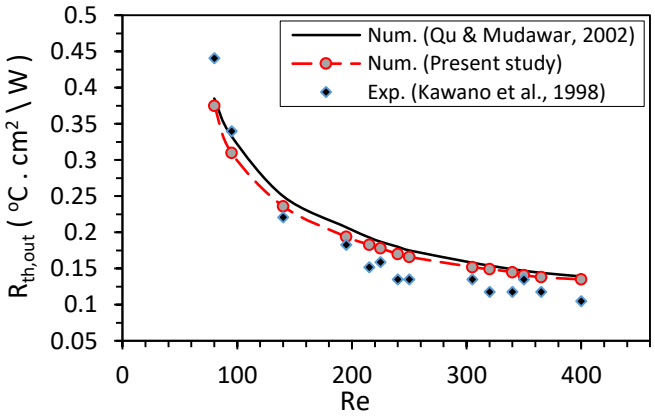

Fig. 6.16: Comparison between the numerical of the present work, Kawano et al. and Qu & Mudawar works for outlet thermal resistance.

6.8 Validation of Numerical Method

In this section, pressure drop, Fanning friction factor, heat transfer coefficient, Nusselt number and total thermal resistance are presented based on the numerical simulation results for both conventional straight rectangular MCHS and serpentine MCHS, and then compared with experimental data of the present work for validation.

6.8.1 Hydraulic Performance

In the present numerical solution, a whole multi-straight rectangular minichannel (SRM) heat sink was used as a computational domain over a wide range of volumetric flow rate ($0.1 \leq Q_{in} \leq 3.0\ l/min$) with a step of $0.1\ l/min$ at input power of 100 W. To validate the numerical predictions, the data obtained for ΔP_t from experimental work at input power of 100 W were used. As shown in Fig. 6.17, a reasonable agreement was achieved between experimental measurements and numerical predictions with a MAE of 9%. Also, it can be seen that all the experimental values are higher than the predictions and this may be due to minor pressure losses in the male run tee union which was not taken into account in the numerical simulation.

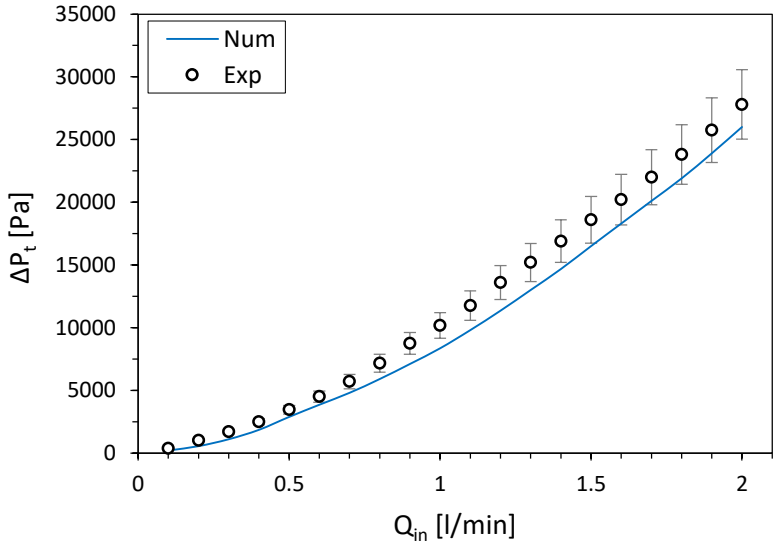

Fig. 6.17: Comparison between the measured and numerical predictions total pressure drop with different Q_{in}.

Another comparison has been conducted between experimental measurements and numerical predictions for friction factor in channel (f_{ch}) for both laminar and turbulent flow regimes. Numerically, the Fanning friction factor inside the straight minichannel for the SRM heat sink was calculated using Eq. (4.25), and the value of ΔP_{ch} was obtained from a CFD solution at an input power of 100 W with water inlet temperature set at 20 °C. As can be seen from

Fig. 6.18, the results of the experimental friction factors reported here at different water flow rate are in reasonable agreement with numerical predictions with a MAE of around 11%.

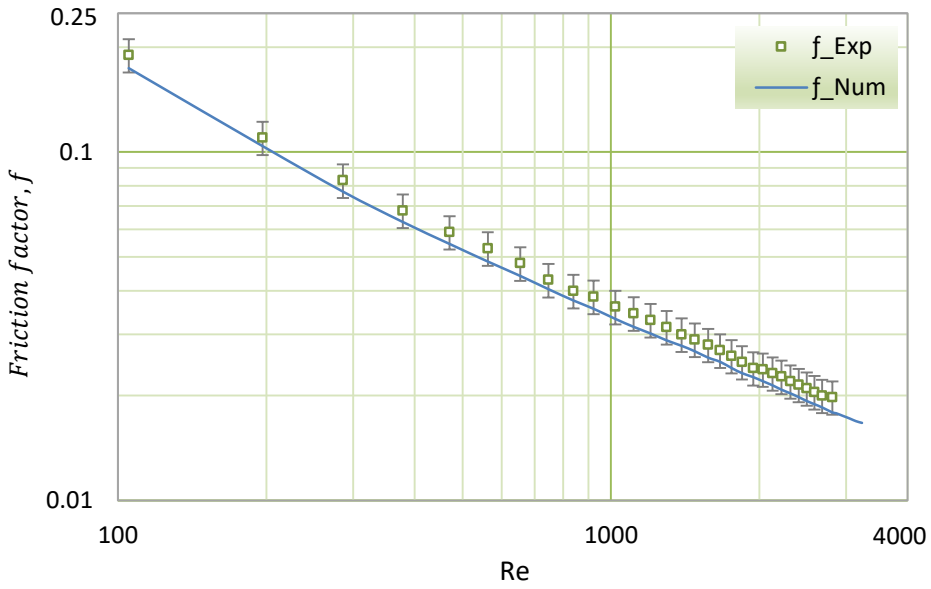

Fig. 6.18: Comparison between the measured and numerical predictions of total pressure drop with different Re.

With respect to the other three types of a serpentine MCHS test sections used experimentally, which are single (SPSM), double (DPSM) and triple path multi-serpentine minichannel (TPSM) heat sink designs, computational modelling has been carried out for comparison with experiment. Three-dimensional conjugate heat transfer with the whole MCHS as a computational domain was simulated within. Fig. 6.19(a) compares experimental measurements and numerical predictions of the total pressure drops (ΔP_t) versus volumetric flow rate (Q_{in}) for the SPSM design, while Fig. 6.19(b) shows the corresponding data for both the DPSM and TPSM heat sinks at input power of 100 W. In all cases, as Q_{in} is increased ΔP_t increases rapidly due to existence of curved channels. As can be seen from the two figures, an acceptable agreement has been achieved between experimental data and numerical predictions with MAEs of 12.5%, 10.6% and 10.2% for the SPSM, DPSM and TPSM designs, respectively.

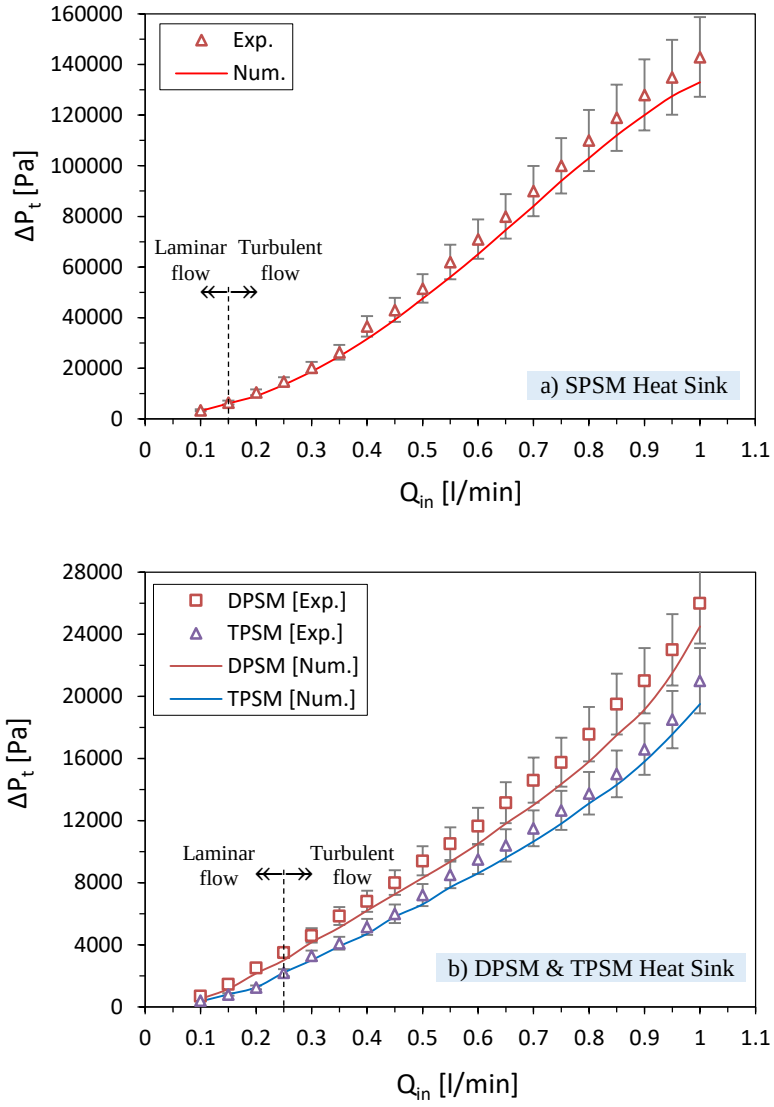

Fig. 6.19: The total pressure drop for (a) SPSM; (b) DPSM and TPSM models at different water flow rate and at input power of 100 W.

For the SPSM heat sink model, the pressure distributions through the twelve – minichannels are illustrated in Fig. 6.20(a), while Fig. 6.20(b) demonstrates the percentage of pressure drop in both straight and bend minichannels at three different volumetric flow rates and input power of 100 W. The markers in Fig. 6.20(a) represent maximum and minimum pressure in each straight portion of the minichannels, while the gaps between adjacent markers denote the pressure loss at bends, see Eqs. (4.21a and 4.21b). The bend loss coefficient, ξ, is determined based on the correlations proposed by Maharudrayya et al. (2004) for single-phase laminar flow. The results obtained from the latter two equations were validated with numerical predictions and good agreement was achieved with a MAE of 8% for three different Q_{in}. As shown in Fig. 6.20(b) the percentage of pressure drop in bends were higher than those in straight channels at each Q_{in}, and this percentage increases as Q_{in} increases.

The data obtained from Eq. (4.20) was compared with experimental pressure drop and acceptable agreement was found, with MAE of 13% at each Q_{in} examined.

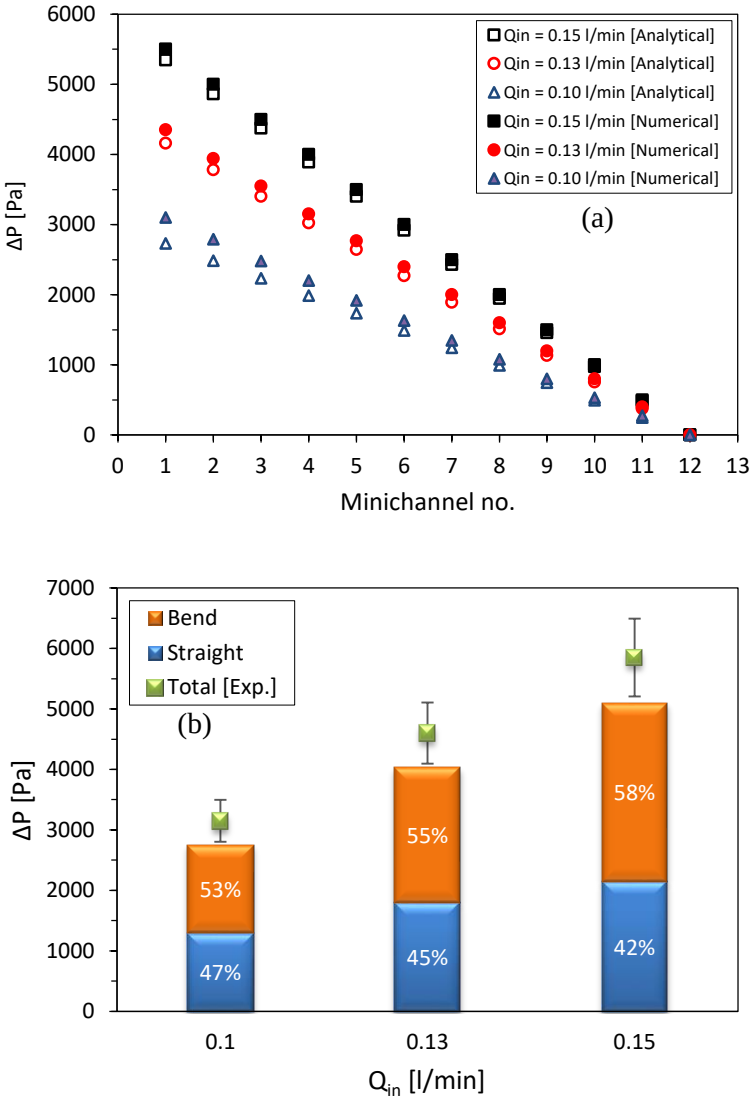

Fig. 6.20: The total pressure drop in SPSM design at different water flow rate and at input power of 100 W; (a) pressure distribution through 12-serpentine channels; and (b) pressure drop percentage.

Fig. 6.21 shows the pressure drop contours of the four MCHS designs used at the mid-depth plane of the channel ($Z = H_{ch}/2$) for laminar flow with $Q_{in} = 0.15\ l/min$ and an input power of 100 W. It can be seen that the SPSM creates a larger pressure drop than other cases. This is due to the fact that water in the SPSM flows inside one channel only, unlike the DPSM and TPSM where fluid is distributed into two and three minichannels respectively, leading to reductions in both the velocity and pressure drop in the latter two cases, and the larger minichannel length in the SPSM.

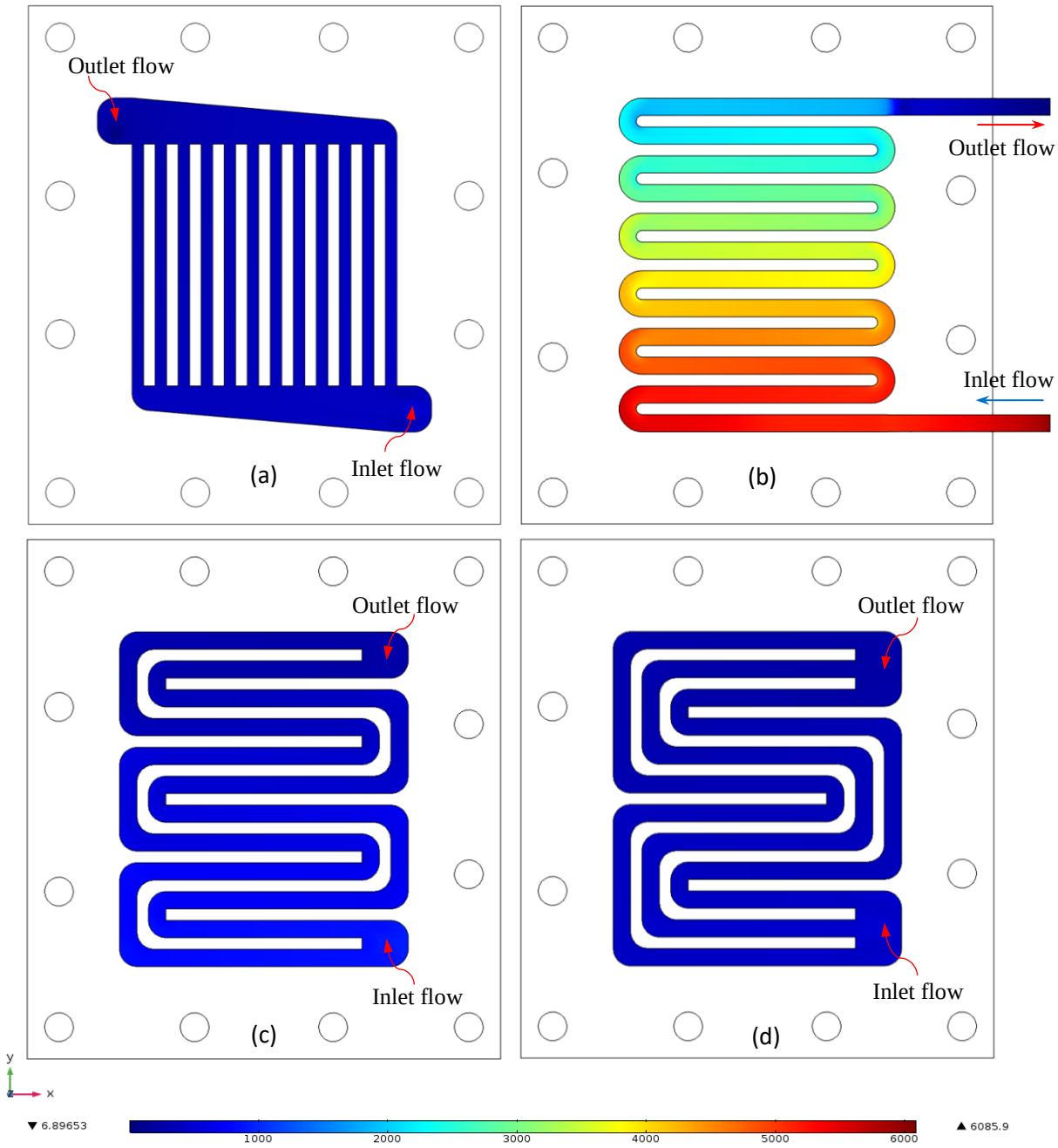

Fig. 6.21: Pressure drop contours (Pa) of four MCHS at the mid-depth plane of the channel ($Z = H_{ch}/2$) : (a) SRM; (b) SPSM ; (c) DPSM; (d) TPSM.

6.8.2 Heat Transfer Performance

Fig. 6.22 presents experimental data and numerical predictions of the channel bottom temperature distribution along the minichannel length for the SRM test section, together with the inlet and outlet water temperatures measured using thermocouples inserted at the inlet and outlet of the MCHS. Good agreement between theory and experiment was obtained, with MAE of 3.8% for the minichannel base temperature and 2.4% for the fluid bulk temperature.

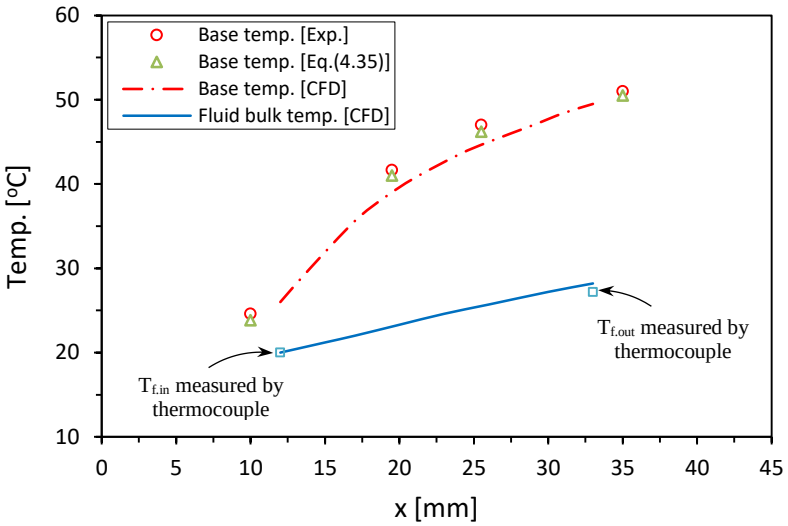

Fig. 6.22: Distribution of base and fluid bulk temperature along the minichannel axis distance for SRM design for $Q_{in} = 0.2\ l/min$ at input power of 100 W.

The data shows how the minichannel base temperature increases along the flow direction and that the difference in temperature between the water and channel base along the axial flow direction is not constant which indicates that the flow is thermally developing throughout the whole of the MCHS, a desirable feature which leads to enhanced heat transfer.

Fig. 6.23 depicts the comparison between the measured base temperature ($T_{w,tci}$) and those obtained by numerical simulation for the SRM heat sink test section. Experimentally, four thermocouples are inserted inside the MCHS model along the minichannel flow direction, which are located 1.75 mm underneath the minichannel (see Fig. 4.7 and Fig. 4.22). The measured base temperatures were taken at input power of 100 W with a wide range of Reynolds number. It can clearly be seen from the given figure that good agreement was achieved between experimental and numerical predictions with a MAE of 2.5%.

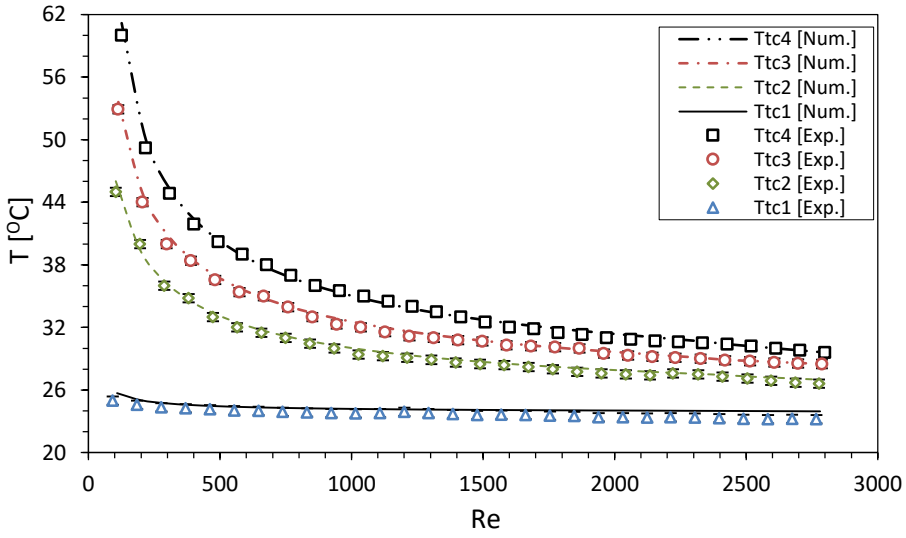

Fig. 6.23: Thermocouple temperature readings at different locations inside MCHS versus Reynolds number for input power of 100 W.

Fig. 6.24 compares the values of the average Nusselt number (Nu_{avg}) obtained experimentally and numerically for the four MCHS test sections. The values of Nu_{avg} are calculated at input power of 100 W with different volumetric flow rates (Q_{in}) ranging from 0.1 to 1.0 l/min with a step of 0.1 l/min. The agreement between experiment and numerical predictions is once again good with a MAE of 6.5% for all MCHSs used, and all values of Nu_{avg} increase monotonically with Q_{in}.

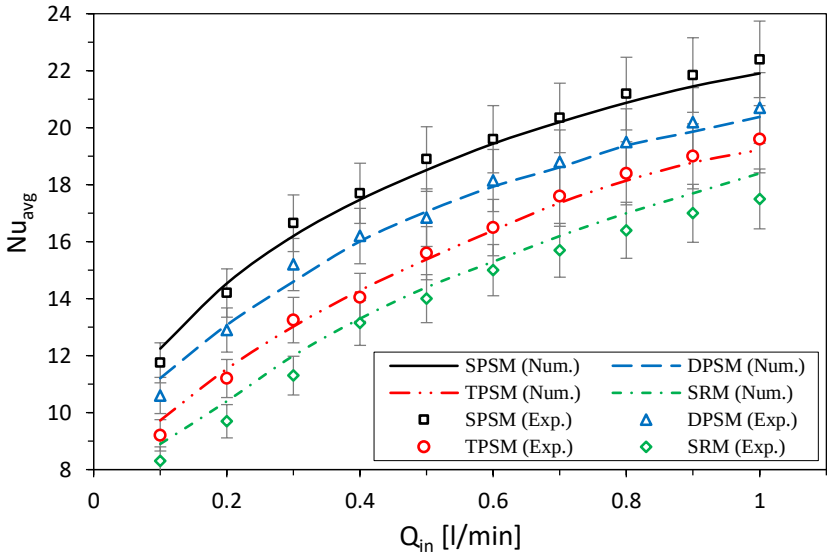

Fig. 6.24: The average Nusselt number versus water flow rate (Q_{in}) for four MCHS designs at input power of 100 W.

Fig. 6.25(a-d) depicts the temperature contours for the four MCHS designs, which are taken at the half depth of the minichannel ($H_{ch}/2$), $Q_{in} = 0.15\ l/min$ and input power of 100 W. For all MCHS, it can be seen that the temperature difference between the near wall fluid and the core fluid increases downstream. The side wall temperature distribution of the SPSM along the flow length was smaller than other MCHSs, while that for the SRM design was higher.

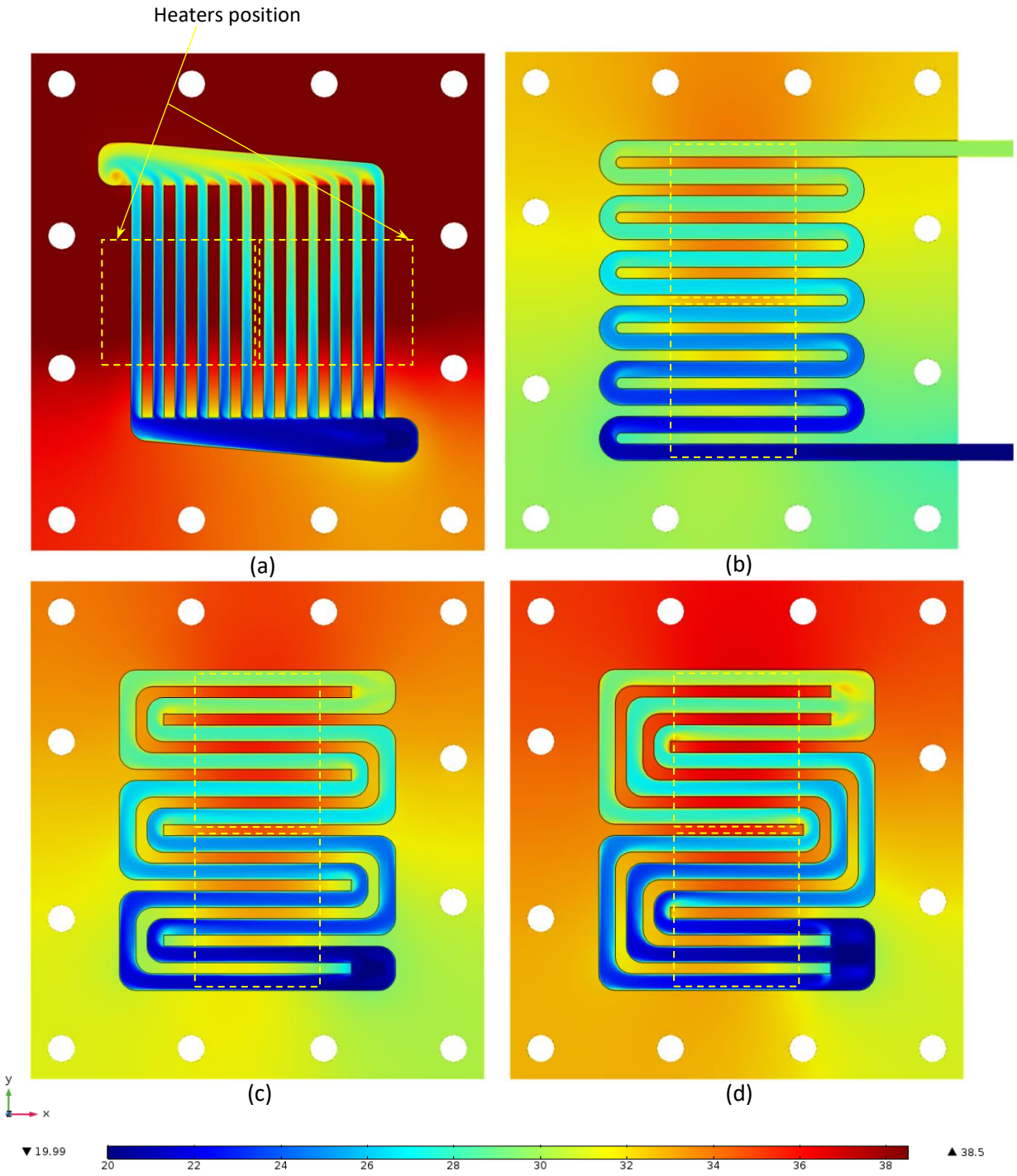

Fig. 6.25: Temperature contours (°C) of the four MCHSs: (a) SRM; (b) SPSM; (c) DPSM; (d) TPSM.

Figs. 6.26 – 6.29 demonstrate the temperature contour for both fluid and solid at different plane along the flow direction for four MCHS models used. Four cross-sectional planes on the $y - z$ section at x = 0 – 33.5 mm were presented for all MCHSs. The temperature contours of all MCHSs adopted are presented at $Q_{in} = 0.15\ l/min$ and input power of 100 W. The examination of the three-dimensional temperature distribution of all MCHS designs

clearly shows the lower wall temperatures of the SPSM heat sink, with the SRM temperatures the highest.

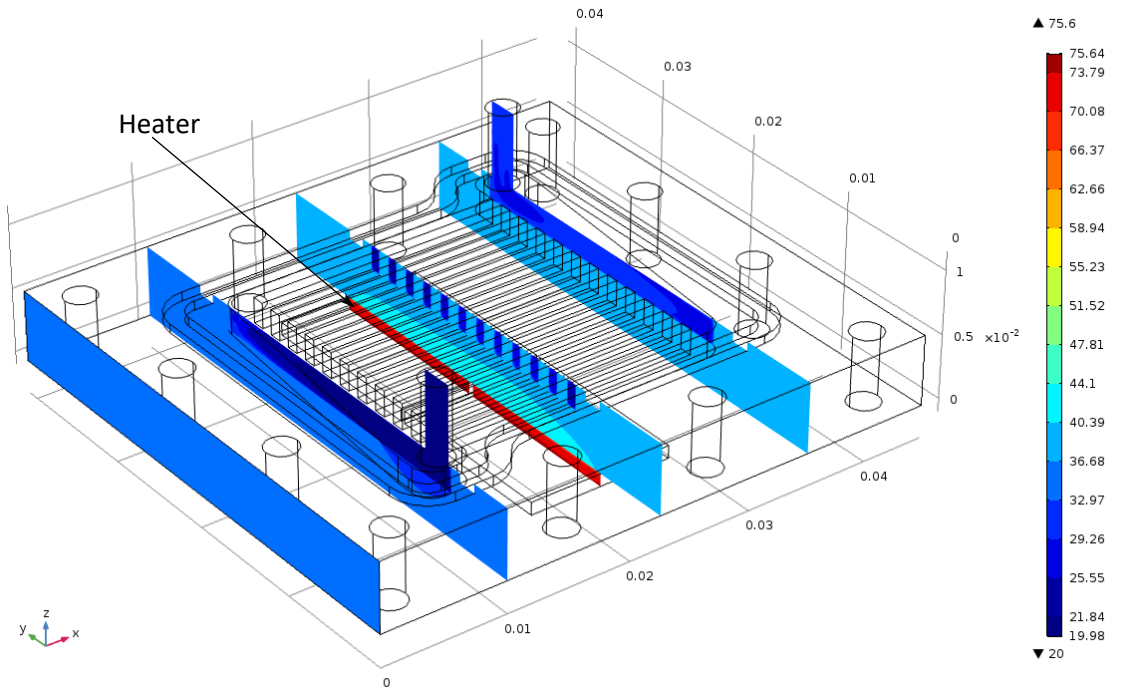

Fig. 6.26: Temperature contours (°C) of the SRM heat sink design.

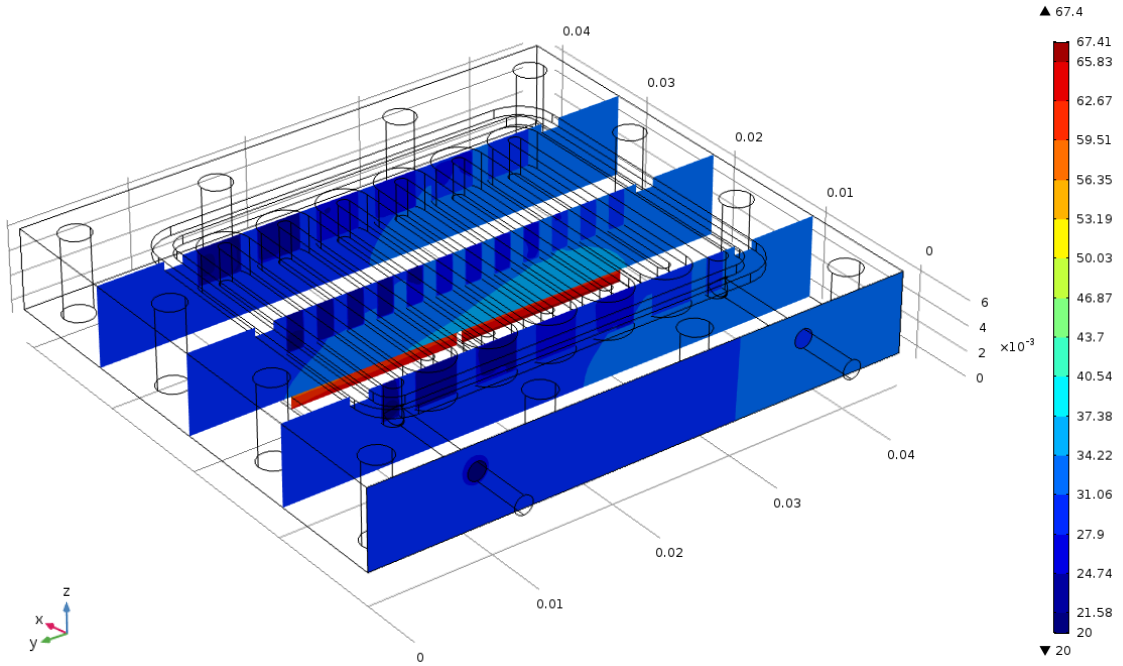

Fig. 6.27: Temperature contours (°C) of the SPSM heat sink design.

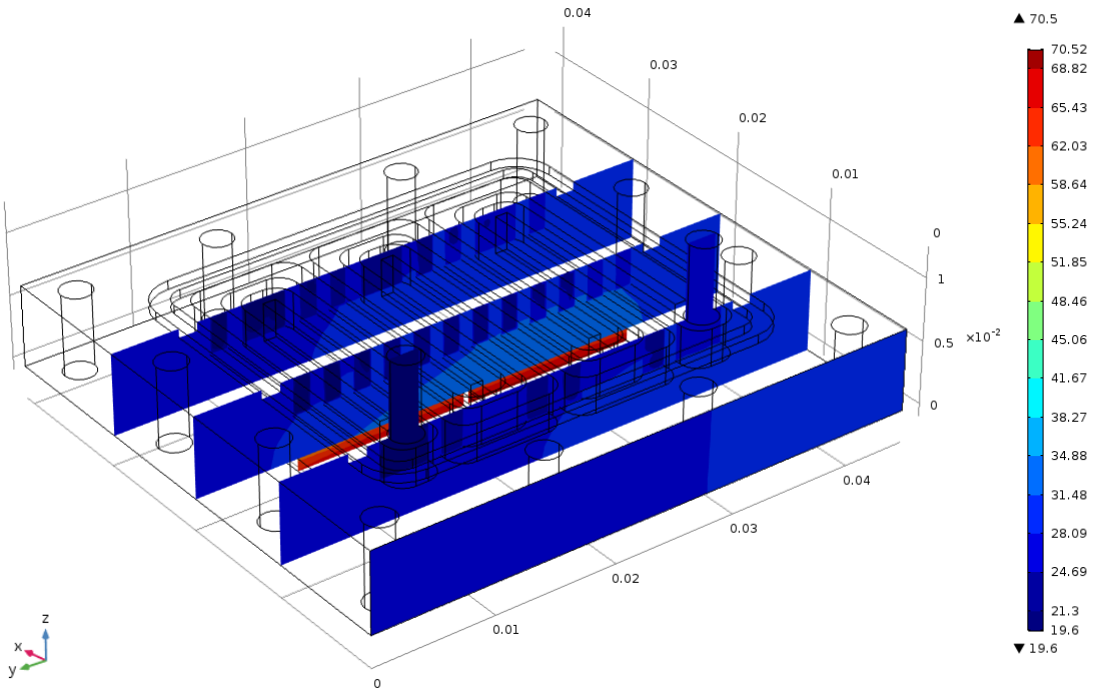

Fig. 6.28: Temperature contours (°C) of the DPSM heat sink design.

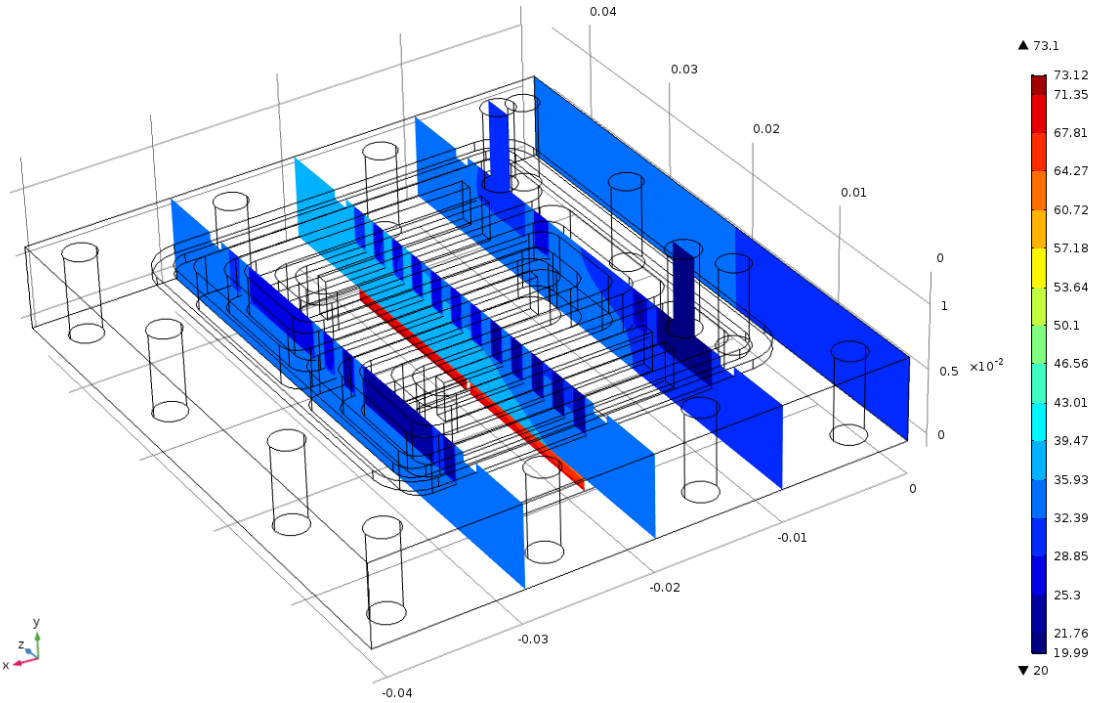

Fig. 6.29: Temperature contours (°C) of the TPSM heat sink design.

Fig. 6.30(a) shows the temperature distribution for the SPSM test section, at a volumetric flow rate (Q_{in}) of 0.15 l/min and an input power of 100 W, while Figs. 6.30(b and c) illustrate the velocity distribution and the velocity vector at the mid-depth plane of the channel ($H_{ch}/2$), respectively. Due to flow continuity, the SPSM model has higher velocities

compared with the other two types of serpentine minichannel designs, and it can be seen that a small region of recirculating flow is created near the inner surface of the bend, which is expected to aid the transportation of heat from the walls into water and disrupts the hydrodynamic and thermal boundary layers, thus improving the convective heat transfer (Dai et al., 2015).

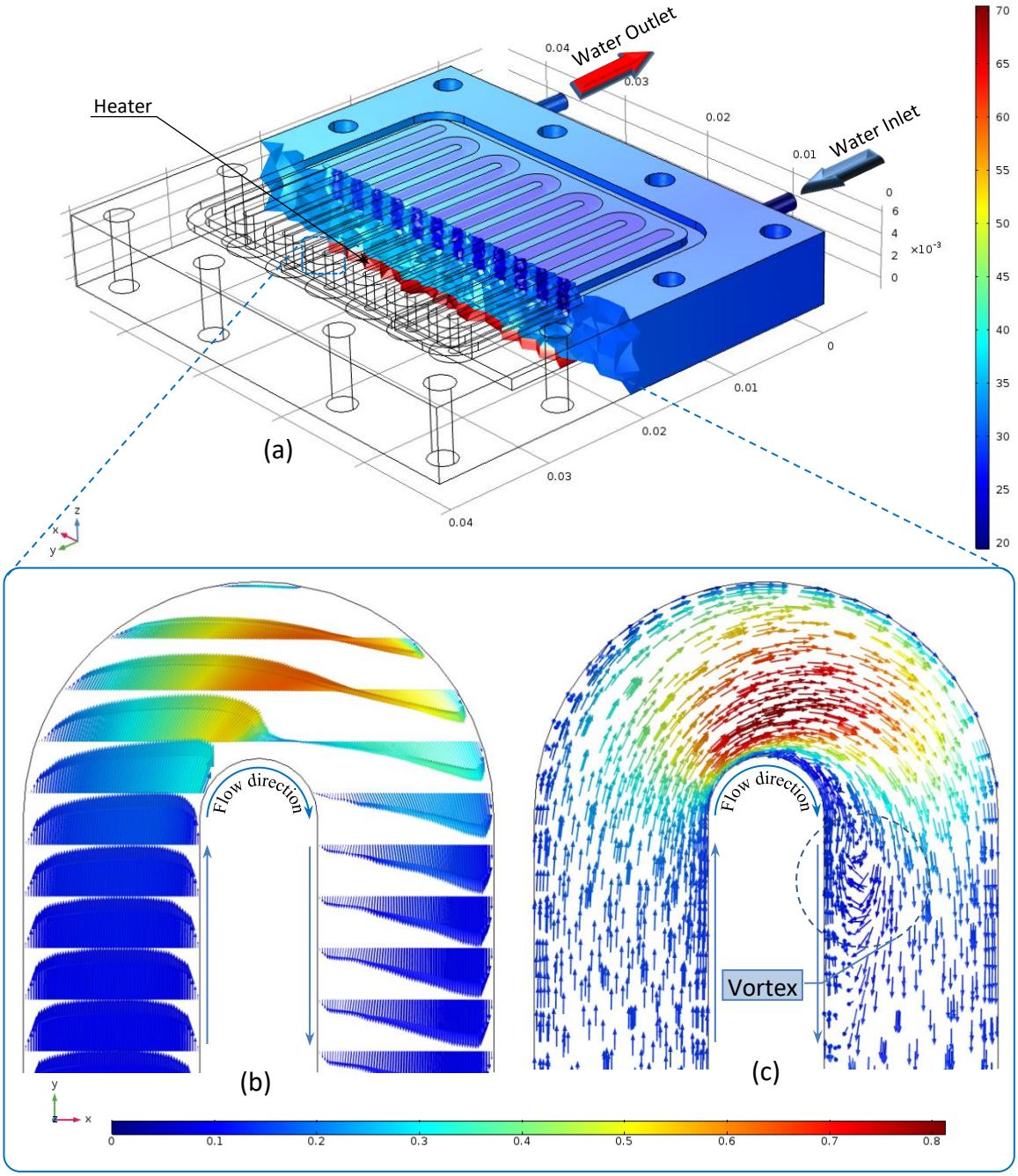

Fig. 6.30: (a) Temperature distribution (°C); (b) velocity distribution (m/s) and (c) velocity vectors (m/s) for the SPSM design at $Q_{in} = 0.15\ l/min$ and input power of 100 W.

6.8.3 Thermal Resistance

A numerical and analytical study was carried out to calculate the total thermal resistance (R_{th}) in the SRM heat sink. In the numerical simulations, a whole MCHS design was used as a computational domain as shown in Fig. 6.9(a). Grid 3 is employed with greater than of 2.6 million elements, as shown in Fig 6.31. Simulations were conducted at four different water flow rates ($0.1 \leq Q_{in} \leq 0.25\ l/min$) with increments of $0.05\ l/min$, and water inlet temperature set to 20 ^{o}C with input power of 100 W.

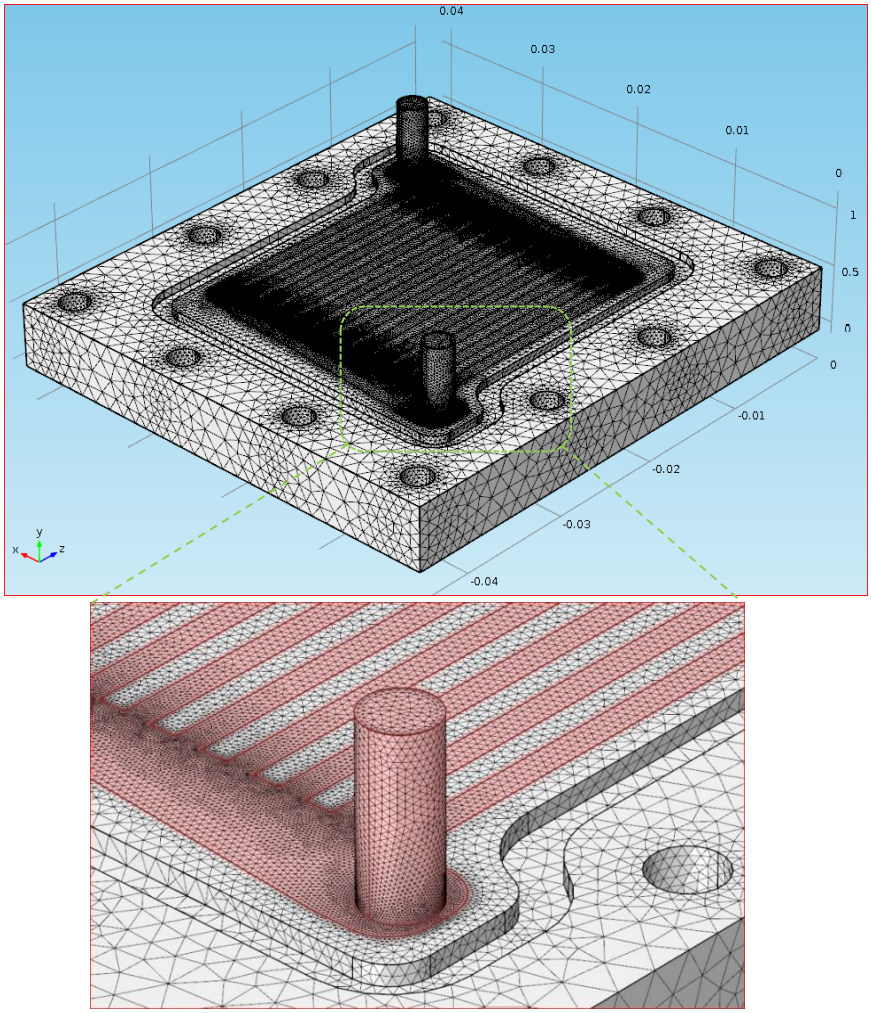

Fig. 6.31: Numerical mesh for a SRM design.

With regard to the analytical study, Eq. (3.77) proposed by Phillips (1987, 1988 and 1990) was used, which is applicable for straight rectangular mini/microchannels. A one-dimensional thermal resistance model was adopted by using four components of thermal resistance which are the conductive, convective, bulk and construction thermal resistances. In the convective thermal resistance component, the value of Nusselt number was calculated by using a correlation equation suggested by Lee and Garimella (2006) to take into account

of the effect of the thermally developing flow, see Eq. (3.49), since most of the flow inside the minichannel was hydrodynamically and thermally developing.

Fig. 6.32 compares the numerical predictions and analytical solutions for the total thermal resistance (R_{th}) values obtained from the SRM heat sink with the measurements of input power of 100 W, and good agreement has been achieved with a MAE of 6%. Phillips's equation is therefore useful for predicting the R_{th} of the MCHS.

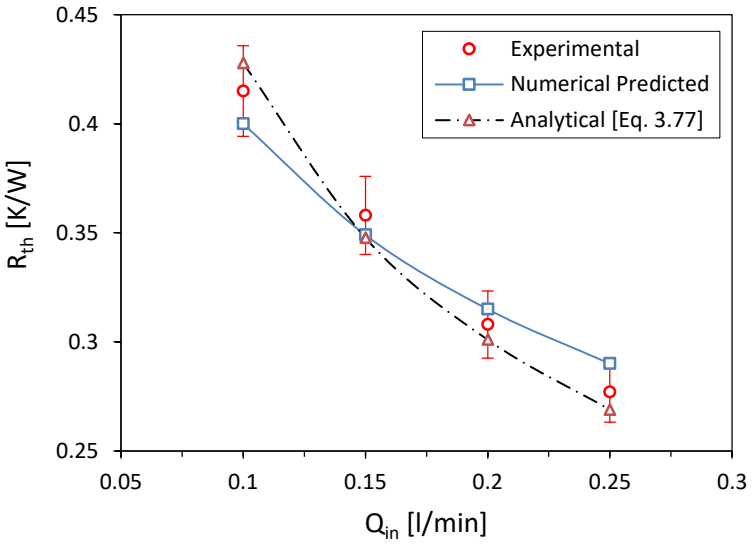

Fig. 6.32: Total thermal resistance versus volumetric flow rate at input power of 100 W.

6.9 Optimisation Strategy of the SPSM Design

In electronics, heat sinks are designed to maintain processors below critical temperatures for minimal energy input into the system. This final section considers the optimisation of the SPSM heat sink design subject to the conflicting objectives of minimising both ΔP and R_{th}.

Optimisation has been carried out on the SPSM heat sink to determine the effect of two design variables; namely the minichannel width (W_{ch}) and the number of minichannels (N_{ch}) to minimize simultaneously R_{th} and ΔP, since these two design variables have significant effects on the pressure drop and heat transfer.

The optimisation was carried out at constant volumetric flow rate of $Q_{in} = 0.16\ l/min$ with an inlet water temperature to the MCHS set to 20 °C, and constant heat flux of 75 W/cm^2 supplied underneath the heat sink. The area ($W \times L$), substrate thickness (H_b) and minichannels depth (H_{ch}) of the heat sink are constrained to be respectively 25×25 mm^2, 0.5 mm and 2 mm. The goal is to construct a Pareto front of non-dominated solutions, from which an appropriate compromise design can be chosen. The Pareto front is obtained by building

accurate metamodels of both ΔP and R_{th}, as a function of the two design variables. The optimisation problem is defined as follow:

Objective function: min (R_{th}) and min (ΔP)

Subject to: $0.5\ mm \leq W_{ch} \leq 1.5\ mm$

$$8 \leq N_{ch} \leq 13$$

After selecting the range of two design variables, thirty of design of experiment (DoE) points were created using an Optimal Latin Hypercube (OLHC) approach. To distribute the DoE points as uniformly as possible, a permutation genetic algorithm was used (Narayanan et al., 2007), see Fig. 6.33.

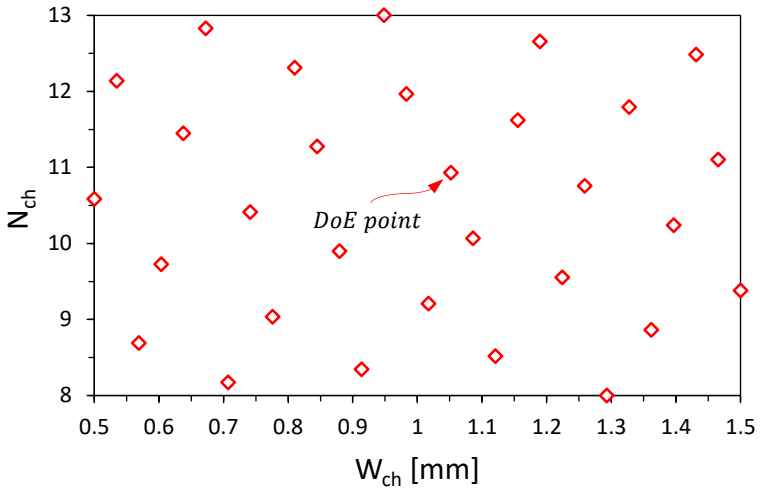

Fig. 6.33: Distribution of Uniform Optimal Latin hypercube DoE points used for metamodel building, 30 points.

Three-dimensional CFD solutions were then obtained at all thirty of the DoE points selected for the SPSM heat sink using COMSOL Multiphysics, and the predicted temperature and pressure drop values are extracted from the CFD solutions. Response surface approximations (Metamodels) of total thermal resistance (R_{th}) and pressure drop (ΔP) throughout the design space are built using a Moving Least Squares (MLS) approximation, with a second order (Quadratic) base polynomial, where a Gaussian weight decay function, w_{ij}, is used to determine the weighting of points in the regression coefficients at each point, see Eq. (3.90). By adjusting the closeness of fit parameter, θ, the influence of numerical noise in the response can be adjusted. The optimum value of θ can be determined by minimising the Root Mean Square Error (RMSE) between the metamodel prediction and the actual numerical predictions at each DoE point (Loweth et al., 2011).

The global minimum of the surrogate model for R_{th} and ΔP is found using a multi-objective genetic algorithm (MOGA) approach based on (Fonseca and Fleming, 1995 and Deb et al., 2002). Graphical examples of surface functions R_{th} and ΔP in terms of the design variables

W_{ch} and N_{ch} are shown in Figs. 6.34 and 6.35 respectively, which are built using HyperStudy v12 software (HyperWorks, 2015). In Fig. 6.34, it can be seen that the R_{th} is reduced by decreasing W_{ch} and increasing N_{ch}, whereas the ΔP_t is decreased by increasing W_{ch} and decreasing N_{ch} as shown in Fig. 6.35.

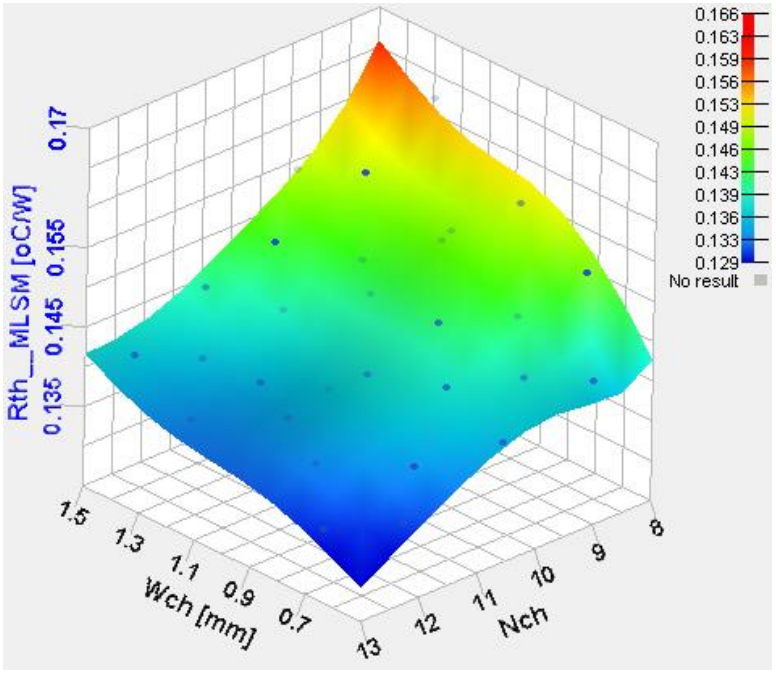

Fig. 6.34: Response surface function using MLSM of total thermal resistance for SPSM heat sink model.

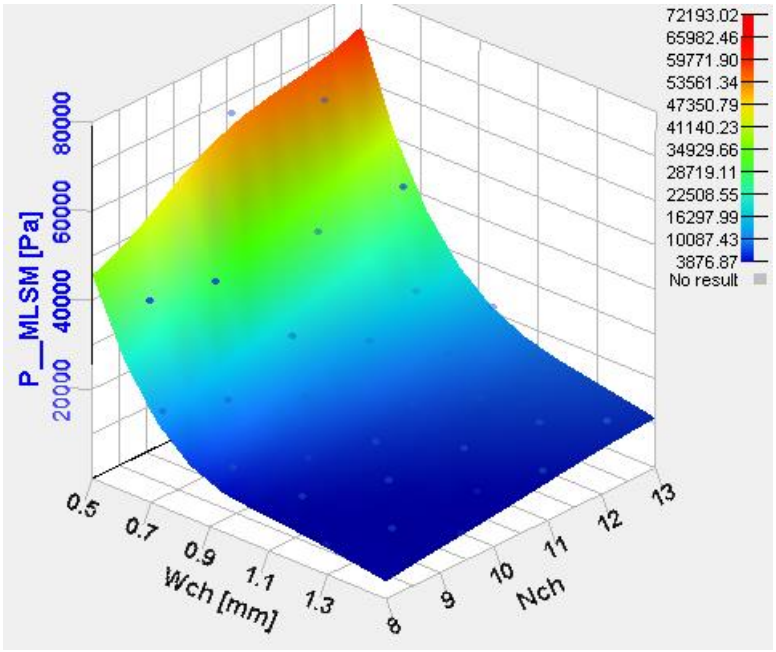

Fig. 6.35: Response surface function using MLSM of total pressure drop for SPSM heat sink model.

From the metamodels obtained, it can be inferred that the design variables have significant effect on the objective functions. It is shown that changes in W_{ch} and N_{ch} lead to conflicting

requirements for each objective function. Fig. 6.36 is a simple design trends which show how the objective functions are influenced by the design variables.

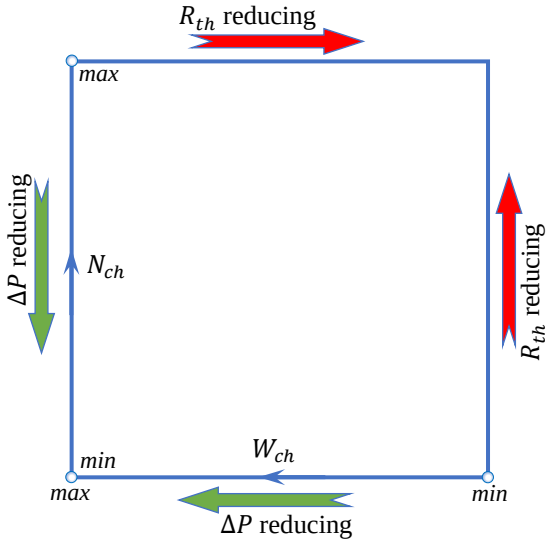

Fig. 6.36: Global design trends obtained from the metamodels.

In a multi-objective optimisation problem, a Pareto front can be used by designers to select the most suitable compromise between the various objective functions that have been distinguished and for which the goal is to minimise the objective functions. It is not possible to move along the design points on the Pareto front to decrease any of the objective functions without increasing at least one other objective function, and Pareto points are often referred to as being 'non-dominated'. In the present case with two objective functions the Pareto front showing the impact of the two objectives of interest here is shown in Fig. 6.37.

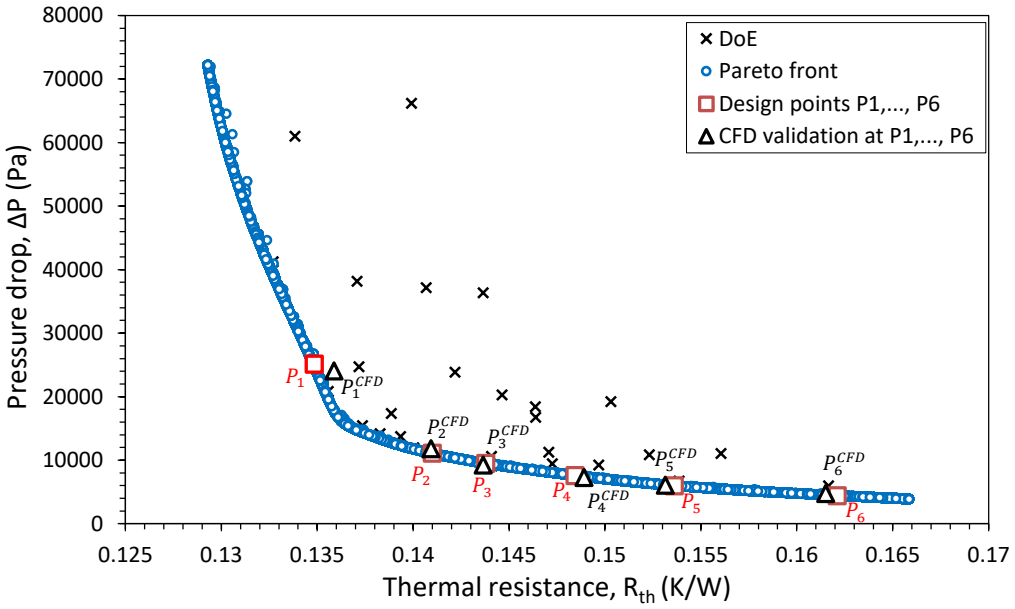

Fig. 6.37: Pareto front showing the compromises that can be struck in minimising both R_{th} and ΔP together with six representative design points (e.g. P_1 ,…, P_6) used for the minichannel performance analysis illustrated in Table 6.4.

As a demonstration, the minichannel of six representative operating conditions designs on the Pareto front as indicated in Fig. 6.37 is formulated in Table 6.4. The corresponding design variables, namely W_{ch} and N_{ch} with the two objectives R_{th} and ΔP are also specified. The optimised designs from the metamodels have been validated against corresponding CFD solutions with the same design variables. These are generally in good agreement with a MAE of less than 0.8% for R_{th} and 7% for ΔP.

Table 6.4: Minichannel design performance at six operating conditions points located on the Pareto front together with CFD validation as shown in Fig. 6.37.

Design point Pareto front	W_{ch} *(mm)*	N_{ch}	R_{th} *(K/W)*	ΔP *(Pa)*	*CFD validation*	R_{th} *(K/W)*	ΔP *(Pa)*	*MAE* (× 100)	
								R_{th}*(%)*	ΔP*(%)*
P_1	0.864374	13	0.13486	25107.598	P_1^{CFD}	0.13587	24040.4	0.746	4.439
P_2	1.342584	12	0.14101	11105.142	P_2^{CFD}	0.14093	11804.1	0.056	5.921
P_3	1.459745	11	0.14379	9518.4099	P_3^{CFD}	0.14366	9267.13	0.091	2.711
P_4	1.494707	10	0.14844	7582.2650	P_4^{CFD}	0.14890	7257.07	0.312	4.481
P_5	1.499419	9	0.15361	5992.6536	P_5^{CFD}	0.15315	6049.74	0.300	0.943
P_6	1.499930	8	0.16211	4415.6202	P_6^{CFD}	0.16151	4743.70	0.368	6.916

6.10 Summary

In this chapter, CFD has been used to simulate the conjugate heat transfer in both laminar and turbulent flow regimes of water through straight rectangular and serpentine MCHS designs. The numerical predictions of fluid flow and heat transfer obtained for the four MCHS models have been validated successfully against experimental results in terms of pressure drop, friction factor, surface temperature, average Nusselt number and thermal resistance.

From the experimental and numerical results, it was found that the single path serpentine minichannel (SPSM) heat sink has higher heat transfer coefficient and low thermal resistance compared with other three MCHS models, albeit with a significantly larger pressure drop. The latter can, however, be reduced by carful optimisation of the MCHS geometry parameters and the multi-objective optimisation carried out here has demonstrated clearly the compromise that can be struck between maximum heat transfer and minimum pressure drop for serpentine MCHSs.

In the optimisation of the SPSM heat sink design, Optimal Latin Hypercube (OLH) approach is used to create thirty of design of experiment (DoE) points, using a permutation genetic algorithm, whereas Moving Least Squares (MLS) approximation is used to build the response surface approximations (Metamodels) of total thermal resistance (R_{th}) and pressure drop (ΔP) throughout the design space. A Pareto front is constructed which enables designers to explore appropriate compromises between designs with low pressure drop and those with low thermal resistance.

Chapter 7: Thermo-hydraulic Performance Analysis of Serpentine Chevron Fin MCHS

7.1 Introduction

According to the results obtained experimentally and numerically from Chapters 5 and 6, it was found that the incorporation of serpentine minichannels in heat sink design will significantly increase the heat-removal ability. The results revealed that the heat transfer coefficient in single path serpentine minichannel (SPSM) heat sinks was larger than for the other three types of minichannel heat sinks (MCHSs). However, this enhancement in heat transfer for SPSM heat sinks is at the expense of a large increase in pressure drop, it was observed that the pressure drop (ΔP) in the SPSM is up to ten-times higher than the straight rectangular minichannel (SRM) heat sink, which in turn leads to high pumping power consumption. Based on these results, it is demonstrated that the thermal enhancement comes together with a higher pressure drop.

To reduce the pressure drop along with the increase in thermal enhancement, the single path serpentine minichannel (SPSM) heat sink design has been modified through integrated it within chevron fins. Therefore, a novel MCHS was designed, fabricated and tested to reduce the pressure drop in SPSM heat sinks while further enhancing the heat transfer coefficient. To authors' best knowledge, no previous studies have considered serpentine channels integrated within chevron fins to generate secondary flow. In this chapter, the heat sink test section of the novel design will be described. Experimental data and CFD solutions will be presented in terms of pressure drop, average Nusselt number and thermal resistance. The design optimisation of the new design will be explained in the last of this chapter.

7.2 Design and Fabrication of the Novel MCHS Test Section

In the present study, the single path serpentine MCHS that investigated experimentally and numerically in chapters 4, 5 and 6 has been modified by cutting the continuous serpentine fin into small chevron fins. The two different configurations of the serpentine MCHSs were designed using SolidWorks (Shih and Schilling, 2015). These were then manufactured and tested to investigate the effect of flow velocity on the heat transfer characteristics and pressure drop.

In order to facilitate a fair comparison between two different MCHS models, both heat sink models share the same channel depth (H_{ch}), channel width (W_{ch}), fin width (W_w), footprint area ($W \times L$), heat sink depth (H) and substrate thickness (H_b). The first model was a single path serpentine MCHS with plate fins (SMPF) (Fig. 7.1(a)), and the second a single path

serpentine MCHS with chevron fins (SMCF) (Fig. 7.1(b)), with an oblique angle of 30°. Fig. 7.1 shows isometric and top views of the two types of MCHSs considered here.

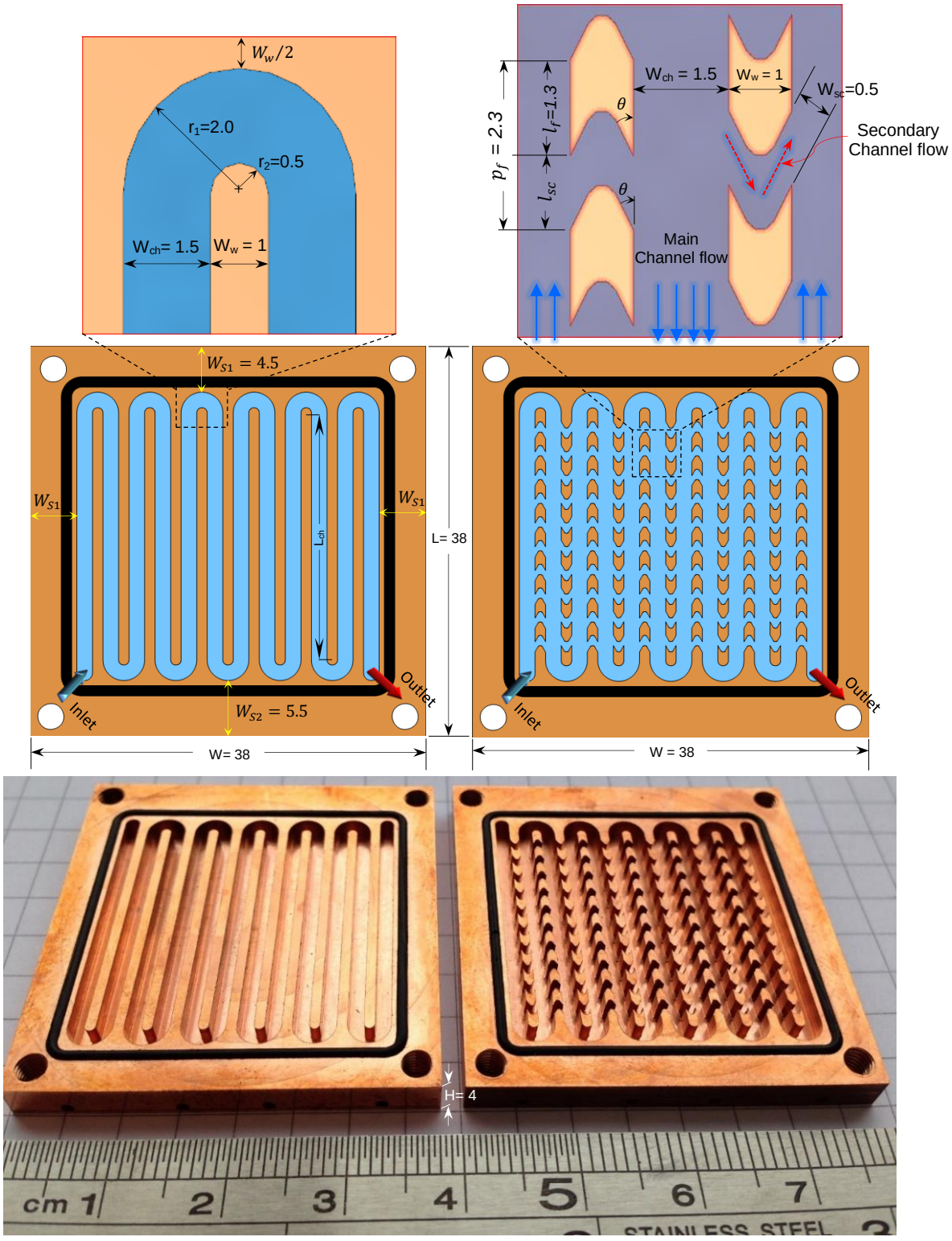

(a) (b)

Fig. 7.1: 3-D isometric actual and top view of (a) serpentine rectangular MCHS with plate fins (SMPF); (b) serpentine rectangular MCHS with chevron fins (SMCF), all dimensions in mm.

The MCHSs were fabricated from copper, using a high-accuracy Computer Numerical Control (CNC) milling machine (FANUC ROBODRIL). With regard to the SMCF design, the continuous plate fin is broken into small chevron fins with 9 fins per row. At the oblique angle (θ) of 30º, the length of the chevron fin (l_f) is 1.3 mm, whereas the fin pitch (p_f) and the secondary channel width (W_{sc}) were 2.3 mm and 0.5 mm, respectively. The dimensions for both sets of MCHS are listed in Table 7.1.

Table 7.1: Dimensional details for SMPF and SMCF heat sinks.

Characteristic	SMPF	SMCF
Material	Copper	
Heat sink dimensions, width×length×height, W×L×H (mm)	38×38×4	
Main channel width, W_{ch} (mm)	1.5	
Fin width, W_w (mm)	1	
Channel depth, H_{ch} (mm)	2	
Substrate thickness, H_b (mm)	2	
Number of minichannels, n	12	
Hydraulic diameter, D_h (mm)	1.714	
Number of chevron fins per row, N_{cf}	––	9
Secondary channel width, W_{sc} (mm)	––	0.5
Secondary channel length, l_{sc} (mm)	––	1
Chevron fin length, l_f (mm)	––	1.3
Chevron fin pitch, p_f (mm)	––	2.3
Chevron oblique angle, θ (deg)	––	30

To provide a good balance between heat transfer and pressure drop, the current design follows the recommendation of Suga and Aoki (1995) for louvered-fin heat exchangers that the ratio of fin pitch in the spanwise direction to the fin length has to be 1.5 times the tangent of oblique angle ($F_p/L_p = 1.5 \times tan\,\theta$, as shown in Fig. 7.2). The chevron oblique angle that denotes the angle between the main channel and oblique channel is set as 30° in the present experimental work, which is within the range of louver angles (20° to 45°) suggested by Suga and Aoki (1995). This approach also adopted by Lee et al. (2012 and 2013) and Fan et al. (2013).

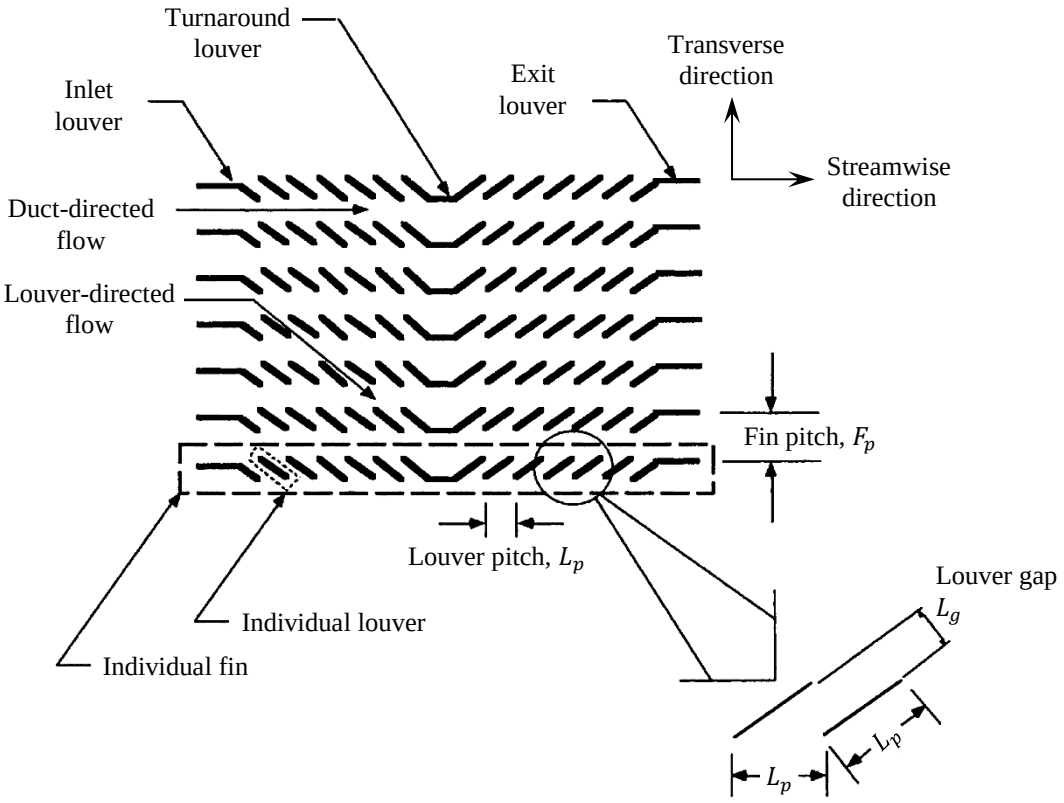

Fig. 7.2: Schematic of a louvered-fin array, Suga and Aoki (1995).

Uncertainties for the main parameters are tabulated in Table 7.2. These were found by using the same procedures used previously in section 4.8.

Table 7.2: Uncertainty for various critical parameter of serpentine MCHSs.

Variable	Absolute uncertainties
Channel width (W_{ch})	4 μm
Channel height (H_{ch})	5 μm
Channel length (L_{ch})	15 μm
Fin width (W_w)	3 μm
Oblique angle (θ)	0.3 deg
Hydraulic diameter (D_h)	1.2%
Volumetric flow rate (Q_{in})	0.65 – 1.27%
Temperature (T)	0.3 °C
Pressure drop (ΔP)	3.6 – 9.2%
Thermal resistance (R_{th})	2.8 – 7.3%
Nusselt number (N_u)	3.0 – 6.8.3%

Around the top of each heat sink there is a groove made for an O-ring seal with a depth and width of 0.7 mm and 1.0 mm respectively to prevent water leakage. Each MCHS sample was assembled with an Acrylic Perspex plastic sheet cover which is held onto the copper block by four stainless steel mounting screws (M3×0.5) and sealed with an O-ring. Two 3 mm holes of depth 3 mm were drilled on the top side surfaces of the plastic covers and male run tee union adapters (M3×0.5) are fixed into these threaded holes to provide the inlet and outlet for the water, and also to measure the temperature of the water at the inlet and outlet of the MCHS

test section. To measure the differential pressure drop between the inlet and outlet MCHS test section, a further two 3 mm holes with depths of 3 mm were drilled into the sides of the plastic cover (at the inlet and outlet positions), with barb fitting adapters (M3×0.5) used to connect the pressure gauge, see Fig. 7.3.

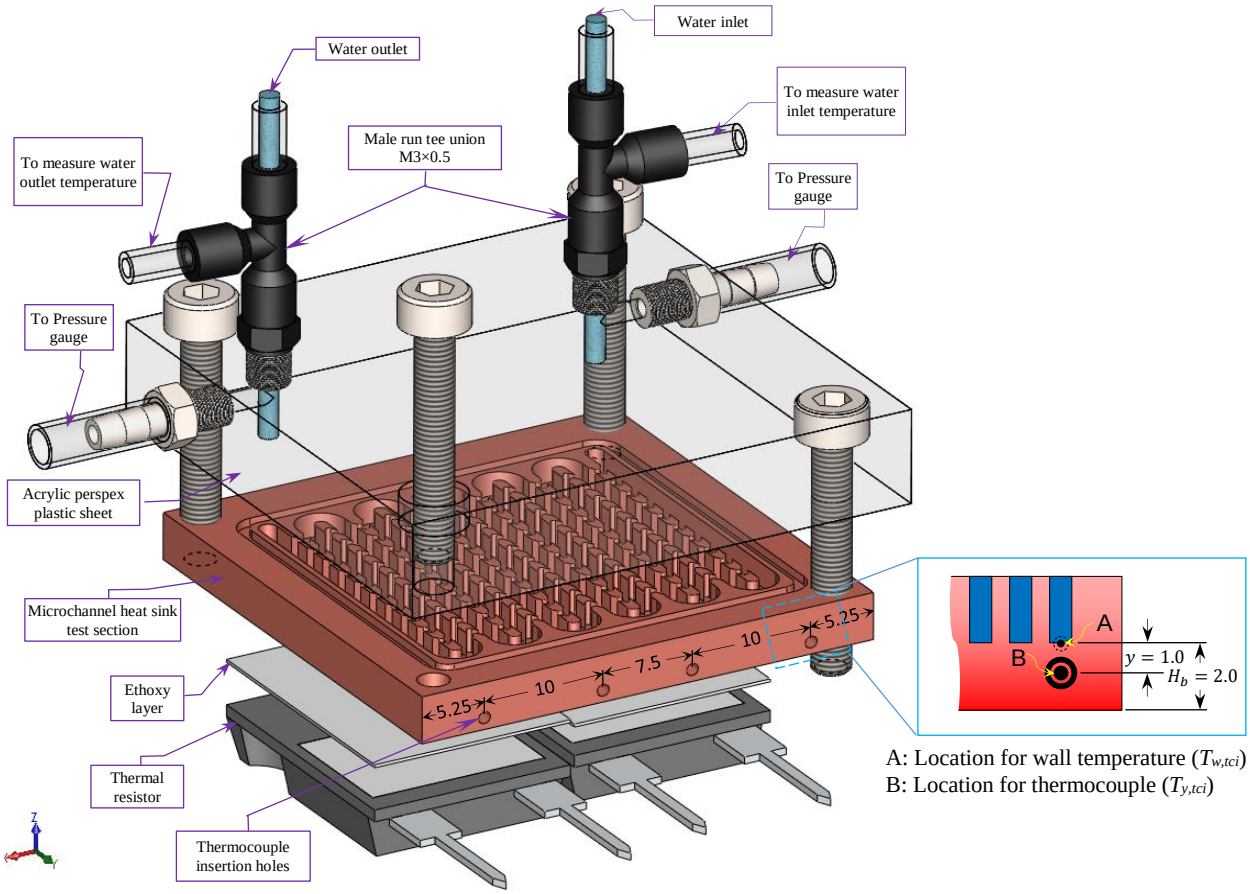

Fig. 7.3: Exploded view of serpentine MCHS model with chevron fins.

Two power film resistors of resistance 10 Ω (MP9100 (TO-247)) were used as heat sources, and each one has cross-sectional area of 11.5 mm × 14 mm with the maximum power reaching 100 W (62 W/cm^2). These were permanently adhered on the bottom side of each MCHS test section using a thin layer of thermal Ethoxy (Electrolube, TCER) with thermal conductivity of 2.2 W/m.K. The thickness of the thermal Ethoxy layer is measured manually for all the MCHS designs using a digital Vernier caliper, and was found to be $200 \pm 7\mu m$. To record the junction (maximum) temperature of the resistor as accurately as possible, the procedure described in the subsection 4.2.2 was adopted, see Fig. 4.9.

To measure the wall temperature distribution along the MCHS sample, four K-type sheathed thermocouples with a 0.5 mm probe diameter were inserted in the copper block at a distance of 1 mm below the minichannel base until it reaches half the width of the MCHS specimen. The locations of the thermocouple holes, as measured from the inlet of the MCHS and along its length are shown in Fig. 7.3. Thermal paste was used to fill the holes to ensure accurate

temperature measurement. The experimental test rig used with the SMPF and SMCF designs was the same as used previously with four MCHS models (see Fig. 4.1), except the test section is changed. A digital pressure gauge was used to measure the total pressure drop (ΔP) directly using two plastic tubes connected to the barb fitting adapters as shown in Fig. 7.3. The procedures used to calculate ΔP in the present experimental work are described in detail in subsection 4.7.1.

In the experiments, the relative surface roughness, ε/D_h, for both serpentine MCHS test sections studied was found to be $\sim 0.583 \times 10^{-3}$, which was measured by using the same procedures used previously with the four MCHS models, see section 4.3. This is less than the ε/D_h of stainless steel micro-tubes (1.76×10^{-3} to 2.80×10^{-3}) in the study of Kandlikar et al. (2003); consequently the effect of the surface roughness (ε) on the pressure drop and heat transfer coefficient is neglected here.

Before conducting any experiments, the rate of heat loss that is dissipated from the MCHS specimen to the surroundings was first determined. In the present work, the procedure described in the section 4.6 has been used, and the maximum average heat loss was found to be approximately 6% of the input power from each model.

In the present work, the heat is transferred to the fluid through three minichannel walls only and the fourth top wall is assumed to be adiabatic. Hence, A_{eff} which represents the surface area available for convective heat transfer for both serpentine MCHS models, can be calculated by:

$$A_{eff} = A_{base} + \eta_f \cdot A_{fin} \tag{7.1}$$

where A_{base} and A_{fin} represent the minichannel base and fin area available for heat transfer, respectively. The A_{base} of the serpentine MCHS with plate fins (SMPF) and with chevron fins (SMCF) can be calculated respectively as:

$$A_{base,SMPF} = nW_{ch} \cdot L_{ch} + \frac{\pi}{2}(n-1)(r_1^2 - r_2^2) + 2W_{ch}\left(L - \left(W_{s1} + W_{s2} + r_1 + L_{ch} + \frac{W_{ch}}{2}\right)\right) + \pi\left(\frac{W_{ch}}{2}\right)^2 \tag{7.2a}$$

$$A_{base,SMCF} = A_{base,SMPF} + W_w(n-1)\left(N_{cf}+1\right)l_{sc} \tag{7.2b}$$

where L_{ch} represents the length of the straight minichannel (m), $L_{ch} = L - (2r_1 + W_{s1} + W_{s2})$, W_{s1}, W_{s2} the outside wall thicknesses (m) and l_{sc} the secondary channel length (m), see Fig. 7.1. The symbols r_1 and r_2 denote the outer and inner radius of the curved minichannel (m) respectively, whereas n and N_{cf} represent respectively the number of minichannels and chevron fins.

The A_{fin} of both the SMPF and the SMCF can be determined respectively by:

$$A_{fin,SMPF} = 2nH_{ch} \cdot L_{ch} + \pi H_{ch}(n-1)(r_1 + r_2) + 4H_{ch}\left(L - \left(W_{s1} + W_{s2} + r_1 + L_{ch} + \frac{W_{ch}}{2}\right)\right) + \pi W_{ch} \cdot H_{ch} \quad (7.3a)$$

$$A_{fin,SMCF} = 2H_{ch}\left(L - \left(W_{s1} + W_{s2} + r_1 + \frac{W_{ch}}{2}\right)\right) + \pi H_{ch}(n-1)(r_1 + r_2) + N_{cf}(n-1)P_{cf} \cdot H_{ch} + 2H_{ch}(n-1)\left(L_{ch} - \left(N_{cf} \cdot p_f + l_{sc} + x\right)\right) + 2H_{ch}(n-1)(2S + l_{arc}) + \pi W_{ch} \cdot H_{ch} + 2H_{ch}(n-1)x + 2H_{ch}\left(L - \left(W_{s1} + W_{s2} + r_1 + L_{ch} + \frac{W_{ch}}{2}\right)\right) \quad (7.3b)$$

The symbol p_f denotes the fin pitch, $\left(p_f = l_f + l_{sc}\right)$, while P_{cf} represents the perimeter of the chevron fin, $\left(P_{cf} = 2\left(l_f + 2S + l_{arc}\right)\right)$, and l_{arc} denotes the length of the curved chevron fin, $\left(l_{arc} = 0.5W_{sc}(\pi - 2\theta)\right)$, where θ is in radians. Fig. 7.4 is a schematic sketch for two chevron fins to explain the parameters used for calculating A_{eff} in the SMCF heat sink model.

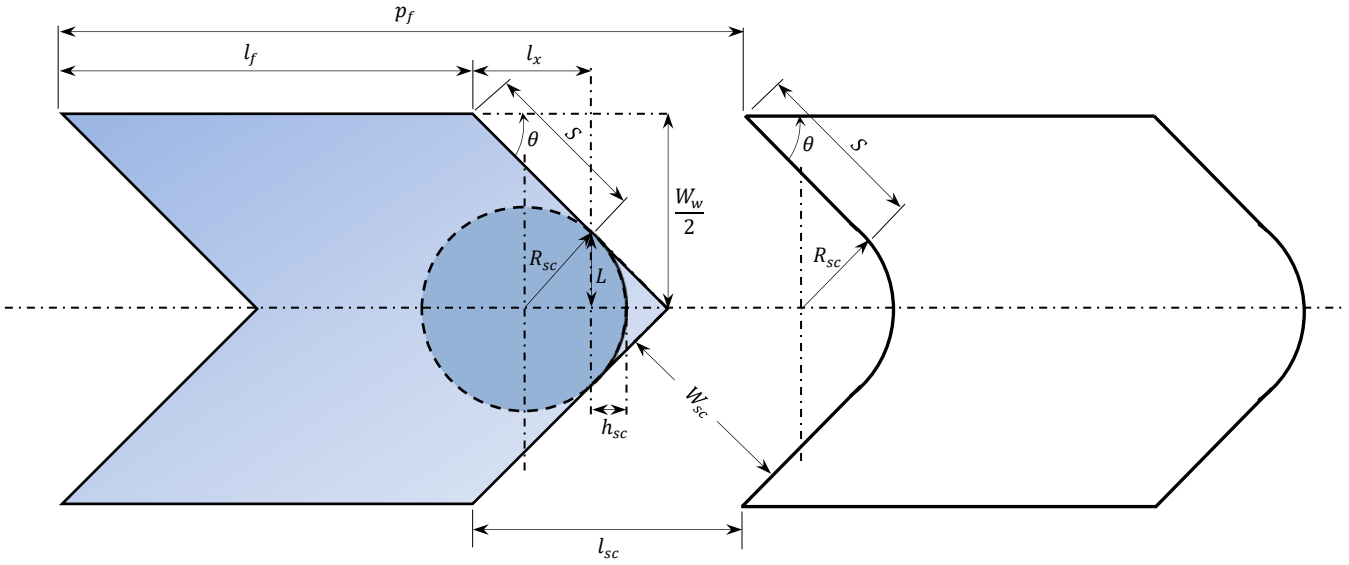

Fig. 7.4: Top view of two chevron fins to explain the parameters used for calculating A_{eff}.

$$R_{sc} = \frac{W_{sc}}{2} \quad (7.4)$$

$$W_{sc} = l_{sc} sin\theta \quad (7.5)$$

$$S = \frac{0.5W_w - L}{sin\theta} \quad (7.6)$$

$$l_x = \frac{0.5W_w - L}{tan\theta} \quad (7.7)$$

$$h_{sc} = R_{sc}(1 - sin\theta) \quad (7.8)$$

$$L = \sqrt{(2h_{sc} \cdot R_{sc}) - h_{sc}^2} \tag{7.9}$$

$$x = \frac{L_{ch} - \left(N_{cf} \cdot l_f + l_{sc}\left(N_{cf} + 1\right) + l_x + h_{sc}\right)}{2} \tag{7.10}$$

θ which represents the chevron fin oblique angle in degrees for Eqs. (7.5-7.8), and in the present experimental work is 30^o.

7.3 CFD Simulation Approach

In the simulations, both geometries of the serpentine minichannel heat sink (MCHS) with and without chevron fins were configured in Solidworks software. In the COMSOL Multiphysics software v.5.2, the geometry plotted by Solidworks was imported for simulation. The governing equations, assumptions and boundary conditions, mesh independent and validation of the numerical solution will be presented in the following subsections below.

7.3.1 Governing Equations

In order to further understand the heat transfer and fluid flow phenomena in MCHS, a finite element method within COMSOL has been employed to perform the simulation within a range of volumetric flow rate ($53 \leq Q_{in} \leq 318\ ml/min$), which corresponds to Reynolds number of 747–4482 using a three-dimensional conjugate numerical simulation. This software has the ability to solve the governing equations which represent the continuity, momentum and energy equation for MCHS test sections. For steady and single-phase laminar and turbulent flow regimes, the Navier-Stokes momentum equations for an incompressible fluid are used as the governing equations of the flow along with the continuity equation (see Eqs. (6.6, 6.13 and 6.14)). While the heat transfer (Energy) equations for the liquid and the solid are described respectively in Eqs. (6.23 and 6.24).

7.3.2 Assumptions and Boundary Conditions

To simplify the numerical solution and analyse the thermal and flow characteristics of the two designs adopted, some simplifications are made as employed by other studies such as Sui et al. (2011); Chai et al. (2013a and 2013b); Kuppusamy et al. (2014); and Lee et al. (2015). A numerical model of the three-dimensional flow and heat transfer in the MCHS was developed under the assumptions that: (1) the fluid flow and heat transfer are steady; (2) flow is incompressible and single-phase in both laminar and turbulent flow regimes; (3) the effect of radiation and buoyancy are negligible; (4) negligible viscous dissipation; (5) smooth surface of the channel.

The computational domain and boundary conditions are shown in Fig. 7.5. No-Slip velocity boundary condition $\mathbf{u_s} = 0$ are used at solid walls and wall temperatures are defined by $T_s = T_{f\ at\ wall}$. At liquid-solid boundaries the conductive and convective heat transfer to the fluid are coupled by imposing heat flux continuity at the interface between the fluid and the solid walls (Qu and Mudawar, 2002b), see Fig. 6.8 in subsection 6.4.2. The boundary conditions of inlet flow are Q_{in} (m^3/s) and $T_{f,in} = 20$ ℃, while the outlet flow boundary condition is $p = p_o$, where p_o is pressure at the outlet (0 Pa), as shown in Fig. 7.5(a).

Except at the bottom of the MCHS, all the outer surface boundaries are considered to be adiabatic. Heating power, q, was applied at the bottom surface of the MCHS using $(-\boldsymbol{n}.(-k_s\nabla T) = q/A_h)$, where $\boldsymbol{n}$ denotes the outward normal vector on the boundary of the domain. To define the thickness and thermal conductivity of a material (Ethoxy) located between the heater and the base of the heat sink, a thin layer boundary condition was employed since COMSOL Multiphysics has the ability to define this boundary as shown in Fig. 7.5(b). The thermal conductivity (k_l) and thickness (d_l) of the Ethoxy layer are respectively 2.2 W/(m.K) and 200 μm.

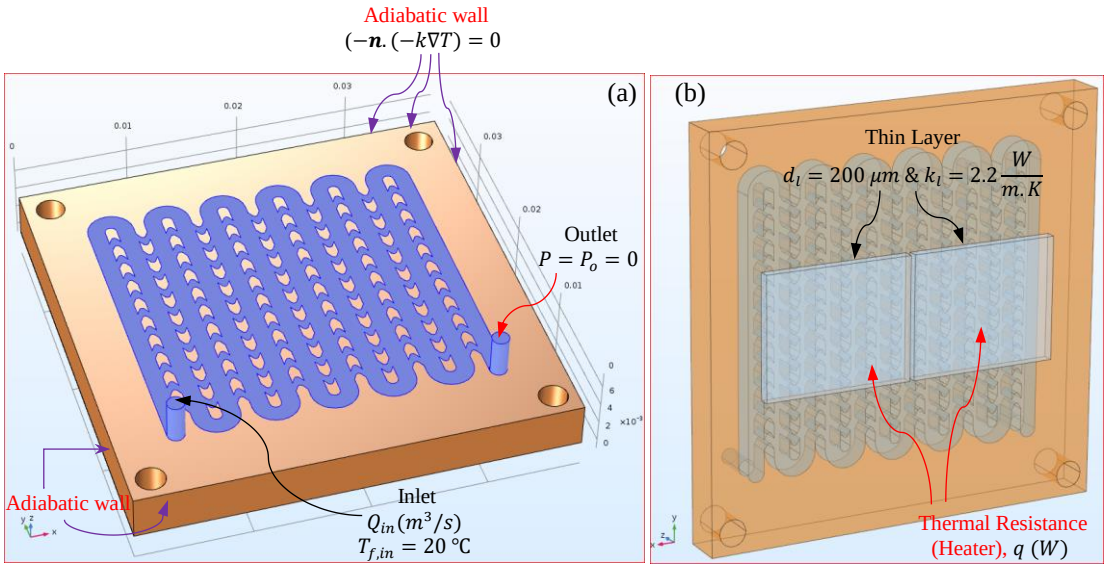

Fig. 7.5: 3-D view and back side of a SMCF design used in simulation to explain the boundary conditions; a) Isometric view; b) Bottom side of the MCHS.

7.3.3 Grid Sensitivity

Grid-dependence of the numerical solutions was tested for the SMPF and SMCF designs. The effects of grid density on the predicted values of the temperature between the heater and heat sink bottom ($T_{junction}$) and the total pressure drop (ΔP) for the MCHS are listed in Table 7.3, where grid 1 is the coarsest and grid 4 is the finest for each MCHS design. Flow in the whole MCHS was solved by employing meshes with additional refinement around the bends and

chevron fins, while the remaining geometry was meshed with a fine mesh element size, see Fig. 7.6. The numerical simulations are carried out at a water flow rate of 106 ml/min (U_{in} = 1 m/s), water inlet temperature set at 20 °C and heat flux of 31 W/cm^2 per heater (two heaters were used as a heat source, and each one give power 50 W (31 W/cm^2)) supplied underneath the MCHS, see Fig. 7.5(b).

Table 7.3: Grid dependency tests.

Heat sink model	Grid No.	Number of elements×10^6	$T_{junction}$ (°C)	E%	ΔP (Pa)	E%
SMPF	1	1.655	57.9	6.2	6632	7.6
	2	2.269	56.4	3.5	6411	4.0
	3	3.372	55.1	1.1	6243	1.3
	4	4.200	54.5	—	6162	—
SMCF	1	4.364	56.42	6.0	1790	9.7
	2	7.116	54.90	3.1	1870	5.7
	3	9.715	53.80	1.0	1941	2.1
	4	11.31	53.25	—	1983	—

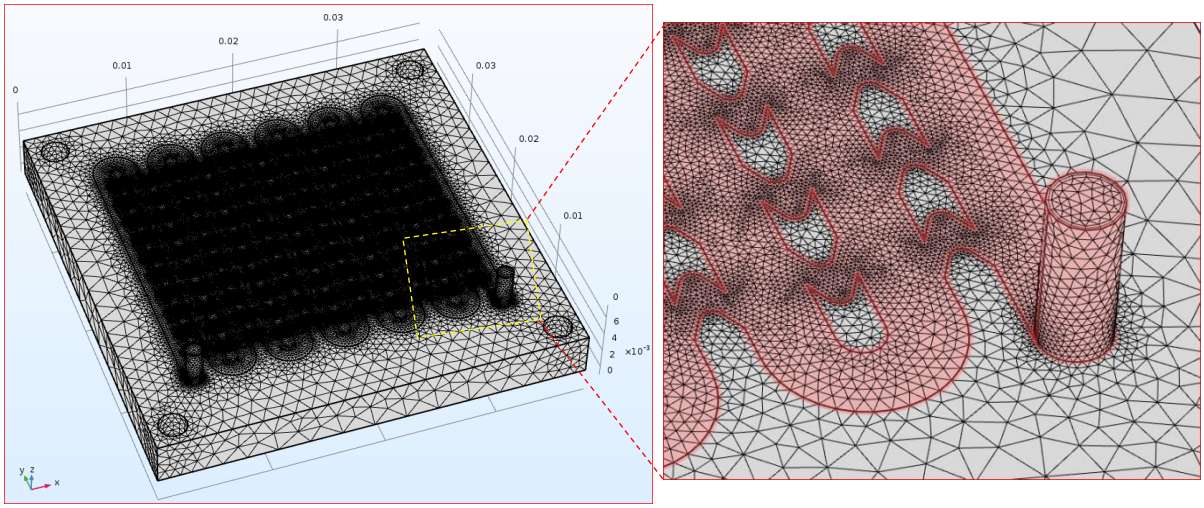

Fig. 7.6: Grid independent mesh for a SMCF design using grid 3.

The heat sink used for both models has the same parameters as used in the experimental work, see Fig. 7.1. The deviation percentage, E, of $T_{junction}$ and ΔP are calculated with respect to the solutions on grid 4 in each case; these are small (~2%), thus grid 3 is employed for all MCHS computations reported below as a suitable compromise between efficiency and accuracy. To avoid the effect of low mesh quality on the solution, mesh quality in the laminar flow regime should be larger than 0.1, and in the present numerical simulation was 0.65. For the turbulent flow regime, the value of y^+ should be equal to 11.06 for the greatest accuracy, this is the value used in grids 3 and 4 in the present work.

7.3.4 Validation Against Previous Studies

The numerical method was validated by comparison with the experimental results of Lee et al. (2012) for oblique fins in microchannels. The dimensions of the straight rectangular MCHS with oblique fins used for validation are tabulated in Table 7.4. Water was used as the coolant with flow rates varying from 375 to 950 *ml/min*, corresponding to a Reynolds number (Re) of 325-780. A uniform heat flux of 65 W/cm^2 was applied in the bottom of the copper heat sink. To reduce the size of the computational problem, symmetry was exploited, and flow was solved in a domain comprising using full width oblique fins and two half–width main microchannels Lee et al. (2013), see Fig. 7.7.

Table 7.4: Details of MCHS dimensions with oblique fin used for validation, all dimensions in mm.

Parameter	MCHS with oblique fin
Size of heat sink	25×25
Main channel width	0.539
Fin width	0.465
Channel depth	1.487
Oblique channel width	0.298
Oblique angle (θ)	26.4
Oblique fin pitch	1.995
Oblique fin length	1.331

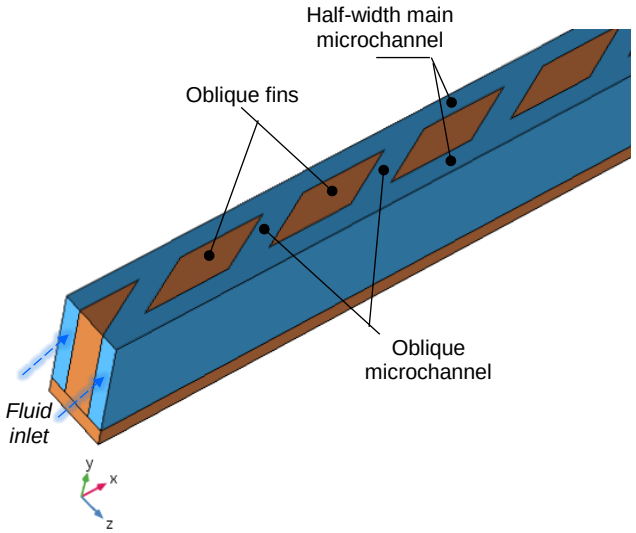

Fig. 7.7: Enlarged view of the computation domain used in the present validation with Lee et al. (2012).

Results were obtained in terms of the Nu_{avg} versus Re as shown in Fig. 7.8, and these agreed reasonably well with those of Lee et al. (2012) with a MAE between their numerical and experimental results of less than 5% and 8%, respectively.

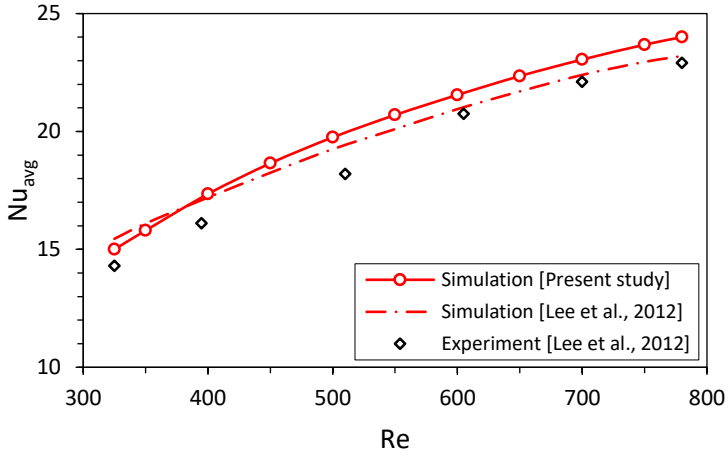

Fig. 7.8: Results of validation with experimental and numerical study of Lee et al. (2012).

7.4 Results and Discussion

7.4.1 The Effect of Volumetric Flow Rate

The effect of volumetric flow rate (Q_{in}) for both of the proposed serpentine MCHSs designs has been studied in terms of total pressure drop (ΔP), total thermal resistance (R_{th}) and average Nusselt number (Nu_{avg}) both experimentally and computationally. Single-phase laminar and turbulent flow regimes are considered depending on the hydraulic diameter of the water inlet tube, which is 1.5 mm for both MCHS models. Fig. 7.9 depicts the experimental data and numerical prediction of ΔP for both MCHSs for heat flux of 31 W/cm^2 per heater supplied underneath the MCHS (two heaters were used and each one dissipate 31 W/cm^2) and volumetric flow rates ranging from 0.053 to 0.318 *l/min*, which corresponds to Reynolds number of 747–4482. The oblique angle (θ), the fin length (l_f) and the fin pitch (p_f) of the chevron fins are respectively 30^o, 1.3 mm and 2.3 mm, (see Fig. 7.1b).

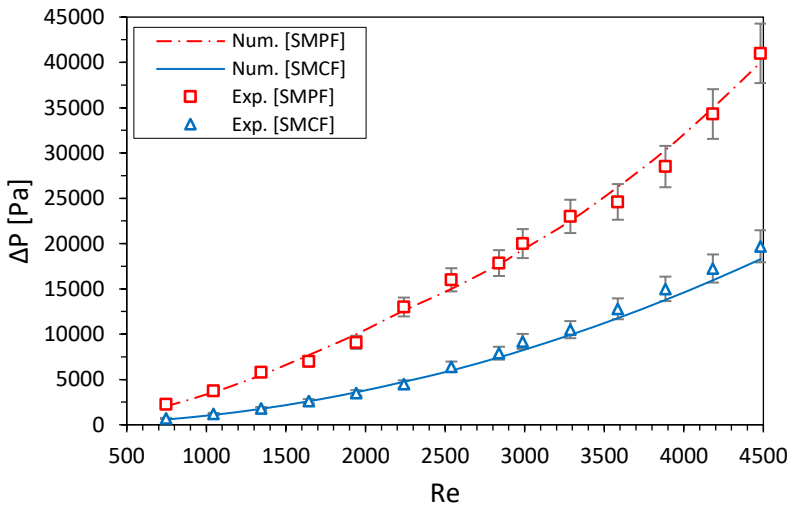

Fig. 7.9: Total pressure drop versus volumetric flow rate for both serpentine MCHSs proposed at input power of 100 W.

Fig. 7.9 shows that generally good agreement was achieved between the experimental and numerical studies for both MCHS designs with MAE of 9.3% and 7.8% for the SMCF and SMPF designs respectively. The ΔP increases as Re increases for both MCHSs. The SMCF heat sink has a lower ΔP compared to a SMPF. This significant reduction in ΔP for the SMCF design is attributed to the flow of water between the chevron fins that form the secondary channels.

From Fig. 7.10, R_{th} decreases monotonically with Re as a result of the decrease in the surface temperature of the MCHS. Good agreement was found between the experimental data and corresponding numerical prediction for both MCHSs, with MAE around 3.2% for both the SMCF and SMPF models. The experimental results indicated that using the SMCF design typically led to a 11% reduction in the thermal resistance, compared with the SMPF, from 0.31 to 0.276 K/W at Re=2240.5 ($Q_{in} = 0.159\ l/min$), see Fig. 7.10. This decrease in the R_{th} is probably due to the re-initialization of both the hydrodynamic and the thermal boundary layers at the leading edge of each oblique fin, which in turn lead to reductions in the thickness of the boundary layers as discussed in subsection 7.4.2. In addition, the effective heat transfer area (A_{eff}) for the SMCF design (2243.6 mm^2) is roughly 17.7% larger than the SMPF one (1846.5 mm^2).

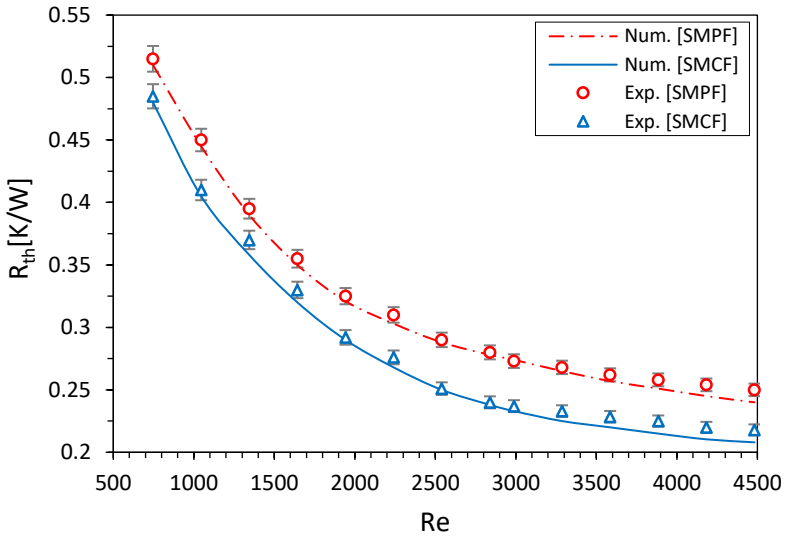

Fig. 7.10: Total thermal resistance versus volumetric flow rate for both serpentine MCHSs proposed at input power of 100 W.

The three components of the thermal resistances at various Reynolds number ranging from 747 to 2832 ($0.053 \leq Q_{in} \leq 0.201\ l/min$) and heat flux of 31 W/cm^2 per heater have been plotted according to Eqs. (3.66, 3.67 and 3.74) proposed by Phillips (1987 and 1990) to give R_{cond}, R_{conv} and R_{bulk}. The experimental total thermal resistance for the present work

calculated by $\left(R_{th} = \frac{T_{surf,max} - T_{f,in}}{q}\right)$ is presented besides the thermal resistance components for both SMPF and SMCF heat sinks for comparison as depicted in Fig. 7.11. Both R_{conv} and R_{bulk} were found to decrease as Re increases, the first is due to the higher heat transfer coefficient while the second is due to the higher flow rate; R_{cond} was constant since the heat sink base thickness is unchanged. For the SMPF design, R_{bulk} was found to be higher than R_{conv} by 33%, this difference is reduced to 28% with the SMCF design, and this is mainly due to the availability of larger flow area which is provided by secondary channels for the SMCF heat sink compared with SMPF, and thereby produce further flow mixing.

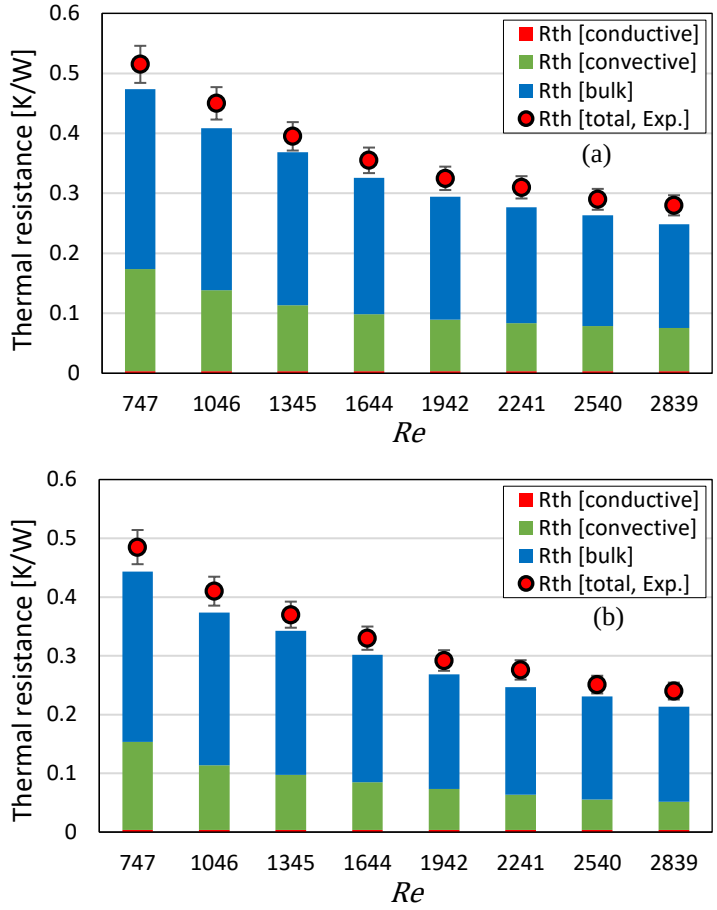

Fig. 7.11: Comparison between the experimental total thermal resistance and three components of thermal resistance suggested by Phillips (1987), versus Re for: (a) SMPF heat sink; and (b) SMCF heat sink at heat flux of 31 W/cm^2 per heater.

Fig. 7.12 shows the contours of pressure along the channel flow at the mid-depth plane of the channel ($H_{ch}/2$) at Re = 2240.5 with heat flux of 31 W/cm^2 per heater for both the SMPF and SMCF designs. It shows that the pressure drop across the SMCF heat sink is around 40% of that for the SMPF. This significant decrease in pressure drop is due to the secondary channel which draws a portion of coolant from the main channel into it and thus reduces the

velocity in the main channel. Fig. 7.12(a) also shows that ΔP in the SMCF is approximately uniform along the channel flow, unlike the SMPF design.

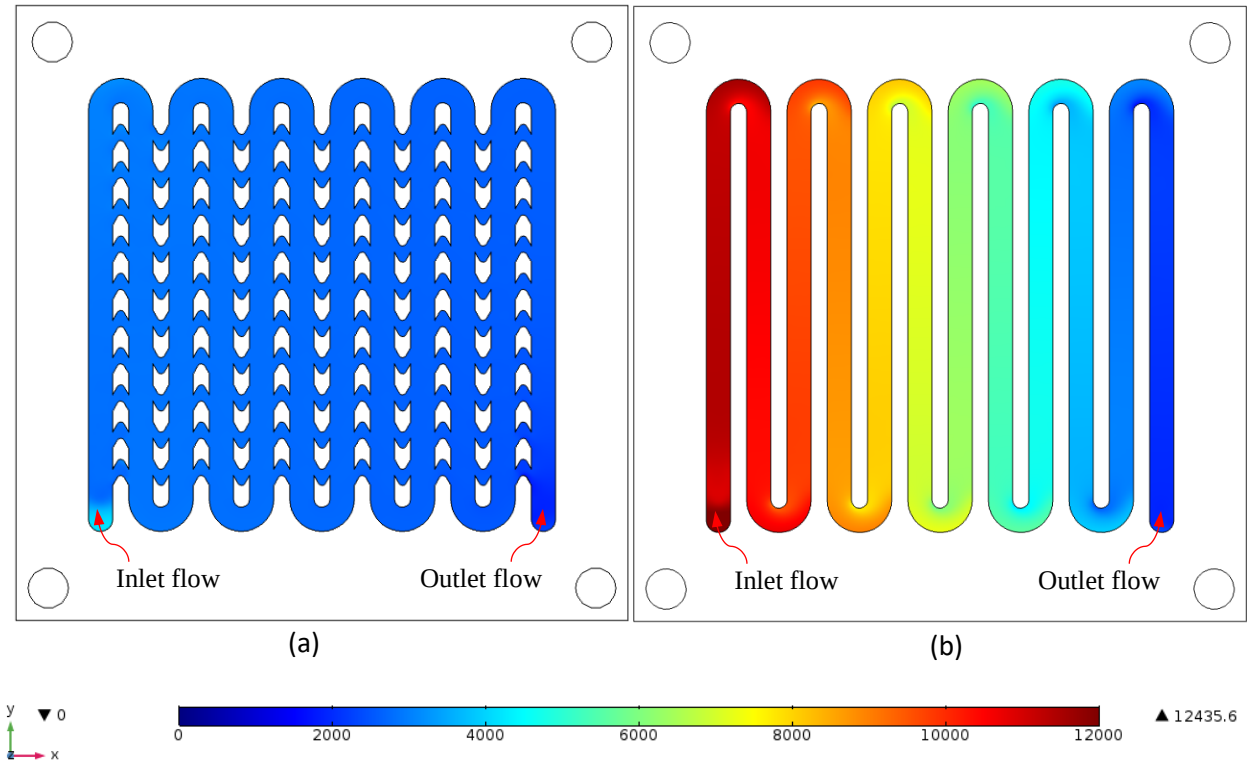

Fig. 7.12: Pressure contours (Pa) for both serpentine MCHSs proposed at Q_{in} of 0.159 *l/min* and heat flux of 31 W/cm^2 per heater; (a) SMCF heat sink; (b) SMPF heat sink.

Fig. 7.13 shows the temperature contours at the mid-depth plane of the channel ($H_{ch}/2$) for Re = 2240.5 with heat flux of 31 W/cm^2 per heater for both the SMPF and SMCF heat sink models. The temperature distributions on the heating surface of the two MCHSs are clearly different, and the wall temperature increases with the flow length due to the sensible heat gain by the coolant. For the SMCF heat sink, the figure demonstrates that breaking the continuous serpentine fin into chevron shaped fins has a significant influence on the temperature field; better fluid mixing between the main and secondary flow channels due to the formation of vortices (as will be explained later in Fig. 7.17), leads to a high temperature gradient over the heating microchannel wall. In addition, the chevron fins lead to a larger convective heat transfer area, thereby enhancing the heat transfer.

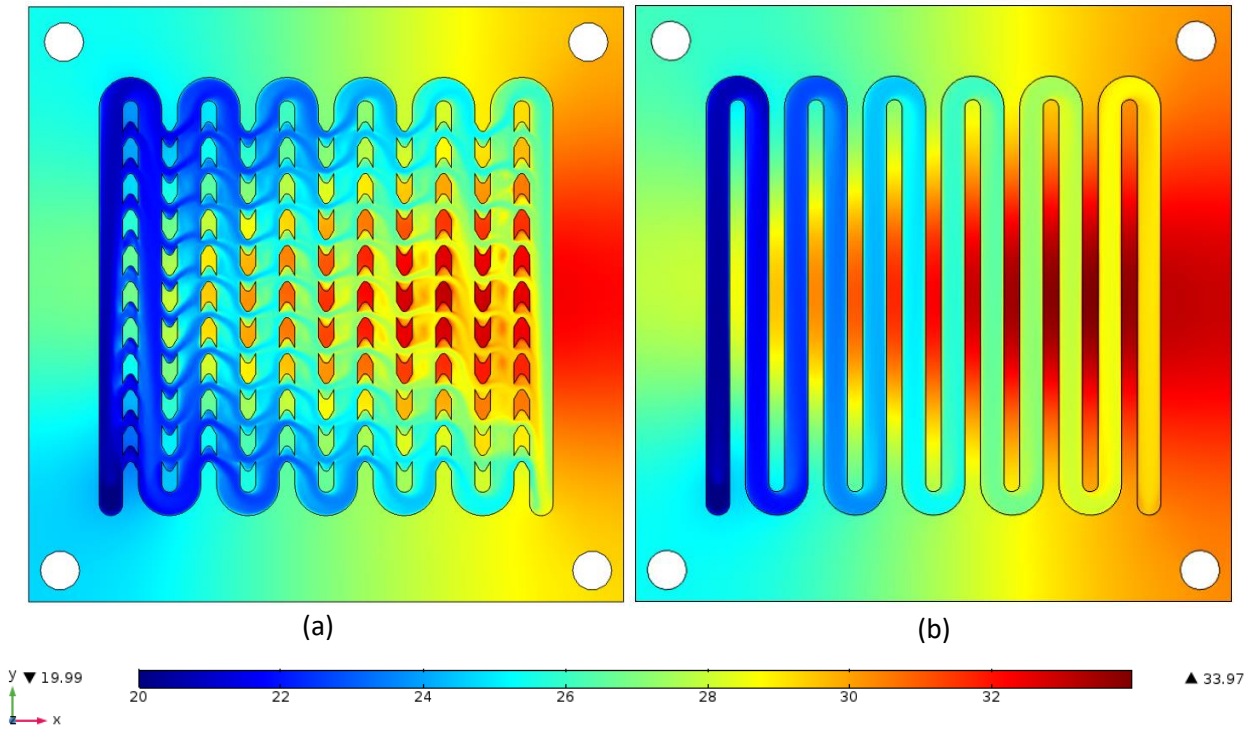

Fig. 7.13: Temperature contours (°C) on the $x-y$ section at $H_{ch}/2$ for both serpentine MCHSs proposed at Q_{in} of 0.159 *l/min* and heat flux of 31 W/cm^2 per heater; (a) SMCF heat sink; (b) SMPF heat sink.

The average channel base temperatures ($T_{w,avg}$) are plotted in Fig. 7.14 at different Re ranging from 747 to 2988 ($0.053 \leq Q_{in} \leq 0.212\ l/min$) with heat flux of 31 W/cm^2 per heater. $T_{w,avg}$ was estimated using the four thermocouples closest to the minichannel base (see Eqs. (4.33 and 4.35) and Fig. 7.3). The $T_{w,avg}$ decreases with Re for both MCHS designs, and SMCF has a lower $T_{w,avg}$ than the SMPF heat sink.

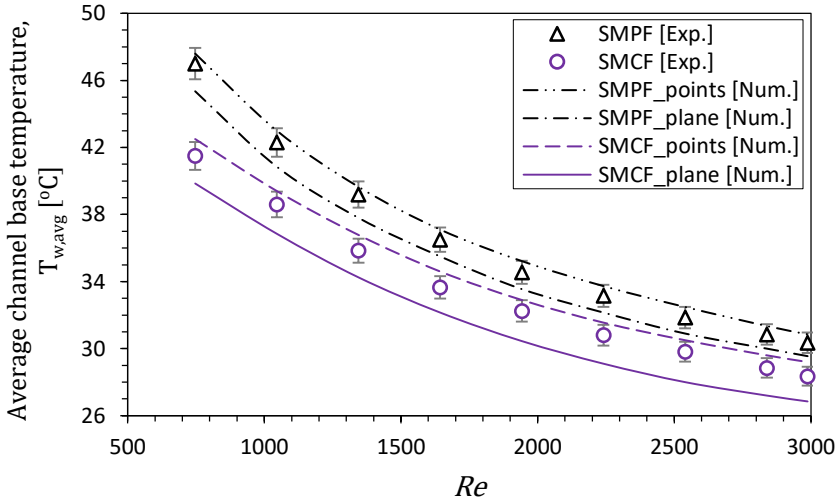

Fig. 7.14: Average channel base temperature versus different Reynolds number for both serpentine MCHSs proposed at heat flux of 31 W/cm^2 per heater.

At the range of Reynolds number, the $T_{w,avg}$ of the SMCF is 6.9–13.2% lower than that of SMPF. The rationale behind the reduction of the wall temperature in the SMCF is due to the

combined effects of thermal boundary layer re-development at the leading edge of each chevron fin and the transfer fluid from the main minichannel to the secondary microchannel through the chevron fin, resulting in better heat transfer.

The average minichannel base temperature $T_{w,avg}$ was estimated using two numerical approaches. The first values, shown in Fig. 7.14, were obtained by calculating the average temperature over the whole minichannel base by creating a cut plane on the $x-y$ section. The second set of values, were obtained using the same approach in the experiments, by taking average temperature of four points distributed at the water inlet side as (5.25, 15.25, 22.75 and 32.75 mm) and located directly below the minichannel base. The use of the four thermocouple locations to calculate average base temperature leads to an over-estimate in base temperature. However, when these are compared with corresponding experimental data, good agreement was found for both heat sinks proposed with MAE of 6.8% for the first case and 2.4% for the second.

Fig. 7.15 shows the average Nusselt numbers (Nu_{avg}) obtained from experiments of both of the SMPF and SMCF heat sinks as a function of Reynolds number varying from 747 to 2988 ($0.053 \leq Q_{in} \leq 0.212\ l/min$) with heat flux of 31 W/cm^2 per heater. To calculate the Nu_{avg} values for the two different serpentine MCHS configurations, Eq. (3.40) was used while Eq. (4.28) was used to determine the average heat transfer coefficient (h_{avg}). Generally, the Nu_{avg} for both configurations increase with Re as the thermal boundary layer thickness decreases with the increased fluid velocity (Lee et al., 2015). However, the heat transfer for the enhanced minichannel with chevron fins is higher than the SMPF heat sink. The simulation predictions are in good agreement with the experimental results, with MAE of 3.2% for both heat sinks.

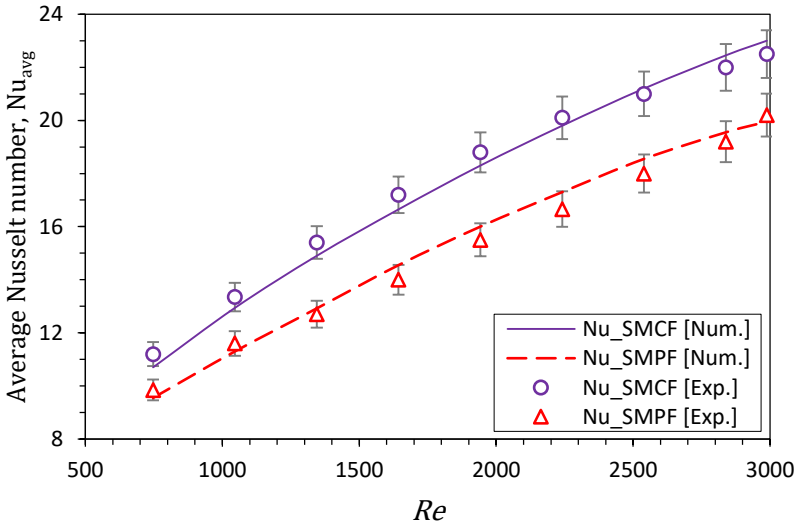

Fig. 7.15: Average Nusselt numbers versus Reynolds number for both serpentine MCHSs proposed at heat flux of 31 W/cm^2 per heater.

7.4.2 The Effect of Fin Oblique Angle

To study effect of the chevron fin oblique angle (θ), solutions are obtained for $\theta = 20^o, 25^o, 30^o, 35^o, 40^o$ and 45^o. The MCHS parameters of base surface area, minichannel height (H_{ch}), minichannel width (W_{ch}), fin width (W_w), fin length (l_f), fin pitch (p_f) and thickness base plate (H_b) are constant for all oblique angles, taking values of 20 × 20 mm^2, 2 mm, 1 mm, 1 mm, 1.4 mm, 2 mm and 0.5 mm respectively, yielding ten parallel minichannels. The volumetric flow rate for these simulations was fixed at 0.2 *l/min* (Re = 2213) with constant heat flux of 100 W/cm^2 supplied underneath the heat sink. The Reynolds number of these simulations was calculated depending on the hydraulic diameter of the minichannel entrance which is D_h=1.334 mm.

Fig. 7.16(a) quantifies the average secondary flow rate diverted from the main minichannel to the secondary microchannel along the streamwise direction at $\theta = 20^0, 30^0$ and 45^0, and the eight secondary microchannels of the minichannel located in the middle heat sink have been chosen for comparison as highlighted in Fig. 7.16(b). As can be seen when θ increases, the secondary flow rate also increases. For example, at $\theta = 20^0$ the average percentage of secondary flow across the heat sink is only 11.4%, indicating that the majority of the flow is confined in the main minichannel and only a small portion of flow is diverted to the secondary microchannel. For $\theta = 45^0$, this percentage increases to 16.6%.

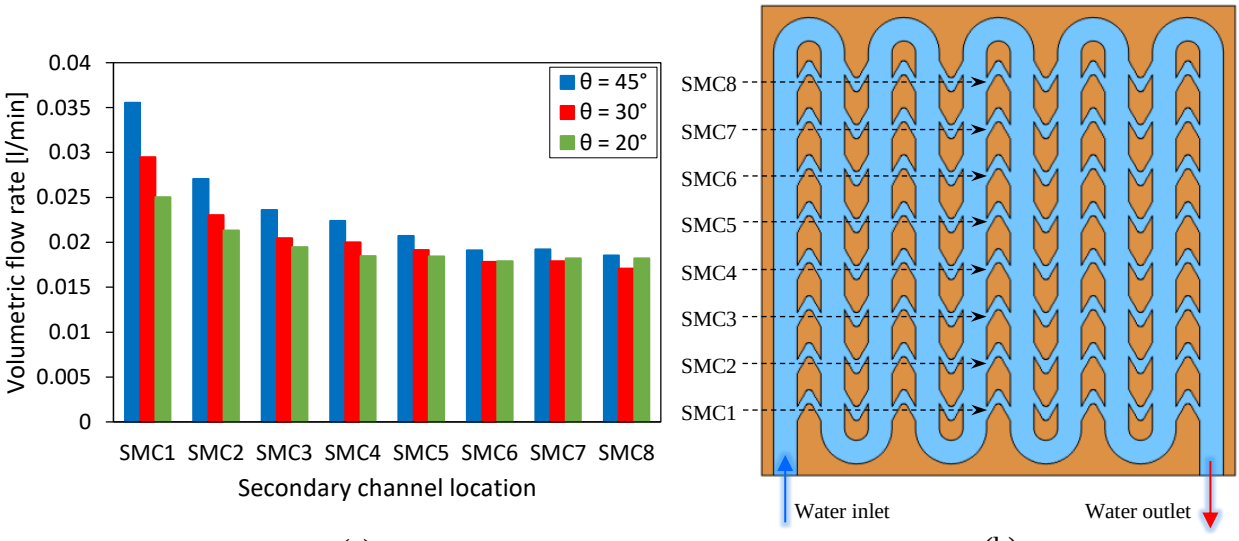

(a) (b)

Fig. 7.16: : Bar chart and top view of a) amount of the secondary flow diverted from the main minichannel to the secondary microchannel at different θ with Q_{in} of 0.2 *l/min* and heat flux of 100 W/cm^2; and b) top view to explain the location of the secondary microchannels (SMC).

Fig. 7.17 shows predicted velocity vectors for the SMCF heat sink design for $\theta = 20^o, 30^o$ and 45^o. The vectors are taken at the mid-depth plane of the minichannel ($H_{ch}/2$) at $Q_{in} = 0.2\ l/min$ and uniform heat flux of 100 W/cm^2. The chevron fin located near the main curved

minichannel was enlarged to show the flow structures more clearly. The figure shows that when θ decreases from 45^o to 20^o the velocity in the main curved minichannel increases, since a greater proportion of the water flows in the mainstream minichannel due to the decreasing secondary microchannel width.

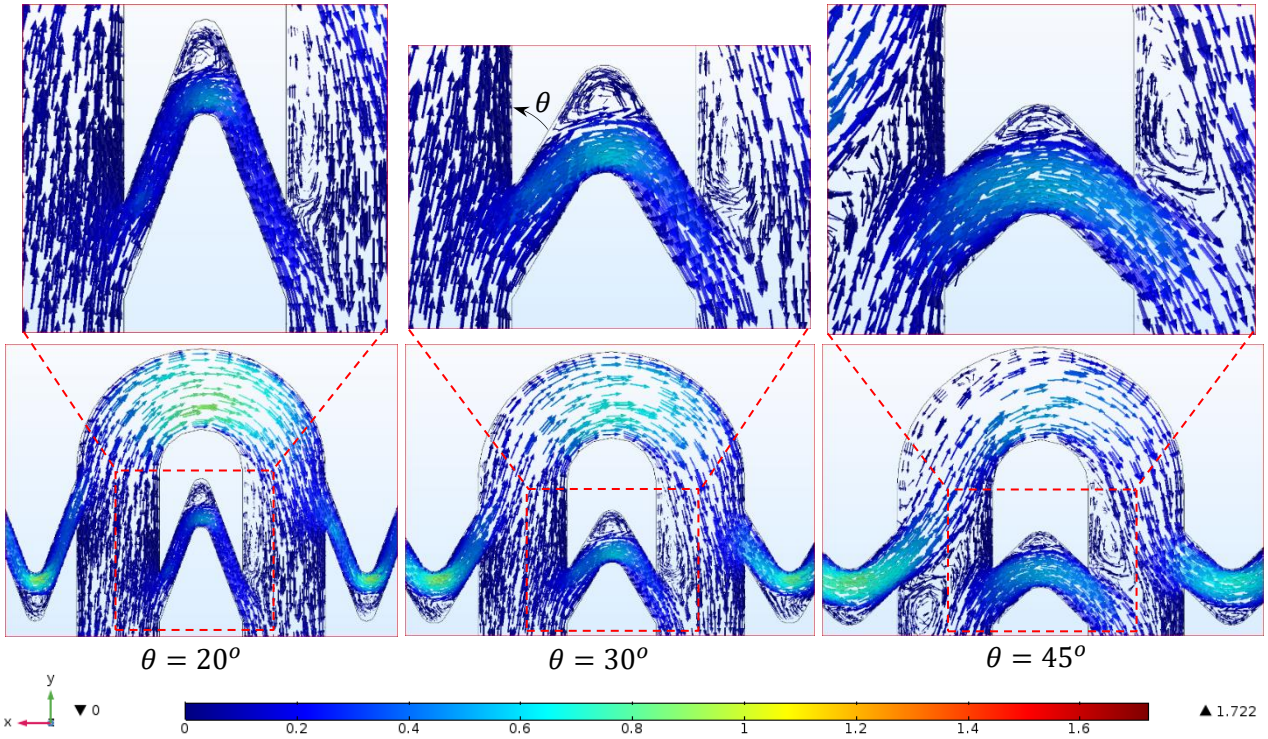

Fig. 7.17: Velocity vectors (m/s) for SMCF models with three different θ proposed at $Q_{in} = 0.2\ l/min$ and heat flux of 100 W/cm^2.

In all cases, a vortex is generated at the lower corner of the chevron fin. The recirculating flow region becomes bigger as θ increases and this diverts more liquid from the main minichannel into the secondary microchannel (see Fig. 7.16). This is due to a wider secondary microchannel which led to an increase in the momentum of the secondary flow and disrupts the recirculation region and boundary layer development. This behaviour has also been reported by Lee et al. (2012), who concluded that it enhances fluid mixing and heat transfer.

Fig. 7.18 shows the velocity vectors in the SMCF heat sink design which is taken at the first two of the minichannels from the inlet side at the mid-depth plane of the channel ($z = H_{ch}/2$) in the $x - y$ plane with $\theta = 30^o$, $Q_{in} = 0.2\ l/min$ and heat flux of 100 W/cm^2. As seen in the figure, fluid is diverted from the secondary microchannel to the main flow of the adjacent minichannel enhancing fluid mixing. In addition, the presence of the chevron fin in the enhanced microchannel configuration disrupts the momentum and thermal boundary layers at the leading and trailing edges of each section, and this re-development of the boundary layer reduces its thickness, promoting improved heat transfer.

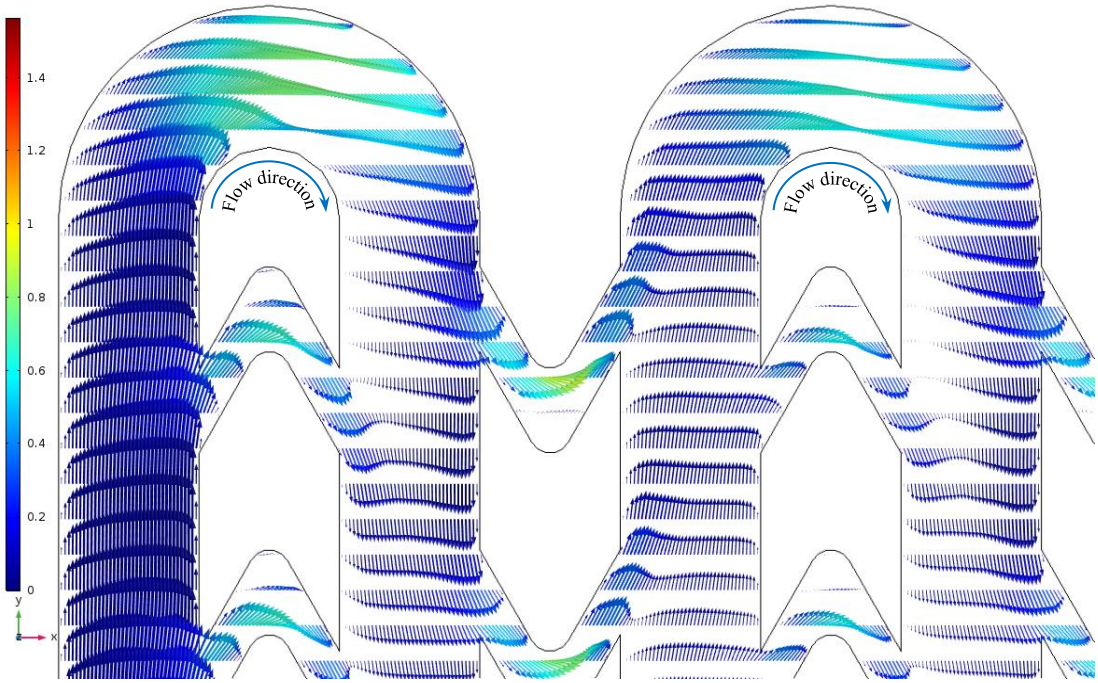

Fig. 7.18: Velocity vector (m/s) distribution along the streamwise at $Q_{in} = 0.2\ l/min$ and heat flux of 100 W/cm^2.

Fig. 7.19 shows predictions of the pressure drop (ΔP) and total thermal resistance (R_{th}) for six different angles used with a constant volumetric flow rate of $Q_{in} = 0.2\ l/min$ and uniform heat flux of 100 W/cm^2. The ΔP of the SMCF heat sink with $\theta = 20^o$ is the highest, as most of the coolant flows through the main minichannel and only a small fraction of coolant enters the secondary microchannel. The ΔP of the MCHS with $\theta = 45^o$ is lower than the MCHS with $\theta = 30^o$. This is due to the large distance (gap) formed in the secondary microchannel as θ increases. The width of the secondary microchannels (W_{sc}) for oblique angles of $\theta = 20^o, 30^o$ and 45^o were found to be respectively 0.2, 0.3 and 0.42 mm.

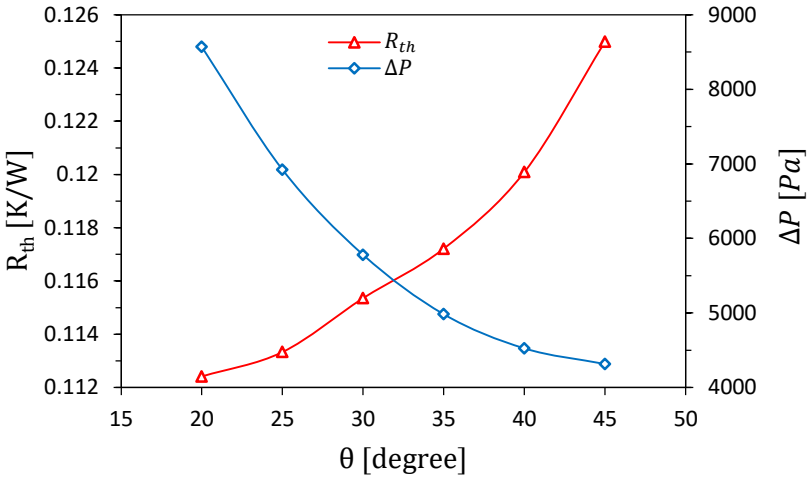

Fig. 7.19: Total pressure drop and total thermal resistance at different θ in a SMCF design with $Q_{in} = 0.2\ l/min$ and heat flux of 100 W/cm^2.
[201]

Fig. 7.19 also shows that R_{th} decreases as θ decreases: R_{th} decreases from 0.125 K/W at $\theta = 45^o$ to 0.112 K/W at $\theta = 20^o$. This decrease in R_{th} for smaller θ values is caused by an increase in the convective heat transfer area (A_{eff}). For example, when θ is decreased from 45° to 20°, A_{eff} increases by 30.6%, from 1212.8 mm^2 at $\theta = 45^o$ to 1583.7 mm^2 at $\theta = 20^o$. Decreasing θ also leads to a reduction in the secondary microchannel width (W_{sc}), which in turn leads to larger flow velocities in the main straight and curved minichannels, which in combination with the larger A_{eff} leads to enhanced heat transfer and correspondingly lower values of R_{th}.

7.4.3 The Effect of the Secondary Microchannel Width

Fig. 7.20 shows the effect of varying the secondary microchannel width W_{sc} on the pressure drop ΔP and total thermal resistance R_{th} at a volumetric flow rate Q_{in} = 0.2 l/min with uniform heat flux of 100 W/cm^2. Five different values of W_{sc} were analysed, and both the minichannel width W_{ch} and fin width W_w were set at 1 mm, while the chevron fin length l_f varies between 0.8 mm and 1.6 mm to produce designs with W_{sc} = 0.2, 0.3, 0.4, 0.5 and 0.6 mm. The fin pitch p_f and the oblique angle θ for these five cases are fixed at 2 mm and 30°, respectively. Fig. 7.20 shows that ΔP increases monotonically when W_{sc} decreases; for example, ΔP increases threefold from 3110.4 Pa at $W_{sc} = 0.6$ mm to 9462.1 Pa at $W_{sc} = 0.2$ mm. This is due to the fact that the majority of the flow for $W_{sc} = 0.2$ mm is confined in the main minichannel, with only a small fraction being diverted to the secondary microchannel.

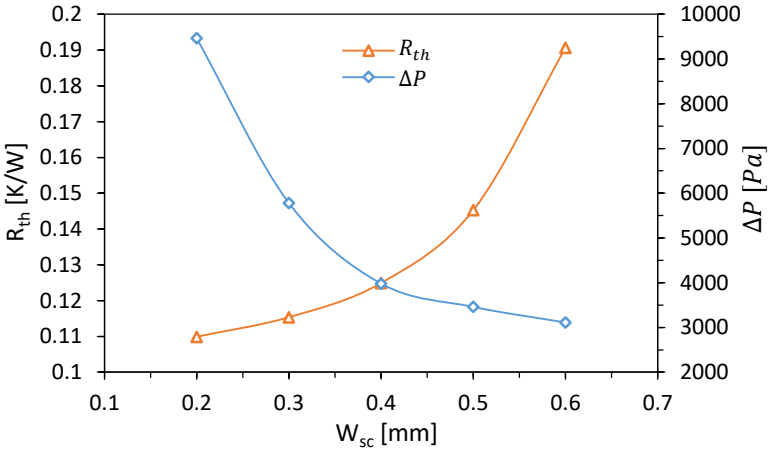

Fig. 7.20: Total pressure drop and total thermal resistance at different W_{sc} in a SMCF design with $Q_{in} = 0.2\ l/min$ and heat flux of 100 W/cm^2.

When W_{sc} decreases from 0.6 mm to 0.2 mm, R_{th} also decreases by 42%, from 0.19 K/W at $W_{sc} = 0.6$ mm to 0.11 K/W at $W_{sc} = 0.2$ mm. This is due to an increase in convective heat transfer area (A_{eff}) between the coolant and the minichannel wall and it was found that when W_{sc} decreases from 0.6 mm to 0.2 mm, A_{eff} increases by 18%. Additionally, this increase in

A_{eff} leads to a reduction in the maximum surface temperature ($T_{surf,max}$), which also decreases the thermal resistance. For example, $T_{surf,max}$ for the SMCF heat sink type with $W_{sc} = 0.2$ mm is 64.0 °C, compared to 96.3 °C with $W_{sc} = 0.6$ mm. The numerical results also showed that the water velocity in the main serpentine minichannel for the SMCF heat sink with a narrow secondary microchannel width is always higher than those for the SMCF heat sinks having a wide secondary microchannel width, since a small portion of the water is diverted into secondary microchannels. These results suggest that reducing W_{sc} can disrupt the thermal boundary layer more effectively, reducing the wall temperature and leading to higher heat transfer and smaller R_{th}.

7.4.4 The Effect of Heat Flux

The heat flux is now varied at 25 W/cm^2 increments to 25, 50 and 75 W/cm^2 to examine its effect on the SMCF heat sink design in terms of pressure drop (ΔP) and maximum surface temperature ($T_{surf,max}$). Each heat flux condition is examined for a volumetric flow rate of 0.06, 0.084, 0.12, 0.156 and 0.18 *l/min*, which corresponds to Reynolds number of 664–1992. The parameters of the SMCF heat sink used in these simulations were the same as in subsection 7.4.2, with $\theta = 30^0$. Fig. 7.21 demonstrates that ΔP decreases with increasing heat flux; for example, when heat flux is increased from 25 to 75 W/cm^2 at $Q_{in} = 0.12\ l/min$ (Re = 1328) ΔP decreases by 6.5%. This is due to the reductions in viscosity and density of water with increasing temperature.

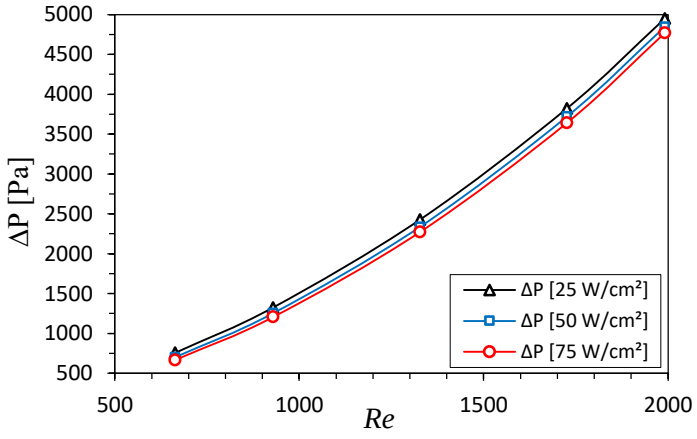

Fig. 7.21: Variation in pressure drop through SMCF with different applied heat flux and Reynolds number.

Fig. 7.22 quantifies the effect of heat flux and volumetric flow rate on the maximum surface temperature ($T_{surf,max}$). As expected $T_{surf,max}$ increases with increasing heat flux and reduces with increasing volumetric flow rate. For example, at the lowest $Q_{in} = 0.06\ l/min$ (Re = 664), $T_{surf,max}$ increases from 50.13 °C at 25 W/cm^2 to 108.65 °C at 75 W/cm^2,

whereas at the highest $Q_{in} = 0.18\ l/min$ (Re = 1992), $T_{surf,max}$ increases from 32.7 °C at 25 W/cm^2 to 57.5 °C at 75 W/cm^2.

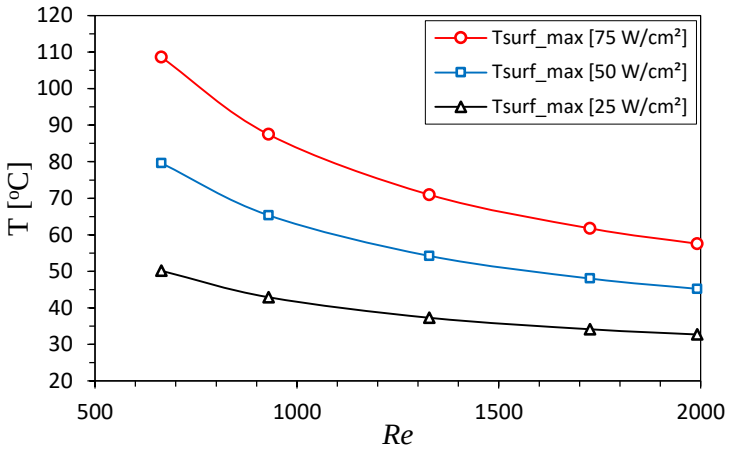

Fig. 7.22: Maximum surface temperature versus Reynolds number at different heat flux.

7.5 Performance Evaluation Analysis

The experimental and numerical results showed that the SMCF heat sink design can simultaneously reduce both the total thermal resistance and pressure drop and enhance Nu_{avg} when compared to the SMPF heat sink model. Therefore, the benefits and disadvantages of the new serpentine MCHS are assessed using a standard metric, the thermal performance factor (P_f) based on the same pumping power consumption, as defined in (Gong et al., 2011 and Zhao et al., 2016):

$$P_f = \frac{Nu_{SMCF}/Nu_{SMPF}}{\sqrt[3]{\Delta P_{SMCF}/\Delta P_{SMPF}}} = \frac{E_{Nu}}{\sqrt[3]{E_{\Delta P}}} \tag{7.11}$$

where, Nu_{SMCF}, ΔP_{SMCF} and Nu_{SMPF}, ΔP_{SMPF} represent the average Nusselt number, pressure drop of comparison model (SMCF) and standard model (SMPF) obtained from numerical simulation, respectively. While E_{Nu} and $E_{\Delta P}$ denote the average heat transfer enhancement and pressure drop penalty parameters (Chai et al., 2013b), respectively. The values of the normalized enhancement parameters E_{Nu} and $E_{\Delta P}$ as well as the P_f are plotted as functions of θ and β ($\beta = W_{sc}/W_{ch}$) as depicted in Figs. 7.23 and 7.24, at uniform heat flux of 100 W/cm^2 and $Q_{in} = 0.138\ l/min$ ($Re = 1524$) for the SMPF and SMCF heat sinks. The geometrical parameters of the heat sink such as base surface area, minichannel height (H_{ch}), minichannel width (W_{ch}), fin width (W_w) and thickness base plate (H_b) of both heat sink models were kept constant to be as follows; 20×20 mm^2, 2 mm, 1 mm, 1 mm and 0.5 mm, respectively. For the SMCF heat sink the fin pitch (p_f) is constrained at 2 mm for all θ and β numerical analysis, yielding ten parallel minichannels. With θ, the chevron fin

length (l_f) was fixed at 1.4 mm, whereas for the β analysis it is varied ($0.8 \leq l_f \leq 1.6$ mm) to produce designs with W_{sc} between 0.2 mm and 0.6 mm.

Fig. 7.23 shows the variation of E_{Nu}, $E_{\Delta P}$ and P_f with θ ($20^o \leq \theta \leq 45^o$). As shown by the E_{Nu} line, since the value is always > 1, this implies that the SMCF is superior to SMPF in heat transfer performance. It is found that E_{Nu} increased slightly from θ= 20° to 30° and then gradual reduction was observed when $\theta > 30^o$. This phenomenon is probably due to the recirculation (vortex) generated at a larger chevron oblique angle which degrades convective heat transfer. This approach is consistent with the findings of DeJong and Jacobi (DeJong and Jacobi, 2003), who found that the size of the recirculation zone increases with louvre angle and decreases heat transfer significantly for louvered-fin arrays. Additionally, the heat transfer area has a significant effect on the heat transfer performance since A_{eff} increases as θ decreases in the SMCF heat sink. Furthermore, less fluid is transferred from the main minichannels when θ decreases thereby enhancing heat transfer.

The increase of E_{Nu} is accompanied by a reduction in $E_{\Delta P}$, and since $E_{\Delta P}$ is always < 1 the pressure drop in the SMCF is lower than for the SMPF. It is observed that $E_{\Delta P}$ decreases by 21.3% within the θ range. As a result, improvements in P_f were obtained since all values are > 1. It is found that P_f increases significantly until θ= 40°, followed by a slight reduction when $\theta > 40^o$.

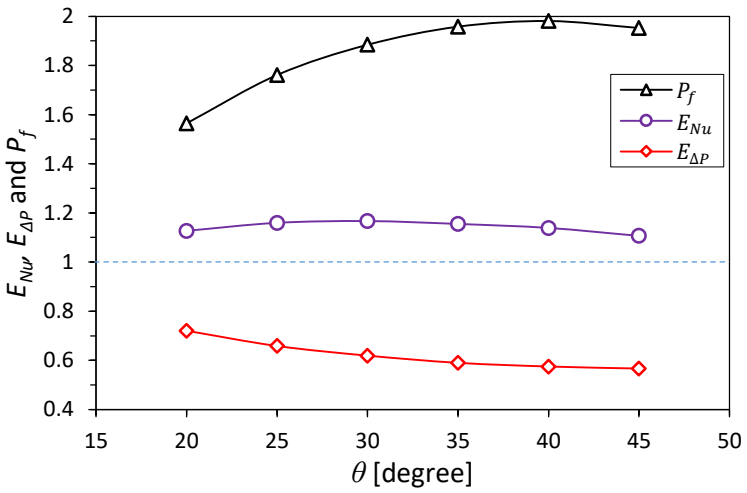

Fig. 7.23: Variation of E_{Nu}, $E_{\Delta P}$ and P_f versus θ with $Q_{in} = 0.138\ l/min$ and heat flux of 100 W/cm^2.

The effect of β is analysed for cases with $\theta = 30^o$. Fig. 7.24 demonstrates the variations of E_{Nu}, $E_{\Delta P}$ and P_f with β in the range ($0.2 \leq \beta \leq 0.6$). A tremendous reduction is observed in E_{Nu} with increasing β, and the value of E_{Nu} became approximately 1 at $\beta = 0.4$, which signifies that the Nu_{avg} of the SMCF heat sink equals that of the SMPF model. When $\beta >$ 0.4, E_{Nu} reduces drastically to reach 0.76 at $\beta = 0.6$. It can be inferred that the Nu_{avg} of the

SMCF model increases as W_{sc} reduces and this contributes to the increase of the convective heat transfer area (A_{eff}) as described previously. Additionally, when W_{sc} decreases the flow rate diverted from the main minichannel to the secondary microchannel also decreases which in turn leads to larger velocities in the minichannel and hence increased fluid mixing and heat transfer in the bends.

With regard to $E_{\Delta P}$ it reduces monotonically when β increases. Since $E_{\Delta P} < 1$ for all values of β, the values of P_f is higher than one for all values of β. In fact P_f reduces sharply when $\beta > 0.3$. As mentioned earlier, the increase of β or W_{sc} reflects the reductions in A_{eff} and, consequently, reductions in E_{Nu} or Nu_{avg}.

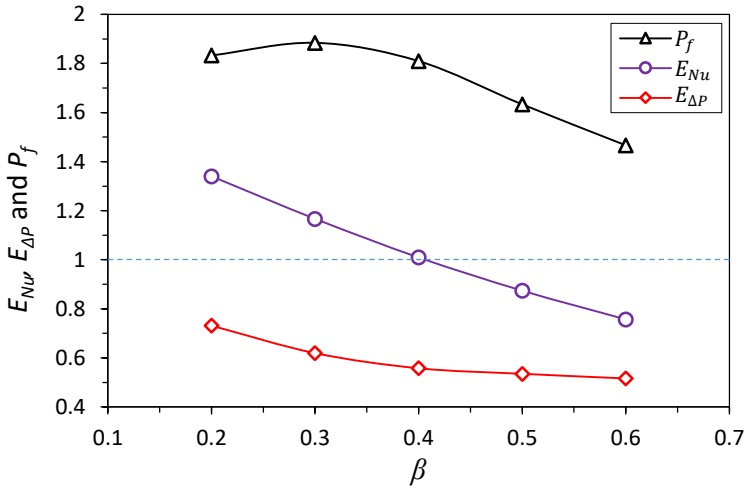

Fig. 7.24: Variation of E_{Nu}, $E_{\Delta P}$ and P_f versus β with $Q_{in} = 0.138\ l/min$ and heat flux of 100 W/cm^2.

7.6 Design Optimisation of the SMCF

An optimisation analysis of the SMCF heat sink has explored the effect of three design variables; namely the minichannel width, W_{ch}, the number of the minichannels, N_{ch}, and the chevron fin oblique angle, θ, on R_{th} and ΔP. The optimisation problem is defined as follow:

Objective function: min (R_{th}) and min (ΔP)

Subject to: $0.5\ mm \leq W_{ch} \leq 1.5\ mm$

$$8 \leq N_{ch} \leq 13$$

$$20^o \leq \theta \leq 45^o$$

The heat sink surface area, substrate thickness, minichannel depth (H_{ch}), fin length (l_f) and fin pitch (p_f) were fixed to be respectively 25 × 25 mm^2, 0.5 mm, 2 mm, 1.4 mm and 2 mm. A constant heat flux of 75 W/cm^2 was supplied under the heat sink with a volumetric flow

rate of 0.16 l/min at 20 ^{o}C. The goal is to construct a Pareto front of non-dominated solutions, from which an appropriate compromise design can be chosen.

The Pareto front is obtained by building accurate metamodels of both ΔP and R_{th}, as a function of the three design variables. The metamodels are constructed using the R_{th} and ΔP values extracted from numerical simulations carried out at 50 Design of Experiments (DoE) points obtained using Optimal Latin Hypercubes (OLHCs), via a permutation genetic algorithm using the Audze-Eglais potential energy criterion to create an efficient distribution of DoE points (Gilkeson et al., 2014). The points are distributed as uniformly as possible using a criterion of minimising the potential energy of repulsive forces which are inverse square functions of the separation of DoE points (Narayanan et al., 2007), see Eq. (3.79). Fig. 7.25 illustrates the distribution of 50 DoE points with the three design variables used.

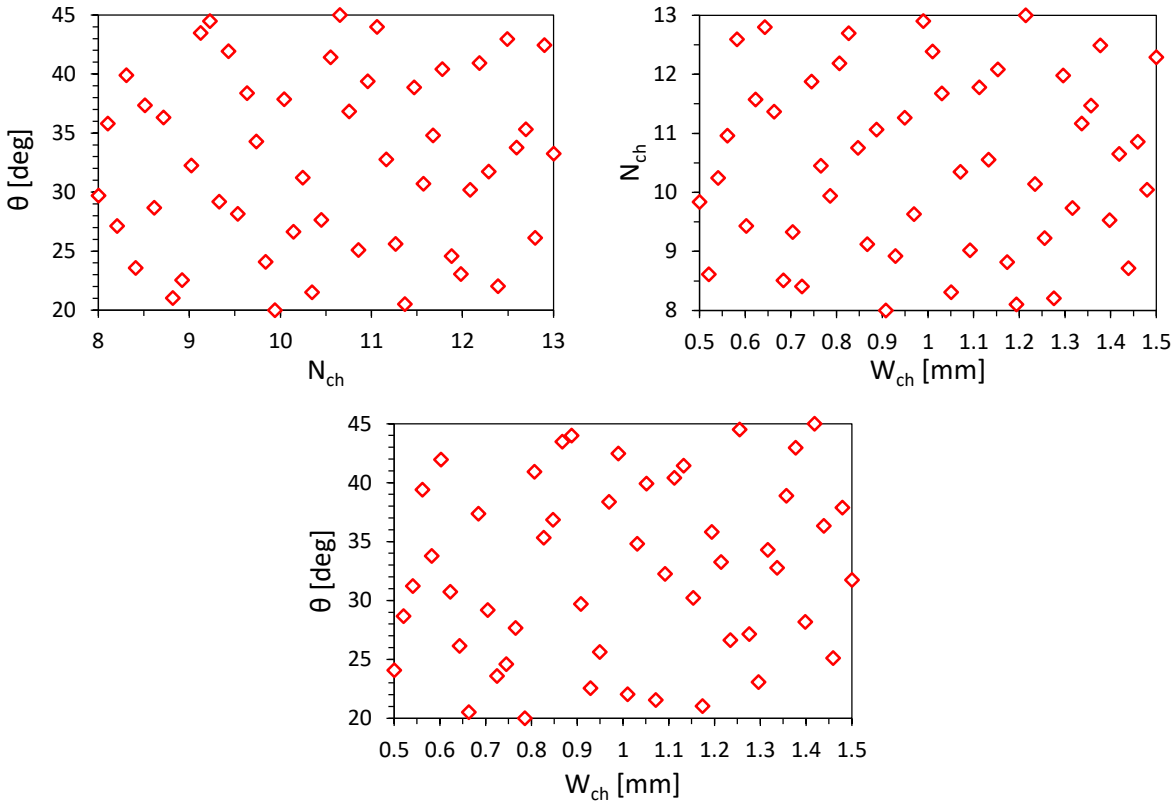

Fig. 7.25: Distribution of uniform Optimal Latin Hypercube DoE points used for metamodel building, 50 points.

Metamodels for R_{th} and ΔP throughout the design space are built using a Moving Least Squares (MLS) method (Leitão et al., 2007), with a second order (Quadratic) base polynomial, where a Gaussian weight decay function, w_i, is used to determine the weighting of points in the regression coefficients at each point, see Eq. (3.90). The surface functions R_{th} and ΔP in terms of the design variables W_{ch}, N_{ch} and θ are shown in Figs. 7.26 and 7.27 respectively, which are built using HyperStudy v12 software (HyperWorks, 2015).

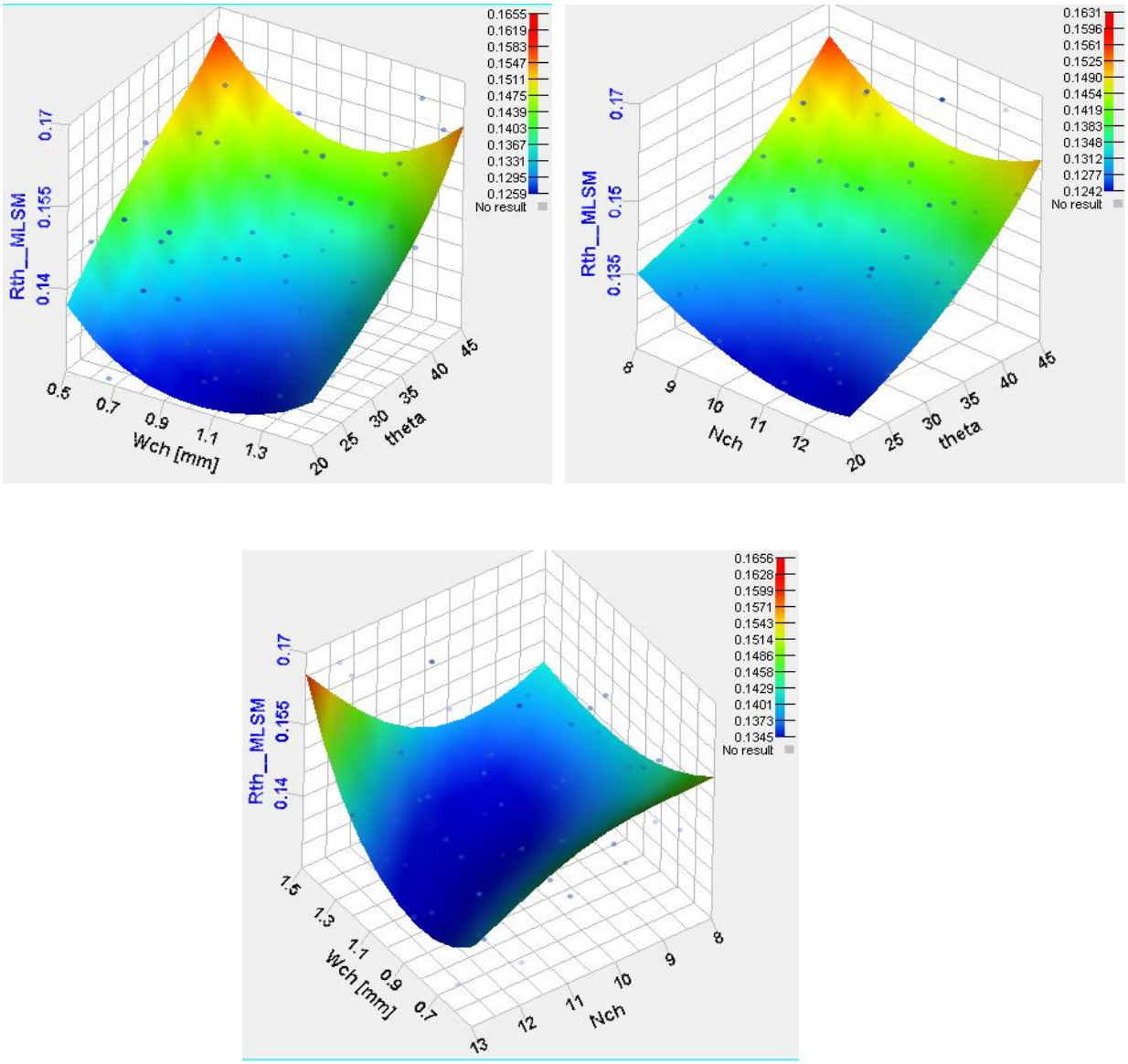

Fig. 7.26: MLS method response surfaces of total thermal resistance for the SMCF heat sink model.

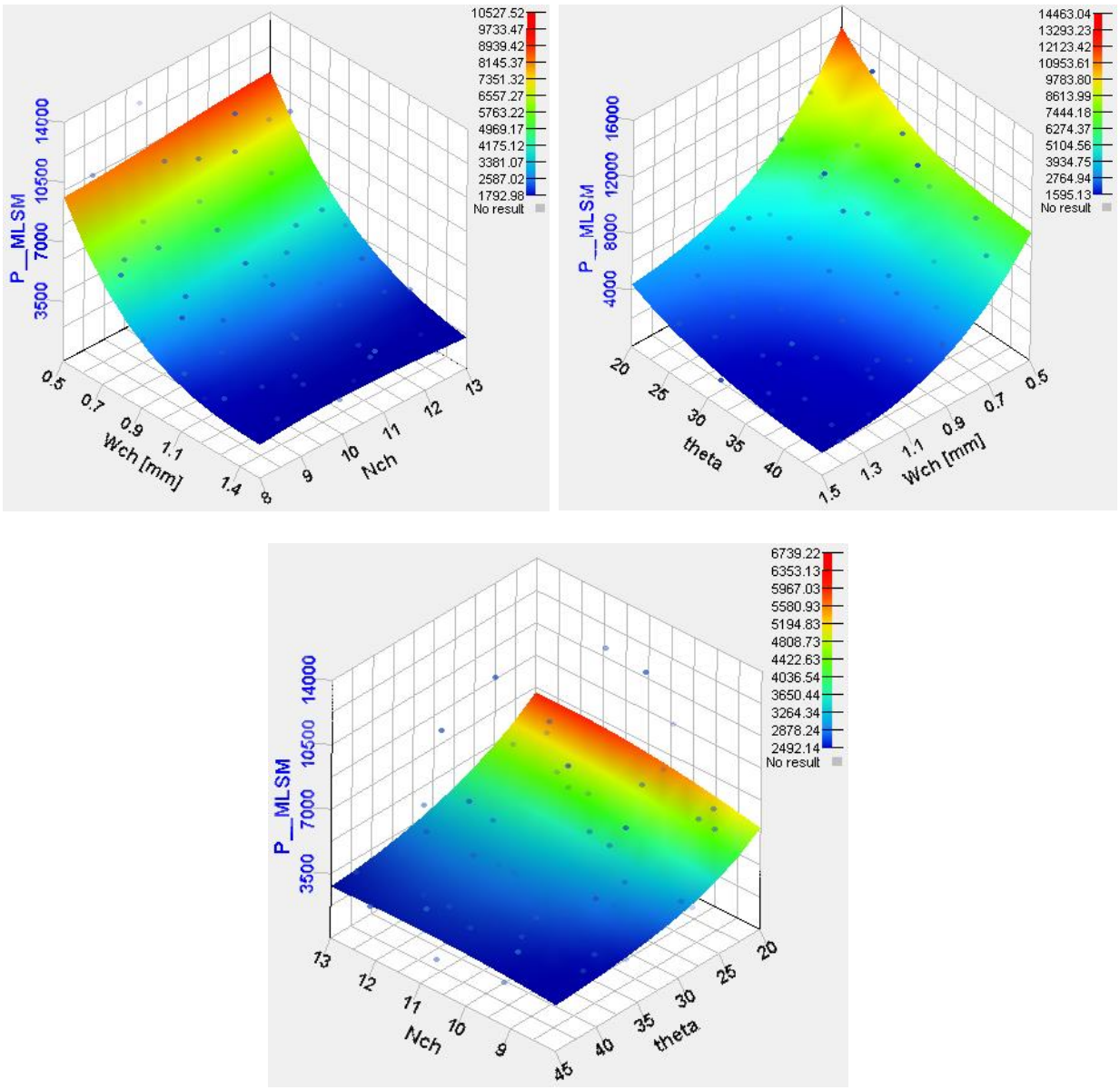

Fig. 7.27: MLS method response surfaces of total pressure drop for the SMCF heat sink model.

From the metamodels obtained, it is observed that changes in W_{ch}, N_{ch} and θ lead to conflicting requirements for each objective function. Fig. 7.28 is a simple design trends which show how the objective functions are influenced by the design variables.

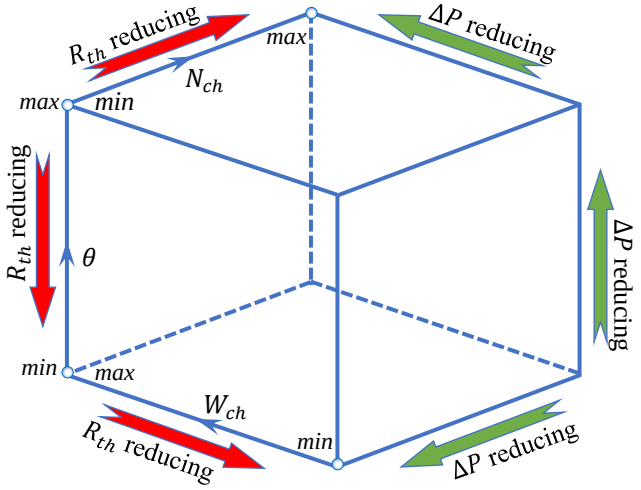

Fig. 7.28: Global design trends obtained from the metamodels.

The Pareto front is calculated using a multi-objective genetic algorithm (MOGA) approach based on the work of (Deb et al., 2002 and Abraham et al., 2005). Points on the Pareto front are non-dominated in the sense that it is not possible to decrease any of the objective functions (i.e. ΔP or R_{th}) without increasing the other objective function. Fig. 7.29 shows the values of ΔP and R_{th} at all of the DoE points and the Pareto front that is constructed from them.

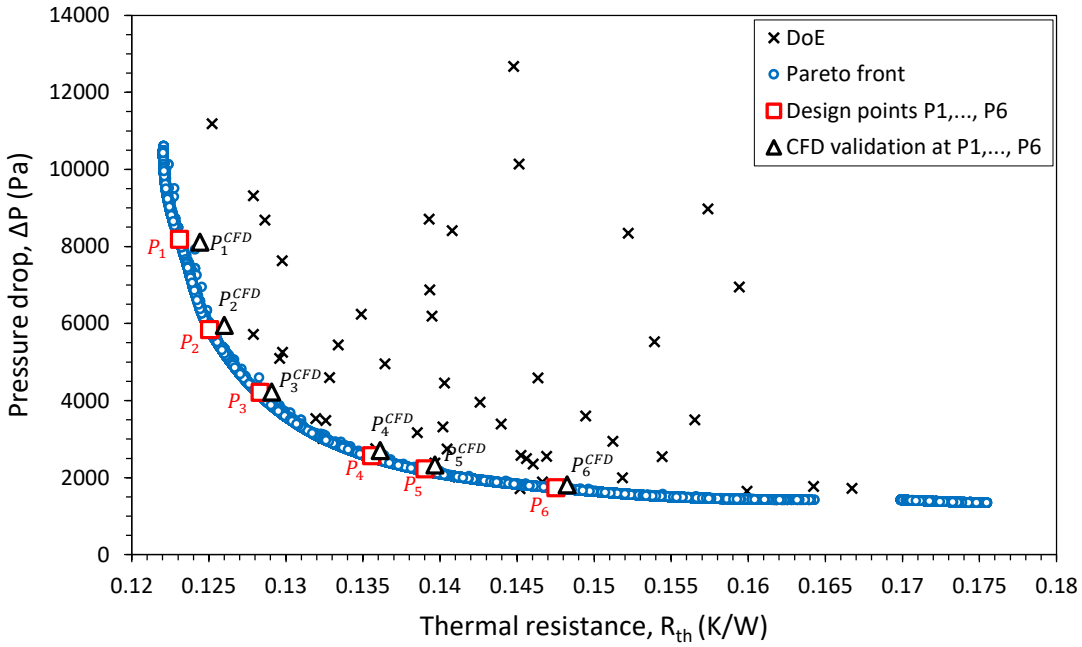

Fig. 7.29: Pareto front showing the compromises that can be struck in minimising both R_{th} and ΔP together with six representative design points (e.g. P_1 ,…, P_6) used for the minichannel performance analysis illustrated in Table 7.5.

Table 7.5 shows six points on the Pareto front (P_1-P_6) and a comparison between the calculated values of ΔP and R_{th} from the metamodels at these points and from the full numerical simulations (CFD). Agreement between the metamodel and full numerical

predictions is good in all cases, demonstrating the accuracy of the metamodelling approach. Table 7.5 also shows the compromise that must be struck between low pressure drop and low thermal resistance. It shows, for example, that achieving the relatively low thermal resistance at P_1 (0.124) requires more than five times the pressure drop than for the higher thermal resistance of 0.148 at P_6. Clearly the most appropriate compromise depends on the particular manufacturing and operating cost and functionality requirements for a specific heat sink.

Table 7.5: Minichannel design performance at six operating conditions points located on the Pareto front together with CFD validation as shown in Fig. 7.29.

Design point Pareto front	W_{ch} *(mm)*	N_{ch}	θ *(deg)*	R_{th} *(K/W)*	ΔP *(Pa)*	*CFD validation*	R_{th} *(K/W)*	ΔP *(Pa)*	*MAE* (× 100)	
									R_{th}*(%)*	ΔP*(%)*
P_1	0.8580	13	20.060	0.1231	8188.959	P_1^{CFD}	0.12442	8115.92	1.061	0.899
P_2	1.1097	12	20.084	0.1250	5847.967	P_2^{CFD}	0.12599	5950.15	0.753	1.717
P_3	1.2086	11	23.497	0.1283	4216.400	P_3^{CFD}	0.12906	4220.41	0.578	0.095
P_4	1.2944	10	31.721	0.1356	2570.773	P_4^{CFD}	0.13611	2704.30	0.401	4.937
P_5	1.3409	9	33.712	0.1390	2229.936	P_5^{CFD}	0.13967	2327.33	0.468	4.184
P_6	1.3969	8	37.561	0.1475	1736.041	P_6^{CFD}	0.14824	1811.26	0.485	4.152

The surface temperature distribution and pressure drop for the SMCF heat sink design having 13 and 8 minichannels number are shown in Fig. 7.30, where the design parameters can be seen in the Table 7.5 at P_1^{CFD} and P_6^{CFD}, respectively. It can be observed that the maximum temperature is for the heat sink with smaller numbers of minichannels (P_6^{CFD}) compared with the heat sink that has more channels (P_1^{CFD}) and the lowest temperatures. However, a higher pressure drop was found with P_1^{CFD} compared to P_6^{CFD}. The maximum temperature for P_6^{CFD} was found to be 89.49 ^{o}C, while for P_1^{CFD} was 78.32 ^{o}C, however the pressure drop was 1811.26 Pa for P_6^{CFD} and 8115.92 Pa for P_1^{CFD}, see Table 7.5.

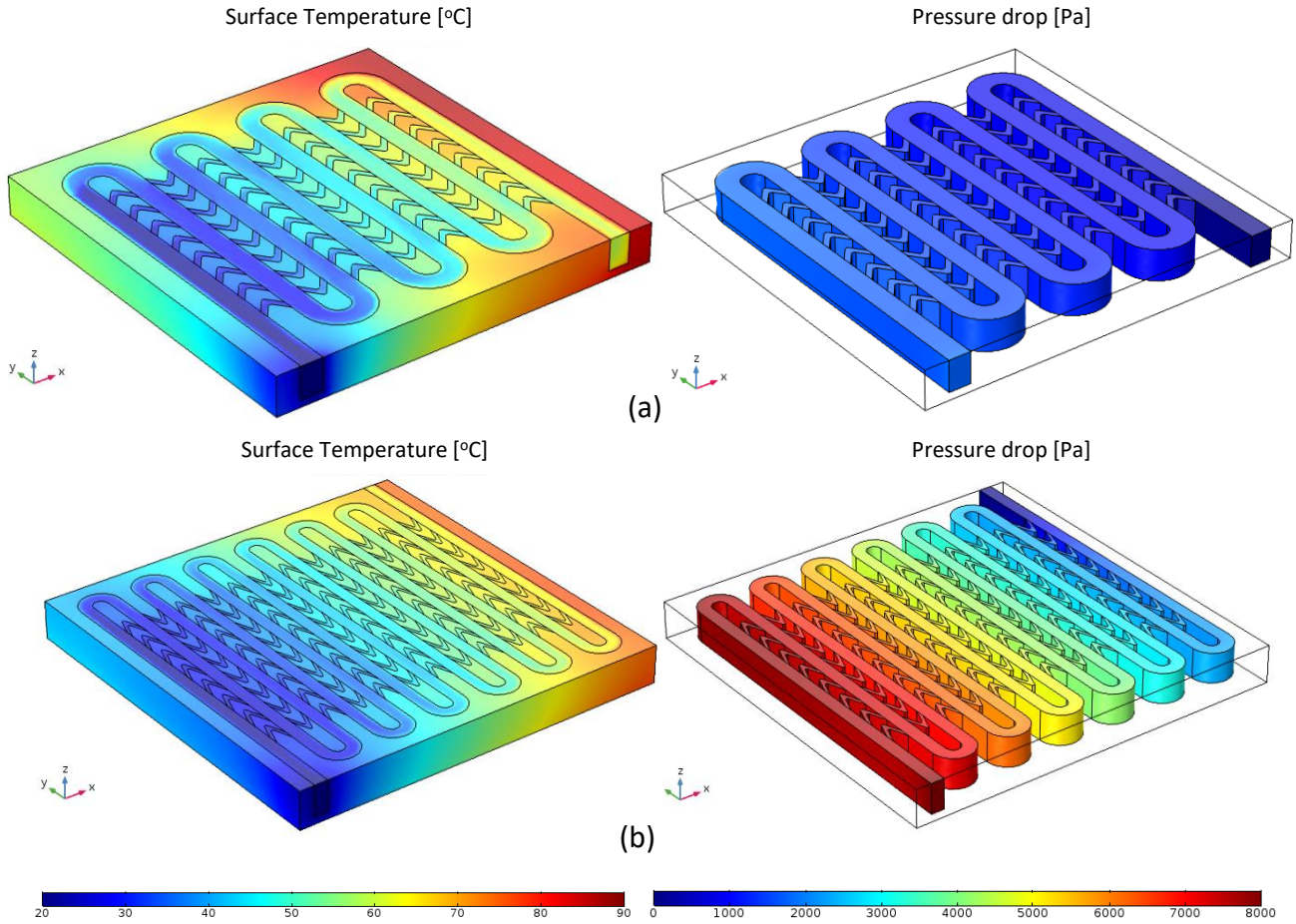

Fig. 7.30: Isometric views of temperature and pressure drop for SMCF heat sink model with $Q_{in} = 0.16\ l/min$ and constant heat flux of 75 W/cm^2; (a) P_6 ; and (b) P_1 from Table 7.5.

7.7 Summary

Liquid-cooled micro/minichannel heat sinks are of increasing interest as a means of dissipating high heat fluxes encountered in, for example, electronics cooling. This study has demonstrated that employing chevron fins within serpentine channels to disrupt the hydrodynamic and thermal boundary layers and transferring fluid between main and secondary channels can lead to substantial reductions in thermal resistance and pressure drop with corresponding enhancements of the heat transfer coefficient.

The experimental and numerical results have demonstrated that the total thermal resistance, R_{th}, of both MCHS designs decrease monotonically with water flow rate due to the increased convective heat transfer. The experiments have shown the SMCF design can reduce R_{th} compared to the SMPF design by around 11% for $Q_{in} = 0.159\ l/min$ and that decreasing the chevron fin oblique angle, θ , from 45^0 to 20^0 can reduce R_{th} by a further 10%. At the same time, the inclusion of the chevron fins reduces the overall pressure drop; with $\theta = 30^0$ and $Q_{in} = 0.159\ l/min$ the pressure drop is reduced to approximately one third of that for

the corresponding SMPF heat sink. This demonstrates that by introducing chevrons into the serpentine MCHSs, it is possible to reduce the thermal resistance without creating additional pressure drop; indeed the chevron design significantly reduces the pressure drop as well. The secondary microchannel width, W_{sc}, is also very influential. For example, when W_{sc} is decreased from 0.6 mm to 0.2 mm at $Q_{in} = 0.2\ l/min$, R_{th} reduces by 42%, mainly as a result of increasing the convective heat transfer area and disturbances to the thermal boundary layer.

When the variations of E_{Nu}, $E_{\Delta P}$ and P_f with both θ and β are investigated, the numerical results indicate that $P_f > 1$ for all values of θ and β. It is observed that P_f increases significantly until θ= 40°, followed by slight reductions when $\theta > 40^o$. Also it is shown that when $\beta > 0.3$, P_f is reduces sharply, and this reflects the reduction of A_{eff} and, consequently, the reduction in Nu_{avg}.

The Pareto front from the formal design optimisation of a SMCF heat sink demonstrates vividly the compromise that must be struck between the conflicting objectives of low thermal resistance and low pressure drop designs. The numerical analysis predicts that reducing thermal resistance by 16.2% (from 0.148 to 0.124) is at the expense of a greater than fivefold increase in pressure drop. In practice, the most appropriate design would balance the competing demands for low manufacturing and operating costs against the requirements on thermal resistance that deliver the critical cooling performance objectives.

Chapter 8: Thermal Management of GaN HEMT Devices

8.1 Introduction

Owing to the unique properties of gallium nitride (GaN) high electron mobility transistors (HEMTs), such as wide bandgap, high thermal conductivity and high breakdown field that enable them to function in harsh environments. However, self-heating effects must be suppressed using some appropriate way for most GaN HEMTs, which indeed degrade their electrical performance seriously. To significantly reduce this temperature rise, the benefits of using single path serpentine minichannel heat sinks (MCHSs) will be considered, since the previous results showed they have the ability to enhance flow mixing and hence heat transfer albeit with a higher pressure drop. Therefore, three-dimensional CFD simulations of the conjugate heat transfer of a serpentine MCHS, combined with a range of different heat spreader materials (i.e. Si, SiC, diamond and graphene), on the cooling of CREE CGHV1J070D GaN HEMT dies (CREE, 2012) have been explored. The details of the computational methodology and results will be explained in the following sections.

8.2 Cooling of GaN HEMTs Using Serpentine MCHSs

This section presents a numerical investigation into the capability of a water-cooled copper serpentine MCHS with a footprint of 25 × 25 mm^2 and a thickness of 2.5 mm, based on the design parameters at Pareto point P_4 with 10 minichannels shown in Table 6.4, to dissipate heat generate from the GaN HEMT. The minichannel width (W_{ch}), fin width (W_w), and minichannel depth (H_{ch}) are kept at 1.495 mm, 0.914 mm, and 2 mm, respectively. The inlet water temperature is set at 20 ^{o}C. A heat spreader having the same base area as the serpentine MCHS with a thickness of 300 μm was attached directly at the bottom of the heat sink base, with a 50 μm thick 80Au/20Sn solder mounted between the heat spreader and the MCHS as a bounding material. The thermal conductivity of the solder is set to 57 W/m.K (Han et al., 2014).

As a typical heat source, a CREE CGHV1J070D GaN HEMT die (CREE, 2012) shown in Fig. 8.1(a) is considered. Fig. 8.1(b) shows a schematic of the transistor layout showing multi-fingered configurations, where source (S), gate (G), and drain (D) metallizations are indicated. Three GaN HEMTs are simulated, each having an area of 4800 × 800 μm^2 and a thickness of 2 μm, and evenly distributed across the centre line of the MCHS. Each transistor is composed of 72 gate fingers that are mounted on the top surface of the GaN transistor to dissipate a total power of 70 W. The length (l_G) and width (W_G) of each gate are respectively 0.25 μm and 250 μm. Almost all of the heat is generated under each gate finger (Han et al., 2014).

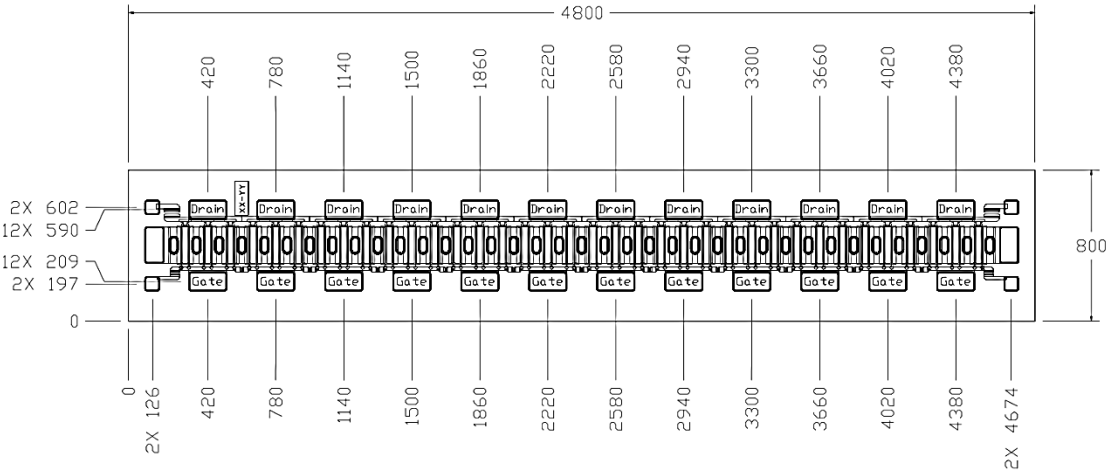

(a)

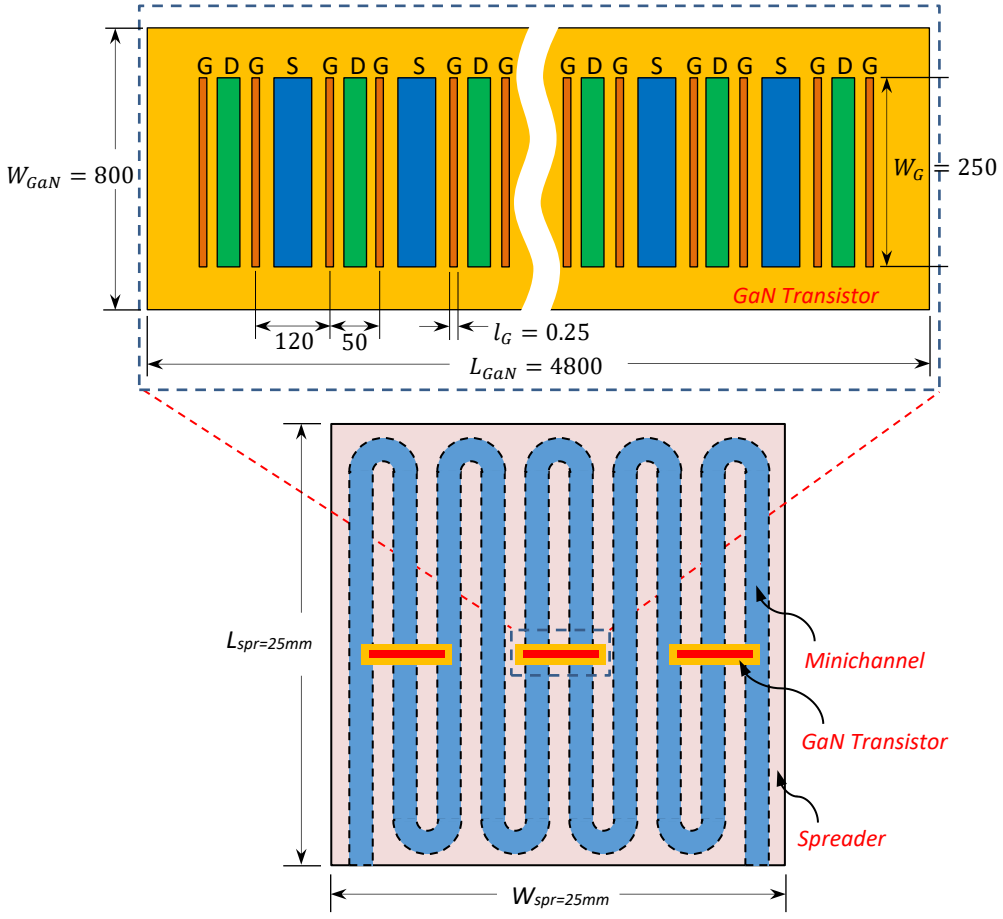

(b)

Fig. 8.1: (a) Layout of a representative GaN HEMT type CREE CGHV1J070D (CREE, 2012); (b) Top view of transistor layout, showing multi-fingered configurations. Source (S), gate (G), and drain (D) metallizations are indicated. All dimensions in μm.

Single-phase, laminar flow conjugate heat transfer simulations are performed for a whole serpentine MCHS using COMSOL Multiphysics v.5.2 and the same assumptions used in section 6.5. The computational domain and boundary conditions used are shown in Fig. 8.2. Except at the bottom of the MCHS, all the outer surface boundaries (other than the flow inlet

and outlet) are considered to be adiabatic. A total power of 210 W (power on each transistor is 70 W to generate heat flux of 1823 W/cm^2) is applied to the 216 gate fingers (3 GaN × 72 gates) resulting in a heat flux of 1.556 MW/cm^2 loaded on each gate finger, with a power density of 3.89 W/mm. The effect of four different heat spreader materials is investigated: silicon (Si), silicon carbide (SiC), diamond and graphene.

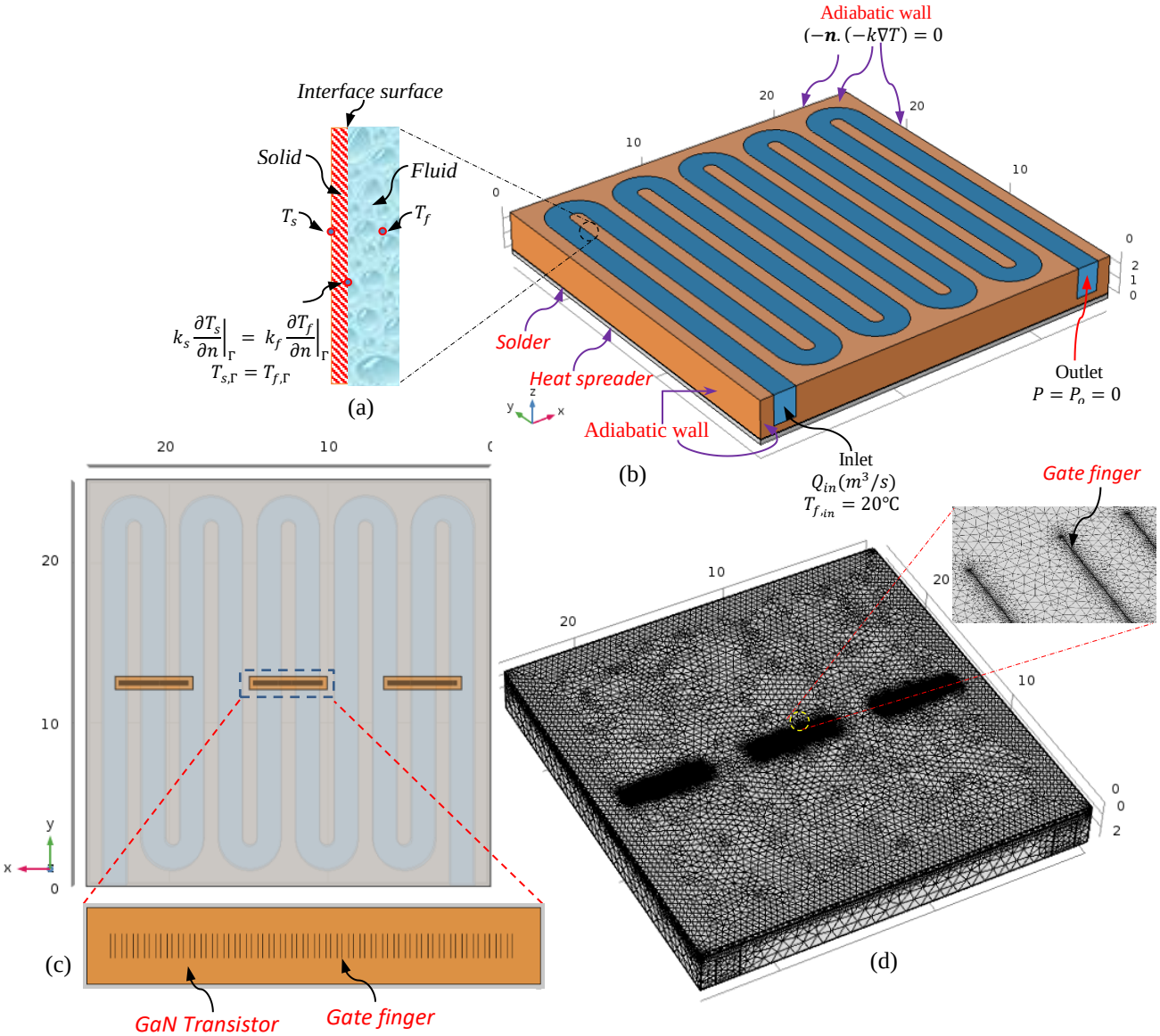

Fig. 8.2: 3-D and back side view of the serpentine MCHS design with boundary conditions: (a) Conjugate heat transfer of the MCHS; (b) Isometric view; (c) Bottom side of the MCHS; and (d) the finite element mesh using grid 4 as shown in Fig. 8.3.

The temperature-dependent thermal conductivity of the Si, SiC, the diamond heat spreaders and the GaN layers are taken from references (Han et al., 2014 and Chen et al., 2014), while for both the copper heat sink and graphene heat spreader conductivity is taken to be constant, with the latter assumed to be 5000 W/m·K (Balandin, 2008; Barua et al., 2012; and Reddy and Dulikravich, 2017). The thermal boundary resistance (TBR) between GaN and heat

spreader is included, and the value is assumed to be 3.3×10^{-8} m^2.K/W for all heat spreaders used (Sarua et al., 2007; Han et al., 2014; and Reddy and Dulikravich, 2017). The TBR, also known as thermal interface resistance or Kapitza resistance is expressed with dimensions of area × temperature/power (inverse of the heat transfer coefficient). This TBR is resistance to heat flow caused by thermal reflections at interfaces between two materials due to differences in the electronic properties of the two materials (Babić, 2014). The thermal properties and thickness of each material used in the simulations are listed in Table 8.1.

Table 8.1: Thickness and thermal conductivity of the materials used for simulation.

Material	Thickness [μm]	Thermal conductivity [W/(m.K)]
Si	100 - 600	$k_{Si} = 152 \times (298/T)^{1.334}$
SiC	100 - 600	$k_{SiC} = 387 \times (293/T)^{1.49}$
Diamond	100 - 600	$k_{Diam} = 1832 \times (298/T)^{1.305}$
GaN	2	$k_{GaN} = 141 \times (298/T)^{1.211}$
Graphene	100 - 600	5000
Cu	2500	385
80Au/20Sn solder	50	57

8.3 Effect of Grid Density

The effect of grid density on the numerical solution of the conjugate heat transfer problem with both serpentine and straight rectangular MCHSs, a SiC heat spreader and three GaN transistors (see Fig. 8.2(c)) is explored using five different mesh sizes, as indicated in Fig. 8.3. In order to facilitate a fair performance comparison between the two different MCHS both heat sink models share the same design parameters, and the dimensions of the Pareto point P_4 is selected as the optimum design for the serpentine MCHS model (see Table 6.4).

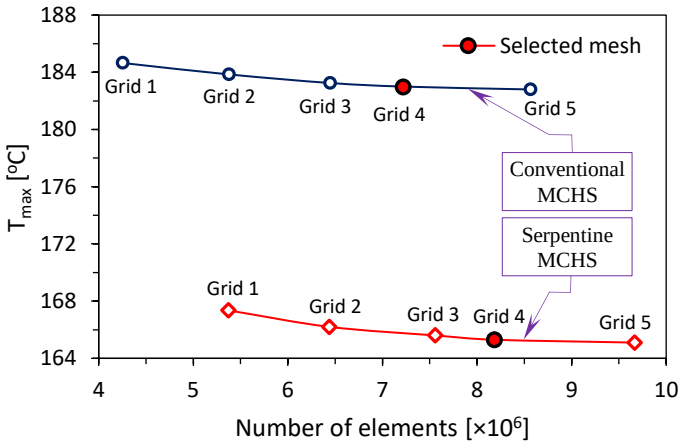

Fig. 8.3: Grid independence test for serpentine and conventional MCHS at $Q_{in} = 0.16\ l/min$ and total power of 210 W.

A tetrahedral mesh is generated to discretize the domain, with increasing grid refinement in the region of the GaN HEMT and gate fingers where the local heat flux is very high, as shown in Fig. 8.2(d). The volumetric flow rate and inlet temperature of the water are set to be 0.16 *l/min* and 20 ^{o}C, respectively. The heat flux density applied for each gate finger was 1.556 MW/cm^2 (total power is 210 W, 70 W on each GaN HEMT), and a 300 μm thick SiC heat spreader is used. As shown in Fig. 8.3, for the conventional straight rectangular MCHS, compared to the results of a grid 4 (7.23×10^6 elements), grid 3 showed a 2.1% change in the maximum chip temperature (T_{max}), whereas using grid 5 resulted in only a 1% change in T_{max}. Similar behaviour was found for the serpentine MCHS so that grid 4 was used in all subsequent numerical solutions.

8.4 Validation Against Previous Studies

The numerical solutions for the GaN HEMTs cases were validated against the experimental results of Han et al. (2014), which used eight GaN resistors (each size 350 × 150 μm^2 with a heat flux between 2.38–11.9 kW/cm^2) with 10–50 W total power mounted on a diamond heat spreader to enhance the hotspot cooling capability of a single-phase water-cooled straight rectangular microchannel heat sink. The conjugate heat transfer problem for the entire straight rectangular microchannel heat sink, heat spreader and GaN HEMTs system was solved numerically for comparison with Han et al. (2014). The water flow rate across the entire microchannel heat sink was fixed at 0.4 *l/min*, leading to a laminar flow regime.

As illustrated in Fig. 8.4(a), good agreement was obtained between Han et al.'s experiments and the simulation results for maximum heater temperature (T_{max}), with MAE of around 4.2% for the cases with and without a diamond heat spreader. Fig. 8.4(b) compares the temperature distribution across all the transistors between those measured by Han et al. (2014) and the current simulation at total power of 50 W for cases with and without a diamond heat spreader. Again good agreement was obtained with MAE of around 5.3%.

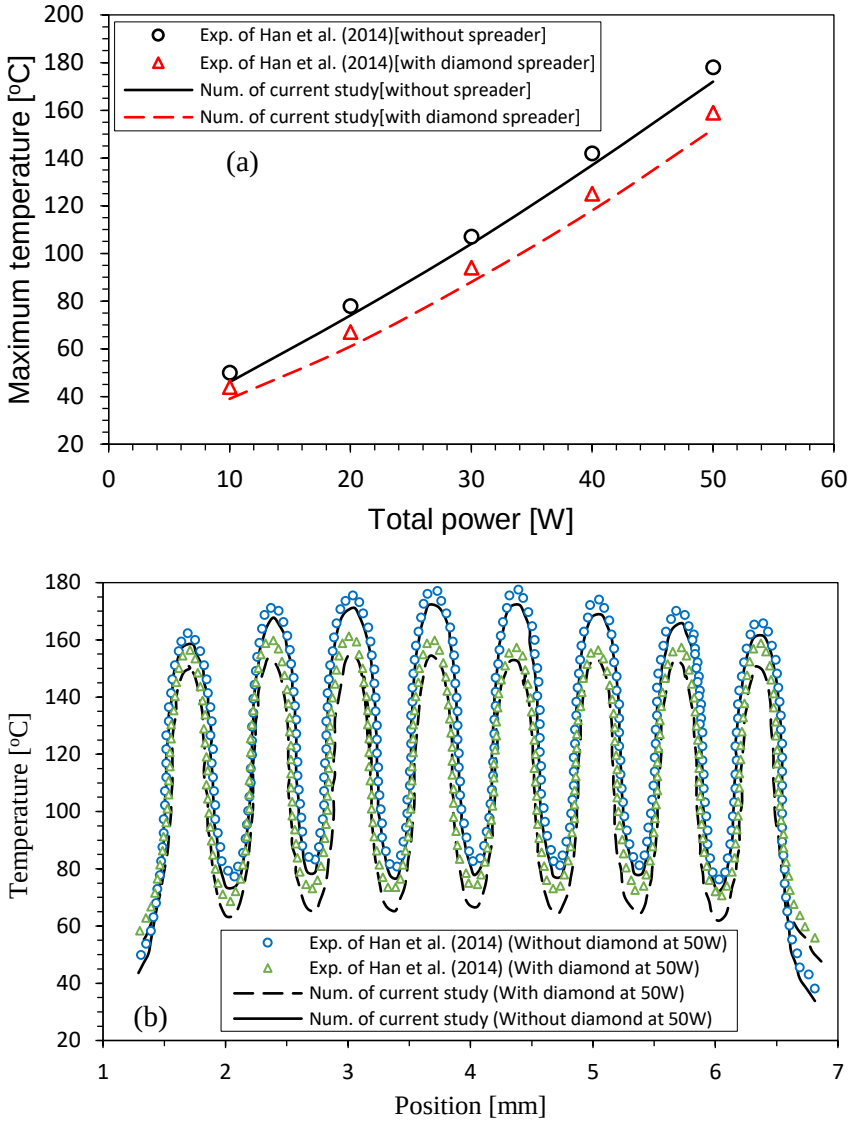

Fig. 8.4: Validation of the current numerical simulation against experimental work of Han et al. (2014) for (a) maximum transistor temperature at different total heating power; (b) temperature distribution along the transistors.

8.5 Effect of Heat Sink Geometry

A comparison between the serpentine and straight rectangular MCHSs has been performed numerically with and without a 300 μm thick graphene heat spreader for different volumetric flow rates ($0.1 \leq Q_{in} \leq 0.22\ l/min$) and an inlet water temperature of 20 °C. For both heat sinks the parameters from Pareto point P_4 are used (see Table 6.4) and the entire heat sink is simulated, with three GaN transistors with a total power of 210 W (generating a heat flux of 1823 W/cm^2 over each GaN transistor) mounted on the bottom surface of the graphene heat spreader (see Fig. 8.2(c)).

In Fig. 8.5 the heat spreader material has the greatest influence on the maximum chip temperature (T_{max}) values and the temperatures for the serpentine MCHS are systematically lower than for the conventional MCHS, both with and without a heat spreader. For example, at Q_{in}= 0.22 *l/min*, T_{max} for the serpentine MCHS with graphene heat spreader is 88 ^{o}C, compared to 102.7 ^{o}C, 133.3 ^{o}C and 156 ^{o}C for the conventional straight rectangular MCHS with graphene heat spreader, the serpentine MCHS without spreader and the conventional MCHS without spreader, respectively. These are due to the fact that the graphene heat spreader has a much higher thermal conductivity than copper (see Table 8.1), and the influence of the minichannel bends in the serpentine MCHS which disrupt the hydrodynamic and thermal boundary layers and maintain a state of developing flow.

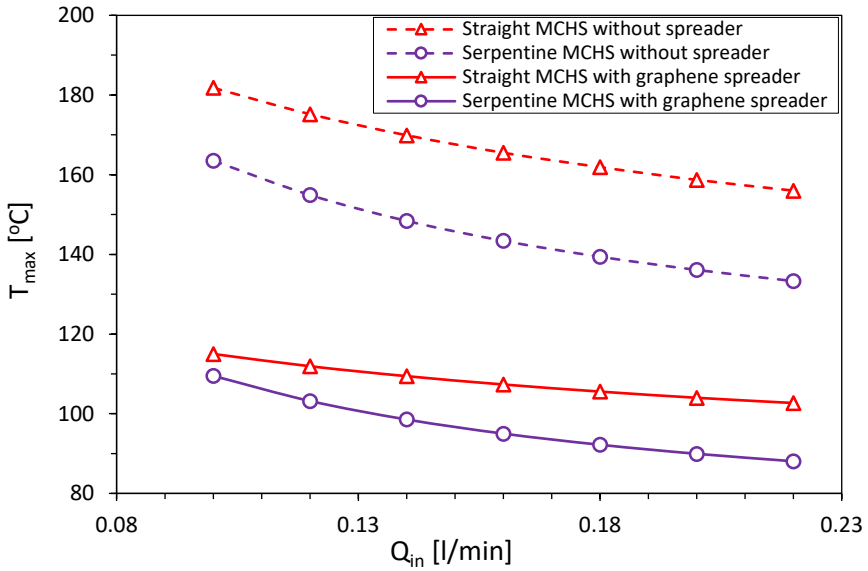

Fig. 8.5: Comparison for maximum temperature between using a serpentine and a straight MCHS with and without graphene heat spreader versus different Q_{in} and total power of 210 W.

Fig. 8.6 compares the pressure drop for the serpentine and a straight rectangular MCHSs with and without a graphene heat spreader as a function of Q_{in} with a total power of 210 W. As shown in Fig. 8.6, the differential pressure between the inlet and outlet of the serpentine channel is significantly higher than those from a straight channel. For example, at $Q_{in} = 0.16\ l/min$ the pressure drop in the serpentine minichannel with graphene heat spreader was 29641 Pa while it was only 46.5 Pa for the straight minichannel. As expected, the influence of the heat spreader is very small.

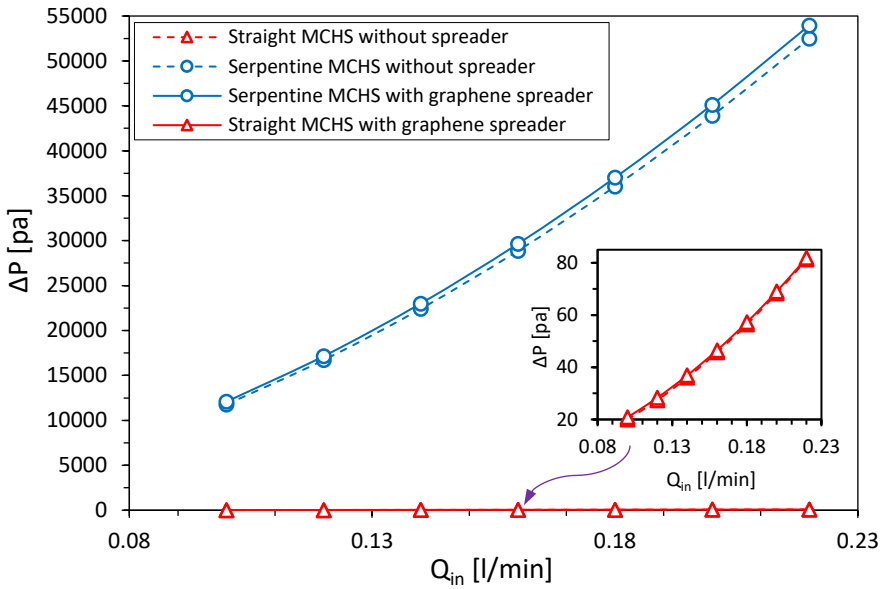

Fig. 8.6: Comparison for pressure drop between using a serpentine and a straight MCHS with and without graphene heat spreader versus different Q_{in} and total power of 210 W.

8.6 Effect of Heat Spreader Materials

The effect of heat spreader material, namely Si, SiC, diamond or graphene is investigated numerically. The thickness of the heat spreaders ($t_{spreader}$) are fixed at 300 µm and a total power of 210 W is dissipated from the three GaN transistors (each transistor dissipating 70 W (1823 W/cm^2)). Once again 10 minichannels of width 1.495 mm and depth of 2 mm are used while the GaN transistor dimension are shown in Fig. 8.1. Fig. 8.7 shows the effect of the heat spreader material and Q_{in} on T_{max} with a water inlet temperature of 20 °C under laminar flow conditions.

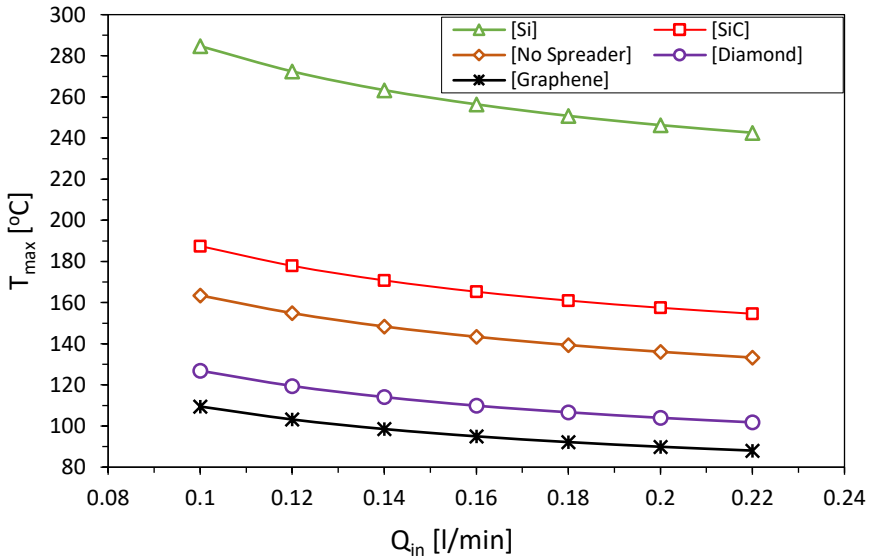

Fig. 8.7: Effect of the Q_{in} on maximum heater temperature at different heat spreaders (Graphene, Diamond, SiC, Si) and without spreader, at total power of 210 W and $t_{spreader} = 300\ \mu m$.

The T_{max} values decrease for higher flow rates and these increase systematically when the graphene is replaced by diamond, whereas the inclusion of the SiC and especially Si heat spreaders have a deleterious effect on T_{max} compared to the case when no heat spreader is used. This is due to the fact that the Si has much lower thermal conductivity than SiC, Copper, diamond and graphene, and that its thermal conductivity reduces further as the temperature increases.

Fig. 8.8 shows the heat flux distribution on the bottom surface of the whole copper serpentine MCHS with diamond and graphene heat spreaders for a total power dissipation of 210 W and Q_{in} of 0.16 l/min. The maximum heat flux for the heat sink with the graphene heat spreader is 285 W/cm^2, while that of the heat sink with the diamond heat spreader is 580 W/cm^2, suggesting that graphene heat spreader is much more effective at alleviating hot spots. Moreover, the use of a graphene heat spreader maintains the GaN transistor temperature at 95 ^{o}C, compared with 110 ^{o}C for diamond, see Fig. 8.7.

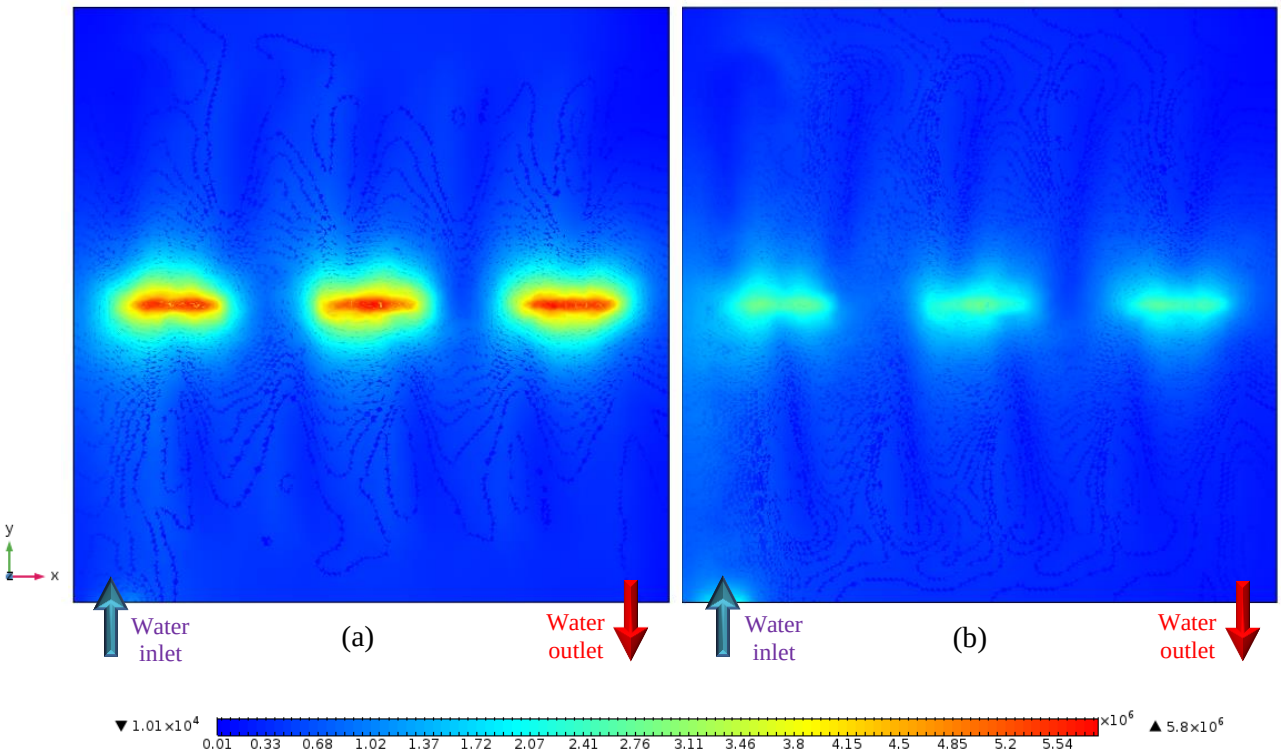

Fig. 8.8: Heat flux distribution (W/m^2) on the top surface of the serpentine MCHS with GaN heaters on different heat spreaders: (a) diamond; and (b) graphene, at 210 W, $Q_{in} = 0.16\ l/min$ and $t_{spreader} = 300\ \mu m$.

Fig. 8.9 shows the temperature profile across the GaN transistor, heat spreader, solder and heat sink material for the graphene and diamond heat spreaders. Cases with three different total powers of 90 W, 150 W and 210 W supplied to the three GaN transistors, leading to heat fluxes on each GaN transistor between 0.78-1.82 kW/cm^2 and heat fluxes on each gate finger

area (A_{gate} = 0.25 × 250 μm^2) between 0.667-1.556 MW/cm^2, are considered with Q_{in} = 0.16 l/min and 300 μm thick graphene and diamond heat spreaders.

The temperature profiles are taken at the gate finger located at the centre of the GaN near the water exit side where the temperature is a maximum. For 210 W total power, significant decrease can be seen in temperature distribution with GaN mounted on the graphene heat spreader compared with those with diamond heat spreader. It is observed that the temperature difference between the top of the GaN transistor and the top of the heat sink, which is about 53.4 ^{o}C for the diamond heat spreader, reduces to 40.5 ^{o}C when a graphene heat spreader is used.

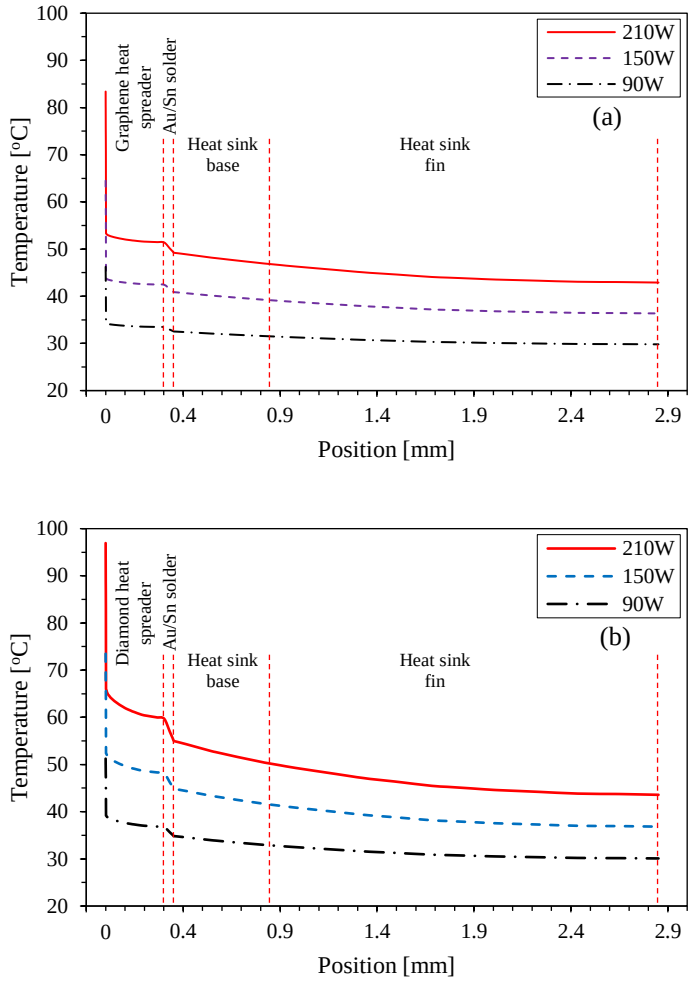

Fig. 8.9: Simulation temperature profile vertically across the structure for heat sink (a) with graphene heat spreader; and (b) with diamond heat spreader; at $Q_{in} = 0.16\ l/min$ and $t_{spreader} = 300\ \mu m$.

Fig. 8.10 shows the effect of heat spreader material on the temperature distribution across 72 gate fingers mounted on the top surface of the GaN transistor located nearest the water exit side where the temperature is a maximum for the case with $Q_{in} = 0.16\ l/min$, $t_{spreader}$ = 300 μm and total power of 210 W. As expected based on the above results, the maximum gate temperature was found for the GaN–on–Si heat spreader case, while that for the GaN–

on–graphene heat spreader was the lowest. Note that the maximum gate finger temperature for all heat spreaders are lower than the critical operating condition temperature ~250 °C (CREE, 2012).

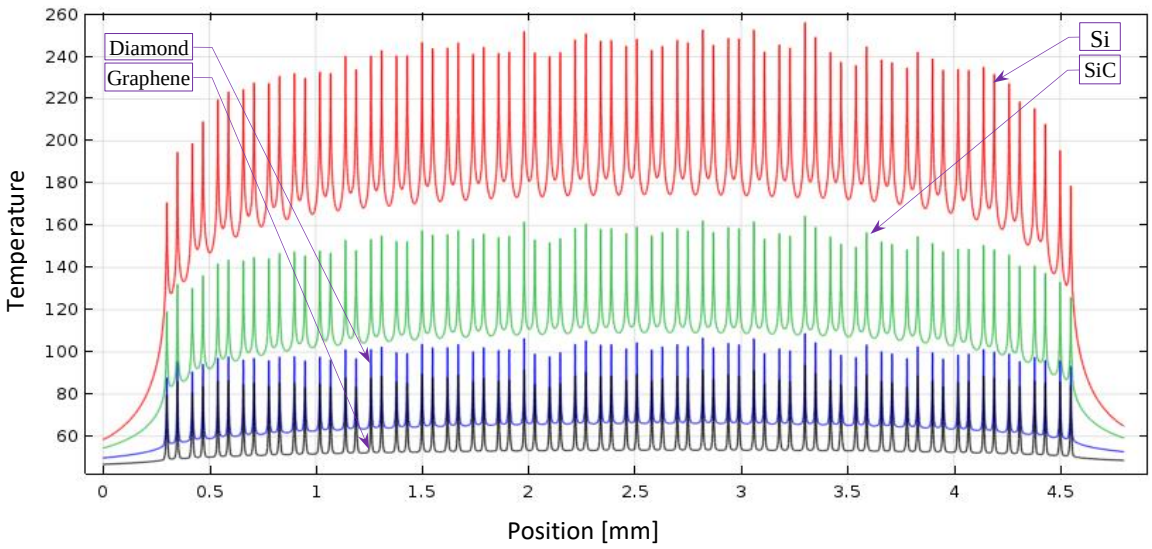

Fig. 8.10: Temperature profile in the longitudinal direction across all gate fingers of last GaN structure at total power of 210 W, $Q_{in} = 0.16\ l/min$ and $t_{spreader} = 300\ \mu m$.

The effect of heat spreader thickness is now investigated, using thicknesses ranging from 100 µm to 600 µm for cases with $Q_{in} = 0.16\ l/min$ and total power of 210 W. Fig. 8.11 shows that increasing the heat spreader thickness has relatively modest benefits for graphene, diamond and SiC heat spreader thicknesses less than about 300 µm, after which increasing spreader thickness has no significant benefit. In all cases T_{max} increases progressively from graphene to diamond then to SiC heat spreaders. In contrast, for the Si heat spreaders, the comparatively low thermal conductivity means that increasing spreader thickness is actually detrimental with T_{max} increasing from around 227 °C to 280 °C as spreader thickness increases from 100 µm to 600 µm.

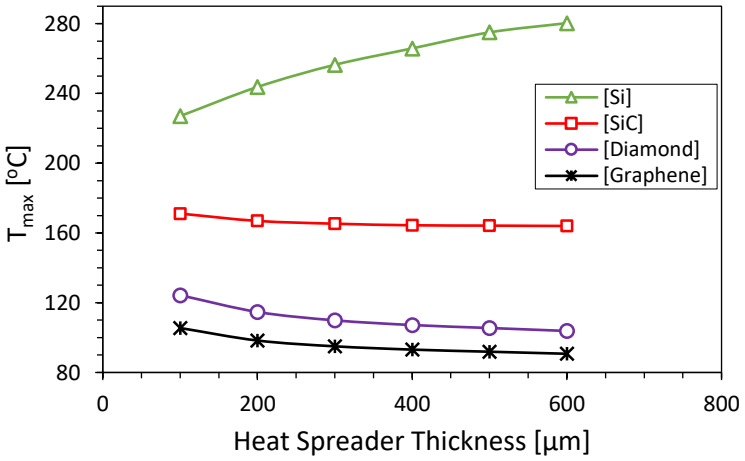

Fig. 8.11: Effect of the heat spreader thickness on the thermal performance of the structure for four different heat spreaders (Graphene, Diamond, SiC and Si).

8.7 Summary

This numerical simulation study has shown that water-cooled serpentine MCHSs can provide effective thermal management of the GaN HEMTs that are increasingly popular for radar frequency and microwave applications. It has also shown that the serpentine channels, which play a crucial role in disrupting thermal boundary layers to improve heat transfer, provide better heat transfer capability than conventional ones based on straight channels, albeit with a significantly larger pressure drop. The latter can, however, be reduced by carful optimisation of the MCHS geometry parameters and the multi-objective optimisation carried out here has demonstrated clearly the compromise that can be struck between maximum heat transfer and minimum pressure drop for serpentine MCHSs.

The role of heat spreaders and heat spreader materials has also been investigated and the numerical simulations have shown that from a list of graphene, diamond, SiC and Si, graphene is the most effective, followed by diamond at reducing both peak chip temperature and peak heat flux over hot spots. However the temperature-dependent conductivity of SiC and Si mean that these heat spreaders are detrimental and increase the maximum chip temperature compared to the case without a heat spreader. Further, the numerical results showed that increasing the heat spreader thickness yields modest benefits for graphene, diamond and SiC heat spreaders with thicknesses less than about 300 μm, after which increasing spreader thickness has no significant benefit. In contrast, for Si heat spreaders the comparatively low thermal conductivity means that increasing spreader thickness is detrimental and leads to an increases in the maximum chip temperature from 227 ^{o}C to 280 ^{o}C as the spreader thickness is increased from 100 μm to 600 μm. These results provide useful information for the optimisation of the thermal design of heat sinks for GaN HEMTs.

Chapter 9: Discussion and Conclusions

9.1 Introduction

In the present work, complementary experimental and numerical methods here used to investigate the fluid flow and heat transfer characteristics of three different configurations of serpentine minichannel heat sink (MCHS) designs which they termed single (SPSM), double (DPSM) and triple (TPSM) path multi-serpentine rectangular minichannels. Their performance was compared with an array of straight rectangular minichannels (SRM) in terms of average Nusselt number (Nu_{avg}), total thermal resistance (R_{th}), friction factor (f) and pressure drop (ΔP). The experimental studies and numerical predictions were conducted over a wide range of volumetric water flow rate ($0.1 \leq Q_{in} \leq 3.0\ l/min$), within single phase laminar and turbulent flow regimes. Following this study, a GaN HEMT type "CREE CGHV1J070D" with a total power of 70 W and area of 4.8×0.8 mm^2 is used as a heat source. A numerical simulation studies were carried out to cooling the later transistor through integrated it with a SPSM heat sink design. To enhance the hotspot cooling capability of the water-cooled copper SPSM heat sink, four different materials of heat spreaders are used which of Si, SiC, diamond and graphene.

To enhance the heat transfer coefficient together with decrease of pressure drop, a novel serpentine MCHS with chevron fins was investigated experimentally and numerically, then compared with the SPSM heat sink model. Finally, an optimisation was carried out on the SPSM heat sink design with and without chevron fins with the aim of reducing the total thermal resistance and pressure drop and consequently lowering the pumping power. This was achieved by using computational technique at different design variables and design of experiment (DoE) points. Key accomplishments of the present study are summarised below together with recommendations for future work and closing concluding remarks.

9.2 Discussion

The discussion of this study can be divided into four main parts: serpentine MCHS design, serpentine MCHS with chevron fins, optimisation technique, recirculating cooling system, and GaN HEMT device cooled by SPSM heat sink model. Collectively, the SPSM heat sink design with chevron fins provides the most effective cooling technique to enhance the thermal hydraulic characteristics of heat sinks by improved water-flow mixing due to existence of secondary channel flow, and increasing of the surface heat transfer area with less pumping power required.

9.2.1 Serpentine MCHS

Depending on the experimental results and numerical predictions for four categorise of the MCHSs (SPSM, DPSM, TPSM and SRM), the following major conclusions have been determined:

1. This study has demonstrated that channel design in MCHS has a strong influence on both heat transfer and pressure drop. Experimental and numerical results show that Nu_{avg} increases monotonically with flow rate, due to reductions in the thickness of the thermal boundary layer, and that the SPSM design provides the most effective heat transfer, followed by the DPSM and TPSM with the SRM heat sink having the poorest heat transfer. The experiments show that the SPSM design has the smallest thermal resistances, with values typically third of those for the poorest performing, SRM heat sink.
2. Comparisons with existing correlations for Nu_{avg} for SRM show that the present experimental results agree well with the correlation of Lee and Garimella (2006) in the laminar flow regime, with MAE of less than 7%, and with that of corrected Dittus-Boelter (1930) in the turbulent flow regime, with MAE of around 5%.
3. The numerical predictions of Nu_{avg} agree well with the experimental measurements for the four MCHS test sections with MAE of around 6.5% for both the laminar and turbulent flow regimes.
4. The numerical solutions show that the channel bends are very influential in preventing the hydrodynamic and thermal boundary layers attaining a fully-developed state and that their greater influence for the SPSM and DPSM designs leads to enhanced heat transfer compared to the other designs. These improvements in heat transfer are, however, achieved at the price of significantly larger pressure drops for the SPSM design, the values of which are reduced by the smaller water density and viscosity at high heating power densities.

9.2.2 Serpentine MCHS with Chevron Fins

For the single path serpentine minichannel (SPSM) heat sink with chevron fins design, the following conclusions can be drawn from this study:

1. The experimental and numerical results have demonstrated that the total thermal resistance, R_{th}, of the SPSM heat sink with and without chevron fins decreases monotonically with increasing of the water flow rate due to increasing the convective heat transfer, also this behaviour was shown with other heat sink models.

2. At the chevron fin oblique angle of $\theta = 30^{o}$ and Reynolds number ranging from 747 to 4482, the experiments have shown that inclusion of the chevron fins within the SPSM heat sink design has ability to reduce R_{th} compared to that one without chevron fins by around 7.7% – 12%, this due to disrupt the hydrodynamic and thermal boundary layers, at the same time, the overall pressure drop, ΔP, is also reduced to approximately 63%, because of transferring fluid between main and secondary channels. This demonstrates that by introducing chevrons into the serpentine MCHSs, it is possible to reduce the thermal resistance without paying the penalty of additional pressure drop; indeed the chevron design significantly reduces the pressure drop.

3. The average Nusselt number, Nu_{avg}, obtained from experiments for the enhanced serpentine minichannel with chevron fins is found to be higher than the SPSM heat sink without chevron fins. For Reynolds number varying from 747 to 2988 with $\theta = 30^{o}$, the Nu_{avg} for the SPSM with chevron fins increased from 8% to 16% compared with the SPSM heat sink without chevron fins. This enhancement is attributed to the reduction of the wall temperature in the enhanced heat sink, due to the combined effects of thermal boundary layer re-development at the leading edge of each chevron fin and the transfer fluid from the main minichannel to the secondary microchannel through the chevron fin, resulting in better heat transfer.

4. From the numerical predictions, it is observed that decreasing the θ from 45^{o} to 20^{o} can reduce R_{th} by a further 10% at $Q_{in} = 0.159\ l/min$. The secondary channel width, W_{sc}, is also found to be very influential, where R_{th} reduces by 42% when W_{sc} is decreased from 0.6 mm to 0.2 mm at $Q_{in} = 0.159\ l/min$, mainly as a result of increasing the convective heat transfer area and disturbances to the thermal boundary layer.

5. The numerical results indicated that the thermal performance factor, P_f, is always larger than one for all values of θ and β. It is shown that P_f increases significantly until $\theta = 40^{o}$, followed by slight reductions when $\theta > 40^{o}$. Also, it is observed that when $\beta > 0.3$, P_f is reduces sharply, and this reflects the reduction of effective area, A_{eff} and, consequently, the reduction in Nu_{avg}.

According to the literature review, pinned heat sinks can be an effective alternative to plate fin heat sinks since they have the advantage of hindering the development of the thermal boundary layer on smooth surfaces responsible for limiting the heat transfer rates in plate fin designs. Using this type of pin-fins can increase the wall surface area, and interrupt the steady flow of the fluid allows better flow mixing and as a result, enhanced

heat transfer. However, this the heat transfer enhancement of pinned heat sinks is always accompanied by a substantial increase in pressure drop (pumping power). Hence, in most pinned heat sink applications, both the heat transfer and pressure drop characteristics should be considered. In this case, the present novel design can be considered better than the pinned heat sinks since the former has ability to reduce both the total thermal resistance and pressure drop.

9.2.3 Optimisation Technique

For numerical simulation, grid independence study on the single straight rectangular microchannel for turbulent flow regime was conducted using two type of cells, namely hexahedral and tetrahedral meshes, and the normal grid size for both meshes provided the best prediction of the maximum temperature (T_{max}) and pressure drop (ΔP), see Table 6.3. The MAE between the hexahedral and tetrahedral cell types for normal grid is found to be 1.38% for T_{max} and 2.24% for ΔP. Furthermore, it is shown there are a slight difference in the velocity and temperature profiles as shown in Figs. 6.13 and 6.14. Hence, to reduce the effort and the time required to generate meshes for complex geometric such as serpentine MCHS, tetrahedral cell type is employed in the present study.

After selecting the mesh type, validation for the numerical results were carried out with the experimental work, and good agreement was achieved. After this match between the experiments and numerical predictions, an optimisation analysis of the serpentine MCHS with plate fins (SMPF) and with chevron fins (SMCF) was carried out, and response surface method (virtual optimization) was used. The SMPF heat sink design is parameterized into two key design variables which of minichannel width (W_{ch}) and number of minichannels (N_{ch}), while the SMCF heat sink design has explored the effect of three design variables; namely W_{ch}, N_{ch}, and the chevron fin oblique angle (θ). After selecting the range of design variables, the optimisation process uses a 30 (SMPF) and 50 (SMCF) point Optimal Latin Hypercubes (OLHCs) Design of Experiments (DoEs), generated from a permutation genetic algorithm. Each design is evaluated using CFD analysis and accurate metamodels built using a Moving Least Square (MLS) method.

The Pareto front is calculated using a multi-objective genetic algorithm (MOGA) approach. Practical design considerations, where the goal is to achieve a high heat transfer without excessive pressure drop, leads to a multi-objective design optimisation problem. The Pareto front from the design optimisation of a SMPF and SMCF heat sink indicates clearly the compromise that must be struck between the conflicting objectives of low thermal resistance and low pressure drop designs.

Table 9.1 shows comparison between the SMPF and SMCF heat sink for total thermal resistance, pressure drop, and pumping power consumed ($P_P = \Delta P \cdot Q_{in}$). Six points on the Pareto front (P_1–P_6) for both heat sink designs were selected with different number of minichannels. The optimisation was carried out under constant volumetric flow rate of 0.16 *l/min* and constant heat flux of 75 W/cm^2. From the results obtained, it is shown that the SMCF design can reduce R_{th} compared to the SMPF design by around 11%, at the same time, the inclusion of the chevron fins reduces the overall pressure drop to approximately one third of that for the corresponding SMPF heat sink. This demonstrates that by introducing chevrons into the serpentine MCHSs, it is capable to reduce the thermal resistance without creating additional pressure drop; indeed the chevron design significantly reduces the pressure drop as well.

Table 9.1: Minichannel design performance at six operating conditions points located on the Pareto front.

Design point Pareto front	N_{ch}	*SMPF heat sink*			*SMCF heat sink*			*Reductions (%)*	
		R_{th} *(K/W)*	ΔP *(Pa)*	P_P *(W)*	R_{th} *(K/W)*	ΔP *(Pa)*	P_P *(W)*	R_{th}*(%)*	ΔP*(%)*
P_1	13	0.13486	25107.598	0.06696	0.1231	8188.959	0.02184	8.72	67.38
P_2	12	0.14101	11105.142	0.02962	0.1250	5847.967	0.01560	11.35	47.34
P_3	11	0.14379	9518.4099	0.02538	0.1283	4216.400	0.01124	10.77	55.70
P_4	10	0.14844	7582.2650	0.02022	0.1356	2570.773	0.00685	8.65	66.10
P_5	9	0.15361	5992.6536	0.01598	0.1390	2229.936	0.00595	9.51	62.79
P_6	8	0.16211	4415.6202	0.01178	0.1475	1736.041	0.00463	9.01	60.68

To quantify the magnitude of the benefit of a typical improvement in pressure drop observed in the novel MCHS design (SMCF), the actual monetary value through one year need to be calculated. This shows that, compared to the SPSM heat sink design, there is money reduction in the range of 20.6% to 50.8% for different volumetric flow rate ($53 \leq Q_{in} \leq 318\ ml/min$).

9.2.4 Recirculating Cooling System

In the present experimental work, a non-recirculating cooling system was used (open loop liquid cooling system). In other words, all the water outlet from the heat sink test section is not recirculated, and this will lead to a significant waste for the water that must be avoided. To solve this dilemma, closed loop liquid cooling system can be used as an option, including:

- A heat sinks to absorb and transfer the heat from a chip.
- A pump to circulate the fluid in the system.
- A small heat exchanger (radiator) to transfer heat from the liquid to the air.
- A radiator fan to remove the heat in then liquid-to-air heat exchanger.

In a recirculating cooling system, the water being circulated by a mini water pump through a microchannel heat sink mounted on the heat source (chip) and out to a heat exchanger, typically a radiator. The radiator is itself usually cooled additionally by means of a fan or by other means, such as a Peltier cooler. Fig. 9.1 is a schematic diagram for the proposed closed loop liquid cooling system. The usage of such a cooling system can significantly reduce the amount of the water waste, but this at the expense of additional electric power consumption that used to operate the radiator. Furthermore, there are increase in the pressure drop between the inlet and outlet of the heat sink due to existence of the heat exchanger (radiator), which in turn leads to increase the pumping power. The water outlet from the radiator can be then returned to the heat sink at a certain temperature.

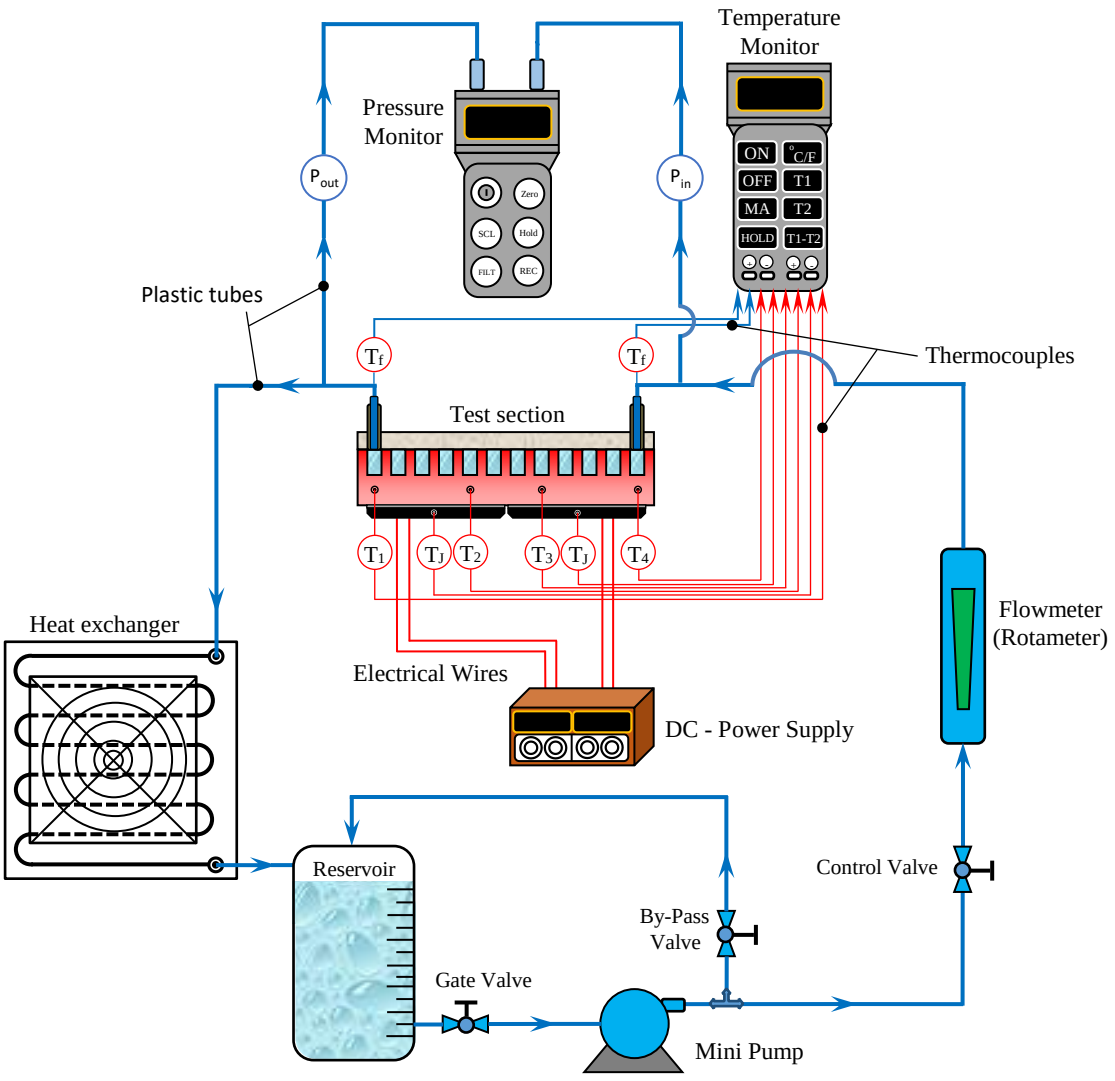

Fig. 9.1: Schematic diagram of the recirculating cooling system.

9.2.5 GaN HEMT Cooled by SPSM Heat Sink

1. From the numerical predictions, it has shown that using a heat sink within serpentine passages can provide effective thermal management of the GaN HEMTs, and this attributed to the existence of the curved channel at the end of each straight channel, which in turn play a crucial role in disrupting thermal boundary layers to improve fluid mixing, provide better heat transfer capability than conventional ones based on straight channels, albeit with a significantly larger pressure drop.
2. In the present study, the heat spreader materials have been investigated by using four different materials, namely graphene, diamond, SiC and Si, and the numerical simulations have demonstrated that graphene is the most effective, followed by diamond at reducing both maximum chip temperature and maximum heat flux over hot spots. However, the inclusion of the SiC and especially Si heat spreaders have a detrimental effect on maximum chip temperature compared to the case without a heat spreader. This is due to the fact that the Si has much lower thermal conductivity than other heat spreaders used, and that its thermal conductivity reduces further as the temperature increases.
3. The effect of heat spreader thickness has also been investigated and the numerical results showed that increasing the heat spreader thickness has relatively modest benefits for graphene, diamond and SiC heat spreader thicknesses less than about 300 μm, after which increasing spreader thickness has no significant benefit. However, increasing spreader thickness of the Si is deleterious and leads to an increase in the maximum chip temperature by around 23.3% as the spreader thickness is increased from 100 μm to 600 μm, due to low thermal conductivity.

9.3 Recommendations for Future Works

From the achievements of the present experimental and numerical investigations, the major extended works for future research are recommended and outlined as follows:

1. The present experimental and numerical work focuses on single-phase liquid-water flow in both of the serpentine minichannel heat sinks with plate fins and with chevron fins and the conventional heat sink designs. In order to develop a more complete understanding of chevron fin structures in a micro/minichannel heat sink, fluid flow and heat transfer characteristics for different fluids and phase change should be investigated. Nanofluids, dielectrics (HFEs and HFOs), Perflouranted poly ketones (Galden HT series) and flow boiling heat transfer in the serpentine MCHS with chevron fin could also be investigated further.

2. In this study, all the heat sinks fabricated were made from copper (Cu) material since it has high thermal conductivity (Cu=385 W/m.K at 20 ^{o}C). Including some consideration of manufacturing practice alongside material selection. For example with a machined block aluminium (Al) (Al=200 W/m.K at 20 ^{o}C) would be much more cost effective from the cost of milling but there would be a reduction in performance due to the lower thermal conductivity. Further simulations would need to be carried out to establish the thermal performance. If stamping then either Cu or Al would be suitable.
3. The serpentine minichannel heat sink with chevron fins could be optimised with more than three design variables. It would be useful if optimisation is implemented with one of these design variables, namely channel depth, secondary channel width, secondary channel length and chevron fin length at different water flow rate.
4. In the present optimisations, total thermal resistance and pressure drop were chosen as an objective functions. The other possible objective function can be used as an alternative to thermal resistance is either heat transfer coefficient or Nusselt number.
5. To further enhance the convective heat transfer in MCHS, fan-shaped reentrant cavities and/or ribs can be incorporated within channel side-wall of the SPSM heat sink design, albeit with a significantly larger pressure drop.
6. For GaN HEMT, gate-to-gate pitch could be optimised to give a minimum gate temperature.

9.4 Conclusions

The complementary nature of experimental and computational analysis has facilitated a detailed and systematic investigation into the passive manipulation of serpentine minichannel design in order to minimise the total thermal resistance (R_{th}) together with the pressure drop (ΔP) and consequently lowering the pumping power (P_P). The experimental data indicated that the single path serpentine minichannel (SPSM) heat sink design leads to a 35% enhancement of the average Nusselt number at a volumetric flow rate of 0.5 *l/min* and a 19% reduction in R_{th} compared to the conventional SRM heat sink. However, this enhancement is at the expense of a large (up to ten-fold) increase in ΔP compared to the SRM heat sink, due to existence of curved channels.

The novel design (SMCF) is found to significantly reduce both the pressure drop across the heat sink and the total thermal resistance by up to 60% and 10%, respectively, and enhance the average Nusselt number by 15% compared with the SMPF heat sink design, due to implementing the chevron fins.

Inclusion the graphene heat spreader into a serpentine MCHS could significantly reduce the maximum temperature (T_{max}) of the GaN HEMT device, whereas the inclusion of the SiC and especially Si heat spreaders have a deleterious effect on T_{max}. This is due to the fact that the graphene has much higher thermal conductivity than Si and SiC.

Companies that concerned in cooling electronic devices can benefit from the application of the optimisation methods that have been developed in this thesis.

References

Abraham, A., Jain, L.C. and Goldberg, R. 2005. *Evolutionary multiobjective optimization, theoretical advances and applications*. New York, Springer.

Agarwal, G., Kazior, T., Kenny, T. and Weinstein, D. 2017. Modeling and analysis for thermal management in Gallium Nitride HEMTs using microfluidic cooling. ASME, *Journal of Electronic Packaging*. **139**(1), pp. 1-11.

Al-Arabi, M. 1982. Turbulent heat transfer in the entrance region of a tube. *Heat Transfer Engineering*. **3**(3-4), pp. 76-83.

Allen, M.J., Tung, V.C. and Kaner, R.B. 2010. Honeycomb carbon: a review of Graphene. *Chem. Rev*. **110**(1), pp. 132–145.

Almaneea, A. H. 2014. Thermal analysis of liquid immersed electronics for data centres. PhD thesis, University of Leeds.

Altenbach, H. and Becker, W. 2003. *Modern trends in composite laminates mechanics, CISM Courses and lectures*. New York, USA: Springer-Verlag Wien GmbH.

Anbumeenakshi, C., Vijaybabu, T. R. and Thansekhar, M. R. 2014. Experimental investigation of flow maldistribution in microchannels. *International Journal of Innovative Research in Science, Engineering and Technology*. **3**(3), pp. 1410 - 1413.

Anderson, T. J., Hobart, K. D., Tadjer, M. J., Koehler, A. D., Imhoff, E. A., Hite, J. K., Feygelson, T. I., Pate, B. B., Eddy Jr., C. R. and Kub, F. J. 2017. Nanocrystalline Diamond Integration with III-Nitride HEMTs. *ECS Journal of Solid State Science and Technology*. **6**(2), pp. 3036-3039.

ASME PTC 19.1-2013.

Audze, P. and Eglais, V. 1977. New approach for planning out of experiments, problems of dynamics and strengths. **35**, pp.104-107. Riga, Zinatne Publishing House (in Russian).

Babić, D. I. 2013. Thermal analysis of AlGaN/GaN HEMTs using angular Fourier-series expansion. Journal of Heat Transfer. 135(11), pp. 1–9.

Babić, D. I. 2014. Optimal AlGaN/GaN HEMT buffer layer thickness in the presence of an embedded thermal boundary. *IEEE Transactions on Electron Devices*. **61**(4), PP. 1047 – 1053.

Bae, S.H., Shabani, R., Lee, J.B. and Baeck, S.J. 2014. Graphene-based heat spreader on flexible electronic devices. *IEEE Transactions on Electron Devices*. **26**, pp. 4171-4175.

Bahrami, M., Jovanovich, M. M. and Culham, J. R. 2006. Pressure drop of fully developed, laminar flow in rough microtubes. *Journal of Fluids Engineering*. **128**, pp. 632-637.

Balandin, A. A., Ghosh, S., Bao, W., Calizo, I., Teweldebrhan, D., Miao, F. and Lau, C. N. 2008. Superior thermal conductivity of single-layer graphene. *Nano Letters*. **8**(3), pp. 902-907.

Balasubramanian, K., Lee, P.S., Jin, L.W., Chou, S.K., Teo, C.J. and Gao, S. 2011. Experimental investigations of flow boiling heat transfer and pressure drop in straight and expanding microchannels – A comparative study. *International Journal of Thermal Sciences*. **50**(12), pp. 2413–2421.

Balasubramanian, K., Lee, P.S., Teo, C.J. and Chou, S.K. 2013. Flow boiling heat transfer and pressure drop in stepped fin microchannels. *International Journal of Heat and Mass Transfer*. **67**, pp. 234-252.

Baliga, J., Ayre, R. W. A., Hinton, K. and Tucker, R.S. 2011. Green cloud computing: Balancing energy in processing, storage, and transport. *Proceedings of the IEEE*. **99**(1), pp. 149–167.

Barua, A., Hossain, Md.S., Massod, K.I. and Subrina, S. 2012. Thermal management in 3-D integrated circuits with graphene heat spreaders. *Physics Procedia*. **25**, pp. 311-316.

Bates, S. J., Sienz, J. and Toropov, V. V. 2004. Formulation of the Optimal Latin Hypercube Designs of Experiments using a Permutation Genetic Algorithm. Proceedings of the 45th AIAA/ ASME/

ASCE/ AHS/ ASC Structures, Structural Dynamics & Materials Conference, 19th-22nd April 2004, Palm Springs, California, USA.

Bayraktar, T. and Pidugu, S.B. 2006. Characterization of liquid flows in microfluidic systems. *International Journal of Heat and Mass Transfer*. **49**, pp. 815-824.

Bejan, A. 2013. *Convection heat transfer*. 4th edition, John Wiley & Sons, Inc.

Bergles, A. E. 2001. The implications and challenges of enhanced heat transfer for the chemical process industries. *Chemical Engineering Research and Design*. **79**(4), pp. 437–444.

Bergman, T. L., Lavine, A. S., Incropera, F. P. and DeWitt, D. P. 2017. *Fundamentals of Heat and Mass Transfer*. 8th edition. New York: John Wiley.

Blevins, R. D. 1984. *Applied Fluid Dynamics Handbook*. New York, NY: Van Nostrand Reinhold.

Bogojevica, D., Sefiane, K., Walton, A.J., Lin, H. and Cummins, G. 2009. Two-phase flow instabilities in a silicon microchannels heat sink. *International Journal of Heat and Fluid Flow*. **30**, pp. 854–867.

Box, G.E.P. and Draper, N.R. 2007. *Response Surfaces, Mixtures and Ridge Analyses*. 2nd edition. New York, USA: Wiley and Sons.

Box, G.E.P. and Wilson, K.B. 1951. On the experimental attainment of optimum conditions. *Journal of the Royal Statistical Society*. **13**, pp.1-45.

Caddock, Inc. MP9100 Series TO-247 Radial Fixed Resistor 20Ω ±1% 100W. Available from: http://uk.rs-online.com/web/p/through-hole-fixed-resistors/3778677/.

Calame, J. P., Myers, R. E., Binari, S. C., Wood, F. N. and Garven, M. 2007. Experimental investigation of microchannel coolers for the high heat flux thermal management of GaN-on-SiC semiconductor devices. *International Journal of Heat and Mass Transfer*. **50**(23), pp. 4767–4779.

Cavazzuti, M. 2013. *Optimization methods: from theory to design scientific and technological aspects in mechanics*. Berlin, Germany: Springer.

Çengel, Y. A. 2002. *Heat transfer: A practical approach*. 2nd edition. New York: McGraw-Hill.

Çengel, Y. A. and Cimbala, J. M. 2013. *Fluid mechanics fundamentals and applications*. 3rd edition. New York: McGraw-Hill.

Chai, L., Xia, G., Wang, L., Zhou, M. and Cui, Z. 2013a. Heat transfer enhancement in microchannel heat sinks with periodic expansion-constriction cross-sections. *International Journal of Heat and Mass Transfer*. **62**, pp. 741–751.

Chai, L., Xia, G.D., Zhou, M.Z., Li, J. and Qi, J. 2013b. Optimum thermal design of interrupted microchannel heat sink with rectangular ribs in the transverse microchambers. *Applied Thermal Engineering*. **51**, pp. 880–989.

Chai, L., Xia, G. D. and Wang, H. S. 2016a. Numerical study of laminar flow and heat transfer in microchannel heat sink with offset ribs on sidewalls. *Applied Thermal Engineering*. **92**, pp. 32-41.

Chai, L., Xia, G. D. and Wang, H. S. 2016b. Laminar flow and heat transfer characteristics of interrupted microchannel heat sink with ribs in the transverse microchamber. *International Journal of Thermal Sciences*. **110**, pp. 1-11.

Chattopadhyay, M. K. and Tokekar, S. 2008. Thermal model for dc characteristics of AlGaN/GaN HEMTs including self-heating effect and non-linear polarization. *Microelectronics Journal*. **39**(10), pp. 1181–1188.

Chein, R. and Chen, J. 2009. Numerical study of the inlet/outlet arrangement effect on microchannel heat sink performance. *International Journal of Thermal Sciences*. **48**, pp. 1627–1638.

Chein, R. and Chuang, J. 2007. Experimental microchannel heat sink performance studies using nanofluids. *International Journal of Thermal Sciences*. **46(**1), pp. 57–66.

Chen, X., Donmezer, F. N., Kumar, S. and Graham, S. 2014. A numerical study on comparing the active and passive cooling of AlGaN/GaN HEMTs. *IEEE Transactions on Electron Devices*. **61**(12), pp. 4056-4061.

Cheng, L. and Xia, G. 2017. Fundamental issues, mechanisms and models of flow boiling heat transfer in microscale channels. *International Journal of Heat and Mass Transfer*. **108**, pp. 97–127.

Chilton, T.H. and Generaux, R.P. 1933. Pressure drop across tube banks. Trans. *The American Institute of Chemical Engineers* (AIChE). **29**, pp. 161–173.

Choi, K. K., Youn, B. and Yang, R.-J. 2001. Moving Least Squares Method for reliability-based design optimization. 4th World Congress of Structural and Multidisciplinary Optimization, Dalian, China.

Choi, S.B., Barron, R.F. and Warrington, R.O. 1991. Fluid flow and heat transfer in microtubes, in: Micromechanical Sensors, Actuators, and Systems, ASME DSC, vol. 32, Atlanta, GA, pp. 123–134.

Chu, J.-C., Teng, J.-T., Xu, T.-T., Huang, S., Jin, S., Yu, X.-f., Dang, T., Zhang, C.-P. and Greif, R. 2012. Characterization of frictional pressure drop of liquid flow through curved rectangular microchannels. *Experimental Thermal and Fluid Science*. **38**, pp. 171–183.

Chu, K. K., Chao, P. C., Diaz, J. A., Yurovchak, T., Schmanski, B. J., Creamer, C. T., Sweetland, S., Kallaher, R. L., McGray, C., Via, G. D. and Blevins, J. D. 2015. High-performance GaN-on-Diamond HEMTs fabricated by low-temperature device transfer process. *IEEE Compound Semiconductor Integrated Circuit Symposium* (CSICS), New Orleans, LA, 11–14 October (2015), pp. 1–4.

Chu, R. C., Simons, R. E., Ellsworth, M. J., Schmidt, R. R., Cozzolino, V. 2004. Review of cooling technologies for computer products. *IEEE Transactions on Device and Materials Reliability*. **4**(4), pp. 568-585.

Churchill, S. W. and Usagi, R. 1972. A general expression for the correlation of rates of transfer and other phenomena. *AIChE Journal*. **18**(6), pp. 1121-1128.

Colebrook, C. F. 1939. Turbulent flow in pipes, with particular reference to the transition region between the smooth and rough pipe laws. *Journal of the Institution of Civil Engineers*. **11**(4), pp. 133-156.

Coleman, H. W. and Steele, W. G. 1995. Engineering application of experimental uncertainty analysis. *AIAA Journal*. **33**(10), pp. 1888-1896.

Coleman, H. W. and Steele, W. G. 2009. *Experimentation, validation, and uncertainty analysis for engineers*. 3rd edition. Hoboken, New Jersey, USA: John Wiley and Son. Inc.

Colgan, E.G., Furman, B., Gaynes, M., Graham, W.S., LaBianca, N.C., Magerlein, J.H., Polastre, R.J., Rothwell, M.B., Bezama, R.J. Choudhary, R., Marston, K.C., Toy, H., Wakil, J., Zitz, J.A. and Schmidt, R.R. 2007. A practical implementation of silicon microchannel coolers for high power chips. *IEEE Transaction on Components and Packaging Technologies*. **30** (2), pp. 218-225.

Comsol Multiphysics v.5.2, Heat Transfer Module User's Guide, 2015.

Copeland, D. 1995. Manifold microchannel heat sinks: Analysis and optimization. *Thermal Science and Engineering*. **3**(1), pp. 7–12.

Copeland, D. 2000. Optimization of parallel plate heatsinks for forced convection, in: Proceedings of 16th Annual *IEEE Semiconductor Thermal Measurement and Management Symposium*, pp. 266-272.

CREE, Inc. 2012. CGHV1J070D. [Online]. Available from:

http://www.wolfspeed.com/downloads/dl/file/id/418/product/131/cghv1j070d.pdf, June 2012.

Curr, R. M., Sharma, D. and Tatchell, D. G. 1972. Numerical predictions of some three-dimensional boundary layers in ducts. *Computer Methods in Applied Mechanics and Engineering*. **1**(2), pp. 143–158.

Dai, Z., Fletcher, D. F. and Haynes, B. S. 2015. Impact of tortuous geometry on laminar flow heat transfer in microchannels. *International Journal of Heat and Mass Transfer*. **83**, pp. 382–398.

Deb, K., Pratap, A., Agarwal, S. and Meyarivan, T. 2002. A fast and elitist Multiobjective Genetic Algorithm: NSGA-II. *IEEE Transactions on evolutionary computation*. **6**(2), pp. 182-197.

de Boer, G. N., Gao, L., Hewson, R. W., Thompson, H. M., Raske, N. and Toropov. V. V. 2016. A multiscale method for optimising surface topography in elastohydrodynamic lubrication (EHL) using metamodels. *Structural and Multidisciplinary Optimization*. **54**(3), pp. 483–497.

de Boer, G. N., Hewson, R. W., Thompson, H. M., Gao, L. and Toropov. V. V. 2014. Two-scale EHL: Three-dimensional topography in tilted-pad bearings. *Tribology International*. **79**, pp. 111–125.

DeJong, N.C. and Jacobi, A.M. 2003. Flow, heat transfer, and pressure drop in the near-wall region of louvered-fin arrays. *Experimental Thermal and Fluid Science*. **27**, pp. 237–250.

Deng, D., Wan, W., Tang, Y., Shao, H. and Huang, Y. 2015a. Experimental and numerical study of thermal enhancement in reentrant copper microchannels. *International Journal of Heat and Mass Transfer*. **91**, pp. 656–670.

Deng, D., Wan, W., Tang, Y., Wan, Z. and Liang, D. 2015b. Experimental investigations on flow boiling performance of reentrant and rectangular microchannels – A comparative study. *International Journal of Heat and Mass Transfer*. **82**, pp. 435–446.

Dhinsa, K., Bailey, C. and Pericleous, K. 2005. Investigation into the performance of turbulence models for fluid flow and heat transfer phenomena in electronic applications. *IEEE Transactions on Components and Packaging Technologies*. **28** (4), pp. 686-699.

Dittus, F. W. and Boelter, L. M. K. 1930. Heat transfer in automobile radiators of the tubular type. *University of California Publications in Engineering*. **2**(13), pp. 443-461; reprinted in *International Communications in Heat and Mass Transfer*. **12**(1) (1985) 3-22.

Dowling, K. M., Suria, A. J., Won, Y., Shankar, A., Lee, H., Asheghi, M., Goodson, K.E. and Senesky, D. G. 2015. Inductive coupled plasma etching of high aspect ratio silicon carbide microchannels for localized cooling. *ASME, International Technical Conference and Exhibition on Packaging and Integration of Electronic and Photonic Microsystems*. San Francisco, California, USA.

EIA, Monthly Energy Review, DOE/EIA-0035 (2011/07), U.S. Energy Information Administration, July 2011.

Fan, Y. F. and Hassan, I. 2011. Investigation of cooling performance of a swirl microchannel heat sink by numerical simulation. Proceedings of 9th ASME: *International Conference on Nanochannels, Microchannels, and Minichannels*.

Fan, Y., Lee, P. S., Jin, L.-W. and Chua, B. W. 2013. A simulation and experimental study of fluid flow and heat transfer on cylindrical oblique-finned heat sink. *International journal of heat and mass transfer*. **61**, pp. 62-72.

Fan, Y., Lee, P. S., Jin, L.-W. and Chua, B. W. 2014. Experimental investigation on heat transfer and pressure drop of a novel cylindrical oblique fin heat sink. *International journal of Thermal Sciences*. 7**6**, pp. 1-10.

Federov, A. G. and Viskanta, R. 2000. Three-dimensional conjugate heat transfer in the microchannel heat sink for electronic packaging. *International Journal of Heat and Mass Transfer*. **43**, pp. 399 - 415.

Felbinger, J. G., Chandra, M.V.S., Sun, Y., Eastman, L. F., Wasserbauer, J., Faili, F., Babic, D., Francis, D. and Ejeckam, F. 2007. Comparison of GaN HEMTs on Diamond and SiC Substrates. *IEEE Electron Device Letters*. **28**(11), pp. 948–950.

Ferhati, A., Karayiannis, T. G., Lewis, J. S., Mcglen, R. J. and Reay, D. A. 2015. Single-phase laminar flow heat transfer from confined electron beam enhanced surfaces. *Heat Transfer Engineering*. **36**(14–15), pp. 1165–1176.

Filonenko, G.K. 1954. Hydraulic resistance in pipes (in Russian), *Teploenergetika*. **1**(4), pp. 40-44.

Flack, T.J., Pushpakaran, B.N. and Bayne, S.B. 2016. GaN technology for power electronic applications: A Review. *Journal of Electronic Materials*. **45**(6), pp. 2673-2682.

Fonseca, C.M. and Fleming, P.J. 1995. An overview of evolutionary algorithms in multiobjective optimization. *Evolutionary Computation*. **3**(1), pp. 1-16.

Gad-el-Hak, M. 2005. The MEMS Handbook: Introduction and Fundamentals. 2nd edition. Taylor & Francis.

Ghani, I. A., Sidik, N. A. C. and Kamaruzaman, N. 2017a. Hydrothermal performance of microchannel heat sink: The effect of channel design. *International Journal of Heat and Mass Transfer*. **107**, pp. 21–44.

Ghani, I.A., Kamaruzaman, N. and Sidik, N.A.C. 2017b. Heat transfer augmentation in a microchannel heat sink with sinusoidal cavities and rectangular ribs. *International Journal of Heat and Mass Transfer*. **108**, pp. 1969–1981.

Ghani, I.A., Sidik, N.A.C., Mamat, R., Najafi, G., Ken, T.L., Asako, Y. and Japar, W. M. A. A. 2017c. Heat transfer enhancement in microchannel heat sink using hybrid technique of ribs and secondary channels. *International Journal of Heat and Mass Transfer*. **114**, pp. 640–655.

Ghosh, S., Calizo, I., Teweldebrhan, D., Pokatilov, E. P., Nika, D. L., Balandin, A. A., Bao, W., Miao, F. and Lau, C. N. 2008. Extremely high thermal conductivity of graphene: Prospects for thermal management applications in nanoelectronic circuits. *Applied Physics Letters*. **92**, 151911.

Gilkeson, C. A., Toropov, V.V., Thompson, H.M., Wilson, M.C.T., Foxley, N. A. and P. H. Gaskell 2014. Dealing with numerical noise in CFD-based design optimization. *Computers and Fluids*. **94**, pp. 84–97.

Gnielinski, V. 1976. New equations for heat and mass transfer in turbulent pipe and channel flow. *International Chemical Engineering*. **16**(2), pp. 359-368.

Gong, L., Kota, K., Tao, W. and Joshi, Y. 2011. Parametric numerical study of flow and heat transfer in microchannels with wavy walls. *Journal of Heat Transfer*. **133**, (051702-1-10).

Gong, L., Lu, H., Li, H. and Xu, M. 2016. Parametric numerical study of the flow and heat transfer in a dimpled wavy microchannel. *Heat Transfer Research*. **47**(2), pp. 105–118.

Greiner, M., Chen, R.-F. and Wirtz, R. 1991. Enhanced heat transfer/pressure drop measured from a flat surface in a grooved channel. *Journal of Heat Transfer*. **113**, pp. 498–501.

Gunnasegaran, P., Mohammed, H. A., Shuaib, N. H. and Saidur, R. 2010. The effect of geometrical parameters on heat transfer characteristics of microchannels heat sink with different shapes. *International communications in heat and mass transfer*. **37**, pp. 1078-1086.

Haaland, S. E. 1983. Simple and explicit formulas for the friction factor in turbulent flow. *Journal of Fluids Engineering*. **105** (1), pp. 89–90.

Hager, W.H. 2003. Blasius: A life in research and education. *Experiments in fluids*. **34**, pp. 566–571.

Han, Y., Lau, B. L., Zhang, X., Leong, Y. C. and Fah, K. 2014. Enhancement of hotspot cooling with diamond heat spreader on Cu microchannel heat sink for GaN-on-Si device. *IEEE Transactions on Components, Packaging and Manufacturing Technology*. **4**(6), pp. 983-990.

Hao, X. H., Li, X. K., Peng, B., Zhang, M. and Zhu, Y. 2013. Thermal resistance network model for heat sink with serpentine channel. *International Journal of Numerical Modelling: Electronic Networks, Devices and Fields*. **27**(2), pp. 298–308.

Harirchian, T. and Garimella, S.V. 2008. Microchannel size effects on local flow boiling heat transfer to a dielectric fluid. *International Journal of Heat and Mass Transfer*. **51**(15–16), pp. 3724 – 3735.

Harirchian, T. and Grimella, S.V. 2009. The critical role of channel cross sectional area in microchannel flow boiling heat transfer. *International Journal of Multiphase Flow*. **35**(10), pp. 904 – 913.

Ho., C.J., Wei, L.C. and Li, Z.W. 2010. An experimental investigation of forced convective cooling performance of a microchannel heat sink with Al_2O_3/water nanofluid. *Applied Thermal Engineering*. **30** (2–3), pp. 96–103.

Holman, J. P. 2012. *Experimental methods for engineers*. 8th Edition. New York, NY: McGraw-Hill Series in Mechanical Engineering.

Hong, F. and Cheng, P. 2009. Three dimensional numerical analyses and optimization of offset strip-fin microchannel heat sinks. *International Communications in Heat and Mass Transfer*. **36**, pp. 651–656.

Hong, F. J., Cheng, P., Ge, H. and Joo, G. T. 2007. Conjugate heat transfer in fractal-shaped microchannel network heat sink for integrated microelectronic cooling application. *International Journal of Heat and Mass Transfer*. **50**, pp. 4986–4998.

Hua, S.-Z. and Yang, X.-N. 1985. Actual fluid friction manual, National Defence Industry Press, Beijing, P. 269.

Hwu, R. and Qu, W. 2010. Heat transfer correlations for thermally developing flow in rectangular micro-channels subject to four-sided and three-sided H1 boundary conditions. Proceedings of the 14th *International Heat Transfer Conference*. **6**, pp. 239-244.

HyperWorks_12. 2015. Available from: http://www.altairhyperworks.co.uk/product/HyperStudy.

Idelchik, I. E. 1986. Handbook of Hydraulic Resistance. New York, NY: Hemisphere Publishing.

ITRS, The International Technology Roadmap for Semiconductors (2011). Available from:

https://www.semiconductors.org/clientuploads/directory/DocumentSIA/ITRS_2011ExecSum.pdf

ITRS, The International Technology Roadmap for Semiconductors 2.0 (2015). Available from: *http://www.semiconductors.org/clientuploads/Research_Technology/ITRS/2015/0_2015%20ITRS%202.0%20Executive%20Report%20(1).pdf*.

Jacob, M. 1938. Discussion-heat transfer and flow resistance in cross flow of gases over tube banks. *ASME, Mech. Eng*. **60**, pp. 381–392.

Jiang, J., Hao, Y. and Shi, M. 2008. Fluid flow and heat transfer characteristics in rectangular microchannel. *Heat Transfer-Asian Research*. **37**, pp. 197 – 207.

Jiang, L., Mikkelsen, J., Koo, J.-M., Huber, D., Yao, S., Zhang, L., Zhou, P. and Goodson, K.E. 2002. Closed-loop electroosmotic microchannel cooling system for VLSI circuits. *IEEE Transactions on Components and Packaging Technologies*. **25** (3), pp. 347–355.

Jiang, P.-X., Fan, M.-H., Si, G.-S. and Ren, Z.-P. 2001. Thermal-hydraulic performance of small scale micro-channel and porous-media heat-exchangers. *International Journal of Heat and Mass Transfer*. **44**, pp. 1039-1051.

Jiang, X. N., Zhou, Z. Y., Huang, X. Y. and Liu, C. Y. 1997. Laminar flow through microchannels used for microscale cooling systems. in: Proceedings of 97 IEEE/CPMT Electronic Packaging Technology Conference. pp. 119–122.

Jiang, X. N., Zhou, Z. Y., Yao, J., Li, Y. and Ye, X. Y. 1995. Micro-fluid flow in microchannel. in: Proceedings of Transducers '95 . Eurosensors IX, the 8th international conference on Solid-state Sensors and Actuators, and Eurosensors IX , in Stockholm, Sweden, June 25-29. 2, pp. 317–320.

Johnson, R. W. 2016. *Handbook of Fluid dynamics*. 2nd edition. By CRC Press.

Jones, O. C. 1976. An improvement in the calculation of turbulent friction in rectangular ducts. ASME, *Journal of Fluids Engineering*. **98**(2), pp. 173-180.

Joshi, Y. and Wei, X. 2005. Micro and Meso-scale compact heat exchangers in electronics thermal management - A Review, in: R.K. Shah, M. Ishizuka, V.V. Wadekar (Eds.), Proceedings of Fifth International Conference on Enhanced, Compacted and Ultra-Compact Heat Exchangers: Sciebcd, Engineering and Technology, Engineering Conferences International, Hoboken, NJ, USA, pp. 162–179.

Jung, J. -Y., Oh, H. -S. and Kwak, H. -Y. 2009. Forced convective heat transfer of nanofluids in microchannels. *International Journal of Heat and Mass Transfer*. **52**(1-2), pp. 466–472.

Kakaç, S., Shah, R.K. and Aung, W. 1987. Handbook of single-phase convective heat transfer. 1st edition, Wiley-Interscience.

Kaminski, N. and Hilt, O. 2014. SiC and GaN devices – wide bandgap is not all the same. *IET Circuits, Devices & Systems*. **8**(3), pp. 227-236.

Kandlikar, S.G. 2002. Two-Phase flow patterns, pressure drop, and heat transfer during boiling in minichannel flow passages of compact evaporators. *Heat Transfer Engineering*. **23**(1), pp. 5–23.

Kandlikar, S.G. 2003. Microchannels and Minichannels: History, Terminology, Classification and Current research needs. ASME, 1st International Conference on Microchannels and Minichannels. ICMM2003-1000, pp. 1-6

Kandlikar, S. G. 2014. Chapter 3-Single-phase liquid flow in minichannels and microchannels, in: Kandlikar, S. G., Garimella, S., Li, D., Colin, S. and King, M.R. (Eds.) Heat Transfer and Fluid Flow in Minichannels and Microchannels, Elsevier Science Ltd, Oxford, pp. 103-174. Kandlikar, S. G. and Grande, W. J. 2003. Evolution of microchannel flow passages - thermohydraulic performance and fabrication technology. *Heat Transfer Engineering*. **24**(1), pp. 3-17.

Kandlikar, S. G. and Grande, W. J. 2004. Evaluation of single phase flow in microchannels for high heat flux chip cooling-thermohydraulic performance enhancement and fabrication technology. Heat Transf. Eng. 25, pp. 5–16.

Kandlikar, S. G., Joshi, S. and Tian, S. 2003. Effect of surface roughness on heat transfer and fluid flow characteristics at low Reynolds numbers in small diameter tubes. *Heat Transfer Engineering*. **24**(3), pp. 4 – 16.

Kandlikar, S.G., Kuan, W.K., Willistein, D.A. and Borrelli, J. 2006. Stabilization of flow boiling in microchannels using pressure drop elements and fabricated nucleation sites. *Journal of Heat Transfer*. **128**(4), pp. 389–396.

Kandlikar, S.G., Widger, T., Kalani, A. and Mejia, V. 2013. Enhanced flow boiling over open microchannels with uniform and tapered gap manifolds. ASME *Journal of Heat Transfer*. 135(6), 061401.

Kant, K. 2009. Data center evolution: A tutorial on state of the art, issues, and challenges. *Computer Networks*. **53**, pp. 2939–2965.

Karayiannis, T.G., Shiferaw, D., Kenning, D.B.R., Wadekar, V.V. 2010. Flow pattern and heat transfer for flow boiling in small to micro diameter tubes. *Heat Transfer Engineering*. **31**(4), pp. 257 – 275.

Karayiannis, T.G. and Mahmoud, M.M. 2017. Flow boiling in microchannels: Fundamentals and applications. *Applied Thermal Engineering*. **115**, pp. 1372–1397.

Kawano, K., Minikami K., Iwasaki H. and Ishizuka M. 1998. Micro channel heat exchanger for cooling electrical equipment. Proc. ASME Heat Transfer Division. **3**, pp. 173–180.

Kays, W. M. 1994. Turbulent Prandtl number–Where Are We?, *ASME Journal of Heat Transfer*. **116**, pp. 284-295.

Kays, W. M., and London, A. L. 1984. *Compact heat exchangers*. 3rd edition. New York: McGraw-Hill Series in Mechanical Engineering.

Keane, A. J. and Nair, P. B. 2005. Computational approaches for aerospace design the pursuit of excellence. West Sussex, England: John Wiley & Sons Ltd.

Kew, P. A. and Cornwell, K. 1997. Correlation for the prediction of boiling heat transfer in small-diameter channels. *Applied Thermal Engineering*. **17**(8-10), pp.705-715.

Khan, T. S., Khan, M. S. Chyu, M. C. and Ayub, Z. H. 2010. Experimental investigation of single phase convective heat transfer coefficient in a corrugated plate heat exchanger for multiple plate configurations. *Applied Thermal Engineering*. **30**, pp. 1058–1065.

Khan, T. S., Khan, M. S. and Ayub, Z. H. 2017. Single-phase flow pressure drop analysis in a plate heat exchanger. *Heat Transfer Engineering*. **38**(2), pp. 256-264.

Khatir, Z., Taherkhani, A.R., Paton, J., Thompson, H., Kapur, N. and Toropov, V. 2015. Energy thermal management in commercial bread-baking using a multi-objective optimisation framework. *Applied Thermal Engineering*. **80**, pp. 141-149.

Khodabandeh, R. and Palm, B. 2002. An experimental investigation of influence of the threaded surface on the boiling heat transfer coefficients in vertical narrow channels. *Microscale Thermophysical Engineering*. **6**(2), pp. 131-139.

Kline, S. J. and McClintock, F. A. 1953. Describing uncertainties in single-sample experiments. *Mechanical Engineering*. **75**(1), pp. 3-8.

Knight, R. W., Goodling, J. S. and Hall, D. J. 1991. Optimal thermal design of forced convection heat sinks-analytical. ASME, *Journal of Electronic Packaging*. **113**(3), pp. 313-321.

Koomey, J. G. 2011. Growth in Data Center Electricity use 2005 to 2010.

Koşar, A. 2010. Effect of substrate thickness and material on heat transfer in microchannel heat sinks. *International Journal of Thermal Sciences*. **49**, pp. 635-642.

Koşar, A., Kuo, C.-J. and Peles, Y. 2006. Suppression of boiling flow oscillations in parallel microchannels by inlet restrictors. *Journal of Heat Transfer*. **128**, pp. 251–260.

Koşar, A., Mishra, C. and Peles, Y. 2005. Laminar flow across a bank of low aspect ratio micro pin fins. ASME, *Journal of Fluids Engineering*. **127**, pp. 419–430.

Koşar, A. and Peles, Y. 2006. Thermal-hydraulic performance of MEMS based pin fin heat sink. ASME, *Journal of Heat Transfer*. **128**, pp. 121–131.

Koşar, A. and Peles, Y. 2007. Critical Heat Flux of R-123 in Silicon-based microchannels. ASME *Journal of Heat Transfer*. **129**(7), pp. 844–851.

Kraus A. 2013. Air- and Liquid-Cooled Cold Plates. Vol. 2 in the Encyclopedia of thermal packaging. Singapore, World Scientific Publishing Co. Pte. Ltd.

Kuo, C.-J. and Peles, Y. 2007. Local measurement of flow boiling in structured surface microchannels. *International Journal of Heat and Mass Transfer*. **50**, pp. 4513–4526.

Kuo, C.-J. and Peles, Y. 2009. Pressure effects on flow boiling instabilities in parallel microchannels. *International Journal of Heat and Mass Transfer*. **52**, pp. 271–280.

Kuppusamy, N. R., Saidur, R., Ghazali, N.N.N. and Mohammed H. A. 2014. Numerical study of thermal enhancement in micro channel heat sink with secondary flow. *International Journal of Heat and Mass Transfer*. **78**, pp. 216–223.

Kuzmin, D., Mierka, O. and Turek, S. 2007. On the implementation of the k–ε turbulence model in incompressible flow solvers based on a finite element discretization. *International Journal of Computing Science and Mathematics*. **1**(2–4), pp. 193–206.

Law, M. and Lee, P.S. 2015. A comparative study of experimental flow boiling heat transfer and pressure characteristics in straight- and oblique-finned microchannels. *International Journal of Heat and Mass Transfer*. **85**, pp. 797–810.

Lee, H., Agonafer, D.D., Won, Y., Houshmand, F., Gorle, C., Asheghi, M. and Goodson, K.E. 2016. Thermal modeling of extreme heat flux microchannel coolers for GaN-on-SiC semiconductor devices. ASME *Journal of Electronic Packaging*. **138**(1), In Press, 010907-1.

Lee, H., Won, Y., Houshmand, F., Gorle, C., Asheghi, M., and Goodson, K. E. 2015. Computational modeling of extreme heat flux microcooler for GaN-Based HEMT. ASME Paper No. IPACK2015-48670.

Lee, J. and Mudawar, I. 2007. Assessment of the effectiveness of nanofluids for single-phase and two-phase heat transfer in micro-channels. *International Journal of Heat and Mass Transfer*. **50**(3-4), pp. 452–463.

Lee, P.C. and Pan, C. 2008. Boiling heat transfer and two-phase flow of water in a single shallow microchannel with uniform or diverging cross section, *Journal of Micromechanics and Microengineering*. **18**, pp. 1–13.

Lee, P. S. and Garimella, S. V. 2006. Thermally developing flow and heat transfer in rectangular microchannels of different aspect ratios. *International Journal of Heat and Mass Transfer*. **49**(17–18), pp. 3060–3067.

Lee, P. S., Garimella, S. V. and Liu, D. 2005. Investigation of heat transfer in rectangular microchannels. *International Journal of Heat and Mass Transfer*. **48**, pp. 1688–1704.

Lee, S. W. and Qu, W. 2007. Thermal design methodology for low flow rate single-phase and two-phase micro-channel heat sinks. *IEEE Transactions on Components and Packaging Technologies*. **30**(4), pp. 830-841.

Lee, Y. J., Lau, B. L., Leong, Y. C., Choo, K. F., Zhang, X. and Chan, P. K. 2012. GaN-on-Si hotspot thermal management using direct-die-attached microchannel heat sink, in Proc. IEEE 14th Electron. Packag. Technol. Conf., Singapore, pp. 121–125.

Lee, Y. J., Lee, P. S. and Chou, S. K. 2012. Enhanced thermal transport in micro channels using oblique fins. *Journal of Heat Transfer*. **134**(9), 101901-1-10.

Lee, Y. J., Lee, P. S. and Chou, S. K. 2013. Numerical study of fluid flow and heat transfer in the enhanced microchannel with oblique fins. *Journal of heat transfer*. **135**(4), 041901-1-10.

Lee, Y. J., Singh, P. K. and Lee, P. S. 2015. Fluid flow and heat transfer investigations on enhanced microchannel heat sink using oblique fins with parametric study. *International Journal of Heat and Mass Transfer*. **81**, pp. 325–336.

Leitão, V.M.A., Alves, C.J.S. and Duarte, C.A. 2007. *Advances in Meshfree Techniques*. Netherlands: Springer.

Leng, C., Wang, X.-D., Wang, T.-H. and Yan, W.-M. 2015. Multi-parameter optimization of flow and heat transfer for a novel double-layered microchannel heat sink. *International Journal of Heat and Mass Transfer*. **84**, pp. 359-369.

Leonard, P.L. and Phillips, A.L. 2005. The thermal bus opportunity–A quantum leap in data center cooling potential. Presented at the ASHRAE Annual Meeting, Denver, CO.

Li, J., Peterson, G. P. and Cheng, P. 2004. Three-dimensional analysis of the heat transfer in a micro-heat sink with single phase flow. *International Journal of Heat and Mass Transfer*. **47**(19-20), pp. 4215–4231.

Li, X. K., Hao, X. H., Chen, Y., Zhang, M. H. and Peng, B. 2013. Multi-objective optimizations of structural parameter determination for serpentine channel heat sink. in: Proceedings of 16th European Conference on the Applications of Evolutionary Computation, Vienna, Austria. pp. 449-458.

Li, Y., Xia, G., Jia, Y., Cheng, Y. and Wang, J. 2017. Experimental investigation of flow boiling performance in microchannels with and without triangular cavities – a comparative study. *International Journal of Heat and Mass Transfer*. **108**, pp. 1511–1526.

Li, Y., Zhang, F., Sunden, B. and Xie, G. 2014. Laminar thermal performance of microchannel heat sinks with constructal vertical Y-shaped bifurcation plates. *Applied Thermal Engineering*. **73**, pp. 185-195.

Liu, C., Teng, J.-T., Chu, J.-C., Chiu, Y.-L., Huang, S., Jin, S., Dang, T., Greif, R. and Pan, H.-H. 2011. Experimental investigations on liquid flow and heat transfer in rectangular microchannel with longitudinal vortex generators. *International Journal of Heat and Mass Transfer*. **54**, pp. 3069–3080.

Liu, D. and Garimella, S.V. 2007. Flow boiling heat transfer in microchannels. *Journal of Heat Transfer*. **129**(10), pp. 1321-1332.

Loweth, E. L., de Boer, G. N., and Toropov, V. V. 2011. Practical recommendations on the use of Moving Least Squares Metamodel building. In Topping, B. H. V., and Tsompanakis, Y. (Eds.) Proceedings of the 13th International Conference on Civil, Structural and Environmental Engineering Computing, 96, Civil Comp Press, Stirlingshire.

Lu, C.T. and Pan, C. 2008. Stabilization of flow boiling in microchannel heat sinks with a diverging cross-section design, *Journal of Micromechanics and Microengineering*. **18**, pp. 1–13.

Lu, C.T. and Pan, C. 2011. Convective boiling in a parallel microchannels heat sink with a diverging cross-section and artificial nucleation sites. *Experimental Thermal and Fluid Sciences*. **35**, pp. 810–815.

Lu, M.-C. and Wang, C.-C. 2006. Effect of the Inlet Location on the Performance of Parallel-Channel Cold-Plate. *IEEE Transactions on Components and Packaging Technologies*. **29**(1), pp. 30-38.

Luo, X. and Mao, Z. 2012. Thermal modeling and design for microchannel cold plate with high temperature uniformity subjected to multiple heat sources. *International Communications in Heat and Mass Transfer*. **39** (6), pp. 781–785.

Maharudrayya, S., Jayanti, S. and Deshpande, A.P. 2004. Pressure losses in laminar flow through serpentine channels in fuel cell stacks. *Journal of Power Sources*. **138**, pp. 1–13.

Manca, O., Nardini, S. and Ricci, D. 2012. A numerical study of nanofluid forced convection in ribbed channels. *Applied Thermal Engineering*. **37**, pp. 280-292.

Megahed, A. 2011. Experimental investigation of flow boiling characteristics in a cross-linked microchannel heat sink. *International Journal of Multiphase Flow*. **37**, pp. 380–393.

Mehendale, S. S., Jacobi, A. M. and Shah, R. K. 2000. Fluid flow and heat transfer at Micro- and Meso-scales with application to heat exchanger design. *Applied Mechanics Reviews*. **53**(7), pp. 175-193.

Metzger, W.B., Fan, D.E. and Shepard, Z.N. 1982. Pressure loss and heat transfer through multiple rows of short pin fins. *Journal of Heat Transfer*. **3**, pp. 137–142.

Meyer, D. J., Feygelson, T. I., Anderson, T. J., Roussos, J. A., Tadjer, M. J., Downey, B. P., Katzer, D. S., Pate, B. B., Ancona, M. G., Hobart, K. D. and Eddy Jr., C. R. 2014. Large-signal RF performance of Nanocrystalline diamond coated AlGaN/GaN High Electron Mobility Transistors. *IEEE Electron Device Letters*. **35**(10), pp. 1013-1015.

Millan, J., Godignon, P., Perpina, X., Perez-Tomas, A. and Rebollo, J. 2014. A survey of wide bandgap power semiconductor devices. *IEEE Transactions on Power Electronics*. **29**(5), pp. 2155-2163.

Minkowycz, W. J., Sparrow, E. M. and Murthy, J. Y. 2006. Handbook of Numerical Heat Transfer, second edition, John Wiley & Sons, Inc.

Mishra, U. and Shen, L. 2008. GaN-based RF power devices and amplifiers. *Proceedings of the IEEE*. **96**(2), pp. 1-19.

Mochizuki, M., Nguyen, T., Mashiko, K., Saito, Y., Nguyen, T. and Wuttijumnong, V. 2011. A review of heat pipe application including new opportunities. *Frontiers in Heat Pipes*. **2**, pp. 1-15.

Moffat, R.J. 1985. Using uncertainty analysis in the planning of an experiment. Transactions of the ASME, *Journal of Fluids Engineering*. **107**(2), pp. 173-178.

Moffat, R.J. 1988. Describing the uncertainties in experimental results. *Experimental Thermal and Fluid Science*. **1**(1), pp. 3-17.

Mohammed, H.A., Gunnasegaran, P. and Shuaib, N.H. 2011a. The impact of various nanofluid types on triangular microchannels heat sink cooling performance. *International Communication in Heat and Mass Transfer*. **38**(6), pp. 767 - 773.

Mohammed, H.A., Gunnasegaran, P. and Shuaib, N.H. 2011b. Numerical simulation of heat transfer enhancement in wavy microchannel heat sink. *International Communication in Heat Mass Transfer*. **38**(1), pp. 63-68.

Mohammed, H.A., Gunnasegaran, P. and Shuaib, N.H. 2011c. Influence of channel shape on the thermal and hydraulic performance of microchannel heat sink. *International Communication in Heat and Mass Transfer*. **38**(4), pp. 474–480.

Montgomery, D. C. 2013. *Design and Analysis of Experiments*. 8th edition, John Wiley & Sons, Inc.

Moore, G. E. 1965. Cramming More Components onto Integrated Circuits. *Electronics*. **38**(8), pp.114-117.

Morini, G. L. 2004. Single-phase convective heat transfer in microchannels: A Review of experimental results. *International Journal of Thermal Sciences.* **43**(7), pp. 631–651.

Moriyama, K., Inoue, A. and Ohira, H. 1992. The themohydraulic characteristics of two-phase flow in extremely narrow channels: The frictional pressure drop and heat transfer of boiling two-phase flow, analytical model. *Heat Transfer*. **58**(546), p. 393–400.

Mudawar, I., Bharathan, D., Kelly, K. and Narumanchi, S. 2009. Two-phase spry cooling of hybrid vehicle electronics. *IEEE Transactions on Components and Packaging Technologies*. **32** (2), pp. 501–512.

Myers, R. H., Montgomery, D. C. and Anderson-Cook, C. M. 2016. Response Surface Methodology: Process and product optimization using designed experiments, 4th Edition, John Wiley and sons, Inc.

Naphon, P. and Nakharintr, L. 2013. Heat transfer of nanofluids in the mini-rectangular fin heat sinks. *International Communications in Heat and Mass Transfer*. **40**, pp. 25–31.

Narayanan, A., Toropov, V.V., Wood A., Campean, I.F. 2007. Simultaneous model building and validation with uniform designs of experiments. *Engineering Optimization*. **39**(5), pp. 497-512.

Nellis, G. and Klein, S. 2009. *Heat transfer*. 1st edition, USA.

Nesis, E.I. Shatalov, A.F. and Karmatskii, N. P. 1994. Dependence of the heat transfer coefficient on the vibration amplitude and frequency of a vertical thin heater. *Journal of Engineering Physics and Thermophysics*. **67**(1-2), pp. 696–698.

Nguyen, C.T., Roy, G., Gauthier, C. and Galanis, N. 2007. Heat transfer enhancement using Al_2O_3–water nanofluid for an electronic liquid cooling system. *Applied Thermal Engineering*. **27** (8–9), pp. 1501–1506.

Nilpueng, K., Keawkamrop, T., Ahn, H.S. and Wongwises, S. 2018. Effect of chevron angle and surface roughness on thermal performance of single-phase water flow inside a plate heat exchanger. *International Communications in Heat and Mass Transfer*. **91**, pp. 201-209.

Nithiarasu, P., Lewis, R.W. and Seetharamu, K. N. 2016. *Fundamentals of the Finite Element Method for Heat and Mass Transfer*. 2nd Edition, John Wiley & Sons, Ltd.

Norris, R. H. 1971. Some simple approximate heat transfer correlations for turbulent flow in ducts with surface roughness. *Augmentation of Convection Heat and Mass Transfer*, American Society of Mechanical Engineers, New York.

Nukiyama, S. 1934. The maximum and minimum values of heat Q transmitted from metal to boiling water under atmospheric pressure. *Journal of Japanese Society of Mechanical Engineering*. **37**, pp. 367-374. (translated in *International Journal of Heat and Mass Transfer*. **27**(7) (1984), pp. 959-970).

Nuttinck, S., Gebara, E., Laskar, J. and Harris, M. 2002. Development of GaN wide bandgap technology for microwave power applications. *IEEE Microwave Magazine*. **3**(1), pp. 80-87.

Obot, N. T. 2003. Toward a better understanding of friction and heat/mass transfer in microchannels – A Literature Review. *Microscale Thermophysical Engineering*. **6**, pp. 155- 173.

Oh, H. W. 2012. Applied Computational Fluid Dynamics. InTech.

Pantzali, M.N., Kanaris, A.G., Antoniadis, K.D., Mouza, A.A. and Paras, S.V. 2009. Effect of nanofluids on the performance of a miniature plate heat exchanger with modulated surface. *International Journal of Heat and Fluid Flow*. **30**, pp. 691-699.

Patankar, S. V. 1980. *Numerical heat transfer and fluid flow*. Taylor and Francis.

Peles, Y., Koşar, A., Mishra, C., Kuo, C. and Schneider, B. 2005. Forced convective heat transfer across a pin fin micro heat sink. *International Journal of Heat and Mass Transfer*. **48**(17), pp. 3615–3627.

Peng, X. F., Peterson, G. P. and Weng, B. X. 1994a. Frictional flow characteristics of water flowing through rectangular microchannels. *Experimental Heat Transfer*. **7**(4), pp. 249-264.

Peng, X. F., Peterson, G. P. and Weng, B. X. 1994b. Heat transfer characteristics of water flowing through microchannels. *Experimental Heat Transfer*. **7**(4), pp. 265-283.

Peng, X. F. and Peterson, G. P. 1996. Convective heat transfer and flow friction for water flow in microchannel structures. *International Journal of Heat and Mass Transfer*. **39**(12), pp. 2599-2608.

Pengelly, R. S., Wood, S. M., Milligan, J. W., Sheppard, S. T.and Pribble, W. L. 2012. A review of GaN on SiC High Electron-Mobility Power Transistors and MMICs. *IEEE Transactions on Microwave Theory and Techniques*. **60**(6), pp. 1764-1783.

Petukhov, B. S. 1970. Heat transfer and friction in turbulent pipe flow with variable physical properties. *Advances in Heat Transfer*. **6**, pp. 503-565.

Phillips, R. J. 1987. *Forced-Convection, Liquid-Cooled, Microchannel Heat Sinks*. M.S. Thesis, Department of Mechanical Engineering, Massachusetts Institute of Technology, Cambridge.

Phillips R. J. 1988. Microchannel heat sinks. *The Lincoln Laboratory Journal*. **1**(1), pp. 31-48.

Phillips, R. J. 1990. Microchannel heat sinks, Advances in thermal modelling of electronic components and systems, Hemisphere Publishing Corporation, New York, NY. Chapter 3.

Pijnenburg, R., Dekker, R., Nicole, C., Aubry, A. and Eummelen, E. 2004. Integrated micro-channel cooling in silicon. in Proceeding of the European Solid-State Device Research conference. 10.1109/ESSDER.2004.1356506. pp. 129-132.

Poh, S. T. and Ng, E. Y. K. 1998. Heat transfer and flow issues in manifold microchannel heat sinks: A CFD Approach. Proceedings of 2nd Electronics Packaging Technology Conference. pp. 246-250.

Popiel, C. O. and Wojtkowiak, J. 1998. Simple formulas for thermophysical properties of liquid water for heat transfer calculations (from 0 ºC to 150 ºC). *Journal of Heat Transfer Engineering*. **19**(3), pp. 87-101.

Prajapati, Y. K., Pathak, M. and Khan, M. K. 2015. A comparative study of flow boiling heat transfer in three different configurations of microchannels. *International Journal of Heat and Mass Transfer*. **85**, pp. 711–722.

Prajapati, Y. K. and Bhandari, P. 2017. Flow boiling instabilities in microchannels and their promising solutions – A review. *Experimental Thermal and Fluid Science*. **88**, pp. 576–593.

Qu, W., Mala, G.M. and Li, D. 2000a. Pressure-driven water flows in trapezoidal silicon microchannels. *International Journal of Heat and Mass Transfer*. **43**, pp. 353– 364.

Qu, W., Mala, G.M. and Li, D. 2000b. Heat transfer for water flow in trapezoidal silicon microchannels. *International Journal of Heat and Mass Transfer*. **43**, pp. 3925-3936.

Qu, W. and Mudawar, I. 2002a. Experimental and numerical study of pressure drop and heat transfer in a single-phase micro-channel heat sink. *International Journal of Heat and Mass Transfer*. **45**(12), pp. 2549 – 2565.

Qu, W. and Mudawar, I. 2002b. Analysis of three-dimensional heat transfer in micro-channel heat sinks. *International Journal of Heat and Mass Transfer*. **45**(19), pp. 3973-3985.

Qu, W., Mudawar, I., Lee, S.-Y. and Wereley, S. T. 2006. Experimental and computational investigation of flow development and pressure drop in a rectangular micro-channel. ASME, *Journal of Electronic Packaging*. **128**(1), pp.1-9.

Qu, W.L. and Siu-Ho, A. M. 2008a. Liquid single-phase flow in an array of micro-pin-fins part I: Heat transfer characteristics. *Journal of Heat Transfer*. **130**(12), pp. 1-11.

Qu, W.L. and Siu-Ho, A. M. 2008b. Liquid single-phase flow in an array of micro-pin-fins part II: Pressure drop characteristics. *Journal of Heat Transfer*. **130**(12), pp. 1-4.

Rainieri, S., Bozzoli, F. and Cattani, L. 2014. Passive techniques for the enhancement of convective heat transfer in single phase duct flow. *Journal of Physics*: Conference Series 547 (2014) 012002, pp. 1-10.

Reddy, S.R. and Dulikravich, G.S. 2017. Analysis of anisotropic graphene platelet heat spreaders to reduce hot spot temperature and temperature non-uniformity. *16th IEEE Intersociety Conference on Thermal and Thermomechanical Phenomena in Electronic Systems (ITherm)*. pp. 135-142.

Reeser, A., Bar-Cohen, A. and Hetsroni, G. 2014. High vapor quality two phase heat transfer in staggered and inline micro pin fin arrays. 14th *IEEE Intersociety Conference on Thermal and Thermomechanical Phenomena in Electronic Systems* (ITherm), Orlando, FL, May 27–30, pp. 213–221.

Rohsenow, W. M., Hartnett, J. P. and Cho, Y. I. 1998. *Handbook of Heat Transfer*. 3rd edition. New York, McGraw-Hill Companies, Inc.

Rosaguti, N.R., Fletcher, D.F. and Haynes, B.S. 2006. Laminar flow and heat transfer in a periodic serpentine channel with semi-circular cross-section. *International Journal of Heat and Mass Transfer*. **49**, pp. 2912–2923.

Rubio-Jimenez, C. A., Kandlikar, S. G. and Hernandez-Guerrero, A. 2013. Performance of online and offset micro pin-fin heat sinks with variable fin density. *IEEE Transactions on Components, Packaging and Manufacturing Technology*. **3**(1), pp. 86–93.

Saenen, T. 2013. Modeling a two-phase microchannel electronics cooling system. PhD thesis, Katholieke Universiteit Leuven.

Sahin, B., Yakut, K., Kotcioglu, I. and Celik, C. 2005. Optimum design parameters of a heat exchanger. *Applied Energy*. **82**, pp. 90-106.

Salman, B. H., Mohammed, H. A. and Kherbeet, A. S. 2014. Numerical and experimental investigation of heat transfer enhancement in a microtube using nanofluids. International Communication in Heat and Mass Transfer. **59**, pp. 88–100.

Sarua, A., Ji, H., Hilton, K.P., Wallis, D.J., Uren, M.J., Martin, T. and Kuball, M. 2007. Thermal boundary resistance between GaN and substrate in AlGaN/GaN electronic devices. *IEEE Transactions on Electron Devices*. **54**(12), pp. 3152-3158.

Seal, S. and Mantooth, H. A. 2017. High performance silicon carbide power packaging-past trends, present practices, and future directions. *Energies*. **10**(3), pp. 1-30.

Sehgal, S. S., Murugesan, K. and Mohapatra, S. K. 2011. Experimental Investigation of the Effect of Flow Arrangements on the Performance of a Micro-Channel Heat Sink. *Experimental Heat Transfer*. **24**, pp. 215–233.

Seyf, H. R. and Feizbakhshi, M. 2012. Computational analysis of nanofluid effects on convective heat transfer enhancement of micro-pin-fin heat sinks. *International Journal of Thermal Sciences*. **58**, pp. 168-179.

Shah, R. K. 1978. A correlation for laminar hydrodynamic entry length solutions for circular and noncircular ducts. ASME, *Journal of Fluids Engineering*. **100**, pp. 177-179.

Shah, R. K. and Bhatti, M. S. 1987. *Laminar Convection Heat Transfer in Ducts*. In: Handbook of single-phase convective heat transfer. eds. Kakaç, S., Shah, R. K. and Aung, W., New York, Wiley-Interscience, John Wiley & Sons.

Shah, R. K., and London, A. L. 1978. *Laminar Flow Forced Convection in Ducts*: a source book for compact heat exchanger analytical data. Advances in Heat Transfer Supplement 1, Academic Press, New York.

Shao, B., Wang, L., Li, J. and Sun, Z. 2009. Application of thermal resistance network model in optimization design of micro-channel cooling heat sink. *International Journal of Numerical Methods for Heat and Fluid Flow*. **19**(3/4), pp. 535-54.

Sharma, C.S., Tiwari, M.K., Michel, B. and Poulikakos, D. 2013. Thermofluidics and energetics of a manifold microchannel heat sink for electronics with recovered hot water as working fluid. *International Journal of Heat and Mass Transfer*. **58**, pp. 135–151.

Sharma, C.S., Tiwari, M.K., Zimmermann, S., Brunschwiler, T., Schlottig, G., Michel, B. and Poulikakos, D. 2015. Energy efficient hotspot-targeted embedded liquid cooling of electronics. *Applied Energy*. **138**, pp. 414–422.

Shehabi, A., Smith, S. J., Horner, N., Azevedo, I., Brown, R., Koomey, J., Masanet, E., Sartor, D., Herrlin, M. and Lintner, W. 2016. United States data center energy usage report, Lawrence Berkeley National Laboratory, Berkeley, California. LBNL-1005775 Page, vol. 4.

Siddique, M. Khaled, A.-R. A., Abdulhafiz, N. I. and Boukhary, A. Y. 2010. Recent Advances in Heat Transfer Enhancements: A Review Report. *International Journal of Chemical Engineering*. Vol (2010), pp. 1-28.

Shih, R. H., Schilling, P. J. 2015. Parametric Modeling with SolidWorks 2015, New Orleans, Louisiana.

Silk, E.A., Golliher, E.L. and Selvam, R.P. 2008. Spray cooling heat transfer: technology overview and assessment of future challenges for micro-gravity application. *Energy Conversion and Management*. **49**(3), pp. 453–468.

Siu-Ho, A. M., Qu, W. and Pfefferkorn, F. E. 2007. Experimental study of pressure drop and heat transfer in a single-phase micro-pin-fin heat sink. ASME, *Journal of Electronic Packaging*. **129**, pp. 479–487.

Steinke, M. E. and Kandlikar, S. G. 2004. Review of single–phase heat transfer enhancement techniques for application in microchannels, mini-channels and microdevices. *International Journal of Heat and Technology*. **22**(2), pp. 3–11.

Steinke, M. E. and Kandlikar, S. G. 2004. Single-phase heat transfer enhancement techniques in microchannel and minichannel flows, in: Second International Conference on Microchannels and Minichannels. Rochester, NY USA, pp. 141–148.

Steinke, M. E. and Kandlikar, S. G. 2006a. Single-phase liquid heat transfer in plain and enhanced microchaneels, in: Proceedings of 4th International conference on Nanochannels, Microchannels and Minichannels, Limerick, Ireland, pp. 943-951.

Steinke, M. E. and Kandlikar, S. G. 2006b. Single-phase liquid friction factors in microchannels. *International Journal of Thermal Sciences*. **45**(11), pp. 1073-1083.

Subrina, A., Kotchethov, D. and Balandin, A.A. 2009. Heat removal in silicon-on-insulator integrated circuits with graphene lateral heat spreaders. *IEEE Electron Device Letters*. **30**, pp. 1281-1283.

Suga, K. and Aoki, H. 1995. Numerical study on heat transfer and pressure drop in multilouvered fins. *Journal of Enhanced Heat Transfer*. **2**, pp. 231–238.

Sui, Y., Teo, C. J. and Lee, P. S. 2010. Fluid flow and heat transfer in wavy microchannels. *International Journal of Heat and Mass Transfer*. **53**(13-14), pp. 2760-2772.

Sui, Y., Lee, P. S. and Teo, C. J. 2011. An experimental study of flow friction and heat transfer in wavy microchannels with rectangular cross section. *International Journal of Thermal Sciences*. **50**(12), pp. 2473-2482.

Sundar, L. S., Sharma, K.V., Singh, M.K. and Sousa, A.C.M. 2017. Hybrid nanofluids preparation, thermal properties, heat transfer and friction factor – A review. *Renewable and Sustainable Energy Reviews*. **68** (1), pp. 185–198.

Sverdlik, Y. 2016. Here's how much energy all US data centers consume, data center knowledge.

Tadjer, M. J., Anderson, T. J., Hobart, K. D., Feygelson, T. I., Caldwell, J. D., Eddy Jr., C. R., Kub, F. J., Butler, J. E., Pate, B. and Melngailis, J. 2012. Reduced Self-Heating in AlGaN/GaN HEMTs Using Nanocrystalline Diamond Heat-Spreading Films. *IEEE Electron Device Letters*. 33, pp. 23-25.

Tadjer, M. J., Anderson, T. J., Feygelson, T. I., Hobart, K. D., Hite, J. K., Koehler, A. D., Wheeler, V. D., Pate, B. B., Eddy Jr., C. R. and Kub, F. J. 2016. Nanocrystalline diamond capped AlGaN/GaN high electron mobility transistors via a sacrificial gate process. Physica Status Solidi A 213 (4), pp. 893–897.

Toh, K. C., Chen, X. Y. and Chai, J. C. 2002. Numerical computation of fluid flow and heat transfer in micro channels. *International Journal of Heat and Mass Transfer*. **45**(26), pp. 5133 -5141.

Tsou, C.-W., Lin, C.-Y., Lian, Y.-W. and Hsu, S.S.H. 2015. 101-GHz InAlN/GaN HEMTs on Silicon with high Johnson's Figure-of-Merit. *IEEE Transactions on Electron Devices*. **62**(8), pp. 2675-2678.

Tsuzuki, N., Kato, Y. and T. Ishizuka. 2007. High performance printed circuit heat exchanger. *Applied Thermal Engineering*. **30**, pp. 1702–1707.

Tuckerman, D. B. and Pease, R. F. W. 1981. High-performance heat sinking for VLSI. *IEEE Electron Device Letters*. EDL-**2**(5), pp. 126-129.

Tuckerman, D. B. and Pease, R. F. W. 1982. Optimized convective cooling using micromachined structures. *Journal of the Electrochemical Society*. **129**(3), p. C98.

Tullius, J.F., Vajtai, R. and Bayazitoglu, Y. 2011. A review of cooling in microchannels. *Heat Transfer Eng*. **32** (7–8), pp. 527–541.

Tummala, R.R. 2001. *Fundamentals of Microsystems Packaging*. McGraw-Hill.

Utsler, J. Computing in 3D, IBM Systems Magazine, November 2010.

Vafai, K. and Zhu, L. 1999. Analysis of two-layered micro-channel heat sink concept in electronic cooling. *International Journal of Heat and Mass Transfer*. **42**(12), pp. 2287–2297.

Versteeg, H. K. and Malalasekera, W. 2007. An introduction to computational fluid dynamics: the finite volume method. 2nd edition, Harlow: Prentice Hall, England.

Vinodhan, V. L. and Rajan, K. S. 2014. Computational analysis of new microchannel heat sink configurations. *Energy Conversion and Management*. **86**, pp. 595–604.

Wang, B. X. and Peng, X. F. 1994. Experimental investigation on liquid forced convection heat transfer through microchannels. *International Journal of Heat and mass Transfer*. **37**, pp. 73-82.

Wang, G., Cheng, P. and Bergles, A. 2008. Effects of inlet/outlet configurations on flow boiling instability in parallel microchannels. *International Journal of Heat and Mass Transfer*. **51**, pp. 2267–2281.

Wang, G., Niu, D., Xie, F., Wang, Y., Zhao, X., and Ding, G. 2015. Experimental and numerical investigation of a microchannel heat sink (MCHS) with micro-scale ribs and grooves for chip cooling. *Applied Thermal Engineering*. **85**, pp. 61-70.

Wei, X. and Joshi, Y. 2003. Optimization study of stacked micro-channel heat sinks for micro-electronic cooling. *IEEE Transactions on Components and Packaging Technologies*. **26**(1), pp. 55–61.

Wei, X. and Joshi, Y. 2004. Stacked microchannel heat sinks for liquid cooling of microelectronic components. *ASME Transactions Journal of electronic packaging*. **126**(1), pp. 60–66.

White, F. M. 2011. Fluid mechanics. 7th edition. New York, NY: McGraw Hill.

Wilcox, D. C. 2006. Turbulence modelling for CFD. 3rd edition. DCW Industries, Inc.

Williams, O.A. 2011. Nanocrystalline diamond. *Diamond and Related Materials*. 20 (5-6), pp. 621–640.

Wirtz, R., Huang, F. and Greiner, M. 1999. Correlation of fully developed heat transfer and pressure drop in a symmetrically grooved channel. *Journal of Heat Transfer*. **113**, pp. 590–596.

Wort, C.J.H. and Balmer, R.S. 2008. Diamond as an electronic material. *Materialstoday*. **11**(1-1). pp. 22-28.

Wu, H. Y. and Cheng, P. 2003. An experimental study of convective heat transfer in silicon microchannels with different surface conditions. *International Journal of Heat and Mass Transfer*. **46**, pp. 2547–2556.

Wu, P. and Little, W. A. 1983. Measurement of friction factors for the flow of gases in very fine channels used for microminiature Joule-Thomson refrigerators. *Cryogenics*. **23**(5), pp. 273-277.

Wu, P. and Little, W. A. 1984. Measurement of the heat transfer characteristics of gas flow in fine channel heat exchangers used for microminiature refrigerators. *Cryogenics*. **24**(8), pp. 415-420.

Xia, G. D., Jiang, J., Wang, J., Zhai, Y. L. and Ma, D. D. 2015. Effects of different geometric structures on fluid flow and heat transfer performance in microchannel heat sinks. *International Journal of Heat and Mass Transfer*. **80**, pp. 439–447.

Xie, G., Li, S., Sundén, B., Zhang, W. and Li, H. 2014. A numerical study of the thermal performance of microchannel heat sinks with multiple length bifurcation in laminar liquid flow. *Numerical Heat Transf.* Part A, **65**, pp. 107-126.

Xie, G., Shen, H. and Wang, C.-C. 2015. Parametric study on thermal performance of microchannel heat sinks with internal vertical Y-shaped bifurcations. *International Journal of Heat and Mass Transfer*. **90**, pp. 948–958.

Xie, X.L., Liu, Z.J., He, Y.L. and Tao, W.Q. 2009. Numerical study of laminar heat transfer and pressure drop characteristics in a water-cooled minichannel heat sink. *Applied Thermal Engineering*. **29**, pp. 64–74.

Xu, B., Ooi, K. T., Wong, N. T. and Choi, W. K. 2000. Experimental investigation of flow friction for liquid flow in microchannels. *International Communications in Heat and Mass Transfer*. **27**, pp.1165-1176.

Xu, J. L., Gan, Y. H., Zhang, D. C. and Li, X. H. 2005. Microscale heat transfer enhancement using thermal boundary layer redeveloping concept. *International Journal of Heat and Mass Transfer*. **48** (9), pp. 1662-1674.

Xu, J. L., Song, Y. X., Zhang, W., Zhang, H. and Gan, Y. H. 2008. Numerical simulations of interrupted and conventional microchannel heat sinks. *International Journal of Heat and Mass Transfer*. **51**(25-26), pp. 5906-5917.

Xu, J.L., Zhang, W., Wang, Q.W. and Su, Q.C. 2006. Flow boiling instability and transient flow patterns inside intercrossed silicon microchannel array in a micro-timescale. *International Journal of Multiphase Flow*. **32**, pp. 568–592.

Yadav, V., Baghel, K., Kumar, R. and Kadam, S. T. 2016. Numerical investigation of heat transfer in extended surface microchannels. *International Journal of Heat and Mass Transfer*. **93**, pp. 612–622.

Yang, D., Wang, Y., Ding, G., Jin, Z., Zhao, J. and Wang, G. 2017. Numerical and experimental analysis of cooling performance of single-phase array microchannel heat sinks with different pin-fin configurations. *Applied Thermal Engineering*. **112**, pp. 1547–1556.

Yang, W.-H., Zhang, J.-Z. and Cheng, H.-E. 2005. The study of flow characteristics of curved microchannel. *Applied Thermal Engineering*. **25**, pp. 1894–1907.

Yang, Y. T. and Liao, S. C. 2014. Numerical optimization of trapezoidal microchannel heat sinks. *International Journal of Mechanical, Aerospace, Industrial and Mechatronics Engineering*. **8**(8), pp. 1374 - 1377.

Yong, J. Q. and Teo, C. J. 2014. Mixing and heat transfer enhancement in microchannels containing converging-diverging passages. *Journal of Heat Transfer*. **136**(4), pp. 1-11.

Yu, X., Woodcock, C., Plawsky, J. and Peles, Y. 2016a. An investigation of convective heat transfer in microchannel with Piranha Pin Fin. *International Journal of Heat and Mass Transfer*. **103**, pp.1125–1132.

Yu, X., Woodcock, C., Wang, Y., Plawsky, J. and Peles. Y. 2016b. A comparative study of flow boiling in a microchannel with piranha pin fins. *Journal of Heat transfer*. **138**(11), 111502-1.

Zhang, M. L., Wang, X. J., Liu, H. J. and Wang, G. L. 2008. Numerical simulation of the micro-channel heat sink on non-uniform heat source. Proceedings of International Conference on Electronic Packaging Technology & High Density Packaging, pp. 3-6.

Zhao, J., Huang, S., Gong, L., Huang, Z. 2016. Numerical study and optimizing on micro square pin-fin heat sink for electronic cooling. *Applied Thermal Engineering*. **93**, pp. 1347–1359.

Zhao, Z., Peles, Y. and Jensen, M.K. 2013. Water jet impingement boiling from structures-porous surface. *International Journal of Heat and Mass Transfer*. **63**, pp. 445–453.

Zhuo, L., Wen-Quan, T., and Ya-Ling, H. 2006. A numerical study of laminar convective heat transfer in microchannel with non-circular cross-section. *International Journal of Thermal Sciences*. **45**(12), pp. 1140–1148.

Zienkiewicz, O.C., Taylor, R.L. and Zhu, J.Z. 2013. The Finite Element Method: Its Basis and Fundamentals. 7th edition, McGraw-Hill.

APPENDIX A: Experimental Uncertainty Analysis

A.1 Introduction

The experimental uncertainty has been estimated in the present work in order to get acceptable and reliable results. The ASME PTC 19.1 (2013) standard was used in this study to calculate the total uncertainty. The total uncertainty in a measurement is the difference between the true value and the measured value, which is the sum of the bias (systematic) errors and the precision (random) errors. Bias errors are those fixed errors that do not vary during a measurement and can be determined from calibration or manufacturers' specifications. Precision errors result from unsteady influences that cause scatter in measurements and the associated uncertainty and can be obtained by repeated measurements under nominally fixed operating conditions. Fig. (A.1) describes both of the bias and precision uncertainty.

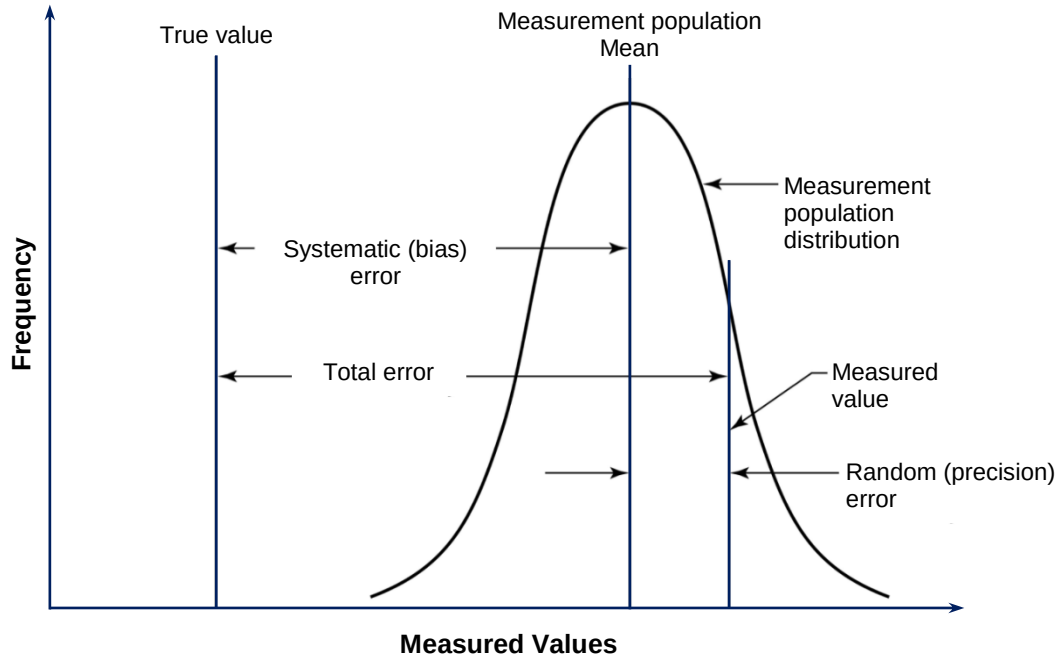

Fig. A.1: Graphic representation of bias and precision uncertainty (ASME PTC 19.1, 2013).

In order to understand the method used to compute uncertainties throughout this work, a short review of statistics and uncertainty will be presented. The precision uncertainties of measured variables $X_1, X_2, X_3, \dots, X_N$ are estimated as the sample standard deviation, P_x, of a sample of N measurements of the variables and can be calculated as follows (Coleman and Steele, 2009):

$$P_x = \sqrt{\frac{1}{N-1}\sum_{i=1}^{N}(X_i - \bar{X})^2} \qquad (A.1)$$

where $\bar{X}$ is called the mean value which is the sum of measurement values divided by the number of measurements as given by:

$$\bar{X} = \frac{1}{N}\sum_{i=1}^{N} X_i \quad (A.2)$$

The random standard uncertainty of the sample mean is determined as:

$$P_{\bar{x}} = t_{95\%} \cdot \frac{P_x}{\sqrt{N}} \quad (A.3)$$

where $t_{95\%} = 2$, and represents the student's t at 95% confidence level for the appropriate degrees of freedom (DOF). When the DOF is sufficiently large (> 30), the random error of a measurement with 95% confidence level is approximately twice its standard deviation (ASME PTC 19.1, 2013). By using the root sum square (RSS) method, the bias uncertainty of a measured variable, X, can be obtained as given by:

$$B_{\bar{x}} = \sqrt{\sum_{k=1}^{N} (B_x)_k^2} \quad (A.4)$$

where $(B_x)_k$ represents the k^{th} of the elemental systematic uncertainties $(B_x)_1$, $(B_x)_2$, $(B_x)_3$, …, $(B_x)_N$, and can be estimated from calibration data and instrument specifications given by the manufacturers. In order to get an overall uncertainty in a measured quantity, the bias and precision errors are combined using a root sum square method.

$$U_x = \pm\sqrt{P_{\bar{x}}^2 + B_{\bar{x}}^2} \quad (A.5)$$

Therefore, we can report the true average value for variable during the measurement in the standard form of uncertainty as, $X \pm U_x$, which is expected to lie within the interval value with 95% confidence.

Generally, two kinds of parameters are involved in the experiment, one is independent or primary parameters and another is dependent or secondary parameters. The independent variables are the parameters that are directly measured in current study using various instruments, which include the basic geometric dimensions of the test specimens such as the channel length, channel depth, channel width, fin width, temperatures, pressure and mass flow rate of water. While the dependent parameters are not directly measured but they are considered to be a function of the independent parameter such as Reynolds number (Re), heat transfer coefficient (h), Nusselt number (Nu), thermal resistance (R_{th}), friction coefficient (f) and so on.

In the present study, the Root-Sum-Square (RSS) method was used to find the uncertainty of the dependent (Secondary) parameters which is based on the method described by Coleman and Steele (2009). By assuming that a quantity R is the dependent parameter, and is a function of different independent (Primary) parameters $X_1, X_2, X_3, \ldots, X_N$.

$$R = f(X_1, X_2, X_3, \ldots, X_N) \quad (A.6)$$

Therefore, the absolute uncertainty of the dependent variable 'R' can be obtained by using the RSS method as given by:

$$U_R = \pm \sqrt{\left(\frac{\partial R}{\partial X_1} \cdot U_{X_1}\right)^2 + \left(\frac{\partial R}{\partial X_2} \cdot U_{X_2}\right)^2 + \left(\frac{\partial R}{\partial X_3} \cdot U_{X_3}\right)^2 + \cdots + \left(\frac{\partial R}{\partial X_N} \cdot U_{X_N}\right)^2} \quad (A.7)$$

where U_R refers to the uncertainty in R as a result of the uncertainty in the X_N measurement. The individual uncertainties of the independent parameters $U_{X_1}, U_{X_2}, U_{X_3}, \ldots, U_{X_N}$ are estimated from the bias and precision errors of both the experiments and the instruments. While, the partial derivatives $\frac{\partial R}{\partial X_1}, \frac{\partial R}{\partial X_2}, \frac{\partial R}{\partial X_3}$ and $\frac{\partial R}{\partial X_N}$ of the dependent (Secondary) parameters are derived from their relationship with the independent (Primary) parameters. The uncertainty of any parameter can be represented in the absolute value as $R \pm U_R$.

$$R \pm U_R = R \pm \sqrt{\left(\frac{\partial R}{\partial X_1} \cdot U_{X_1}\right)^2 + \left(\frac{\partial R}{\partial X_2} \cdot U_{X_2}\right)^2 + \left(\frac{\partial R}{\partial X_3} \cdot U_{X_3}\right)^2 + \cdots + \left(\frac{\partial R}{\partial X_N} \cdot U_{X_N}\right)^2} \quad (A.8)$$

The absolute uncertainty of any parameter in Eq. (A.7) can also be written in the dimensionless form to give the relative uncertainty, $\frac{U_R}{R}$ of the result, as follows:

$$\frac{U_R}{R} = \sqrt{\frac{1}{R^2}\left[\left(\frac{\partial R}{\partial X_1} \cdot U_{X_1}\right)^2 + \left(\frac{\partial R}{\partial X_2} \cdot U_{X_2}\right)^2 + \left(\frac{\partial R}{\partial X_3} \cdot U_{X_3}\right)^2 + \cdots + \left(\frac{\partial R}{\partial X_N} \cdot U_{X_N}\right)^2\right]} \quad (A.9)$$

The relative uncertainty $\frac{U_R}{R}$ was used to carry out the propagated uncertainty analysis for all parameters.

A.2 Uncertainty in Measured Values (Independent Variables)

A.2.1 Channel Geometry Uncertainties

In our experimental work, an electronic digital Vernier caliper is used to measure various geometric dimensions of the MCHS test sections. The digital caliper has a resolution of $B_{res.}$ = 3 μm and an accuracy of $B_{accur.}$ = 5 μm as given by manufacturer's specification. So, by using Eq. (A.4), the bias uncertainty can be found to be as follows:

$$B_{caliper} = \sqrt{(B_{res.})^2 + (B_{accur.})^2} = \sqrt{(3)^2 + (5)^2} = 5.83\ \mu m$$

In the present work, twenty five measurements of the minichannel width, depth and length are made by using a digital caliper to get the uncertainty. A straight rectangular minichannanel width (W_{ch}), depth (H_{ch}) and length (L_{ch}) have been chosen as an example to estimate the uncertainty based on the random standard deviation of the sample mean, as shown in Table (A.1). By using Eq. (A.5), it can be found the total uncertainty for any independent geometric parameter 'X' of the straight rectangular minichannel heat sink as follows:

$$U_x = \pm \sqrt{\left(B_{caliper}\right)^2 + (P_{\bar{x}})^2}$$

$$U_{W_{ch}} = \pm\sqrt{(5.83)^2 + (1.4063)^2} = \pm 6\ \mu m$$

$$\therefore \frac{U_{W_{ch}}}{\bar{W}_{ch}} = \frac{6}{1000.12} = \pm 0.006 = \pm 0.6\%$$

$$U_{H_{ch}} = \pm\sqrt{(5.83)^2 + (1.32665)^2} = \pm 5.979\ \mu m$$

$$\frac{U_{H_{ch}}}{\bar{H}_{ch}} = \frac{5.979}{2000.2} = \pm 0.00299 = \pm 0.299\%$$

$$U_{L_{ch}} = \pm\sqrt{(5.83)^2 + (1.9497)^2} = \pm 6.1474\ \mu m$$

$$\frac{U_{L_{ch}}}{\bar{L}_{ch}} = \frac{6.1474}{21001.48} = \pm 0.000293 = \pm 0.0293\ \%$$

$$U_{W_w} = \pm\sqrt{(5.83)^2 + (1.6424)^2} = \pm 6.0569\ \mu m$$

$$\frac{U_{W_w}}{\bar{W}_w} = \frac{6.0569}{999.12} = \pm 0.00606 = \pm 0.606\ \%$$

For the other MCHS geometric parameters the same procedures have been conducted to find the total uncertainty.

Table A.1: Measurement uncertainty summary for the straight rectangular MCHS design.

Straight rectangular MCHS dimensions				
X_i	Channel Width (W_{ch}), μm	Channel Height (H_{ch}), μm	Channel Length (L_{ch}), μm	Fin Width (W_w), μm
X_1	1006	2004	21009	1001
X_2	1004	2007	21010	998
X_3	997	1999	21005	999
X_4	1002	1996	20998	997
X_5	1001	2001	20995	994
X_6	995	2000	21000	996
X_7	999	2002	21002	999
X_8	996	2005	21001	1000
X_9	1000	1997	20995	1002
X_{10}	1005	1998	20996	1004
X_{11}	1003	1995	20996	1007
X_{12}	1003	2000	21001	1005
X_{13}	997	2002	21004	1004
X_{14}	996	2004	21009	1001
X_{15}	994	1999	21005	1003
X_{16}	1003	1998	21011	999
X_{17}	1005	1998	21007	996
X_{18}	1000	1996	21002	992
X_{19}	1002	1999	20999	991
X_{20}	1004	2001	20997	993
X_{21}	998	2004	20998	996
X_{22}	999	2001	21000	1000
X_{23}	1001	2005	21002	1001
X_{24}	996	1999	20998	1002
X_{25}	997	1995	20997	998
$\sum X_i$	25003	50005	525037	24978
$\bar{X} = \frac{\sum X_i}{N}$	1000.12	2000.2	21001.48	999.12
$P_x = \sqrt{\frac{\sum (X_i - \bar{X})^2}{N-1}}$	3.515679	3.316625	4.874423	4.106093
$P_{\bar{x}} = t_{95\%} \cdot \frac{P_x}{\sqrt{N}}$	*1.406271666*	*1.326649916*	*1.949769217*	*1.642437213*

A.2.2 Uncertainties of the Temperature Measurements

In the present work, two types of a digital thermometer monitor (DTM) within thermocouples have been used to read the inlet and outlet water temperatures, wall temperature and junction temperature. The first one was from RS, Model Kane-May KM340 with an accuracy of (±0.2% of reading +1 °C) at a range temperature of 0 to 1100 °C used to measure the junction temperature. While the other digital thermometer monitor was from Thermosense, Model HH-747UD with an accuracy of (±0.1% of reading +0.7°C) over a temperature range of -100 to 1300 °C and resolution of 0.1 °C to measure inlet and outlet water temperatures and also the wall distribution temperature along the channel flow. The thermocouple used for measuring the junction temperature was K-type from RS with tolerance ±1.5 °C at temperature range of -40 °C to 375 °C as mentioned in the manufacturer's specification, whereas the other type of thermocouple used to measure the other parameters has a tolerance of ±1.5 °C over at temperature range of -40 °C to 375 °C.

The bias uncertainty for "HH-747UD" model and thermocouples can be determined as follows:

$$B_{DTM+thermocouple} = \sqrt{(B_{accur.})^2 + (B_{reso.})^2 + (B_{tolerance.})^2}$$

In the present work, the inlet water temperature was fixed at 20 °C. Therefore, the systematic (Bias) uncertainty for the "$B_{DTM+thermocouple}$" was found to be ±0.3 °C as mentioned in the manufacturer's specification.

Twenty five measurements have been conducted to measure inlet water temperature by using K-type thermocouple and HH-747UD digital thermometer monitor model to estimate the uncertainty based on the random standard deviation of the sample mean, as shown in Table (A.2).

$$U_T = \pm\sqrt{\left(B_{DTM+thermocouple}\right)^2 + (P_{\bar{x}})^2}$$

$$U_T = \pm\sqrt{(0.3)^2 + (0.05)^2} = \pm 0.304$$

The uncertainty in the temperature measurement is given as:

$$\frac{U_T}{T} = \pm\frac{0.304}{T}$$

Therefore, the uncertainty of inlet water temperature ($T_{f,in}$) was found to be:

$$\frac{U_{T_{f,in}}}{T_{f,in}} = \pm\frac{0.304}{20} = \pm 0.0152 = \pm 1.52\%$$

Table A.2: Measurement uncertainty summary for inlet water temperature.

X_i	Water Inlet Temperature ($T_{f,in}$) ^oC
X_1	20.08
X_2	20.1
X_3	19.9
X_4	19.94
X_5	20.05
X_6	20.1
X_7	19.92
X_8	19.93
X_9	19.85
X_{10}	20.12
X_{11}	20.15
X_{12}	19.6
X_{13}	20.04
X_{14}	20.15
X_{15}	20.2
X_{16}	19.98
X_{17}	19.99
X_{18}	20
X_{19}	20.15
X_{20}	20.06
X_{21}	20.1
X_{22}	20.07
X_{23}	20
X_{24}	19.97
X_{25}	19.95
$\sum X_i$	500.4
$\overline{X} = \frac{\sum X_i}{N}$	20.016
$P_x = \sqrt{\frac{\sum (X_i - \overline{X})^2}{N-1}}$	0.125133
$P_{\overline{x}} = t_{95\%} \cdot \frac{P_x}{\sqrt{N}}$	0.050053

A.2.3 Uncertainties for Voltage and Current of Resistor

The voltage and current applied to the power film resistors embedded underneath the base plate of the MCHS is measured using the Aim-TTi EX354RT model from RS. The range of voltage used in the present study is 15 V <V_{heater}< 33 V, and the corresponding accuracy of the measurements from the calibration specifications of the instrument (Aim-TTi EX354RT) is 0.3% of reading ±3 digits. For the 30 V applied to the resistor, the resulting uncertainty of the heater supplied voltage is found to be from 29.88 V to 30.12 V.

The current accuracy in the heater is calculated based on the calibration specifications of the instrument (Aim-TTi EX354RT), which is found to be 0.5% of reading ±3 digits. The resulting uncertainty for the 2 A is found from 1.96 A to 2.04 A.

A.2.4 Water Flow Rate Uncertainties

The flow rate of water was measured by using rotameter and calibration was made at different flow rate by using a collecting container (volumetric beaker) and stopwatch as shown in Fig. 4.15. The accuracy was determined to be ±2.5 *ml/min* of reading over the range of 0.2 to 3.0 *l/min*.

A.2.5 Pressure Gauge Uncertainties

The uncertainty of pressure gauge was found to be ±75 Pa of reading depends on the calibration made by using an inclined manometer. The calibration has been conducted over the range of 0 to 90000 Pa as shown in Fig. 4.16. The total uncertainties of each measured parameter mentioned in the previous section are summarized in Table A.3.

Table A.3: Measurement uncertainty summary.

Parameter	Symbol	Measuring instrument	Total uncertainty of a measurement
Channel width	W_{ch} [mm]	Vernier caliper	± 6.00 µm
Channel depth	H_{ch} [mm]	Vernier caliper	± 5.98 µm
Channel length	L_{ch} [mm]	Vernier caliper	± 6.15 µm
Fin width	W_w [mm]	Vernier caliper	± 6.06 µm
Temperature	T [°C]	Calibration	± 0.30 °C
DC-Power Supply Current	I [Ampere]	Calibrated by manufacturer	± 0.04 A
DC-Power Supply Voltage	V [Voltage]	Calibrated by manufacturer	± 0.12 V
Volumetric flow rate	Q_{in} [l/min]	Calibration	± 2.5 ml/min
Pressure drop	ΔP [Pa]	Calibration	± 75 Pa

A.3 Uncertainty in Calculated Quantities (Dependent Variables)

A.3.1 Minichannel Aspect Ratio (∝)

$$\propto = \frac{W_{ch}}{H_{ch}} \tag{A.10}$$

$$U_{\propto} = \pm \sqrt{\left(\frac{\partial \propto}{\partial W_{ch}} \cdot U_{W_{ch}}\right)^2 + \left(\frac{\partial \propto}{\partial H_{ch}} \cdot U_{H_{ch}}\right)^2} \tag{A.11}$$

$$\frac{\partial \propto}{\partial W_{ch}} = \frac{H_{ch}}{H_{ch}^2} = \propto \cdot \frac{1}{W_{ch}} \tag{A.12}$$

$$\frac{\partial \propto}{\partial H_{ch}} = \frac{-W_{ch}}{H_{ch}^2} = -\propto \cdot \frac{1}{H_{ch}} \tag{A.13}$$

$$\frac{U_{\propto}}{\propto} = \pm \sqrt{\left(\frac{U_{W_{ch}}}{W_{ch}}\right)^2 + \left(\frac{U_{H_{ch}}}{H_{ch}}\right)^2} \tag{A.14}$$

$$\therefore \frac{U_{\propto}}{\propto} = \pm \sqrt{(0.006)^2 + (0.00299)^2} = \pm 0.0067$$

A.3.2 Fin Spacing Ratio (β)

$$\beta = \frac{W_w}{W_{ch}} \tag{A.15}$$

$$U_{\beta} = \pm \sqrt{\left(\frac{\partial \beta}{\partial W_w} \cdot U_{W_w}\right)^2 + \left(\frac{\partial \beta}{\partial W_{ch}} \cdot U_{W_{ch}}\right)^2} \tag{A.16}$$

$$\frac{\partial \beta}{\partial W_w} = \frac{1}{W_{ch}} = \beta \cdot \frac{1}{W_w} \tag{A.17}$$

$$\frac{\partial \beta}{\partial W_{ch}} = \frac{-W_w}{W_{ch}^2} = -\beta \cdot \frac{1}{W_{ch}} \quad (A.18)$$

$$\frac{U_\beta}{\beta} = \pm \sqrt{\left(\frac{U_{W_w}}{W_w}\right)^2 + \left(\frac{U_{W_{ch}}}{W_{ch}}\right)^2} \quad (A.19)$$

$$\frac{U_\beta}{\beta} = \pm \sqrt{(0.00606)^2 + (0.006)^2} = \pm 0.00853$$

A.3.3 Channel Cross-Sectional Area (A_{ch})

$$A_{ch} = H_{ch} \cdot W_{ch} \quad (A.20)$$

$$U_{A_{ch}} = \pm \sqrt{\left(\frac{\partial A_{ch}}{\partial H_{ch}} \cdot U_{H_{ch}}\right)^2 + \left(\frac{\partial A_{ch}}{\partial W_{ch}} \cdot U_{W_{ch}}\right)^2} \quad (A.21)$$

$$\frac{\partial A_{ch}}{\partial H_{ch}} = W_{ch} = A_{ch} \cdot \frac{1}{H_{ch}} \quad (A.22)$$

$$\frac{\partial A_{ch}}{\partial W_{ch}} = H_{ch} = A_{ch} \cdot \frac{1}{W_{ch}} \quad (A.23)$$

$$\frac{U_{A_{ch}}}{A_{ch}} = \pm \sqrt{\left(\frac{U_{H_{ch}}}{H_{ch}}\right)^2 + \left(\frac{U_{W_{ch}}}{W_{ch}}\right)^2} \quad (A.24)$$

$$\frac{U_{A_{ch}}}{A_{ch}} = \pm \sqrt{(0.00299)^2 + (0.006)^2} = \pm 0.0067$$

A.3.4 Fin Area (A_{fin})

$$A_{fin} = L_{ch} \cdot H_{ch} \quad (A.25)$$

$$\frac{U_{A_{fin}}}{A_{fin}} = \pm \sqrt{\left(\frac{U_{L_{ch}}}{L_{ch}}\right)^2 + \left(\frac{U_{H_{ch}}}{H_{ch}}\right)^2} \quad (A.26)$$

$$\frac{U_{A_{fin}}}{A_{fin}} = \pm \sqrt{(0.000293)^2 + (0.00299)^2} = \pm 0.003$$

A.3.5 Fin Base Area (A_{base})

$$A_{base} = L_{ch} \cdot W_{ch} \quad (A.27)$$

$$\frac{U_{A_{base}}}{A_{base}} = \pm \sqrt{\left(\frac{U_{L_{ch}}}{L_{ch}}\right)^2 + \left(\frac{U_{W_{ch}}}{W_{ch}}\right)^2} \quad (A.28)$$

$$\frac{U_{A_{base}}}{A_{base}} = \pm \sqrt{(0.000293)^2 + (0.006)^2} = \pm 0.006$$

A.3.6 Minichannel Hydraulic Diameter (D_h)

The hydraulic diameter of the rectangular cross-sectional channels is calculated using Eq. (A.29), where the channel width, W_{ch}, and height, H_{ch}, are measured quantities as given in Table A.1. The propagated uncertainty of D_h is obtained from Eq. (A.33).

$$D_h = \frac{2W_{ch} \cdot H_{ch}}{W_{ch} + H_{ch}} \quad (A.29)$$

$$U_{D_h} = \pm \sqrt{\left(\frac{\partial D_h}{\partial W_{ch}} \cdot U_{W_{ch}}\right)^2 + \left(\frac{\partial D_h}{\partial H_{ch}} \cdot U_{H_{ch}}\right)^2} \quad (A.30)$$

By using quotient rule for derivatives of D_h

$$\frac{\partial D_h}{\partial W_{ch}} = \frac{2H_{ch}(W_{ch} + H_{ch}) - 2W_{ch} \cdot H_{ch}}{(W_{ch} + H_{ch})^2} = \frac{2H_{ch}^2}{(W_{ch} + H_{ch})^2} = D_h \cdot \frac{H_{ch}}{W_{ch}(W_{ch} + H_{ch})} \quad (A.31)$$

$$\frac{\partial D_h}{\partial H_{ch}} = \frac{2W_{ch}(W_{ch} + H_{ch}) - 2W_{ch} \cdot H_{ch}}{(W_{ch} + H_{ch})^2} = \frac{2W_{ch}^2}{(W_{ch} + H_{ch})^2} = D_h \cdot \frac{W_{ch}}{H_{ch}(W_{ch} + H_{ch})} \quad (A.32)$$

$$\frac{U_{D_h}}{D_h} = \pm \sqrt{\left(\frac{H_{ch}}{W_{ch} + H_{ch}} \cdot \frac{U_{W_{ch}}}{W_{ch}}\right)^2 + \left(\frac{W_{ch}}{W_{ch} + H_{ch}} \cdot \frac{U_{H_{ch}}}{H_{ch}}\right)^2} \quad (A.33)$$

By applying the uncertainty equation above, it can be obtained the hydraulic diameter uncertainty for the rectangular mini/microchannel as shown:

$$\frac{U_{D_h}}{D_h} = \pm \sqrt{\left(\frac{2000}{1000 + 2000} \times 0.006\right)^2 + \left(\frac{1000}{1000 + 2000} \times 0.00299\right)^2} = \pm 0.00412 = \pm 0.412\ \%$$

A.3.7 Convective (effective) Heat Transfer Area for Single Channel ($U_{A_{eff}}$)

The effective area available for heat transfer in the straight rectangular MCHS is given by:

$$A_{eff} = \left(A_{base} + A_{fin}\right) = L_{ch}(W_{ch} + 2H_{ch}) \quad (A.34)$$

$$U_{A_{eff}} = \pm \sqrt{\left(\frac{\partial A_{eff}}{\partial L_{ch}} \cdot U_{L_{ch}}\right)^2 + \left(\frac{\partial A_{eff}}{\partial W_{ch}} \cdot U_{W_{ch}}\right)^2 + \left(\frac{\partial A_{eff}}{\partial H_{ch}} \cdot U_{H_{ch}}\right)^2} \quad (A.35)$$

$$\frac{\partial A_{eff}}{\partial L_{ch}} = W_{ch} + 2H_{ch} = \frac{A_{eff}}{L_{ch}} \quad (A.36)$$

$$\frac{\partial A_{eff}}{\partial W_{ch}} = L_{ch} = \frac{A_{eff}}{W_{ch} + 2H_{ch}} \quad (A.37)$$

$$\frac{\partial A_{eff}}{\partial H_{ch}} = 2L_{ch} = 2\left(\frac{A_{eff}}{W_{ch} + 2H_{ch}}\right) \quad (A.38)$$

$$\frac{U_{A_{eff}}}{A_{eff}} = \pm \sqrt{\left(\frac{U_{L_{ch}}}{L_{ch}}\right)^2 + \left(\frac{U_{W_{ch}}}{W_{ch} + 2H_{ch}}\right)^2 + \left(\frac{2U_{H_{ch}}}{W_{ch} + 2H_{ch}}\right)^2} \quad (A.39)$$

$$\frac{U_{Aeff}}{A_{eff}} = \pm \sqrt{\left(\frac{U_{L_{ch}}}{L_{ch}}\right)^2 + \left(\left(\frac{W_{ch}}{W_{ch} + 2H_{ch}}\right)\frac{U_{W_{ch}}}{W_{ch}}\right)^2 + \left(\left(\frac{2H_{ch}}{W_{ch} + 2H_{ch}}\right)\frac{U_{H_{ch}}}{H_{ch}}\right)^2} \quad (A.40)$$

In order to get an uncertainty of the effective heat transfer area for multiple channels, we need to multiply $U_{A_{eff}}$ by the number of channels (n).

$$U_{A_{eff,m}} = n \cdot U_{A_{eff}} \quad (A.41)$$

A.3.8 Water Properties

Properties of water such as fluid density, dynamic viscosity, specific heat, Prandtl number and thermal conductivity were determined based on correlation equations proposed by Popiel and Wojtkowiak (1998) which are a function of water temperature, see Appendix B. It was found that the correlations deviate from the tabulated values in Bergman et al. (2017) by less than 0.5%. Therefore, the uncertainty in the fluid properties is:

$$\frac{U_{Property}}{Property} = \pm 0.5\ \% \tag{A.42}$$

A.3.9 Mass Flux ($\dot{m}$)

$$\dot{m} = \rho_f \cdot Q_{in} \tag{A.43}$$

$$Q_{in} = A_{ch} \cdot u \tag{A.44}$$

$$U_{\dot{m}} = \pm \sqrt{\left(\frac{\partial \dot{m}}{\partial \rho_f} \cdot U_{\rho_f}\right)^2 + \left(\frac{\partial \dot{m}}{\partial Q_{in}} \cdot U_{Q_{in}}\right)^2} \tag{A.45}$$

$$\frac{\partial \dot{m}}{\partial \rho_f} = Q_{in} = \frac{\dot{m}}{\rho_f} \qquad \text{And} \qquad \frac{\partial \dot{m}}{\partial Q_{in}} = \rho_f = \frac{\dot{m}}{Q_{in}} \tag{A.46}$$

$$\frac{U_{\dot{m}}}{\dot{m}} = \pm \sqrt{\left(\frac{U_{\rho_f}}{\rho_f}\right)^2 + \left(\frac{U_{Q_{in}}}{Q_{in}}\right)^2} \tag{A.47}$$

A.3.10 Reynolds Number (Re)

$$Re = \frac{\rho_f \cdot u \cdot D_h}{\mu_f} = \frac{\dot{m} \cdot D_h}{\mu_f \cdot A_{ch}} = \frac{2\dot{m}}{\mu_f (W_{ch} + H_{ch})} \tag{A.48}$$

$$\frac{U_{Re}}{Re} = \pm \sqrt{\left(\frac{U_{\dot{m}}}{\dot{m}}\right)^2 + \left(\frac{U_{H_{ch}}}{W_{ch} + H_{ch}}\right)^2 + \left(\frac{U_{W_{ch}}}{W_{ch} + H_{ch}}\right)^2 + \left(\frac{U_{\mu_f}}{\mu_f}\right)^2} \tag{A.49}$$

$$\frac{U_{Re}}{Re} = \pm \sqrt{\left(\frac{U_{\rho_f}}{\rho_f}\right)^2 + \left(\frac{U_{Q_{in}}}{Q_{in}}\right)^2 + \left(\frac{U_{\mu_f}}{\mu_f}\right)^2 + \left(\frac{U_{H_{ch}}}{W_{ch} + H_{ch}}\right)^2 + \left(\frac{U_{W_{ch}}}{W_{ch} + H_{ch}}\right)^2} \tag{A.50}$$

A.3.11 Heat Supply (q_{in})

The heat supplied to the minichannel heat sink test section using DC-power supply can be expressed by:

$$q_{in} = V \times I \tag{A.51}$$

$$\frac{U_{q_{in}}}{q_{in}} = \pm \sqrt{\left(\frac{U_V}{V}\right)^2 + \left(\frac{U_I}{I}\right)^2} \tag{A.52}$$

A.3.12 Heat Flux (q'')

The steady state single phase heat gained by the fluid flow as a coolant from the minichannel heat sink is determined by:

$$q = m^{\cdot} \cdot C_{p_f}\left(T_{f,out} - T_{f,in}\right) = V \cdot I - q_{loss} = 0.92(V \cdot I) \quad (A.53)$$

$$U_q = \pm\sqrt{\left(\frac{\partial q}{\partial m^{\cdot}} \cdot U_{m^{\cdot}}\right)^2 + \left(\frac{\partial q}{\partial C_{p_f}} \cdot U_{C_{p_f}}\right)^2 + \left(\frac{\partial q}{\partial T_{f,out}} \cdot U_{T_{f,out}}\right)^2 + \left(\frac{\partial q}{\partial T_{f,in}} \cdot U_{T_{f,in}}\right)^2} \quad (A.54)$$

$$\frac{\partial q}{\partial m^{\cdot}} = C_{p_f}\left(T_{f,out} - T_{f,in}\right) = \frac{q}{m^{\cdot}} \quad (A.55)$$

$$\frac{\partial q}{\partial C_{p_f}} = m^{\cdot}\left(T_{f,out} - T_{f,in}\right) = \frac{q}{C_{p_f}} \quad (A.56)$$

$$\frac{\partial q}{\partial T_{f,out}} = m^{\cdot} \cdot C_{p_f} = \frac{q \cdot T_{f,out}}{T_{f,out}\left(T_{f,out} - T_{f,in}\right)} \quad (A.57)$$

$$\frac{\partial q}{\partial T_{f,in}} = m^{\cdot} \cdot C_{p_f} = \frac{q \cdot T_{f,in}}{T_{f,in}\left(T_{f,out} - T_{f,in}\right)} \quad (A.58)$$

$$\frac{U_q}{q} = \pm\sqrt{\left(\frac{U_{m^{\cdot}}}{m^{\cdot}}\right)^2 + \left(\frac{U_{C_{p_f}}}{C_{p_f}}\right)^2 + \left(\left(\frac{T_{f,out}}{T_{f,out} - T_{f,in}}\right)\frac{U_{T_{f,out}}}{T_{f,out}}\right)^2 + \left(\left(\frac{T_{f,in}}{T_{f,out} - T_{f,in}}\right)\frac{U_{T_{f,in}}}{T_{f,in}}\right)^2} \quad (A.59)$$

The heat flux is equal to be:

$$q^{"} = \frac{q}{A_{eff}} \quad (A.60)$$

Then the uncertainty of the heat flux can be estimated as given by:

$$\frac{U_{q^{"}}}{q^{"}} = \pm\sqrt{\left(\frac{U_q}{q}\right)^2 + \left(\frac{U_{A_{eff}}}{A_{eff}}\right)^2} \quad (A.61)$$

A.3.13 Heat Transfer Coefficient (h)

$$h = \frac{q^{"}}{n\left(T_w - T_f\right)} \quad (A.62)$$

$$U_h = \pm\sqrt{\left(\frac{\partial h}{\partial q^{"}} \cdot U_{q^{"}}\right)^2 + \left(\frac{\partial h}{\partial T_w} \cdot U_{T_w}\right)^2 + \left(\frac{\partial h}{\partial T_f} \cdot U_{T_f}\right)^2} \quad (A.63)$$

$$\frac{U_h}{h} = \pm\sqrt{\left(\frac{U_{q^{"}}}{q^{"}}\right)^2 + \left(\left(\frac{T_w}{T_w - T_f}\right)\frac{U_{T_w}}{T_w}\right)^2 + \left(\left(\frac{T_f}{T_w - T_f}\right)\frac{U_{T_f}}{T_f}\right)^2} \quad (A.64)$$

A.3.14 Nusselt Number (Nu)

$$Nu = \frac{h \cdot D_h}{k_f} \quad (A.65)$$

$$\frac{U_{Nu}}{Nu} = \pm\sqrt{\left(\frac{U_h}{h}\right)^2 + \left(\frac{U_{D_h}}{D_h}\right)^2 + \left(\frac{U_{k_f}}{k_f}\right)^2} \quad (A.66)$$

A.3.15 Thermal Resistance (R_{th})

$$R_{th} = \frac{T_w - T_{f,in}}{q} \quad , \quad \left(\frac{℃}{W}\right) \tag{A.67}$$

$$\frac{U_{R_{th}}}{R_{th}} = \pm \sqrt{\left(\frac{U_q}{q}\right)^2 + \left(\left(\frac{T_w}{T_w - T_{f,in}}\right)\frac{U_{T_w}}{T_w}\right)^2 + \left(\left(\frac{T_{f,in}}{T_w - T_{f,in}}\right)\frac{U_{T_{f,in}}}{T_{f,in}}\right)^2} \tag{A.68}$$

A.3.16 Total Measured Pressure Drop (ΔP_t) and Minichannel Pressure Drop (ΔP_{ch})

$$\Delta P_t = P_{in} - P_{out} \tag{A.69}$$

$$\frac{U_{\Delta P_t}}{\Delta P_t} = \pm \sqrt{\left(\frac{U_{P_{in}}}{P_{in} - P_{out}}\right)^2 + \left(\frac{U_{P_{out}}}{P_{in} - P_{out}}\right)^2} \tag{A.70}$$

$$U_{\Delta P_t} = \pm \sqrt{\left(U_{P_{in}}\right)^2 + \left(U_{P_{out}}\right)^2} \tag{A.71}$$

The channel pressure drop in the straight rectangular minichannel is equal to the total pressure drop which was measured directly using pressure gauge minus the minor pressure losses which formed by sudden expansion (κ_e), sudden contraction (κ_c) and bends (κ_{90}) as described previously by Eq. (4.8) in subsection (4.7.1.1), and in order to simplify the uncertainty problem the terms $\kappa_{e_{inlet}}, \kappa_{c_{outlet}}$ and minor losses in plastic tubes are not taken into account. Hence, the uncertainty in the channel pressure drop for the straight rectangular MCHS is given by:

$$\Delta P_{ch} = \Delta P_t - \frac{\rho_f}{2} \cdot \frac{Q_{in}^2}{A_{ch}^2}\left(\kappa_c + \kappa_e + 2\kappa_{90}\left(\frac{A_{ch}}{A_p}\right)^2\right) \tag{A.72}$$

$$U_{\Delta P_{ch}} = \pm \sqrt{\left(U_{\Delta P_t}\right)^2 + \left(U_{\frac{\rho_f \cdot Q_{in}^2}{2A_{ch}^2}\left(\kappa_c + \kappa_e + 2\kappa_{90}\left(\frac{A_{ch}}{A_p}\right)^2\right)}\right)^2} \tag{A.73}$$

$$\frac{U_{\Delta P_{ch}}}{\Delta P_{ch}} = \pm \sqrt{\left(\frac{U_{\Delta P_t}}{\Delta P_t - \frac{\rho_f \cdot Q_{in}^2}{2A_{ch}^2}\left(\kappa_c + \kappa_e + 2\kappa_{90}\left(\frac{A_{ch}}{A_p}\right)^2\right)}\right)^2 + \left(\frac{U_{\frac{\rho_f \cdot Q_{in}^2}{2A_{ch}^2}\left(\kappa_c + \kappa_e + 2\kappa_{90}\left(\frac{A_{ch}}{A_p}\right)^2\right)}}{\Delta P_t - \frac{\rho_f \cdot Q_{in}^2}{2A_{ch}^2}\left(\kappa_c + \kappa_e + 2\kappa_{90}\left(\frac{A_{ch}}{A_p}\right)^2\right)}\right)^2} \tag{A.74}$$

$$\frac{U_{\frac{\rho_f \cdot Q_{in}^2}{2A_{ch}^2}\left(\kappa_c + \kappa_e + 2\kappa_{90}\left(\frac{A_{ch}}{A_p}\right)^2\right)}}{\frac{\rho_f \cdot Q_{in}^2}{2A_{ch}^2}\left(\kappa_c + \kappa_e + 2\kappa_{90}\left(\frac{A_{ch}}{A_p}\right)^2\right)} = \pm \sqrt{\left(\frac{U_{\rho_f}}{\rho_f}\right)^2 + 4\left(\frac{U_{Q_{in}}}{Q_{in}}\right)^2 + 4\left(\frac{U_{A_{ch}}}{A_{ch}}\right)^2 + \left(\frac{U_{\kappa_c + \kappa_e + 2\kappa_{90}\left(\frac{A_{ch}}{A_p}\right)^2}}{\kappa_c + \kappa_e + 2\kappa_{90}\left(\frac{A_{ch}}{A_p}\right)^2}\right)^2} \tag{A.75}$$

$$\frac{U_{\kappa_c+\kappa_e+2\kappa_{90}\left(\frac{A_{ch}}{A_p}\right)^2}}{\kappa_c+\kappa_e+2\kappa_{90}\left(\frac{A_{ch}}{A_p}\right)^2}$$

$$= \pm\sqrt{\left(\frac{U_{\kappa_c}}{\kappa_c+\kappa_e+2\kappa_{90}\left(\frac{A_{ch}}{A_p}\right)^2}\right)^2+\left(\frac{U_{\kappa_e}}{\kappa_c+\kappa_e+2\kappa_{90}\left(\frac{A_{ch}}{A_p}\right)^2}\right)^2+\left(\frac{U_{2\kappa_{90}\left(\frac{A_{ch}}{A_p}\right)^2}}{\kappa_c+\kappa_e+2\kappa_{90}\left(\frac{A_{ch}}{A_p}\right)^2}\right)^2} \quad (A.76)$$

$$\frac{U_{2\kappa_{90}\left(\frac{A_{ch}}{A_p}\right)^2}}{2\kappa_{90}\left(\frac{A_{ch}}{A_p}\right)^2} = \pm\sqrt{\left(\frac{U_{\kappa_{90}}}{\kappa_{90}}\right)^2+4\left(\frac{U_{A_{ch}}}{A_{ch}}\right)^2+4\left(\frac{U_{A_P}}{A_P}\right)^2} \quad (A.77)$$

$$\therefore\ U_{\frac{\rho_f\cdot Q_{in}^2}{2A_{ch}^2}\left(\kappa_c+\kappa_e+2\kappa_{90}\left(\frac{A_{ch}}{A_p}\right)^2\right)} = \frac{\rho_f\cdot Q_{in}^2}{2A_{ch}^2}\left(\kappa_c+\kappa_e+2\kappa_{90}\left(\frac{A_{ch}}{A_p}\right)^2\right).$$

$$\sqrt{\left(\frac{U_{\rho_f}}{\rho_f}\right)^2+4\left(\frac{U_{Q_{in}}}{Q_{in}}\right)^2+4\left(\frac{U_{A_{ch}}}{A_{ch}}\right)^2+\left(\sqrt{\left(\frac{U_{\kappa_c}}{\kappa_c+\kappa_e+2\kappa_{90}\left(\frac{A_{ch}}{A_p}\right)^2}\right)^2+\left(\frac{U_{\kappa_e}}{\kappa_c+\kappa_e+2\kappa_{90}\left(\frac{A_{ch}}{A_p}\right)^2}\right)^2+\left(\frac{2\kappa_{90}\left(\frac{A_{ch}}{A_p}\right)^2\cdot\sqrt{\left(\frac{U_{\kappa_{90}}}{\kappa_{90}}\right)^2+4\left(\frac{U_{A_{ch}}}{A_{ch}}\right)^2+4\left(\frac{U_{A_P}}{A_P}\right)^2}}{\kappa_c+\kappa_e+2\kappa_{90}\left(\frac{A_{ch}}{A_p}\right)^2}\right)^2}\right)^2} \quad (A.78)$$

Now, by substituting Eq. (A.78) into Eq. (A.74), the uncertainty of $\frac{U_{\Delta P_{ch}}}{\Delta P_{ch}}$ for the straight rectangular minichannel can be estimated.

A.3.17 Fanning Friction Factor (f)

$$f_{ch} = \frac{\Delta P_{ch}}{2\rho_f\cdot u^2}\cdot\frac{D_h}{L_{ch}} = \frac{\Delta P_{ch}\cdot D_h\cdot A_{ch}^2}{2\rho_f\cdot L_{ch}\cdot Q_{in}^2} \quad (A.79)$$

$$U_{f_{ch}} = \pm\sqrt{\left(\frac{\partial f_{ch}}{\partial\Delta P_{ch}}\cdot U_{\Delta P_{ch}}\right)^2+\left(\frac{\partial f_{ch}}{\partial D_h}\cdot U_{D_h}\right)^2+\left(\frac{\partial f_{ch}}{\partial A_{ch}}\cdot U_{A_{ch}}\right)^2+\left(\frac{\partial f_{ch}}{\partial\rho_f}\cdot U_{\rho_f}\right)^2+\left(\frac{\partial f_{ch}}{\partial L_{ch}}\cdot U_{L_{ch}}\right)^2+\left(\frac{\partial f_{ch}}{\partial Q_{in}}\cdot U_{Q_{in}}\right)^2} \quad (A.80)$$

$$\frac{U_{f_{ch}}}{f_{ch}} = \pm\sqrt{\left(\frac{U_{\Delta P_{ch}}}{\Delta P_{ch}}\right)^2+\left(\frac{U_{D_h}}{D_h}\right)^2+4\left(\frac{U_{A_{ch}}}{A_{ch}}\right)^2+\left(\frac{U_{\rho_f}}{\rho_f}\right)^2+\left(\frac{U_{L_{ch}}}{L_{ch}}\right)^2+4\left(\frac{U_{Q_{in}}}{Q_{in}}\cdot\right)^2} \quad (A.81)$$

A.3.18 Poiseuille Number (Po)

$$Po = f_{ch}\cdot Re \quad (A.82)$$

$$U_{Po} = \pm\sqrt{\left(\frac{\partial Po}{\partial f_{ch}}\cdot U_{f_{ch}}\right)^2+\left(\frac{\partial Po}{\partial Re}\cdot U_{Re}\right)^2} \quad (A.83)$$

$$\frac{U_{Po}}{Po} = \pm\sqrt{\left(\frac{U_{f_{ch}}}{f_{ch}}\right)^2+\left(\frac{U_{Re}}{Re}\right)^2} \quad (A.84)$$

APPENDIX B: Thermophysical Properties of the Water

The properties of water such as the fluid density (ρ_f), specific heat (C_{p_f}), dynamic viscosity (μ_f), thermal conductivity (k_f) and Prandtl number (Pr) are required for the data analysis. In this study, the thermophysical properties of water were calculated using the equations proposed by Popiel and Wojtkowiak (1998), where these equations are developed for temperature varying between 0 °C and 150 °C. They proposed five equations (Eqs (B.1 – B.5)) to calculate the properties of water which are based on temperature in Celsius degree only with coefficients A_0, A_1, A_2, A_3 and A_4 for each respective equation, given in Table (B.1). To calculate the water properties, a MATLAB code was developed for this purpose to solve Eqs (B.1 – B.5).

$$\rho_f = A_0 + A_1 T + A_2 T^2 + A_3 T^{2.5} + A_4 T^3 \quad (B.1)$$

$$C_{p_f} = A_0 + A_1 T + A_2 T^{1.5} + A_3 T^2 + A_4 T^{2.5} \quad (B.2)$$

$$k_f = A_0 + A_1 T + A_2 T^{1.5} + A_3 T^2 + A_4 \cdot \sqrt{T} \quad (B.3)$$

$$\mu_f = \frac{1}{A_0 + A_1 T + A_2 T^2 + A_3 T^3} \quad (B.4)$$

$$Pr = \frac{1}{A_0 + A_1 T + A_2 T^2 + A_3 T^3} \quad (B.5)$$

Table B.1: List of coefficient for equations of water properties (Popiel and Wojtkowiak, 1998).

Constants	ρ_f	C_{p_f}	k_f	μ_f	Pr
A_0	999.79684	4.2174356	0.5650285	557.82468	0.074763403
A_1	0.068317355	-0.0056181625	0.0026363895	19.408782	0.002902098
A_2	-0.010740248	0.001299253	-0.00012516934	0.1360459	2.8606181×10^{-5}
A_3	8.21409×10^{-4}	-1.15354×10^{-4}	$-1.5154915 \times 10^{-6}$	$-3.1160832 \times 10^{-4}$	$-8.1395537 \times 10^{-8}$
A_4	-2.3031×10^{-5}	4.15×10^{-6}	-0.000941295	---	---

APPENDIX C: Drawing of Experimental Heat Sink Designs

[267]

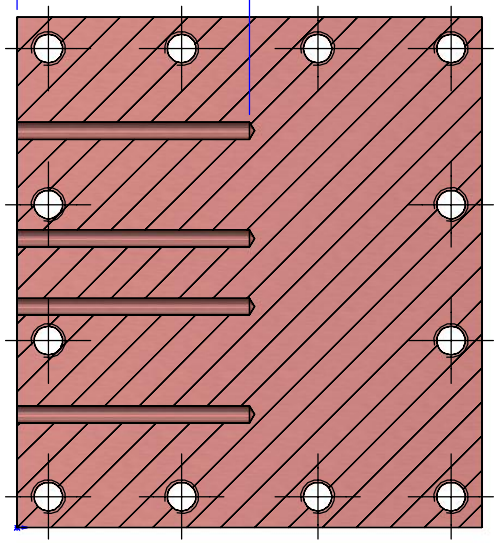

SECTION B-B
SCALE 1.5 : 1

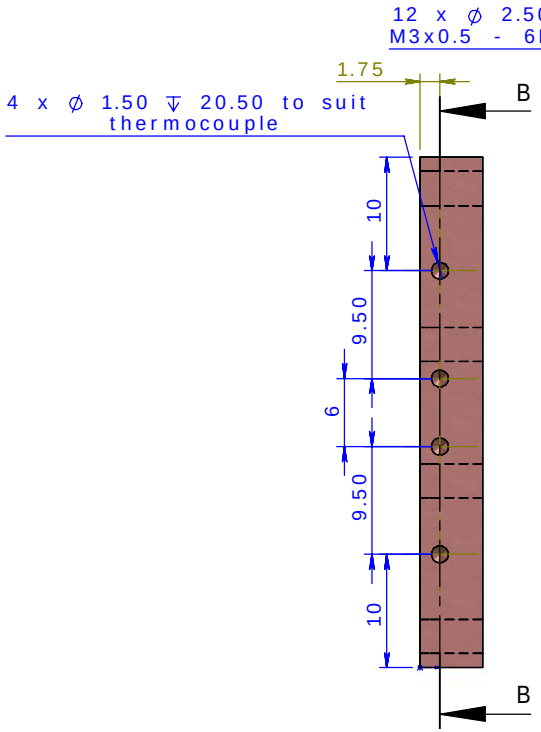

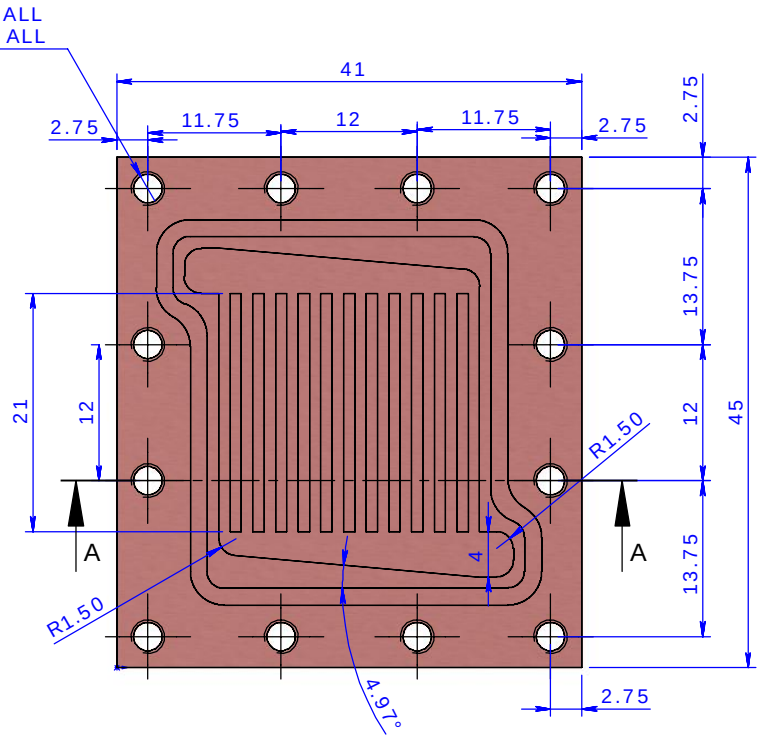

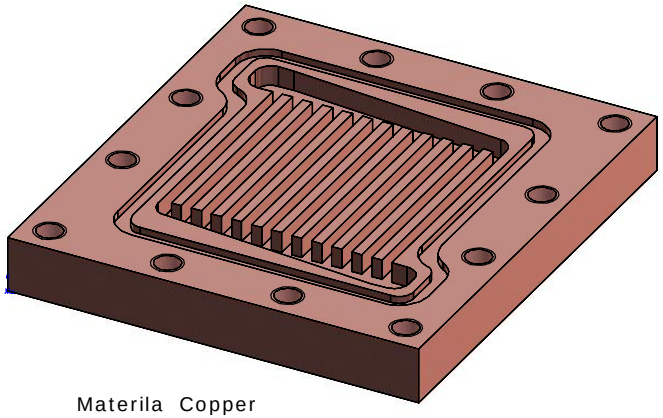

Materila Copper
Quantity 1 off
Remove all sharp edges

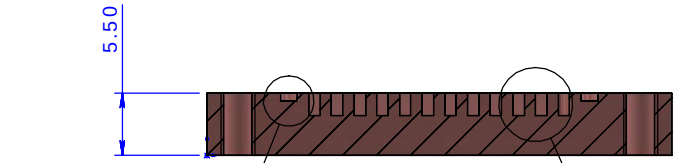

SECTION A-A
SCALE 1.5 : 1

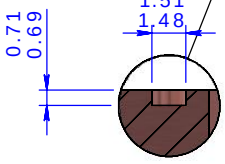

DETAIL C
SCALE 3 : 1
O-Ring Groove

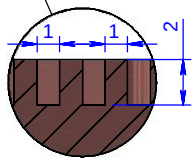

DETAIL D
SCALE 3 : 1
Channel profile

DO NOT SCALE IF IN DOUBT ASK	UNLESS OTHERWISE STATED 1) MACHINE AT ▽ TO 3.2 um Ra MAX 2) TOLERANCE ON MACHINED DIMENSIONS AS FOLLOWS: 0 - 500 ±0.2; 500 - 1000 ±0.4		LUMED THE UNIVERSITY OF LEEDS SCHOOL OF MECHANICAL ENGINEERING	DATE	TITLE *Multi-Straight rectangular MCHS All Dimensions in mm*	DRAWN BY
				SCALE		DRG No

[268]

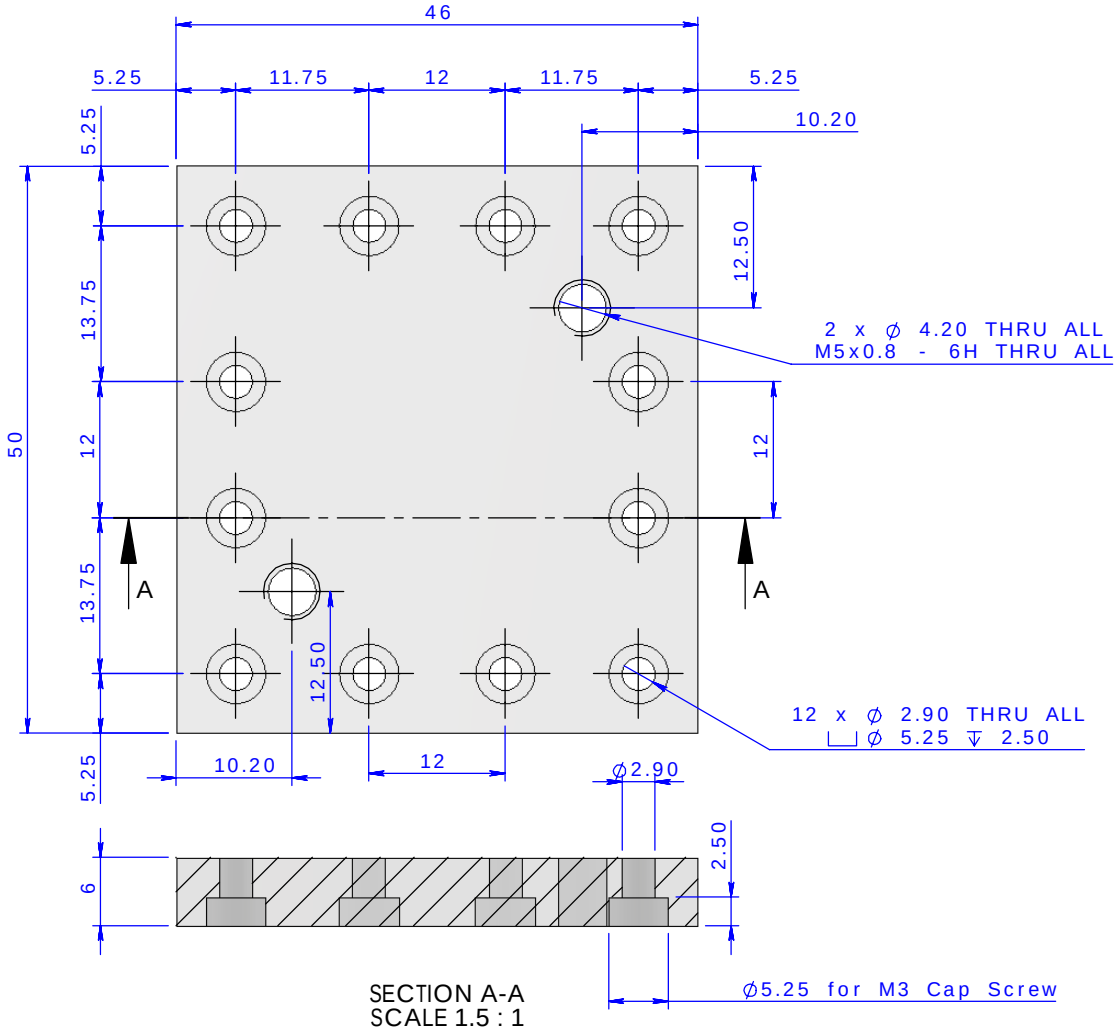

SECTION A-A
SCALE 1.5 : 1

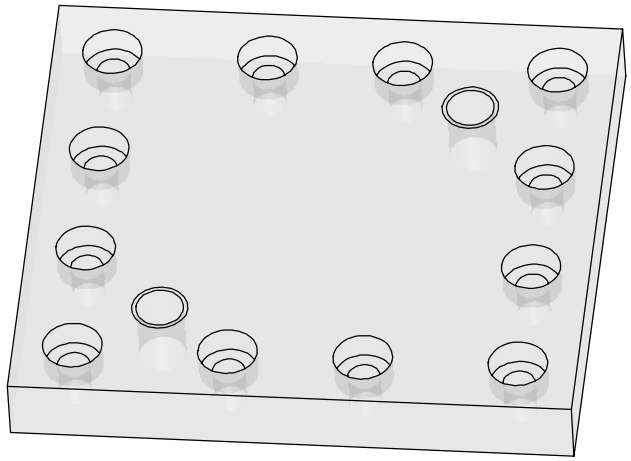

Material Perspex
Quantity 1 off
Remove all sharp Corners

DO NOT SCALE IF IN DOUBT ASK	UNLESS OTHERWISE STATED 1) MACHINE AT ▽ TO 3.2 um Ra MAX 2) TOLERANCE ON MACHINED DIMENSIONS AS FOLLOWS: 0 - 500 ±0.2; 500 - 1000 ±0.4		LUMED THE UNIVERSITY OF LEEDS SCHOOL OF MECHANICAL ENGINEERING	DATE / SCALE	TITLE *Cover of the multi-straight rectangular MCHS All Dimensions in mm*	DRAWN BY / DRG No

[269]

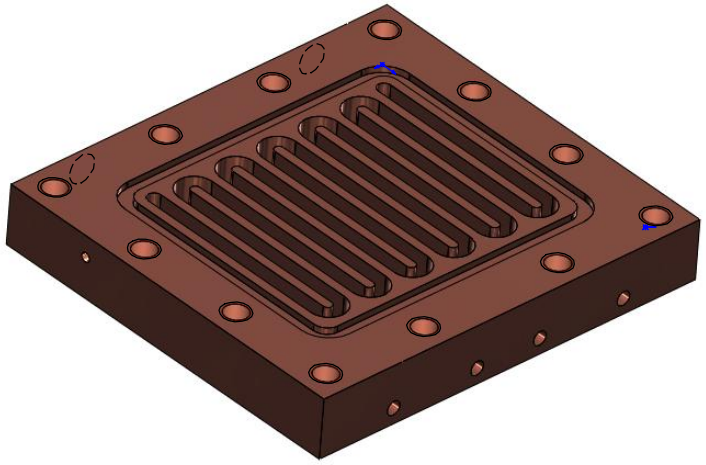

Material Copper
Quantity 1 off
Remove all sharp edges

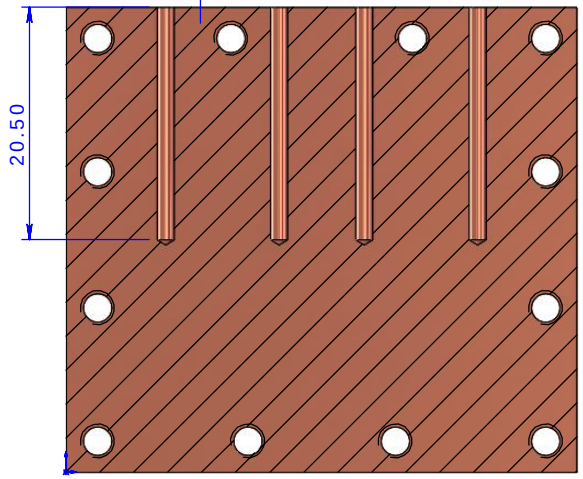

SECTION B-B
SCALE 1.5 : 1

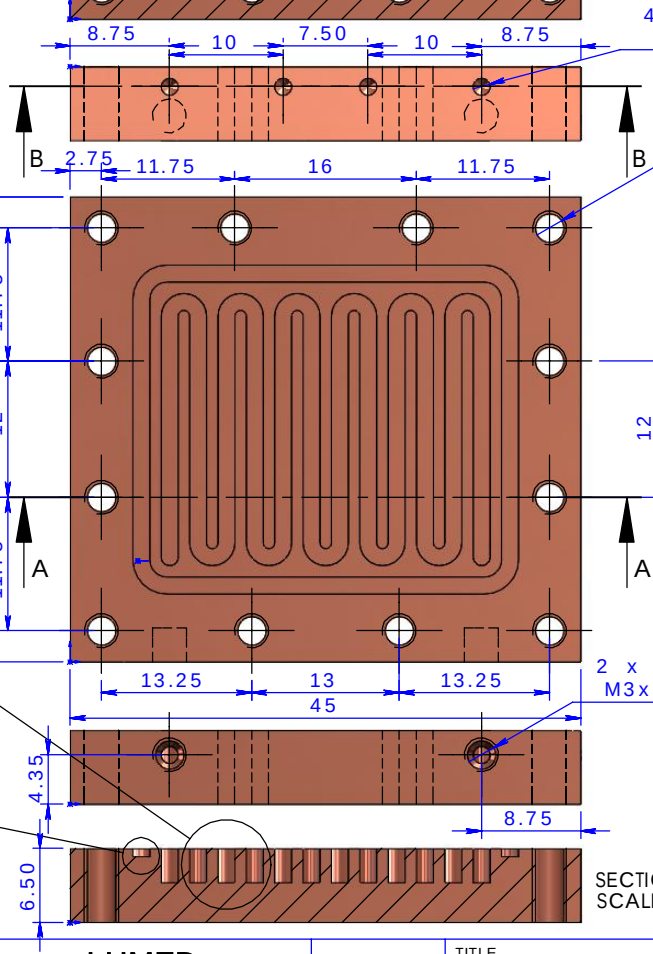

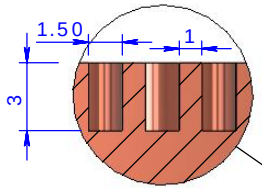

DETAIL C
SCALE 3 : 1
Channel Profile

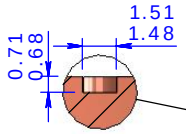

DETAIL D
SCALE 3 : 1
O-Ring Groove

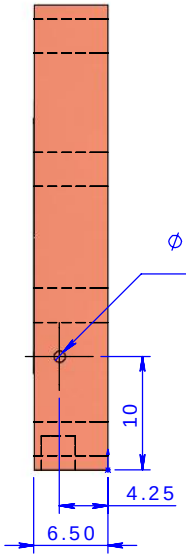

SECTION A-A
SCALE 1.5 : 1

DO NOT SCALE IF IN DOUBT ASK	UNLESS OTHERWISE STATED	1) MACHINE AT ▽ TO 3.2 um Ra MAX 2) TOLERANCE ON MACHINED DIMENSIONS AS FOLLOWS: 0 - 500 ±0.2; 500 - 1000 ±0.4	LUMED THE UNIVERSITY OF LEEDS SCHOOL OF MECHANICAL ENGINEERING	DATE SCALE	TITLE *Single Path Multi-Serpentine Microchannel (SPSM) Heat Sink* *All Dimenssions in mm*	DRAWN BY DRG No

[270]

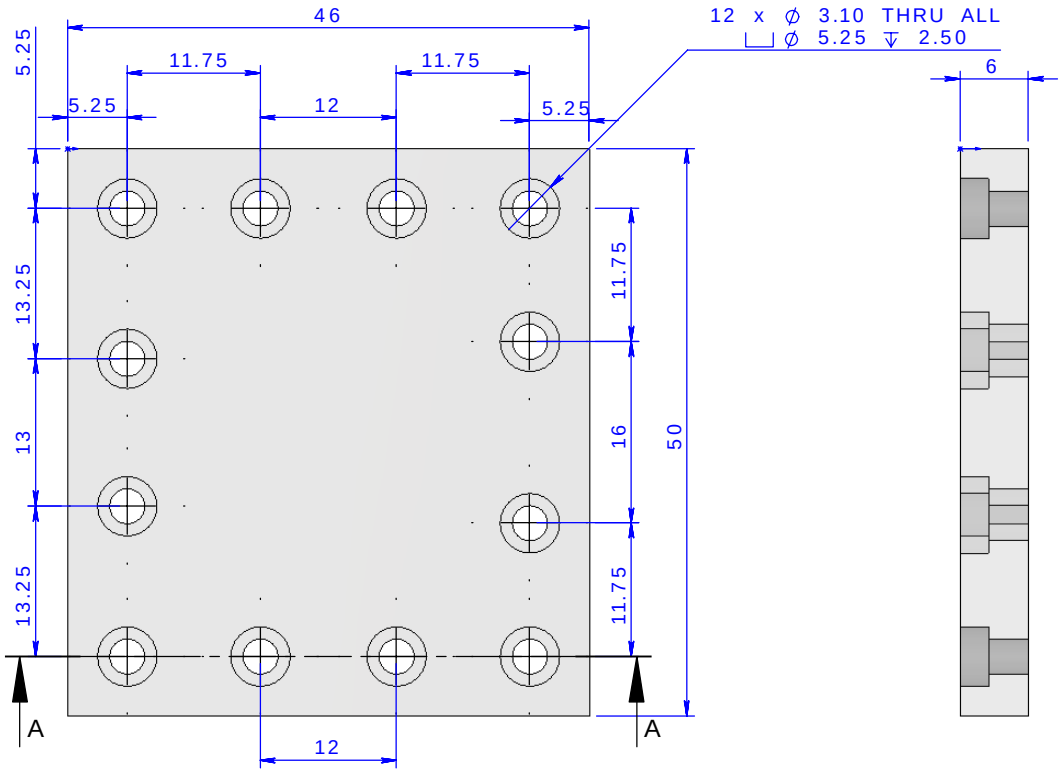

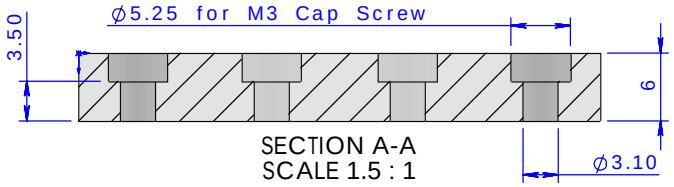

SECTION A-A
SCALE 1.5 : 1

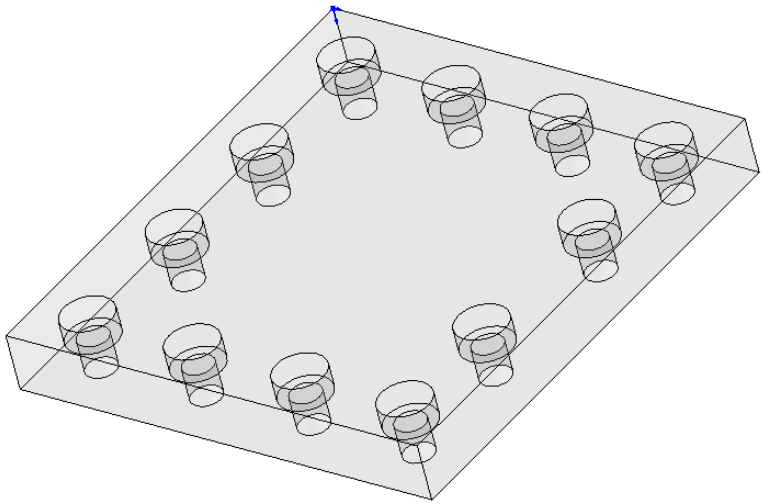

Material Perspex
Quantity 1 off
Remove all sharp Corners

DO NOT SCALE IF IN DOUBT ASK	UNLESS OTHERWISE STATED 1) MACHINE AT ▽ TO 3.2 um Ra MAX 2) TOLERANCE ON MACHINED DIMENSIONS AS FOLLOWS: 0 - 500 ±0.2; 500 - 1000 ±0.4		LUMED THE UNIVERSITY OF LEEDS SCHOOL OF MECHANICAL ENGINEERING	DATE / SCALE	TITLE: *Cover of the SPSM Heat Sink* *All Dimenssions in mm*	DRAWN BY / DRG No

[271]

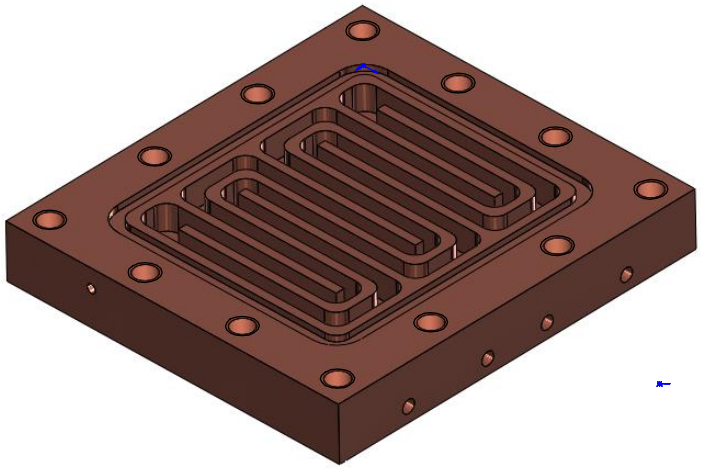

Material Copper
Quantity 1 off
Remove all sharp edges

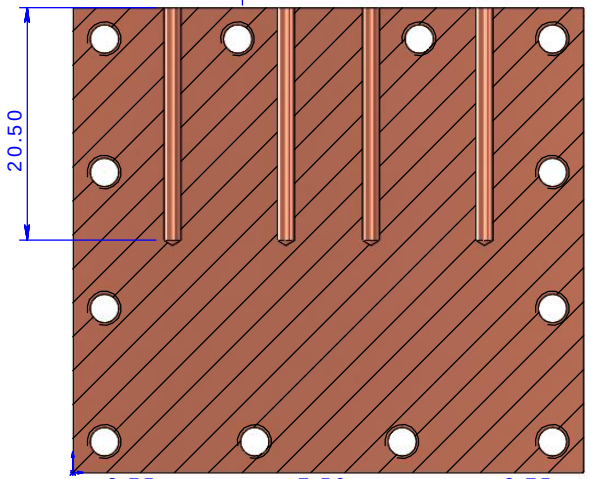

SECTION A-A
SCALE 1.5 : 1

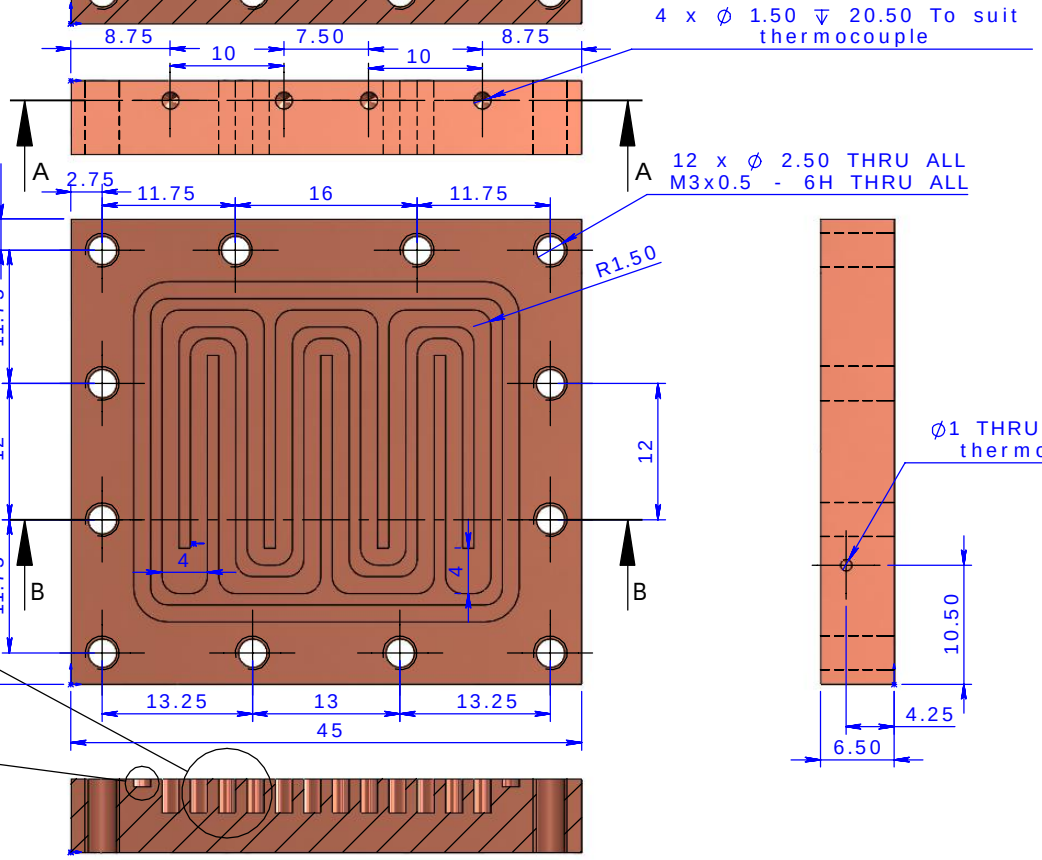

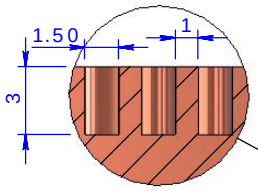

DETAIL C
SCALE 3 : 1
Channel Profile

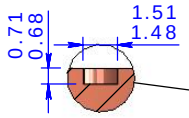

DETAIL D
SCALE 3 : 1
O-Ring Groove

SECTION B-B
SCALE 1.5 : 1

DO NOT SCALE IF IN DOUBT ASK	UNLESS OTHERWISE STATED 1) MACHINE AT ▽ TO 3.2 um Ra MAX 2) TOLERANCE ON MACHINED DIMENSIONS AS FOLLOWS: 0 - 500 ±0.2; 500 - 1000 ±0.4		LUMED THE UNIVERSITY OF LEEDS SCHOOL OF MECHANICAL ENGINEERING	DATE / SCALE	TITLE *Double Path Multi-Serpentine Microchannel (DPSM) Heat Sink* *All Dimenssions in mm*	DRAWN BY / DRG No

[272]

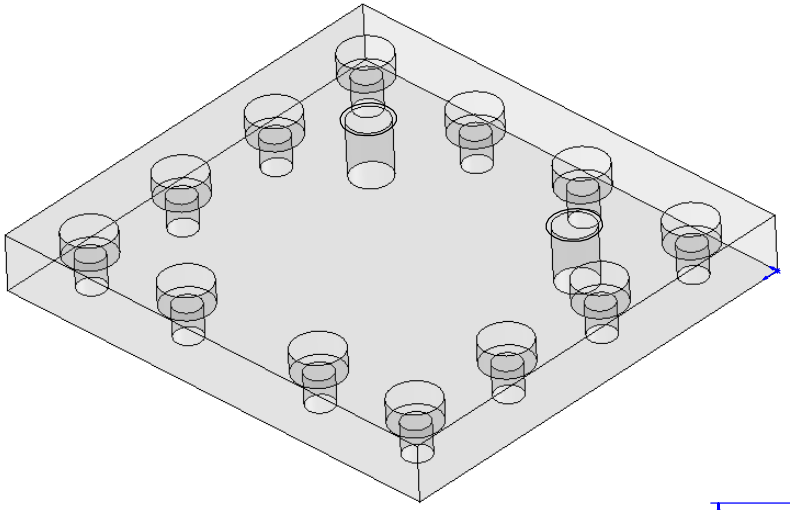

Material Perspex
Quantity 1 off
Remove all Sharp Corners

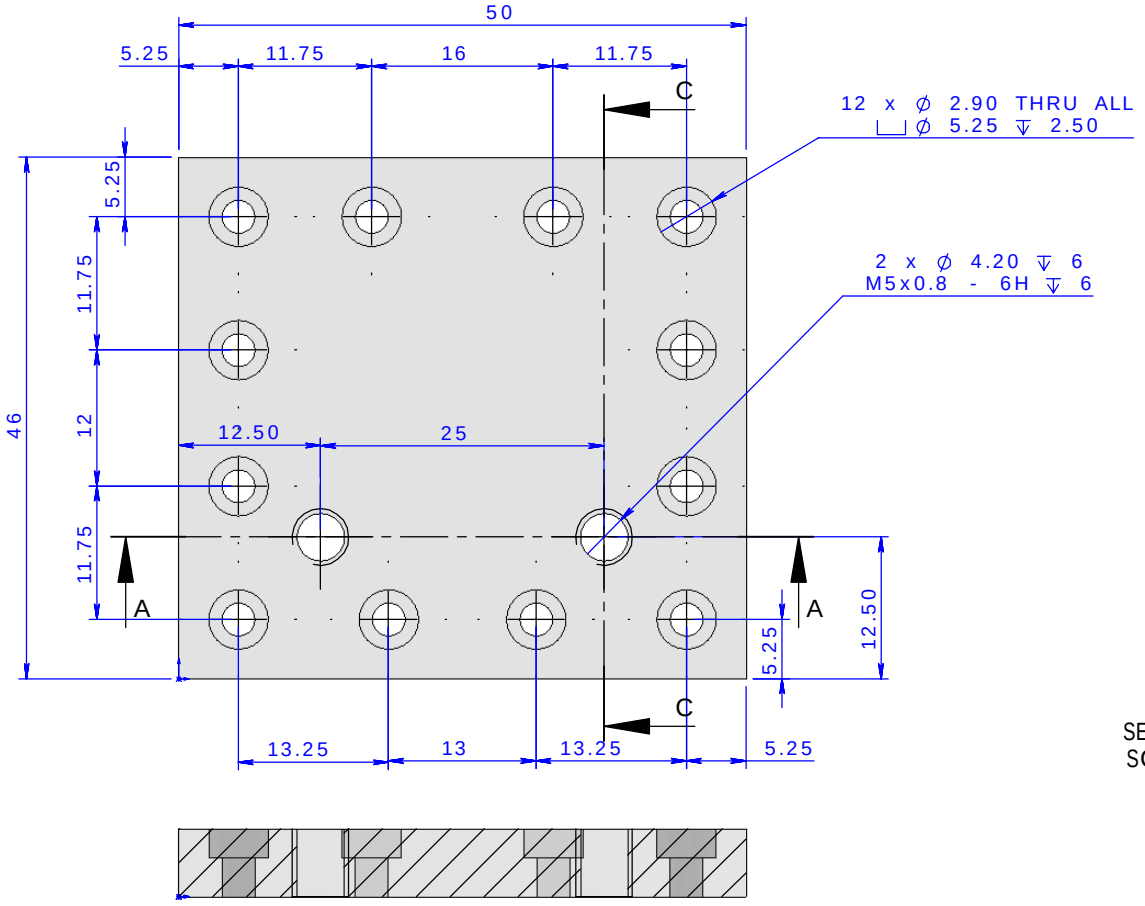

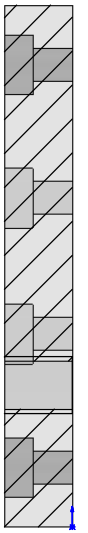

SECTION C-C
SCALE 1.5 : 1

SECTION A-A
SCALE 1.5 : 1

DO NOT SCALE IF IN DOUBT ASK	UNLESS OTHERWISE STATED 1) MACHINE AT ▽ TO 3.2 um Ra MAX 2) TOLERANCE ON MACHINED DIMENSIONS AS FOLLOWS: 0 - 500 ±0.2; 500 - 1000 ±0.4		LUMED THE UNIVERSITY OF LEEDS SCHOOL OF MECHANICAL ENGINEERING	DATE	TITLE *Cover of the DPSM Heat Sink* *All Dimenssions in mm*	DRAWN BY
				SCALE		DRG No

[273]

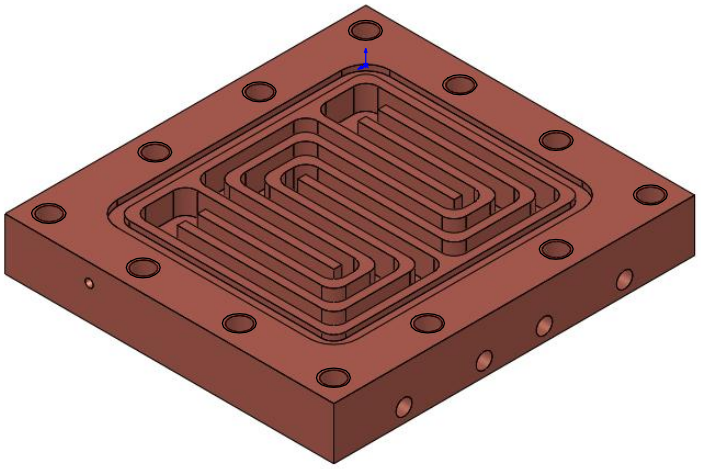

Material Copper
Quantity 1 off
Remove all sharp edges

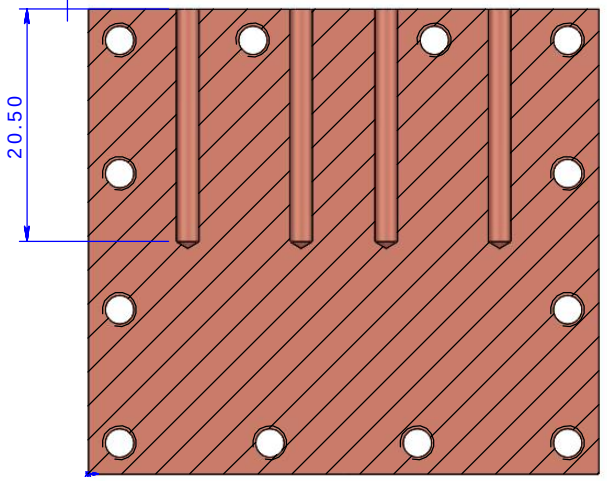

SECTION A-A
SCALE 1.5 : 1

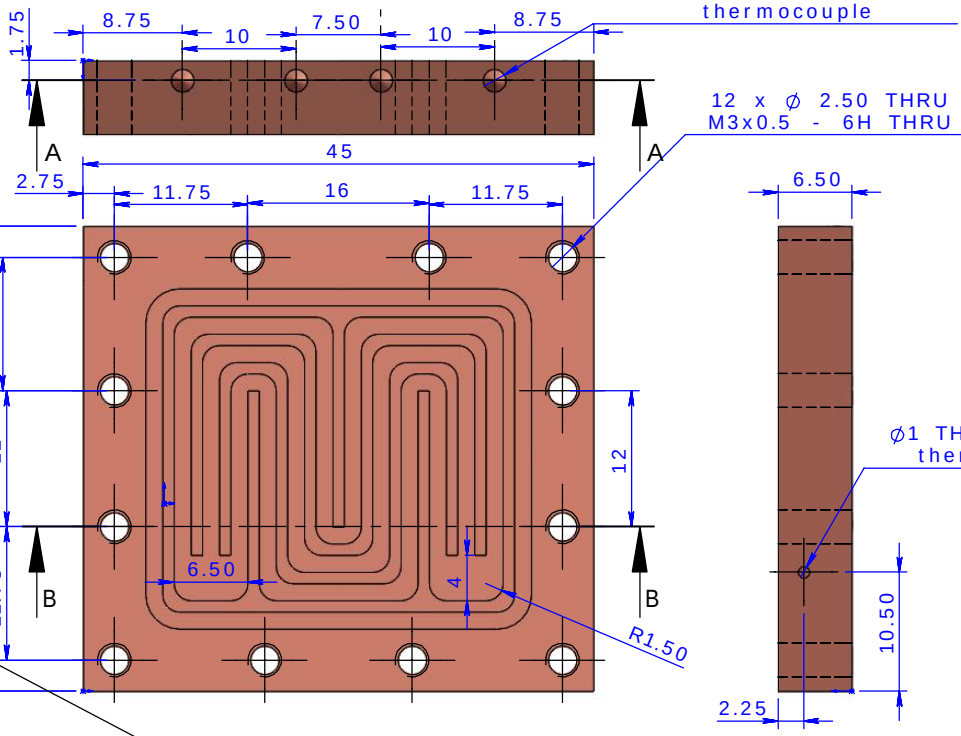

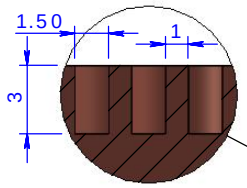

DETAIL C
SCALE 3 : 1
Channel Profile

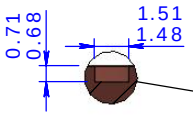

DETAIL D
SCALE 3 : 1
O-Ring Groove

SECTION B-B
SCALE 1.5 : 1

DO NOT SCALE IF IN DOUBT ASK	UNLESS OTHERWISE STATED	1) MACHINE AT ▽ TO 3.2 um Ra MAX 2) TOLERANCE ON MACHINED DIMENSIONS AS FOLLOWS: 0 - 500 ±0.2; 500 - 1000 ±0.4	LUMED THE UNIVERSITY OF LEEDS SCHOOL OF MECHANICAL ENGINEERING	DATE SCALE	TITLE *Triple Path Multi-Serpentine Microchannel (TPSM) Heat Sink* *All Dimensions in mm*	DRAWN BY DRG No

[274]

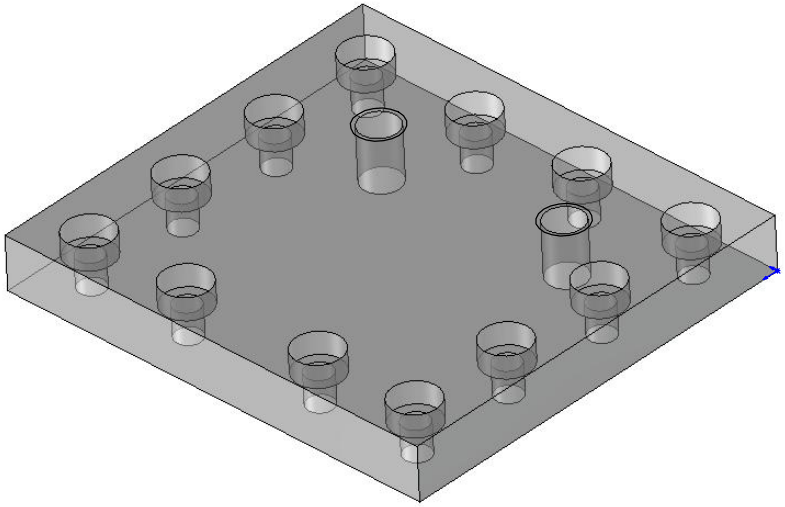

Material Perspex
Quantity 1 off
Remove all Sharp Corners

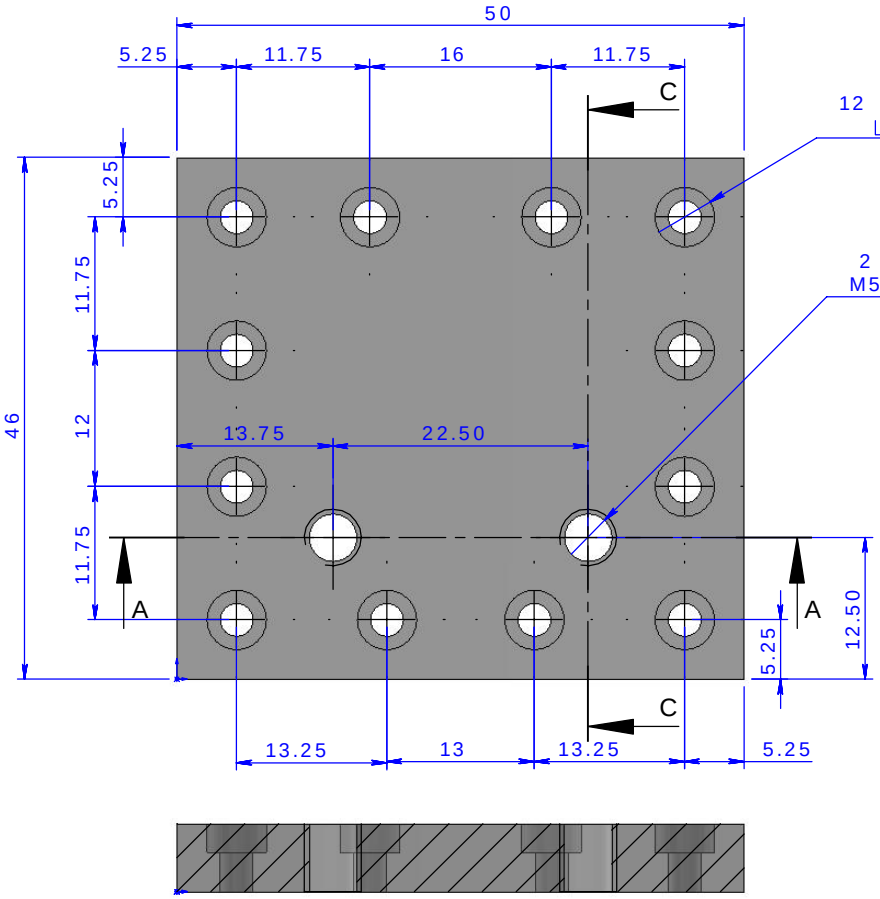

SECTION A-A
SCALE 1.5 : 1

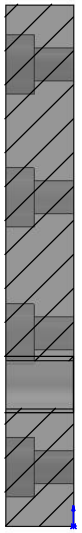

SECTION C-C
SCALE 1.5 : 1

DO NOT SCALE IF IN DOUBT ASK	UNLESS OTHERWISE STATED	1) MACHINE AT ▽ TO 3.2 um Ra MAX 2) TOLERANCE ON MACHINED DIMENSIONS AS FOLLOWS: 0 - 500 ±0.2; 500 - 1000 ±0.4	LUMED THE UNIVERSITY OF LEEDS SCHOOL OF MECHANICAL ENGINEERING	DATE SCALE	TITLE *Cover of the TPSM Heat Sink* *All Dimenssions in mm*	DRAWN BY DRG No

[275]

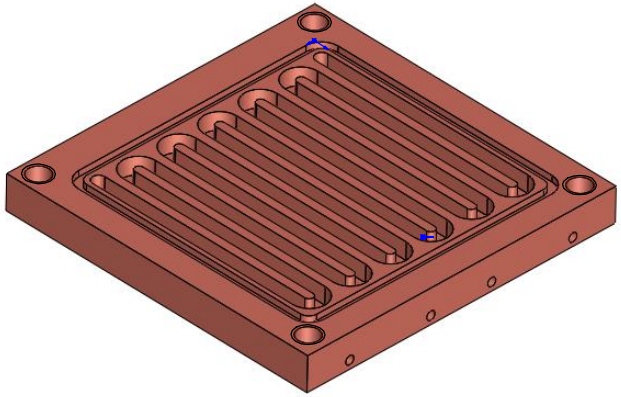

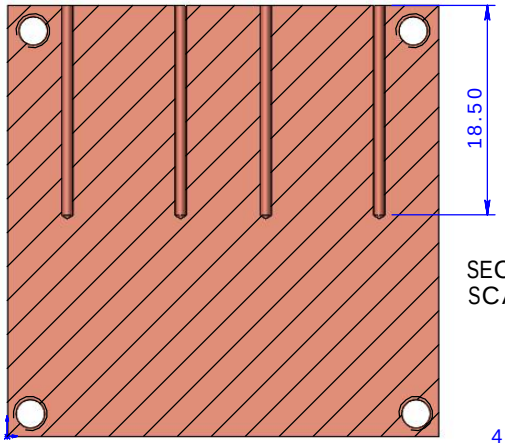

SECTION A-A
SCALE 1.5 : 1

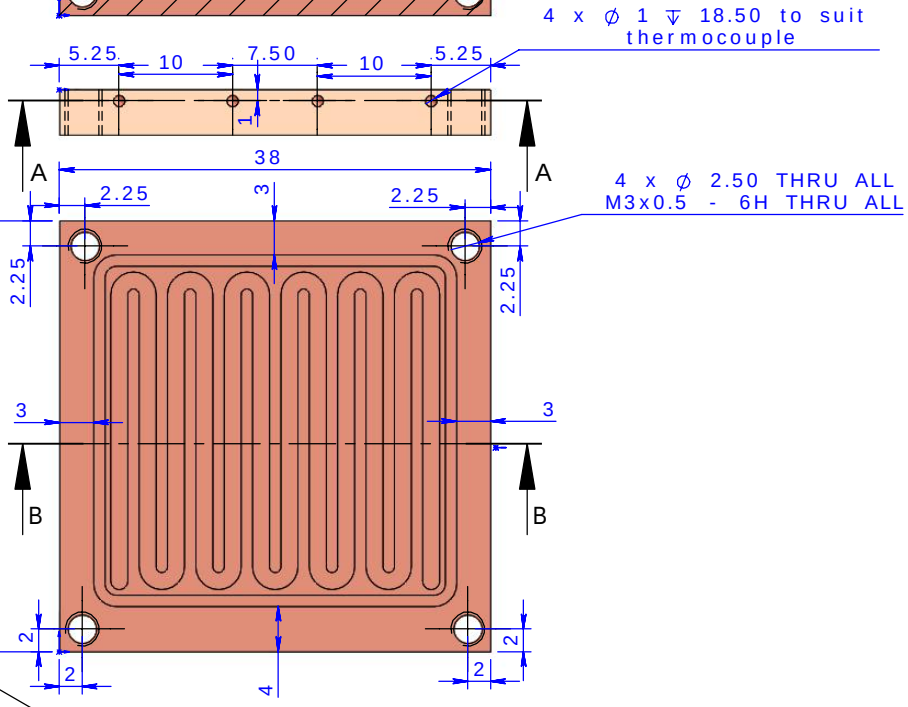

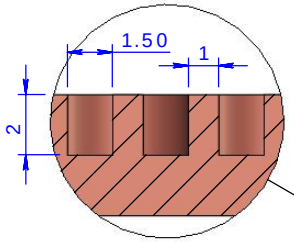

DETAIL C
SCALE 4 : 1
Channel Profile

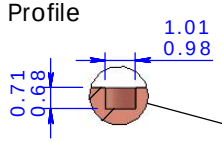

DETAIL D
SCALE 4 : 1
O-Ring Groove

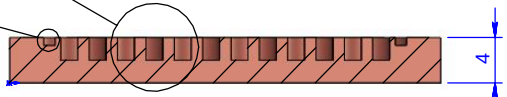

SECTION B-B
SCALE 1.5 : 1

DO NOT SCALE IF IN DOUBT ASK	UNLESS OTHERWISE STATED	1) MACHINE AT ▽ TO 3.2 um Ra MAX 2) TOLERANCE ON MACHINED DIMENSIONS AS FOLLOWS: 0 - 500 ±0.2; 500 - 1000 ±0.4		LUMED THE UNIVERSITY OF LEEDS SCHOOL OF MECHANICAL ENGINEERING	DATE SCALE	TITLE *Serpentine MCHS with plate fins* *Note: All Dimensions in mm*	DRAWN BY DRG No

[276]

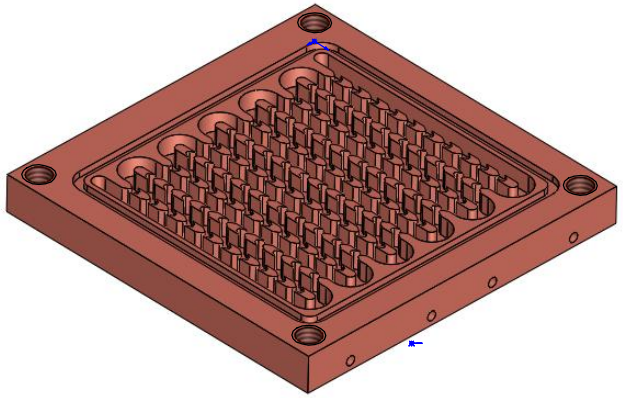

Material Copper
Quality 1 off
Remove all sharp edges

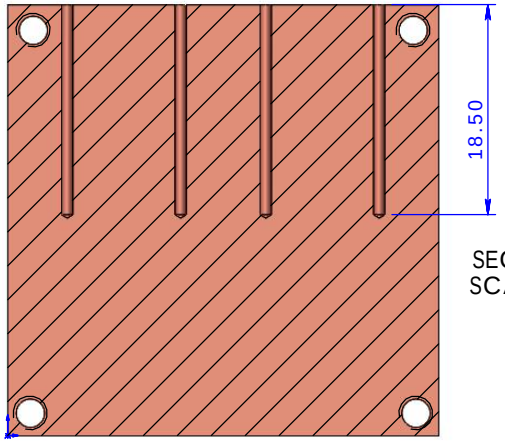

SECTION B-B
SCALE 1.5 : 1

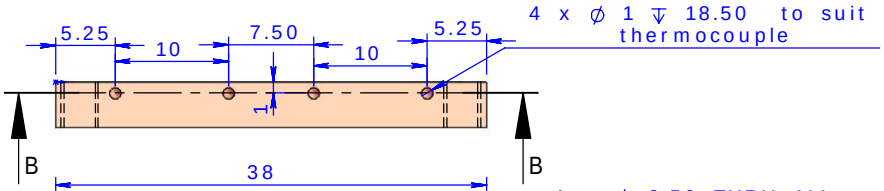

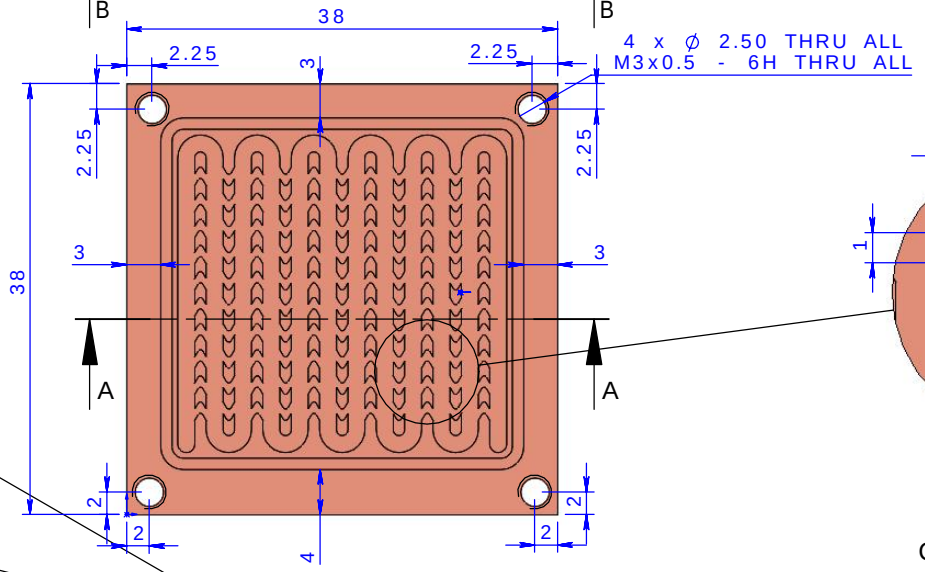

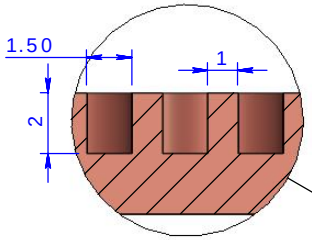

DETAIL C
SCALE 4 : 1
Channel Profile

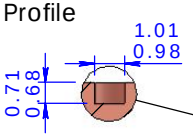

DETAIL D
SCALE 4 : 1
O-Ring Groove

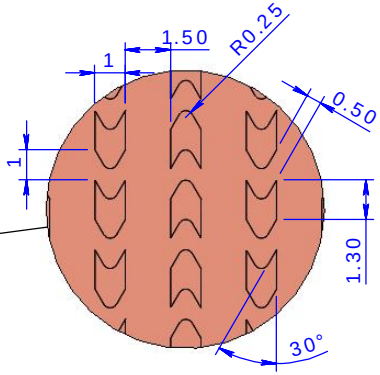

DETAIL E
SCALE 4 : 1
Chevron fin details

SECTION A-A
SCALE 1.5 : 1

DO NOT SCALE IF IN DOUBT ASK	UNLESS OTHERWISE STATED	1) MACHINE AT ▽ TO 3.2 um Ra MAX 2) TOLERANCE ON MACHINED DIMENSIONS AS FOLLOWS: 0 - 500 ±0.2; 500 - 1000 ±0.4		LUMED THE UNIVERSITY OF LEEDS SCHOOL OF MECHANICAL ENGINEERING	DATE SCALE	TITLE *Serpentine MCHS with chevron fins* *Note: All Dimensions in mm*	DRAWN BY DRG No

[277]

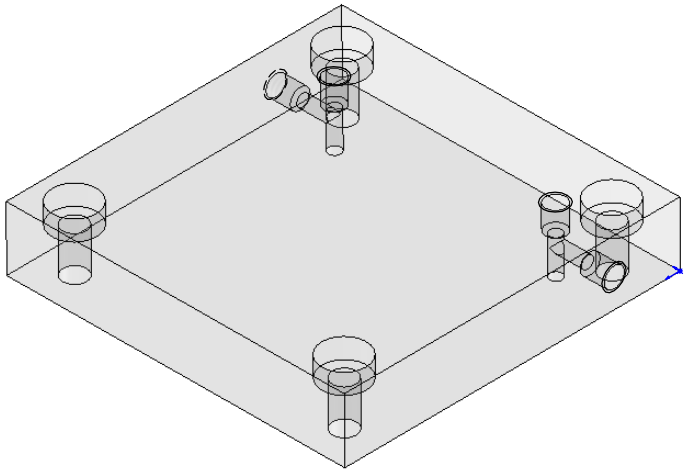

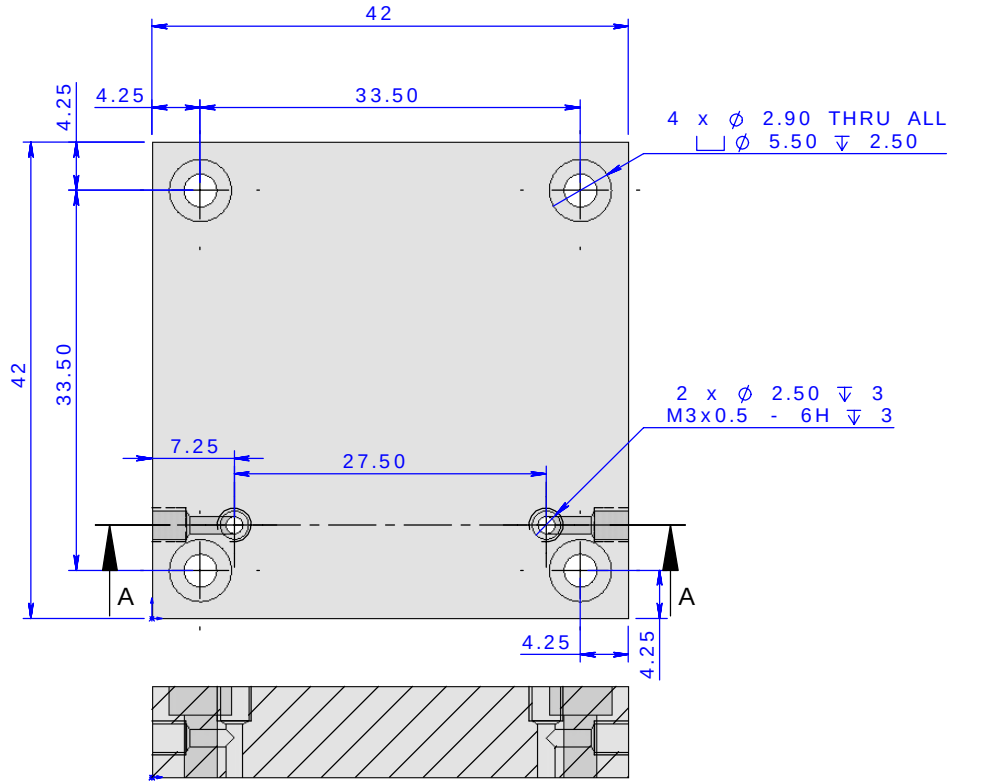

SECTION A-A
SCALE 1.5 : 1

DO NOT SCALE IF IN DOUBT ASK	UNLESS OTHERWISE STATED 1) MACHINE AT ▽ TO 3.2 um Ra MAX 2) TOLERANCE ON MACHINED DIMENSIONS AS FOLLOWS: 0 - 500 ±0.2; 500 - 1000 ±0.4		LUMED THE UNIVERSITY OF LEEDS SCHOOL OF MECHANICAL ENGINEERING	DATE SCALE	TITLE *Cover of the SMPF and SMCF Heat Sink* *Note: All Dimensions in mm*	DRAWN BY DRG No